CMS Draft Analysis Note

The content of this note is intended for CMS internal use and distribution only

2021/07/06
Archive Hash: 9b426ff-D
Archive Date: 2021/06/30

Search for resolved and boosted heavy neutrinos decaying from right-handed W_R bosons in pp collisions at CMS using $\sqrt{s} = 13$ TeV Run2 Data

Jae Sung Kim[1], Si Hyun Jeon[1], John Almond[1], S.B. Oh[1], U.K. Yang[1], Jeremy Mans[2], Andrew Evans[2], Michael Krohn[2], and Josh Hiltbrand[2]

[1] Seoul National University
[2] University of Minnesota

Abstract

A search for right-handed charged gauge bosons (W_R) and heavy neutrinos (N) using data collected with the CMS detector at the LHC. The data were collected during 2016, 2017, and 2018 in proton-proton collisions at a center-of-mass energy of 13 TeV, corresponding to an integrated luminosity of 137.4 fb^{-1}. The W_R and N can be produced from a $SU_C(3) \otimes SU_L(2) \otimes SU_R(2) \otimes U(1)$ left-right symmetric model, giving an event signature of two same flavor leptons (e or μ) and jets. This search is done for both the resolved and boosted signatures and in both cases the signal is characterized as a peak over the invariant mass spectrum of final state objects. In the case of no signal, a set of limits will be placed on the production cross section in the m_N vs m_{W_R} phase space.

Contents

1 Introduction

Experimental observations have shown that parity is violated in weak interactions predicted by the standard model (SM). Left-right symmetric models [1–4] which extend the Electroweak sector of the SM by a right-handed SU(2) group provide a possible explanation for parity violation as the consequence of spontaneous symmetry breaking at a multi-TeV mass scale. This analysis note summarizes a search for such a heavy partner, a heavy right-handed W boson (W_R), using the collision data collected by the Compact Muon Solenoid (CMS) detector in proton-proton (pp) collisions at $\sqrt{s} = 13$ TeV from the years 2016-2018 corresponding to an integrated luminosity of 137.4 fb^{-1}.

The W_R is produced through an interaction between a quark and an anti-quark, and decays to a right-handed neutrino (N) and either an electron or a muon. Subsequently, the N decays to a second SM charged lepton and an off-shell W_R which decays hadronically. The dominant Feynman diagram for this process is shown in Fig. 1.

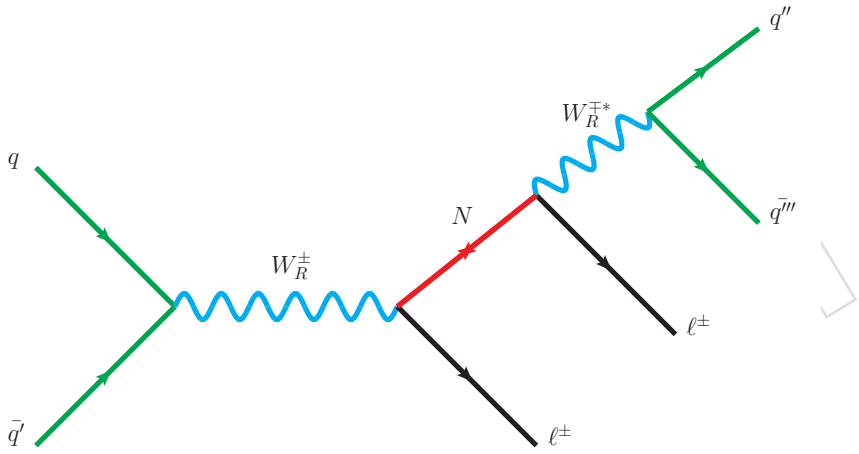

Figure 1: Feynman diagram for the production of the heavy neutrino via the decay of a W_R boson.

Several assumptions are made in this analysis. Firstly, we search for W_R in a mass range between 800 and 6000 GeV, and the mass of N between 100 GeV and the mass of W_R. This is considered a sensible search region based on the fact that previous searches have excluded W_R bosons up to 3.3 (3.5) TeV in the electron (muon) channel with a N mass between 10% and 90% of the W_R mass, under the assumption that the coupling strength of W_R with the SM particles, g_R, is the same as the SM coupling constant g_L. However, the coupling strength g_R is a free parameter in most LR models and smaller values allow for smaller W_R cross sections. We assume that lepton number is conserved in the process and consequently the flavor of the two final state leptons are the same. The search summarized in this note focuses on final states with either electrons or muons.

While the W_R production and decay mode (in Fig. 1) represents the benchmark signal, the search for evidence confirming the W_R model is not the sole focus of this analysis. This analysis is designed to be sensitive to any heavy resonance which can be produced through pp interactions, that subsequently decays to two leptons and quarks. Specific details of the W_R decay chain and correlations between final state particles are not exploited to make this analysis as model independent as possible.

The analysis is performed in two different event topologies, in order to cover as much of the $m_{W_R} - m_N$ phase space as possible. The 'resolved' topology consists of four final state objects, two leptons (e or μ) and two small cone size jets, and occurs roughly when $m_N > m_{W_R}/5$. At smaller m_N values, the signals enter the 'boosted' topology where the final state consists of two reconstructed objects, a lepton and a large cone size jet. The large cone size jet (fatjet) contains the entire decay of the N and is produced roughly back-to-back to the lepton.

The data, simulated samples, and triggers used in this analysis are described in Sec. 2. The lepton and jet reconstruction algorithms, and correction factors to account for known differences between data and simulations are described in Sec. 3. The online and offline event selections are described in Sec. 4. The details about the estimate of non-reducible background events are reported in Sec. 5. The uncertainties are described in Sec. 6, followed by the results in Sec. 7.

2 Datasets and triggers

2.1 Data samples

The analysis is performed using pp interactions recorded with the CMS detector at $\sqrt{s} = 13\,\text{TeV}$ from 2016-2018 corresponding to an integrated luminosity of $137.4\,\text{fb}^{-1}$. Data were preselected for "good" luminosity sections using the JSON files listed in Table 1. The SingleElectron and SingleMuon primary datasets are used in our control and signal regions. These data samples are summarized in Tables 2 and 3. The global tags used in the analysis for each year of data taking are summarized in Tab. 4.

Table 1: The golden JSON files used for each year.

Year	Golden JSON
2016	ReReco/Final/Cert_271036-284044_13TeV_ReReco_07Aug2017_Collisions16_JSON.txt
2017	ReReco/Cert_294927-306462_13TeV_EOY2017ReReco_Collisions17_JSON.txt
2018	ReReco/Cert_314472-325175_13TeV_17SeptEarlyReReco2018ABC_PromptEraD_Collisions18_JSON.txt

Table 2: SingleMuon dataset used in this analysis, the run-ranges for each data period and the integrated luminosities for each dataset.

Dataset	Run Range	Int. Lum.(fb^{-1})
/SingleMuon/Run2016B-17Jul2018-v*/MINIAOD	272007 – 275376	
/SingleMuon/Run2016C-17Jul2018-v1/MINIAOD	275657 – 276283	
/SingleMuon/Run2016D-17Jul2018-v1/MINIAOD	276315 – 276811	
/SingleMuon/Run2016E-17Jul2018-v1/MINIAOD	276831 – 277420	
/SingleMuon/Run2016F-17Jul2018-v1/MINIAOD	277772 – 278808	
/SingleMuon/Run2016G-17Jul2018-v1/MINIAOD	278820 – 280385	
/SingleMuon/Run2016H-17Jul2018-v1/MINIAOD	280919 – 284044	
2016 Total		**35.92**
/SingleMuon/Run2017B-31Mar2018-v1/MINIAOD	297046 – 299329	
/SingleMuon/Run2017C-31Mar2018-v1/MINIAOD	299368 – 302029	
/SingleMuon/Run2017D-31Mar2018-v1/MINIAOD	302030 – 303434	
/SingleMuon/Run2017E-31Mar2018-v1/MINIAOD	303824 – 304797	
/SingleMuon/Run2017F-31Mar2018-v1/MINIAOD	305040 – 306462	
2017 Total		**41.53**
/SingleMuon/Run2018A-17Sep2018-v2/MINIAOD	315252 – 316995	
/SingleMuon/Run2018B-17Sep2018-v1/MINIAOD	316998 – 319312	
/SingleMuon/Run2018C-17Sep2018-v1/MINIAOD	319313 – 320393	
/SingleMuon/Run2018D-22Jan2019-v2/MINIAOD	320394 – 325273	
2018 Total		**59.97**
2016-2018 Total		**137.4**

2.2 Simulated samples

For both the signal and background samples, the Moriond2017, Winter2017, and June2018 pileup scenarios were used to approximate the number of inelastic collisions per bunch crossing of the LHC for the 2016, 2017 and 2018 data-taking periods, respectively. Appropriate event reweighting is applied to reproduce the distribution of the number of primary vertices in data. The distributions of the number of primary vertices, and their ratios are shown in Fig. 2. The global tags used in the analysis with the monte carlo (MC) samples are listed in Table 5.

Table 3: SingleElectron and EGamma dataset used in this analysis, the run-ranges for each data period and the integrated luminosities for each dataset.

Dataset	Run-range	Int. Lum.(fb^{-1})
/SingleElectron/Run2016B-17Jul2018-v*/MINIAOD	272007 – 275376	
/SingleElectron/Run2016C-17Jul2018-v1/MINIAOD	275657 – 276283	
/SingleElectron/Run2016D-17Jul2018-v1/MINIAOD	276315 – 276811	
/SingleElectron/Run2016E-17Jul2018-v1/MINIAOD	276831 – 277420	
/SingleElectron/Run2016F-17Jul2018-v1/MINIAOD	277772 – 278808	
/SingleElectron/Run2016G-17Jul2018-v1/MINIAOD	278820 – 280385	
/SingleElectron/Run2016H-17Jul2018-v1/MINIAOD	280919 – 284044	
2016 Total		**35.92**
/SingleElectron/Run2017B-31Mar2018-v1/MINIAOD	297046 – 299329	
/SingleElectron/Run2017C-31Mar2018-v1/MINIAOD	299368 – 302029	
/SingleElectron/Run2017D-31Mar2018-v1/MINIAOD	302030 – 303434	
/SingleElectron/Run2017E-31Mar2018-v1/MINIAOD	303824 – 304797	
/SingleElectron/Run2017F-31Mar2018-v1/MINIAOD	305040 – 306462	
2017 Total		**41.53**
/EGamma/Run2018A-17Sep2018-v2/MINIAOD	315252 – 316995	
/EGamma/Run2018B-17Sep2018-v1/MINIAOD	316998 – 319312	
/EGamma/Run2018C-17Sep2018-v1/MINIAOD	319313 – 320393	
/EGamma/Run2018D-22Jan2019-v2/MINIAOD	320394 – 325273	
2018 Total		**59.97**
2016-2018 Total		**137.4**

Table 4: Global tags used for data in this analysis for each year. In 2018, RunD uses the Prompt global tag and the remaining runs us the Sep2018Rereco global tag.

Year	Global tag
2016	`102X_dataRun2_v12`
2017	`102X_dataRun2_v12`
2018	`102X_dataRun2_v12 (Run2018A-C) 102X_dataRun2_Prompt_v15 (Run2018D)`

Table 5: Global tags used on MC samples in this analysis for each year.

Year	Global Tag
2016	`102X_mcRun2_asymptotic_v7`
2017	`102X_mc2017_realistic_v7`
2018	`102X_upgrade2018_realistic_v20`

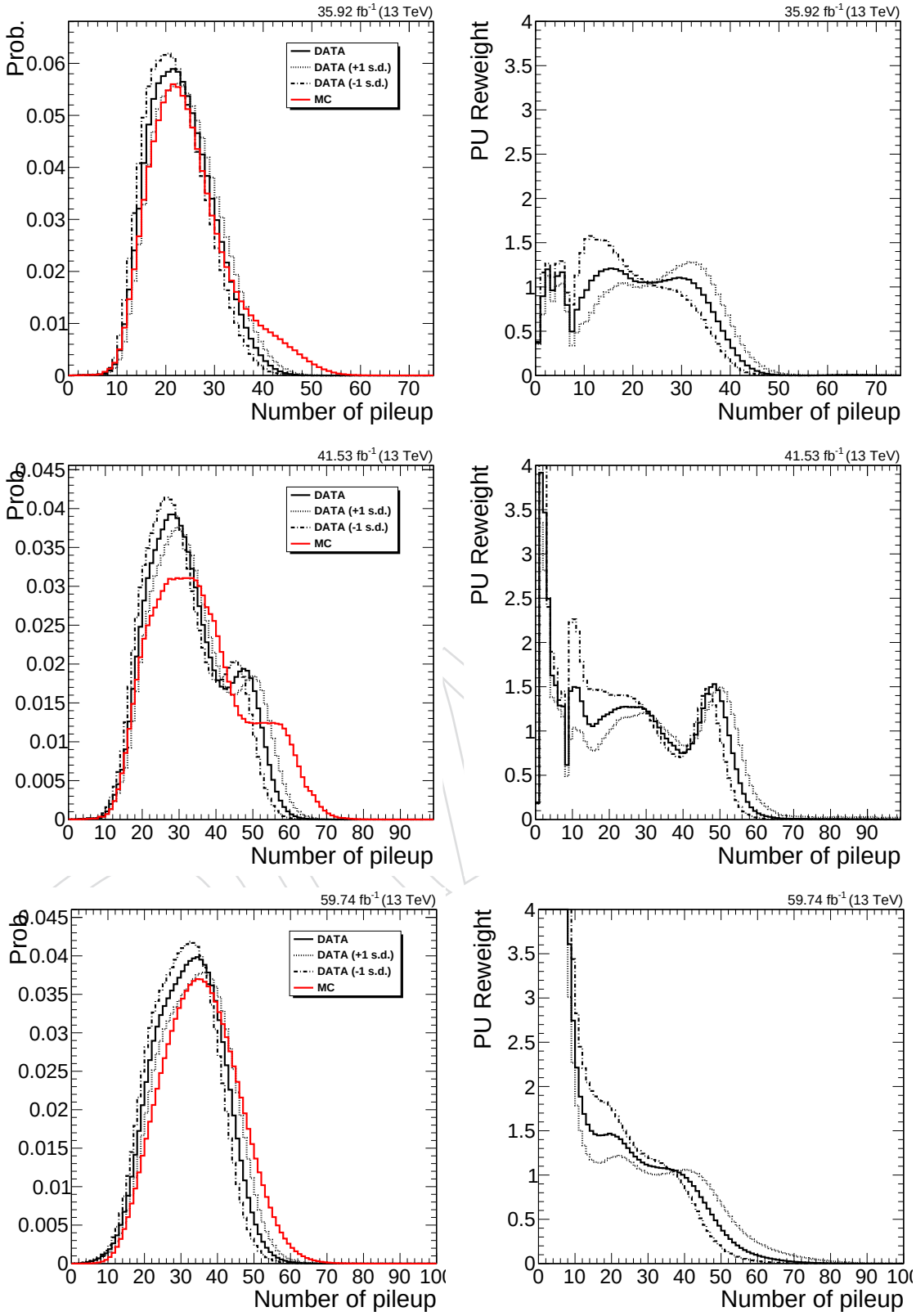

Figure 2: The number of primary vertices (left) and the ratios of primary vertices between data and MC (right) for each data-taking year.

Table 6: The list of MC samples and corresponding cross-sections used in 2016 analysis.

Process	DAS name	Xsec. (pb)	Xsec. computed order
DY ($10 < m(\ell\ell) < 50\,\text{GeV}$)	/DYJetsToLL_M-10to50_TuneCUETP8M1_13TeV-madgraphMLM-pythia8/†	18610	NLO
DY ($m(\ell\ell) > 50\,\text{GeV}$)	/DYJetsToLL_M-50_TuneCUETP8M1_13TeV-madgraphMLM-pythia8/†	6077.22	NNLO
DY ($m(\ell\ell) > 50\,\text{GeV}$)	/DYJetsToLL_M-50_HT-70to100_TuneCUETP8M1_13TeV-madgraphMLM-pythia8/†	208.977	NNLO
DY ($m(\ell\ell) > 50\,\text{GeV}$)	/DYJetsToLL_M-50_HT-100to200_TuneCUETP8M1_13TeV-madgraphMLM-pythia8/†	181.30	NNLO
DY ($m(\ell\ell) > 50\,\text{GeV}$)	/DYJetsToLL_M-50_HT-200to400_TuneCUETP8M1_13TeV-madgraphMLM-pythia8/†	50.4177	NNLO
DY ($m(\ell\ell) > 50\,\text{GeV}$)	/DYJetsToLL_M-50_HT-400to600_TuneCUETP8M1_13TeV-madgraphMLM-pythia8/†	6.98394	NNLO
DY ($m(\ell\ell) > 50\,\text{GeV}$)	/DYJetsToLL_M-50_HT-600to800_TuneCUETP8M1_13TeV-madgraphMLM-pythia8/†	1.68141	NNLO
DY ($m(\ell\ell) > 50\,\text{GeV}$)	/DYJetsToLL_M-50_HT-800to1200_TuneCUETP8M1_13TeV-madgraphMLM-pythia8/†	0.775392	NNLO
DY ($m(\ell\ell) > 50\,\text{GeV}$)	/DYJetsToLL_M-50_HT-1200to2500_TuneCUETP8M1_13TeV-madgraphMLM-pythia8/†	0.186222	NNLO
DY ($m(\ell\ell) > 50\,\text{GeV}$)	/DYJetsToLL_M-50_HT-2500toInf_TuneCUETP8M1_13TeV-madgraphMLM-pythia8/†	0.00438495	NNLO
$t\bar{t}$ (semi-leptonic)	/TTToSemilepton_TuneCUETP8M2_ttHtranche3_13TeV-powheg-pythia8/†	365.34	NNLO
$t\bar{t}$ (leptonic)	/TTTo2L2Nu_TuneCUETP8M2_ttHtranche3_13TeV-powheg-pythia8/†	88.29	NNLO
W+Jets	/WJetsToLNu_TuneCUETP8M1_13TeV-madgraphMLM-pythia8/†	61526.7	NNLO
W+Jets	/WJetsToLNu_HT-70To100_TuneCUETP8M1_13TeV-madgraphMLM-pythia8/†	1637.1	NNLO
W+Jets	/WJetsToLNu_HT-100To200_TuneCUETP8M1_13TeV-madgraphMLM-pythia8/†	1627.45	NNLO
W+Jets	/WJetsToLNu_HT-200To400_TuneCUETP8M1_13TeV-madgraphMLM-pythia8/†	435.237	NNLO
W+Jets	/WJetsToLNu_HT-400To600_TuneCUETP8M1_13TeV-madgraphMLM-pythia8/†	59.1811	NNLO
W+Jets	/WJetsToLNu_HT-600To800_TuneCUETP8M1_13TeV-madgraphMLM-pythia8/†	14.5805	NNLO
W+Jets	/WJetsToLNu_HT-800To1200_TuneCUETP8M1_13TeV-madgraphMLM-pythia8/†	6.65621	NNLO
W+Jets	/WJetsToLNu_HT-1200To2500_TuneCUETP8M1_13TeV-madgraphMLM-pythia8/†	1.60809	NNLO
W+Jets	/WJetsToLNu_HT-2500ToInf_TuneCUETP8M1_13TeV-madgraphMLM-pythia8/†	0.0389136	NNLO
WW	/WW_TuneCUETP8M1_13TeV-pythia8/†	118.7	NLO
WZ	/WZ_TuneCUETP8M1_13TeV-pythia8/†	47.13	NLO
ZZ	/ZZ_TuneCUETP8M1_13TeV-pythia8/†	16.523	NLO
WWW	/WWW_4F_TuneCUETP8M1_13TeV-amcatnlo-pythia8/†	0.2086	NLO
WWZ	/WWZ_TuneCUETP8M1_13TeV-amcatnlo-pythia8/†	0.1651	NLO
WZZ	/WZZ_TuneCUETP8M1_13TeV-amcatnlo-pythia8/†	0.05565	NLO
ZZZ	/ZZZ_TuneCUETP8M1_13TeV-amcatnlo-pythia8/†	0.01398	NLO
ttW	/TTWJetsToLNu_TuneCUETP8M1_13TeV-amcatnloFXFX-madspin-pythia8/†	0.2043	NLO
ttW	/TTWJetsToQQ_TuneCUETP8M1_13TeV-amcatnloFXFX-madspin-pythia8/†	0.4062	NLO
ttZ	/ttZJets_13TeV_madgraphMLM-pythia8/†	0.5407	NLO
Single-top, s-channel	/ST_s-channel_4f_leptonDecays_13TeV_PSweights-amcatnlo-pythia8/†	3.36	NLO
Single-top, tW-channel	/ST_tW_antitop_5f_NoFullyHadronicDecays_13TeV-powheg_TuneCUETP8M1/†	19.20	NNLO
Single-top, tW-channel	/ST_tW_top_5f_NoFullyHadronicDecays_13TeV-powheg_TuneCUETP8M1/†	19.20	NNLO
Single-top, t-channel	/ST_t-channel_antitop_4f_inclusiveDecays_13TeV_PSweights-powhegV2-madspin/†	80.95	NLO
Single-top, t-channel	/ST_t-channel_top_4f_inclusiveDecays_13TeV_PSweights-powhegV2-madspin/†	136.02	NLO

† RunIISummer16MiniAODv3-PUMoriond17_94X_mcRun2_asymptotic_v3*/MINIAODSIM

2.2.1 Background samples

A list of all 2016, 2017, and 2018 background MC samples and their corresponding cross sections are given in Table 6, Table 7, and Table 8, respectively.

2.3 Signal samples

2.3.1 PYTHIA vs MADGRAPH

In the previous CMS analysis, which used data collected in 2016 at $\sqrt{s} = 13\,\text{TeV}$ [5], PYTHIA was used in the production of signal samples. A similar search was also performed by the ATLAS Collaboration using data collected in 2015 and 2016 [6], with signal samples produced using MADGRAPH. In this section, we show comparisons between these two generators.

Firstly we looked at the transverse momentum (p_T), pseudorapidity (η), and W_R invariant mass distributions of the true particles (Fig 3–5). We observed that the p_T of the leading jet is softer in signal samples produced with PYTHIA when compared to MADGRAPH. This will reduce the signal efficiencies due to the p_T requirement on the reconstructed jets. We applied the event selections of the two signal regions (Section 4), and compare the signal efficiencies in Table 9. As expected, MADGRAPH shows higher signal efficiencies across all mass points.

2.3.2 Signal sample production

Signal samples were generated with MADGRAPH, containing both ee and $\mu\mu$ final states (i.e., eejj or $\mu\mu$jj). A left-right symmetry model is included in the MADGRAPH generator with the W_R mass, N mass, and couplings as input parameters. The assumptions for this search are those described above. Events were generated with the W_R mass ranging from 200 GeV to 7 TeV, in

Table 7: The list of MC samples and corresponding cross-sections used in 2017 analysis.

Process	DAS name	Xsec. (pb)	Xsec. computed order
DY ($10 < m(\ell\ell) < 50$ GeV)	/DYJetsToLL_M-10to50_TuneCP5_13TeV-madgraphMLM-pythia8/†	18610	NLO
DY ($m(\ell\ell) > 50$ GeV)	/DYJetsToLL_M-50_TuneCP5_13TeV-amcatnloFXFX-pythia8/†	6077.22	NNLO
DY ($m(\ell\ell) > 50$ GeV)	/DYJetsToLL_M-50_HT-70to100_TuneCP5_13TeV-madgraphMLM-pythia8/†	208.977	NNLO
DY ($m(\ell\ell) > 50$ GeV)	/DYJetsToLL_M-50_HT-100to200_TuneCP5_13TeV-madgraphMLM-pythia8/†	181.30	NNLO
DY ($m(\ell\ell) > 50$ GeV)	/DYJetsToLL_M-50_HT-200to400_TuneCP5_13TeV-madgraphMLM-pythia8/†	50.4177	NNLO
DY ($m(\ell\ell) > 50$ GeV)	/DYJetsToLL_M-50_HT-400to600_TuneCP5_13TeV-madgraphMLM-pythia8/†	6.98394	NNLO
DY ($m(\ell\ell) > 50$ GeV)	/DYJetsToLL_M-50_HT-600to800_TuneCP5_13TeV-madgraphMLM-pythia8/†	1.68141	NNLO
DY ($m(\ell\ell) > 50$ GeV)	/DYJetsToLL_M-50_HT-800to1200_TuneCP5_13TeV-madgraphMLM-pythia8/†	0.775392	NNLO
DY ($m(\ell\ell) > 50$ GeV)	/DYJetsToLL_M-50_HT-1200to2500_TuneCP5_13TeV-madgraphMLM-pythia8/†	0.186222	NNLO
DY ($m(\ell\ell) > 50$ GeV)	/DYJetsToLL_M-50_HT-2500toInf_TuneCP5_13TeV-madgraphMLM-pythia8/†	0.00438495	NNLO
$t\bar{t}$ (semi-leptonic)	/TTToSemiLeptonic_TuneCP5_13TeV-powheg-pythia8/†	365.34	NNLO
$t\bar{t}$ (leptonic)	/TTTo2L2Nu_TuneCP5_PSweights_13TeV-powheg-pythia8/†	88.29	NNLO
W+Jets	/WJetsToLNu_TuneCP5_13TeV-madgraphMLM-pythia8/†	61530	NNLO
W+Jets	/WJetsToLNu_HT-70To100_TuneCP5_13TeV-madgraphMLM-pythia8/†	1637.1	NNLO
W+Jets	/WJetsToLNu_HT-100To200_TuneCP5_13TeV-madgraphMLM-pythia8/†	1627.45	NNLO
W+Jets	/WJetsToLNu_HT-200To400_TuneCP5_13TeV-madgraphMLM-pythia8/†	435.237	NNLO
W+Jets	/WJetsToLNu_HT-400To600_TuneCP5_13TeV-madgraphMLM-pythia8/†	59.1811	NNLO
W+Jets	/WJetsToLNu_HT-600To800_TuneCP5_13TeV-madgraphMLM-pythia8/†	14.5805	NNLO
W+Jets	/WJetsToLNu_HT-800To1200_TuneCP5_13TeV-madgraphMLM-pythia8/†	6.65621	NNLO
W+Jets	/WJetsToLNu_HT-1200To2500_TuneCP5_13TeV-madgraphMLM-pythia8/†	1.60809	NNLO
W+Jets	/WJetsToLNu_HT-2500ToInf_TuneCP5_13TeV-madgraphMLM-pythia8/†	0.0389136	NNLO
WW	/WW_TuneCP5_13TeV-pythia8/†	118.7	NLO
WZ	/WZ_TuneCP5_13TeV-pythia8/†	47.13	NLO
ZZ	/ZZ_TuneCP5_13TeV-pythia8/†	16.523	NLO
WWW	/WWW_4F_TuneCP5_13TeV-amcatnlo-pythia8/†	0.2086	NLO
WWZ	/WWZ_4F_TuneCP5_13TeV-amcatnlo-pythia8/†	0.1651	NLO
WZZ	/WZZ_TuneCP5_13TeV-amcatnlo-pythia8/†	0.05565	NLO
ZZZ	/ZZZ_TuneCP5_13TeV-amcatnlo-pythia8/†	0.01398	NLO
ttW	/ttWJets_TuneCP5_13TeV_madgraphMLM_pythia8/†	0.4611	NLO
ttZ	/ttZJets_TuneCP5_13TeV_madgraphMLM_pythia8/†	0.5407	NLO
Single-top, s-channel	/ST_s-channel_4f_leptonDecays_TuneCP5_PSweights_13TeV-amcatnlo-pythia8/†	3.36	NLO
Single-top, tW-channel	/ST_tW_antitop_5f_NoFullyHadronicDecays_TuneCP5_13TeV-powheg-pythia8/†	19.2	NNLO
Single-top, tW-channel	/ST_tW_top_5f_NoFullyHadronicDecays_TuneCP5_PSweights_13TeV-powheg-pythia8/†	19.2	NNLO
Single-top, t-channel	/ST_t-channel_antitop_5f_TuneCP5_PSweights_13TeV-powheg-pythia8/†	80.95	NLO
Single-top, t-channel	/ST_t-channel_top_5f_TuneCP5_13TeV-powheg-pythia8/†	136.02	NLO

† RunIIFall17MiniAODv2-PU2017_12Apr2018_*94X_mc2017_realistic_v14*/MINIAODSIM

Table 8: The list of MC samples and corresponding cross-sections used in 2018 analysis.

Process	DAS name	Xsec. (pb)	Xsec. computed order
DY ($10 < m(\ell\ell) < 50$ GeV)	/DYJetsToLL_M-10to50_TuneCP5_13TeV-madgraphMLM-pythia8/†	18610	NLO
DY ($m(\ell\ell) > 50$ GeV)	/DYJetsToLL_M-50_TuneCP5_13TeV-madgraphMLM-pythia8/†	6077.22	NNLO
DY ($m(\ell\ell) > 50$ GeV)	/DYJetsToLL_M-50_HT-70to100_TuneCP5_PSweights_13TeV-madgraphMLM-pythia8/†	208.977	NNLO
DY ($m(\ell\ell) > 50$ GeV)	/DYJetsToLL_M-50_HT-100to200_TuneCP5_PSweights_13TeV-madgraphMLM-pythia8/†	181.30	NNLO
DY ($m(\ell\ell) > 50$ GeV)	/DYJetsToLL_M-50_HT-200to400_TuneCP5_PSweights_13TeV-madgraphMLM-pythia8/†	50.4177	NNLO
DY ($m(\ell\ell) > 50$ GeV)	/DYJetsToLL_M-50_HT-400to600_TuneCP5_PSweights_13TeV-madgraphMLM-pythia8/†	6.98394	NNLO
DY ($m(\ell\ell) > 50$ GeV)	/DYJetsToLL_M-50_HT-600to800_TuneCP5_PSweights_13TeV-madgraphMLM-pythia8/†	1.68141	NNLO
DY ($m(\ell\ell) > 50$ GeV)	/DYJetsToLL_M-50_HT-800to1200_TuneCP5_PSweights_13TeV-madgraphMLM-pythia8/†	0.775392	NNLO
DY ($m(\ell\ell) > 50$ GeV)	/DYJetsToLL_M-50_HT-1200to2500_TuneCP5_PSweights_13TeV-madgraphMLM-pythia8/†	0.186222	NNLO
DY ($m(\ell\ell) > 50$ GeV)	/DYJetsToLL_M-50_HT-2500toInf_TuneCP5_PSweights_13TeV-madgraphMLM-pythia8/†	0.00438495	NNLO
$t\bar{t}$ (semi-leptonic)	/TTToSemiLeptonic_TuneCP5_13TeV-powheg-pythia8/†	365.34	NNLO
$t\bar{t}$ (leptonic)	/TTTo2L2Nu_TuneCP5_13TeV-powheg-pythia8/†	88.29	NNLO
W+Jets	/WJetsToLNu_TuneCP5_13TeV-madgraphMLM-pythia8/†	61530	NNLO
W+Jets	/WJetsToLNu_HT-70To100_TuneCP5_13TeV-madgraphMLM-pythia8/†	1637.1	NNLO
W+Jets	/WJetsToLNu_HT-100To200_TuneCP5_13TeV-madgraphMLM-pythia8/†	1627.45	NNLO
W+Jets	/WJetsToLNu_HT-200To400_TuneCP5_13TeV-madgraphMLM-pythia8/†	435.237	NNLO
W+Jets	/WJetsToLNu_HT-400To600_TuneCP5_13TeV-madgraphMLM-pythia8/†	59.1811	NNLO
W+Jets	/WJetsToLNu_HT-600To800_TuneCP5_13TeV-madgraphMLM-pythia8/†	14.5805	NNLO
W+Jets	/WJetsToLNu_HT-800To1200_TuneCP5_13TeV-madgraphMLM-pythia8/†	6.65621	NNLO
W+Jets	/WJetsToLNu_HT-1200To2500_TuneCP5_13TeV-madgraphMLM-pythia8/†	1.60809	NNLO
W+Jets	/WJetsToLNu_HT-2500ToInf_TuneCP5_13TeV-madgraphMLM-pythia8/†	0.0389136	NNLO
WW	/WW_TuneCP5_PSweights_13TeV-pythia8/†	118.7	NLO
WZ	/WZ_TuneCP5_PSweights_13TeV-pythia8/†	47.13	NLO
ZZ	/ZZ_TuneCP5_13TeV-pythia8/†	16.523	NLO
WWW	/WWW_4F_TuneCP5_13TeV-amcatnlo-pythia8/†	0.2086	NLO
WWZ	/WWZ_TuneCP5_13TeV-amcatnlo-pythia8/†	0.1651	NLO
WZZ	/WZZ_TuneCP5_13TeV-amcatnlo-pythia8/†	0.05565	NLO
ZZZ	/ZZZ_TuneCP5_13TeV-amcatnlo-pythia8/†	0.01398	NLO
ttW	/ttWJets_TuneCP5_13TeV_madgraphMLM_pythia8/†	0.4611	NLO
ttZ	/ttZJets_TuneCP5_13TeV_madgraphMLM_pythia8/†	0.5407	NLO
Single-top, s-channel	/ST_s-channel_4f_leptonDecays_TuneCP5_13TeV-madgraph-pythia8/†	3.36	NLO
Single-top, tW-channel	/ST_tW_antitop_5f_NoFullyHadronicDecays_TuneCP5_13TeV-powheg-pythia8/†	19.20	NNLO
Single-top, tW-channel	/ST_tW_top_5f_NoFullyHadronicDecays_TuneCP5_13TeV-powheg-pythia8/†	19.20	NNLO
Single-top, t-channel	/ST_t-channel_antitop_5f_TuneCP5_13TeV-powheg-pythia8/†	80.95	NLO
Single-top, t-channel	/ST_t-channel_top_5f_TuneCP5_13TeV-powheg-pythia8/†	136.02	NLO

† RunIIAutumn18MiniAOD-102X_upgrade2018_realistic_v15*/MINIAODSIM

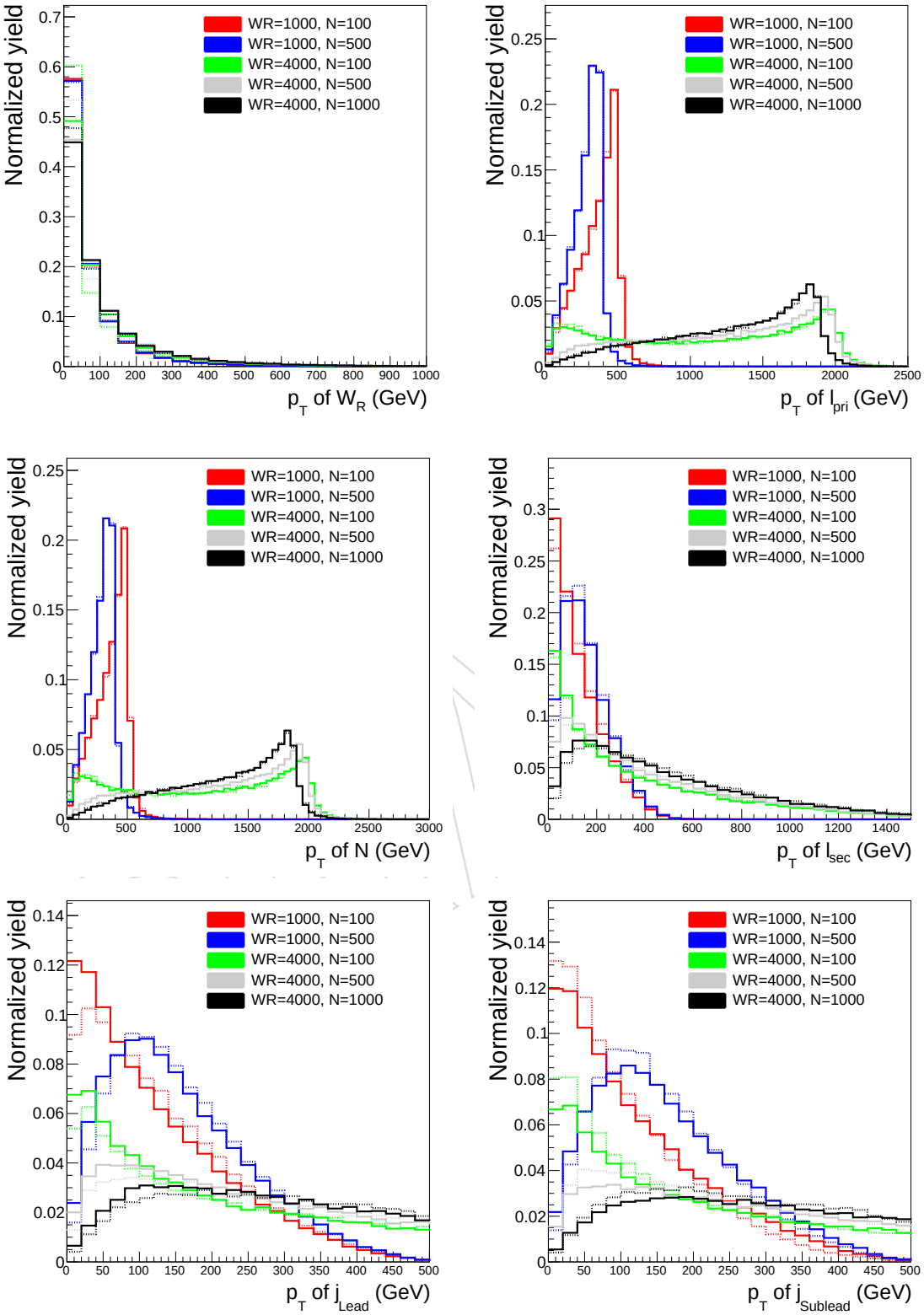

Figure 3: The p_{T} distributions of the $\mathrm{W_R}$, primary lepton, N, secondary lepton, and jets, divided by the total number of signal events. The solid (dashed) line shows the signal samples produced with PYTHIA (MADGRAPH).

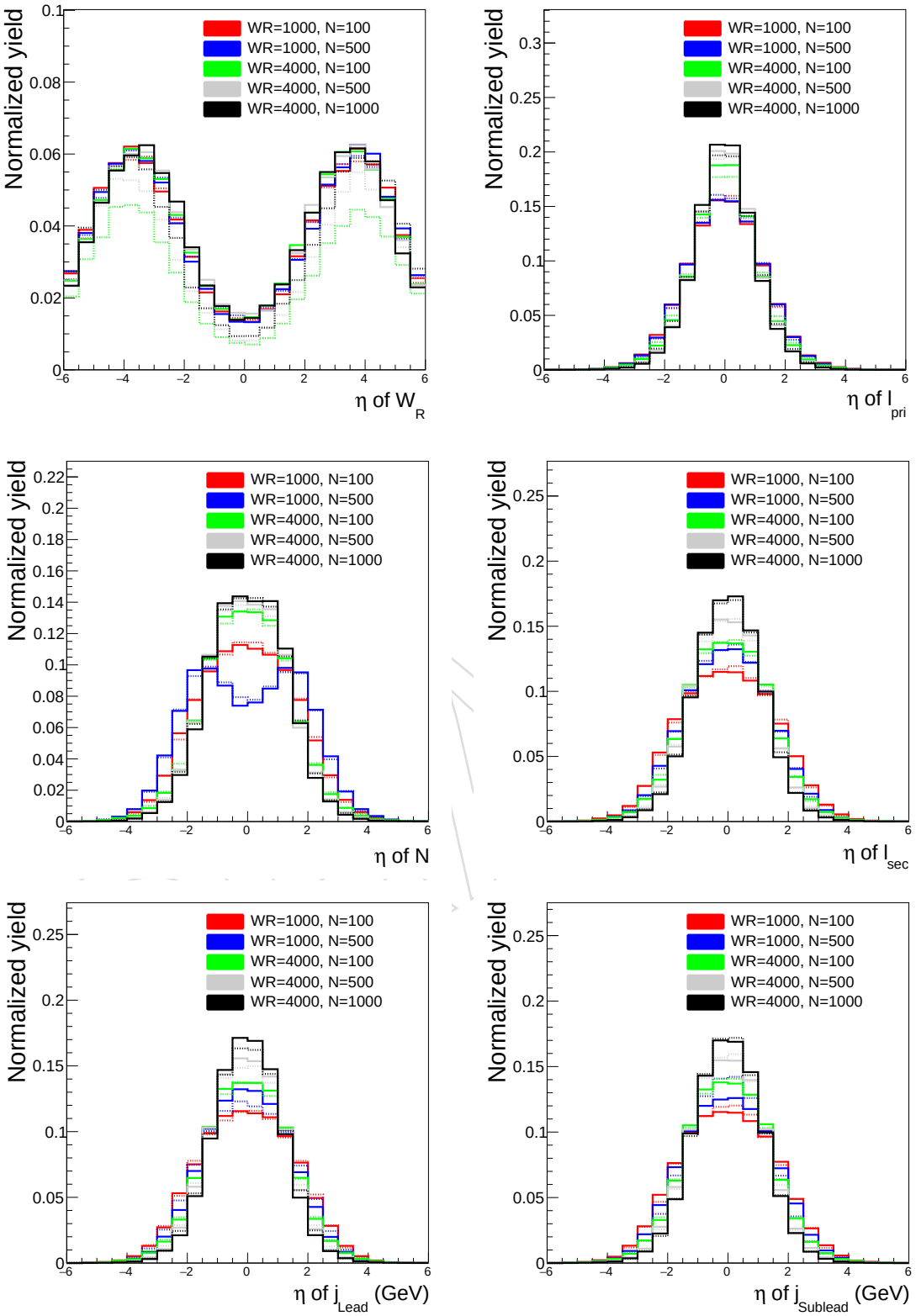

Figure 4: The η distributions of the W_R, primary lepton, N, secondary lepton, and jets, divided by the total number of signal events. The solid (dashed) line shows the signal samples produced with PYTHIA (MADGRAPH).

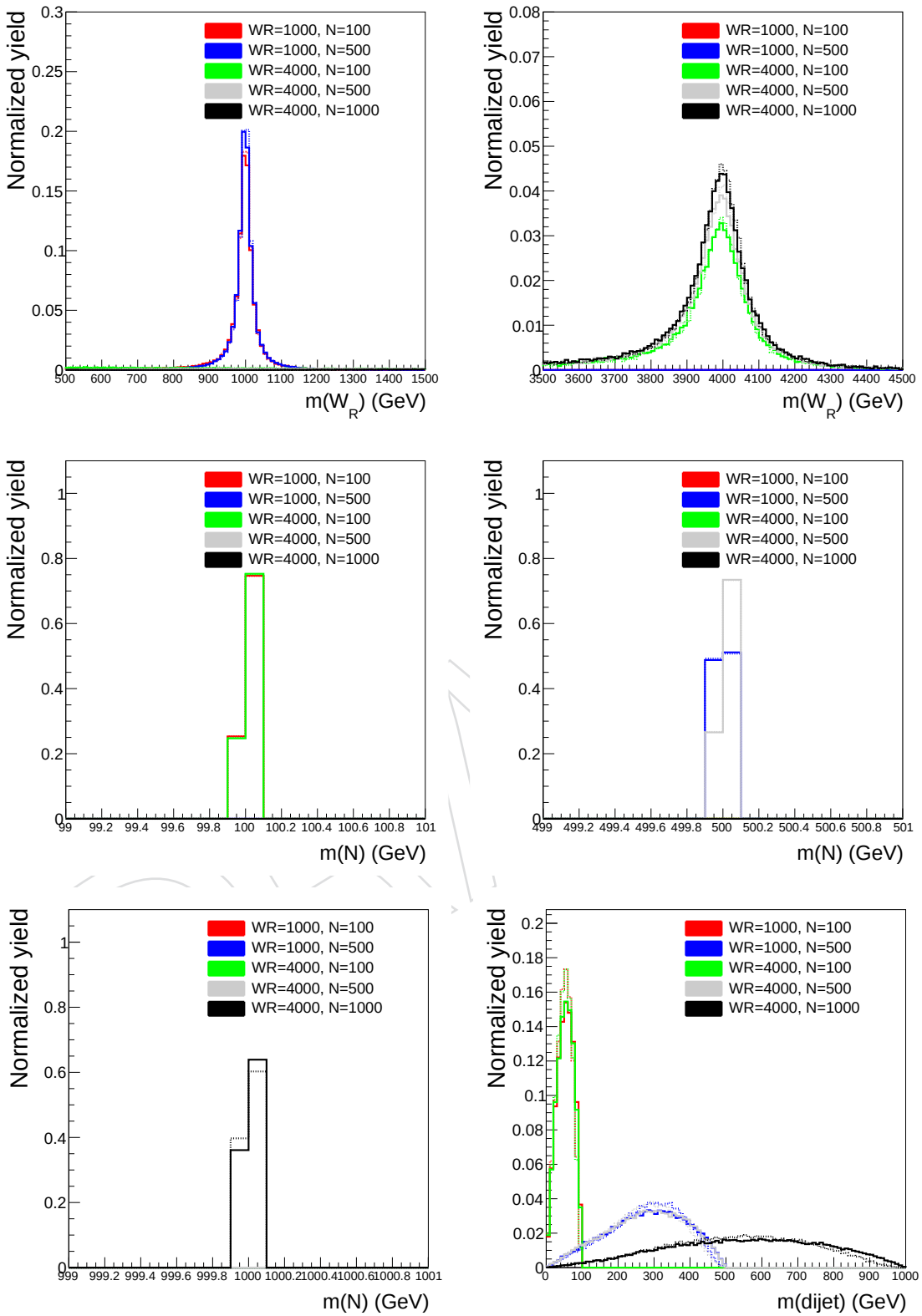

Figure 5: The invariant mass distributions of the W_R, N, and dijet, divided by the total number of signal events. The solid (dashed) line shows the signal samples produced with PYTHIA (MADGRAPH).

Table 9: Signal efficiencies obtained using PYTHIA and MADGRAPH generators.

m_{W_R} (GeV)	m_N (GeV)	Resolved		Boosted	
		PYTHIA	MADGRAPH	PYTHIA	MADGRAPH
ee					
1000	100	4.94 %	5.82 %	27.24 %	30.58 %
1000	500	37.30 %	39.91 %	3.08 %	2.76 %
4000	100	1.35 %	1.45 %	11.04 %	12.19 %
4000	500	26.50 %	28.55 %	22.37 %	21.99 %
4000	1000	48.77 %	51.72 %	9.12 %	7.57 %
$\mu\mu$					
1000	100	10.35 %	11.66 %	35.87 %	38.12 %
1000	500	51.70 %	54.82 %	2.52 %	2.30 %
4000	100	2.79 %	3.12 %	49.18 %	50.60 %
4000	500	44.63 %	46.42 %	23.06 %	22.28 %
4000	1000	68.01 %	70.12 %	7.55 %	6.04 %

steps of 200 GeV; the N mass ranges from 100 GeV up to W_R mass, and the couplings between W_R and N were set equal to the couplings between the SM W boson and SM neutrinos. These sets were produced privately, and validated with the official samples. The complete list of the signal samples is given in App. A in Tab. 23–41, and the cross sections of ee channel are shown if Fig. 6, which are identical to the cross sections for the $\mu\mu$ channel. We calculated NLO-to-LO K factor which is summairzed in App. A.

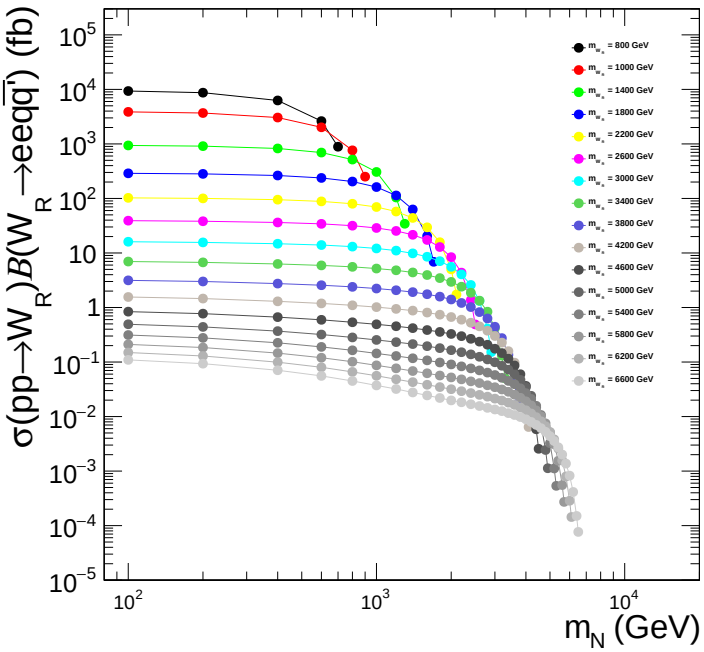

Figure 6: Signal cross sections, in fb, for the process pp $\to$ eN $\to$ eejj, as a function of the mass of N.

2.4 Triggers

The primary triggers that are used for the $\mu\mu$ channel in this analysis are the lowest p_T unprescaled single muon triggers that contain no requirements on the muon ID. Our signals con-

tain muons with $p_T \gg 100$ GeV, so the single muon triggers are used to not lose any efficiency in the higt p_T region. For the ee channel, the single-electron trigger with the lowest p_T threshold are used, along with a single-photon trigger to make up for an inefficiency at high p_T. For the flavor sideband control region, requiring an electron-muon pair, eμ, the $\mu\mu$ triggers are used except for the boosted control region where the electron is the lead lepton. In this region, the ee triggers are used. The triggers are listed for each data-taking year in Tab. 10. In 2017 ee channel, HLT_Ele115_CaloIdVT_GsfTrkIdT_v is dropped because this trigger was not included in the first ~ 5 fb^{-1}. The trigger efficiency loss per electron is 3–4 % for p_T between 100 and 200 GeV, while our signal events are expected to have more energetic. The impact of excluding HLT_Ele115_CaloIdVT_GsfTrkIdT_v trigger is less than 0.1 % in both resolved and boosted signal regions, so we decided to drop this trigger in 2017 only.

Table 10: Triggers used during each year of data taking.

Year	$\mu\mu$	ee
2016	HLT_Mu50_v* or HLT_TkMu50_v*	HLT_Ele27_WPTight_Gsf_v* or HLT_Photon175_v* or HLT_Ele115_CaloIdVT_GsfTrkIdT_v*
2017	HLT_Mu50_v* or HLT_OldMu100_v* or HLT_TkMu100_v*	HLT_Ele35_WPTight_Gsf_v* or HLT_Photon200_v*
2018	HLT_Mu50_v* or HLT_OldMu100_v* or HLT_TkMu100_v*	HLT_Ele32_WPTight_Gsf_v* or HLT_Photon200_v* or HLT_Ele115_CaloIdVT_GsfTrkIdT_v*

2.4.1 Application of the trigger scale factors

The trigger efficiencies we measure in the following sections are measure per lepton, and we estimated the efficiency of a dilepton event fires the triggers ($\epsilon(\ell_1, \ell_2)$) as follows :

$$\epsilon(\ell_1, \ell_2) = 1 - (\text{both lepton fails the trigger}) = 1 - (1 - \epsilon(\ell_1))(1 - \epsilon(\ell_2)) \quad (1)$$

$$\text{Trigger SF} = \epsilon(\text{dimuon, data})/\epsilon(\text{dimuon, MC}) \quad (2)$$

, where $\epsilon(\text{dimuon, data (MC)})$ is the measured per-lepton trigger efficiency in data (MC).

2.4.2 EGamma High Level Trigger efficiency

We measured EGamma High Level Trigger (HLT) efficiency listed in Tab. 10 using the tag-and-probe method. Events with a Z boson decaying into two electrons with high purity can be obtained by requiring a dielectron pair whose mass falls into nominal the Z boson mass window. One of the electrons (the tag electron) should pass a tight identification requirement, to ensure the other electron (probe electron) is a prompt electron. For the data pair-mass distributions, the signal is extracted by fitting the shape with a functional form of "Signal (taken from DY MC) + Background (RooCMSShape [7])".

Detailed requirements are listed in Table 11.

Table 11: Tag-and-probe and electron pair requirements used in the EGamma HLT efficiency measurement.

	2016	2017	2018
Tag	Cut-based tight ID $p_T > 30$ GeV $\eta_{SC} < 2.1$ HLT_Ele27_eta2p1_WPTight_Gsf_v hltEle27erWPTightGsfTrackIsoFilter	Cut-based tight ID $p_T > 35$ GeV $\eta_{SC} < 2.5$ No $1.4442 < \eta_{SC} < 1.566$ HLT_Ele32_WPTight_Gsf_L1DoubleEG_v hltEle32L1DoubleEGWPTightGsfTrackIsoFilter and hltEGL1SingleEGOrFilter	Cut-based tight ID $p_T > 35$ GeV $\eta_{SC} < 2.5$ HLT_Ele32_WPTight_Gsf_v hltEle32WPTightGsfTrackIsoFilter
Probe	HEEPV70 ID $p_T > 5$ GeV $\eta_{SC} < 2.5$		
Passing probe	hltEle27WPTightGsfTrackIsoFilter or hltEG175HEFilter or hltEle115CaloIdVTGsfTrkIdTGsfDphiFilter	hltEle35noerWPTightGsfTrackIsoFilter or hltEG200HEFilter	hltEle32WPTightGsfTrackIsoFilter or hltEG200HEFilter or hltEle115CaloIdVTGsfTrkIdTGsfDphiFilter
Pair	$50 < m(\text{pair}) < 130$ GeV		

Table 12: Systematics uncertainties considered in the EGamma HLT efficiency measurement.

2016	2017	2018
Alternate signal fit		
Alternate background fit		
Alternate DY MC (LO to NLO)		—
Tag $p_T > 35$ GeV	Tag $p_T > 40$ GeV	Tag $p_T > 40$ GeV

The systematic uncertainties considered are listed in Table 12. For 2018, NLO Drell–Yan MC have very low statistics, which leads to unreliably large uncertainties. Instead of considering this source, we estimated the impact of this source from the 2016 and 2017 samples, and assign a conservative value (3 %) in the 2018 analysis. The measured efficiencies are shown in Fig. 7, and are approved by EGamma POG [8].

2.4.3 Muon HLT efficiency

The single muon trigger efficiencies used in our $\mu\mu$ regions were officially measured by the Muon POG as a function of the p_T of a muon passing the HighpT ID [9]. Our signals contain muons with $p_T \gg 100$ GeV and as seen in the following subsection the single muon triggers are fully efficient in this region, therefore these triggers are used to not lose any efficiency in the higt p_T region. The efficiencies were measured in data and MC, and the ratio is used as a correction factor that is applied to MC. The weights can be seen in Fig. 8.

2.4.4 L1 pre-firing trigger inefficiency

The L1 detector performance group discovered that ECAL trigger primitives (TPs), located in the innermost rings of the endcap region ($2.5 < |\eta| < 3.0$), exhibit a timing drift during 2016 and 2017 data-taking, leading to an increase of the L1 pre-firing rate for any calorimeter based trigger.

Pre-firing of L1 triggers represents a problem because of the unfortunate CMS trigger rules, which were developed to prevent buffer overflows. Trigger rules are enforced by the timing and control distribution system (TCDS) right after the final decision of the Global Trigger (GT). They prevent the acceptance of more than one L1 trigger (L1A) in three consecutive bunch crossing (BX), more than two L1A in 25 consecutive BXs, etc. A given L1 trigger pre-fires when the decision of a mis-timed TP, with energy above a minimum threshold required in the

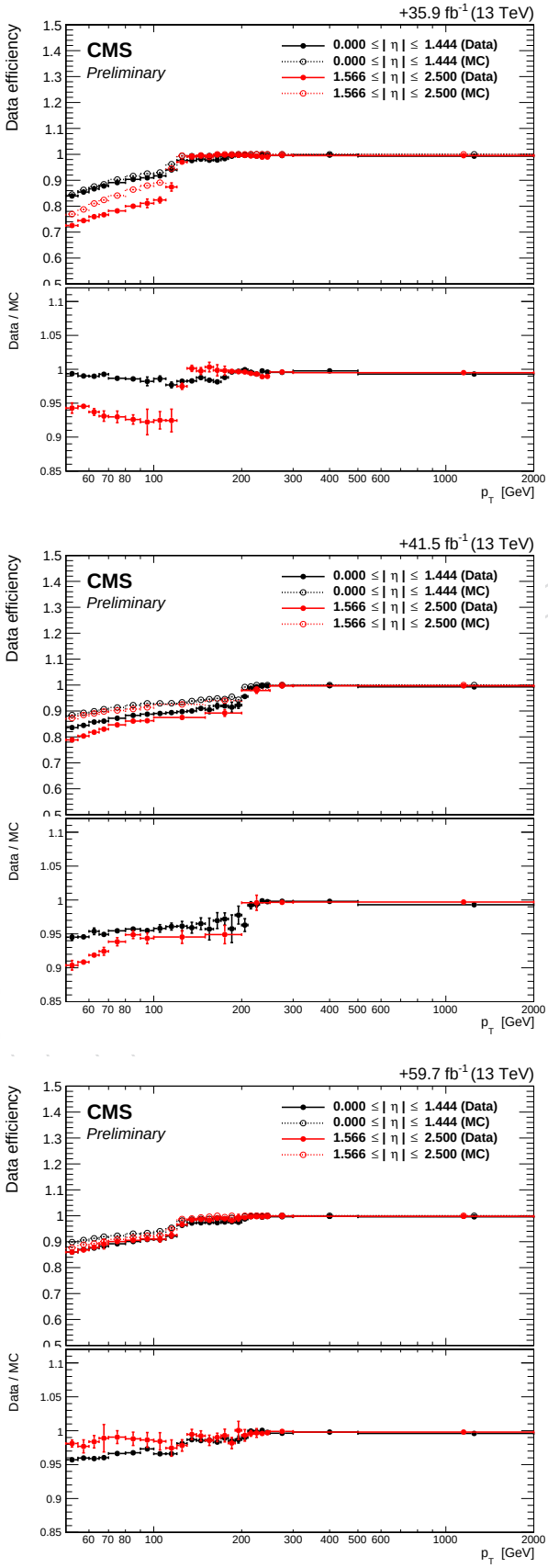

Figure 7: EGamma HLT efficiencies for each year; 2016 (top), 2017 (center), and 2018 (bottom).

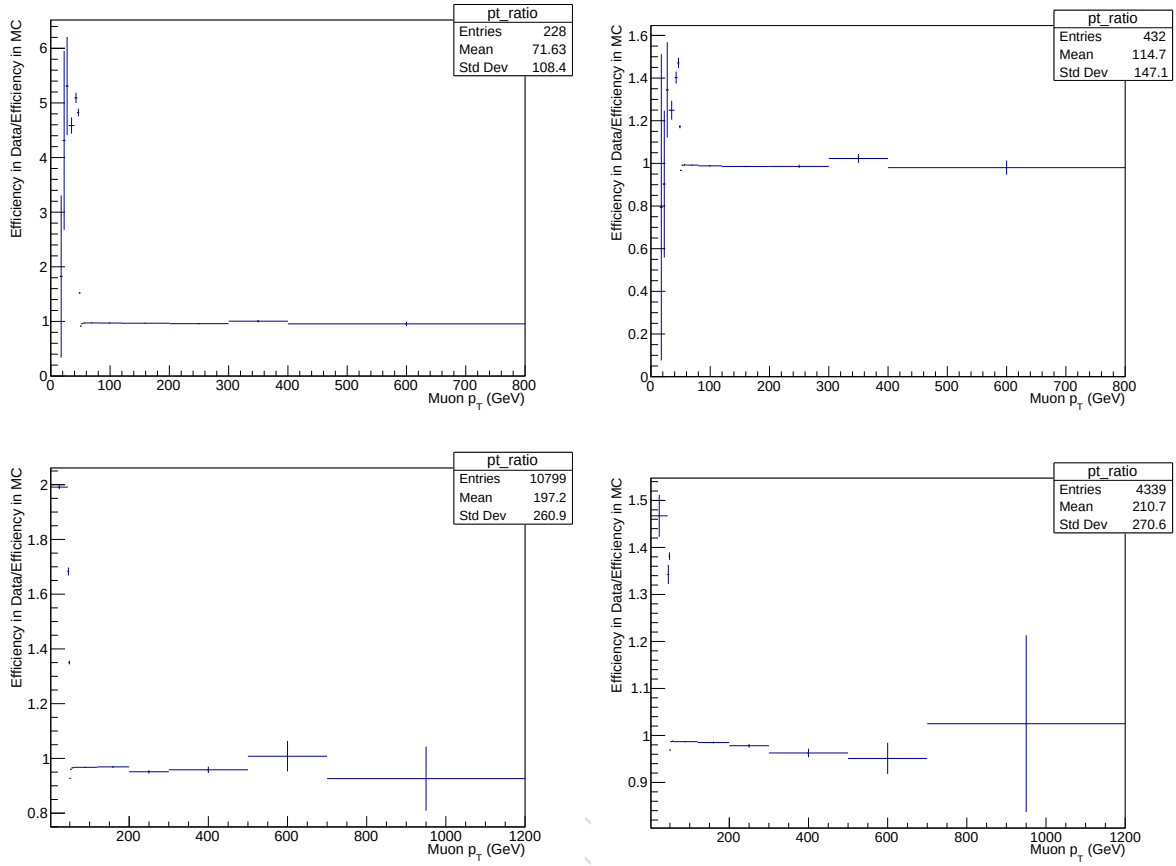

Figure 8: Trigger weights in Runs B-F of 2016 (top left), Runs G-H of 2016 (top right), 2017 (bottom left), and 2018 (bottom right).

L1 menu, is wrongly assigned to the earlier interaction (BX-1) compared to the current one (BX0). Due to the trigger rules, the interesting event in BX0 is discarded by the TCDS, while the previous one in BX-1 will be readout. In addition, the readout event in BX-1 will likely be rejected by the HLT. In fact, the event in BX-1 corresponds to a set minimum-bias interactions, which are typically rejected by the HLT decision. Therefore, the main consequence of the pre-firing is an inefficiency in recording potentially interesting event by the L1 trigger system.

The pre-firing rate cannot be measured with standard techniques because, even if a pre-fired event passes the HLT decision, it is not possible to know whether it has been selected because of a pre-firing or because it is a genuine interesting event. To estimate the pre-firing rate, the standard technique is to use the trigger rules to collect a set of un-prefirable events, which are used as a denominator in the pre-firing measurement. An event in BX0 is called "un-prefirable" when the event in BX-3 was already accepted by the L1 trigger. In fact, because of the trigger rules, BX-2 and BX-1 are vetoed by the TCDS system and cannot prevent the acquisition of BX0. Therefore, even if a mis-timed TP in BX0 pre-fires, BX-1 will not be readout. In addition, for every interesting event accepted by the L1 trigger, all L1-objects and GT decision bits are stored in a window of ± 2 BXs. Therefore, from a set of selected un-prefirable events, the pre-firing probability can be computed for a specific analysis selection. This set of events can be used to estimate the probability of a wrong BX assignment by performing a standard tag-and-probe method making sure that the tag candidate is not responsible for the pre-firing.

The pre-firing probabilities are measured as a function of the p_{T} and η of a given object. In this analysis, a set of pre-firing probability maps are used for jet objects. These probability maps are measured using events from the SingleMuon dataset. The event selection requires exactly one muon matched to HLT IsoMu24/27. An electron veto is also required. The probed jet is requested to pass the tight identification requirements and is required to be the only jet with $p_{\mathrm{T}} > 40\,\mathrm{GeV}$ found in the $1.75 < |\eta| < 3.5$ region. This ensures that the probe is the object responsible for the possible pre-firing. The jet pre-firing probability maps for 2016 and 2017 are shown in Fig. 9, and are used to correct the MC, for 2016–2017, to account for the probability of an event not to pre-fire.

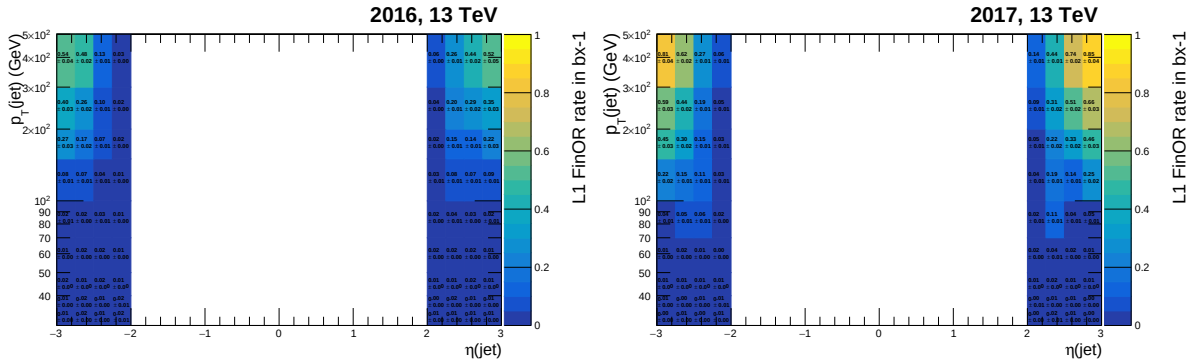

Figure 9: Jet pre-firing probability maps for 2016 (left) and 2017 (right).

The impact of pre-firing is calculated for $m_{\mathrm{W_R}} = 5\,\mathrm{TeV}$ (Table 13).

Table 13: The fraction (%) of prefirable events of signals in ee ($\mu\mu$) channel.

(m_{W_R}, m_N) GeV	2016		2017	
	Resolved	Boosted	Resolved	Boosted
(5000,100)	3.50 (1.31)	2.17 (0.66)	6.61 (2.19)	3.99 (1.13)
(5000,200)	2.76 (1.17)	1.40 (0.63)	4.94 (1.94)	2.58 (1.08)
(5000,400)	2.43 (1.16)	0.92 (0.70)	4.24 (1.86)	1.64 (1.08)
(5000,600)	2.20 (1.11)	0.89 (0.73)	3.82 (1.81)	1.67 (1.04)
(5000,800)	1.87 (1.05)	0.89 (0.81)	3.32 (1.66)	1.44 (1.54)
(5000,1000)	1.87 (1.03)	1.14 (0.75)	3.31 (1.74)	1.67 (1.71)
(5000,1200)	1.89 (1.14)	1.19 (0.89)	3.23 (1.77)	2.43 (1.74)
(5000,1400)	1.73 (1.03)	1.40 (1.05)	3.19 (1.90)	2.35 (2.12)
(5000,1600)	1.80 (1.09)	1.47 (1.16)	3.41 (1.72)	2.37 (1.97)
(5000,1800)	1.88 (1.12)	1.62 (1.07)	3.28 (1.80)	2.85 (2.10)
(5000,2000)	1.83 (1.11)	1.78 (1.08)	3.22 (1.69)	2.35 (2.24)
(5000,2200)	1.85 (1.14)	1.79 (1.47)	3.30 (1.79)	2.86 (1.94)
(5000,2400)	1.87 (1.12)	1.99 (1.58)	3.29 (1.80)	2.40 (2.07)
(5000,2600)	1.86 (1.15)	1.78 (1.11)	3.16 (1.84)	2.95 (2.10)
(5000,2800)	1.92 (1.24)	2.12 (1.42)	3.44 (1.88)	3.35 (1.51)
(5000,3000)	1.90 (1.18)	1.65 (1.39)	3.39 (1.92)	3.22 (2.19)
(5000,3200)	1.92 (1.23)	1.96 (1.37)	3.50 (2.07)	2.33 (1.96)
(5000,3400)	1.96 (1.26)	1.77 (1.10)	3.54 (2.06)	2.94 (2.00)
(5000,3600)	1.95 (1.28)	1.71 (1.12)	3.52 (2.15)	2.77 (2.10)
(5000,3800)	1.99 (1.33)	2.55 (1.39)	3.53 (2.19)	3.13 (2.50)
(5000,4000)	1.96 (1.39)	1.84 (1.24)	3.54 (2.22)	3.30 (2.30)
(5000,4200)	2.08 (1.41)	1.66 (1.20)	3.66 (2.32)	3.20 (2.45)
(5000,4400)	2.11 (1.45)	1.91 (1.31)	3.58 (2.45)	3.14 (2.04)
(5000,4600)	2.06 (1.48)	1.96 (1.45)	3.36 (2.38)	2.77 (2.39)
(5000,4800)	2.04 (1.57)	1.76 (1.48)	3.64 (2.44)	2.55 (2.62)
(5000,4900)	1.97 (1.48)	1.69 (1.70)	3.59 (2.47)	2.59 (2.07)

3 Object definition, Identification and Corrections

3.1 Jets

3.1.1 Reconstruction

The jets used in this analysis are reconstructed by clustering particle flow candidates in the events using the anti-k$_T$ algorithm [10] with a distance parameter, R=$\sqrt{(\Delta\eta)^2 + (\Delta\phi)^2}$, of either 0.4 (AK4) or 0.8 (AK8). To mitigate the effect of multiple interactions in the same bunch crossing, the so-called pileup jets, two methods are used. For the AK4 jets, charged hadron subtraction (CHS) is applied, where the charged particles from non-primary vertices are removed. For the AK8 jets, the pileup per particle identification (PUPPI) algorithm [11] is used to weight the particle flow candidates prior to jet clustering. The pileup jet discriminator is built based on event pileup properties, local shape and tracking information.

3.1.2 Identification

The AK4 jets pass the official JetMET POG "tight jet ID with lepton veto". These reconstructed jets must pass the following requirements:

- the neutral hadron and EM fractions must be less than 90%,
- there were at least two constituents in the jet,
- the muon energy fraction must be less than 80%,
- there is at least one charged hadron in the jet and the charged hadronic fraction must be greater than zero,
- the charged EM fraction must be less than 90% (2016) or 80% (2017,2018)

The AK8 jets pass the official JETMET POG "tight" jet ID. These reconstructed jets must pass the following requirements:

- the neutral hadron and EM fractions must be less than 90%,
- there were at least two constituents in the jet,
- there is at least one charged hadron in the jet and the charged hadronic fraction must be greater than zero,
- the charged EM fraction must be less than 99% for 2016 only.

Requirements made to select jets in this analysis are summarized in Table 14.

Table 14: Jet selection requirements.

Cut	AK8	AK4
$\lvert\eta\rvert$	< 2.4	< 2.4
p_{T}	$> 200\,\mathrm{GeV}$	$> 40\,\mathrm{GeV}$
POG ID	Tight	Tight w/ Lepton Veto
Soft drop Mass	$> 40\,\mathrm{GeV}$	—
LSF	> 0.75	—

3.1.3 Corrections

For both types of jets, further corrections are applied as a function of jet η and p_{T} (L2, L3 corrections) to account for detector non-linearities. Differences between data and simulation after the L2 and L3 corrections are removed by applying a specific calibration to data events.

Residual corrections are extracted from data using the p_T balance in γ+jets and Z+jets events. These corrections have been computed directly for AK4 CHS and AK8 PUPPI jets.

Following the JME POG recommendations [12], the latest jet energy corrections (JEC) are applied to data and MC and are summarized in Table 15. Since the jet energy resolution (JER) differs in data and MC, in order to improve the agreement an additional smearing is applied to the simulation. The JER scale factors are listed in Table 16.

Table 15: The JEC tags used for each data taking year.

Year	Data	MC (FullSim)	MC (FastSim)
2016	Summer16_07Aug2017(BCD,EF,GH)_V11_DATA	Summer16_07Aug2017_V11_MC	Summer16_FastsimV1_MC
2017	Fall17_17Nov2017(B,C,D,E,F)_V32_DATA	Fall17_17Nov2017_V32_MC	Fall17_FastSimV1_MC
2018	Autumn18_Run(A,B,C,D)_V19_DATA	Autumn18_V19_MC	Autumn18_FastSimV1_MC

Table 16: The JER scale factors used for each data taking year.

Year	SF tag
2016	Summer16_25nsV1
2017	Fall17_V3
2018	Autumn18_V7

In our boosted analysis, where the heavy neutrino is reconstructed as an AK8 jet, a lepton makes up a large portion of the jets energy. JECs are derived using a QCD sample with a parton-made object and therefore we verified that the JECs are suitable for our neutrino jets. Figure 10 shows the GEN level energy of a boosted neutrino compared to the RECO level energy of an AK8 jet with and without the JECs applied. The JECs have very minimal effect on the RECO jet energy distribution and the RECO energy roughly peaks in the same location as the GEN energy. The RECO distribution is broader than the GEN distribution, as expected, due to reconstruction effects.

3.1.4 Jet mass

The soft drop algorithm [13] has been used to calculate the mass of the AK8 jets. Like any grooming method, soft drop declustering removes wide-angle soft radiation from a jet in order to mitigate the effects of contamination from initial state radiation (ISR), the underlying event (UE), and multiple hadron scattering (pileup). Given a jet of radius R_0 with only two constituents, the soft drop procedure removes the softer constituent unless:

$$\frac{\min(p_T^1, p_T^2)}{p_T^1 + p_T^2} > z_{\text{cut}} \left(\frac{\Delta R_{12}}{R_0} \right)^{\beta}$$

. This algorithm controls the soft wide-angle radiation by a soft radiation fraction threshold z_{cut} and an angular exponent parameter β, where $\beta = 0$ corresponds roughly to the (modified) mass-drop procedure (mMDT) detailed in [14]. The default parameters used by CMS are $\beta = 0$ and $z_{\text{cut}} = 1$. The soft drop algorithm has the benefit of performing jet grooming in a theoretically safer way [13, 15] and its behavior is constant across different clustering distance parameters R and p_T, which is not true for the pruning technique [16, 17]. Although the soft drop algorithm is primarily aimed at separating boosted W-jets from light quark/gluon-jets, it can fully reject contributions from UE and pileup when combined with the PUPPI algorithm.

In Figure 11 the jet soft drop mass and pruned mass distributions are shown for the p_T-leading jet for several simulated signal samples. The soft drop mass distributions have much sharper peaks closer to the N mass than the pruned mass distributions.

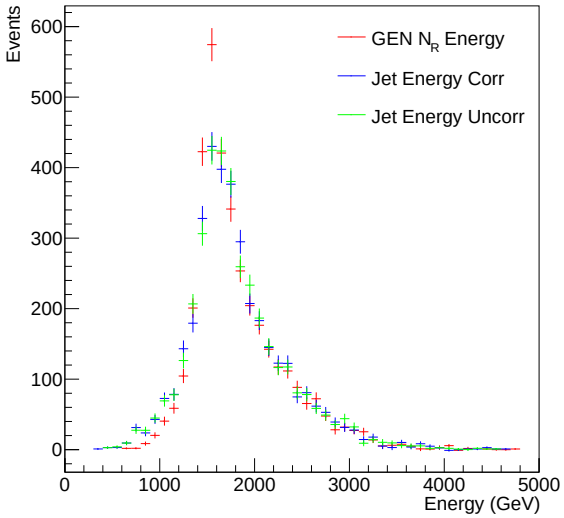

Figure 10: The GEN level energy of a boosted neutrino compared to RECO level energy of an AK8 jet, with and without the JECs applied. The boosted neutrino decay products are reconstructed within the AK8 jet. The RECO and GEN level distributions show good agreement. The signal sample used was simulated with a right-handed W mass of 3000 GeV and a neutrino mass of 400 GeV, decaying through the dimuon channel.

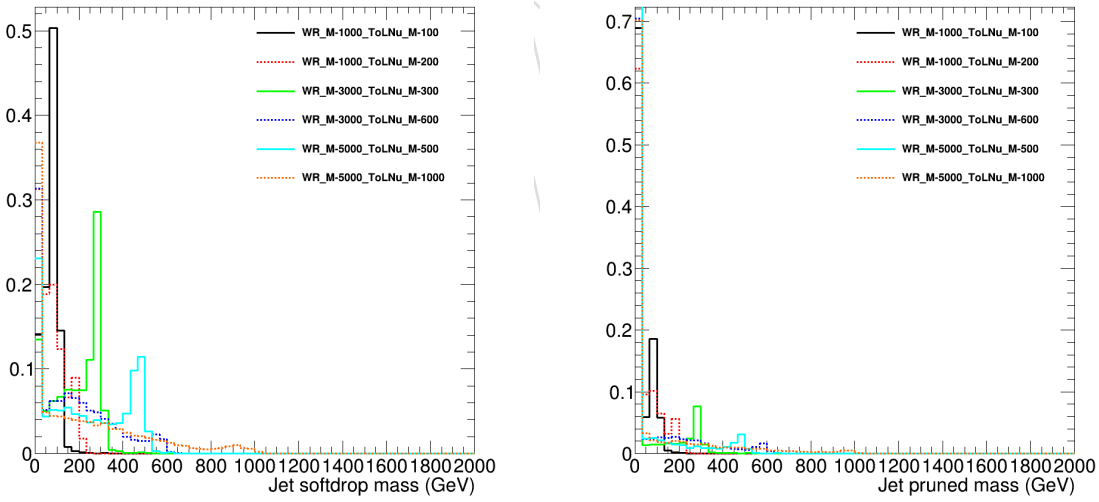

Figure 11: Lead jet soft drop mass (left) and pruned mass (right) distributions for a variety of signal sample mass points.

3.1.5 Jet LSF

Traditional isolation of a reconstructed event object, such as a final state lepton, is computed as the ratio of the sum of p_T within a cone of radius R around the event object to the p_T of the event object itself. Here a smaller ratio corresponds to a higher degree of isolation.

In [18] it was demonstrated that in highly boosted signal topologies traditional isolation re-

quirements on final state leptons can only reject backgrounds at the cost of significant signal losses. A SUSY signal model and $b\bar{b}$ backgrounds are considered and the final state lepton in the SUSY model is collimated with the final state quarks and is less isolated than a lepton produced in the decay of a b-quark which is displaced from the jet axis. Thus, making isolation requirements in the signal event selection not at all useful.

The LSF variable is proposed to be able to better discriminate signal from background in this highly boosted regime. The LSF variable is calculated very much in the spirit of traditional isolation and proceeds by first clustering objects (including leptons) in an event into "fat" jets using the anti-k_T algorithm with a radius parameter of $R = 0.8$. Then the exclusive k_T algorithm is used to cluster the constituents of each fat jet into n-subjets, where n is chosen based on the exact final state topology. Finally, the LSF_n quantity is calculated as

$$\mathrm{LSF}_n = \frac{p_{\mathrm{T},\ell}}{p_{\mathrm{T,subjet}}} \tag{3}$$

,

where $p_{\mathrm{T,subjet}}$ is the transverse momentum of the subjet containing the lepton in question and $p_{\mathrm{T},\ell}$ is the transverse momentum of the lepton itself. Leptons with high values of LSF (approaching 1) are considered more isolated. From [18], final state leptons in the SUSY model have LSF values peaking near 1, while leptons from background $b\bar{b}$ decays have LSF values peaking around 0.2, further motivating the usefulness of this variable in a highly boosted regime.

The LSF_3 distribution of the leading p_T AK8 jet is shown in Fig. 12 for simulated signal and background events after passing the full boosted event selection. The signal sample distributions have a sharp peak at one. The background distributions also peak at one, however this is due to our event selection removing the majority of low LSF jets. However, the W+jets background primarily has low LSF values, so applying an LSF cut is very beneficial since we do not have a suitable control region to estimate this background.

An S/B study was performed to determine the optimal LSF cut value for our analysis, where $\mathrm{LSF} > 0.7$ was found to give the best signal to background ratio for the majority of our signal mass region. The results of this study are summarized in Appendix G.

3.2 Muons

3.2.1 Reconstruction

Muons reconstruction starts with a track in the muon system and looks for a matching tracker track. More information on muon reconstruction algorithms can be found in [19]. Each algorithm is best suited for a unique range of muon η and p_T values, but no single algorithm is always best for the high-p_T muons studied in this analysis. This degeneracy in algorithm performance results from reductions in the tracker and muon detector momentum resolution with increasing muon p_T. To compensate for this the 'cocktail' algorithm (TuneP) was used to determine the p_T of high energy muons. The p_T of reconstructed muons were recalculated using the TuneP algorithm.

3.2.2 Identification

The high-p_T muon is used in this analysis:

- The muon is reconstructed as a "global" muon.

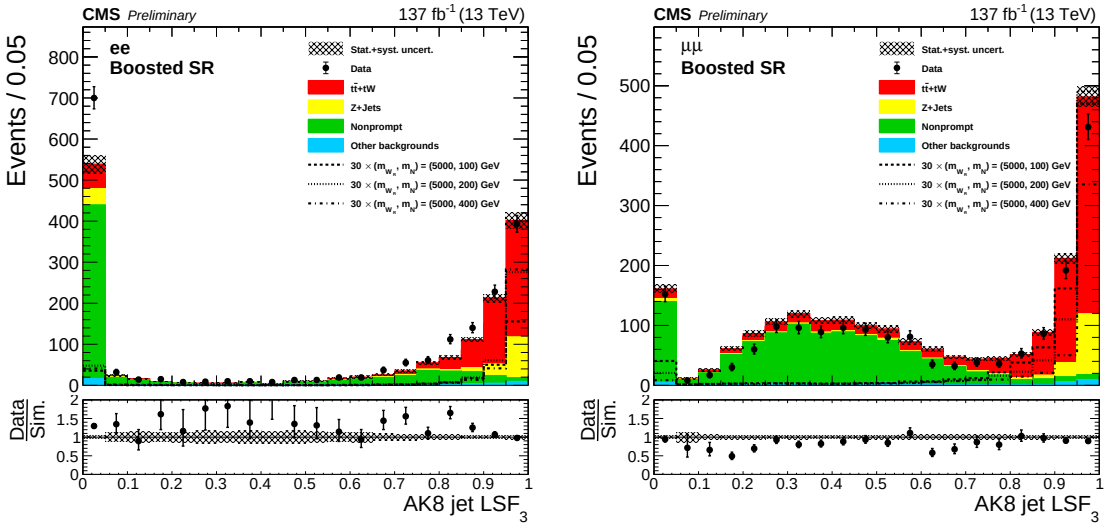

Figure 12: The LSF_3 distributions of the leading AK8 jet. Data and simulated background from three data periods are compared. Also plotted are the distributions for the simulated W_R signals of masses 5 TeV. The number of signal and background events correspond to an integrated luminosity of 137 fb^{-1} and the NLO signal cross sections are scaled by a factor of 30. The events are required to pass the full electron channel (left) and muon channel (right) boosted event selection except for the LSF_3 requirement.

- At least one muon-chamber hit is included in the global-muon track fit.
- There are muon segments in at least two muon stations.
- The p_T relative error, σ_{p_T}/p_T, of the muon best track, is less than 0.3.
- To prevent muons from cosmics and from decays-in-flight, the transverse impact parameter must be less than 2mm, with respect to the primary vertex. The longitudinal distance of the track must be less than 5 mm.
- The muon track has at least one pixel hit.
- At least 6 tracker layer hits are required in the reconstruction.

To reject muons from jets, each muon, other than the second muon in boosted events, must be isolated from other tracks. The energy of all tracks in a cone of $R = \sqrt{(\Delta\phi)^2 + (\Delta\eta)^2} < 0.3$ around the muon, excluding the muon track, must be less than 10% of the muon p_T. After applying muon ID and isolation requirements, simulated events were reweighted according to the muon POG prescriptions to account for differences in the ID and isolation efficiencies between data and simulations [9, 20, 21].

3.2.3 Momentum corrections

For muons with $p_T < 200$ GeV, the momenta are corrected using the Rochester corrections [20]. Muons with $p_T \geq 200$ GeV are corrected with the generalized–endpoint (GE) method [9, 21]. These corrections bring the position and width of the $Z \to \mu\mu$ mass peak in simulations and data into better agreement.

3.3 Electrons

3.3.1 Reconstruction

Electrons are reconstructed from ECAL clusters matched to GSF tracks and must have a shower shape consistent with an electromagnetic interaction. The energy measurement of electrons in data is not perfect and must be corrected based on the standard candle of $Z \rightarrow ee$ events. A scale factor is applied to electrons in the data to correct for this mis-measurement according to the recipe provided by the Egamma POG. A correction to the MC must also be applied to correct for the differences in resolution by smearing the energy of electrons. Smearing, scaling, and reconstruction efficiency scale factors were provided by the POG [22, 23].

3.3.2 Identification

Reconstructed electrons were required to pass the HEEP identification (v7.0) [24–26]. This identification requires a reconstructed electron to contain a high quality, isolated track spatially linked to an isolated ECAL energy deposit. In addition, the shower shape of the ECAL energy deposit must be consistent with a true electromagnetic shower.

Differences in electron ID efficiencies between data and simulation were taken into account by applying a scale factor provided by the EGamma POG.

3.3.3 Energy corrections

Discrepancies in energy scale and resolution between data and simulation were corrected following the EGamma prescriptions for scales and smearings [22]. The electron energy scale was corrected in data, by a multiplicative factor dependent on both the η and R_9 of the electron. The electron energy in simulated events was smeared to take into account the effective resolution in data. A Gaussian smearing which depends on η and R_9 was applied.

3.4 Lepton selections

Both electrons and muons have two selection categories (tight and loose), chosen such that we can optimally reconstruct resolved and boosted signal events. Tight leptons are used to reconstruct isolated leptons, similar to the leptons expected in resolved signals. Loose leptons are similar to non-isolated leptons in boosted signals, and are required to exist inside a wide-cone jet, to reconstruct a merged jet of quarks and a lepton. The requirements for electrons (muons) are summarized in Table 17 (18).

Table 17: Electron selection requirements.

Requirement	Loose	Tight
$\lvert\eta\rvert$	< 2.4	< 2.4
p_T	$> 53\,\text{GeV}$	$> 53\,\text{GeV}$
ID	Cut Based Loose without relIsoWithEA	HEEPV70 (HEEPv7.0-2018Prompt for 2018)

Table 18: Muon selection requirements.

Requirement	Loose	Tight
$\lvert\eta\rvert$	< 2.4	< 2.4
p_T	$> 53\,\text{GeV}$	$> 53\,\text{GeV}$
ID	HighPt	HighPt
Isolation	–	Relative tracker isolation < 0.1

4 Event Selection

The event selection is split into two categories, the first targeting events that have a boosted final state and the second targeting events with a resolved final state. The selection for each of these two signal topologies are designed to be orthogonal and maximize the ratio of the total signal (resolved plus boosted) over backgrounds as well as sideband creation. Before describing the events selections for the two signal topologies, we must define the criteria used to distinguish between resolved and boosted events. An event is labeled "resolved" if it satisfies the follow conditions:

- the number of tight leptons (ℓ_{Tight}) is exactly two,
  - leading lepton $p_{\text{T}} > 60\,\text{GeV}$,
  - subleading lepton $p_{\text{T}} > 53\,\text{GeV}$,
- contains at least two AK4 jets that pass the jet selection,
- ΔR between any pair of the two tight leptons and the two leading AK4 jets are greater than 0.4.

If an event does not satisfy the above resolved criteria then it is a possible "Boosted" event and the boosted event selection is applied.

The selection criteria for the ee and $\mu\mu$ channels are identical except for the triggers. All events must pass the recommended $E_{\text{T}}^{\text{miss}}$ filters as described in [27]. The selection requirements (in the order applied) as used in the resolved and boosted regions are listed below, with signal/sideband regions denoted with ★, and selections applied denoted with a •.

1. Resolved regions and selections:
   - Event is classed as "resolved" as described above.
   - ★ **Resolved DY sideband:**
     - $60 < m(\ell_{\text{Tight}}\ell_{\text{Tight}}) < 150\,\text{GeV}$.
   - ★ **Resolved signal region and flavor-sideband:**
     - $m(\ell_{\text{Tight}}\ell_{\text{Tight}}) > 400\,\text{GeV}$,
     - $m(\ell_{\text{Tight}}\ell_{\text{Tight}}\text{jj}) > 800\,\text{GeV}$.
   - ★ **Resolved low-mass control region:**
     - $m(\ell_{\text{Tight}}\ell_{\text{Tight}}) > 200\,\text{GeV}$,
     - $m(\ell_{\text{Tight}}\ell_{\text{Tight}}\text{jj}) < 800\,\text{GeV}$.
2. Boosted regions and selections:
   - Event is not "resolved".
   - The leading (ℓ_{Tight}) has $p_{\text{T}} > 60\,\text{GeV}$.
   - ★ **Boosted DY sideband:**
     - at least one loose lepton, ℓ_{Loose}, satisfies $60 < m(\ell_{\text{Tight}}\ell_{\text{Loose}}) < 150\,\text{GeV}$,
     - at least one AK8 jet (J) without LSF requirement satisfies $\Delta\phi(\ell_{\text{Tight}}, \text{J}) > 2.0$,
   - If none of the loose lepton satisfies $60 < m(\ell_{\text{Tight}}\ell_{\text{Loose}}) < 150\,\text{GeV}$:
     - at least one AK8 jets with LSF requirement satisfies $\Delta\phi(\ell_{\text{Tight}}, \text{J}) > 2.0$; leading jet is selected,

- at least one loose lepton satisfies $\Delta R(\ell_{\text{Loose}}, J) < 0.8$; leading lepton is selected,
- only one flavor of ℓ_{Loose} can exist; e.g., if a loose muon satisfies the requirement above, no loose electron satisfies the same requirement,
- no extra lepton pass tight ID except ℓ_{Tight} and ℓ_{Loose}.

★ **Boosted signal region and flavor-sideband:**

- $m(\ell_{\text{Tight}}\ell_{\text{Loose}}) > 200\,\text{GeV}$,
- $m(\ell_{\text{Tight}}J) > 800\,\text{GeV}$.

★ **Boosted low-mass control region:**

- $m(\ell_{\text{Tight}}\ell_{\text{Loose}}) > 200\,\text{GeV}$,
- $m(\ell_{\text{Tight}}J) < 800\,\text{GeV}$.

The reconstructed mass distributions of W_R for the boosted and resolved signal regions is shown in Fig. 43–46, respectively.

4.1 Signal efficiencies

The signal efficiencies after applying the signal selections are shown in Appendix B, as a function m_N, for each value of m_{W_R}.

5 Background Estimation

As $t\bar{t}$, single-top+W, and DY+jets have the same final state as the signal, they are the main sources of background in both the resolved and boosted regions of this analysis. A schematic diagram presenting the control regions used to estimate the $t\bar{t}$, single-top+W, and DY+jets backgrounds and the signal region is shown in Fig. 13. The contributions from other processes are more minor and have been estimated by counting the number of events in the simulated samples in the signal region. We have grouped these minor backgrounds into 2 categories: "nonprompt" and "other". Nonprompt corresponds to backgrounds with one real lepton and a second energetic fake lepton (single top s- and t-channel and W+jets) and other corresponds to rare processes with two real leptons (multiboson and $t\bar{t}V$).

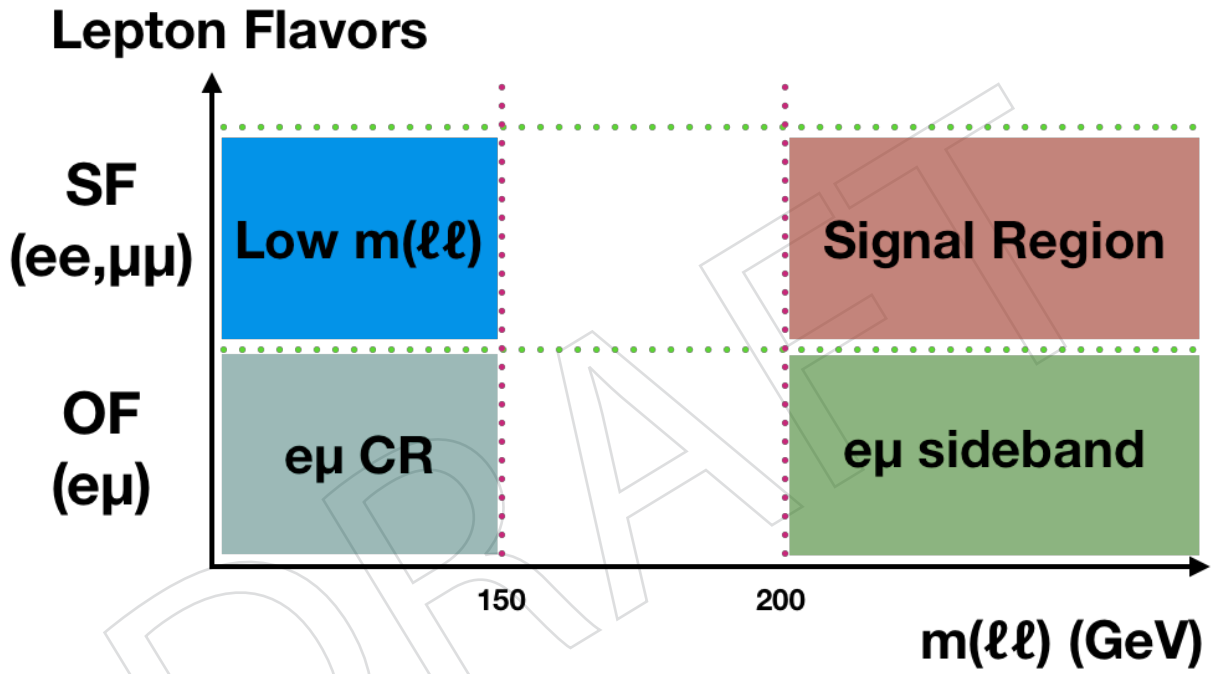

Figure 13: A schematic diagram of the analysis regions.

5.1 DY+jets background estimation

To estimate the background from high-mass DY lepton pairs produced in association with additional jets, we used MC simulation. We validated the DY simulation in the DY sideband as described in Section 4).

It has been reported [28] that the p_T of the Z boson in DY simulation is not well-modeled. The dedicated p_T correction for the true Z is derived in a sample of dimuon events [29], but they are measured in the events containing isolated dimuon events without any further requirements to reject our signal events. We observed a good agreement in the Z p_T distributions with the NLO DY MC, thus we used the NLO-to-LO ratio as our reweighting values. The results as a function of the p_T of the true Z boson as shown in Fig. 14. The uncertainties originate from the renormalization/factorization scale, PDF error, and α_S are considered.

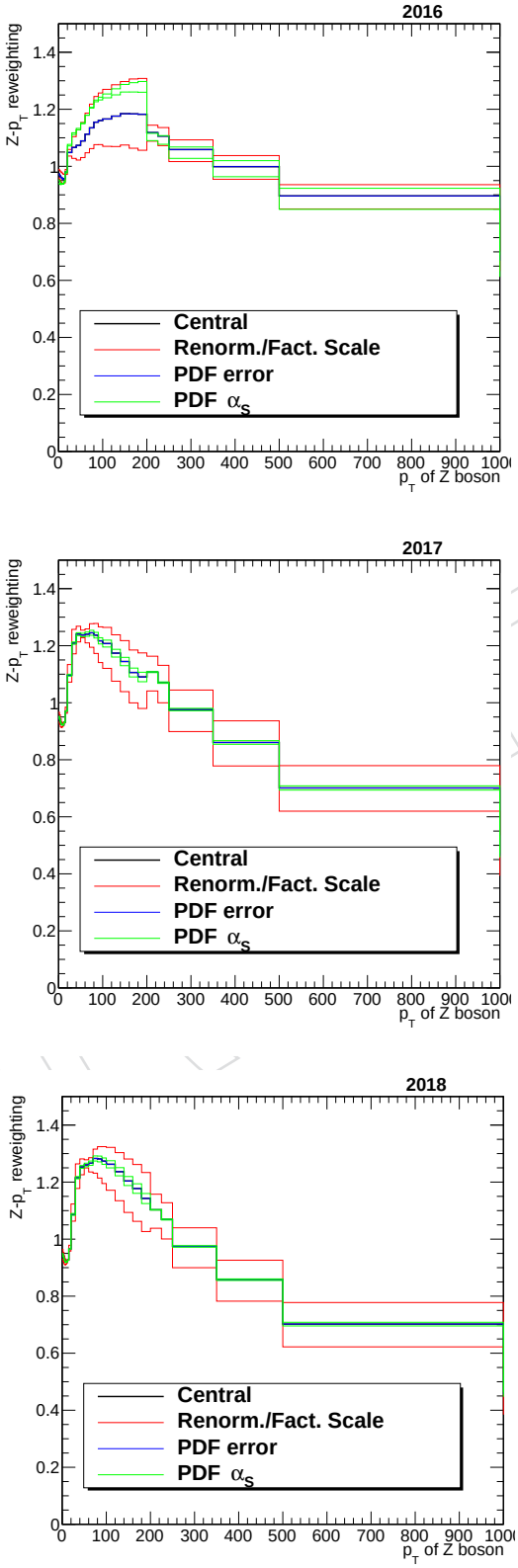

Figure 14: The Z-p_{T} correction functions, for 2016 (upper), 2017 (middle) and 2018 (lower).

The dilepton p_T distributions before and after applying the p_T corrections are shown in Figs. 15–18.

The jet p_T distributions in the DY sideband are shown in Fig. 19–21 after applying the Z-p_T correction. As can be seen, the simulation predicts harder jets than is observed in the data. This is due to the absence of a loop correction in the LO DY sample. The discrepancy is also apparent in $m(\ell\ell jj)$ and $m(\ell J)$ distributions shown in Fig 22–23. To correct this discrepancy, we derive a bin-by-bin jet-p_T reweighting in the DY sideband:

$$(\text{Data} - \text{non-DY})/(\text{DY MC}), \tag{4}$$

which we apply to our DY distributions in all regions. Since the discrepancy originates from higher order corrections on the jets and should be independent of the lepton flavor of the Z decay, we combine the dielectron and dimuon sidebands to obtain the nominal ratio for each year. The systematic uncertainty applied to the corection factor is the combined statistical and systematic uncertainties from data and simulation in the DY CR and since the statistical uncertainty dominates the uncertainty is uncorrelated across bins in the invariant mass spectrum. The ratios and uncertainties for each year are shown in Fig 24. The $m(\ell\ell jj)$ and $m(\ell J)$ distributions in the sideband after the ratios are applied are shown in Fig 25–26.

To validate the DY ratio correction method, a couple of studies were performed. First, the method was validated in our low dilepton invariant mass control region by splitting the region in two, $60 < m_{\ell\ell} < 100\,\text{GeV}$ (DY CR1) and $100 < m_{\ell\ell} < 150\,\text{GeV}$ (DY CR2). The correction ratios are derived in the DY CR1 and applied to the DY CR2. The $m(\ell\ell jj)$ ($m(\ell J)$) distributions in the DY CR2, before and after the ratios obtained in the DY CR1 are applied are shown in Fig 27–30, and show that application of the ratios brings better agreement between data and simulation.

Additionally, to validate the use of the ratios to our higher dilepton invariant mass signal region, we use a NLO DY sample as pseudodata. The NLO sample is limited by a lack of statistics, so we can not use it in our final background estimation, but it is suitable for the validation. First, we compare the NLO/LO DY ratio to the Data/LO DY ratio in the DY control region in Fig 31 and see fairly good agreement across the ratios. Then we compare the NLO/LO ratio in the control region and signal region in Fig 32 and see that most bins agree with the exceptions agreeing within 2σ.

The p_T of jets after the jet-p_T reweighting are shown in Fig 33–35.

The postfit mass distribution in the DY CRs are shown in Fig. 36–37 for each year, and the year-combined results are shwon in Fig 38. The fitted rate parameters of the DY MCS are shown in Table 19.

Table 19: The fitted rate parameters (i.e., normalization scale factors) of the Z+jets MC samples.

Year	Event type	ee	$\mu\mu$
2016	Resolved	1.00 ± 0.09	0.99 ± 0.09
	Boosted	1.04 ± 0.12	1.02 ± 0.16
2017	Resolved	0.99 ± 0.07	0.99 ± 0.07
	Boosted	1.04 ± 0.13	0.96 ± 0.17
2018	Resolved	1.01 ± 0.07	1.00 ± 0.07
	Boosted	1.03 ± 0.13	1.02 ± 0.16

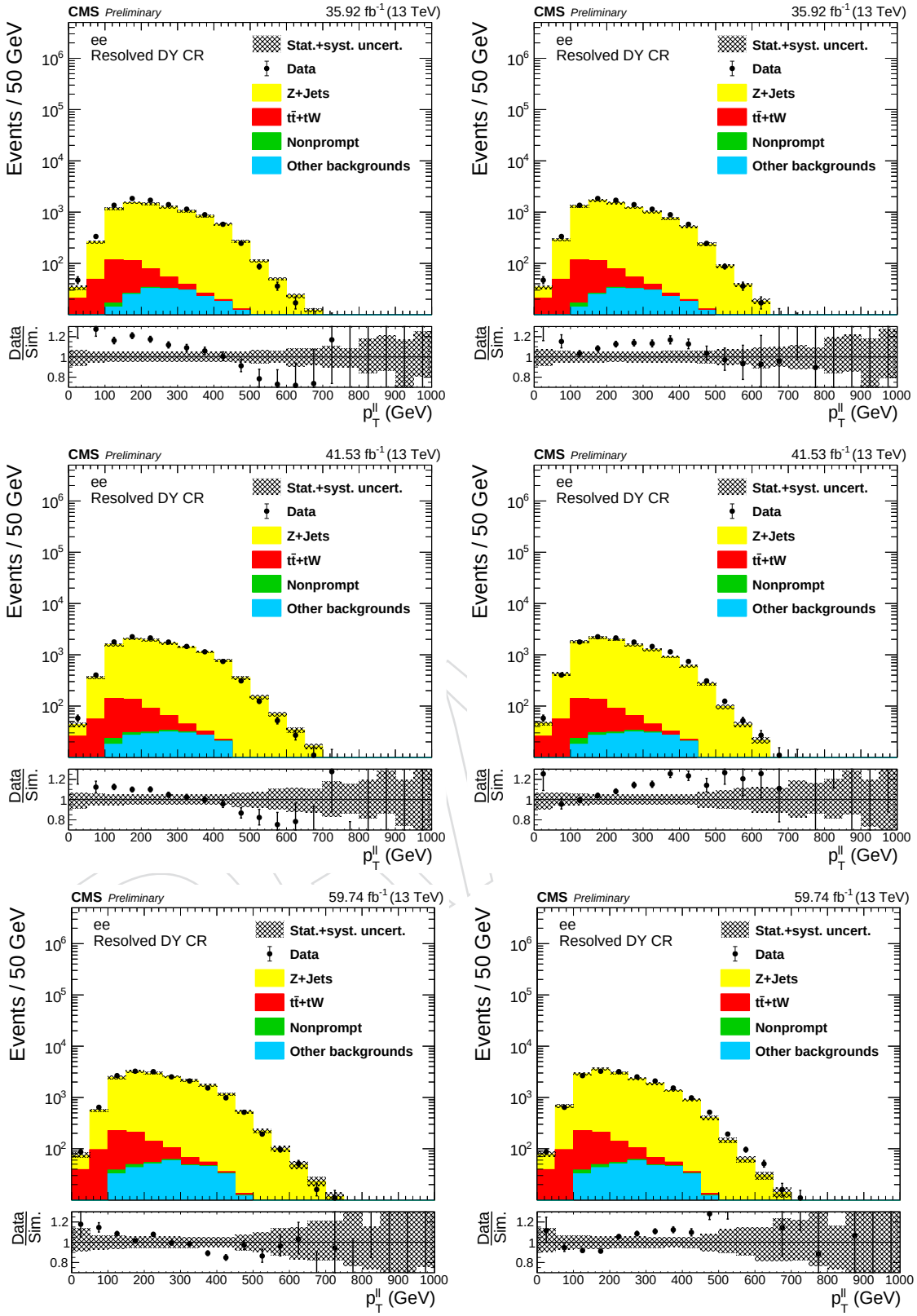

Figure 15: The p_{T} of dilepton in the low $m_{\ell\ell}$ resolved control regions, before (left) and after (right) applying the Z-p_{T} correction. Results for dielectron channel is shown for 2016 (upper), 2017 (middle) and 2018 (lower).

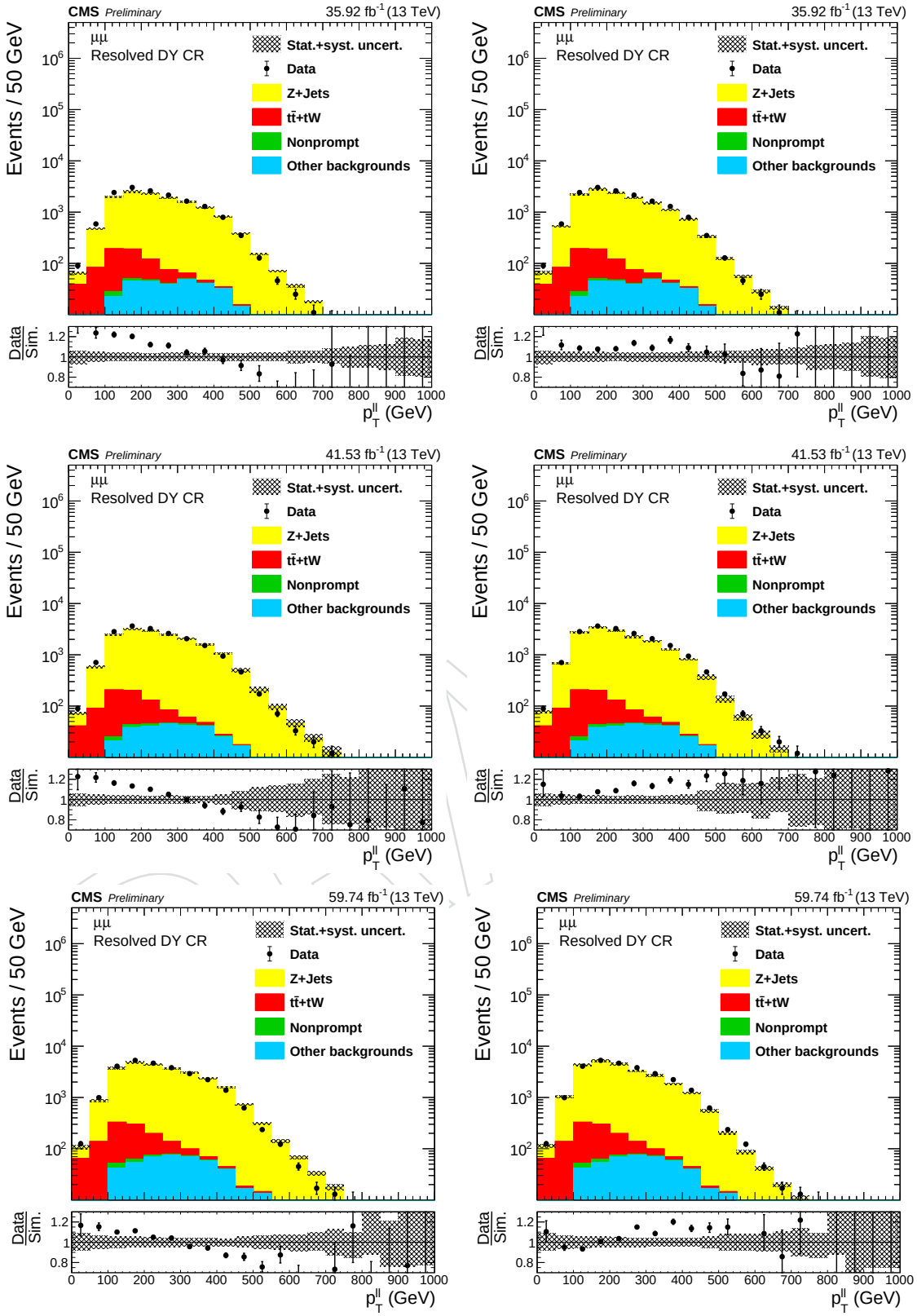

Figure 16: The p_{T} of dilepton in the low $m_{\ell\ell}$ resolved control regions, before (left) and after (right) applying the Z-p_{T} correction. Results for dimuon channel is shown for 2016 (upper), 2017 (middle) and 2018 (lower).

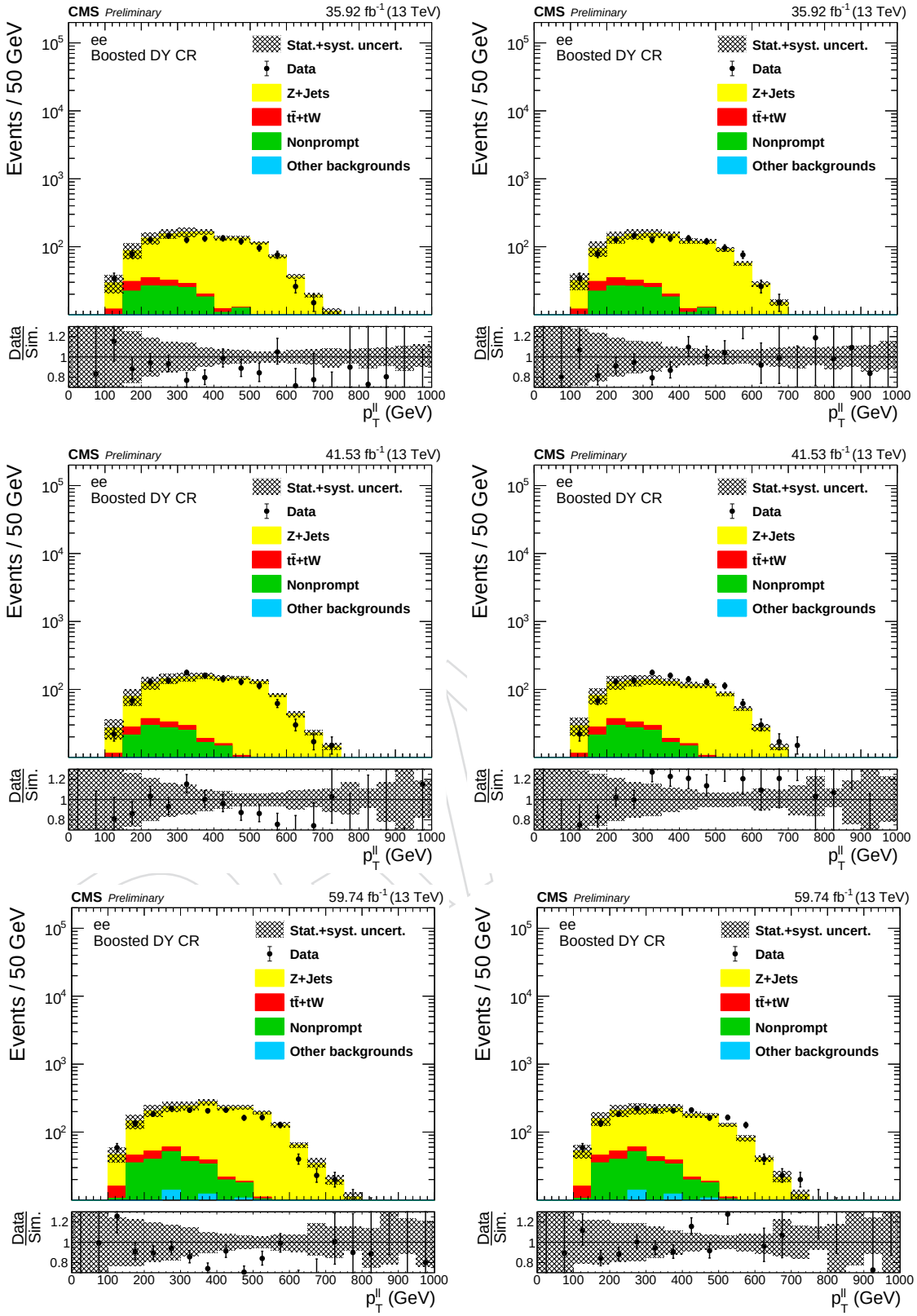

Figure 17: The p_{T} of dilepton in the low $m_{\ell\ell}$ boosted control regions, before (left) and after (right) applying the Z-p_{T} correction. Results for dielectron channel is shown for 2016 (upper), 2017 (middle) and 2018 (lower).

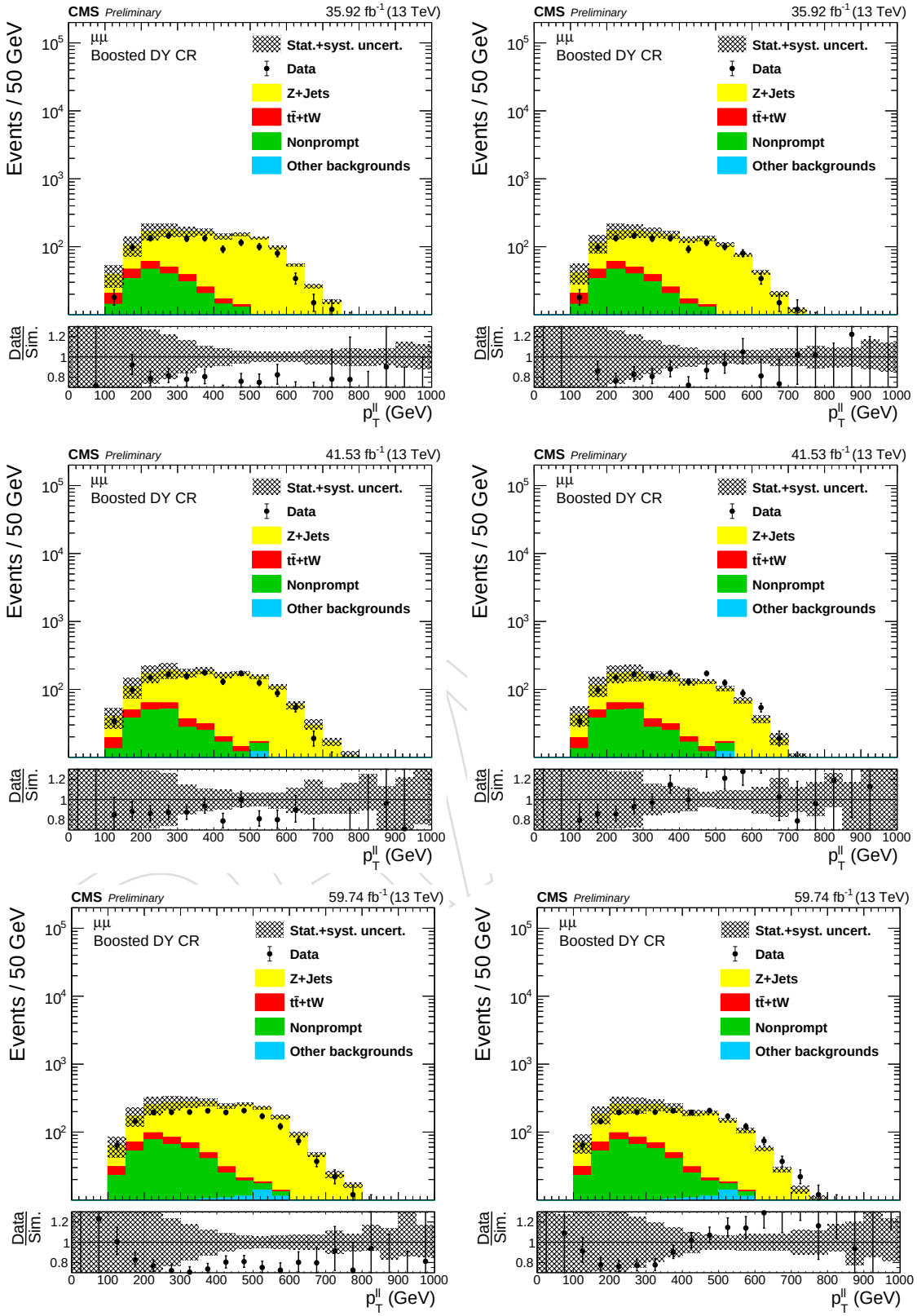

Figure 18: The p_{T} of dilepton in the low $m_{\ell\ell}$ boosted control regions, before (left) and after (right) applying the Z-p_{T} correction. Results for dimuon channel is shown for 2016 (upper), 2017 (middle) and 2018 (lower).

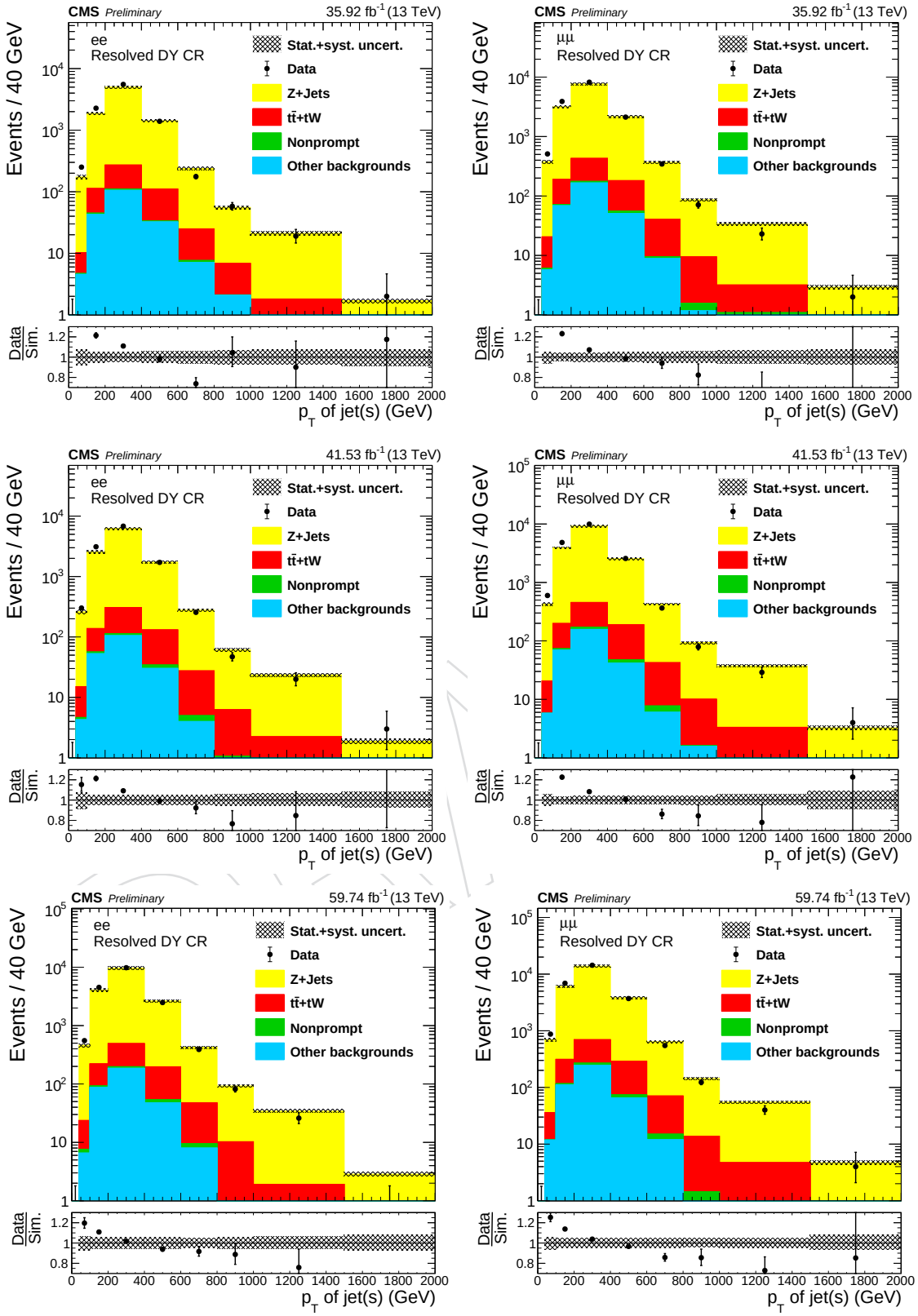

Figure 19: The p_T of the leading AK4 jet in the resolved DY CRs for eacah year; 2016 (top), 2017 (middle), and 2018 (bottom), before applying the jet-p_T reweighting. Results for dielectron (dimuon) channel is shown on the left (right).

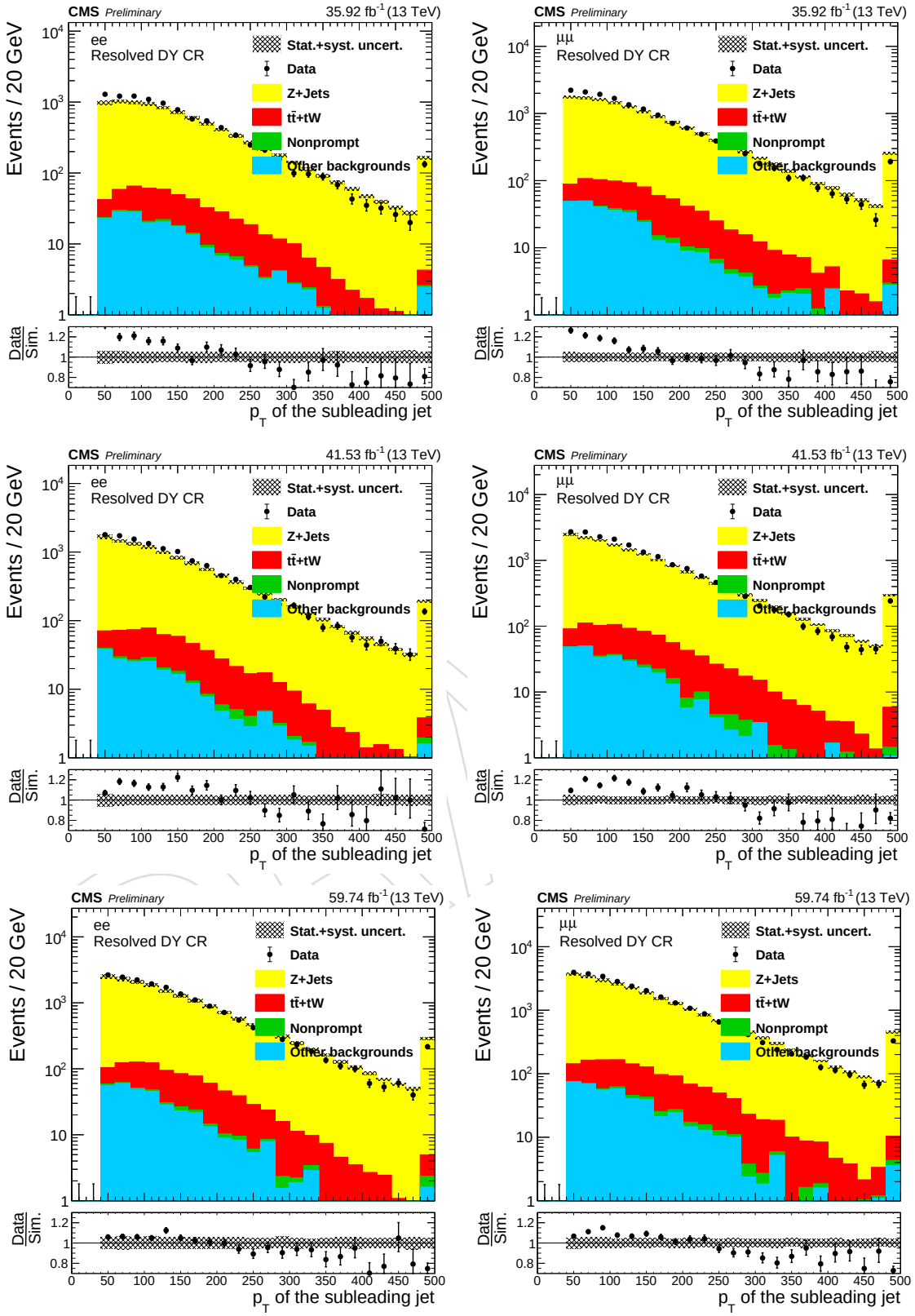

Figure 20: The p_{T} of the subleading AK4 jet in the resolved DY CRs for eacah year; 2016 (top), 2017 (middle), and 2018 (bottom), before applying the jet-p_{T} reweighting. Results for dielectron (dimuon) channel is shown on the left (right).

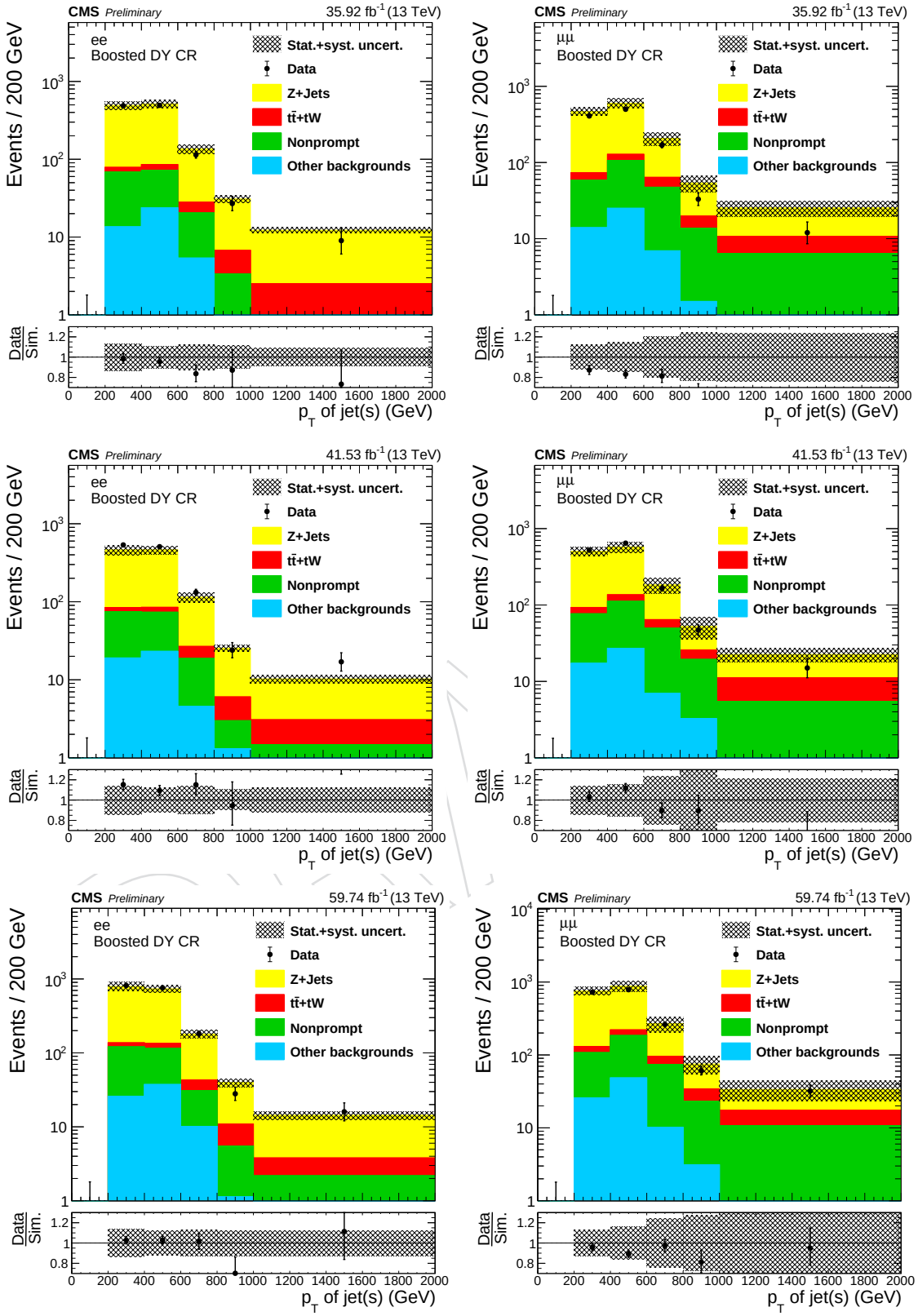

Figure 21: The p_{T} of the leading AK8 jet in the resolved DY CRs for eacah year; 2016 (top), 2017 (middle), and 2018 (bottom), before applying the jet-p_{T} reweighting. Results for dielectron (dimuon) channel is shown on the left (right).

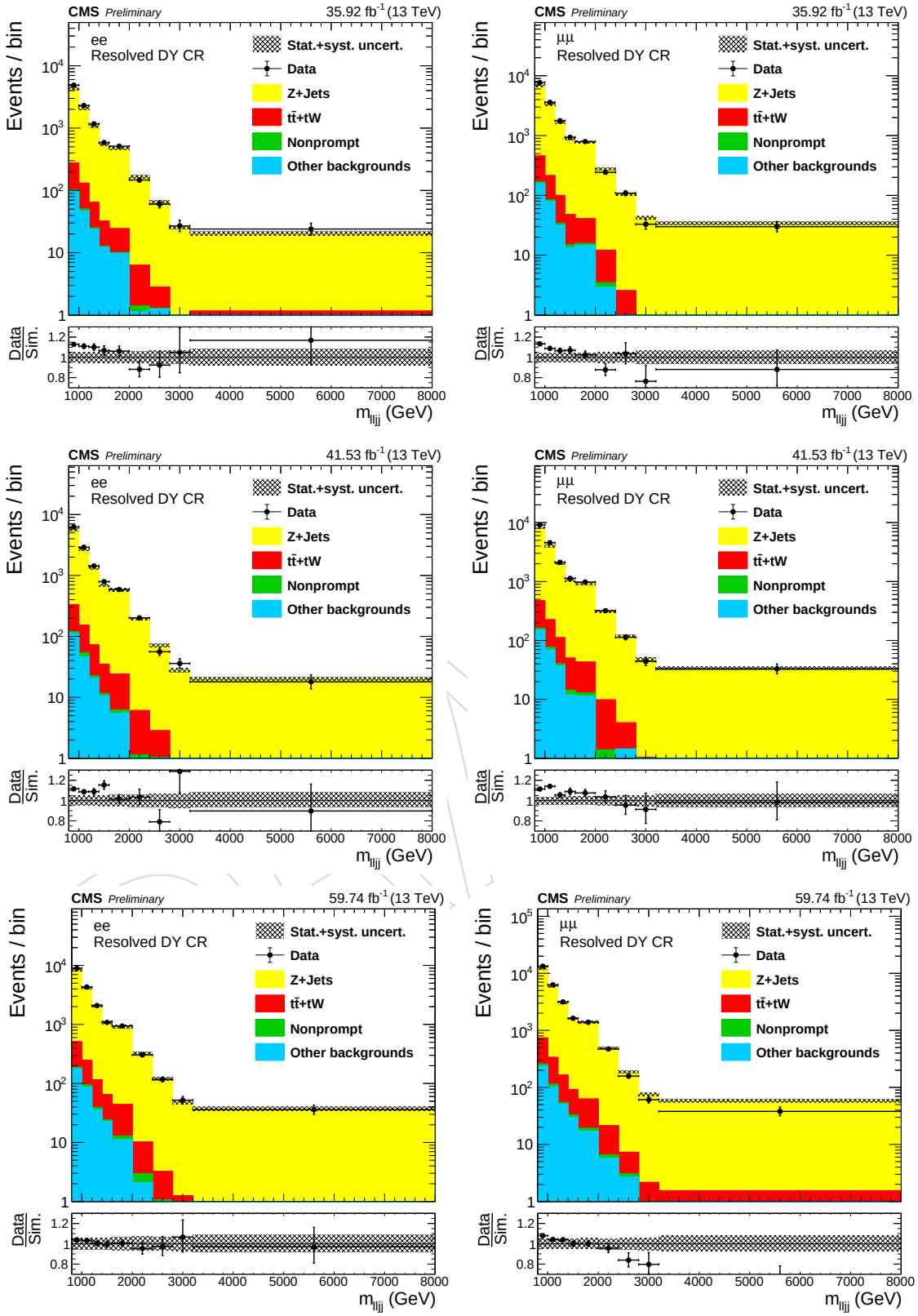

Figure 22: The $m(\ell\ell\mathrm{jj})$ in the low $m_{\ell\ell}$ resolved control regions, after applying the Z-p_{T} correction and the normalization scale factors. Results for dielectron (dimuon) channel is shown on the left (right), for 2016 (upper), 2017 (middle) and 2018 (lower).

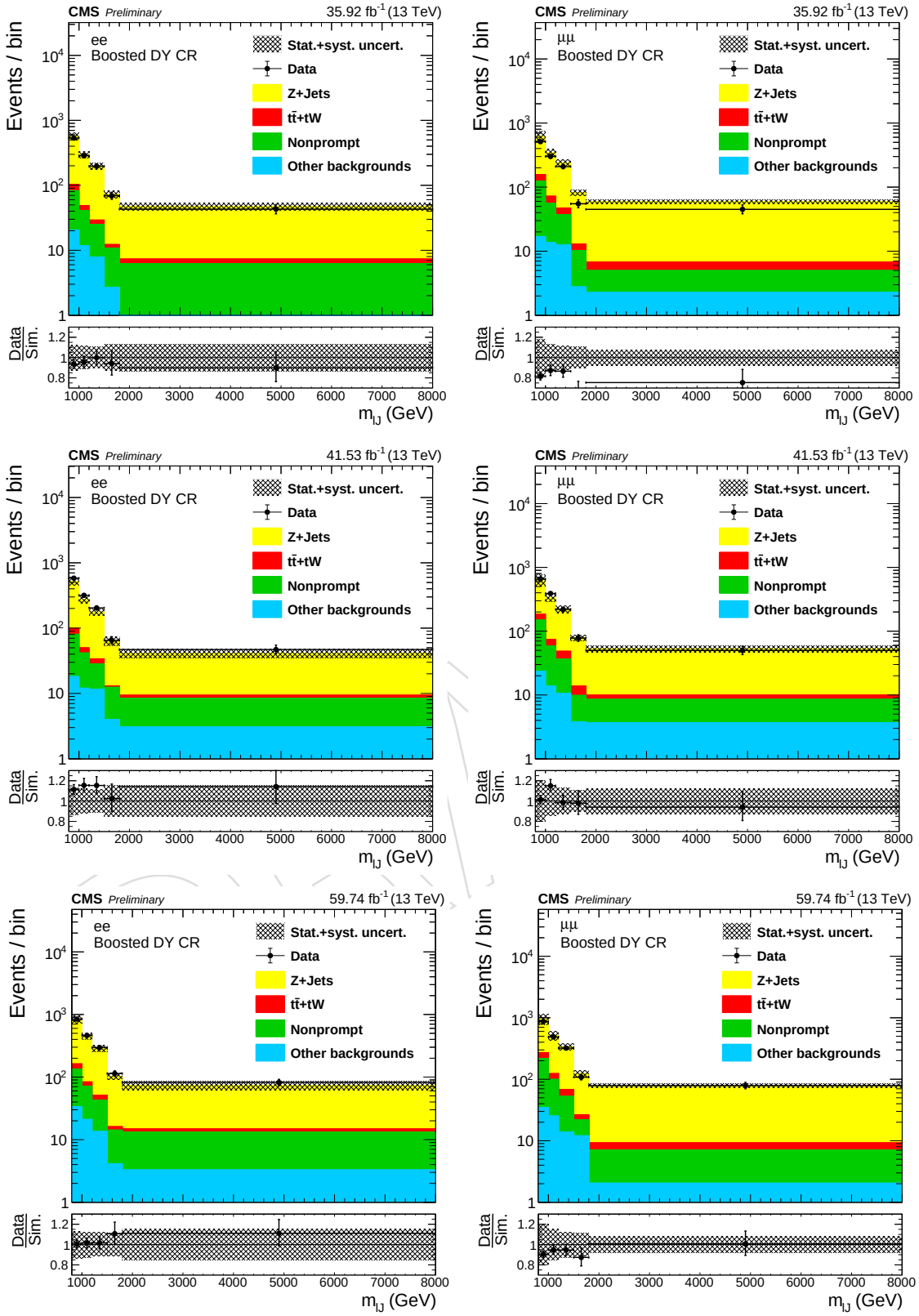

Figure 23: The $m(\ell \mathrm{J})$ of dilepton in the low $m_{\ell\ell}$ boosted control regions, after applying the Z-p_{T} correction and the normalization scale factors. Results for dielectron (dimuon) channel is shown on the left (right), for 2016 (upper), 2017 (middle) and 2018 (lower).

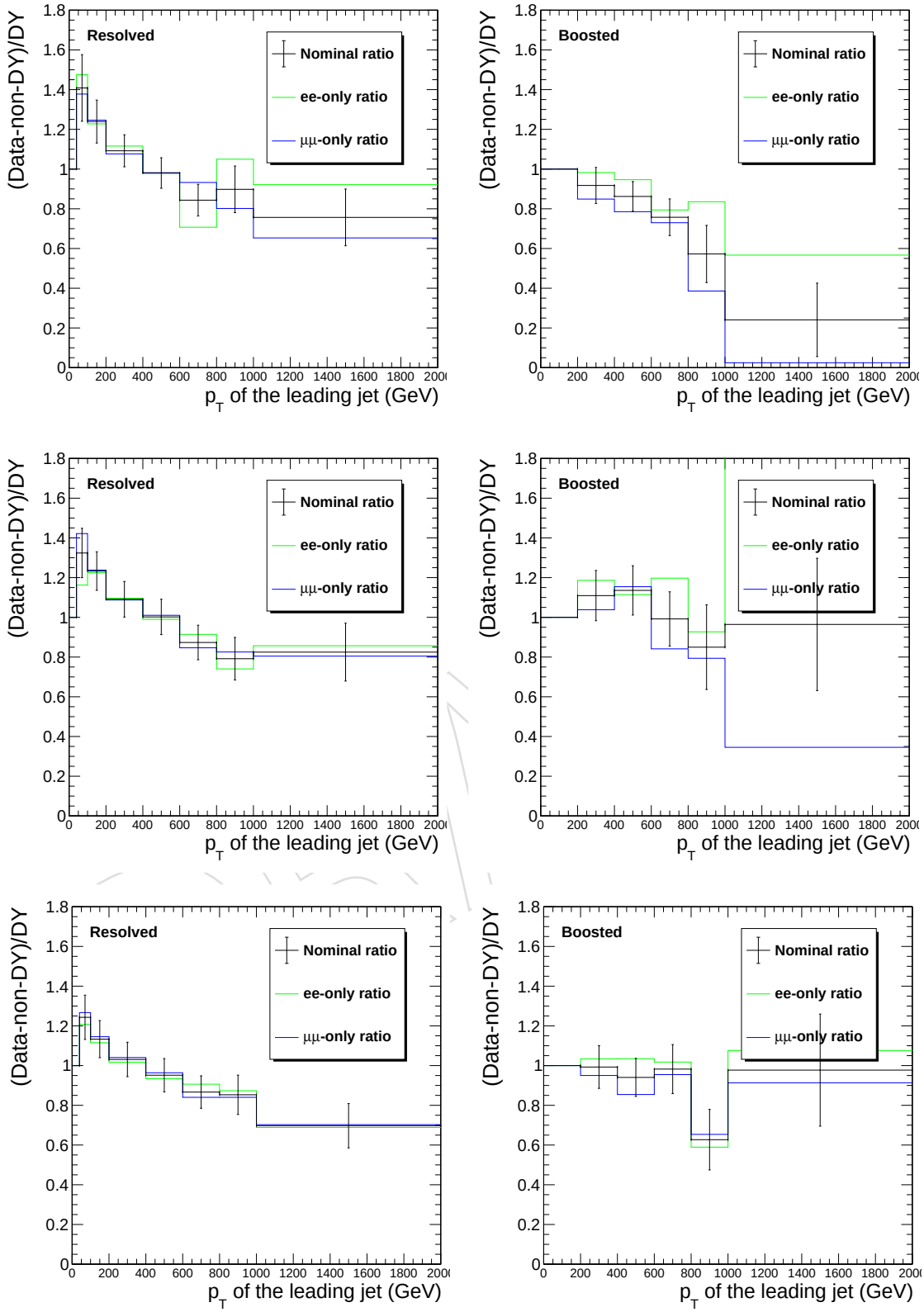

Figure 24: The (Data - nonDY)/(DY MC) obtained in the DY sidebands. The error bars in black solid line indicate the statistical and systematic uncertainties of the data and MCs propagated to the ratios. The green and blue solid lines are the ratios obtained using ee and $\mu\mu$ data, respectively.

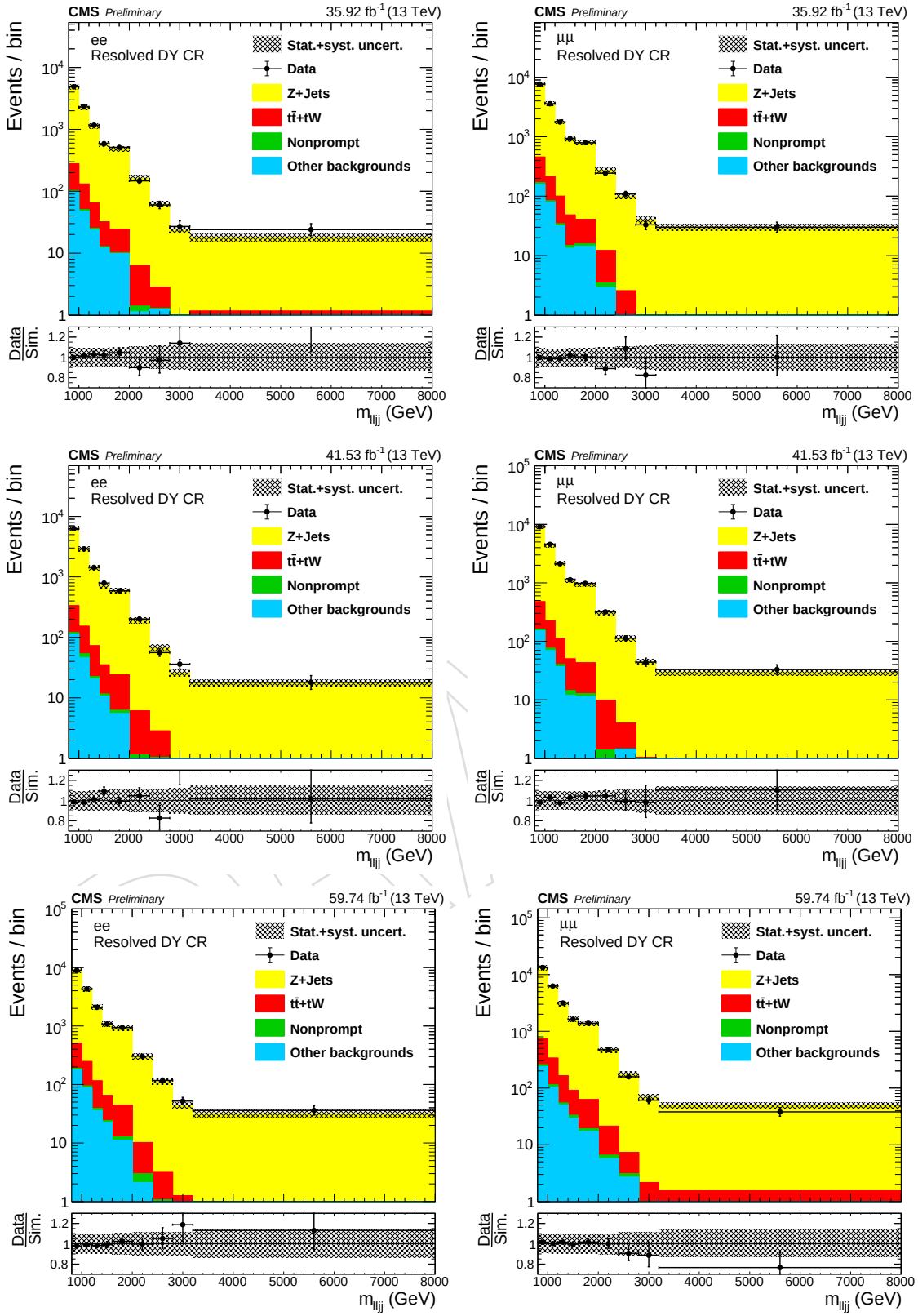

Figure 25: The $m(\ell\ell\mathrm{jj})$ in the low $m_{\ell\ell}$ Resolved control regions, after applying the DY ratio. Results for dielectron (dimuon) channel is shown on the left (right), for 2016 (upper), 2017 (middle) and 2018 (lower).

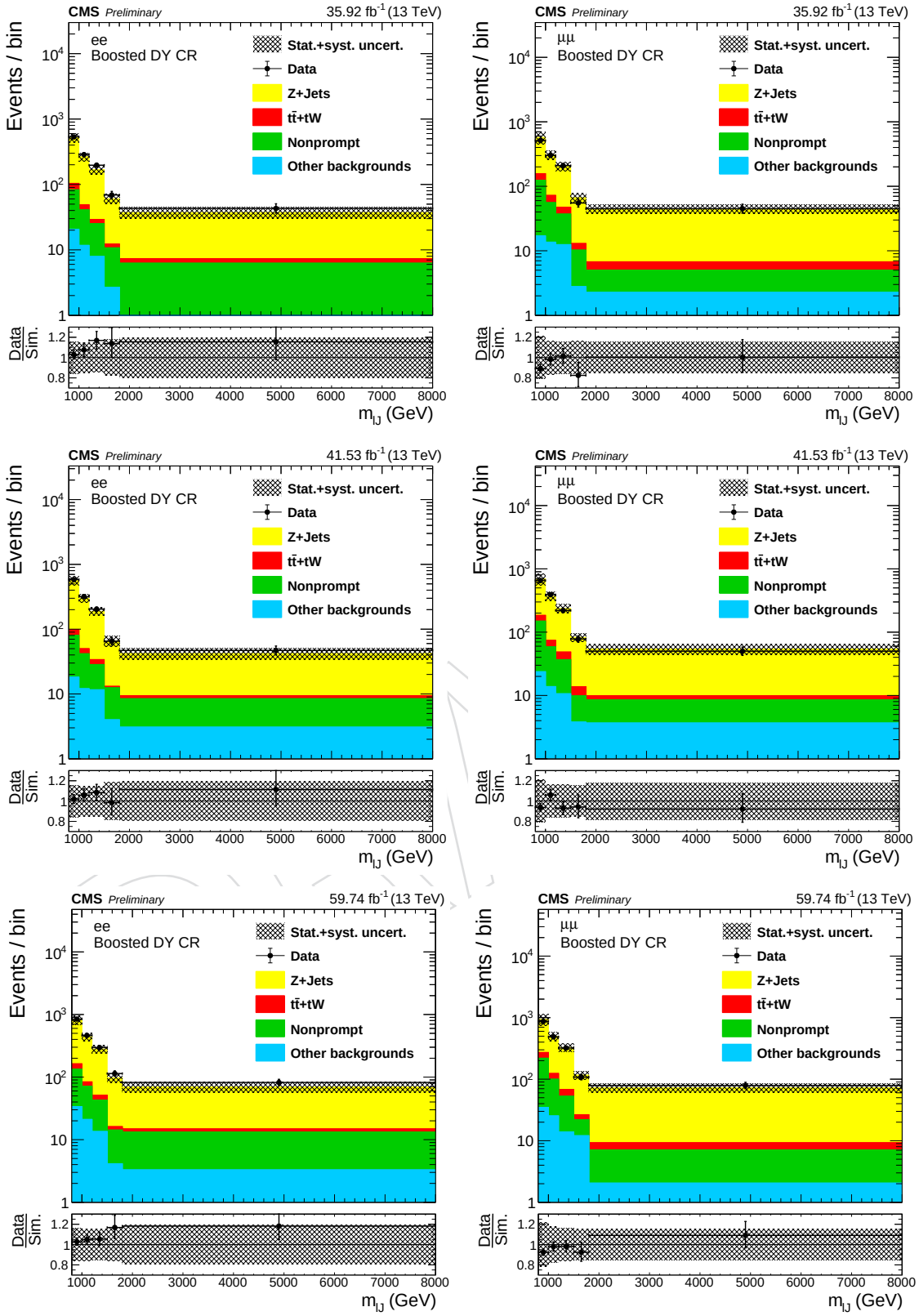

Figure 26: The $m(\ell \mathrm{J})$ of dilepton in the low $m_{\ell\ell}$ boosted control regions, after applying the DY ratio. Results for dielectron (dimuon) channel is shown on the left (right), for 2016 (upper), 2017 (middle) and 2018 (lower).

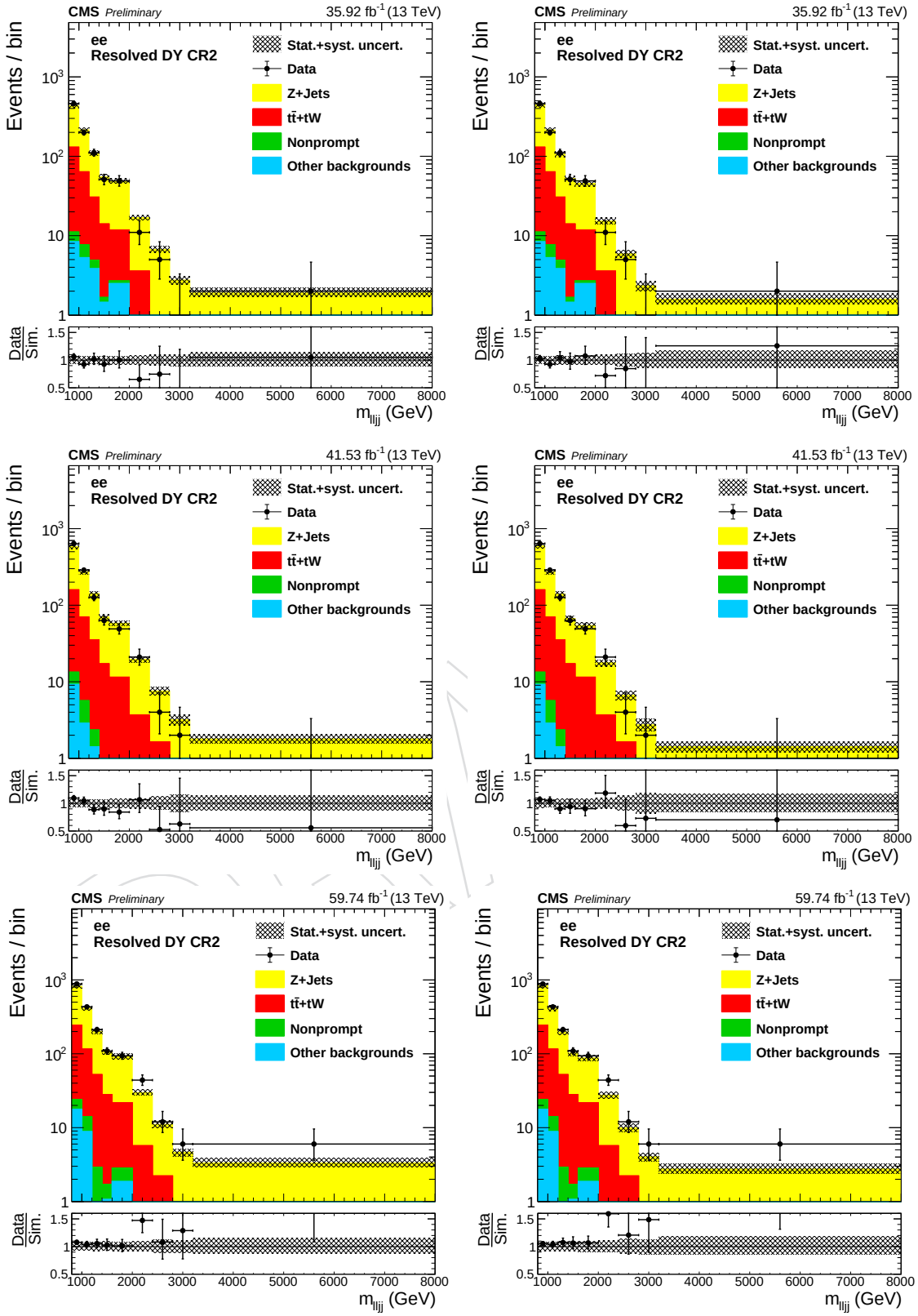

Figure 27: The $m(\ell\ell$jj$)$ in the resolved DY CR2, before (left) and after (right) applying the DY ratio obtained in the DY CR1. Results for dielectron channel is shown, for 2016 (upper), 2017 (middle) and 2018 (lower).

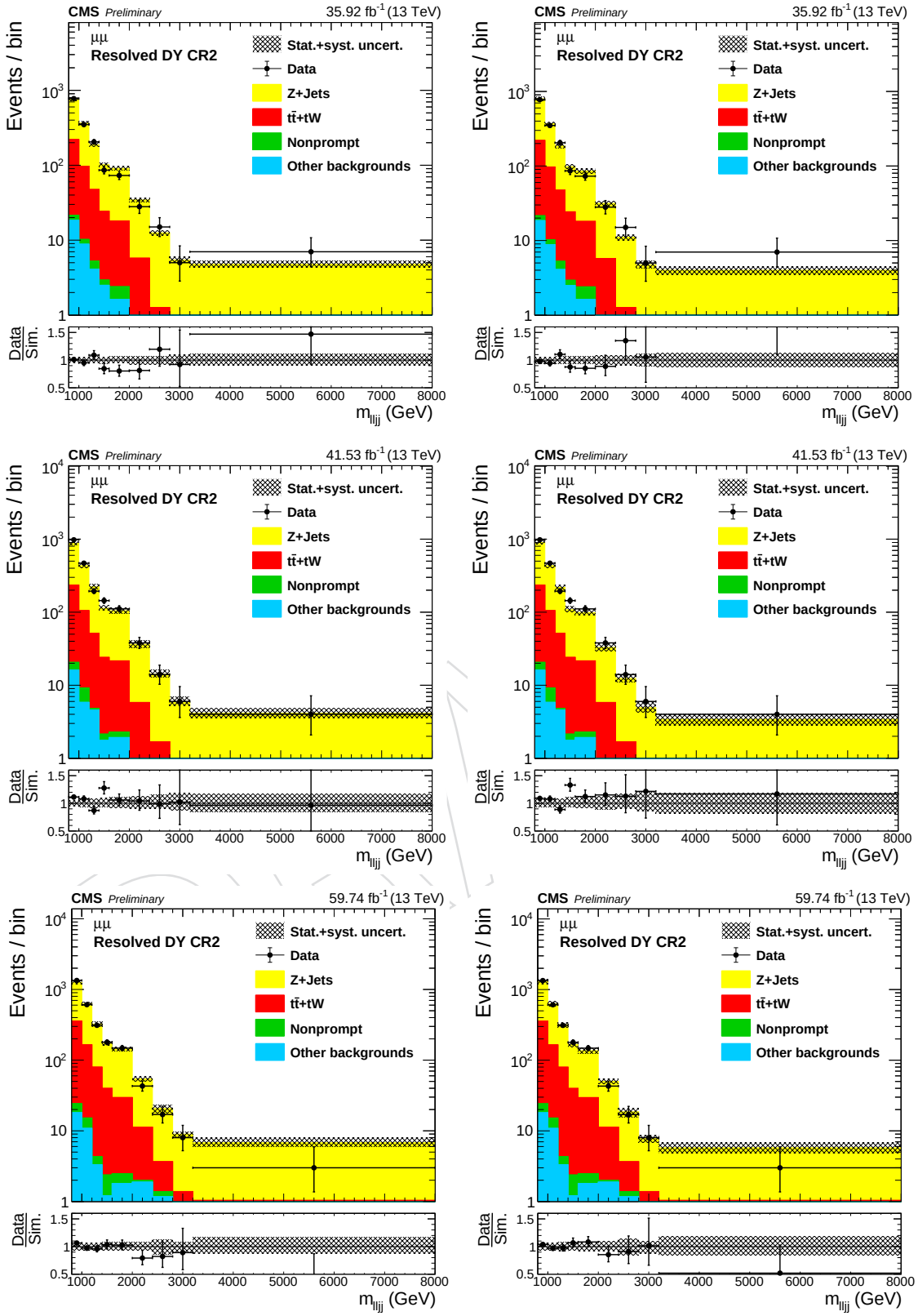

Figure 28: The $m(\ell\ell jj)$ in the resolved DY CR2, before (left) and after (right) applying the DY ratio obtained in the DY CR1. Results for dimuon channel is shown, for 2016 (upper), 2017 (middle) and 2018 (lower).

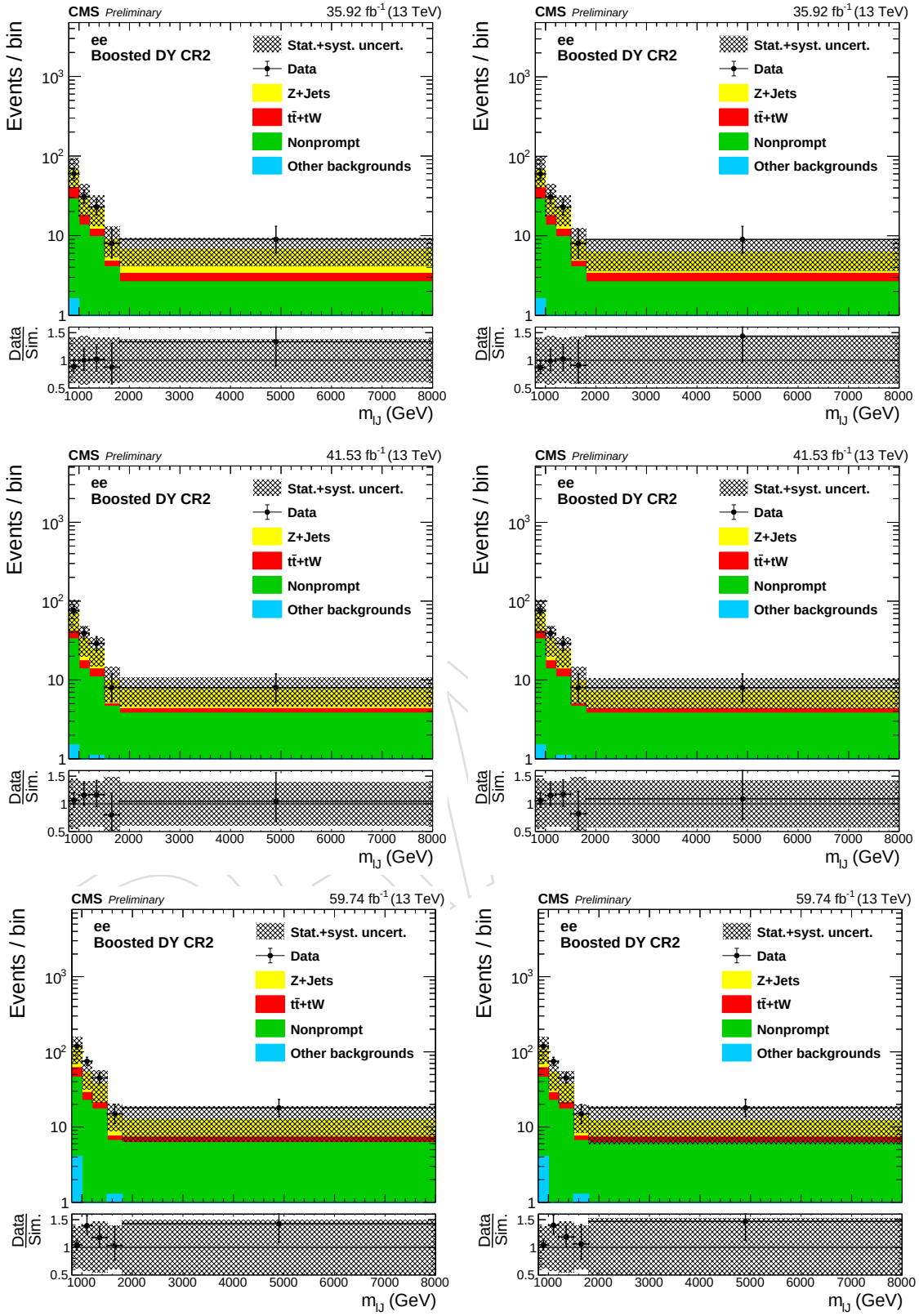

Figure 29: The $m(\ell\ell\mathrm{jj})$ in the boosted DY CR2, before (left) and after (right) applying the DY ratio obtained in the DY CR1. Results for dielectron channel is shown, for 2016 (upper), 2017 (middle) and 2018 (lower).

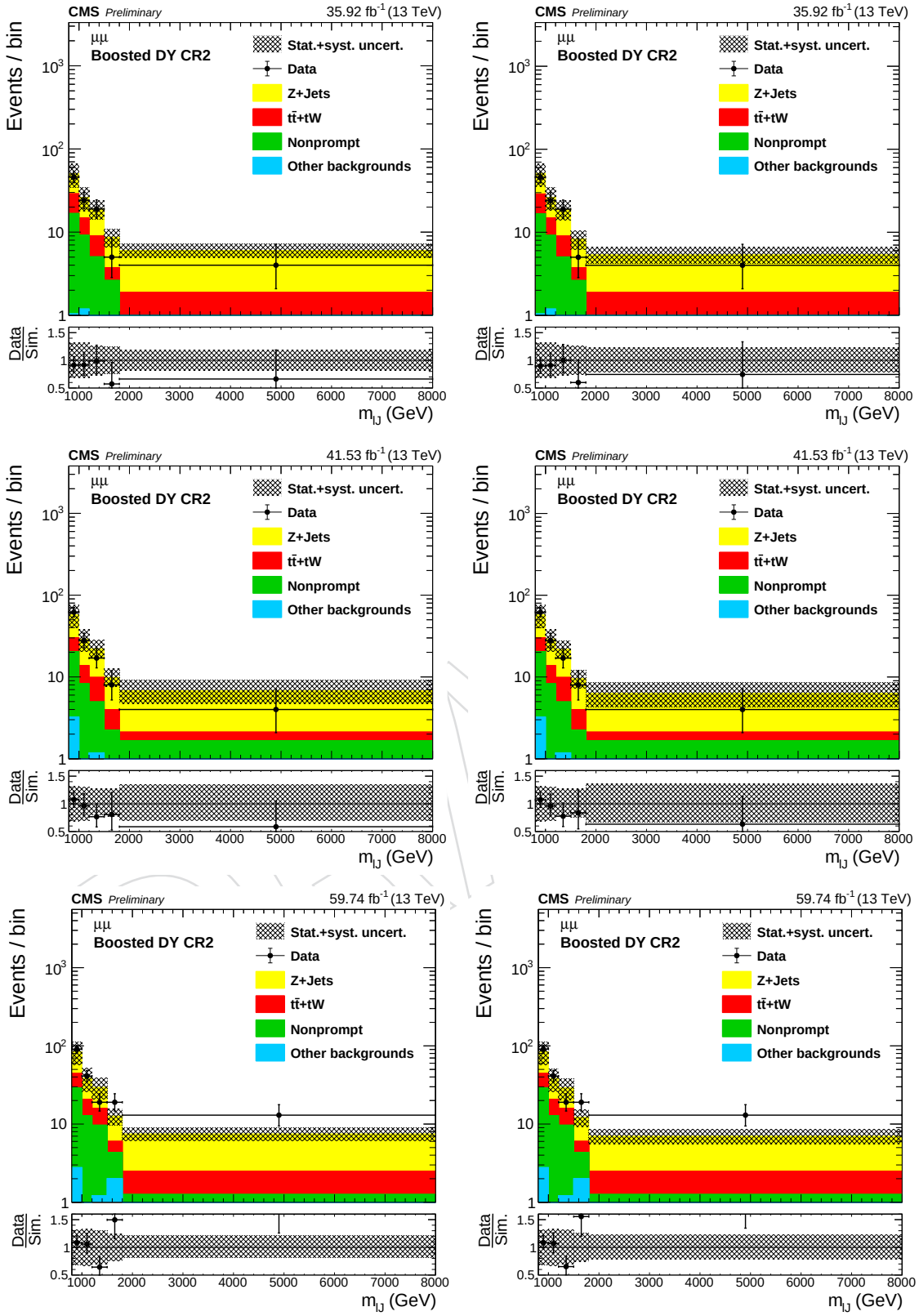

Figure 30: The $m(\ell\ell\mathrm{jj})$ in the boosted DY CR2, before (left) and after (right) applying the DY ratio obtained in the DY CR1. Results for dimuon channel is shown, for 2016 (upper), 2017 (middle) and 2018 (lower).

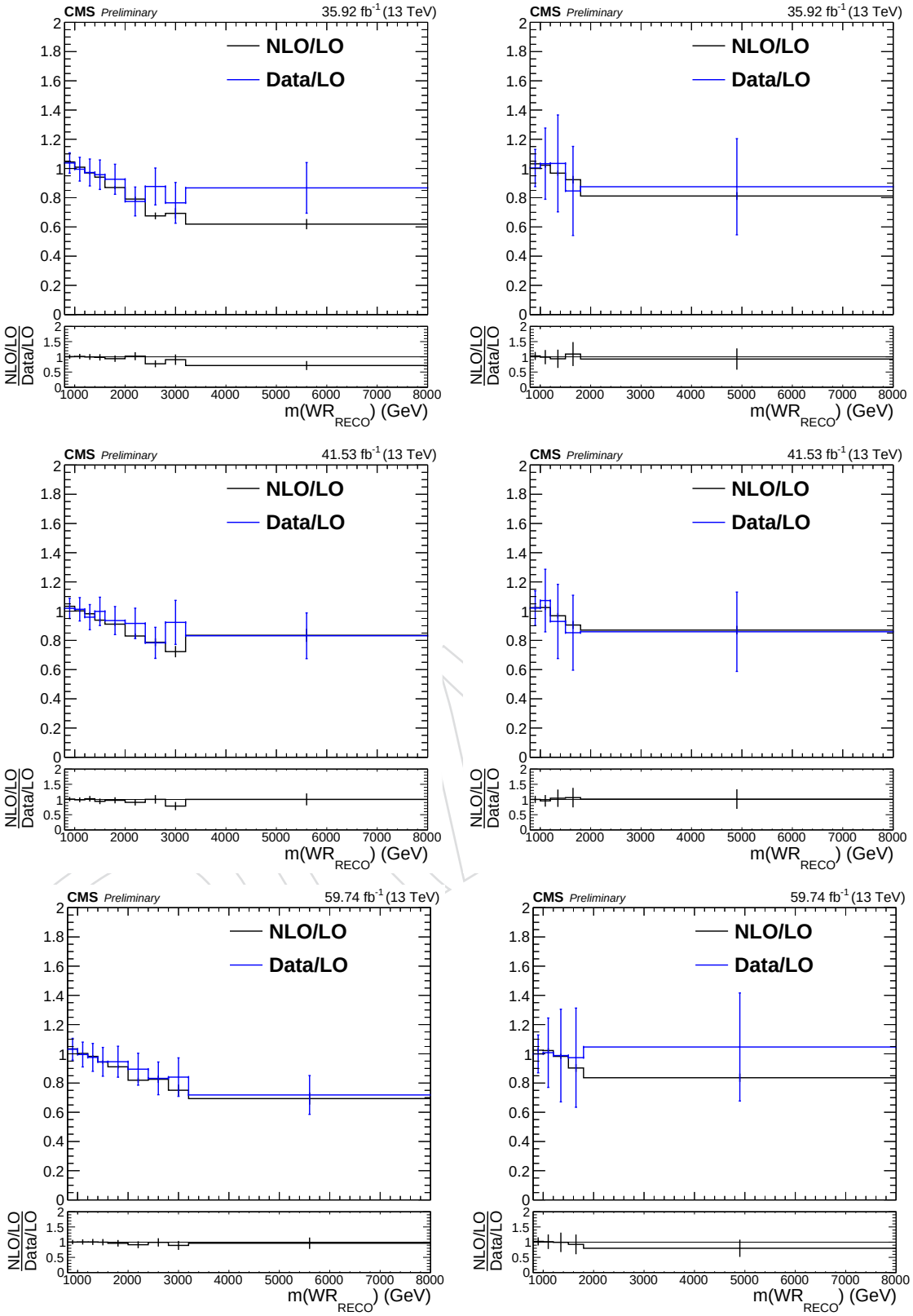

Figure 31: The comparison between NLO/LO (black solide line) and Data/LO (blue solid line) at the DY CRs.

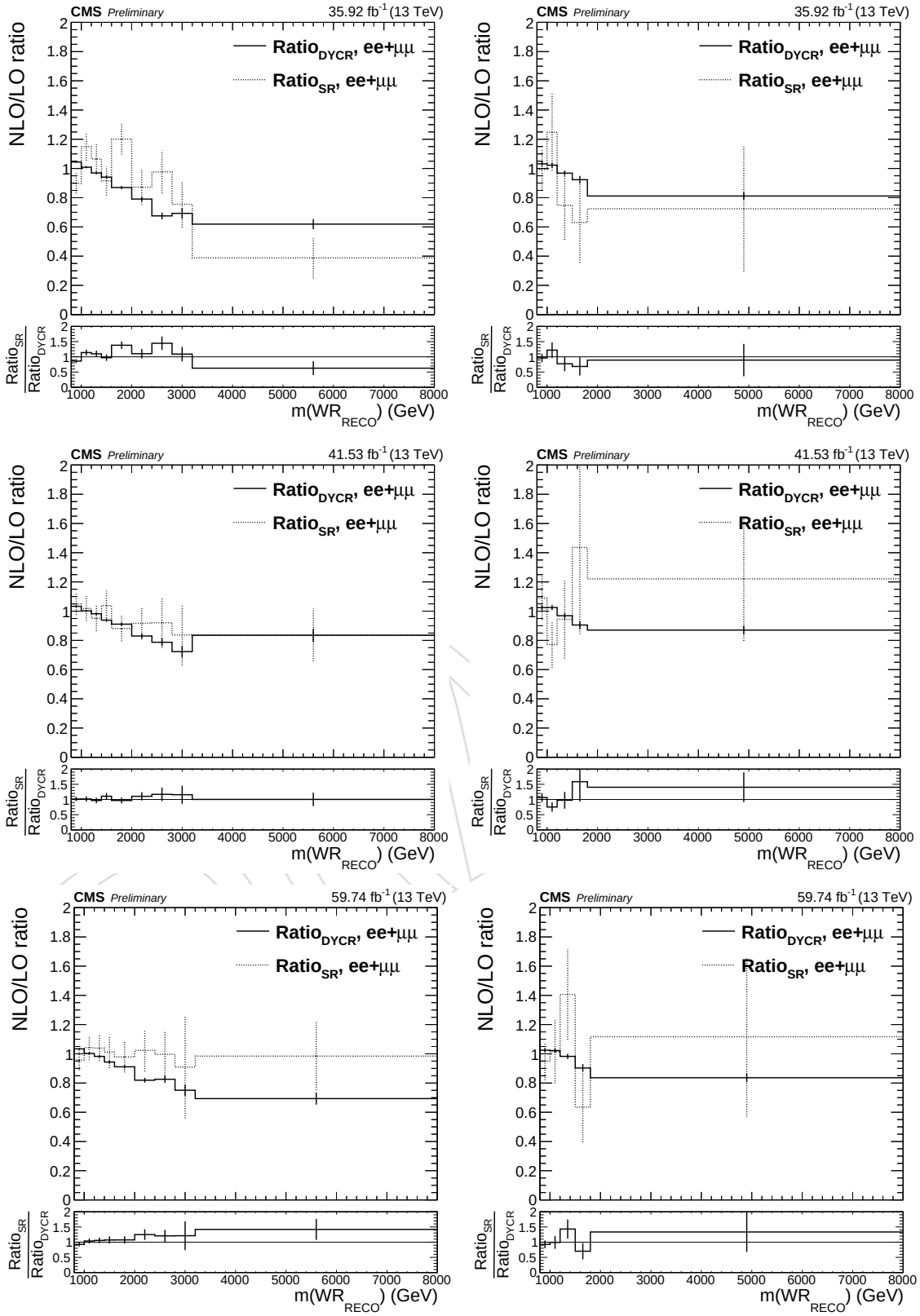

Figure 32: The DY NLO/LO ratios in the DY CR and SR. The ratios obtained from the DY CR (SR) is shown in the black solid (dashed) lines.

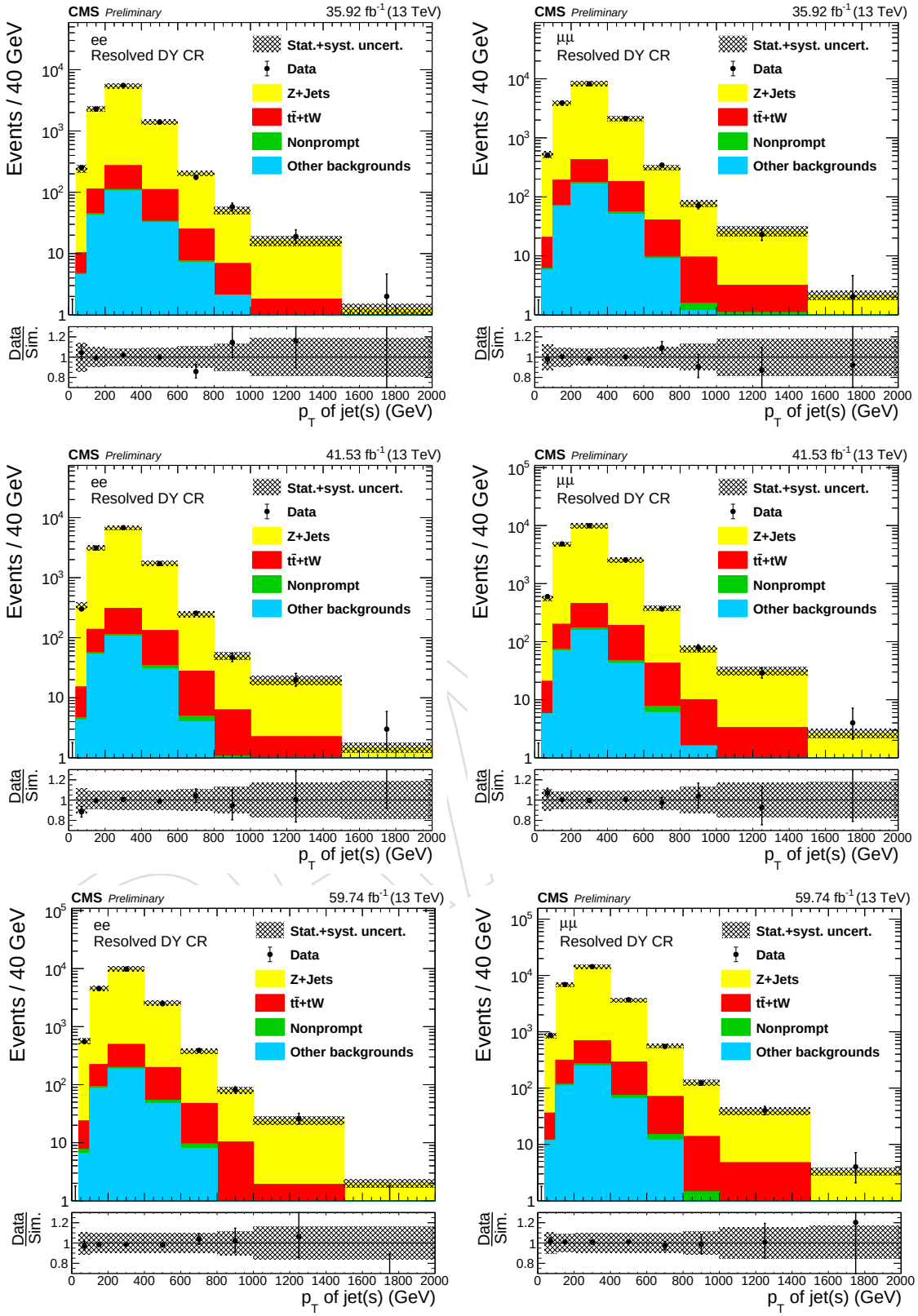

Figure 33: The p_T of the leading AK4 jet in the resolved DY CRs for eacah year; 2016 (top), 2017 (middle), and 2018 (bottom), after applying the jet-p_T reweighting. Results for dielectron (dimuon) channel is shown on the left (right).

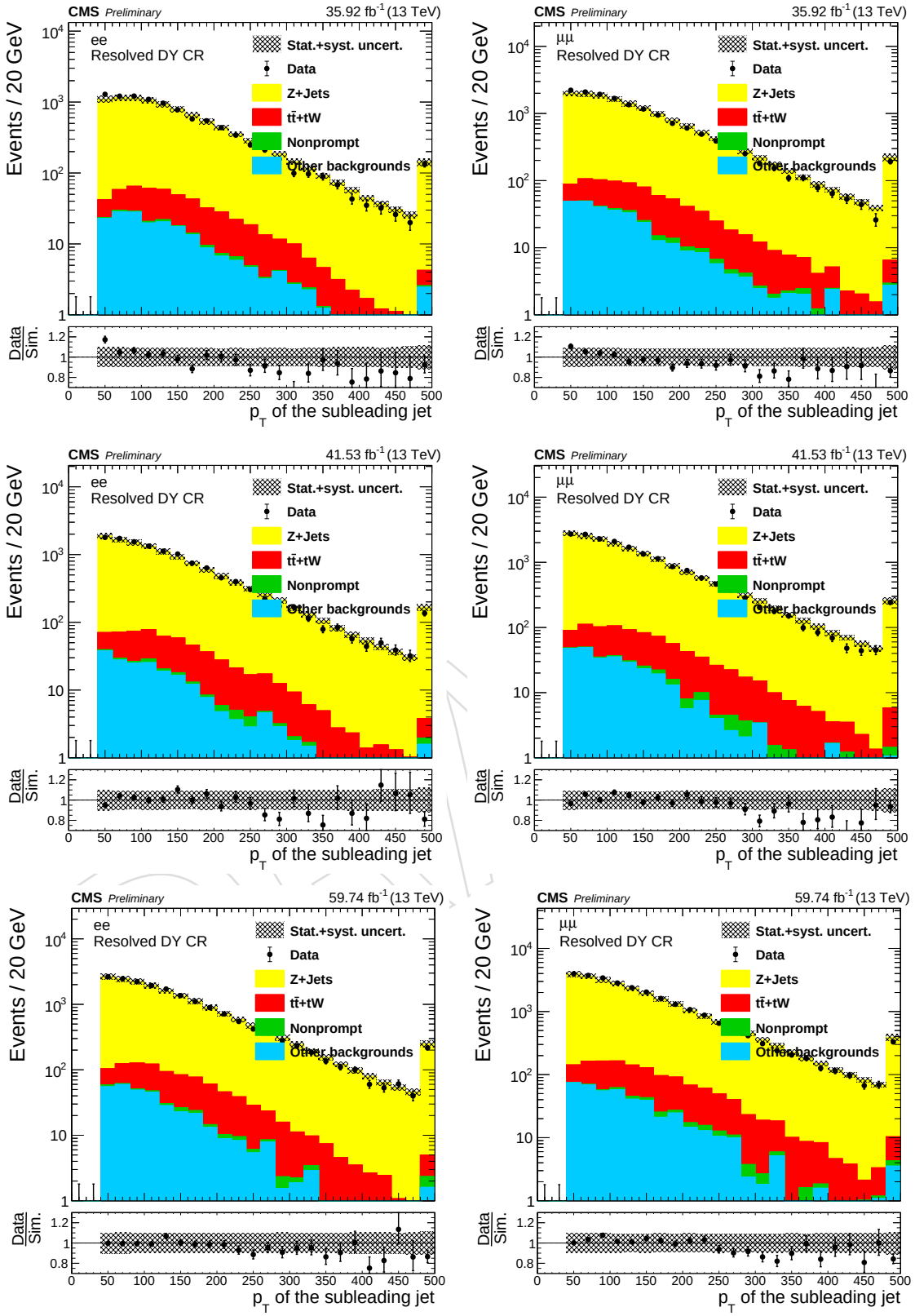

Figure 34: The p_{T} of the subleading AK4 jet in the resolved DY CRs for eacah year; 2016 (top), 2017 (middle), and 2018 (bottom), after applying the jet-p_{T} reweighting. Results for dielectron (dimuon) channel is shown on the left (right).

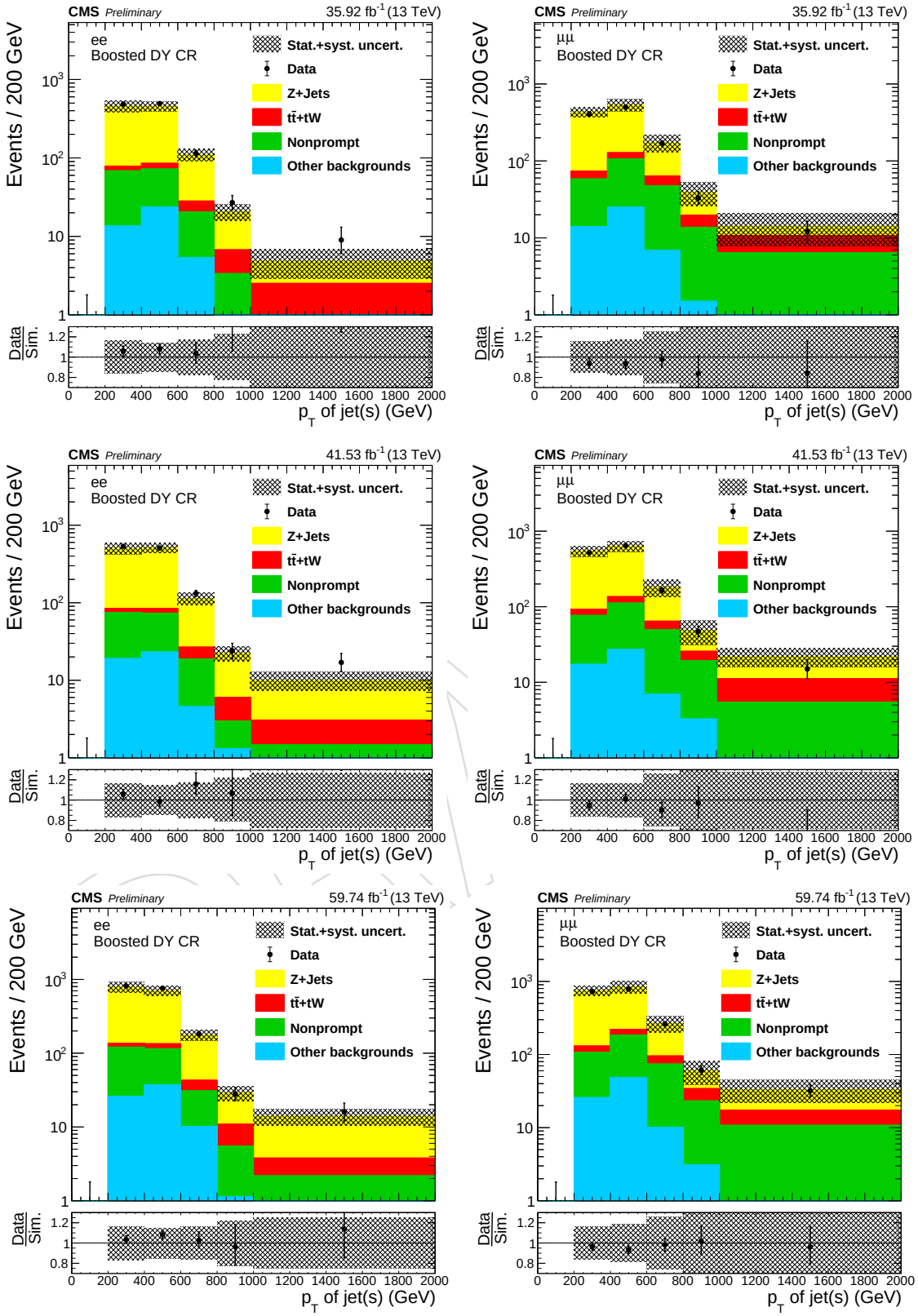

Figure 35: The p_{T} of the leading AK8 jet in the resolved DY CRs for eacah year; 2016 (top), 2017 (middle), and 2018 (bottom), after applying the jet-p_{T} reweighting. Results for dielectron (dimuon) channel is shown on the left (right).

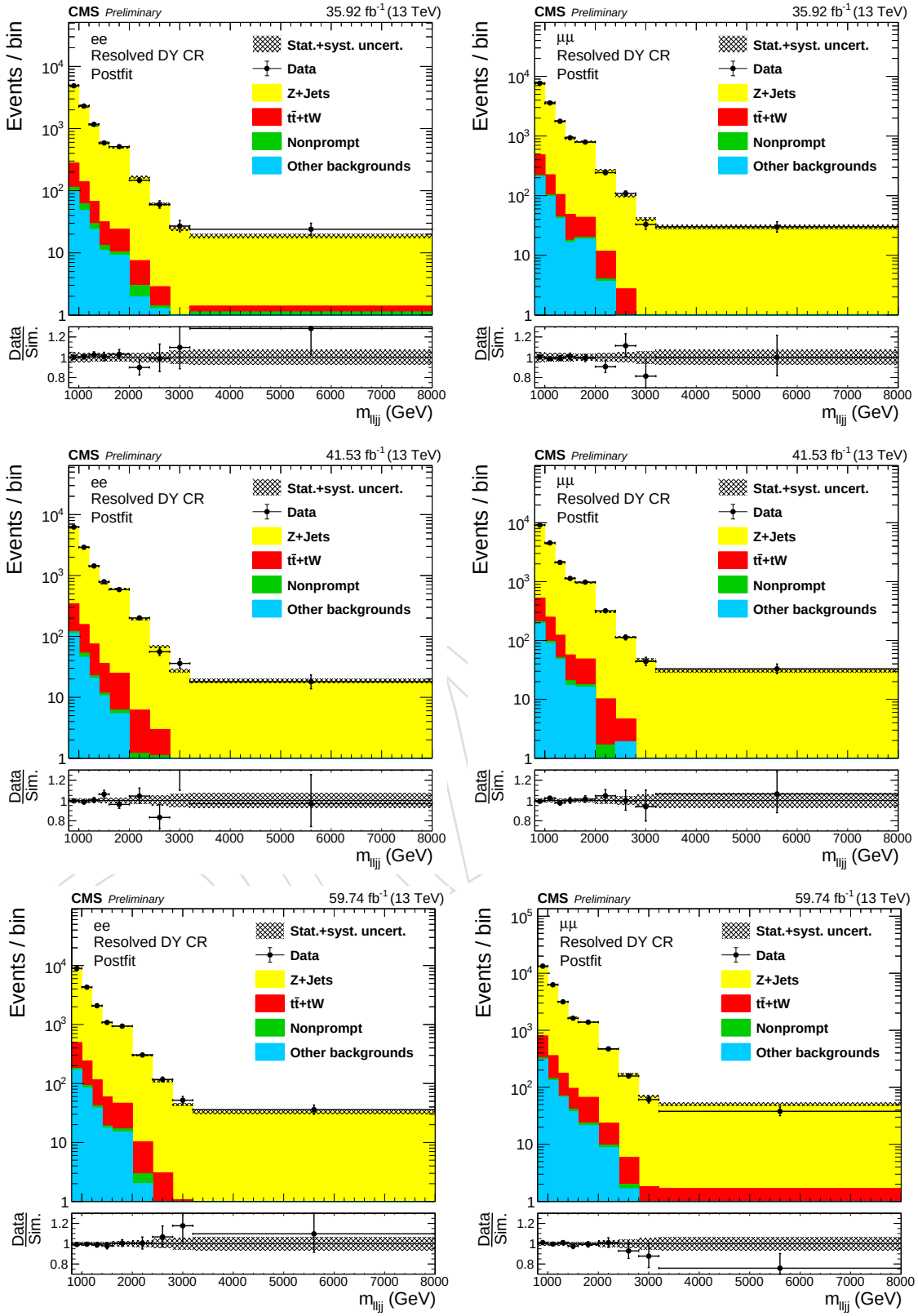

Figure 36: The postfit $m(\ell\ell$jj$)$ in the resolved DY CRs for eacah year; 2016 (top), 2017 (middle), and 2018 (bottom). Results for dielectron (dimuon) channel is shown on the left (right).

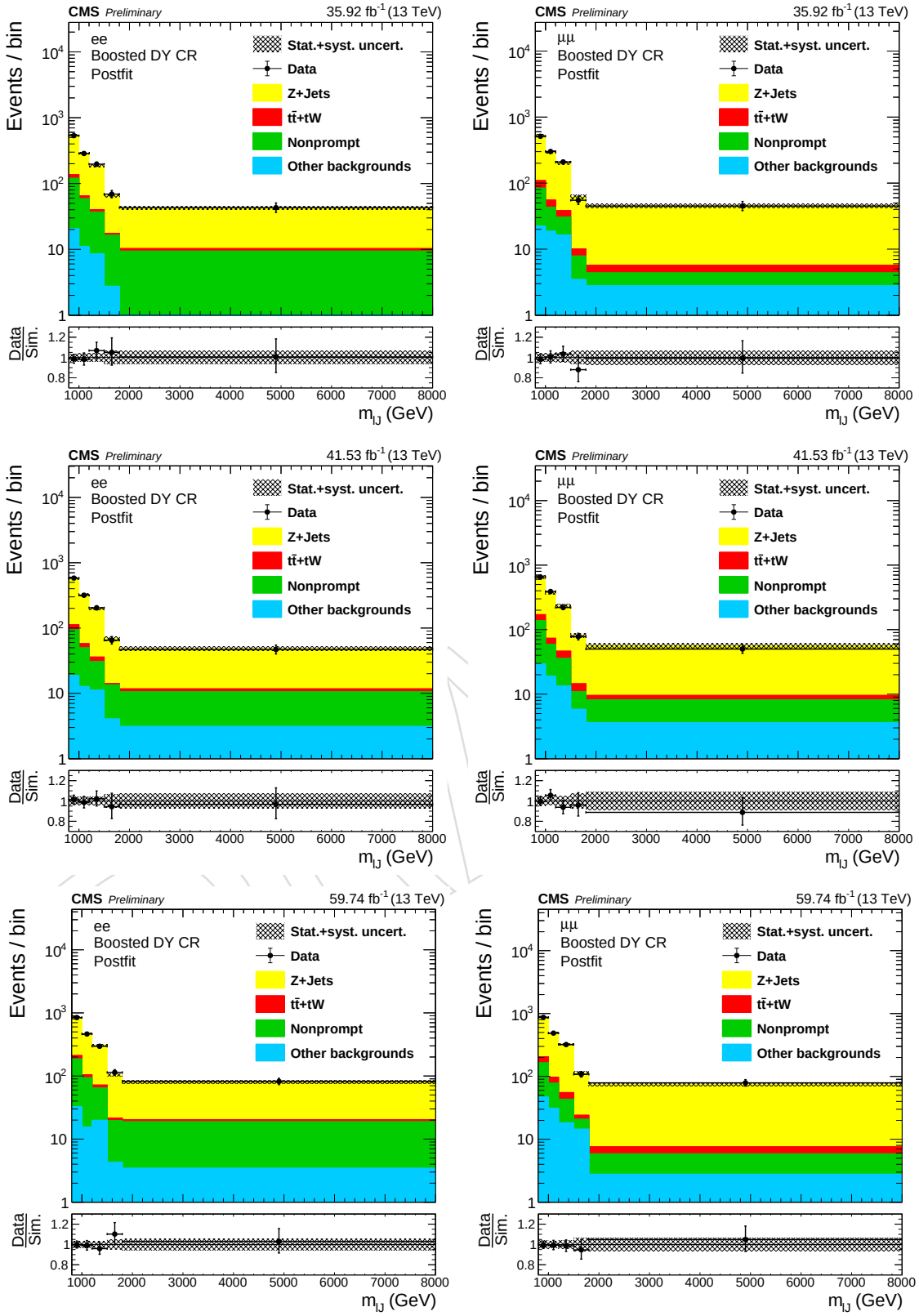

Figure 37: The postfit $m(\ell\ell\text{jj})$ in the boosted DY CRs for eacah year; 2016 (top), 2017 (middle), and 2018 (bottom). Results for dielectron (dimuon) channel is shown on the left (right).

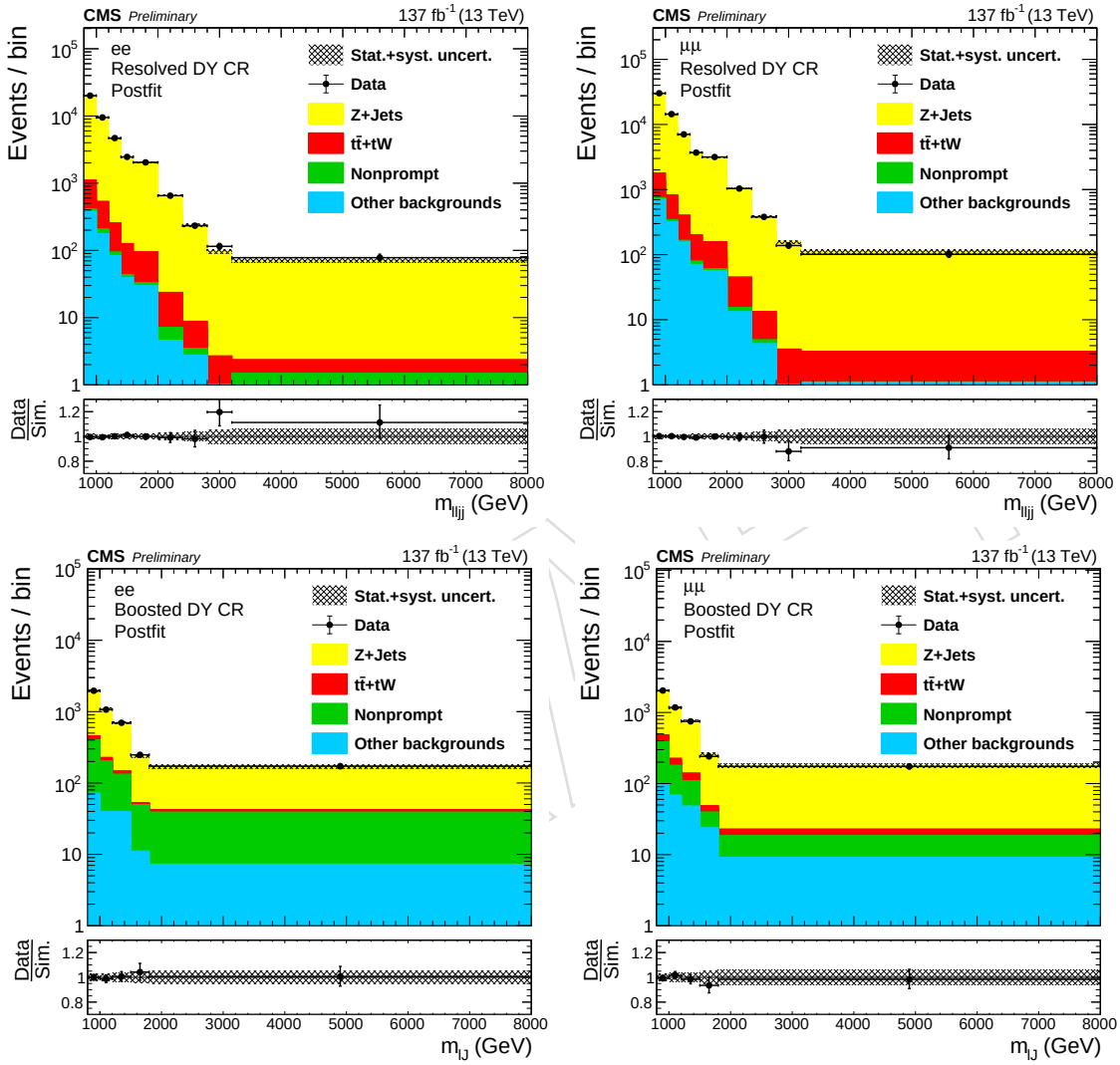

Figure 38: The postfit $m(\ell\ell\mathrm{jj})$ and $m(\ell\mathrm{J})$ in the DY CRs with three years stacked. Results for di-electron (dimuon) channel is shown on the left (right), for resolved (upper) and boosted (lower).

5.2 ttbar+jets and single top+W background estimation

In the previous iteration of the analysis, $t\bar{t}$ contributions in the SRs were estimated from the data events flavor sideband CR, weighted by the eμ–to–$\ell\ell$ ratio ("eμ-method"). In this analysis, we combine the $t\bar{t}$ and single top+W processes (eμ symmetric backgrounds) and use $t\bar{t}$ and single top+W MC and fit its normalization by performing the simulataneous fit with the flavor sideband CR and SRs, which helps contrain the uncertainties. The pre- and post-fit invariant mass distributions in the flavor sideband are shown in Figs. 39–42. The final fitted normalizations are listed in Table 20.

Table 20: The fitted rate parameter of $t\bar{t}$ and single top+W background.

Year	Event type	Fitted with ee SRs	Fitted with $\mu\mu$ SRs
2016	Resolved	0.96 ± 0.05	0.93 ± 0.05
	Boosted with e-Jet	0.79 ± 0.14	0.78 ± 0.14
	Boosted with μ-Jet	0.79 ± 0.09	0.77 ± 0.08
2017	Resolved	1.04 ± 0.05	1.02 ± 0.05
	Boosted with e-Jet	0.98 ± 0.18	0.85 ± 0.19
	Boosted with μ-Jet	0.96 ± 0.12	0.92 ± 0.12
2018	Resolved	1.00 ± 0.04	0.98 ± 0.04
	Boosted with e-Jet	0.87 ± 0.15	0.85 ± 0.15
	Boosted with μ-Jet	0.70 ± 0.08	0.79 ± 0.08

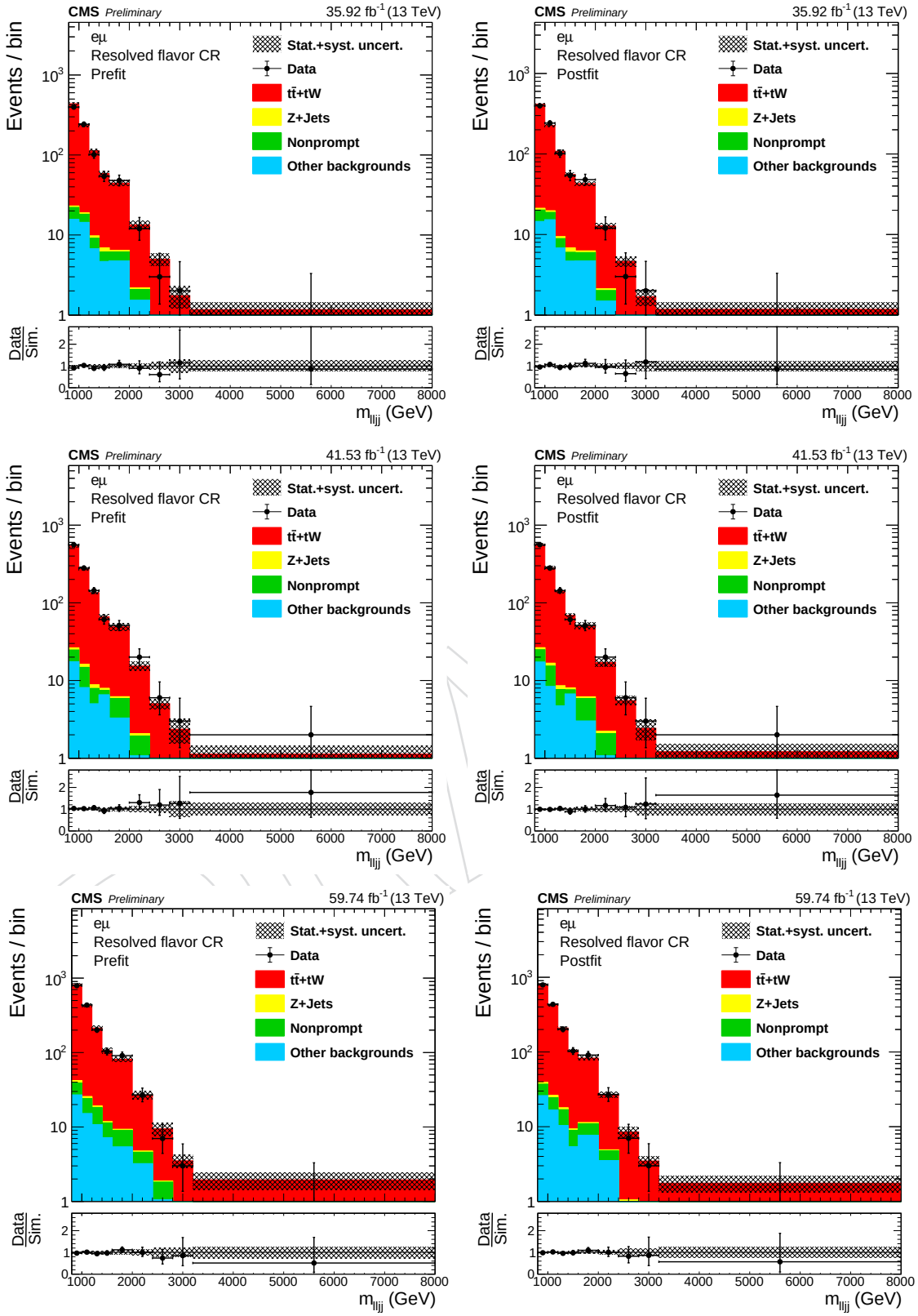

Figure 39: The reconstructed mass of W_R in the resolved flavor sideband, for 2016 (upper), 2017 (middle) and 2018 (lower). Pre(Post)fit results are shown in left (right).

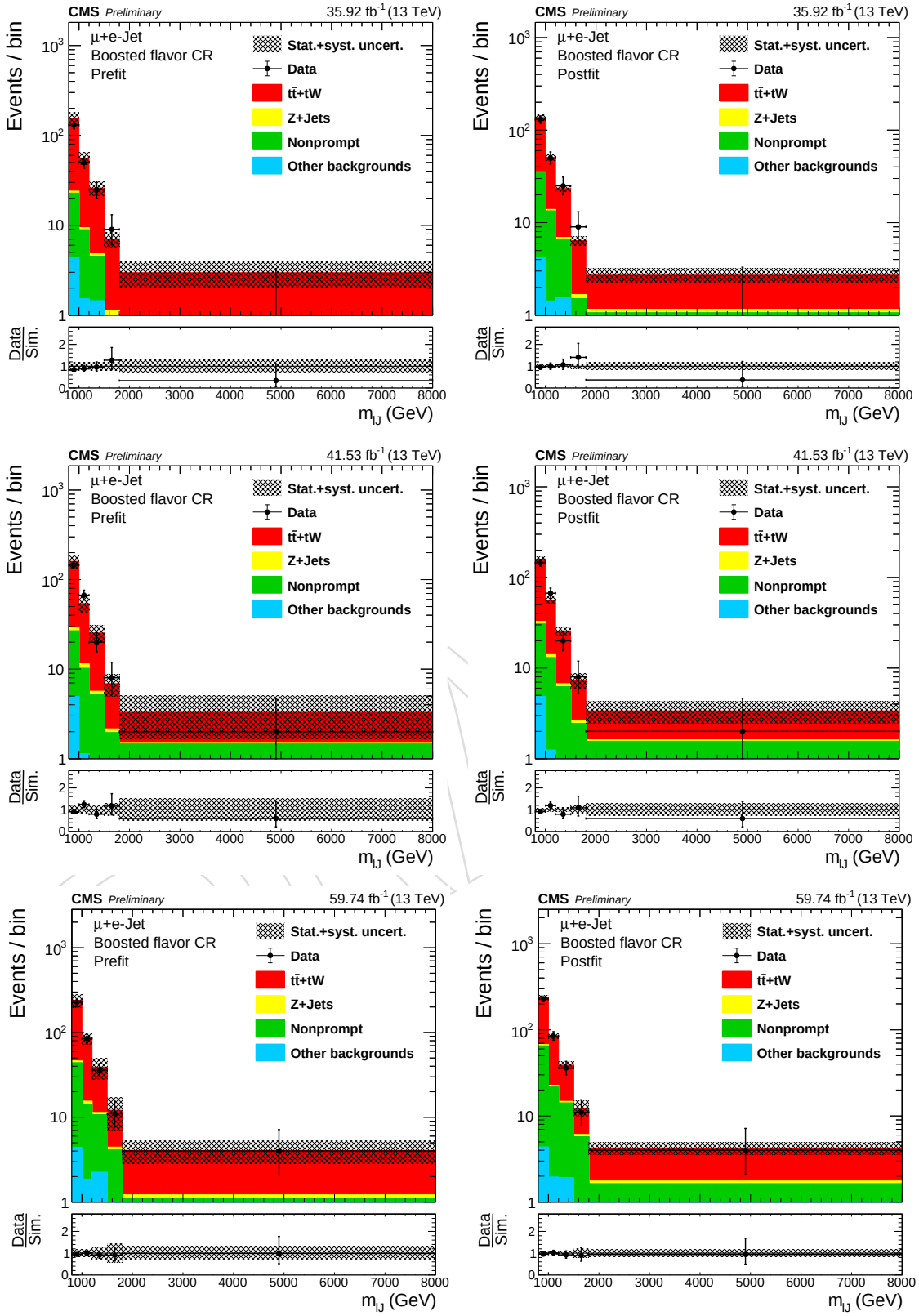

Figure 40: The reconstructed mass of W_R in the boosted flavor sideband with e–jet, for 2016 (upper), 2017 (middle) and 2018 (lower). Pre(Post)fit results are shown in left (right).

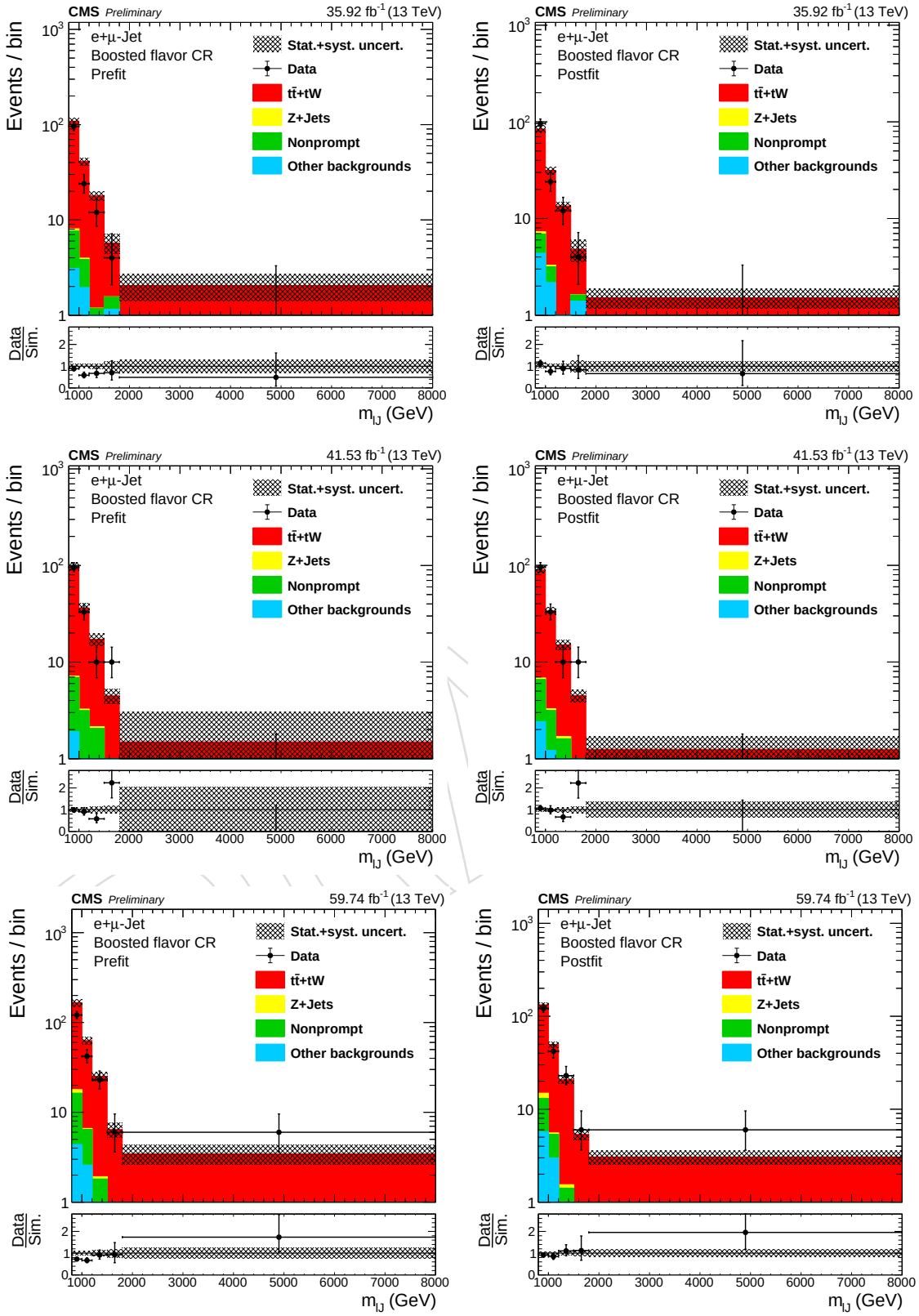

Figure 41: The reconstructed mass of W_R in the boosted flavor sideband with μ–jet, for 2016 (upper), 2017 (middle) and 2018 (lower). Pre(Post)fit results are shown in left (right).

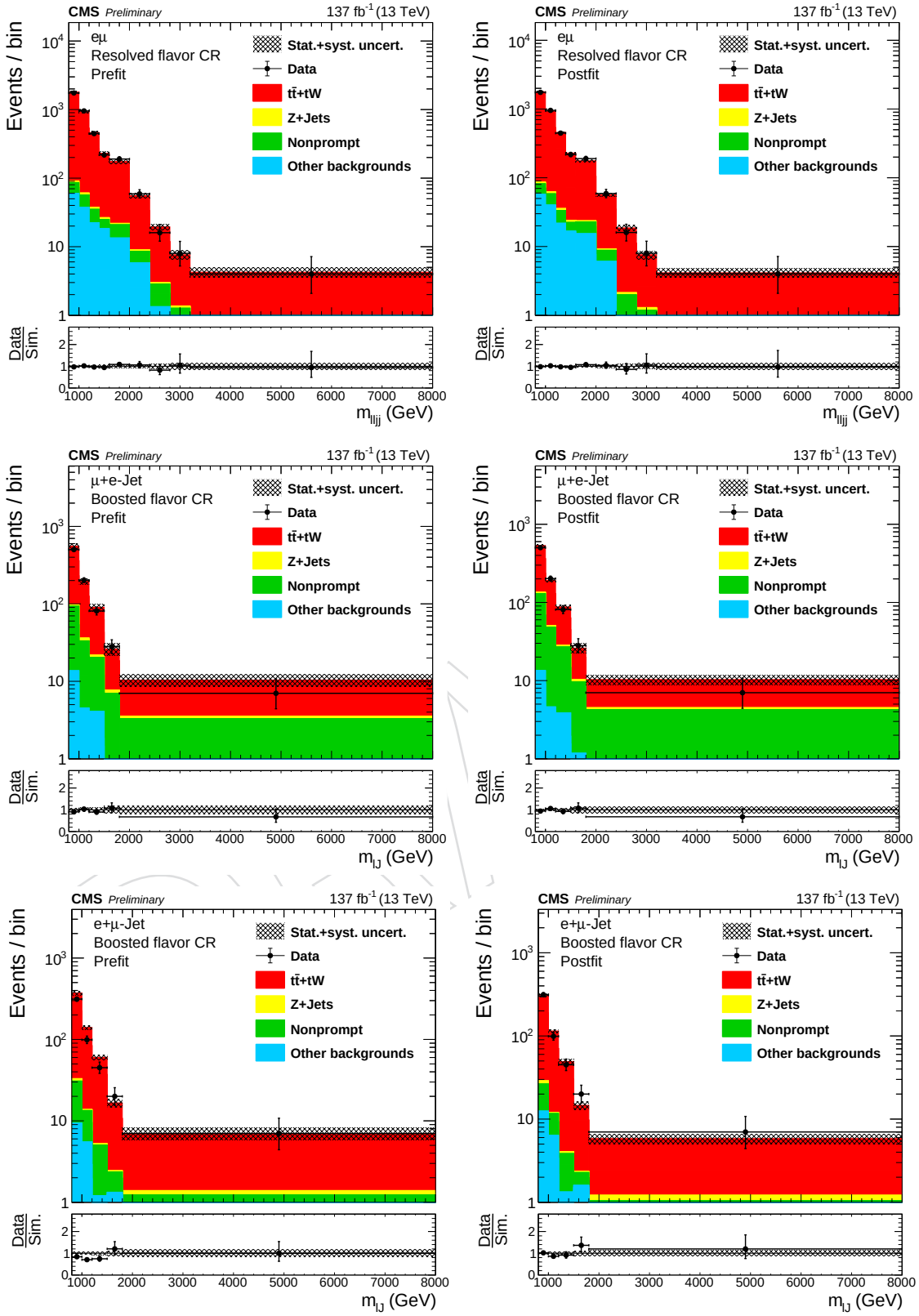

Figure 42: The reconstructed mass of W_R in the resolved flavor sideband (upper), boosted flavor sideband with e–jet (middle), and boosted flavor sideband with *mu*–jet (lower) with three year stacked. Pre(Post)fit results are shown in left (right).

6 Systematic uncertainties

The uncertainties we consider in our analysis for both signal and backgrounds are discussed in the following section in detail.

The major experimental sources of uncertainties for simulated backgrounds and signals include:

- **Integrated luminosity**: The systematic uncertainty on the integrated luminosity are 2.5 %, 2.3 %, and 2.5 % for 2016, 2017 and 2018, respectively [30–32].
- **Pileup**: An uncertainty is estimated by varying the nominal minimum bias cross section of pp collisions at 13 TeV (69.2 mb) by 5 %.
- **Theoretical uncertainties**: For signal only the uncertainties on the rate and acceptance of the signal are derived from the variation of the QCD scale, the parton distribution functions (PDFs) and α_S. The PDF and α_S uncertainties for the MADGRAPH signal samples are estimated from the standard deviation of the weights from the pdf errorsets provided in the NNPDF3.1 parton distribution set. The procedure for estimating the uncertainties associated with the PDF follows the recommendations issued by the PDF4LHC group [33].
- **Lepton trigger and selection**: Discrepancies in the lepton reconstruction, identification, and isolation efficiencies between data and simulation are corrected by applying a scale factor to all the simulated samples. This is explained in Section 3. For the modified loose electron ID, the discrepancy between data and simulation is calculated as part of our LSF SF. The scale factors, which depend on the p_{T} and η, are varied by $\pm\sigma$ and the change in the yield in the signal region is taken as the systematic. Electron identification [25, 26] and trigger [8] give 3.1–3.2 (1.8–1.9)% and 0–0.1 (0.2–0.4)% uncertainties in the background estimation in the resolved (boosted) region. Muon identification, isolation and trigger give 0.2–1.2 (0.1–0.6)%, 0.1–0.2 (0–0.1)%, and 0.1–0.2 (0.1–0.2)% uncertainties in the background estimation in the resolved (boosted) region.
- **Lepton momentum scale and resolution**: The lepton momentum scale uncertainty is computed by varying the momentum of the leptons by their uncertainties.

  For muons with $p_{\mathrm{T}} < 200\,\mathrm{GeV}$, the Rochester corrections were applied to the muon momentum, which removes bias from detector misalignment or magnetic fields [20]. Systematic uncertainties considered are follows; root-mean-squared (RMS) of pregenerated error sets, difference between results without Z momentum reweighting and variation of profile and fitting mass window, For muons with $p_{\mathrm{T}} \geq 200\,\mathrm{GeV}$, generalized–endpoint (GE) method [9] was applied, and the uncertainties on the muon curvature bias are taken from a gaussian distribution. Muon reconstruction and momentum scale give 0.4–1.0 (0.3–0.7)% and 0.4–2.5 (0.4–3.6)% uncertainties in the background estimation in the resolved (boosted) region.

  For electrons, we used the MiniAOD V2 energy corrections [22], and corresponding uncertainties. Electron reconstruction [23], energy resolution, and energy scale [22] give 1.0–1.6 (0.5–0.8)%, $<$ 0.1 ($<$ 0.1)%, and 0.5–1.8 (0.5–2.3)% uncertainties in the background estimation in the resolved (boosted) region.
- **Jet energy scale and resolution**: The versions of JEC and JER are summarized in Table 15 and Table 16. In order to have the resolution in the simulation match that in the data the momentum of the jets is smeared as:

$$p_{\mathrm{T}} \rightarrow \max[0, p_T^{\mathrm{gen}} + c_{\pm 1\sigma} \cdot (p_{\mathrm{T}} = p_T^{\mathrm{gen}})] \tag{5}$$

in which $c_{\pm 1\sigma}$ are the data/MC scale factors, which are shifted by $\pm\sigma$.
This results in a systematic uncertainty of less than 1% for all masses.

- **MC statistics**: A bin-wise statistical uncertainty is included to take into account the limited statistics available in our MC samples. This uncertainty is implemented through the Barlow-Beeston approach, where a single nuisance parameter is used in each bin to scale the sum of the process yields.
- **Monte Carlo normalization**: For our minor backgrounds, we assigned a normalization uncertainty on them to conservatively estimate the directly from simulation. For the nonprompt backgrounds, where an energetic fake lepton passes our selection, we assigned a 100% normalization uncertainty due to fakes not being well modeled in simulation. For the remaining background, we assigned a standard 50% normalization uncertainty.
- **LSF scale factor**: The difference in efficiency between data and MC on our LSF selection is taken into account with a dedicated scale factor. The measurement of this scale factor and the uncertainty on it are explained in Appendix M.
- **Pre-firing probabilities**: Followed by the recommendation [1], a 20 % systematic uncertainty is applied in addition to the statistcial uncertainty.

To combine our results across all three years of data taking, we treat the uncertainties that depend on run conditions as uncorrelated while ones that do not are treated as correlated. A complete list of systematic uncertainties is given in Table 21. One caveat to this, is we also treat the JEC uncertainties as correlated, since the JetMET POG recommends to correlate and uncorrelated certain sources of the JECs and we find that the difference between our expected limits when we fully uncorrelate or fully correlate our JECs is 1%. Therefore, we will treat them as fully correlated in order to take the most conservatice approach.

[1] https://lathomas.web.cern.ch/lathomas/TSGStuff/L1Prefiring/PrefiringMaps_2016and2017/

Table 21: Summary of the relative systematic uncertainties in signal and DY+jets background. The uncertainties are given for the resolved (boosted) SR. The numbers for signal is obtained for $m_{W_R} = 5\,\text{TeV}$. The range given for each systematic uncertainty source covers the variation across the years.

Source	Bkgd./Signal process	Year-to-year treatment	ee bkgd. (%)	ee signal (%)	$\mu\mu$ bkgd. (%)	$\mu\mu$ signal (%)
Integrated luminosity	All bkgd./Signal	Correlated	1.8 (1.8)	1.8 (1.8)	1.8 (1.8)	1.8 (1.8)
Electron reconstruction	All bkgd./Signal	Correlated	1.0–1.6 (0.5–0.8)	0.8–1.4 (0.4–0.8)	—	—
Electron energy resolution	All bkgd./Signal	Correlated	< 0.1 (< 0.1)	< 0.1 (< 0.1)	—	—
Electron energy scale	All bkgd./Signal	Correlated	0.5–1.8 (0.5–2.3)	0–0.3 (0–0.5)	—	—
Electron identification	All bkgd./Signal	Correlated	3.1–3.3 (1.8–1.9)	4.1–4.4 (2.1–2.4)	—	—
Electron trigger	All bkgd./Signal	Uncorrelated	0–0.1 (0.2–0.4)	< 0.1 (0.1–0.2)	—	—
Muon reconstruction	All bkgd./Signal	Correlated	—	—	0.4–1.0 (0.3–0.7)	4.4–36.8 (5.6–30.7)
Muon momentum scale	All bkgd./Signal	Correlated	—	—	0.4–2.5 (0.5–3.7)	0.1–0.2 (0.1–0.3)
Muon identification	All bkgd./Signal	Correlated	—	—	0.2–1.2 (0.1–0.6)	0.2–1.1 (0.1–0.5)
Muon isolation	All bkgd./Signal	Correlated	—	—	0.1–0.2 (0–0.1)	0.1–0.2 (0–0.1)
Muon trigger	All bkgd./Signal	Uncorrelated	—	—	0.1–0.2 (0.1–0.2)	0.7–1.6 (0.5–1.3)
Jet energy scale	All bkgd./Signal	Correlated	1.9–4.4 (0.9–1.9)	0–0.2 (0–0.3)	2.1–3.5 (0.6–0.9)	0–0.2 (0–0.4)
Jet energy resolution	All bkgd./Signal	Uncorrelated	0.5–1.5 (0.7–2.0)	0–0.3 (0–0.4)	0.2–1.3 (0.2–1.1)	0–0.3 (0–0.3)
Jet mass scale	All bkgd./Signal	Correlated	< 0.1 (1.0–1.8)	< 0.1 (0.1–1.0)	< 0.1 (1.4–1.7)	< 0.1 (0.2–1.0)
LSF scale factor	All bkgd./Signal	Uncorrelated	— (6.7–8.7)	— (6.7–8.7)	— (5.8–7.1)	— (5.8–7.1)
Pileup modeling	All bkgd./Signal	Correlated	0.2–1.1 (0.5–1.1)	0.1–0.8 (0.2–0.9)	0.3–0.5 (0.2–1.1)	0.1–0.5 (0–0.6)
Z-p_T correction, MC stat.	DY+jets	Correlated	0.6–2.0 (0.6–2.0)	—	0.6–2.0 (0.6–2.0)	—
Z-p_T correction, QCD scale	DY+jets	Correlated	6.3–7.1 (6.7–7.3)	—	6.1–7.1 (6.8–7.4)	—
Z-p_T correction, QCD PDF error	DY+jets	Correlated	0.6–2.0 (0.6–2.0)	—	0.6–2.0 (0.6–2.0)	—
Z-p_T correction, QCD PDF α_S	DY+jets	Correlated	0.8–4.7 (0.8–5.2)	—	0.8–4.7 (0.8–5.3)	—
Z-p_T correction, EW1 [34]	DY+jets	Correlated	< 0.1 (< 0.1)	—	< 0.1 (< 0.1)	—
Z-p_T correction, EW2 [34]	DY+jets	Correlated	0.3 (0.3)	—	0.3 (0.3)	—
Z-p_T correction, EW3 [34]	DY+jets	Correlated	0.1 (0.1)	—	0.1 (0–0.1)	—
DY reshape	DY+jets	Correlated	8.5–9.1 (10.1–11.6)	—	8.5–9.2 (9.7–11.6)	—
Nonprompt background normalization	Nonprompt	Uncorrelated	100 (100)	—	100 (100)	—
Rare SM background normalization	Others	Correlated	50 (50)	—	50 (50)	—
PDF error	Signal	Correlated	—	5.9–11.1 (8.8–39.9)	—	2.8–6.8 (17.5–40.6)
α_S	Signal	Correlated	—	0–0.2 (0.2–1.3)	—	0–0.2 (0.2–1.2)
renormalization/factorization scales	Signal	Correlated	—	0–0.1 (0.3–2.3)	—	0–0.1 (2.1–2.9)

7 Results

The prefit (postfit) observed invariant mass distributions in the resolved and boosted signal regions including the expected backgrounds, for both ee and $\mu\mu$ channels, are shown for each year of data taking separately in Fig. 43 and 45 (Fig. 44 and 46). Figure 47 and 48 show the prefit and postfit observed invariant mass distributions and expected background for the combination of all three data periods.

Table 22: Yields of the last three mass bins in the signal regions.

Year	Channel	Event type	DY	$t\bar{t} + tW$	Nonprompt	Others	Total background	Data
2016	ee	Resolved	3.72 ± 0.21	2.71 ± 0.27	1.11 ± 0.54	0.69 ± 0.35	8.24 ± 0.77	10
		Boosted	4.74 ± 0.76	18.08 ± 1.67	11.13 ± 2.91	2.07 ± 0.77	36.02 ± 2.96	39
	$\mu\mu$	Resolved	5.58 ± 0.43	4.30 ± 0.30	0.10 ± 0.07	1.36 ± 0.71	11.34 ± 1.14	9
		Boosted	5.06 ± 1.02	22.85 ± 1.44	1.02 ± 0.33	1.68 ± 0.73	30.61 ± 2.18	27
2017	ee	Resolved	5.49 ± 0.40	4.48 ± 0.41	0.34 ± 0.20	1.32 ± 0.73	11.64 ± 1.22	11
		Boosted	7.49 ± 0.97	18.46 ± 2.39	11.27 ± 4.76	0.46 ± 0.13	37.68 ± 3.89	44
	$\mu\mu$	Resolved	6.41 ± 0.40	5.11 ± 0.37	0.10 ± 0.07	2.63 ± 1.39	14.26 ± 1.66	19
		Boosted	6.17 ± 0.76	26.92 ± 1.99	2.48 ± 1.08	1.61 ± 0.64	37.18 ± 2.51	46
2018	ee	Resolved	7.93 ± 0.52	5.40 ± 0.48	0.72 ± 0.43	0.89 ± 0.53	14.94 ± 1.20	27
		Boosted	12.54 ± 1.69	26.72 ± 2.55	15.33 ± 3.89	1.32 ± 0.50	55.92 ± 4.16	60
	$\mu\mu$	Resolved	8.59 ± 0.50	8.30 ± 0.90	0.14 ± 0.09	0.89 ± 0.55	17.93 ± 1.42	26
		Boosted	10.13 ± 1.45	37.83 ± 2.18	3.47 ± 1.05	0.95 ± 0.27	52.38 ± 2.99	46
Combinded	ee	Resolved	17.14 ± 1.12	12.59 ± 1.01	2.18 ± 0.90	2.91 ± 1.18	34.82 ± 2.12	48
		Boosted	24.77 ± 2.97	63.26 ± 4.82	37.73 ± 8.45	3.85 ± 1.43	129.61 ± 7.22	143
	$\mu\mu$	Resolved	20.58 ± 1.26	17.70 ± 1.39	0.34 ± 0.19	4.89 ± 2.07	43.52 ± 2.76	54
		Boosted	21.36 ± 2.68	87.60 ± 3.65	6.97 ± 2.09	4.25 ± 1.55	120.18 ± 4.61	119

The impact of the nuisances and their postfit results are shown in App. N.

Figure 49 shows the 95 % CL asymptotic CL_s limits on $\sigma \times$ BR $\times$ A for each of the three data taking years, taking into account all the systematic and statistical uncertainties described in Section 6. The expected and observed exclusions are also shown. The full Run2 combined limit

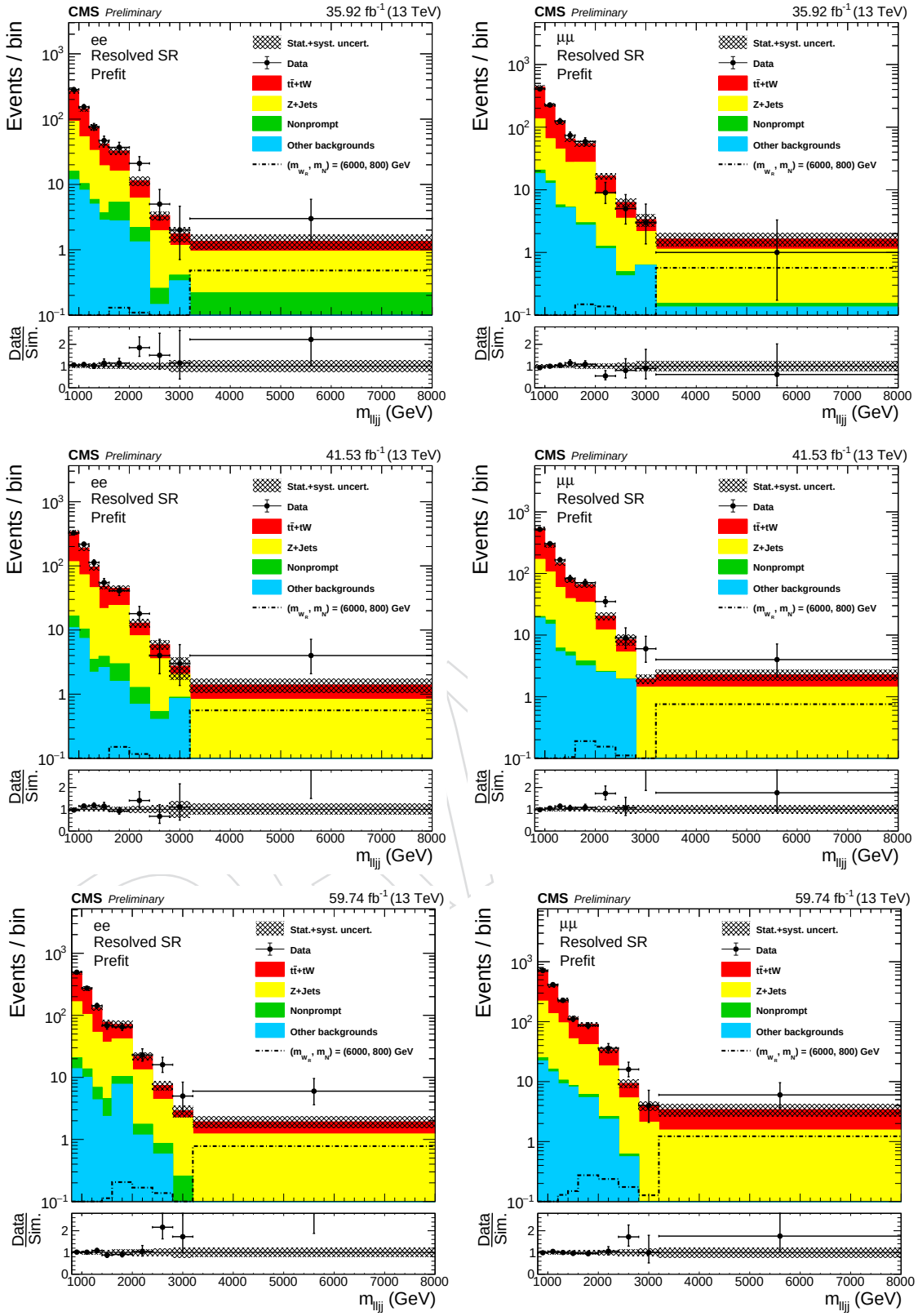

Figure 43: The prefit reconstructed mass of W_R in the resolved signal region. Results for the dielectron (dimuon) channel are shown on the left (right), for 2016 (top), 2017 (middle) and 2018 (bottom).

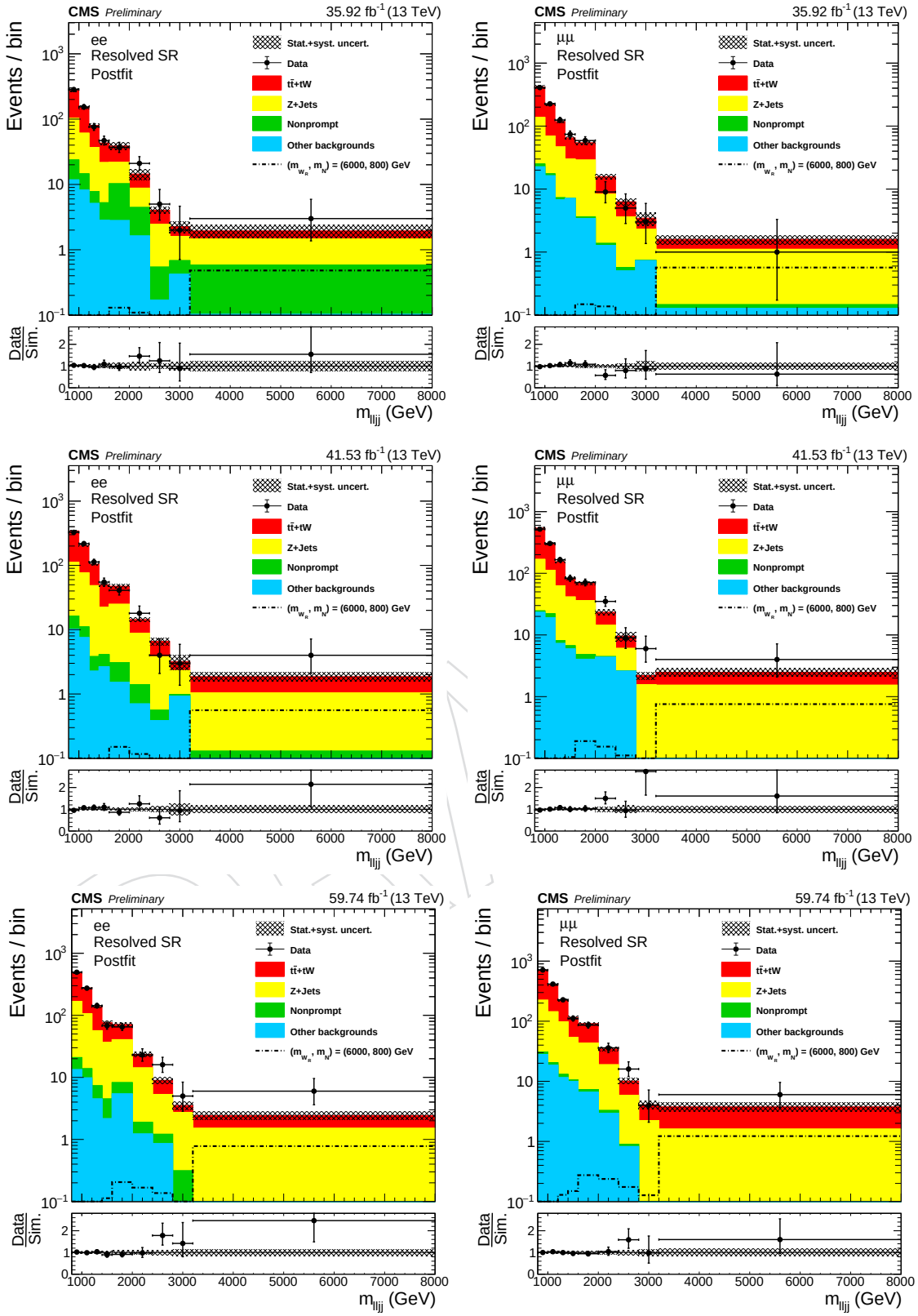

Figure 44: The postfit reconstructed mass of W_R in the resolved signal region. Results for the dielectron (dimuon) channel are shown on the left (right), for 2016 (top), 2017 (middle) and 2018 (bottom).

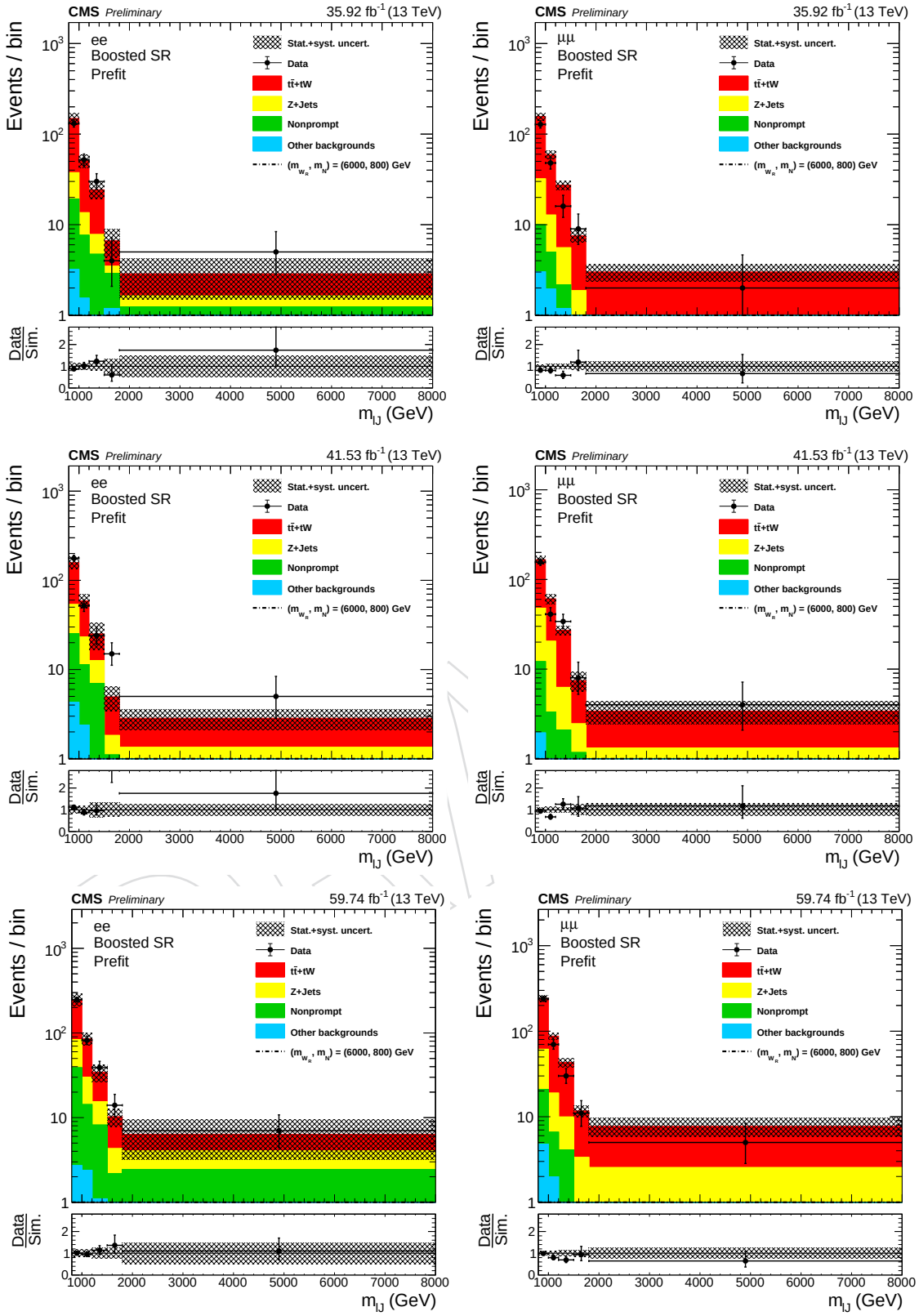

Figure 45: The prefit reconstructed mass of W_R in the boosted signal region. Results for the dielectron (dimuon) channel are shown on the left (right), for 2016 (top), 2017 (middle) and 2018 (bottom).

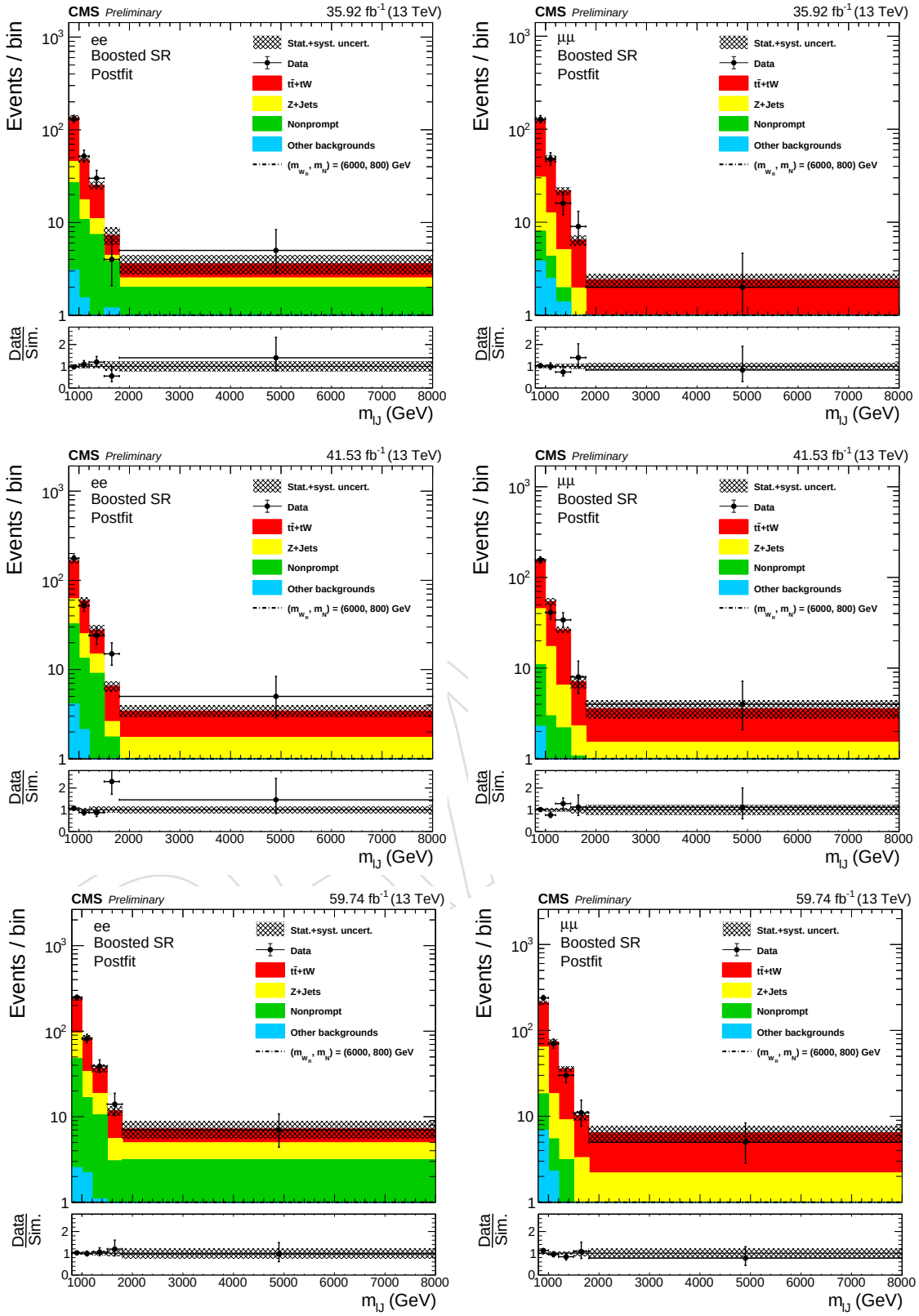

Figure 46: The postfit reconstructed mass of W_R in the boosted signal region. Results for the dielectron (dimuon) channel are shown on the left (right), for 2016 (top), 2017 (middle) and 2018 (bottom).

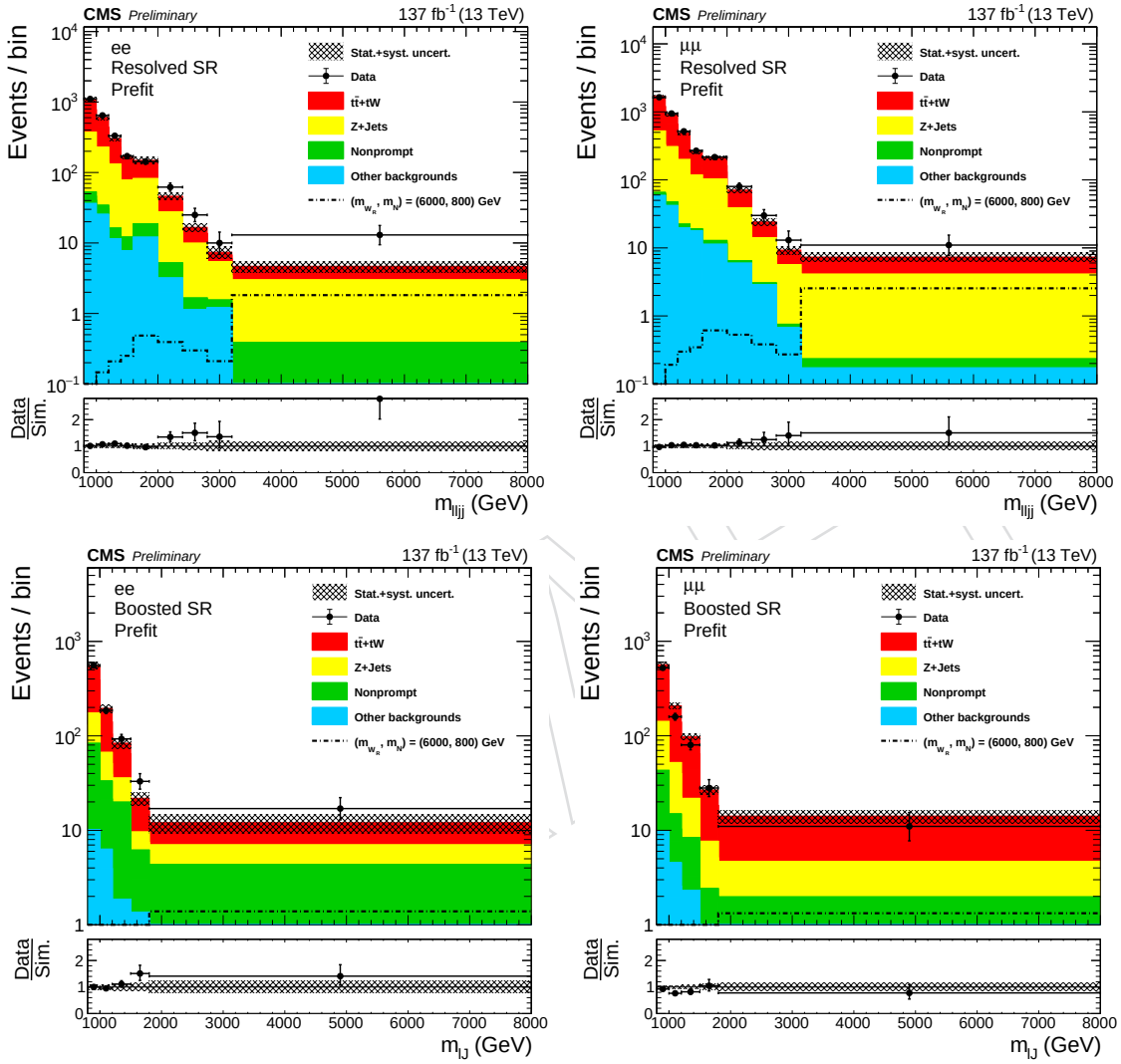

Figure 47: The prefit reconstructed mass of W_R in the signal regions with three year stacked. Results for the dielectron (dimuon) channel are shown on the left (right), for resolved (upper) and boosted (lower).

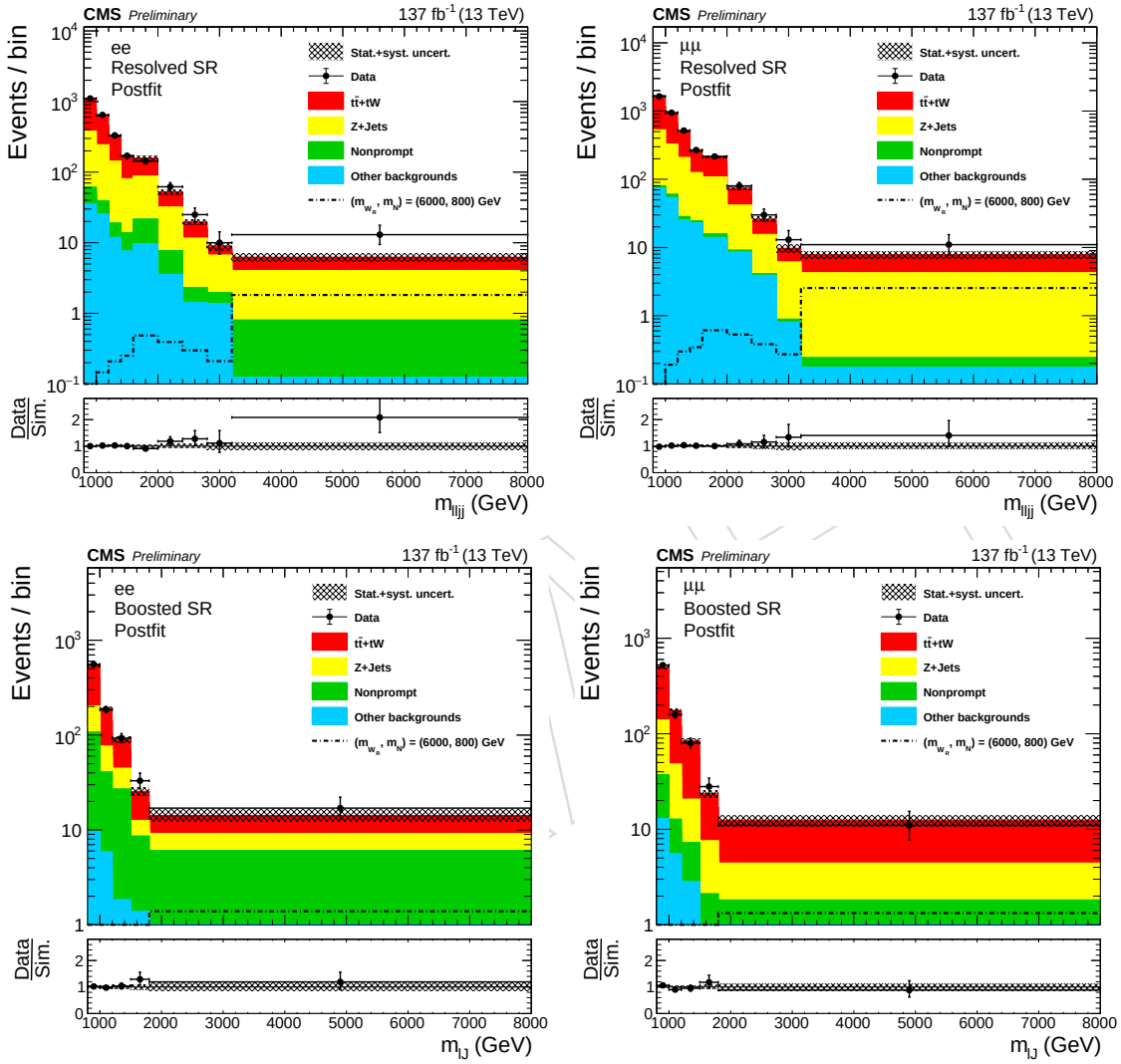

Figure 48: The postfit reconstructed mass of W_R in the signal regions with three year stacked. Results for the dielectron (dimuon) channel are shown on the left (right), for resolved (upper) and boosted (lower).

552 can be seen in Fig. 50.

553 The expected limits for the 2016 analysis alone are shown to be improved when compared
554 to the expected limits from the previous 2016 limits [5]. This is due to the tightening of the
555 dilepton invariant mass cut, the optimization of can be seen in App. H.

556 The expected limits for boosted signals are shown to have improved significantly, which is
557 expected as we now have dedicated signal regions that are designed to probe this phase space.

558 In Fig 51 are the upper limits on the cross section at a fixed W_R mass for $N = \frac{1}{2}m_{W_R}$ using
559 the Full Run2 data. The exclusion has been extended to 5 TeV from approximately 4.4 TeV with
560 only the 2016 data.

561 The observed background-only fit p-values are shown in Fig 52.

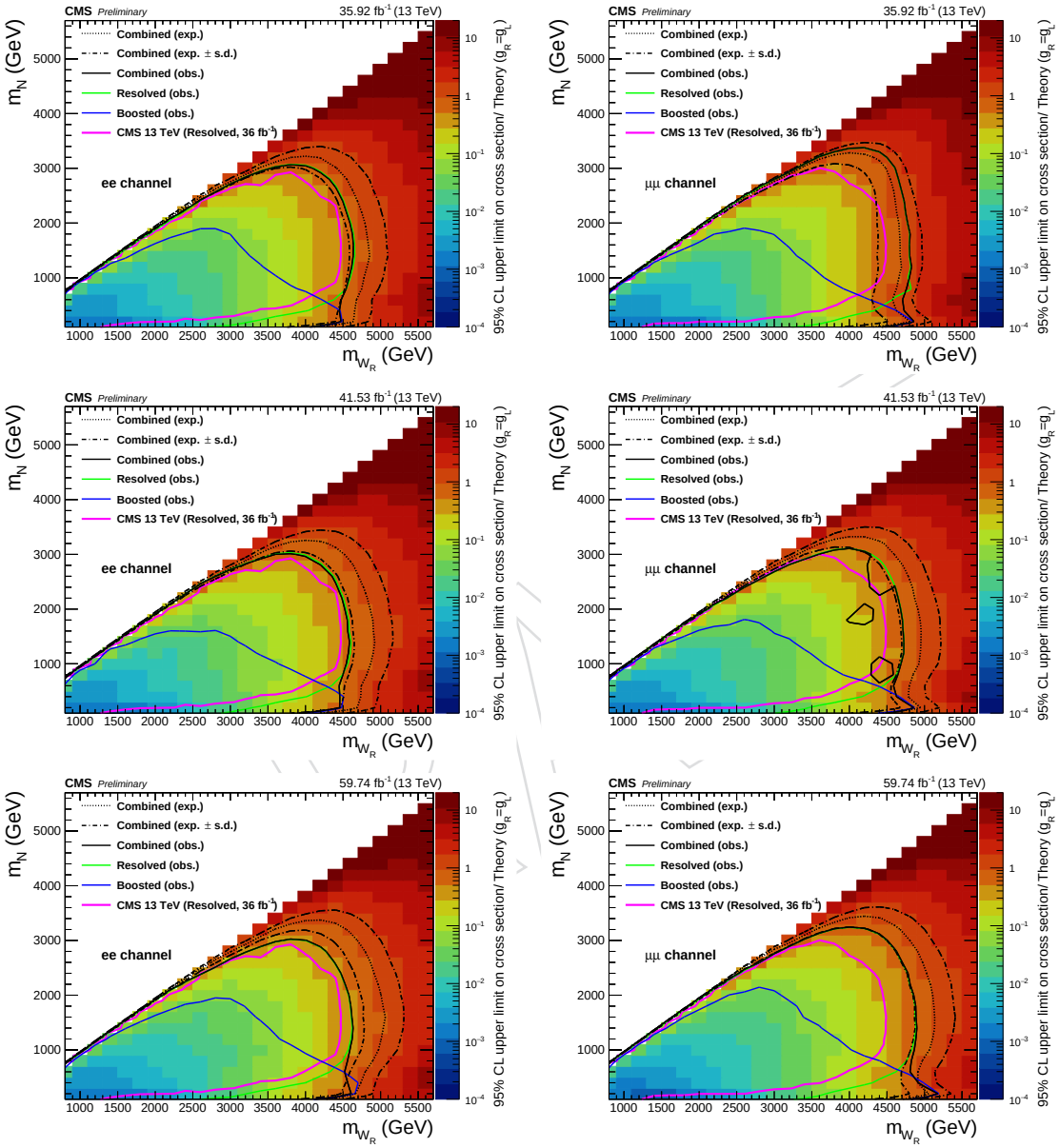

Figure 49: Upper limit on $\sigma(\mathrm{pp} \rightarrow \mathrm{W_R}) \times BR(\mathrm{W_R} \rightarrow \mathrm{ee}(\mu\mu)\mathrm{jj})$ cross section limit are shown on the left (right). Results are obtained from data taken in 2016 (top), 2017 (middle) and 2018 (bottom). The expected exclusions are shown.

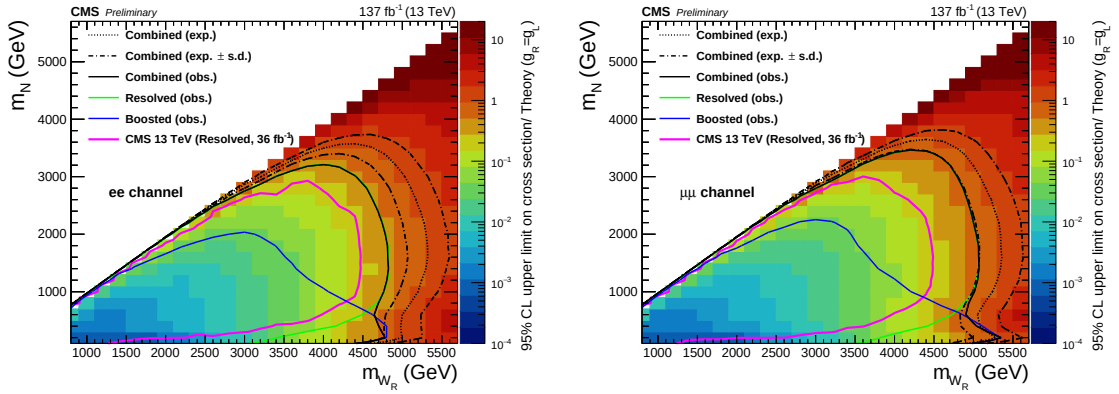

Figure 50: Upper limit on $\sigma(\mathrm{pp} \rightarrow \mathrm{W_R}) \times BR(\mathrm{W_R} \rightarrow \mathrm{e}\mathrm{e}(\mu\mu)\mathrm{jj})$ cross section limit are shown on the left (right) for the entire Run2 dataset. The expected exclusions are shown.

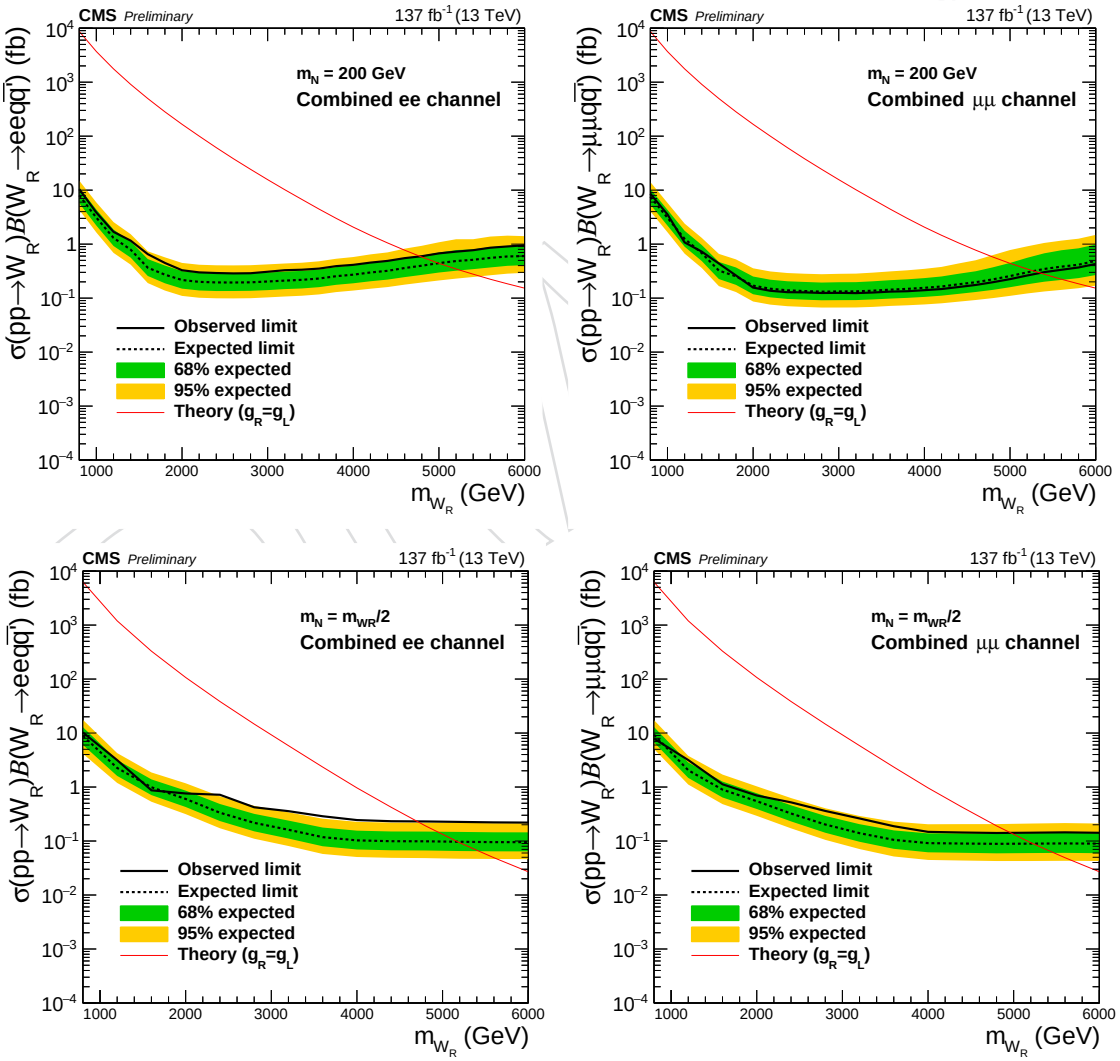

Figure 51: Upper limit on $\sigma(\mathrm{pp} \rightarrow \mathrm{W_R}) \times BR(\mathrm{W_R} \rightarrow \mathrm{e}\mathrm{e}(\mu\mu)\mathrm{jj})$ cross section limit are shown on the left (right) for the entire Run2 dataset. The expected exclusions are shown.

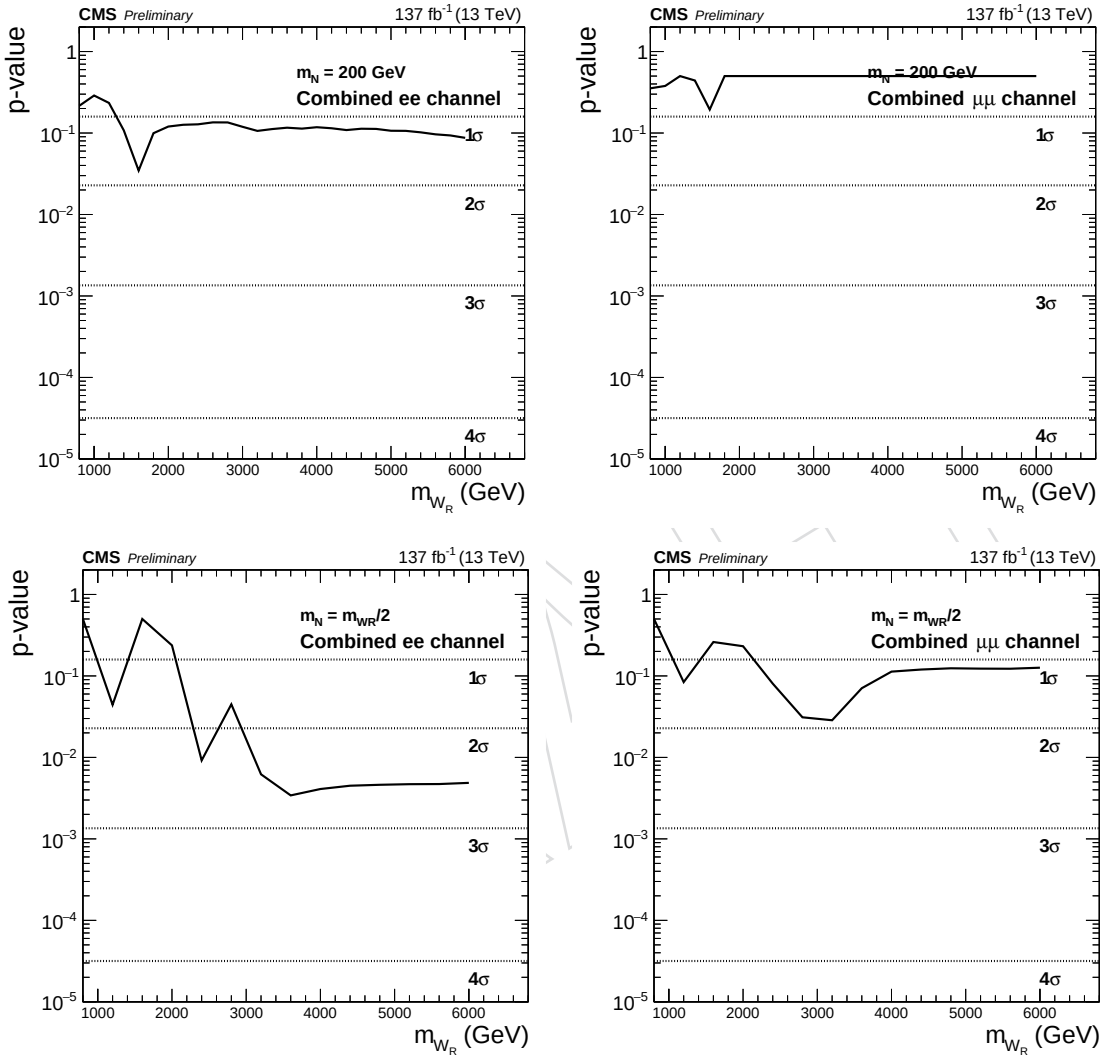

Figure 52: The observed background-only fit p-values for $m_{\mathrm{N}} = 200\,\mathrm{GeV}$ and $m_{\mathrm{N}} = m_{\mathrm{W_R}}/2$ are shown in the top and bottom plots, respectively. Upper limit on $\sigma(\mathrm{pp} \to \mathrm{W_R}) \times BR(\mathrm{W_R} \to \mathrm{ee}(\mu\mu)\mathrm{jj})$ cross section limit are shown on the left (right) for the entire Run2 dataset. The expected exclusions are shown.

8 Conclusion

A search for right-handed charged gauge bosons and heavy neutrinos is conducted using CMS pp collision data collected from 2016–2018 at $\sqrt{s} = 13\,\text{TeV}$ and corresponding to an integrated luminosity of $137\,\text{fb}^{-1}$. The search is done in two event topologies to cover as much m_{W_R} vs m_{N} phase space as possible: the resovled region, where all four decay products are well isolated, and the boosted region, where the entire heavy neutrino decay is reconstructed with a large area jet. The most stringent limits to data are placed on a new W boson-like particle, with standard model couplings, decaying via a new heavy neutrino.

Acknowledgments

References

[1] J. C. Pati and A. Salam, "Lepton number as the fourth "color"", *Phys. Rev. D* **10** (1974) 275, doi:10.1103/PhysRevD.10.275.

[2] R. N. Mohapatra and J. C. Pati, "A natural left-right symmetry", *Phys. Rev. D* **11** (1975) 2558, doi:10.1103/PhysRevD.11.2558.

[3] G. Senjanović and R. N. Mohapatra, "Exact left-right symmetry and spontaneous violation of parity", *Phys. Rev. D* **12** (1975) 1502, doi:10.1103/PhysRevD.12.1502.

[4] W.-Y. Keung and G. Senjanović, "Majorana neutrinos and the production of the right-handed charged gauge boson", *Phys. Rev. Lett.* **50** (1983) 1427, doi:10.1103/PhysRevLett.50.1427.

[5] CMS Collaboration, "Search for a heavy right-handed W boson and a heavy neutrino in events with two same-flavor leptons and two jets at $\sqrt{s} = 13$ TeV", *JHEP* **05** (2018) 148, doi:10.1007/JHEP05(2018)148.

[6] ATLAS Collaboration, "Search for heavy Majorana or Dirac neutrinos and right-handed W gauge bosons in final states with two charged leptons and two jets at $\sqrt{s} = 13$ TeV with the ATLAS detector", *JHEP* **01** (2019) 016, doi:10.1007/JHEP01(2019)016.

[7] A. H. K. N. Adams. https://github.com/cms-sw/cmssw/blob/master/PhysicsTools/TagAndProbe/interface/RooCMSShape.h. PhysicsTools/TagAndProbe/RooCMSShape.

[8] E. POG. https://twiki.cern.ch/twiki/bin/view/CMS/EgHLTScaleFactorMeasurements. Approved and ongoing electron and photon trigger scale factor measurements for Run2 data.

[9] M. POG. https://twiki.cern.ch/twiki/bin/viewauth/CMS/HighPtMuonReferenceRun2. High pt muonrefernces for Run2.

[10] M. Cacciari, G. P. Salam, and G. Soyez, "The anti-k_t jet clustering algorithm", *JHEP* **04** (2008) 063, doi:10.1088/1126-6708/2008/04/063, arXiv:0802.1189.

[11] CMS Collaboration, "Pileup mitigation at CMS in 13 TeV data", *JINST* **15** (2020) P09018, doi:10.1088/1748-0221/15/09/p09018, arXiv:2003.00503.

[12] C. J. POG, "Recommended Jet Energy Corrections and Uncertainties For Data and MC". https://twiki.cern.ch/twiki/bin/view/CMS/JECDataMC, 2017.

[13] A. J. Larkoski, S. Marzani, G. Soyez, and J. Thaler, "Soft Drop", *JHEP* **05** (2014) 146, doi:10.1007/JHEP05(2014)146, arXiv:1402.2657.

[14] M. Dasgupta, A. Fregoso, S. Marzani, and G. P. Salam, "Towards an understanding of jet substructure", *JHEP* **09** (2013) 029, doi:10.1007/JHEP09(2013)029, arXiv:1307.0007.

[15] A. J. Larkoski and J. Thaler, "Unsafe but Calculable: Ratios of Angularities in Perturbative QCD", *JHEP* **09** (2013) 137, doi:10.1007/JHEP09(2013)137, arXiv:1307.1699.

[16] S. D. Ellis, C. K. Vermilion, and J. R. Walsh, "Techniques for improved heavy particle searches with jet substructure", *Phys. Rev.* **D80** (2009) 051501, doi:10.1103/PhysRevD.80.051501, arXiv:0903.5081.

[17] S. D. Ellis, C. K. Vermilion, and J. R. Walsh, "Recombination Algorithms and Jet Substructure: Pruning as a Tool for Heavy Particle Searches", *Phys. Rev.* **D81** (2010) 094023, doi:10.1103/PhysRevD.81.094023, arXiv:0912.0033.

[18] C. Brust et al., "Identifying boosted new physics with non-isolated leptons", *Journal of High Energy Physics* **2015** (Apr, 2015) 79, doi:10.1007/JHEP04(2015)079.

[19] CMS Collaboration, "Performance of the CMS muon detector and muon reconstruction with proton-proton collisions at $\sqrt{s} = 13\,\text{TeV}$", *JINST* **13** (2018) P06015, doi:10.1088/1748-0221/13/06/P06015, arXiv:1804.04528.

[20] A. Khukhunaishvili, "Rochester Correction". https://twiki.cern.ch/twiki/bin/viewauth/CMS/RochcorMuon.

[21] M. POG, "Muon Reference Selection And Calibrations for Run2". https://twiki.cern.ch/twiki/bin/viewauth/CMS/MuonReferenceSelectionAndCalibrationsRun2#Special_systematic_uncertainties.

[22] E. POG, "Electron energy smearing and scale corrections". https://twiki.cern.ch/twiki/bin/viewauth/CMS/EGMSmearer.

[23] E. POG, "EGamma POG Electron Efficiencies and Scale Factors". https://twiki.cern.ch/twiki/bin/view/CMS/EgammaIDRecipesRun2#Electron_efficiencies_and_scale.

[24] E. POG, "HEEPv70 Electron ID and isolation". https://twiki.cern.ch/twiki/bin/view/CMS/HEEPElectronIdentificationRun2#Selection_Cuts_HEEP_V7_0_recomme.

[25] E. POG, "HEEPv70 ID Scale Factors". https://twiki.cern.ch/twiki/bin/view/CMS/EgammaRunIIRecommendations#HEEPV7_0.

[26] E. POG, "HEEPv70 ID Scale Factors, 2018Prompt". https://twiki.cern.ch/twiki/bin/view/CMS/EgammaRunIIRecommendations#HEEPv7_0_2018Prompt.

[27] J. POG, "MET Filter Recommendations for Run II". https://twiki.cern.ch/twiki/bin/viewauth/CMS/MissingETOptionalFiltersRun2, 2019.

[28] CMS Collaboration, "Measurements of inclusive and differential Z boson production cross sections in pp collisions at $\sqrt{s} = 13$ TeV", CMS Physics Analysis Summary CMS-PAS-SMP-15-011, CERN, 2016.

[29] I. Neutelings, Y. Takahashi, and B. Kilminster, "The search for a third-generation leptoquark decaying to a tau lepton and a b quark through single, pair and t-channel production with run-2 data at 13 tev", CMS Analysis Note 2019/019, CERN, 2019.

[30] CMS Collaboration, "CMS luminosity measurements for the 2016 data taking period", CMS Physics Analysis Summary CMS-PAS-LUM-17-001, CERN, 2017.

[31] CMS Collaboration, "CMS luminosity measurement for the 2017 data-taking period at $\sqrt{s} = 13$ TeV", CMS Physics Analysis Summary CMS-PAS-LUM-17-004, CERN, 2018.

[32] CMS Collaboration, "CMS luminosity measurement for the 2018 data taking period at $\sqrt{s} = 13$ TeV", CMS Physics Analysis Summary CMS-PAS-LUM-18-002, CERN, 2017.

[33] J. Butterworth et al., "PDF4LHC recommendations for LHC run II", *J. Phys. G* **43** (2016) 023001, doi:10.1088/0954-3899/43/2/023001, arXiv:1510.03865.

[34] J. M. Lindert et al., "Precise predictions for $V+$ jets dark matter backgrounds", *Eur. Phys. J. C* **77** (2017), no. 12, 829, doi:10.1140/epjc/s10052-017-5389-1, arXiv:1705.04664.

[35] ATLAS Collaboration, "Search for a right-handed gauge boson decaying into a high-momentum heavy neutrino and a charged lepton in pp collisions with the ATLAS detector at $\sqrt{s} = 13$ TeV", *PLB* **798** (134942) 016, doi:10.1016/j.physletb.2019.134942.

[36] I. Moult, L. Necib, and J. Thaler, "New angles on energy correlation functions", *Journal of High Energy Physics* **2016** (Dec, 2016) doi:10.1007/jhep12(2016)153.

[37] N. T. et al., "Search for boosted light diject resonances with 2016 data", CMS Analysis Note 2016/365, CERN, 2016.

A Signal samples

The cross sections of signal samples produced with FastSim are shown in Tab. 23–41. Each sample contains both ee and $\mu\mu$ channels.

Since there more than 600 mass points set for the analysis, we take a simpler approach instead of calculating K factors for all mass points.

A.1 Averaged K factors

We calculate the K factors only for the cases where $m_{\mathrm{N}} = 100, m_{\mathrm{W_R}}/2, m_{\mathrm{W_R}} - 100\,\mathrm{GeV}$ with $m_{\mathrm{W_R}}$ varying from 200 to 7000 GeV. As shown in Fig. 53, $m_{\mathrm{N}} = 100\,\mathrm{GeV}$'s K factors differ a lot compared to the other two cases, while $m(\mathrm{W_R})/2$ and $m(\mathrm{W_R}) - 100\,\mathrm{GeV}$ have similar trends. This difference is due to offshell production of $\mathrm{W_R}$ enhancement when $m(\mathrm{W_R}) >> m(N)$. For mass points where $100 <= m(N) < m(\mathrm{W_R})/2\,\mathrm{GeV}$ we use $m(N) = 100\,\mathrm{GeV}$ K factors and $m(N) = m(\mathrm{W_R}) - 100\,\mathrm{GeV}$ K factors are used for $m(\mathrm{W_R})/2 <= m(N) < m(\mathrm{W_R}) - 100\,\mathrm{GeV}$.

We initially used K factors different for two m_{N} as follows:

- If $m_{\mathrm{N}} < m_{\mathrm{W_R}}/2$, use the K factor at $m_{\mathrm{N}} = 100\,\mathrm{GeV}$ in Fig. 53 for each $m_{\mathrm{W_R}}$
- Otherwise, use the K factor at $m_{\mathrm{N}} = m_{\mathrm{W_R}} - 100\,\mathrm{GeV}$ in Fig. 53 for each $m_{\mathrm{W_R}}$.

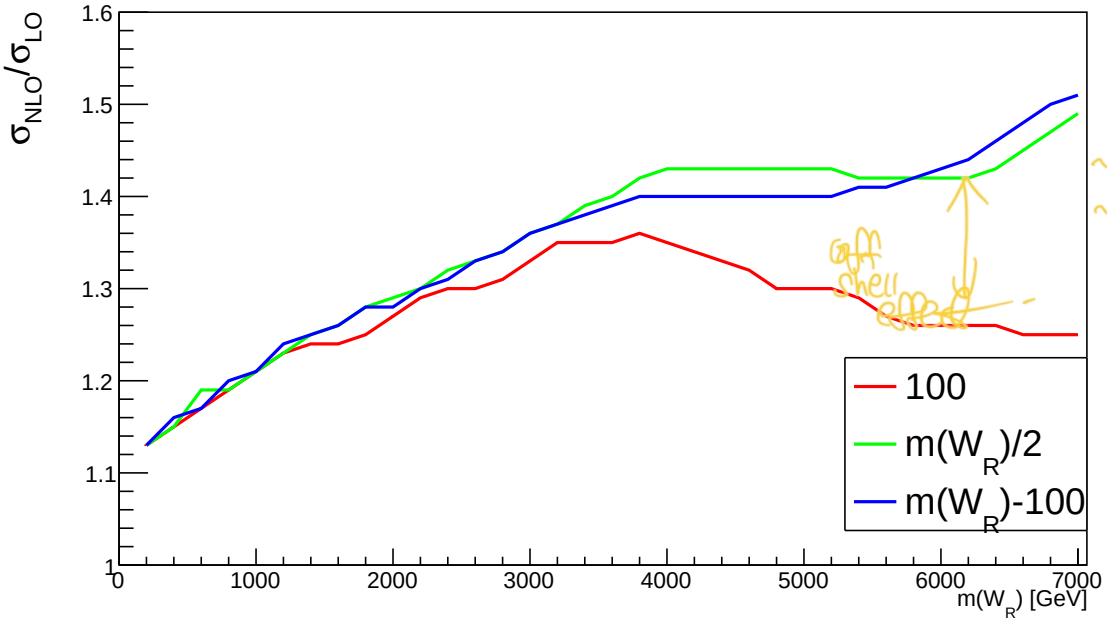

Figure 53: K factor values

The on-shell parts of the signal events are more sensitive to the limit extraction, so we decided to obtain the K factor as a function of $m(\ell\mathrm{N})$, and apply a event-by-event reweighting using the gen-level information.

A.2 K factor as a function of m(lN)

The QCD NLO/LO effect in our signal must be only related to the N production, and the amount of this higher-order effect can be parametrized as a function of $\sqrt{Q^2}$, in this case $m_{\ell\mathrm{N}}$.

We used 6M signal events, varying the combinations of (m_{W_R}, m_N), and obtained the NLO/LO K factor as a function of $m_{\ell N}$ (Fig. 54). For each signal events, we used the gen-level $m_{\ell N}$ value and applied the corresponding K factor. In Fig. 55, we compared the previously used K factor and the newly calcaulted K-factor. For $(m_{W_R}, m_N) = (5, 2)$ TeV, the calcualted K factor is 1.41, while the previous values we used is 1.30.

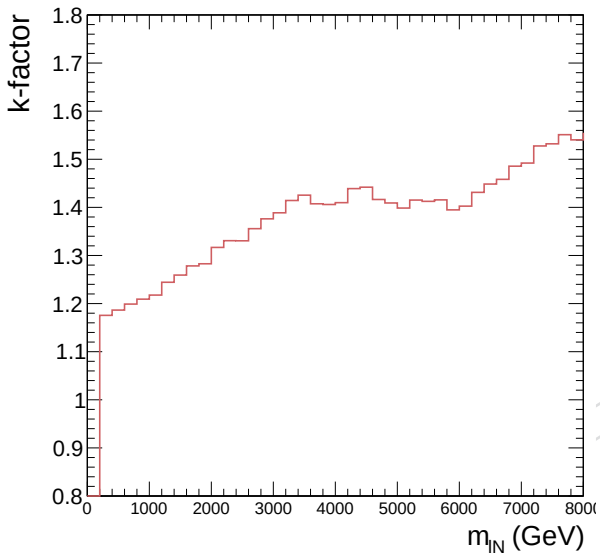

Figure 54: K factor as a function of $m(\ell N)$.

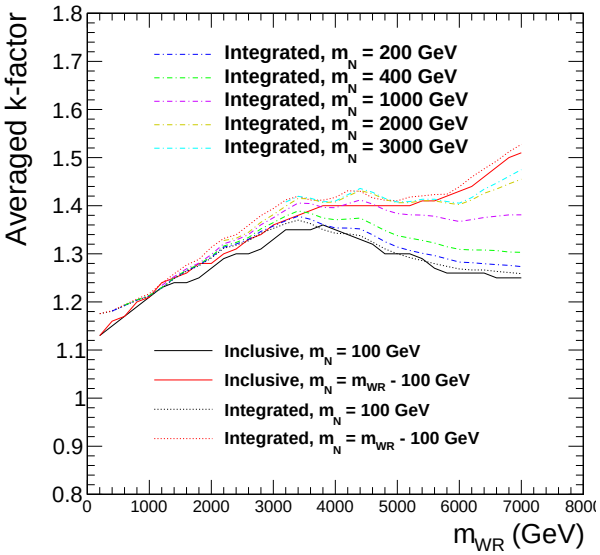

Figure 55: Averaged K factors for each m_{W_R} from Fig. 53 ("Inclusive", solid lines) and the calculated values using Fig. 54 with the gen-level information ("Integrated", dashed lines).

Table 23: MINIAOD datasets, LO cross-sections, and NLO-to-LO k-factor for signal samples.

Sample Name	$\sigma(pb)$, LO	$k^{\mathrm{NLO/LO}}$
WRtoNLtoLLJJ_WR200_N100	$2.041 \times 10^{+03}$	1.18
WRtoNLtoLLJJ_WR400_N100	$1.947 \times 10^{+02}$	1.18
WRtoNLtoLLJJ_WR400_N200	$1.428 \times 10^{+02}$	1.18
WRtoNLtoLLJJ_WR400_N300	$6.158 \times 10^{+01}$	1.18
WRtoNLtoLLJJ_WR600_N100	$4.597 \times 10^{+01}$	1.19
WRtoNLtoLLJJ_WR600_N200	$4.029 \times 10^{+01}$	1.19
WRtoNLtoLLJJ_WR600_N400	$1.983 \times 10^{+01}$	1.19
WRtoNLtoLLJJ_WR600_N500	$7.149 \times 10^{+00}$	1.19
WRtoNLtoLLJJ_WR800_N100	$1.551 \times 10^{+01}$	1.20
WRtoNLtoLLJJ_WR800_N200	$1.446 \times 10^{+01}$	1.20
WRtoNLtoLLJJ_WR800_N400	$1.041 \times 10^{+01}$	1.20
WRtoNLtoLLJJ_WR800_N600	$4.351 \times 10^{+00}$	1.20
WRtoNLtoLLJJ_WR800_N700	$1.473 \times 10^{+00}$	1.21
WRtoNLtoLLJJ_WR1000_N100	$6.383 \times 10^{+00}$	1.21
WRtoNLtoLLJJ_WR1000_N200	$6.083 \times 10^{+00}$	1.21
WRtoNLtoLLJJ_WR1000_N400	$5.023 \times 10^{+00}$	1.21
WRtoNLtoLLJJ_WR1000_N600	$3.323 \times 10^{+00}$	1.21
WRtoNLtoLLJJ_WR1000_N800	$1.256 \times 10^{+00}$	1.21
WRtoNLtoLLJJ_WR1000_N900	4.125×10^{-01}	1.22
WRtoNLtoLLJJ_WR1200_N100	$2.97 \times 10^{+00}$	1.23
WRtoNLtoLLJJ_WR1200_N200	$2.867 \times 10^{+00}$	1.23
WRtoNLtoLLJJ_WR1200_N400	$2.511 \times 10^{+00}$	1.23
WRtoNLtoLLJJ_WR1200_N600	$1.947 \times 10^{+00}$	1.23
WRtoNLtoLLJJ_WR1200_N800	$1.207 \times 10^{+00}$	1.23
WRtoNLtoLLJJ_WR1200_N1000	4.296×10^{-01}	1.23
WRtoNLtoLLJJ_WR1200_N1100	1.406×10^{-01}	1.24
WRtoNLtoLLJJ_WR1400_N100	$1.502 \times 10^{+00}$	1.25
WRtoNLtoLLJJ_WR1400_N200	$1.458 \times 10^{+00}$	1.25
WRtoNLtoLLJJ_WR1400_N400	$1.321 \times 10^{+00}$	1.25
WRtoNLtoLLJJ_WR1400_N600	$1.111 \times 10^{+00}$	1.25
WRtoNLtoLLJJ_WR1400_N800	8.25×10^{-01}	1.25
WRtoNLtoLLJJ_WR1400_N1000	4.887×10^{-01}	1.25
WRtoNLtoLLJJ_WR1400_N1200	1.66×10^{-01}	1.25
WRtoNLtoLLJJ_WR1400_N1300	5.455×10^{-02}	1.26
WRtoNLtoLLJJ_WR1600_N100	8.063×10^{-01}	1.26

Table 24: MINIAOD datasets, LO cross-sections, and NLO-to-LO k-factor for signal samples.

Sample Name	$\sigma(pb)$, LO	$k^{\mathrm{NLO/LO}}$
WRtoNLtoLLJJ_WR1600_N200	7.864×10^{-01}	1.26
WRtoNLtoLLJJ_WR1600_N400	7.256×10^{-01}	1.27
WRtoNLtoLLJJ_WR1600_N600	6.375×10^{-01}	1.27
WRtoNLtoLLJJ_WR1600_N800	5.188×10^{-01}	1.27
WRtoNLtoLLJJ_WR1600_N1000	3.731×10^{-01}	1.27
WRtoNLtoLLJJ_WR1600_N1200	2.129×10^{-01}	1.27
WRtoNLtoLLJJ_WR1600_N1400	7.031×10^{-02}	1.27
WRtoNLtoLLJJ_WR1600_N1500	2.318×10^{-02}	1.28
WRtoNLtoLLJJ_WR1800_N100	4.53×10^{-01}	1.28
WRtoNLtoLLJJ_WR1800_N200	4.422×10^{-01}	1.28
WRtoNLtoLLJJ_WR1800_N400	4.125×10^{-01}	1.28
WRtoNLtoLLJJ_WR1800_N600	3.718×10^{-01}	1.28
WRtoNLtoLLJJ_WR1800_N800	3.192×10^{-01}	1.28
WRtoNLtoLLJJ_WR1800_N1000	2.528×10^{-01}	1.28
WRtoNLtoLLJJ_WR1800_N1200	1.771×10^{-01}	1.28
WRtoNLtoLLJJ_WR1800_N1400	9.803×10^{-02}	1.28
WRtoNLtoLLJJ_WR1800_N1600	3.186×10^{-02}	1.28
WRtoNLtoLLJJ_WR1800_N1700	1.069×10^{-02}	1.29
WRtoNLtoLLJJ_WR2000_N100	2.622×10^{-01}	1.29
WRtoNLtoLLJJ_WR2000_N200	2.565×10^{-01}	1.29
WRtoNLtoLLJJ_WR2000_N400	2.415×10^{-01}	1.29
WRtoNLtoLLJJ_WR2000_N600	2.217×10^{-01}	1.30
WRtoNLtoLLJJ_WR2000_N800	1.962×10^{-01}	1.30
WRtoNLtoLLJJ_WR2000_N1000	1.649×10^{-01}	1.30
WRtoNLtoLLJJ_WR2000_N1200	1.281×10^{-01}	1.30
WRtoNLtoLLJJ_WR2000_N1400	8.748×10^{-02}	1.30
WRtoNLtoLLJJ_WR2000_N1600	4.72×10^{-02}	1.30
WRtoNLtoLLJJ_WR2000_N1800	1.517×10^{-02}	1.31
WRtoNLtoLLJJ_WR2000_N1900	5.147×10^{-03}	1.31
WRtoNLtoLLJJ_WR2200_N100	1.563×10^{-01}	1.31
WRtoNLtoLLJJ_WR2200_N200	1.526×10^{-01}	1.31
WRtoNLtoLLJJ_WR2200_N400	1.443×10^{-01}	1.32
WRtoNLtoLLJJ_WR2200_N600	1.34×10^{-01}	1.32
WRtoNLtoLLJJ_WR2200_N800	1.211×10^{-01}	1.32
WRtoNLtoLLJJ_WR2200_N1000	1.055×10^{-01}	1.32

Table 25: MINIAOD datasets, LO cross-sections, and NLO-to-LO k-factor for signal samples.

Sample Name	$\sigma(pb)$, LO	$k^{\mathrm{NLO/LO}}$
WRtoNLtoLLJJ_WR2200_N1200	8.713×10^{-02}	1.32
WRtoNLtoLLJJ_WR2200_N1400	6.64×10^{-02}	1.32
WRtoNLtoLLJJ_WR2200_N1600	4.463×10^{-02}	1.32
WRtoNLtoLLJJ_WR2200_N1800	2.379×10^{-02}	1.32
WRtoNLtoLLJJ_WR2200_N2000	7.548×10^{-03}	1.33
WRtoNLtoLLJJ_WR2200_N2100	2.602×10^{-03}	1.33
WRtoNLtoLLJJ_WR2400_N100	9.505×10^{-02}	1.32
WRtoNLtoLLJJ_WR2400_N200	9.283×10^{-02}	1.32
WRtoNLtoLLJJ_WR2400_N400	8.794×10^{-02}	1.32
WRtoNLtoLLJJ_WR2400_N600	8.234×10^{-02}	1.33
WRtoNLtoLLJJ_WR2400_N800	7.538×10^{-02}	1.33
WRtoNLtoLLJJ_WR2400_N1000	6.736×10^{-02}	1.33
WRtoNLtoLLJJ_WR2400_N1200	5.781×10^{-02}	1.33
WRtoNLtoLLJJ_WR2400_N1400	4.709×10^{-02}	1.33
WRtoNLtoLLJJ_WR2400_N1600	3.533×10^{-02}	1.33
WRtoNLtoLLJJ_WR2400_N1800	2.333×10^{-02}	1.33
WRtoNLtoLLJJ_WR2400_N2000	1.227×10^{-02}	1.33
WRtoNLtoLLJJ_WR2400_N2200	3.845×10^{-03}	1.33
WRtoNLtoLLJJ_WR2400_N2300	1.352×10^{-03}	1.34
WRtoNLtoLLJJ_WR2600_N100	5.897×10^{-02}	1.33
WRtoNLtoLLJJ_WR2600_N200	5.743×10^{-02}	1.33
WRtoNLtoLLJJ_WR2600_N400	5.436×10^{-02}	1.33
WRtoNLtoLLJJ_WR2600_N600	5.118×10^{-02}	1.34
WRtoNLtoLLJJ_WR2600_N800	4.73×10^{-02}	1.34
WRtoNLtoLLJJ_WR2600_N1000	4.291×10^{-02}	1.34
WRtoNLtoLLJJ_WR2600_N1200	3.784×10^{-02}	1.34
WRtoNLtoLLJJ_WR2600_N1400	3.211×10^{-02}	1.34
WRtoNLtoLLJJ_WR2600_N1600	2.58×10^{-02}	1.34
WRtoNLtoLLJJ_WR2600_N1800	1.914×10^{-02}	1.34
WRtoNLtoLLJJ_WR2600_N2000	1.247×10^{-02}	1.34
WRtoNLtoLLJJ_WR2600_N2200	6.481×10^{-03}	1.35
WRtoNLtoLLJJ_WR2600_N2400	2.025×10^{-03}	1.35
WRtoNLtoLLJJ_WR2600_N2500	7.201×10^{-04}	1.36
WRtoNLtoLLJJ_WR2800_N100	3.711×10^{-02}	1.34
WRtoNLtoLLJJ_WR2800_N200	3.609×10^{-02}	1.35

Table 26: MINIAOD datasets, LO cross-sections, and NLO-to-LO k-factor for signal samples.

Sample Name	$\sigma(pb)$, LO	$k^{\mathrm{NLO/LO}}$
WRtoNLtoLLJJ_WR2800_N400	3.408×10^{-02}	1.35
WRtoNLtoLLJJ_WR2800_N600	3.214×10^{-02}	1.36
WRtoNLtoLLJJ_WR2800_N800	2.99×10^{-02}	1.36
WRtoNLtoLLJJ_WR2800_N1000	2.748×10^{-02}	1.36
WRtoNLtoLLJJ_WR2800_N1200	2.468×10^{-02}	1.36
WRtoNLtoLLJJ_WR2800_N1400	2.155×10^{-02}	1.36
WRtoNLtoLLJJ_WR2800_N1600	1.806×10^{-02}	1.36
WRtoNLtoLLJJ_WR2800_N1800	1.431×10^{-02}	1.36
WRtoNLtoLLJJ_WR2800_N2000	1.053×10^{-02}	1.37
WRtoNLtoLLJJ_WR2800_N2200	6.788×10^{-03}	1.37
WRtoNLtoLLJJ_WR2800_N2400	3.482×10^{-03}	1.37
WRtoNLtoLLJJ_WR2800_N2600	1.081×10^{-03}	1.37
WRtoNLtoLLJJ_WR2800_N2700	3.928×10^{-04}	1.38
WRtoNLtoLLJJ_WR3000_N100	2.376×10^{-02}	1.35
WRtoNLtoLLJJ_WR3000_N200	2.301×10^{-02}	1.36
WRtoNLtoLLJJ_WR3000_N400	2.166×10^{-02}	1.36
WRtoNLtoLLJJ_WR3000_N600	2.042×10^{-02}	1.37
WRtoNLtoLLJJ_WR3000_N800	1.905×10^{-02}	1.37
WRtoNLtoLLJJ_WR3000_N1000	1.762×10^{-02}	1.37
WRtoNLtoLLJJ_WR3000_N1200	1.605×10^{-02}	1.38
WRtoNLtoLLJJ_WR3000_N1400	1.427×10^{-02}	1.38
WRtoNLtoLLJJ_WR3000_N1600	1.236×10^{-02}	1.38
WRtoNLtoLLJJ_WR3000_N1800	1.025×10^{-02}	1.38
WRtoNLtoLLJJ_WR3000_N2000	8.069×10^{-03}	1.38
WRtoNLtoLLJJ_WR3000_N2200	5.861×10^{-03}	1.38
WRtoNLtoLLJJ_WR3000_N2400	3.746×10^{-03}	1.38
WRtoNLtoLLJJ_WR3000_N2600	1.903×10^{-03}	1.39
WRtoNLtoLLJJ_WR3000_N2800	5.913×10^{-04}	1.39
WRtoNLtoLLJJ_WR3000_N2900	2.188×10^{-04}	1.39
WRtoNLtoLLJJ_WR3200_N100	1.545×10^{-02}	1.36
WRtoNLtoLLJJ_WR3200_N200	1.486×10^{-02}	1.37
WRtoNLtoLLJJ_WR3200_N400	1.391×10^{-02}	1.38
WRtoNLtoLLJJ_WR3200_N600	1.308×10^{-02}	1.38
WRtoNLtoLLJJ_WR3200_N800	1.223×10^{-02}	1.39
WRtoNLtoLLJJ_WR3200_N1000	1.134×10^{-02}	1.39

Table 27: MINIAOD datasets, LO cross-sections, and NLO-to-LO k-factor for signal samples.

Sample Name	$\sigma(pb)$, LO	$k^{\mathrm{NLO/LO}}$
WRtoNLtoLLJJ_WR3200_N1200	1.044×10^{-02}	1.39
WRtoNLtoLLJJ_WR3200_N1400	9.417×10^{-03}	1.40
WRtoNLtoLLJJ_WR3200_N1600	8.364×10^{-03}	1.40
WRtoNLtoLLJJ_WR3200_N1800	7.143×10^{-03}	1.40
WRtoNLtoLLJJ_WR3200_N2000	5.881×10^{-03}	1.40
WRtoNLtoLLJJ_WR3200_N2200	4.585×10^{-03}	1.40
WRtoNLtoLLJJ_WR3200_N2400	3.303×10^{-03}	1.40
WRtoNLtoLLJJ_WR3200_N2600	2.092×10^{-03}	1.40
WRtoNLtoLLJJ_WR3200_N2800	1.055×10^{-03}	1.40
WRtoNLtoLLJJ_WR3200_N3000	3.262×10^{-04}	1.41
WRtoNLtoLLJJ_WR3200_N3100	1.23×10^{-04}	1.41
WRtoNLtoLLJJ_WR3400_N100	1.017×10^{-02}	1.37
WRtoNLtoLLJJ_WR3400_N200	9.756×10^{-03}	1.38
WRtoNLtoLLJJ_WR3400_N400	9.058×10^{-03}	1.39
WRtoNLtoLLJJ_WR3400_N600	8.478×10^{-03}	1.40
WRtoNLtoLLJJ_WR3400_N800	7.946×10^{-03}	1.40
WRtoNLtoLLJJ_WR3400_N1000	7.375×10^{-03}	1.41
WRtoNLtoLLJJ_WR3400_N1200	6.836×10^{-03}	1.41
WRtoNLtoLLJJ_WR3400_N1400	6.229×10^{-03}	1.41
WRtoNLtoLLJJ_WR3400_N1600	5.584×10^{-03}	1.41
WRtoNLtoLLJJ_WR3400_N1800	4.898×10^{-03}	1.41
WRtoNLtoLLJJ_WR3400_N2000	4.166×10^{-03}	1.42
WRtoNLtoLLJJ_WR3400_N2200	3.4×10^{-03}	1.42
WRtoNLtoLLJJ_WR3400_N2400	2.632×10^{-03}	1.42
WRtoNLtoLLJJ_WR3400_N2600	1.883×10^{-03}	1.42
WRtoNLtoLLJJ_WR3400_N2800	1.181×10^{-03}	1.42
WRtoNLtoLLJJ_WR3400_N3000	5.894×10^{-04}	1.42
WRtoNLtoLLJJ_WR3400_N3200	1.844×10^{-04}	1.42
WRtoNLtoLLJJ_WR3400_N3300	7.064×10^{-05}	1.42
WRtoNLtoLLJJ_WR3600_N100	6.83×10^{-03}	1.36
WRtoNLtoLLJJ_WR3600_N200	6.49×10^{-03}	1.37
WRtoNLtoLLJJ_WR3600_N400	5.978×10^{-03}	1.38
WRtoNLtoLLJJ_WR3600_N600	5.568×10^{-03}	1.39
WRtoNLtoLLJJ_WR3600_N800	5.185×10^{-03}	1.40
WRtoNLtoLLJJ_WR3600_N1000	4.843×10^{-03}	1.40

Table 28: MINIAOD datasets, LO cross-sections, and NLO-to-LO k-factor for signal samples.

Sample Name	$\sigma(pb)$, LO	$k^{\mathrm{NLO/LO}}$
WRtoNLtoLLJJ_WR3600_N1200	4.483×10^{-03}	1.41
WRtoNLtoLLJJ_WR3600_N1400	4.124×10^{-03}	1.41
WRtoNLtoLLJJ_WR3600_N1600	3.735×10^{-03}	1.41
WRtoNLtoLLJJ_WR3600_N1800	3.318×10^{-03}	1.41
WRtoNLtoLLJJ_WR3600_N2000	2.891×10^{-03}	1.41
WRtoNLtoLLJJ_WR3600_N2200	2.443×10^{-03}	1.41
WRtoNLtoLLJJ_WR3600_N2400	1.987×10^{-03}	1.42
WRtoNLtoLLJJ_WR3600_N2600	1.525×10^{-03}	1.42
WRtoNLtoLLJJ_WR3600_N2800	1.083×10^{-03}	1.42
WRtoNLtoLLJJ_WR3600_N3000	6.751×10^{-04}	1.42
WRtoNLtoLLJJ_WR3600_N3200	3.352×10^{-04}	1.41
WRtoNLtoLLJJ_WR3600_N3400	1.055×10^{-04}	1.41
WRtoNLtoLLJJ_WR3600_N3500	4.113×10^{-05}	1.41
WRtoNLtoLLJJ_WR3800_N100	4.659×10^{-03}	1.35
WRtoNLtoLLJJ_WR3800_N200	4.412×10^{-03}	1.36
WRtoNLtoLLJJ_WR3800_N400	3.996×10^{-03}	1.37
WRtoNLtoLLJJ_WR3800_N600	3.7×10^{-03}	1.38
WRtoNLtoLLJJ_WR3800_N800	3.437×10^{-03}	1.39
WRtoNLtoLLJJ_WR3800_N1000	3.192×10^{-03}	1.40
WRtoNLtoLLJJ_WR3800_N1200	2.961×10^{-03}	1.40
WRtoNLtoLLJJ_WR3800_N1400	2.73×10^{-03}	1.40
WRtoNLtoLLJJ_WR3800_N1600	2.495×10^{-03}	1.40
WRtoNLtoLLJJ_WR3800_N1800	2.251×10^{-03}	1.41
WRtoNLtoLLJJ_WR3800_N2000	1.995×10^{-03}	1.41
WRtoNLtoLLJJ_WR3800_N2200	1.721×10^{-03}	1.41
WRtoNLtoLLJJ_WR3800_N2400	1.448×10^{-03}	1.41
WRtoNLtoLLJJ_WR3800_N2600	1.17×10^{-03}	1.41
WRtoNLtoLLJJ_WR3800_N2800	8.948×10^{-04}	1.41
WRtoNLtoLLJJ_WR3800_N3000	6.3×10^{-04}	1.41
WRtoNLtoLLJJ_WR3800_N3200	3.903×10^{-04}	1.41
WRtoNLtoLLJJ_WR3800_N3400	1.934×10^{-04}	1.41
WRtoNLtoLLJJ_WR3800_N3600	6.13×10^{-05}	1.41
WRtoNLtoLLJJ_WR3800_N3700	2.421×10^{-05}	1.41
WRtoNLtoLLJJ_WR4000_N100	3.258×10^{-03}	1.34
WRtoNLtoLLJJ_WR4000_N200	3.049×10^{-03}	1.35

Table 29: MINIAOD datasets, LO cross-sections, and NLO-to-LO k-factor for signal samples.

Sample Name	$\sigma(pb)$, LO	$k^{\mathrm{NLO/LO}}$
WRtoNLtoLLJJ_WR4000_N400	2.727×10^{-03}	1.37
WRtoNLtoLLJJ_WR4000_N600	2.491×10^{-03}	1.38
WRtoNLtoLLJJ_WR4000_N800	2.299×10^{-03}	1.39
WRtoNLtoLLJJ_WR4000_N1000	2.137×10^{-03}	1.40
WRtoNLtoLLJJ_WR4000_N1200	1.984×10^{-03}	1.40
WRtoNLtoLLJJ_WR4000_N1400	1.829×10^{-03}	1.40
WRtoNLtoLLJJ_WR4000_N1600	1.677×10^{-03}	1.41
WRtoNLtoLLJJ_WR4000_N1800	1.529×10^{-03}	1.41
WRtoNLtoLLJJ_WR4000_N2000	1.37×10^{-03}	1.41
WRtoNLtoLLJJ_WR4000_N2200	1.207×10^{-03}	1.41
WRtoNLtoLLJJ_WR4000_N2400	1.04×10^{-03}	1.41
WRtoNLtoLLJJ_WR4000_N2600	8.684×10^{-04}	1.41
WRtoNLtoLLJJ_WR4000_N2800	6.971×10^{-04}	1.41
WRtoNLtoLLJJ_WR4000_N3000	5.318×10^{-04}	1.41
WRtoNLtoLLJJ_WR4000_N3200	3.718×10^{-04}	1.41
WRtoNLtoLLJJ_WR4000_N3400	2.294×10^{-04}	1.41
WRtoNLtoLLJJ_WR4000_N3600	1.135×10^{-04}	1.41
WRtoNLtoLLJJ_WR4000_N3800	3.594×10^{-05}	1.41
WRtoNLtoLLJJ_WR4000_N3900	1.456×10^{-05}	1.42
WRtoNLtoLLJJ_WR4200_N100	2.323×10^{-03}	1.34
WRtoNLtoLLJJ_WR4200_N200	2.156×10^{-03}	1.35
WRtoNLtoLLJJ_WR4200_N400	1.891×10^{-03}	1.37
WRtoNLtoLLJJ_WR4200_N600	1.715×10^{-03}	1.39
WRtoNLtoLLJJ_WR4200_N800	1.571×10^{-03}	1.40
WRtoNLtoLLJJ_WR4200_N1000	1.448×10^{-03}	1.40
WRtoNLtoLLJJ_WR4200_N1200	1.338×10^{-03}	1.41
WRtoNLtoLLJJ_WR4200_N1400	1.241×10^{-03}	1.41
WRtoNLtoLLJJ_WR4200_N1600	1.141×10^{-03}	1.42
WRtoNLtoLLJJ_WR4200_N1800	1.041×10^{-03}	1.42
WRtoNLtoLLJJ_WR4200_N2000	9.419×10^{-04}	1.42
WRtoNLtoLLJJ_WR4200_N2200	8.416×10^{-04}	1.42
WRtoNLtoLLJJ_WR4200_N2400	7.402×10^{-04}	1.42
WRtoNLtoLLJJ_WR4200_N2600	6.345×10^{-04}	1.42
WRtoNLtoLLJJ_WR4200_N2800	5.277×10^{-04}	1.42
WRtoNLtoLLJJ_WR4200_N3000	4.223×10^{-04}	1.42

Table 30: MINIAOD datasets, LO cross-sections, and NLO-to-LO k-factor for signal samples.

Sample Name	$\sigma(pb)$, LO	$k^{\mathrm{NLO/LO}}$
WRtoNLtoLLJJ_WR4200_N3200	3.192×10^{-04}	1.42
WRtoNLtoLLJJ_WR4200_N3400	2.221×10^{-04}	1.42
WRtoNLtoLLJJ_WR4200_N3600	1.366×10^{-04}	1.43
WRtoNLtoLLJJ_WR4200_N3800	6.727×10^{-05}	1.43
WRtoNLtoLLJJ_WR4200_N4000	2.145×10^{-05}	1.43
WRtoNLtoLLJJ_WR4200_N4100	8.993×10^{-06}	1.43
WRtoNLtoLLJJ_WR4400_N100	1.696×10^{-03}	1.34
WRtoNLtoLLJJ_WR4400_N200	1.556×10^{-03}	1.35
WRtoNLtoLLJJ_WR4400_N400	1.352×10^{-03}	1.37
WRtoNLtoLLJJ_WR4400_N600	1.201×10^{-03}	1.39
WRtoNLtoLLJJ_WR4400_N800	1.092×10^{-03}	1.40
WRtoNLtoLLJJ_WR4400_N1000	9.943×10^{-04}	1.41
WRtoNLtoLLJJ_WR4400_N1200	9.204×10^{-04}	1.42
WRtoNLtoLLJJ_WR4400_N1400	8.498×10^{-04}	1.42
WRtoNLtoLLJJ_WR4400_N1600	7.847×10^{-04}	1.43
WRtoNLtoLLJJ_WR4400_N1800	7.199×10^{-04}	1.43
WRtoNLtoLLJJ_WR4400_N2000	6.561×10^{-04}	1.43
WRtoNLtoLLJJ_WR4400_N2200	5.889×10^{-04}	1.43
WRtoNLtoLLJJ_WR4400_N2400	5.255×10^{-04}	1.43
WRtoNLtoLLJJ_WR4400_N2600	4.588×10^{-04}	1.43
WRtoNLtoLLJJ_WR4400_N2800	3.923×10^{-04}	1.44
WRtoNLtoLLJJ_WR4400_N3000	3.26×10^{-04}	1.44
WRtoNLtoLLJJ_WR4400_N3200	2.587×10^{-04}	1.44
WRtoNLtoLLJJ_WR4400_N3400	1.952×10^{-04}	1.44
WRtoNLtoLLJJ_WR4400_N3600	1.349×10^{-04}	1.44
WRtoNLtoLLJJ_WR4400_N3800	8.271×10^{-05}	1.44
WRtoNLtoLLJJ_WR4400_N4000	4.087×10^{-05}	1.44
WRtoNLtoLLJJ_WR4400_N4200	1.32×10^{-05}	1.43
WRtoNLtoLLJJ_WR4400_N4300	5.639×10^{-06}	1.43
WRtoNLtoLLJJ_WR4600_N100	1.268×10^{-03}	1.32
WRtoNLtoLLJJ_WR4600_N200	1.152×10^{-03}	1.34
WRtoNLtoLLJJ_WR4600_N400	9.786×10^{-04}	1.36
WRtoNLtoLLJJ_WR4600_N600	8.614×10^{-04}	1.38
WRtoNLtoLLJJ_WR4600_N800	7.695×10^{-04}	1.39
WRtoNLtoLLJJ_WR4600_N1000	7.013×10^{-04}	1.40

Table 31: MINIAOD datasets, LO cross-sections, and NLO-to-LO k-factor for signal samples.

Sample Name	$\sigma(pb)$, LO	$k^{\mathrm{NLO/LO}}$
WRtoNLtoLLJJ_WR4600_N1200	6.428×10^{-04}	1.41
WRtoNLtoLLJJ_WR4600_N1400	5.911×10^{-04}	1.42
WRtoNLtoLLJJ_WR4600_N1600	5.437×10^{-04}	1.42
WRtoNLtoLLJJ_WR4600_N1800	5.009×10^{-04}	1.42
WRtoNLtoLLJJ_WR4600_N2000	4.593×10^{-04}	1.42
WRtoNLtoLLJJ_WR4600_N2200	4.184×10^{-04}	1.43
WRtoNLtoLLJJ_WR4600_N2400	3.735×10^{-04}	1.43
WRtoNLtoLLJJ_WR4600_N2600	3.315×10^{-04}	1.43
WRtoNLtoLLJJ_WR4600_N2800	2.908×10^{-04}	1.43
WRtoNLtoLLJJ_WR4600_N3000	2.456×10^{-04}	1.43
WRtoNLtoLLJJ_WR4600_N3200	2.045×10^{-04}	1.43
WRtoNLtoLLJJ_WR4600_N3400	1.613×10^{-04}	1.43
WRtoNLtoLLJJ_WR4600_N3600	1.21×10^{-04}	1.43
WRtoNLtoLLJJ_WR4600_N3800	8.373×10^{-05}	1.43
WRtoNLtoLLJJ_WR4600_N4000	5.118×10^{-05}	1.43
WRtoNLtoLLJJ_WR4600_N4200	2.52×10^{-05}	1.42
WRtoNLtoLLJJ_WR4600_N4400	8.234×10^{-06}	1.42
WRtoNLtoLLJJ_WR4600_N4500	3.62×10^{-06}	1.42
WRtoNLtoLLJJ_WR4800_N100	9.702×10^{-04}	1.31
WRtoNLtoLLJJ_WR4800_N200	8.7×10^{-04}	1.33
WRtoNLtoLLJJ_WR4800_N400	7.256×10^{-04}	1.35
WRtoNLtoLLJJ_WR4800_N600	6.289×10^{-04}	1.37
WRtoNLtoLLJJ_WR4800_N800	5.569×10^{-04}	1.38
WRtoNLtoLLJJ_WR4800_N1000	5.025×10^{-04}	1.39
WRtoNLtoLLJJ_WR4800_N1200	4.574×10^{-04}	1.40
WRtoNLtoLLJJ_WR4800_N1400	4.196×10^{-04}	1.40
WRtoNLtoLLJJ_WR4800_N1600	3.84×10^{-04}	1.41
WRtoNLtoLLJJ_WR4800_N1800	3.578×10^{-04}	1.41
WRtoNLtoLLJJ_WR4800_N2000	3.273×10^{-04}	1.41
WRtoNLtoLLJJ_WR4800_N2200	2.981×10^{-04}	1.41
WRtoNLtoLLJJ_WR4800_N2400	2.699×10^{-04}	1.41
WRtoNLtoLLJJ_WR4800_N2600	2.424×10^{-04}	1.41
WRtoNLtoLLJJ_WR4800_N2800	2.142×10^{-04}	1.42
WRtoNLtoLLJJ_WR4800_N3000	1.864×10^{-04}	1.42
WRtoNLtoLLJJ_WR4800_N3200	1.576×10^{-04}	1.41

Table 32: MINIAOD datasets, LO cross-sections, and NLO-to-LO k-factor for signal samples.

Sample Name	$\sigma(pb)$, LO	$k^{\mathrm{NLO/LO}}$
WRtoNLtoLLJJ_WR4800_N3400	1.3×10^{-04}	1.41
WRtoNLtoLLJJ_WR4800_N3600	1.024×10^{-04}	1.41
WRtoNLtoLLJJ_WR4800_N3800	7.687×10^{-05}	1.41
WRtoNLtoLLJJ_WR4800_N4000	5.298×10^{-05}	1.41
WRtoNLtoLLJJ_WR4800_N4200	3.221×10^{-05}	1.41
WRtoNLtoLLJJ_WR4800_N4400	1.594×10^{-05}	1.41
WRtoNLtoLLJJ_WR4800_N4600	5.282×10^{-06}	1.41
WRtoNLtoLLJJ_WR4800_N4700	2.37×10^{-06}	1.41
WRtoNLtoLLJJ_WR5000_N100	7.581×10^{-04}	1.30
WRtoNLtoLLJJ_WR5000_N200	6.707×10^{-04}	1.31
WRtoNLtoLLJJ_WR5000_N400	5.517×10^{-04}	1.34
WRtoNLtoLLJJ_WR5000_N600	4.704×10^{-04}	1.36
WRtoNLtoLLJJ_WR5000_N800	4.119×10^{-04}	1.37
WRtoNLtoLLJJ_WR5000_N1000	3.676×10^{-04}	1.38
WRtoNLtoLLJJ_WR5000_N1200	3.331×10^{-04}	1.39
WRtoNLtoLLJJ_WR5000_N1400	3.055×10^{-04}	1.40
WRtoNLtoLLJJ_WR5000_N1600	2.788×10^{-04}	1.40
WRtoNLtoLLJJ_WR5000_N1800	2.562×10^{-04}	1.40
WRtoNLtoLLJJ_WR5000_N2000	2.346×10^{-04}	1.41
WRtoNLtoLLJJ_WR5000_N2200	2.151×10^{-04}	1.41
WRtoNLtoLLJJ_WR5000_N2400	1.964×10^{-04}	1.41
WRtoNLtoLLJJ_WR5000_N2600	1.774×10^{-04}	1.41
WRtoNLtoLLJJ_WR5000_N2800	1.586×10^{-04}	1.41
WRtoNLtoLLJJ_WR5000_N3000	1.407×10^{-04}	1.41
WRtoNLtoLLJJ_WR5000_N3200	1.214×10^{-04}	1.41
WRtoNLtoLLJJ_WR5000_N3400	1.03×10^{-04}	1.41
WRtoNLtoLLJJ_WR5000_N3600	8.436×10^{-05}	1.41
WRtoNLtoLLJJ_WR5000_N3800	6.682×10^{-05}	1.41
WRtoNLtoLLJJ_WR5000_N4000	4.939×10^{-05}	1.41
WRtoNLtoLLJJ_WR5000_N4200	3.418×10^{-05}	1.41
WRtoNLtoLLJJ_WR5000_N4400	2.078×10^{-05}	1.41
WRtoNLtoLLJJ_WR5000_N4600	1.03×10^{-05}	1.41
WRtoNLtoLLJJ_WR5000_N4800	3.466×10^{-06}	1.41
WRtoNLtoLLJJ_WR5000_N4900	1.599×10^{-06}	1.41
WRtoNLtoLLJJ_WR5200_N100	6.016×10^{-04}	1.29

Table 33: MINIAOD datasets, LO cross-sections, and NLO-to-LO k-factor for signal samples.

Sample Name	$\sigma(pb)$, LO	$k^{\mathrm{NLO/LO}}$
WRtoNLtoLLJJ_WR5200_N200	5.304×10^{-04}	1.31
WRtoNLtoLLJJ_WR5200_N400	4.292×10^{-04}	1.33
WRtoNLtoLLJJ_WR5200_N600	3.595×10^{-04}	1.35
WRtoNLtoLLJJ_WR5200_N800	3.114×10^{-04}	1.37
WRtoNLtoLLJJ_WR5200_N1000	2.753×10^{-04}	1.38
WRtoNLtoLLJJ_WR5200_N1200	2.448×10^{-04}	1.39
WRtoNLtoLLJJ_WR5200_N1400	2.238×10^{-04}	1.40
WRtoNLtoLLJJ_WR5200_N1600	2.036×10^{-04}	1.40
WRtoNLtoLLJJ_WR5200_N1800	1.877×10^{-04}	1.40
WRtoNLtoLLJJ_WR5200_N2000	1.722×10^{-04}	1.41
WRtoNLtoLLJJ_WR5200_N2200	1.578×10^{-04}	1.41
WRtoNLtoLLJJ_WR5200_N2400	1.447×10^{-04}	1.41
WRtoNLtoLLJJ_WR5200_N2600	1.32×10^{-04}	1.41
WRtoNLtoLLJJ_WR5200_N2800	1.187×10^{-04}	1.41
WRtoNLtoLLJJ_WR5200_N3000	1.064×10^{-04}	1.41
WRtoNLtoLLJJ_WR5200_N3200	9.365×10^{-05}	1.41
WRtoNLtoLLJJ_WR5200_N3400	8.11×10^{-05}	1.41
WRtoNLtoLLJJ_WR5200_N3600	6.86×10^{-05}	1.41
WRtoNLtoLLJJ_WR5200_N3800	5.595×10^{-05}	1.41
WRtoNLtoLLJJ_WR5200_N4000	4.402×10^{-05}	1.41
WRtoNLtoLLJJ_WR5200_N4200	3.286×10^{-05}	1.41
WRtoNLtoLLJJ_WR5200_N4400	2.263×10^{-05}	1.41
WRtoNLtoLLJJ_WR5200_N4600	1.371×10^{-05}	1.41
WRtoNLtoLLJJ_WR5200_N4800	6.813×10^{-06}	1.41
WRtoNLtoLLJJ_WR5200_N5000	2.335×10^{-06}	1.41
WRtoNLtoLLJJ_WR5200_N5100	1.087×10^{-06}	1.42
WRtoNLtoLLJJ_WR5400_N100	4.865×10^{-04}	1.29
WRtoNLtoLLJJ_WR5400_N200	4.262×10^{-04}	1.30
WRtoNLtoLLJJ_WR5400_N400	3.393×10^{-04}	1.33
WRtoNLtoLLJJ_WR5400_N600	2.807×10^{-04}	1.35
WRtoNLtoLLJJ_WR5400_N800	2.399×10^{-04}	1.37
WRtoNLtoLLJJ_WR5400_N1000	2.083×10^{-04}	1.38
WRtoNLtoLLJJ_WR5400_N1200	1.855×10^{-04}	1.39
WRtoNLtoLLJJ_WR5400_N1400	1.676×10^{-04}	1.40
WRtoNLtoLLJJ_WR5400_N1600	1.529×10^{-04}	1.40

Table 34: MINIAOD datasets, LO cross-sections, and NLO-to-LO k-factor for signal samples.

Sample Name	$\sigma(pb)$, LO	$k^{\mathrm{NLO/LO}}$
WRtoNLtoLLJJ_WR5400_N1800	1.394×10^{-04}	1.41
WRtoNLtoLLJJ_WR5400_N2000	1.282×10^{-04}	1.41
WRtoNLtoLLJJ_WR5400_N2200	1.18×10^{-04}	1.41
WRtoNLtoLLJJ_WR5400_N2400	1.083×10^{-04}	1.41
WRtoNLtoLLJJ_WR5400_N2600	9.949×10^{-05}	1.41
WRtoNLtoLLJJ_WR5400_N2800	9.056×10^{-05}	1.41
WRtoNLtoLLJJ_WR5400_N3000	8.175×10^{-05}	1.41
WRtoNLtoLLJJ_WR5400_N3200	7.273×10^{-05}	1.41
WRtoNLtoLLJJ_WR5400_N3400	6.379×10^{-05}	1.41
WRtoNLtoLLJJ_WR5400_N3600	5.541×10^{-05}	1.41
WRtoNLtoLLJJ_WR5400_N3800	4.661×10^{-05}	1.41
WRtoNLtoLLJJ_WR5400_N4000	3.801×10^{-05}	1.41
WRtoNLtoLLJJ_WR5400_N4200	2.978×10^{-05}	1.41
WRtoNLtoLLJJ_WR5400_N4400	2.228×10^{-05}	1.41
WRtoNLtoLLJJ_WR5400_N4600	1.512×10^{-05}	1.41
WRtoNLtoLLJJ_WR5400_N4800	9.22×10^{-06}	1.41
WRtoNLtoLLJJ_WR5400_N5000	4.593×10^{-06}	1.41
WRtoNLtoLLJJ_WR5400_N5200	1.579×10^{-06}	1.42
WRtoNLtoLLJJ_WR5400_N5300	7.552×10^{-07}	1.42
WRtoNLtoLLJJ_WR5600_N100	3.985×10^{-04}	1.28
WRtoNLtoLLJJ_WR5600_N200	3.456×10^{-04}	1.30
WRtoNLtoLLJJ_WR5600_N400	2.72×10^{-04}	1.32
WRtoNLtoLLJJ_WR5600_N600	2.224×10^{-04}	1.35
WRtoNLtoLLJJ_WR5600_N800	1.875×10^{-04}	1.36
WRtoNLtoLLJJ_WR5600_N1000	1.613×10^{-04}	1.38
WRtoNLtoLLJJ_WR5600_N1200	1.422×10^{-04}	1.39
WRtoNLtoLLJJ_WR5600_N1400	1.278×10^{-04}	1.40
WRtoNLtoLLJJ_WR5600_N1600	1.157×10^{-04}	1.40
WRtoNLtoLLJJ_WR5600_N1800	1.057×10^{-04}	1.41
WRtoNLtoLLJJ_WR5600_N2000	9.679×10^{-05}	1.41
WRtoNLtoLLJJ_WR5600_N2200	8.893×10^{-05}	1.41
WRtoNLtoLLJJ_WR5600_N2400	8.211×10^{-05}	1.41
WRtoNLtoLLJJ_WR5600_N2600	7.583×10^{-05}	1.41
WRtoNLtoLLJJ_WR5600_N2800	6.938×10^{-05}	1.41
WRtoNLtoLLJJ_WR5600_N3000	6.324×10^{-05}	1.41

Table 35: MINIAOD datasets, LO cross-sections, and NLO-to-LO k-factor for signal samples.

Sample Name	$\sigma(pb)$, LO	$k^{\mathrm{NLO/LO}}$
WRtoNLtoLLJJ_WR5600_N3200	5.701×10^{-05}	1.41
WRtoNLtoLLJJ_WR5600_N3400	5.059×10^{-05}	1.41
WRtoNLtoLLJJ_WR5600_N3600	4.46×10^{-05}	1.41
WRtoNLtoLLJJ_WR5600_N3800	3.828×10^{-05}	1.41
WRtoNLtoLLJJ_WR5600_N4000	3.211×10^{-05}	1.41
WRtoNLtoLLJJ_WR5600_N4200	2.62×10^{-05}	1.41
WRtoNLtoLLJJ_WR5600_N4400	2.066×10^{-05}	1.41
WRtoNLtoLLJJ_WR5600_N4600	1.518×10^{-05}	1.41
WRtoNLtoLLJJ_WR5600_N4800	1.041×10^{-05}	1.41
WRtoNLtoLLJJ_WR5600_N5000	6.317×10^{-06}	1.41
WRtoNLtoLLJJ_WR5600_N5200	3.174×10^{-06}	1.42
WRtoNLtoLLJJ_WR5600_N5400	1.108×10^{-06}	1.42
WRtoNLtoLLJJ_WR5600_N5500	5.342×10^{-07}	1.42
WRtoNLtoLLJJ_WR5800_N100	3.305×10^{-04}	1.27
WRtoNLtoLLJJ_WR5800_N200	2.862×10^{-04}	1.29
WRtoNLtoLLJJ_WR5800_N400	2.217×10^{-04}	1.31
WRtoNLtoLLJJ_WR5800_N600	1.794×10^{-04}	1.34
WRtoNLtoLLJJ_WR5800_N800	1.491×10^{-04}	1.36
WRtoNLtoLLJJ_WR5800_N1000	1.267×10^{-04}	1.37
WRtoNLtoLLJJ_WR5800_N1200	1.108×10^{-04}	1.38
WRtoNLtoLLJJ_WR5800_N1400	9.829×10^{-05}	1.39
WRtoNLtoLLJJ_WR5800_N1600	8.897×10^{-05}	1.40
WRtoNLtoLLJJ_WR5800_N1800	8.067×10^{-05}	1.40
WRtoNLtoLLJJ_WR5800_N2000	7.43×10^{-05}	1.41
WRtoNLtoLLJJ_WR5800_N2200	6.836×10^{-05}	1.41
WRtoNLtoLLJJ_WR5800_N2400	6.282×10^{-05}	1.41
WRtoNLtoLLJJ_WR5800_N2600	5.84×10^{-05}	1.41
WRtoNLtoLLJJ_WR5800_N2800	5.32×10^{-05}	1.41
WRtoNLtoLLJJ_WR5800_N3000	4.904×10^{-05}	1.41
WRtoNLtoLLJJ_WR5800_N3200	4.456×10^{-05}	1.41
WRtoNLtoLLJJ_WR5800_N3400	4.043×10^{-05}	1.41
WRtoNLtoLLJJ_WR5800_N3600	3.578×10^{-05}	1.41
WRtoNLtoLLJJ_WR5800_N3800	3.137×10^{-05}	1.41
WRtoNLtoLLJJ_WR5800_N4000	2.705×10^{-05}	1.41
WRtoNLtoLLJJ_WR5800_N4200	2.274×10^{-05}	1.41

Table 36: MINIAOD datasets, LO cross-sections, and NLO-to-LO k-factor for signal samples.

Sample Name	$\sigma(pb)$, LO	$k^{\mathrm{NLO/LO}}$
WRtoNLtoLLJJ_WR5800_N4400	1.845×10^{-05}	1.41
WRtoNLtoLLJJ_WR5800_N4600	1.441×10^{-05}	1.41
WRtoNLtoLLJJ_WR5800_N4800	1.067×10^{-05}	1.41
WRtoNLtoLLJJ_WR5800_N5000	7.311×10^{-06}	1.41
WRtoNLtoLLJJ_WR5800_N5200	4.402×10^{-06}	1.41
WRtoNLtoLLJJ_WR5800_N5400	2.195×10^{-06}	1.41
WRtoNLtoLLJJ_WR5800_N5600	7.834×10^{-07}	1.41
WRtoNLtoLLJJ_WR5800_N5700	3.822×10^{-07}	1.42
WRtoNLtoLLJJ_WR6000_N100	2.783×10^{-04}	1.27
WRtoNLtoLLJJ_WR6000_N200	2.388×10^{-04}	1.28
WRtoNLtoLLJJ_WR6000_N400	1.827×10^{-04}	1.31
WRtoNLtoLLJJ_WR6000_N600	1.454×10^{-04}	1.33
WRtoNLtoLLJJ_WR6000_N800	1.202×10^{-04}	1.35
WRtoNLtoLLJJ_WR6000_N1000	1.013×10^{-04}	1.37
WRtoNLtoLLJJ_WR6000_N1200	8.778×10^{-05}	1.38
WRtoNLtoLLJJ_WR6000_N1400	7.75×10^{-05}	1.39
WRtoNLtoLLJJ_WR6000_N1600	6.938×10^{-05}	1.40
WRtoNLtoLLJJ_WR6000_N1800	6.289×10^{-05}	1.40
WRtoNLtoLLJJ_WR6000_N2000	5.7×10^{-05}	1.40
WRtoNLtoLLJJ_WR6000_N2200	5.28×10^{-05}	1.40
WRtoNLtoLLJJ_WR6000_N2400	4.899×10^{-05}	1.40
WRtoNLtoLLJJ_WR6000_N2600	4.509×10^{-05}	1.41
WRtoNLtoLLJJ_WR6000_N2800	4.172×10^{-05}	1.41
WRtoNLtoLLJJ_WR6000_N3000	3.839×10^{-05}	1.41
WRtoNLtoLLJJ_WR6000_N3200	3.512×10^{-05}	1.41
WRtoNLtoLLJJ_WR6000_N3400	3.192×10^{-05}	1.40
WRtoNLtoLLJJ_WR6000_N3600	2.887×10^{-05}	1.40
WRtoNLtoLLJJ_WR6000_N3800	2.564×10^{-05}	1.40
WRtoNLtoLLJJ_WR6000_N4000	2.248×10^{-05}	1.40
WRtoNLtoLLJJ_WR6000_N4200	1.929×10^{-05}	1.40
WRtoNLtoLLJJ_WR6000_N4400	1.615×10^{-05}	1.40
WRtoNLtoLLJJ_WR6000_N4600	1.31×10^{-05}	1.40
WRtoNLtoLLJJ_WR6000_N4800	1.016×10^{-05}	1.40
WRtoNLtoLLJJ_WR6000_N5000	7.596×10^{-06}	1.41
WRtoNLtoLLJJ_WR6000_N5200	5.104×10^{-06}	1.41

Table 37: MINIAOD datasets, LO cross-sections, and NLO-to-LO k-factor for signal samples.

Sample Name	$\sigma(pb)$, LO	$k^{\mathrm{NLO/LO}}$
WRtoNLtoLLJJ_WR6000_N5400	3.108×10^{-06}	1.41
WRtoNLtoLLJJ_WR6000_N5600	1.572×10^{-06}	1.41
WRtoNLtoLLJJ_WR6000_N5800	5.528×10^{-07}	1.42
WRtoNLtoLLJJ_WR6000_N5900	2.731×10^{-07}	1.44
WRtoNLtoLLJJ_WR6200_N100	2.359×10^{-04}	1.27
WRtoNLtoLLJJ_WR6200_N200	2.015×10^{-04}	1.28
WRtoNLtoLLJJ_WR6200_N400	1.519×10^{-04}	1.31
WRtoNLtoLLJJ_WR6200_N600	1.202×10^{-04}	1.33
WRtoNLtoLLJJ_WR6200_N800	9.734×10^{-05}	1.35
WRtoNLtoLLJJ_WR6200_N1000	8.167×10^{-05}	1.37
WRtoNLtoLLJJ_WR6200_N1200	6.978×10^{-05}	1.39
WRtoNLtoLLJJ_WR6200_N1400	6.133×10^{-05}	1.40
WRtoNLtoLLJJ_WR6200_N1600	5.458×10^{-05}	1.40
WRtoNLtoLLJJ_WR6200_N1800	4.93×10^{-05}	1.41
WRtoNLtoLLJJ_WR6200_N2000	4.496×10^{-05}	1.41
WRtoNLtoLLJJ_WR6200_N2200	4.128×10^{-05}	1.41
WRtoNLtoLLJJ_WR6200_N2400	3.807×10^{-05}	1.42
WRtoNLtoLLJJ_WR6200_N2600	3.529×10^{-05}	1.42
WRtoNLtoLLJJ_WR6200_N2800	3.273×10^{-05}	1.42
WRtoNLtoLLJJ_WR6200_N3000	3.011×10^{-05}	1.42
WRtoNLtoLLJJ_WR6200_N3200	2.774×10^{-05}	1.42
WRtoNLtoLLJJ_WR6200_N3400	2.539×10^{-05}	1.42
WRtoNLtoLLJJ_WR6200_N3600	2.313×10^{-05}	1.42
WRtoNLtoLLJJ_WR6200_N3800	2.072×10^{-05}	1.42
WRtoNLtoLLJJ_WR6200_N4000	1.841×10^{-05}	1.42
WRtoNLtoLLJJ_WR6200_N4200	1.606×10^{-05}	1.42
WRtoNLtoLLJJ_WR6200_N4400	1.377×10^{-05}	1.42
WRtoNLtoLLJJ_WR6200_N4600	1.155×10^{-05}	1.42
WRtoNLtoLLJJ_WR6200_N4800	9.384×10^{-06}	1.42
WRtoNLtoLLJJ_WR6200_N5000	7.321×10^{-06}	1.42
WRtoNLtoLLJJ_WR6200_N5200	5.369×10^{-06}	1.42
WRtoNLtoLLJJ_WR6200_N5400	3.64×10^{-06}	1.42
WRtoNLtoLLJJ_WR6200_N5600	2.202×10^{-06}	1.43
WRtoNLtoLLJJ_WR6200_N5800	1.113×10^{-06}	1.43
WRtoNLtoLLJJ_WR6200_N6000	3.959×10^{-07}	1.44

Table 38: MINIAOD datasets, LO cross-sections, and NLO-to-LO k-factor for signal samples.

Sample Name	$\sigma(pb)$, LO	$k^{\mathrm{NLO/LO}}$
WRtoNLtoLLJJ_WR6200_N6100	1.969×10^{-07}	1.46
WRtoNLtoLLJJ_WR6400_N100	2.018×10^{-04}	1.27
WRtoNLtoLLJJ_WR6400_N200	1.703×10^{-04}	1.28
WRtoNLtoLLJJ_WR6400_N400	1.275×10^{-04}	1.31
WRtoNLtoLLJJ_WR6400_N600	9.967×10^{-05}	1.33
WRtoNLtoLLJJ_WR6400_N800	7.972×10^{-05}	1.36
WRtoNLtoLLJJ_WR6400_N1000	6.614×10^{-05}	1.38
WRtoNLtoLLJJ_WR6400_N1200	5.655×10^{-05}	1.39
WRtoNLtoLLJJ_WR6400_N1400	4.885×10^{-05}	1.40
WRtoNLtoLLJJ_WR6400_N1600	4.322×10^{-05}	1.41
WRtoNLtoLLJJ_WR6400_N1800	3.878×10^{-05}	1.42
WRtoNLtoLLJJ_WR6400_N2000	3.541×10^{-05}	1.43
WRtoNLtoLLJJ_WR6400_N2200	3.233×10^{-05}	1.43
WRtoNLtoLLJJ_WR6400_N2400	2.994×10^{-05}	1.43
WRtoNLtoLLJJ_WR6400_N2600	2.771×10^{-05}	1.43
WRtoNLtoLLJJ_WR6400_N2800	2.553×10^{-05}	1.43
WRtoNLtoLLJJ_WR6400_N3000	2.375×10^{-05}	1.43
WRtoNLtoLLJJ_WR6400_N3200	2.198×10^{-05}	1.43
WRtoNLtoLLJJ_WR6400_N3400	2.033×10^{-05}	1.44
WRtoNLtoLLJJ_WR6400_N3600	1.861×10^{-05}	1.44
WRtoNLtoLLJJ_WR6400_N3800	1.678×10^{-05}	1.44
WRtoNLtoLLJJ_WR6400_N4000	1.511×10^{-05}	1.44
WRtoNLtoLLJJ_WR6400_N4200	1.343×10^{-05}	1.44
WRtoNLtoLLJJ_WR6400_N4400	1.164×10^{-05}	1.44
WRtoNLtoLLJJ_WR6400_N4600	9.949×10^{-06}	1.44
WRtoNLtoLLJJ_WR6400_N4800	8.339×10^{-06}	1.44
WRtoNLtoLLJJ_WR6400_N5000	6.753×10^{-06}	1.44
WRtoNLtoLLJJ_WR6400_N5200	5.239×10^{-06}	1.44
WRtoNLtoLLJJ_WR6400_N5400	3.838×10^{-06}	1.44
WRtoNLtoLLJJ_WR6400_N5600	2.611×10^{-06}	1.44
WRtoNLtoLLJJ_WR6400_N5800	1.59×10^{-06}	1.45
WRtoNLtoLLJJ_WR6400_N6000	7.953×10^{-07}	1.45
WRtoNLtoLLJJ_WR6400_N6200	2.833×10^{-07}	1.46
WRtoNLtoLLJJ_WR6400_N6300	1.425×10^{-07}	1.48
WRtoNLtoLLJJ_WR6600_N100	1.734×10^{-04}	1.26

Table 39: MINIAOD datasets, LO cross-sections, and NLO-to-LO k-factor for signal samples.

Sample Name	$\sigma(pb)$, LO	$k^{\mathrm{NLO/LO}}$
WRtoNLtoLLJJ_WR6600_N200	1.461×10^{-04}	1.28
WRtoNLtoLLJJ_WR6600_N400	1.082×10^{-04}	1.31
WRtoNLtoLLJJ_WR6600_N600	8.348×10^{-05}	1.33
WRtoNLtoLLJJ_WR6600_N800	6.625×10^{-05}	1.36
WRtoNLtoLLJJ_WR6600_N1000	5.406×10^{-05}	1.38
WRtoNLtoLLJJ_WR6600_N1200	4.589×10^{-05}	1.40
WRtoNLtoLLJJ_WR6600_N1400	3.926×10^{-05}	1.41
WRtoNLtoLLJJ_WR6600_N1600	3.438×10^{-05}	1.42
WRtoNLtoLLJJ_WR6600_N1800	3.065×10^{-05}	1.43
WRtoNLtoLLJJ_WR6600_N2000	2.757×10^{-05}	1.43
WRtoNLtoLLJJ_WR6600_N2200	2.539×10^{-05}	1.44
WRtoNLtoLLJJ_WR6600_N2400	2.334×10^{-05}	1.44
WRtoNLtoLLJJ_WR6600_N2600	2.162×10^{-05}	1.44
WRtoNLtoLLJJ_WR6600_N2800	1.997×10^{-05}	1.45
WRtoNLtoLLJJ_WR6600_N3000	1.864×10^{-05}	1.45
WRtoNLtoLLJJ_WR6600_N3200	1.739×10^{-05}	1.45
WRtoNLtoLLJJ_WR6600_N3400	1.596×10^{-05}	1.45
WRtoNLtoLLJJ_WR6600_N3600	1.474×10^{-05}	1.45
WRtoNLtoLLJJ_WR6600_N3800	1.353×10^{-05}	1.45
WRtoNLtoLLJJ_WR6600_N4000	1.228×10^{-05}	1.45
WRtoNLtoLLJJ_WR6600_N4200	1.098×10^{-05}	1.45
WRtoNLtoLLJJ_WR6600_N4400	9.688×10^{-06}	1.45
WRtoNLtoLLJJ_WR6600_N4600	8.438×10^{-06}	1.45
WRtoNLtoLLJJ_WR6600_N4800	7.233×10^{-06}	1.45
WRtoNLtoLLJJ_WR6600_N5000	6.013×10^{-06}	1.45
WRtoNLtoLLJJ_WR6600_N5200	4.89×10^{-06}	1.45
WRtoNLtoLLJJ_WR6600_N5400	3.755×10^{-06}	1.46
WRtoNLtoLLJJ_WR6600_N5600	2.759×10^{-06}	1.46
WRtoNLtoLLJJ_WR6600_N5800	1.882×10^{-06}	1.46
WRtoNLtoLLJJ_WR6600_N6000	1.129×10^{-06}	1.46
WRtoNLtoLLJJ_WR6600_N6200	5.651×10^{-07}	1.47
WRtoNLtoLLJJ_WR6600_N6400	2.036×10^{-07}	1.48
WRtoNLtoLLJJ_WR6600_N6500	1.027×10^{-07}	1.49
WRtoNLtoLLJJ_WR6800_N100	1.499×10^{-04}	1.26
WRtoNLtoLLJJ_WR6800_N200	1.259×10^{-04}	1.28

Table 40: MINIAOD datasets, LO cross-sections, and NLO-to-LO k-factor for signal samples.

Sample Name	$\sigma(pb)$, LO	$k^{\mathrm{NLO/LO}}$
WRtoNLtoLLJJ_WR6800_N400	9.183×10^{-05}	1.30
WRtoNLtoLLJJ_WR6800_N600	7.029×10^{-05}	1.33
WRtoNLtoLLJJ_WR6800_N800	5.529×10^{-05}	1.36
WRtoNLtoLLJJ_WR6800_N1000	4.476×10^{-05}	1.38
WRtoNLtoLLJJ_WR6800_N1200	3.721×10^{-05}	1.40
WRtoNLtoLLJJ_WR6800_N1400	3.161×10^{-05}	1.42
WRtoNLtoLLJJ_WR6800_N1600	2.753×10^{-05}	1.43
WRtoNLtoLLJJ_WR6800_N1800	2.435×10^{-05}	1.44
WRtoNLtoLLJJ_WR6800_N2000	2.193×10^{-05}	1.45
WRtoNLtoLLJJ_WR6800_N2200	2.014×10^{-05}	1.45
WRtoNLtoLLJJ_WR6800_N2400	1.838×10^{-05}	1.46
WRtoNLtoLLJJ_WR6800_N2600	1.703×10^{-05}	1.46
WRtoNLtoLLJJ_WR6800_N2800	1.567×10^{-05}	1.46
WRtoNLtoLLJJ_WR6800_N3000	1.471×10^{-05}	1.46
WRtoNLtoLLJJ_WR6800_N3200	1.371×10^{-05}	1.46
WRtoNLtoLLJJ_WR6800_N3400	1.269×10^{-05}	1.46
WRtoNLtoLLJJ_WR6800_N3600	1.175×10^{-05}	1.46
WRtoNLtoLLJJ_WR6800_N3800	1.078×10^{-05}	1.46
WRtoNLtoLLJJ_WR6800_N4000	9.962×10^{-06}	1.47
WRtoNLtoLLJJ_WR6800_N4200	8.946×10^{-06}	1.47
WRtoNLtoLLJJ_WR6800_N4400	7.985×10^{-06}	1.47
WRtoNLtoLLJJ_WR6800_N4600	7.062×10^{-06}	1.47
WRtoNLtoLLJJ_WR6800_N4800	6.14×10^{-06}	1.47
WRtoNLtoLLJJ_WR6800_N5000	5.23×10^{-06}	1.47
WRtoNLtoLLJJ_WR6800_N5200	4.363×10^{-06}	1.47
WRtoNLtoLLJJ_WR6800_N5400	3.502×10^{-06}	1.47
WRtoNLtoLLJJ_WR6800_N5600	2.723×10^{-06}	1.47
WRtoNLtoLLJJ_WR6800_N5800	1.995×10^{-06}	1.48
WRtoNLtoLLJJ_WR6800_N6000	1.349×10^{-06}	1.48
WRtoNLtoLLJJ_WR6800_N6200	8.113×10^{-07}	1.48
WRtoNLtoLLJJ_WR6800_N6400	4.028×10^{-07}	1.49
WRtoNLtoLLJJ_WR6800_N6600	1.453×10^{-07}	1.50
WRtoNLtoLLJJ_WR6800_N6700	7.379×10^{-08}	1.51
WRtoNLtoLLJJ_WR7000_N100	1.304×10^{-04}	1.26
WRtoNLtoLLJJ_WR7000_N200	1.093×10^{-04}	1.27

Table 41: MINIAOD datasets, LO cross-sections, and NLO-to-LO k-factor for signal samples.

Sample Name	$\sigma(pb)$, LO	$k^{\mathrm{NLO/LO}}$
WRtoNLtoLLJJ_WR7000_N400	7.917×10^{-05}	1.30
WRtoNLtoLLJJ_WR7000_N600	5.966×10^{-05}	1.33
WRtoNLtoLLJJ_WR7000_N800	4.659×10^{-05}	1.36
WRtoNLtoLLJJ_WR7000_N1000	3.733×10^{-05}	1.38
WRtoNLtoLLJJ_WR7000_N1200	3.059×10^{-05}	1.40
WRtoNLtoLLJJ_WR7000_N1400	2.581×10^{-05}	1.42
WRtoNLtoLLJJ_WR7000_N1600	2.223×10^{-05}	1.43
WRtoNLtoLLJJ_WR7000_N1800	1.945×10^{-05}	1.45
WRtoNLtoLLJJ_WR7000_N2000	1.747×10^{-05}	1.46
WRtoNLtoLLJJ_WR7000_N2200	1.583×10^{-05}	1.46
WRtoNLtoLLJJ_WR7000_N2400	1.447×10^{-05}	1.47
WRtoNLtoLLJJ_WR7000_N2600	1.333×10^{-05}	1.47
WRtoNLtoLLJJ_WR7000_N2800	1.239×10^{-05}	1.47
WRtoNLtoLLJJ_WR7000_N3000	1.152×10^{-05}	1.47
WRtoNLtoLLJJ_WR7000_N3200	1.067×10^{-05}	1.48
WRtoNLtoLLJJ_WR7000_N3400	9.959×10^{-06}	1.48
WRtoNLtoLLJJ_WR7000_N3600	9.236×10^{-06}	1.48
WRtoNLtoLLJJ_WR7000_N3800	8.562×10^{-06}	1.48
WRtoNLtoLLJJ_WR7000_N4000	7.892×10^{-06}	1.48
WRtoNLtoLLJJ_WR7000_N4200	7.176×10^{-06}	1.48
WRtoNLtoLLJJ_WR7000_N4400	6.497×10^{-06}	1.48
WRtoNLtoLLJJ_WR7000_N4600	5.812×10^{-06}	1.48
WRtoNLtoLLJJ_WR7000_N4800	5.141×10^{-06}	1.49
WRtoNLtoLLJJ_WR7000_N5000	4.436×10^{-06}	1.49
WRtoNLtoLLJJ_WR7000_N5200	3.767×10^{-06}	1.49
WRtoNLtoLLJJ_WR7000_N5400	3.147×10^{-06}	1.49
WRtoNLtoLLJJ_WR7000_N5600	2.523×10^{-06}	1.49
WRtoNLtoLLJJ_WR7000_N5800	1.955×10^{-06}	1.49
WRtoNLtoLLJJ_WR7000_N6000	1.424×10^{-06}	1.49
WRtoNLtoLLJJ_WR7000_N6200	9.628×10^{-07}	1.49
WRtoNLtoLLJJ_WR7000_N6400	5.802×10^{-07}	1.50
WRtoNLtoLLJJ_WR7000_N6600	2.877×10^{-07}	1.50
WRtoNLtoLLJJ_WR7000_N6800	1.036×10^{-07}	1.51
WRtoNLtoLLJJ_WR7000_N6900	5.312×10^{-08}	1.53

B Signal efficiencies

In this section, we present the acceptance times efficiencies ($A\epsilon$) of signal samples. Due to the lower muon reconstruction efficiency [9], we observed increasing $A\epsilon$ in order of years in the dimuon channel.

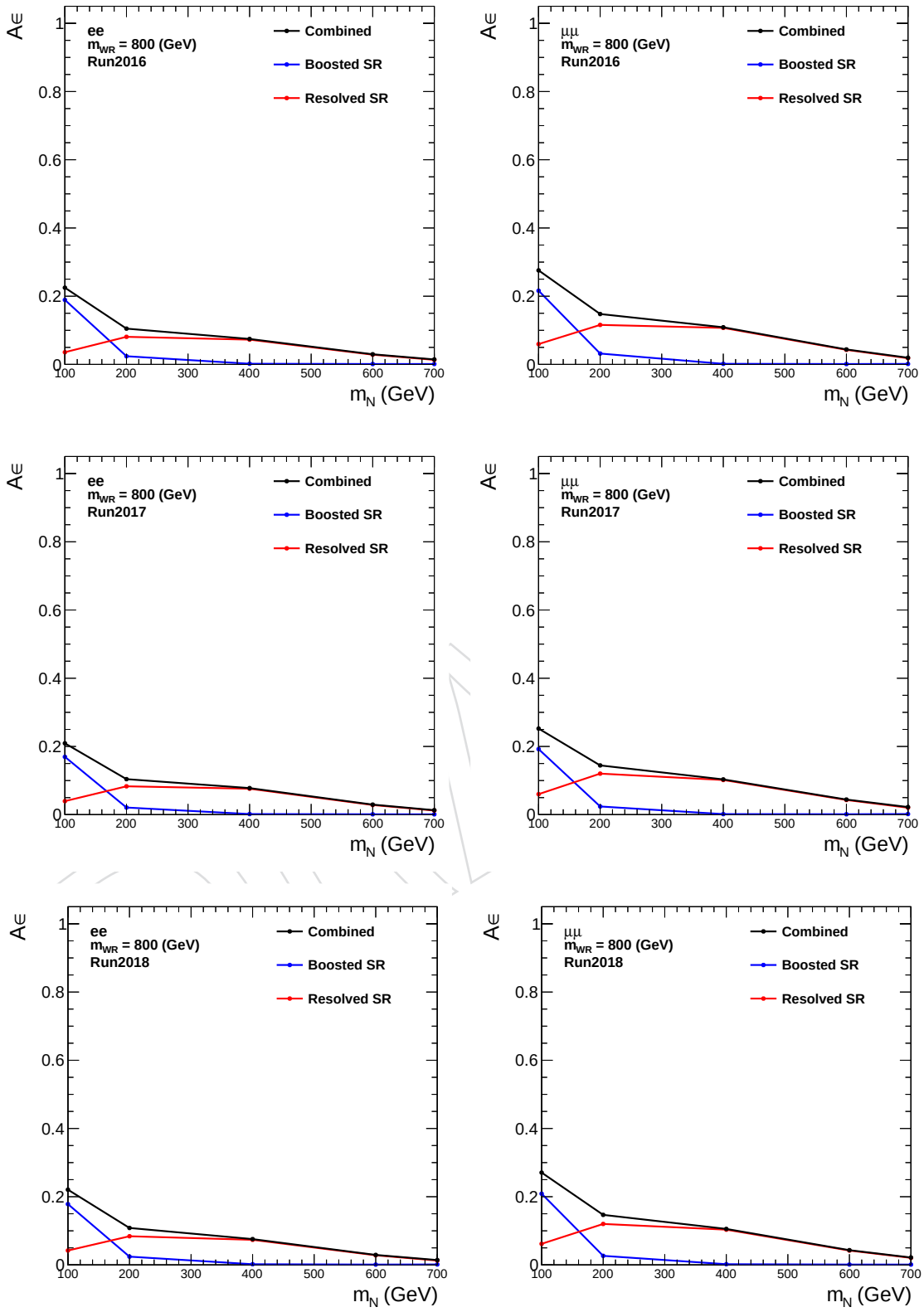

Figure 56: The signal acceptance times efficiencies ($A\epsilon$) in the ee (left) and $\mu\mu$ (right) channels, for $m_{W_R} = 800\,\text{GeV}$. Results with 2016 (top), 2017 (middle) and 2018 (bottom) are shown.

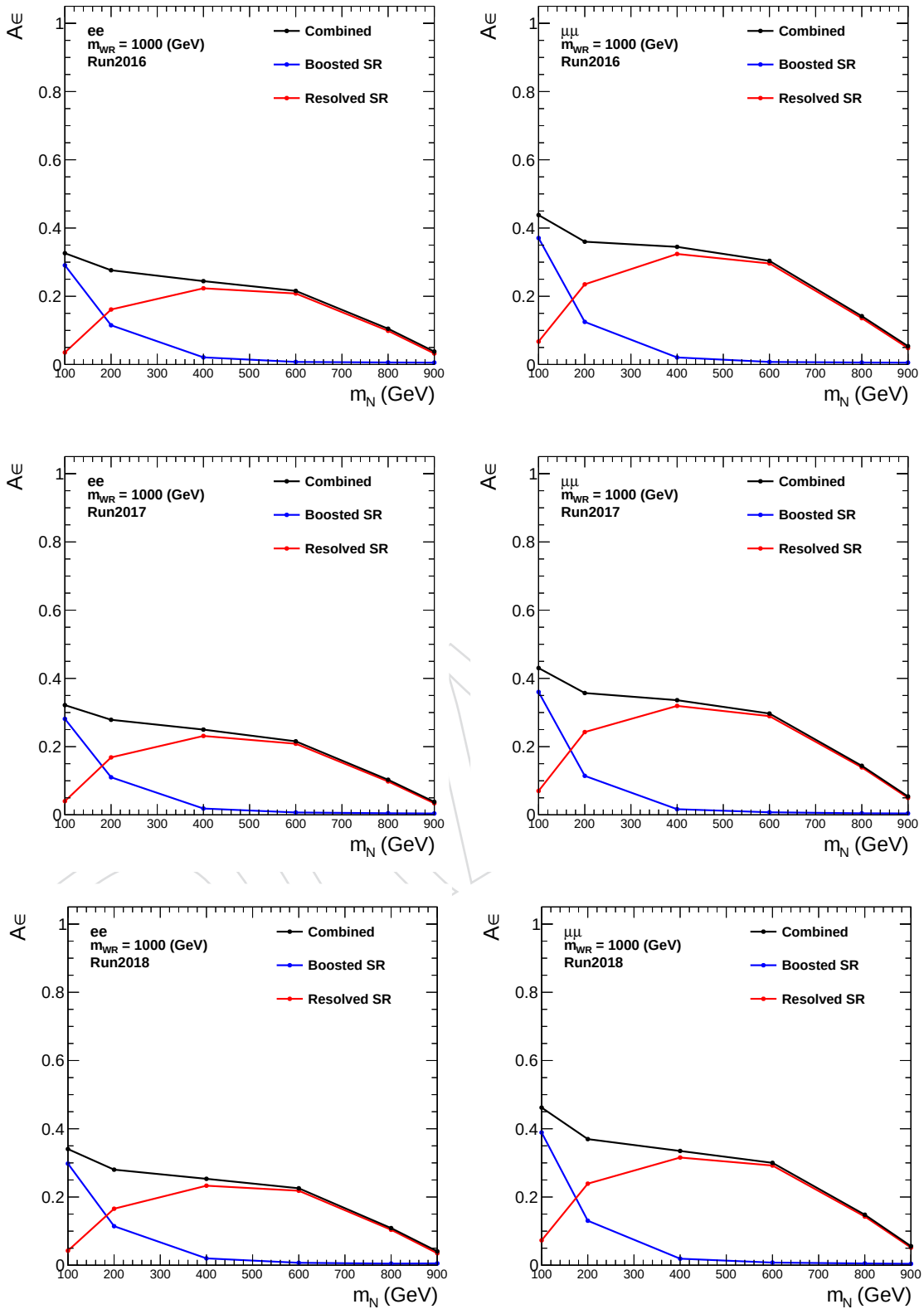

Figure 57: The signal acceptance times efficiencies ($A\epsilon$) in the ee (left) and $\mu\mu$ (right) channels, for $m_{W_R} = 1000\,\text{GeV}$. Results with 2016 (top), 2017 (middle) and 2018 (bottom) are shown.

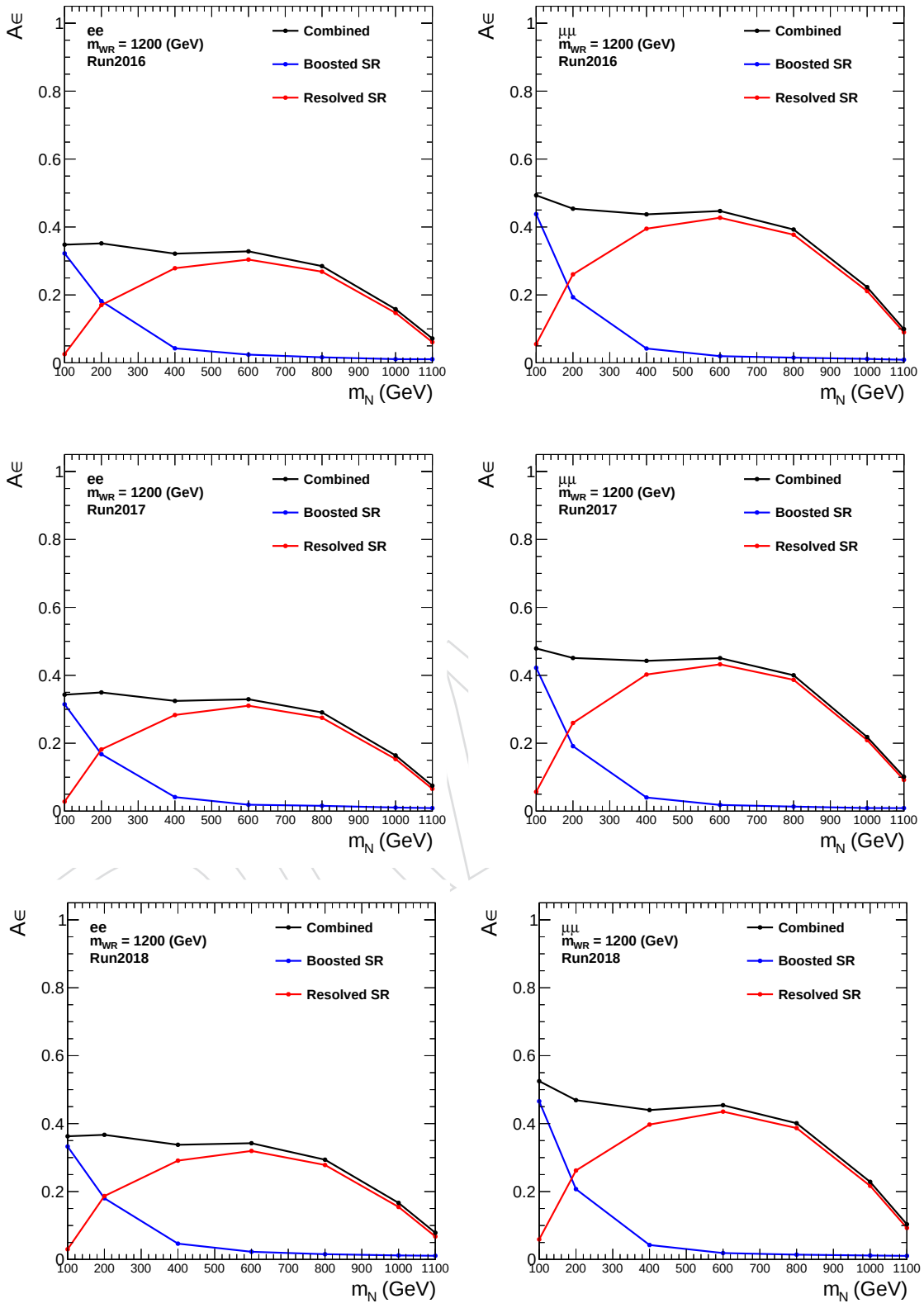

Figure 58: The signal acceptance times efficiencies ($A\epsilon$) in the ee (left) and $\mu\mu$ (right) channels, for $m_{W_R} = 1200\,\text{GeV}$. Results with 2016 (top), 2017 (middle) and 2018 (bottom) are shown.

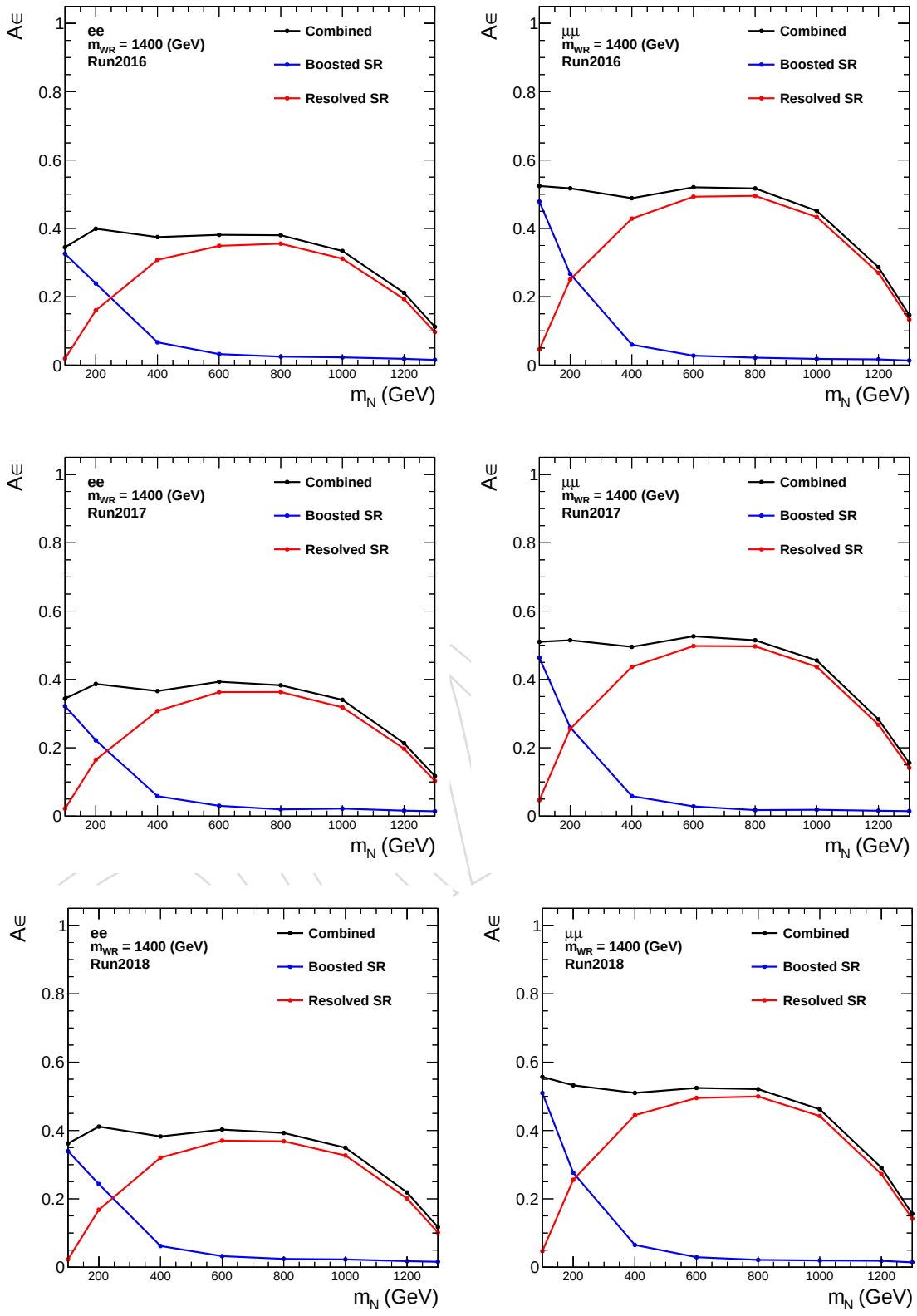

Figure 59: The signal acceptance times efficiencies ($A\epsilon$) in the ee (left) and $\mu\mu$ (right) channels, for $m_{W_R} = 1400\,\text{GeV}$. Results with 2016 (top), 2017 (middle) and 2018 (bottom) are shown.

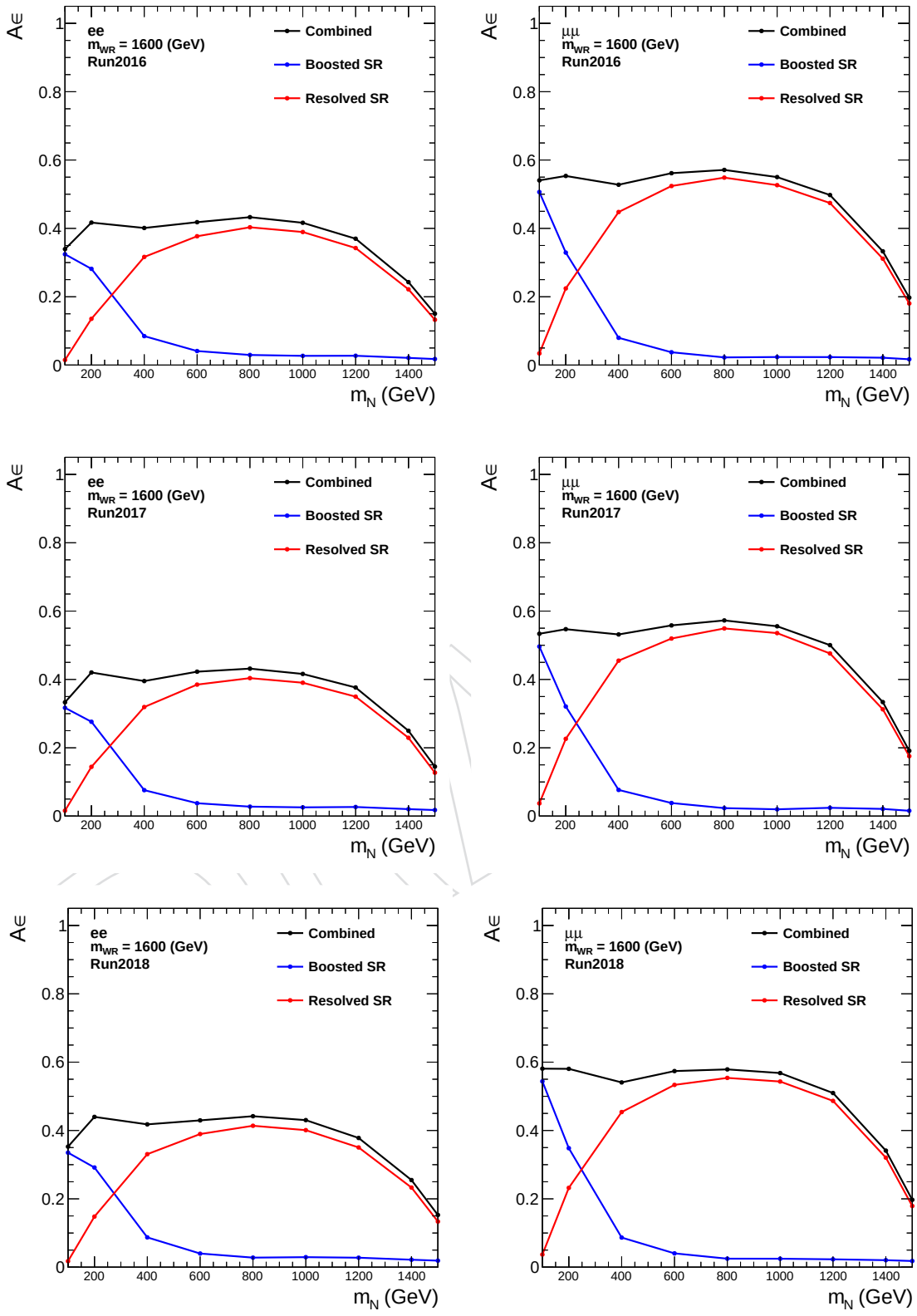

Figure 60: The signal acceptance times efficiencies ($A\epsilon$) in the ee (left) and $\mu\mu$ (right) channels, for $m_{W_R} = 1600\,\text{GeV}$. Results with 2016 (top), 2017 (middle) and 2018 (bottom) are shown.

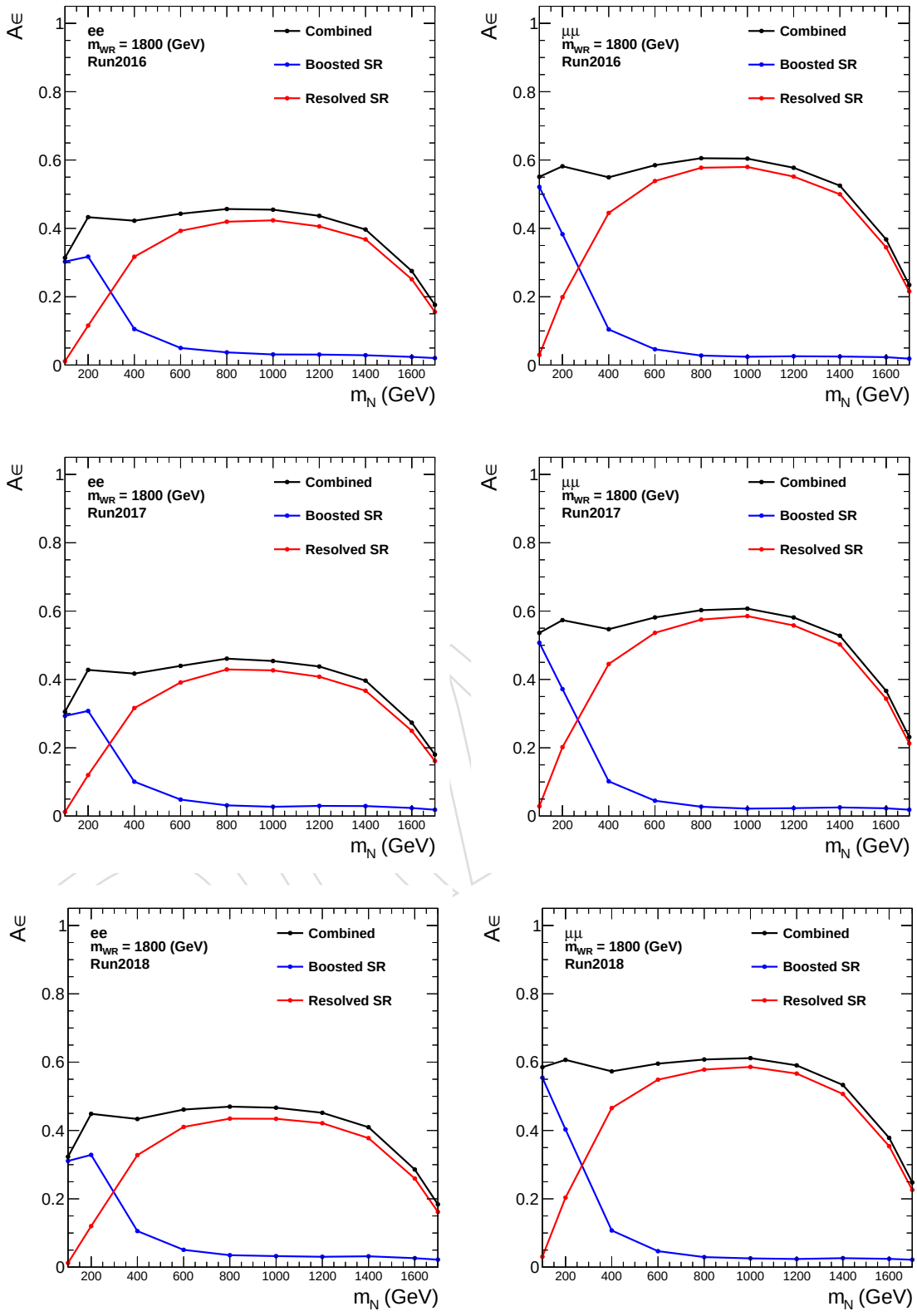

Figure 61: The signal acceptance times efficiencies ($A\epsilon$) in the ee (left) and $\mu\mu$ (right) channels, for $m_{W_R} = 1800\,\text{GeV}$. Results with 2016 (top), 2017 (middle) and 2018 (bottom) are shown.

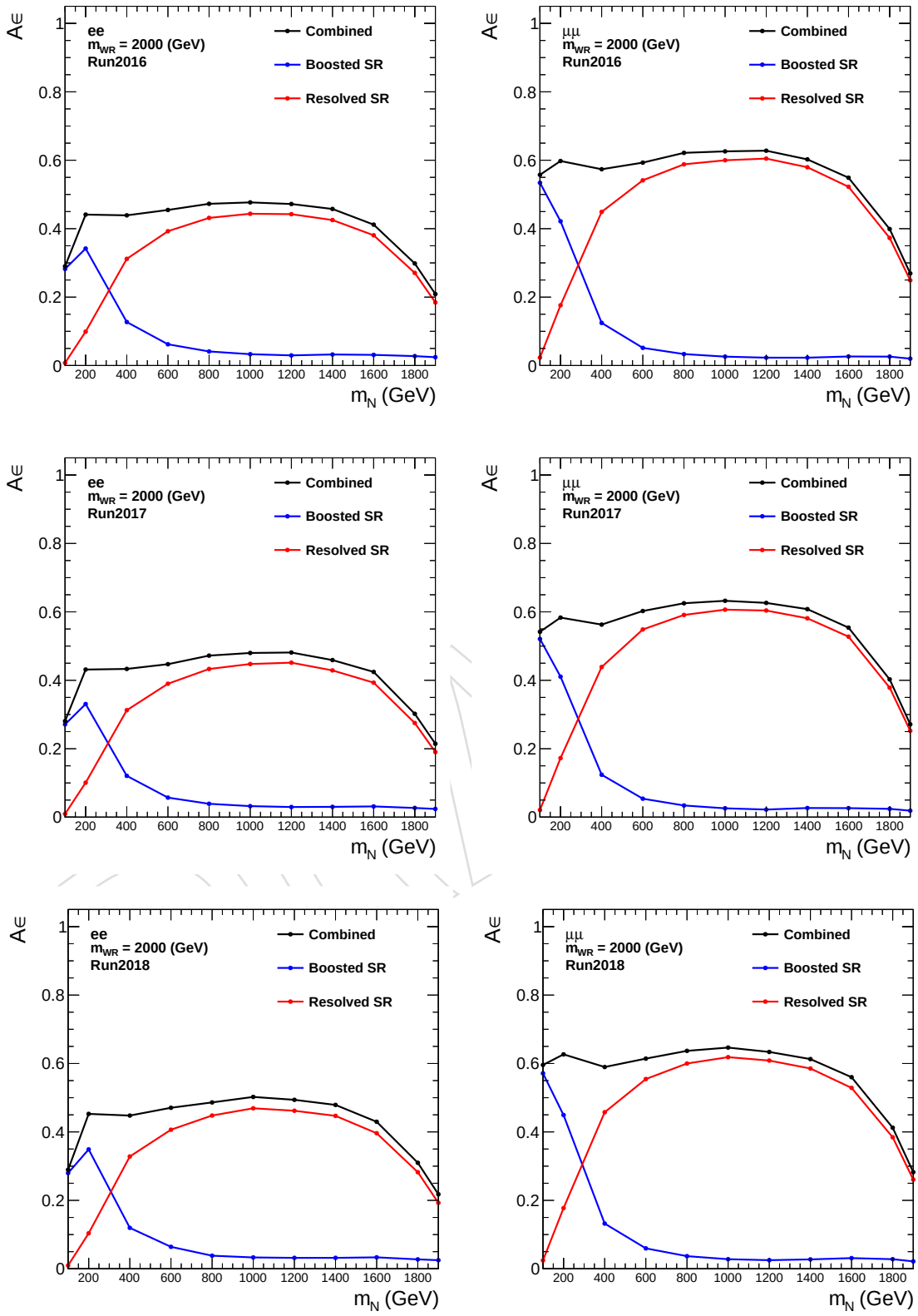

Figure 62: The signal acceptance times efficiencies ($A\epsilon$) in the ee (left) and $\mu\mu$ (right) channels, for $m_{W_R} = 2000\,\text{GeV}$. Results with 2016 (top), 2017 (middle) and 2018 (bottom) are shown.

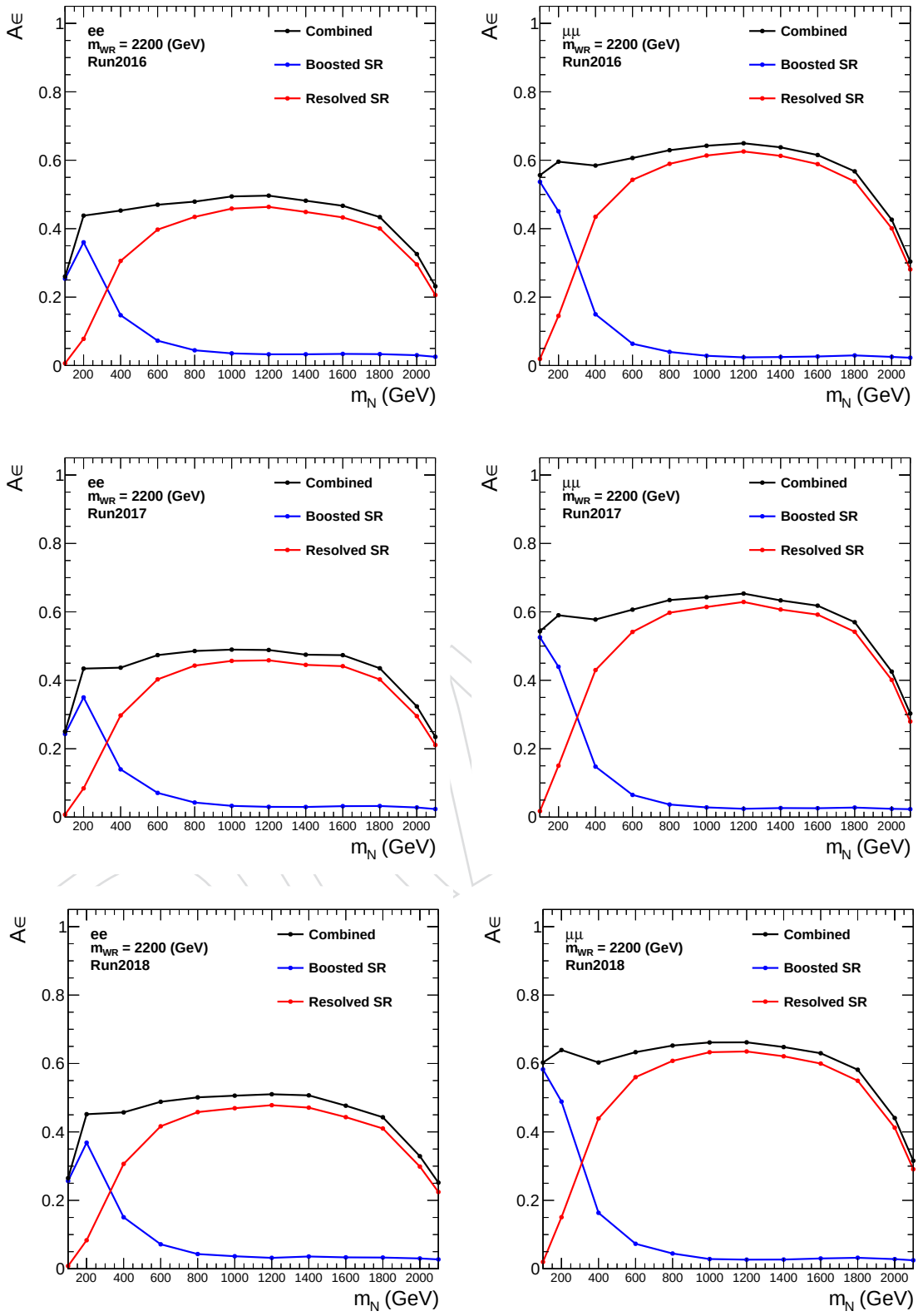

Figure 63: The signal acceptance times efficiencies ($A\epsilon$) in the ee (left) and $\mu\mu$ (right) channels, for $m_{W_R} = 2200\,\text{GeV}$. Results with 2016 (top), 2017 (middle) and 2018 (bottom) are shown.

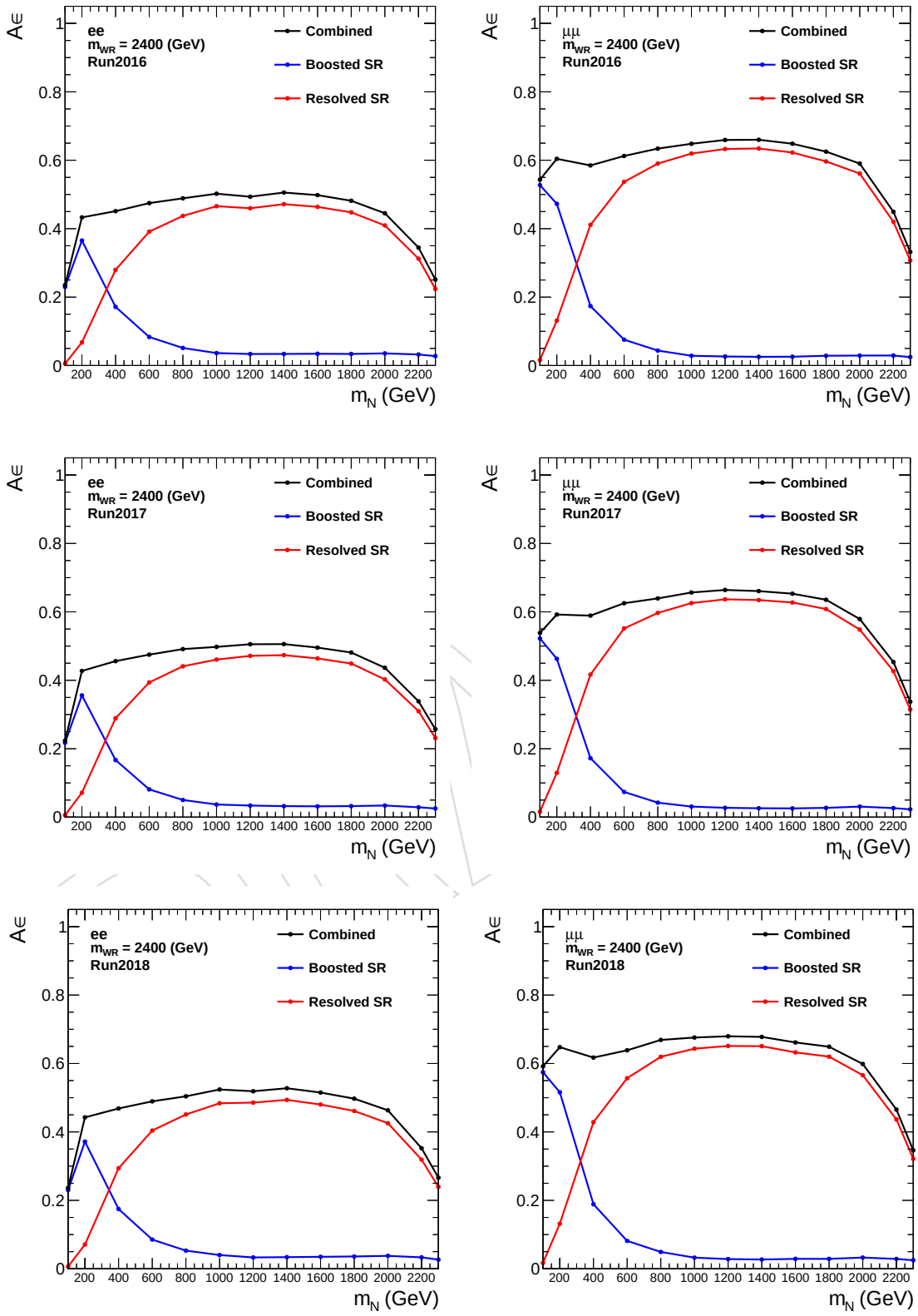

Figure 64: The signal acceptance times efficiencies ($A\epsilon$) in the ee (left) and $\mu\mu$ (right) channels, for $m_{W_R} = 2400\,\text{GeV}$. Results with 2016 (top), 2017 (middle) and 2018 (bottom) are shown.

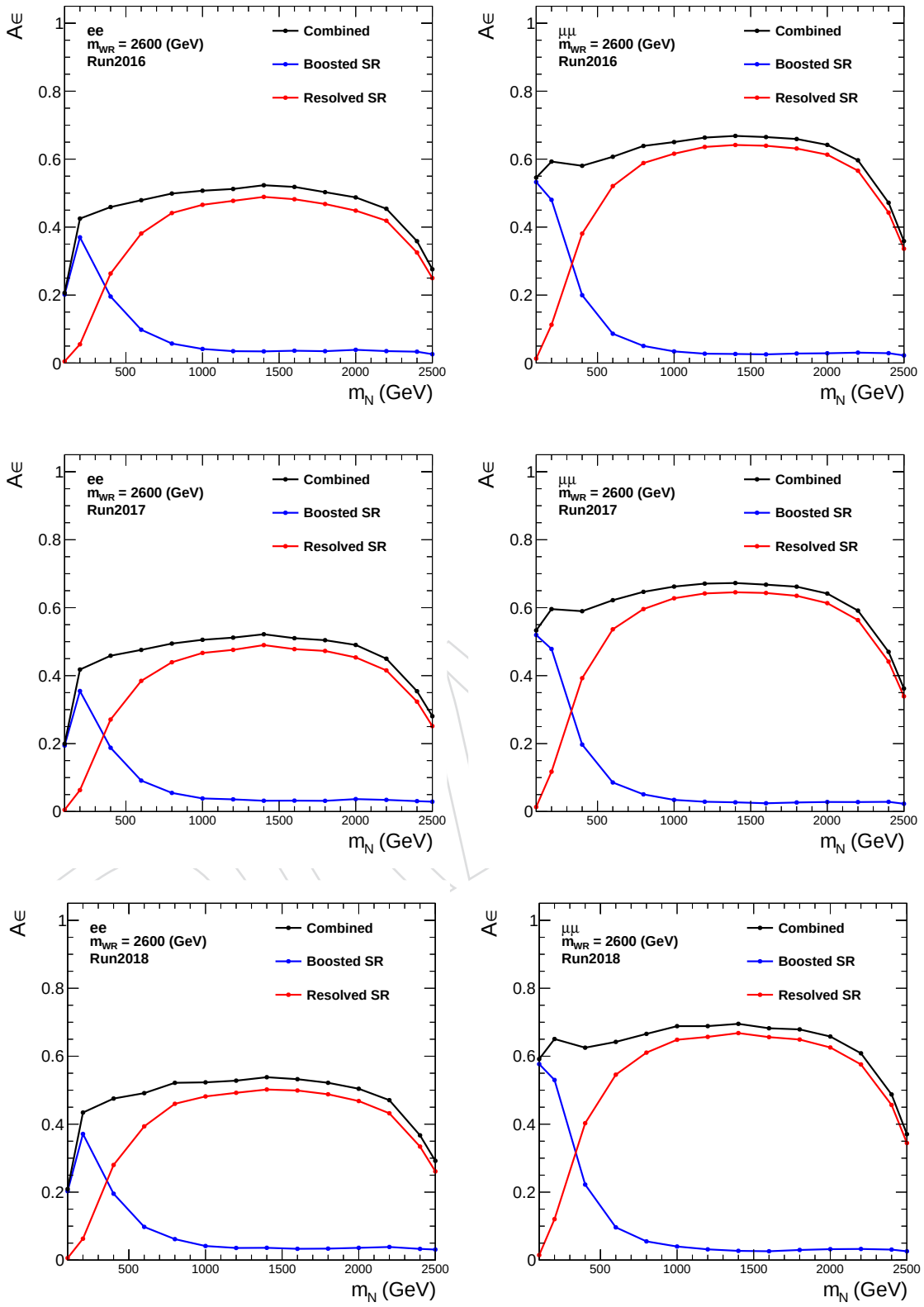

Figure 65: The signal acceptance times efficiencies ($A\epsilon$) in the ee (left) and $\mu\mu$ (right) channels, for $m_{W_R} = 2600\,\text{GeV}$. Results with 2016 (top), 2017 (middle) and 2018 (bottom) are shown.

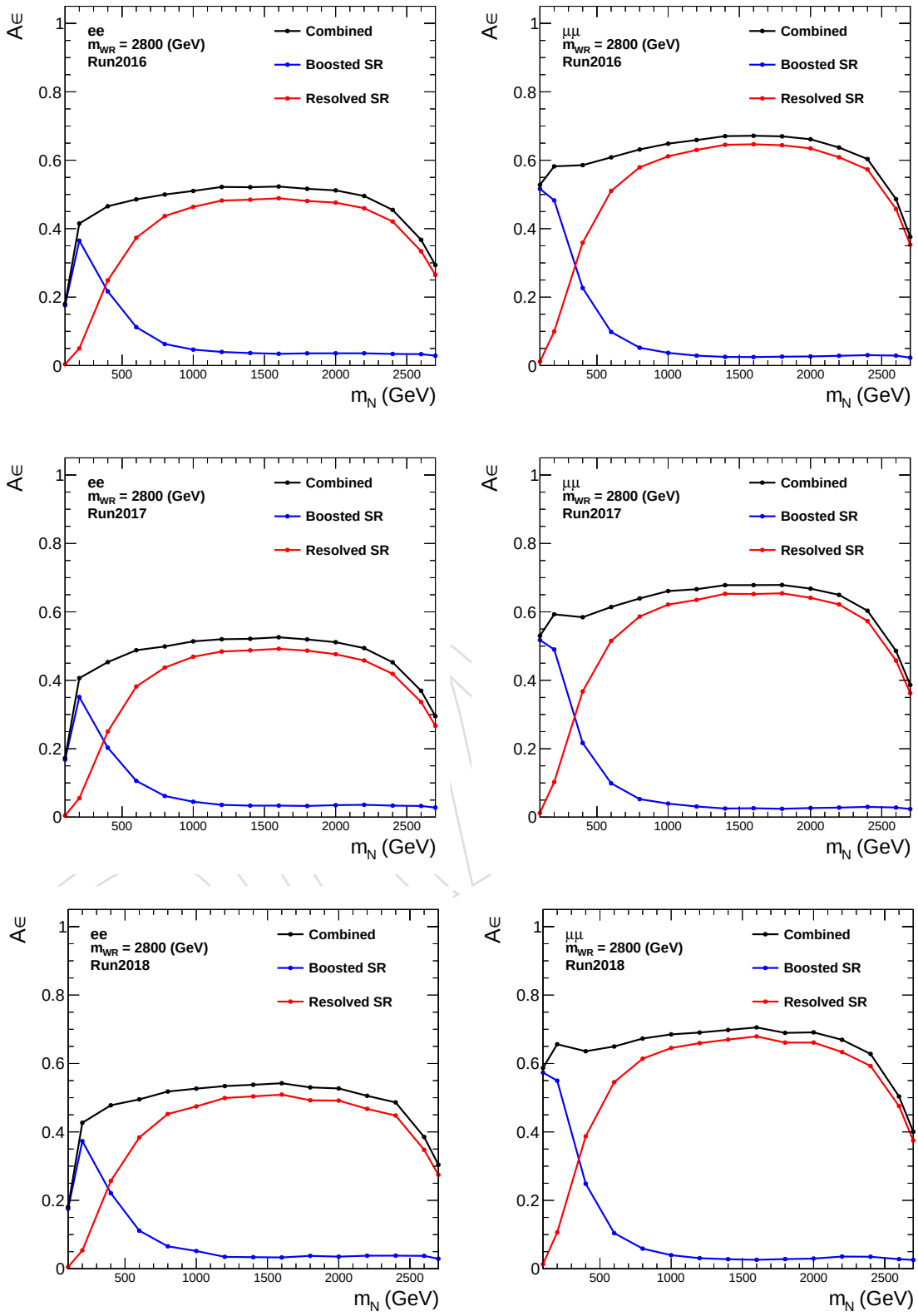

Figure 66: The signal acceptance times efficiencies ($A\epsilon$) in the ee (left) and $\mu\mu$ (right) channels, for $m_{W_R} = 2800\,\text{GeV}$. Results with 2016 (top), 2017 (middle) and 2018 (bottom) are shown.

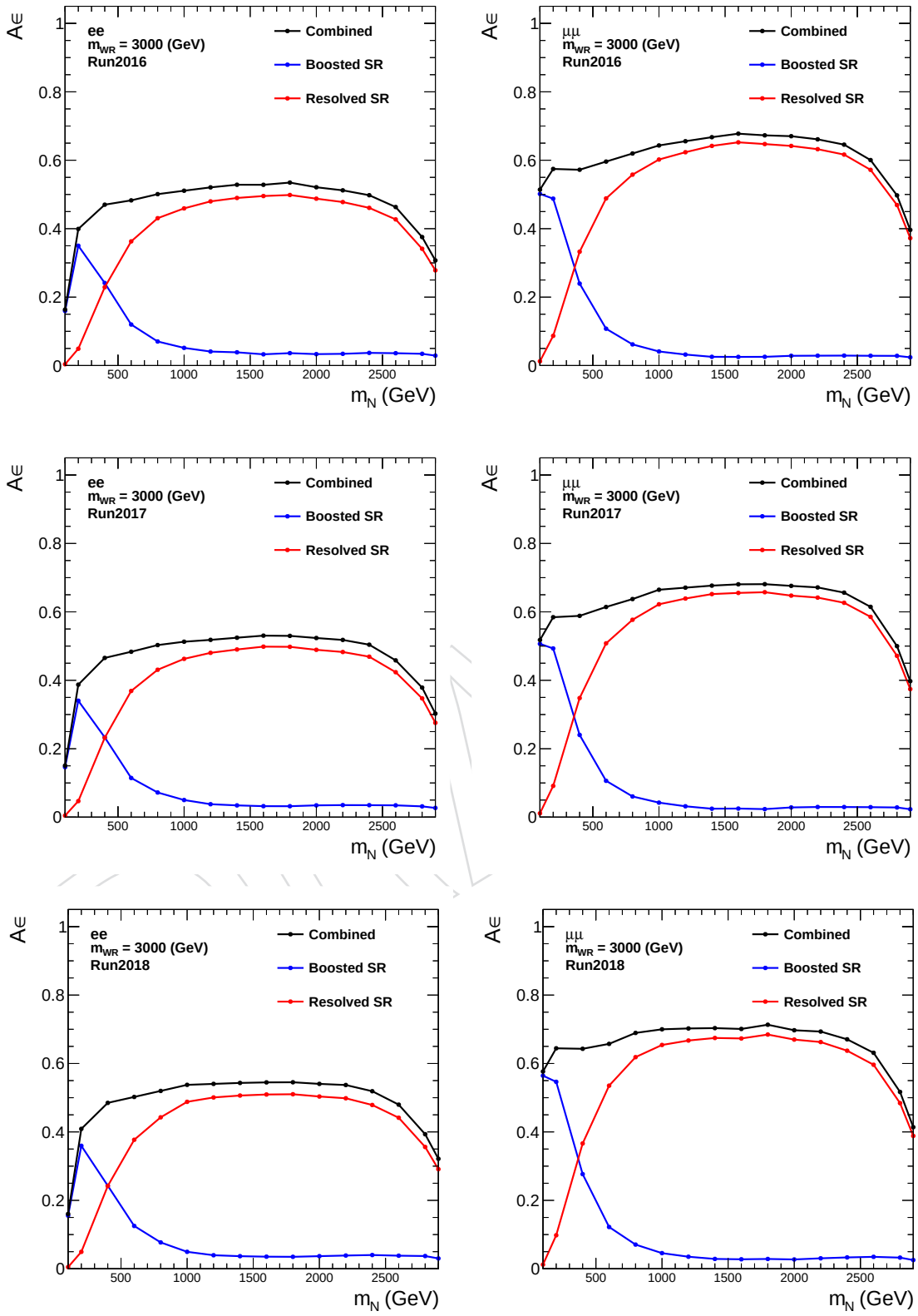

Figure 67: The signal acceptance times efficiencies ($A\epsilon$) in the ee (left) and $\mu\mu$ (right) channels, for $m_{W_R} = 3000\,\text{GeV}$. Results with 2016 (top), 2017 (middle) and 2018 (bottom) are shown.

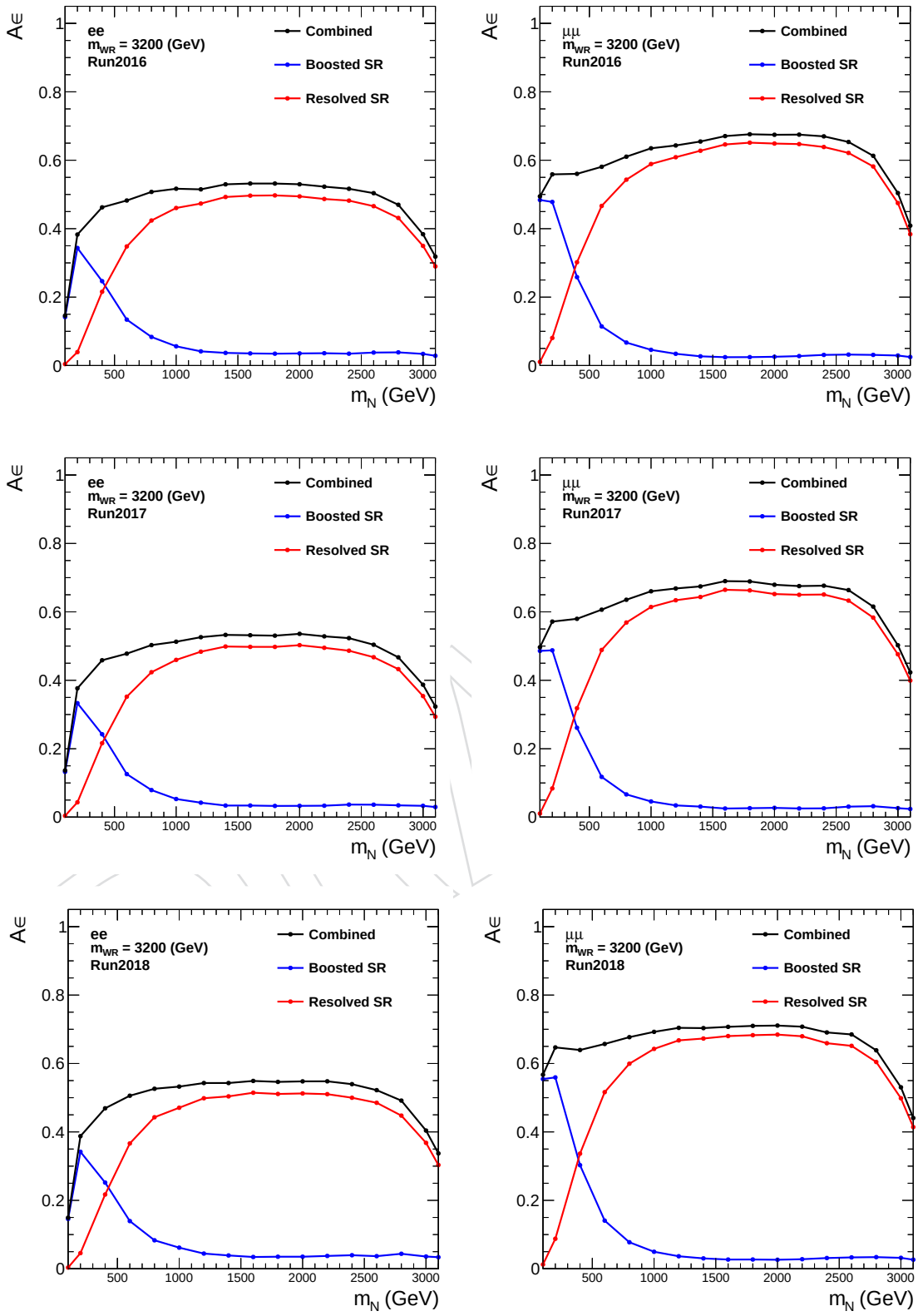

Figure 68: The signal acceptance times efficiencies ($A\epsilon$) in the ee (left) and $\mu\mu$ (right) channels, for $m_{W_R} = 3200\,\text{GeV}$. Results with 2016 (top), 2017 (middle) and 2018 (bottom) are shown.

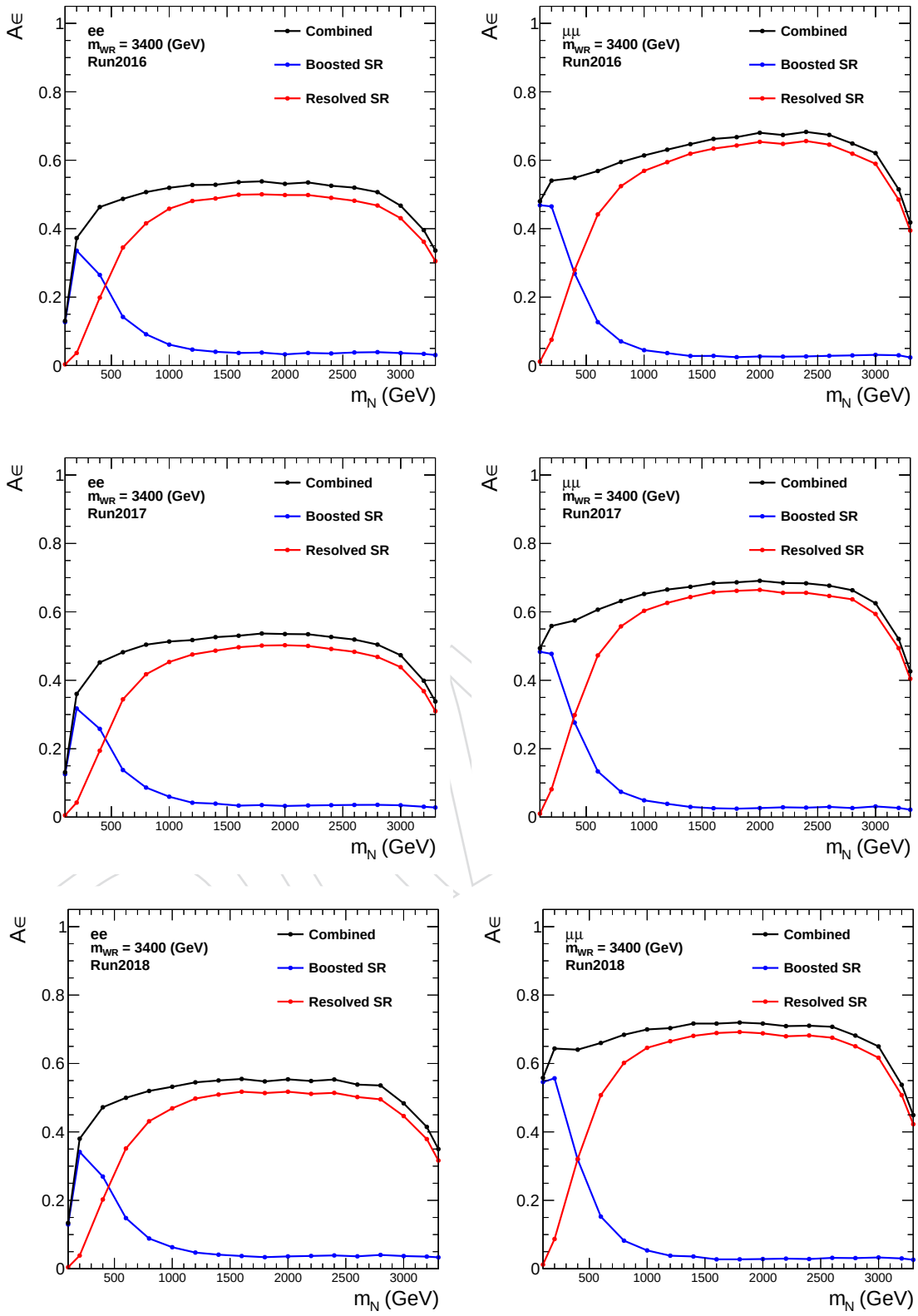

Figure 69: The signal acceptance times efficiencies ($A\epsilon$) in the ee (left) and $\mu\mu$ (right) channels, for $m_{W_R} = 3400\,\text{GeV}$. Results with 2016 (top), 2017 (middle) and 2018 (bottom) are shown.

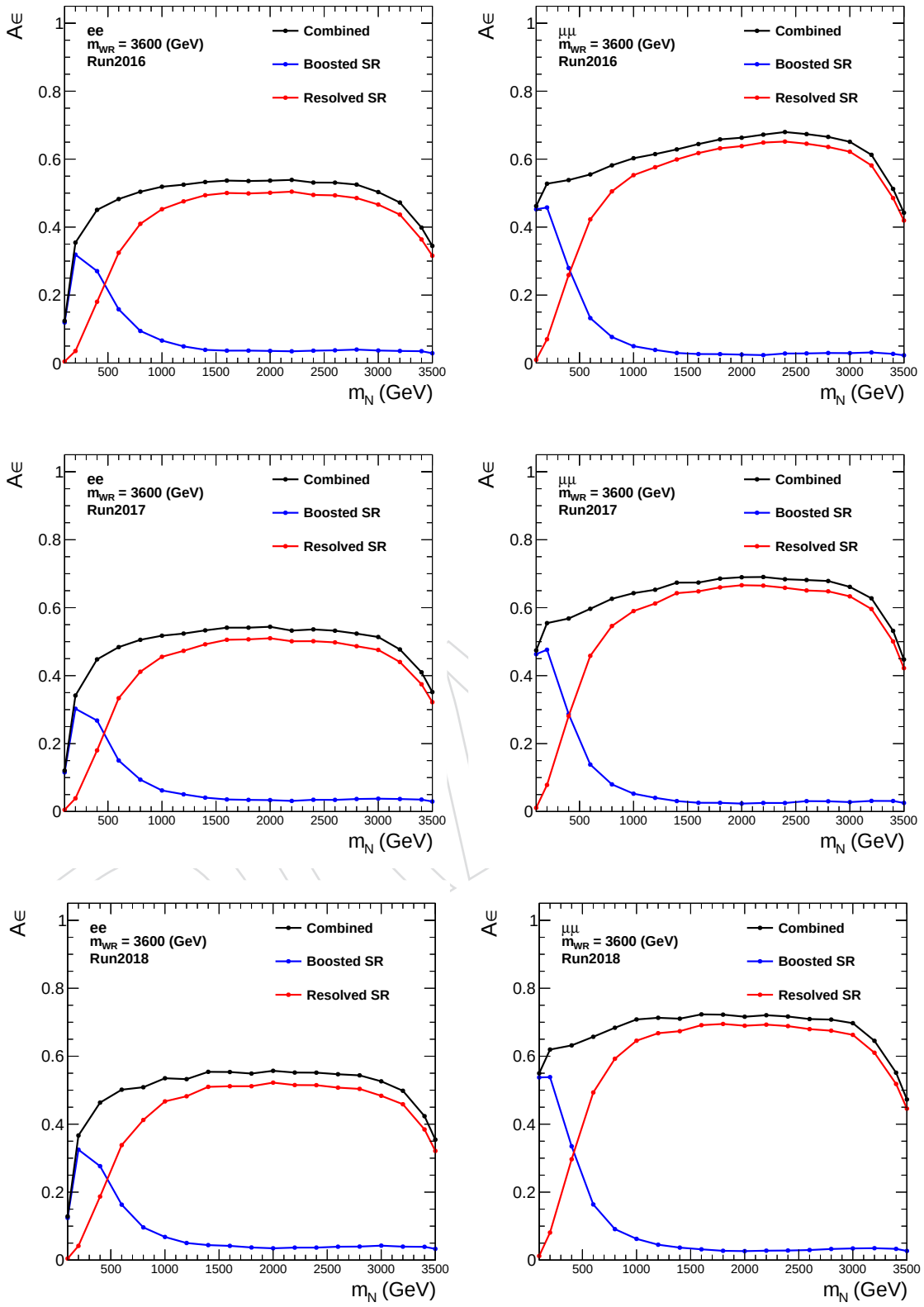

Figure 70: The signal acceptance times efficiencies ($A\epsilon$) in the ee (left) and $\mu\mu$ (right) channels, for $m_{W_R} = 3600\,\text{GeV}$. Results with 2016 (top), 2017 (middle) and 2018 (bottom) are shown.

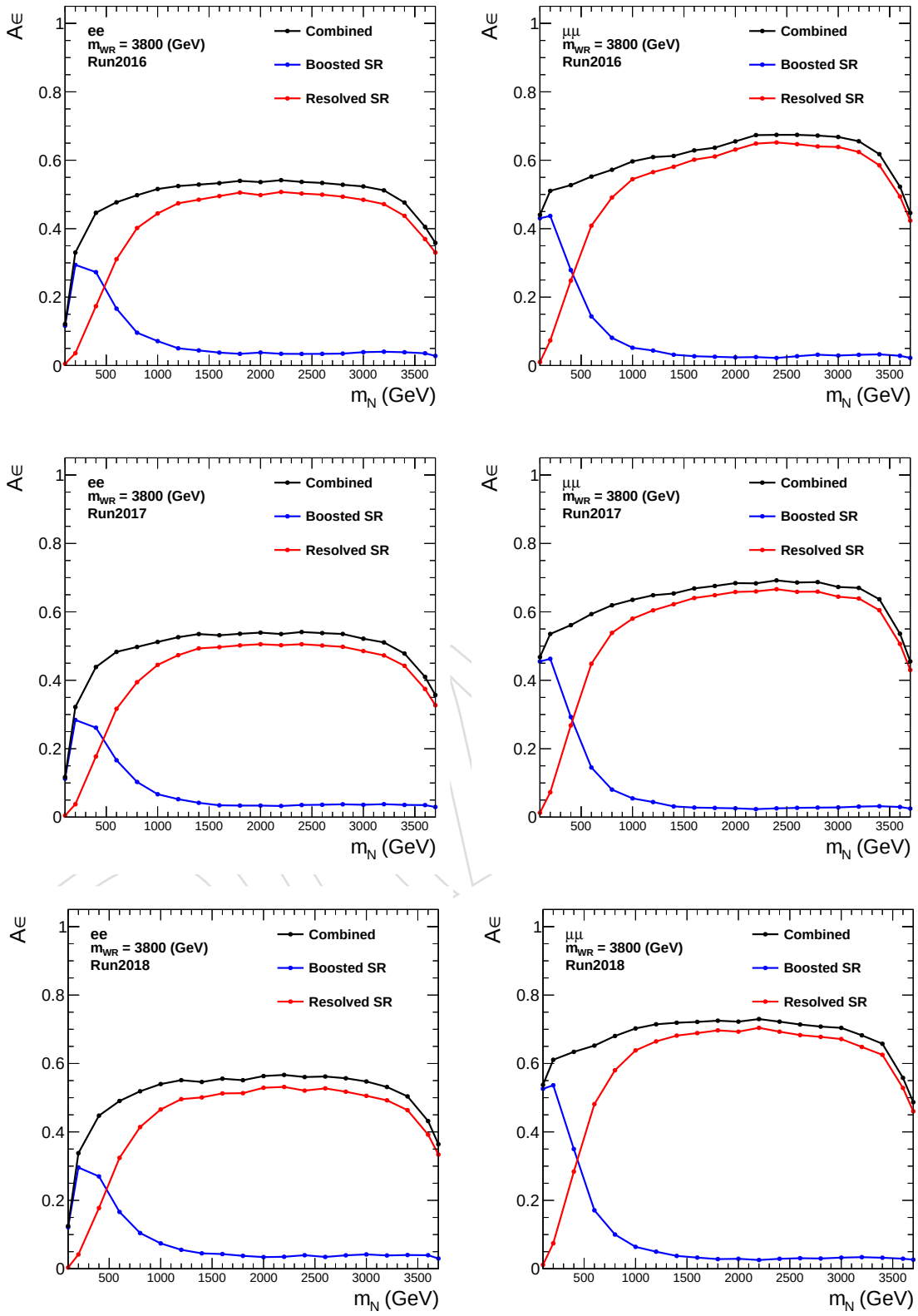

Figure 71: The signal acceptance times efficiencies ($A\epsilon$) in the ee (left) and $\mu\mu$ (right) channels, for $m_{W_R} = 3800\,\text{GeV}$. Results with 2016 (top), 2017 (middle) and 2018 (bottom) are shown.

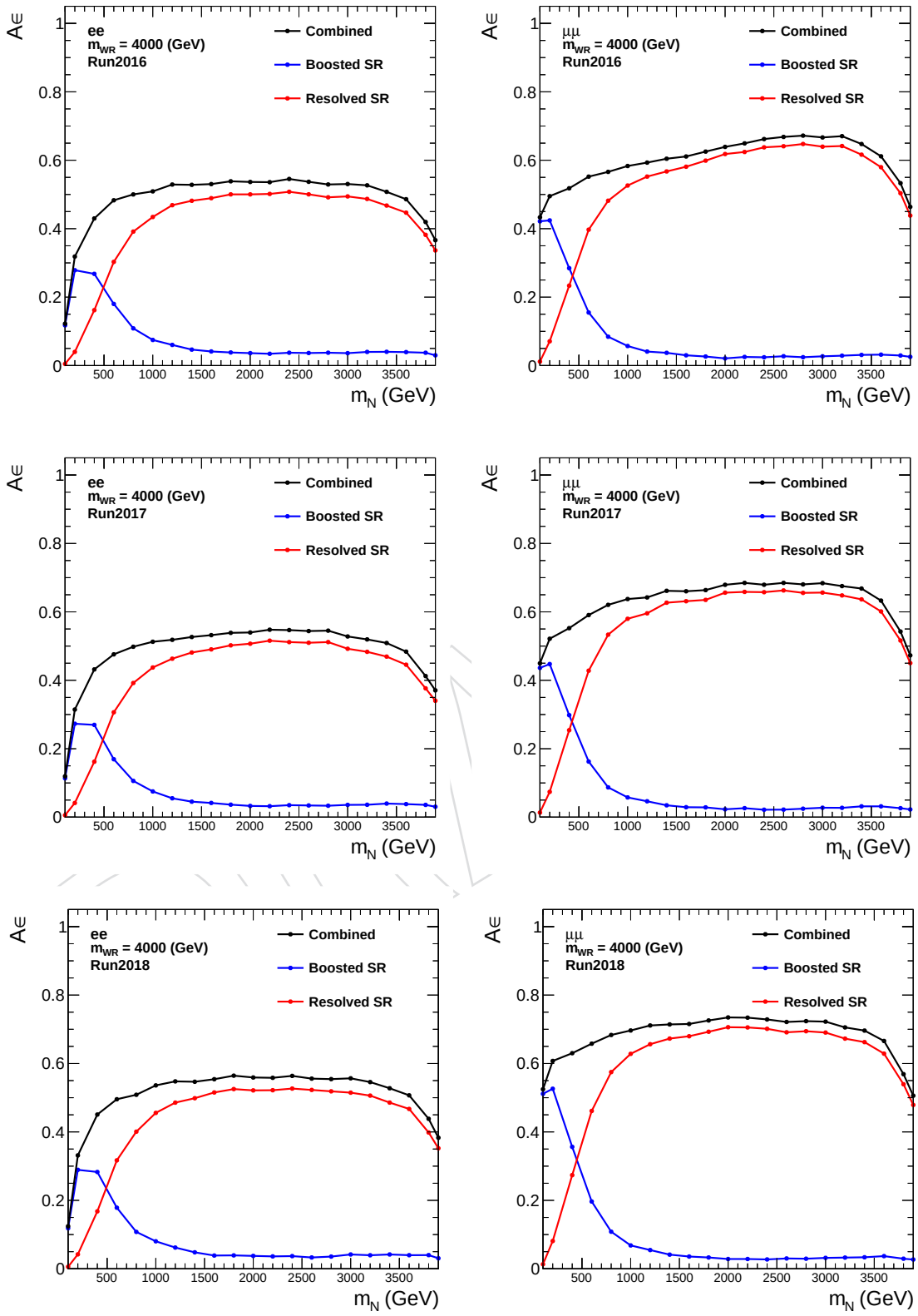

Figure 72: The signal acceptance times efficiencies ($A\epsilon$) in the ee (left) and $\mu\mu$ (right) channels, for $m_{W_R} = 4000\,\text{GeV}$. Results with 2016 (top), 2017 (middle) and 2018 (bottom) are shown.

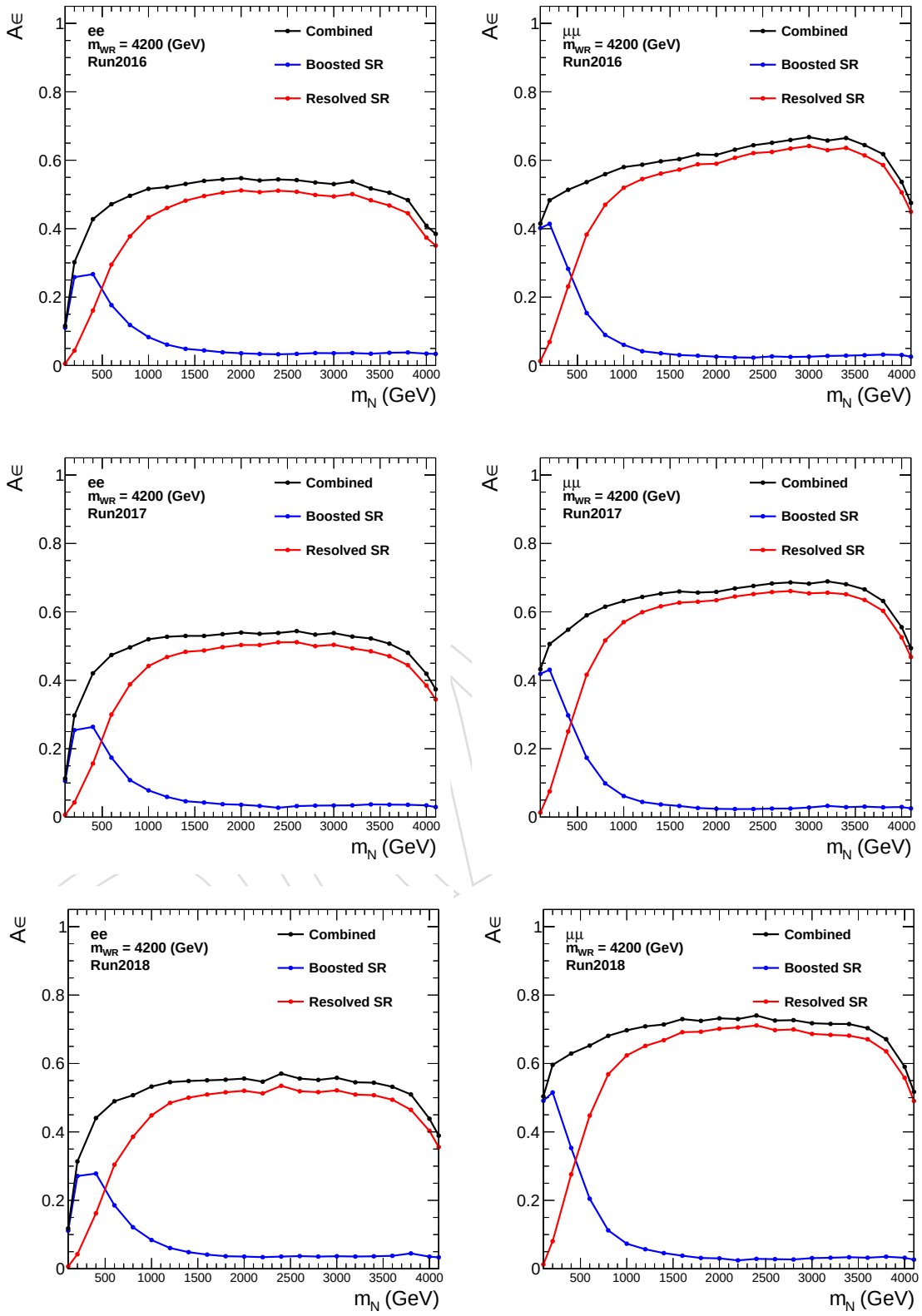

Figure 73: The signal acceptance times efficiencies ($A\epsilon$) in the ee (left) and $\mu\mu$ (right) channels, for $m_{W_R} = 4200\,\text{GeV}$. Results with 2016 (top), 2017 (middle) and 2018 (bottom) are shown.

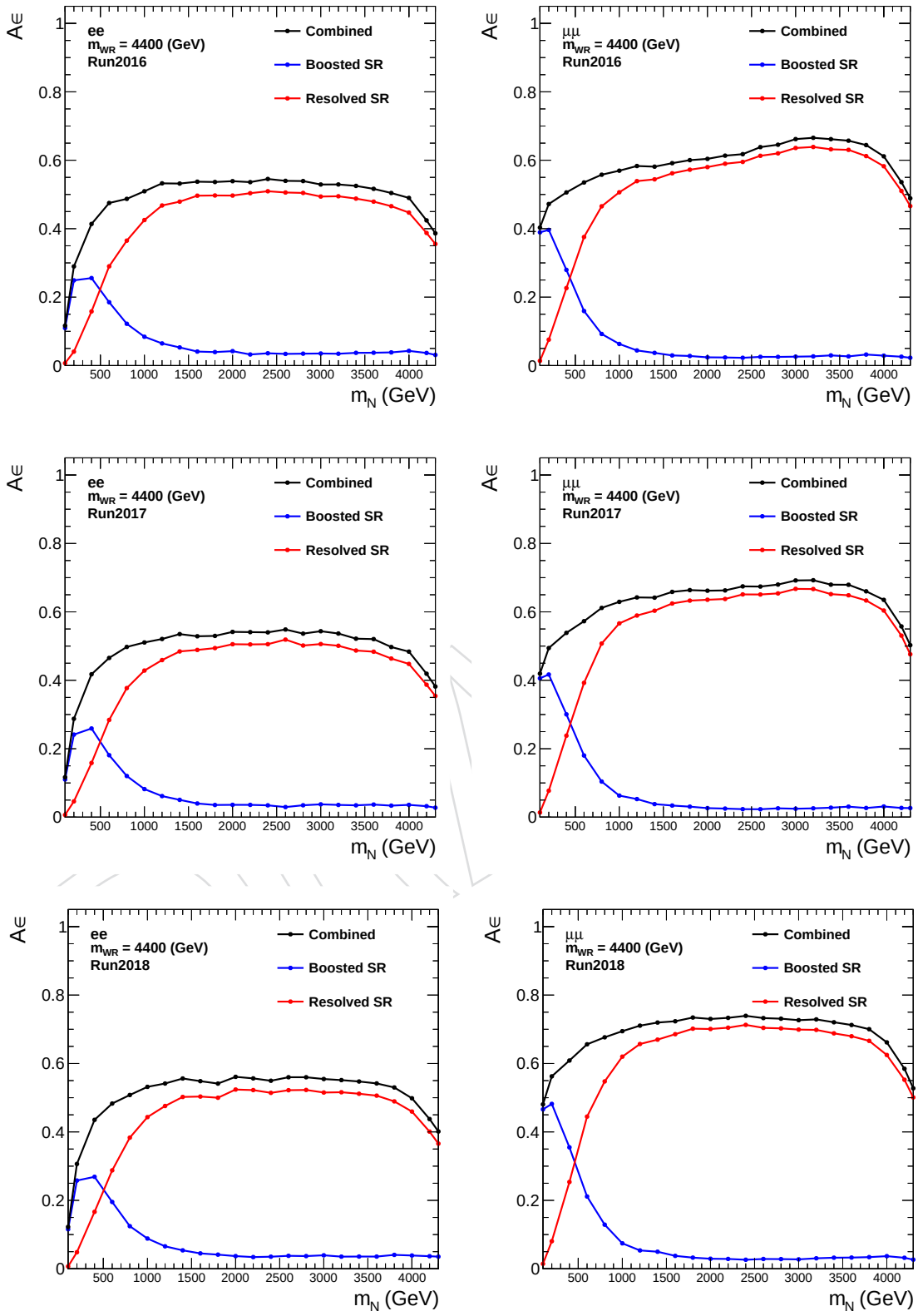

Figure 74: The signal acceptance times efficiencies ($A\epsilon$) in the ee (left) and $\mu\mu$ (right) channels, for $m_{W_R} = 4400\,\text{GeV}$. Results with 2016 (top), 2017 (middle) and 2018 (bottom) are shown.

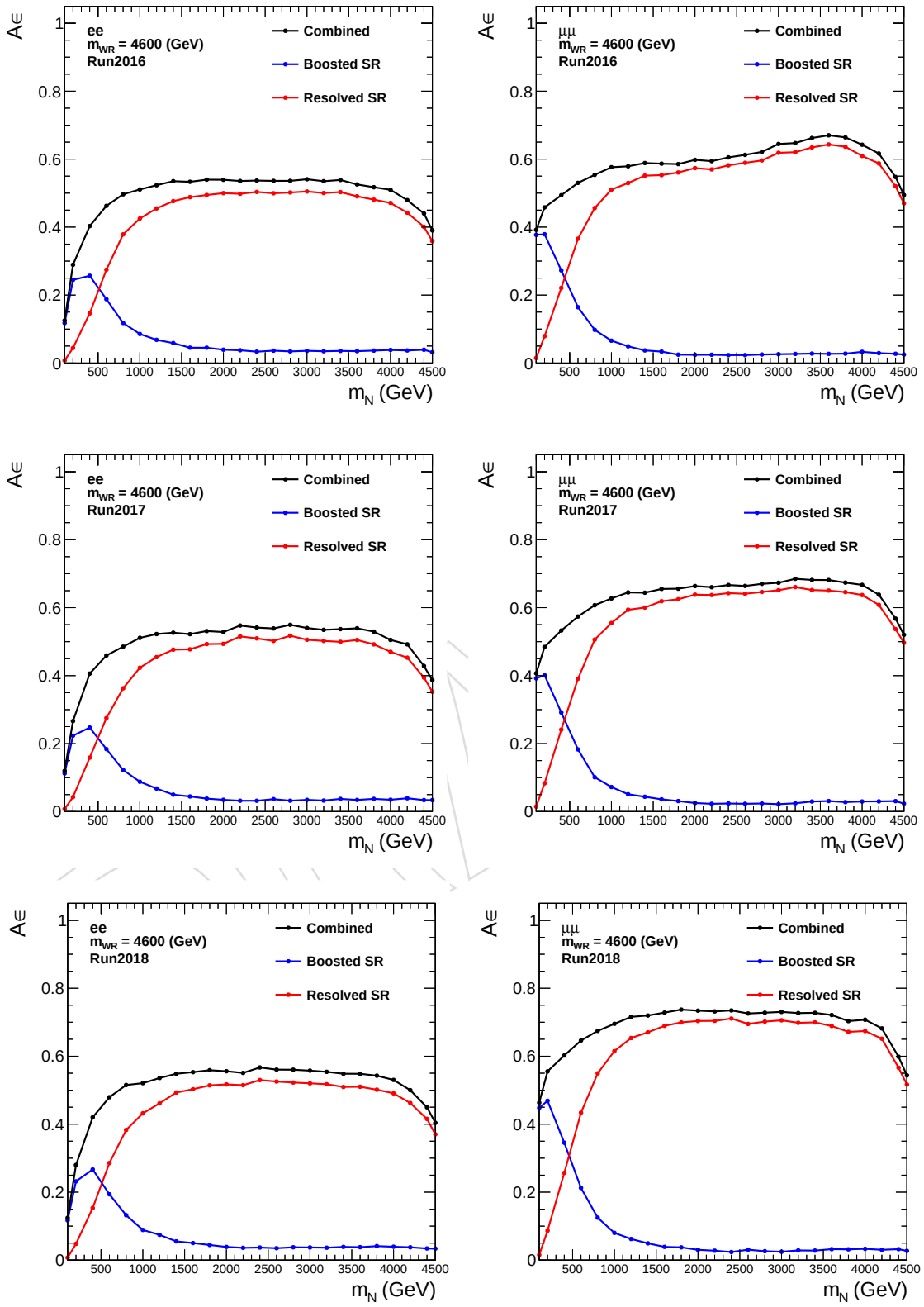

Figure 75: The signal acceptance times efficiencies ($A\epsilon$) in the ee (left) and $\mu\mu$ (right) channels, for $m_{W_R} = 4600\,\text{GeV}$. Results with 2016 (top), 2017 (middle) and 2018 (bottom) are shown.

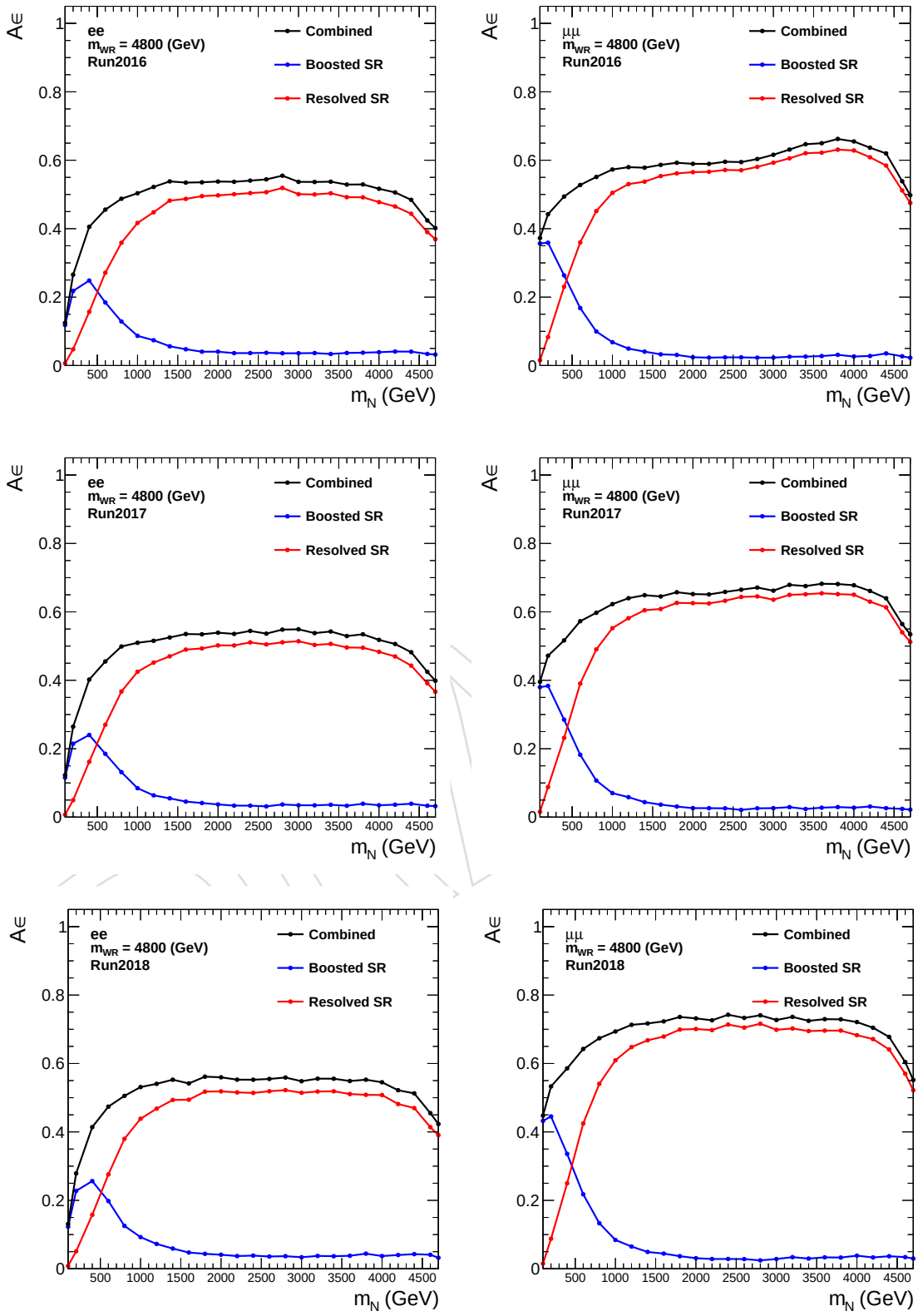

Figure 76: The signal acceptance times efficiencies ($A\epsilon$) in the ee (left) and $\mu\mu$ (right) channels, for $m_{W_R} = 4800\,\text{GeV}$. Results with 2016 (top), 2017 (middle) and 2018 (bottom) are shown.

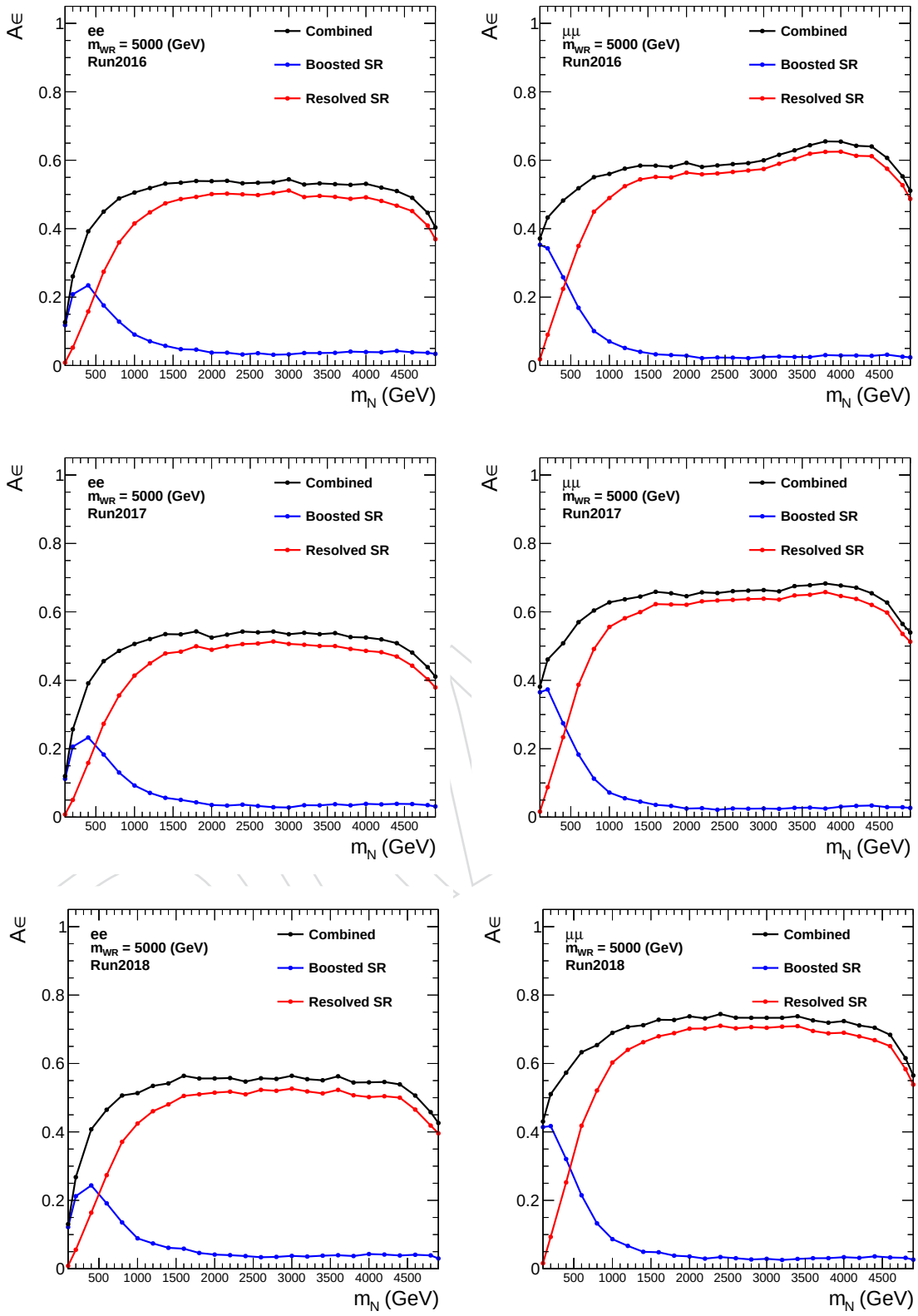

Figure 77: The signal acceptance times efficiencies ($A\epsilon$) in the ee (left) and $\mu\mu$ (right) channels, for $m_{W_R} = 5000\,\text{GeV}$. Results with 2016 (top), 2017 (middle) and 2018 (bottom) are shown.

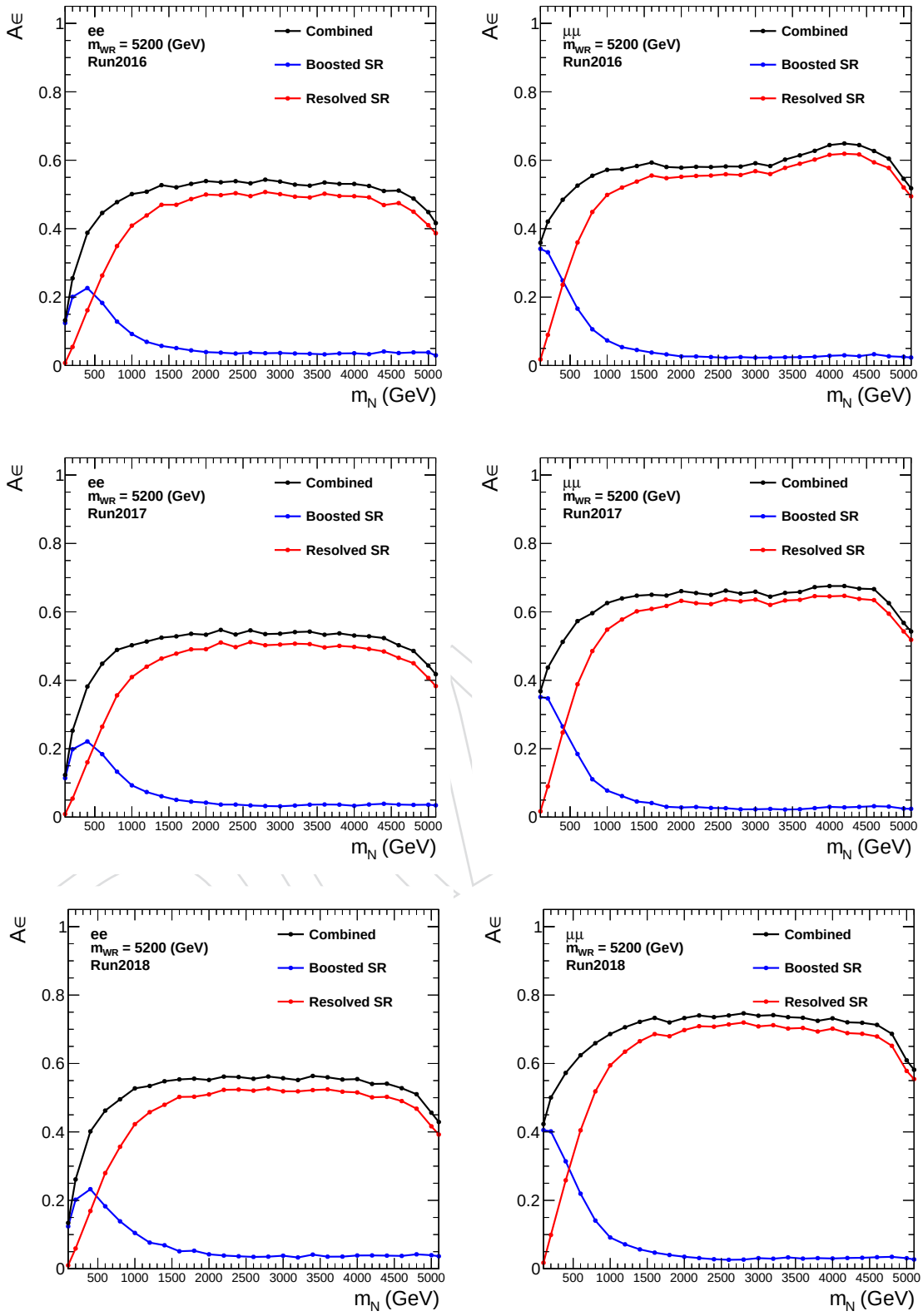

Figure 78: The signal acceptance times efficiencies ($A\epsilon$) in the ee (left) and $\mu\mu$ (right) channels, for $m_{W_R} = 5200\,\text{GeV}$. Results with 2016 (top), 2017 (middle) and 2018 (bottom) are shown.

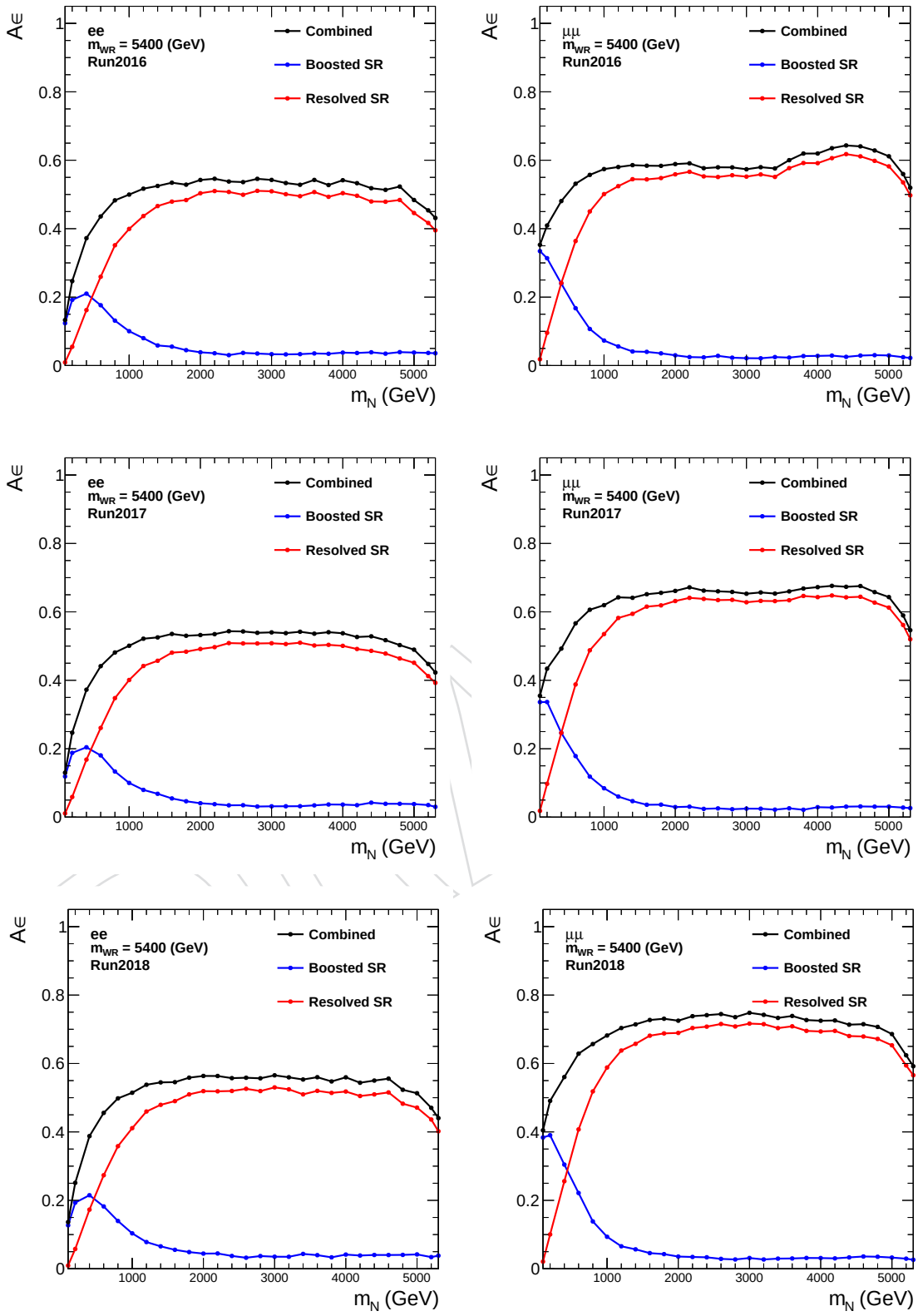

Figure 79: The signal acceptance times efficiencies ($A\epsilon$) in the ee (left) and $\mu\mu$ (right) channels, for $m_{W_R} = 5400\,\text{GeV}$. Results with 2016 (top), 2017 (middle) and 2018 (bottom) are shown.

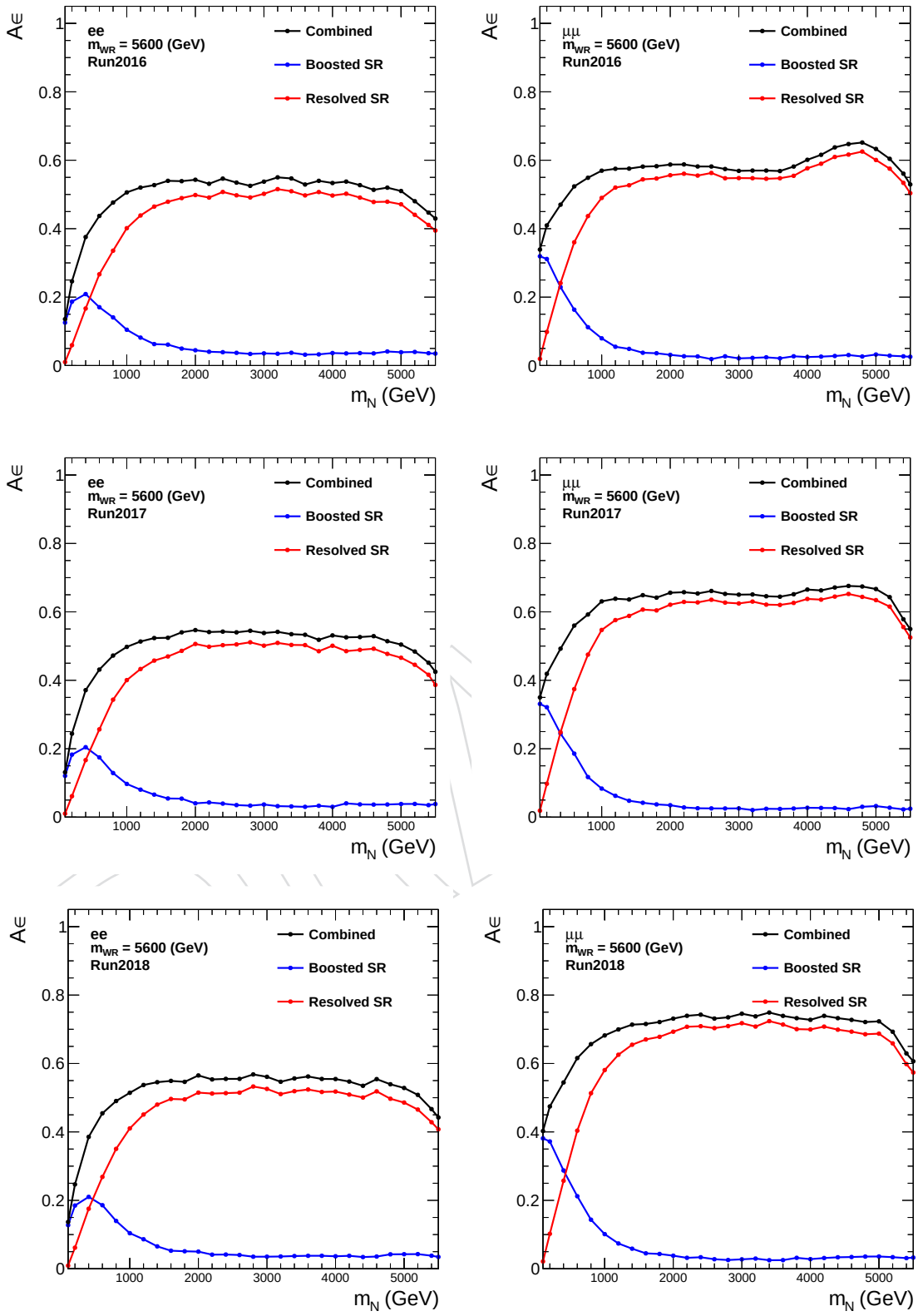

Figure 80: The signal acceptance times efficiencies ($A\epsilon$) in the ee (left) and $\mu\mu$ (right) channels, for $m_{W_R} = 5600\,\text{GeV}$. Results with 2016 (top), 2017 (middle) and 2018 (bottom) are shown.

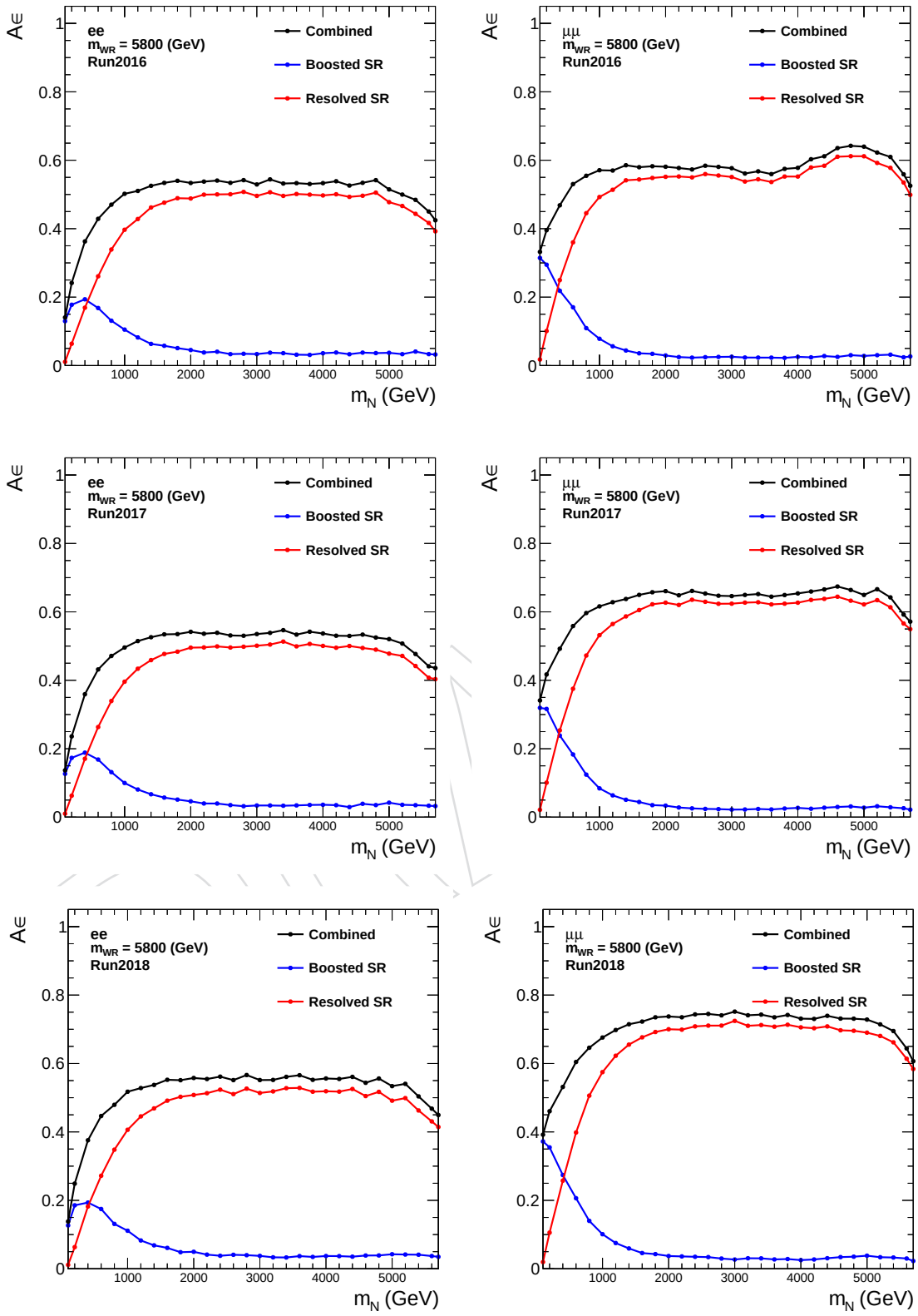

Figure 81: The signal acceptance times efficiencies ($A\epsilon$) in the ee (left) and $\mu\mu$ (right) channels, for $m_{W_R} = 5800\,\text{GeV}$. Results with 2016 (top), 2017 (middle) and 2018 (bottom) are shown.

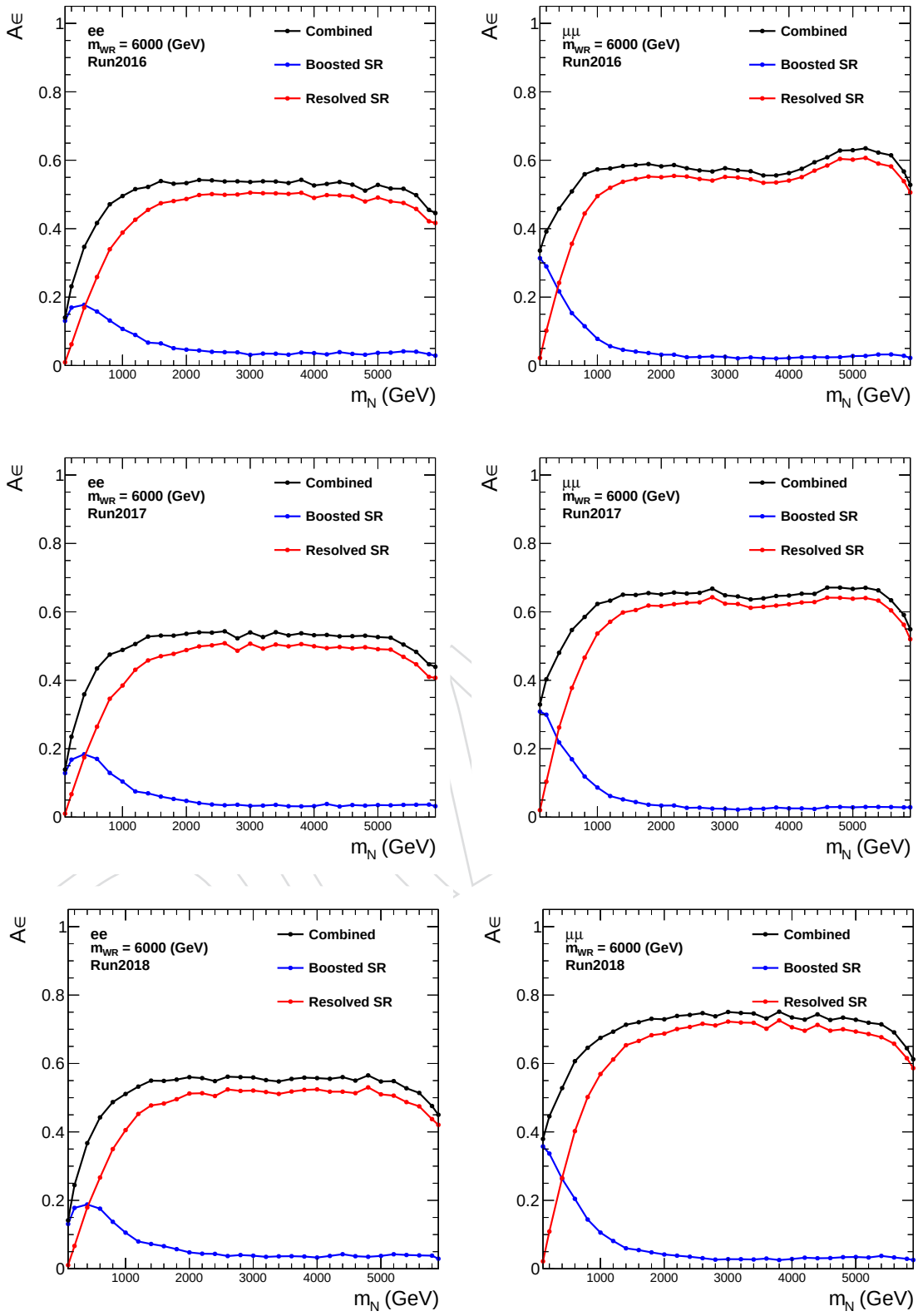

Figure 82: The signal acceptance times efficiencies ($A\epsilon$) in the ee (left) and $\mu\mu$ (right) channels, for $m_{W_R} = 6000\,\text{GeV}$. Results with 2016 (top), 2017 (middle) and 2018 (bottom) are shown.

C Comparison between the FastSim and FullSim signal samples

Since we have a vast ranges of signal mass points—nearly 500—, and producing these with full detector simulations is expensive in both CPU and time, we decided to use fast simulation (FastSim) (add ref). To further reduce time and CPU we used the leading order theoretical calculations for our signal, and combined the two lepton flavors into one sample (ee and $\mu\mu$).

The basic kinematics of the leptons and (fat)jets are compared between the fast and full simulation (Figs 83–86). No significant discrepancy was observed between the two simulation methods.

In this analysis, we consider the case where the N is sufficiently boosted as to create a merged jet, which contains a lepton and two quark jets. To reconstruct such an object, we use a new lepton isolation variable; the lepton subjet fraction (LSF) [18]. The details of this variable are discussed in Section 3. Since this variable has not been previously used within a FastSim sample, we compared the LSF selection efficiency between the two simulation methods. We collected the signal events which has a wide-cone jet matched to a true N, and a loose lepton if reconstructed inside the matched jet. For these jets, the efficiency that this jet passes the requirement LSF > 0.75 (Figure 87 and Table 42).

Table 42: LSF > 0.75 efficiency of the gen-matched wide-cone jet (and a loose lepton is reconstruced inside) for signals using the two simulation methods.

m_{W_R} (GeV)	m_N (GeV)	FullSim	FastSim
ee			
1000	100	91.95 %	92.28 %
4000	100	80.58 %	80.58 %
4000	1000	84.91 %	89.69 %
$\boldsymbol{\mu\mu}$			
1000	100	93.74 %	94.69 %
4000	100	87.80 %	91.37 %
4000	1000	93.33 %	95.03 %

C.0.1 MC pileup profile for the 2016 fast simulation signal samples

Different MC pileup profiles were used between the full and fast simulations 43 for 2016. Figure 88 shows the pileup profiles from data, full-simulated MC and fast-simulated MC for 2016. Fast-simulated samples do not contain any events where the number of pileup vertices is greater than 37. Hence, once the pileup reweighting is applied the normalization of the signal samples is less than 1. To keep the samples correctly normalized we scaled the reweighting histograms accordingly.

Table 43: MC pileup profile used in the full and fast simulation.

Simulation type	MC profile
Full simulation	2016_25ns_Moriond17MC_PoissonOOTPU
Fast simulation	2016_25ns_SpringMC_PUScenarioV1_PoissonOOTPU

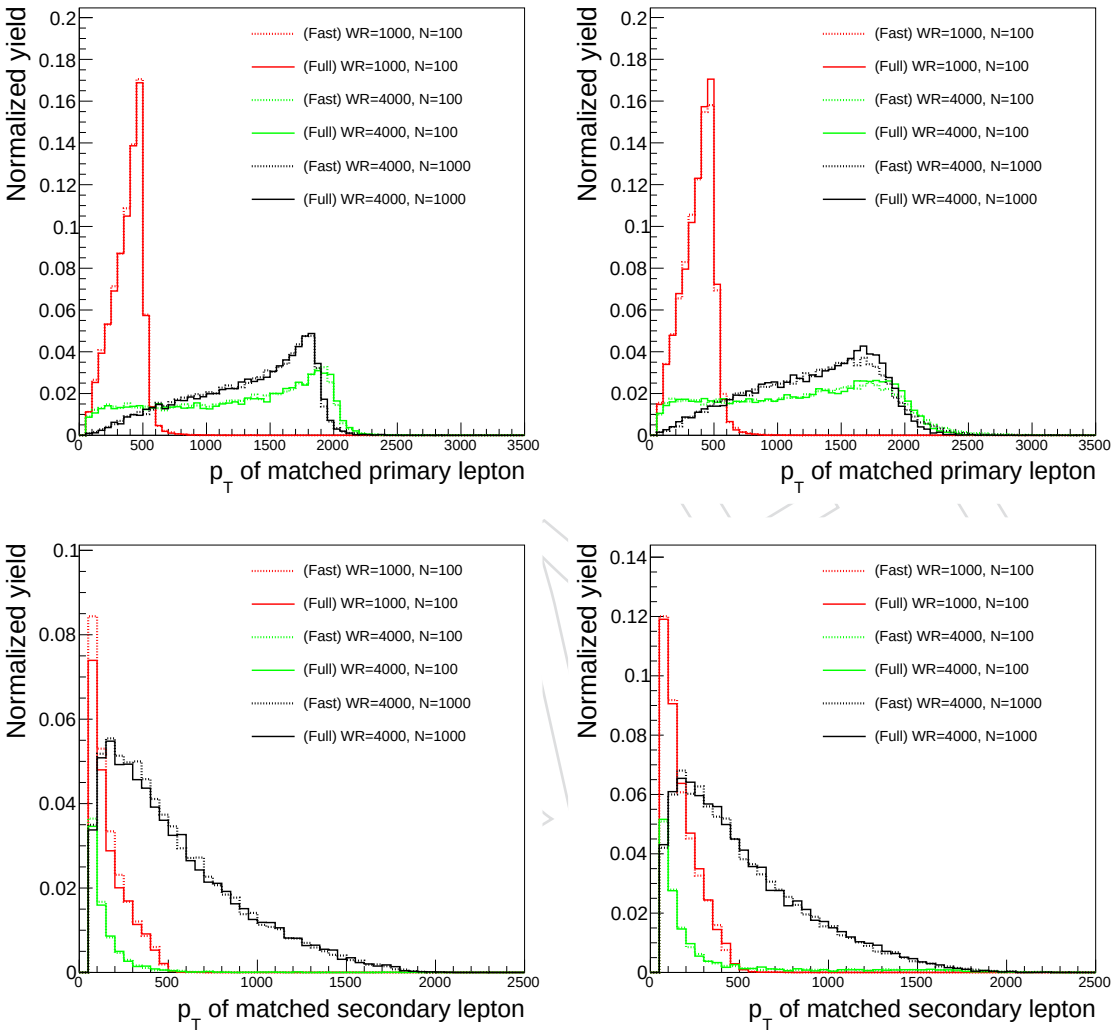

Figure 83: The p_{T} distributions of reconstructed leptons that are matched to true leptons. ee ($\mu\mu$) signal samples are shown in the left (right) plots. The solid (dashed) lines represent the results from full (fast) simulation.

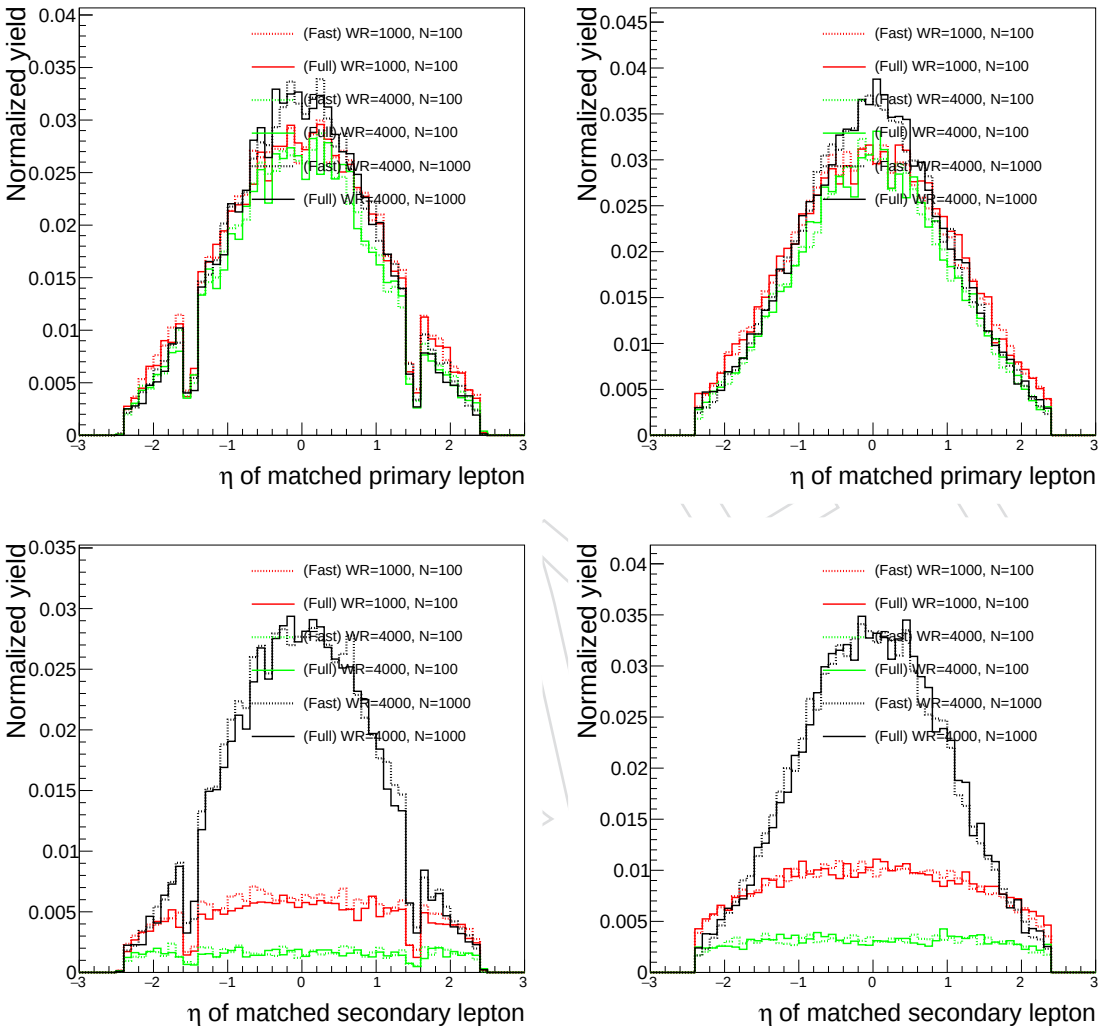

Figure 84: The η distributions of reconstructed leptons that are matched to true leptons. ee ($\mu\mu$) signal samples are shown in the left (right) plots. The solid (dashed) lines represent the results from full (fast) simulation.

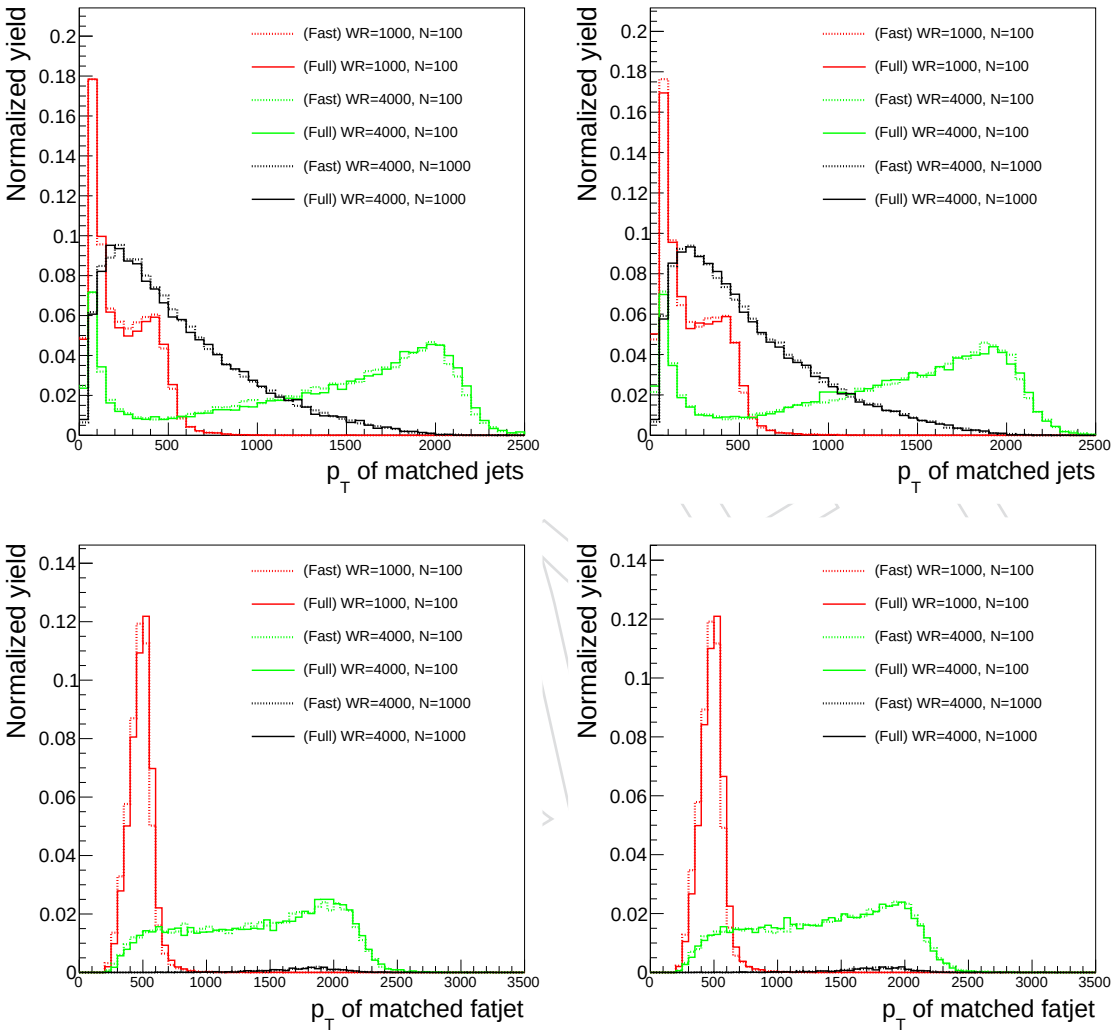

Figure 85: The p_{T} distributions of reconstructed jets (fatjets) that are matched to true quark-jet (N-jet). ee ($\mu\mu$) signal samples are shown in the left (right) plots. The solid (dashed) lines represent the results from full (fast) simulation.

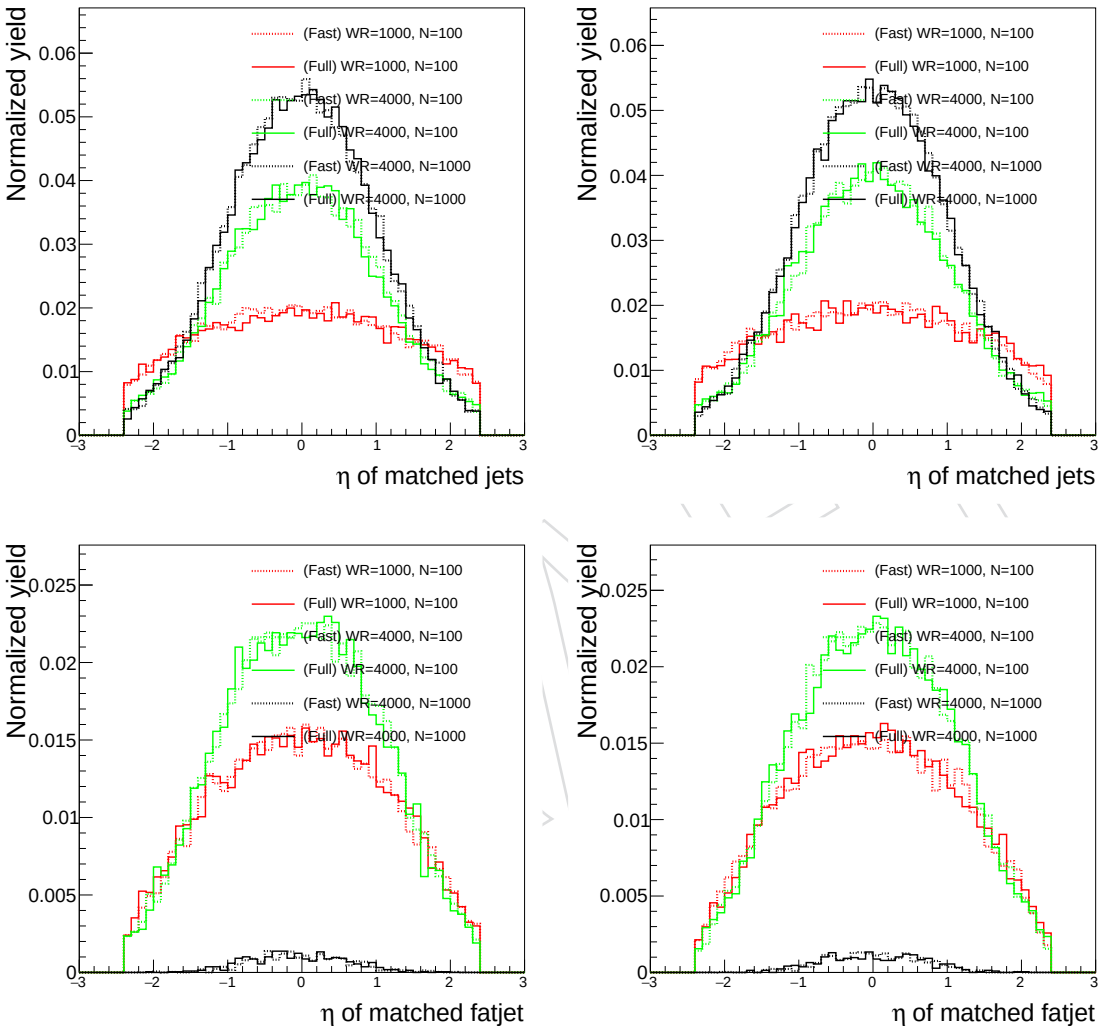

Figure 86: The η distributions of reconstructed jets (fatjets) that are matched to true quark-jet (N-jet). ee ($\mu\mu$) signal samples are shown in the left (right) plots. The solid (dashed) lines represent the results from full (fast) simulation.

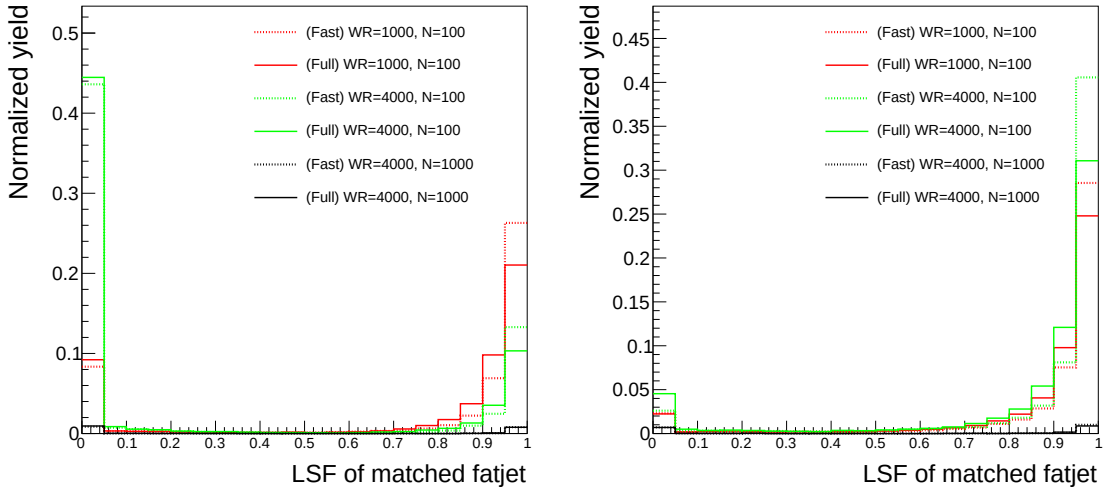

Figure 87: The LSF distributions of reconstructed AK8 jet that are matched to a true N-jet. ee ($\mu\mu$) signal samples are shown in the left (right) plots. The solid (dashed) lines represent the results from full (fast) simulation.

Figure 88: Pileup profiles from data and fast- and full-simulated MCs for 2016.

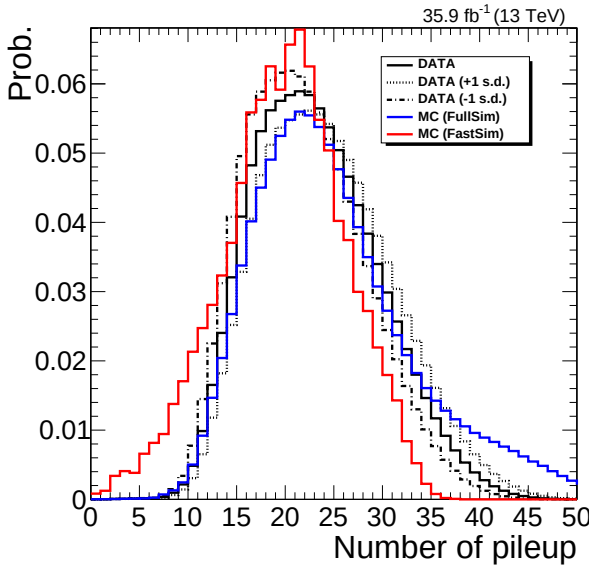

D HEM15/16 Issue

During the Run2018 data taking, the negative endcap HCAL sectors, HEM15 and HEM16 could no longer be operated until the end of the run. The first regular physics run affected is 319077, and a 40 degree section ($-3.0 < \eta < -1.3$ and $-1.57 < \phi < -0.87$) in HCAL is effectively off.

The impact of the issue can be checked by counting the number of merged jet for each η and ϕ sections. We divided the xy-plane into four sections; $(\eta, \phi) = (+,+), (-,+), (-,-), (+,-)$. The HEM 15/16 is located in the third section, $(-,-)$.

Figure 89–90 shows the number of merged jets in the boosted flavor-sideband, but no significant deviations between periodAB and periodCD, or outside-HEM15/16 and inside HEM15/16

728 is observed.

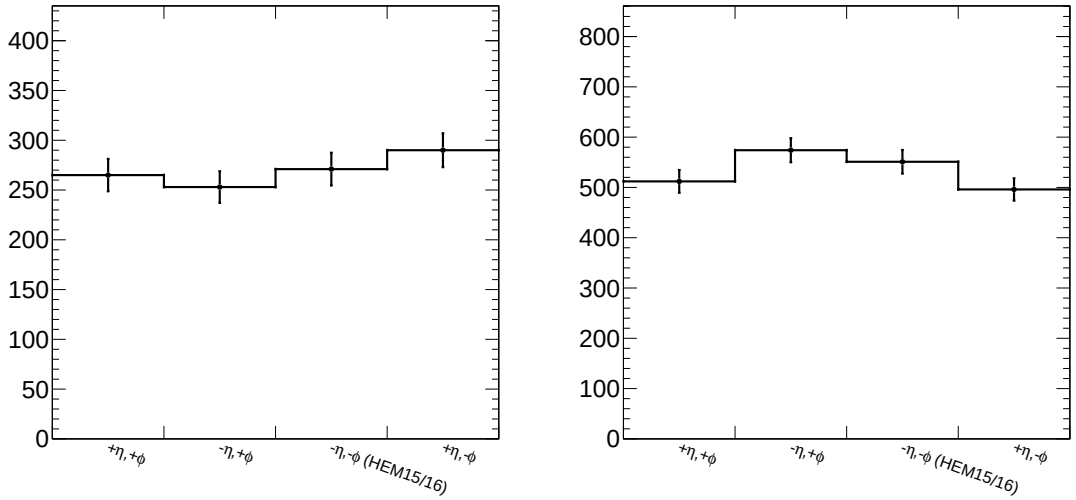

Figure 89: The number of merged jets in the boosted flavor-sideband for each (η, ϕ) section, using EGamma dataset. Results with Run2018 periodAB (periodCD) is shown on the left (right).

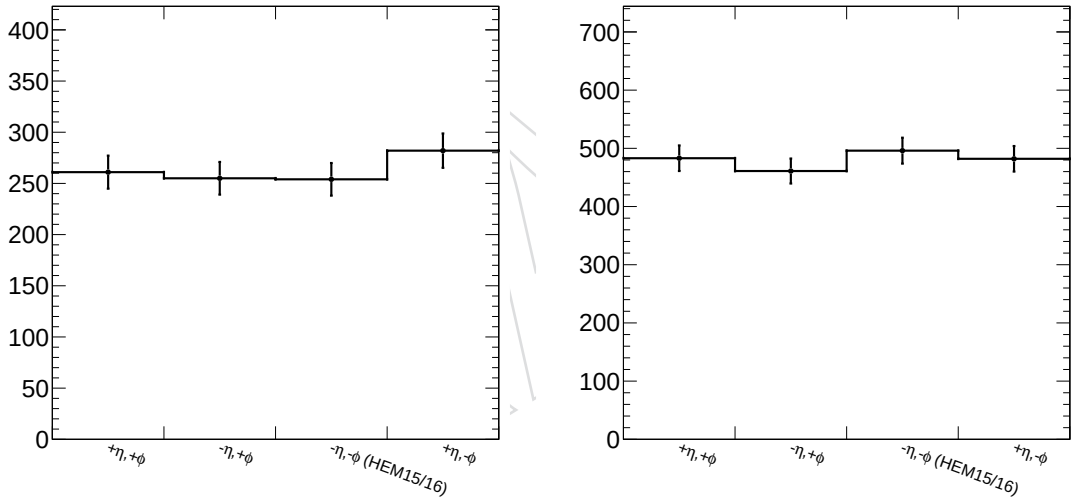

Figure 90: The number of merged jets in the boosted flavor-sideband for each (η, ϕ) section, using SingleMuon dataset. Results with Run2018 periodAB (periodCD) is shown on the left (right).

E HEEP ID in Fast simulation

As we mentioned in Sec. 2, fast simulation (FastSim) is used to simulate our signal samples. We observed the "isEcalDriven==true" requirement, which is included in the HEEP ID, shows lower efficiency in 2017 and 2018 compared to 2016 for the FastSim samples. To validate our FastSim recipes, we used centrally produced FullSim and FastSim $t\bar{t}$ MC samples and compared the same efficiency (Tab. 44). FullSim samples shows similar efficiency throughout the three years (91.8–92.6 %) together with 2016 FastSim (93.9 %), but dropped to 82.1–83.3 % in 2017 and 2018 FastSim samples. This is consistent with the EGamma monitoring results [2].

Table 44: isEcalDriven efficiency.

	2016	2017	2018
Full simulation	92.6 %	92.6 %	91.8 %
Fast simulation	93.9 %	82.3 %	82.1 %

We reported this issue in both EGamma and FastSim group, and the recommendation was to check the "isEcalDriven==true" efficiency within the signals and see if this can be ignored [3]https://hypernews.cern.ch/HyperNews/CMS/get/famos/714/1/1.html. We collected all electrons with $p_{\mathrm{T}} > 35$ GeV and $|\eta| < 2.4$ and passing HEEP ID without "isEcalDriven==true" requirement, and measured the efficiency of them passing "isEcalDriven==true" using 2016 FastSim signal samples (Fig. 91). In our analysis regions, we have one or two HEEP electrons. Both the efficiency of "isEcalDriven==true" and its squared are greater than 98.8 %, hence we concluded to remove this requirement from the 2017 and 2018 HEEP ID selection, and assign extra 2 % uncertainties.

[2]https://hypernews.cern.ch/HyperNews/CMS/get/famos/714/1/1/1.html
[3]https://hypernews.cern.ch/HyperNews/CMS/get/famos/714/1/1.html

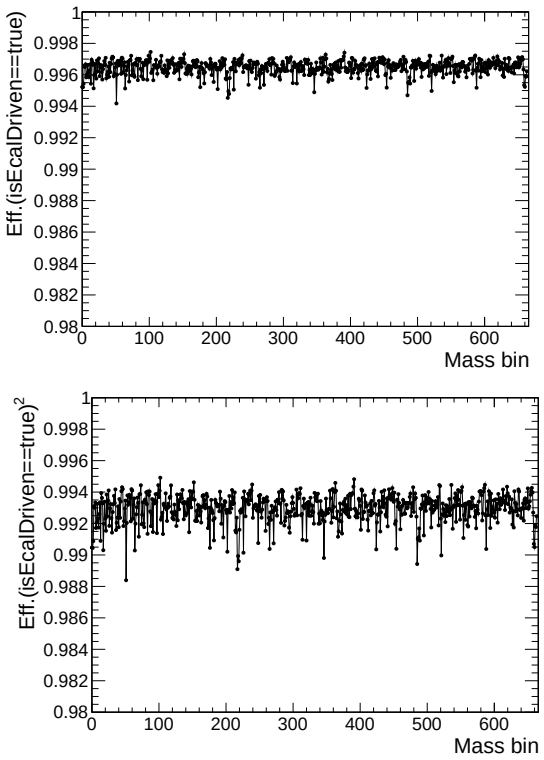

Figure 91: The efficiencies of "isEcalDriven==true" of electrons with $p_{\mathrm{T}} > 35$ GeV and $|\eta| < 2.4$ is shown in the top plot. The x-axis represents signal mass points (in total, 644). The plot on the bottom is the squared value of the top plot.

F Optimization of the soft-drop mass selection

The optimal value of the soft drop mass (m_{SD}) selection in our boosted analysis is chosen using $S/\sqrt{B}$ as a figure of merit, where S is the number of signal events and B is the number of background events. The number of events are integrated so that 90% of the signal invariant mass peak is included for each mass point. The results are shown in Table 45 for different signal sample mass points. All mass points except for the $m_{W_R} = 2500$ and $m_N = 500$ signal have the highest $S/\sqrt{B}$ value when $m_{SD} > 40$ GeV. The Drell-Yan background is reduced the most by the m_{SD} requirement, which is illustrated in Figure 92.

Table 45: $S/\sqrt{B}$ for a variety of signal mass points and different m_{SD} selections.

Signal Sample (m_{W_R}, m_N)	No m_{SD} cut	$m_{SD} > 20$ GeV	$m_{SD} > 30$ GeV	$m_{SD} > 40$ GeV
5000, 1000 GeV	6.692	12.653	11.885	20.228
5000, 500 GeV	2.778	5.803	9.623	10.046
4500, 900 GeV	9.919	27.808	31.225	39.395
4500, 450 GeV	4.225	13.362	15.01	22.144
4000, 800 GeV	14.97	28.094	29.929	39.688
4000, 400 GeV	6.27	21.077	34.052	34.31
3500, 700 GeV	21.505	37.187	36.696	40.811
3500, 350 GeV	14.035	39.847	62.301	64.846
3000, 600 GeV	21.368	28.485	38.558	40.31
3000, 300 GeV	27.603	73.927	75.139	126.549
2500, 500 GeV	14.496	19.548	31.008	30.899
2500, 250 GeV	27.88	58.175	64.341	65.645
2000, 400 GeV	9.578	11.945	13.877	14.33
2000, 200 GeV	20.103	40.557	42.301	44.562
1500, 300 GeV	4.136	5.321	5.188	8.759
1500, 150 GeV	9.432	14.768	16.559	24.483
1000, 200 GeV	1.684	2.241	2.344	2.438
1000, 100 GeV	2.694	4.244	4.549	4.846

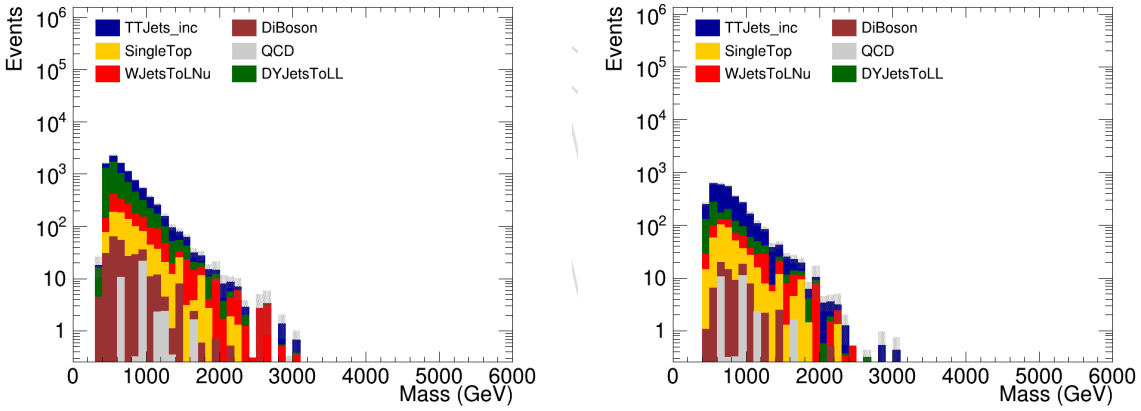

Figure 92: Invariant mass distribution of the background samples with the full event selection applied without (left) and with (right) the $m_{SD} > 40$ GeV selection. The 2016 MC background samples are used.

G Optimization of the LSF selection

The optimal value of the LSF selection in our boosted analysis is chosen using $S/\sqrt{B}$ as a figure of merit, where S is the number of signal events and B is the number of background events. The number of events are integrated so that 90% of the signal invariant mass peak is included for each mass point. The results are shown in Table 93 for different signal sample mass points. In order to be optimal for as many mass points as possible, an LSF > 0.75 is used since tighter requirements show a drop in $S/\sqrt{B}$ for some of the mass points. The $W + Jets$ background is almost completely removed with the LSF selection, as illustrated in Figure 94.

Figure 93: $S/\sqrt{B}$ for a variety of signal mass points and different LSF selections.

Sample	LSF > 0.5	LSF > 0.55	LSF > 0.6	LSF > 0.65	LSF > 0.7	LSF > 0.75	LSF > 0.8	LSF > 0.85	LSF > 0.9	LSF > 0.95
W_R 3000 GeV, N_R 100 GeV	105.03746	104.58982	105.03746	107.41769	109.8119	114.63871	114.51767	111.24252	112.66141	107.76144
W_R 3000 GeV, N_R 200 GeV	95.51158	95.07797	95.51158	97.87751	100.13971	104.74952	104.94336	102.76459	105.74093	107.74615
W_R 3000 GeV, N_R 400 GeV	44.85286	44.99218	44.85286	45.62606	46.19692	47.66982	47.00475	45.53538	46.74589	48.9643
W_R 3000 GeV, N_R 600 GeV	19.03773	19.08723	19.03773	19.33575	19.60256	20.27276	19.94252	19.30974	19.78254	20.55756
W_R 5000 GeV, N_R 100 GeV	1.81474	1.80232	1.81474	1.85444	1.89023	1.97251	1.97065	1.91124	1.94705	1.91849
W_R 5000 GeV, N_R 200 GeV	1.82466	1.81477	1.82466	1.86408	1.90368	1.98626	1.99231	1.93641	1.99677	2.0533
W_R 5000 GeV, N_R 400 GeV	1.16012	1.15955	1.16012	1.17565	1.19425	1.23662	1.23072	1.19866	1.2302	1.30539
W_R 5000 GeV, N_R 600 GeV	0.06941	0.06936	0.06941	0.07064	0.07156	0.07394	0.07286	0.07062	0.07257	0.07598
W_R 5000 GeV, N_R 800 GeV	0.03842	0.03836	0.03842	0.03895	0.03952	0.04089	0.04039	0.03919	0.04069	0.04352
W_R 5000 GeV, N_R 1000 GeV	0.02294	0.02285	0.02294	0.02338	0.02386	0.02462	0.02458	0.02406	0.02473	0.02639
W_R 7000 GeV, N_R 100 GeV	0.18652	0.18538	0.18652	0.19095	0.19513	0.2035	0.20056	0.19482	0.19967	0.19411
W_R 7000 GeV, N_R 200 GeV	0.16785	0.16717	0.16785	0.17199	0.17593	0.18396	0.18451	0.18018	0.18545	0.18923
W_R 7000 GeV, N_R 400 GeV	0.10015	0.1001	0.10015	0.10189	0.10291	0.10687	0.10651	0.10324	0.10693	0.11468
W_R 7000 GeV, N_R 600 GeV	0.06235	0.06228	0.06235	0.06348	0.06471	0.06675	0.06691	0.06432	0.06549	0.07
W_R 7000 GeV, N_R 800 GeV	0.04058	0.0406	0.04058	0.0413	0.0422	0.0424	0.04242	0.04169	0.04303	0.04591
W_R 7000 GeV, N_R 1000 GeV	0.0264	0.02632	0.0264	0.02703	0.02752	0.02863	0.02837	0.02674	0.02775	0.03014
W_R 7000 GeV, N_R 1200 GeV	0.01642	0.01641	0.01642	0.01678	0.01703	0.01776	0.01768	0.01723	0.0178	0.01924
W_R 7000 GeV, N_R 1400 GeV	0.012	0.01198	0.012	0.01223	0.01239	0.01285	0.01282	0.01248	0.01304	0.01393

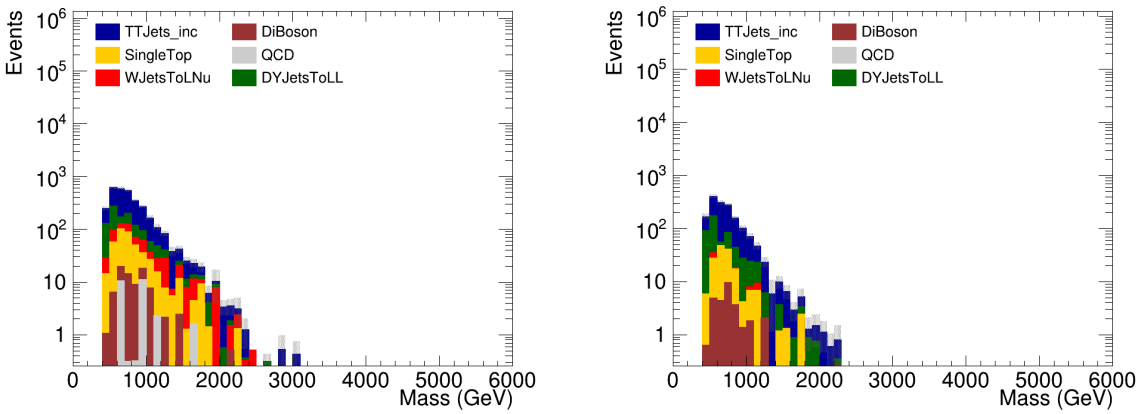

Figure 94: Invariant mass distribution of the background samples with the full event selection applied without (left) and with (right) the LSF $>$ 0.75 selection. The 2016 MC background samples are used.

H Optimization of the dilepton invariant mass selection

The optimal value of the m_{ll} selection in our resolved analysis is chosen using the expected limit as a figure of merit. A comparison between the expected limits with $m_{ll} > 200$ GeV and $m_{ll} > 400$ GeV selections in the muon channel can be seen in Figure 95. The $m_{ll} > 400$ GeV has at least a $10 - 20\%$ improvement for all signals with $m_{W_R} > 1$ TeV.

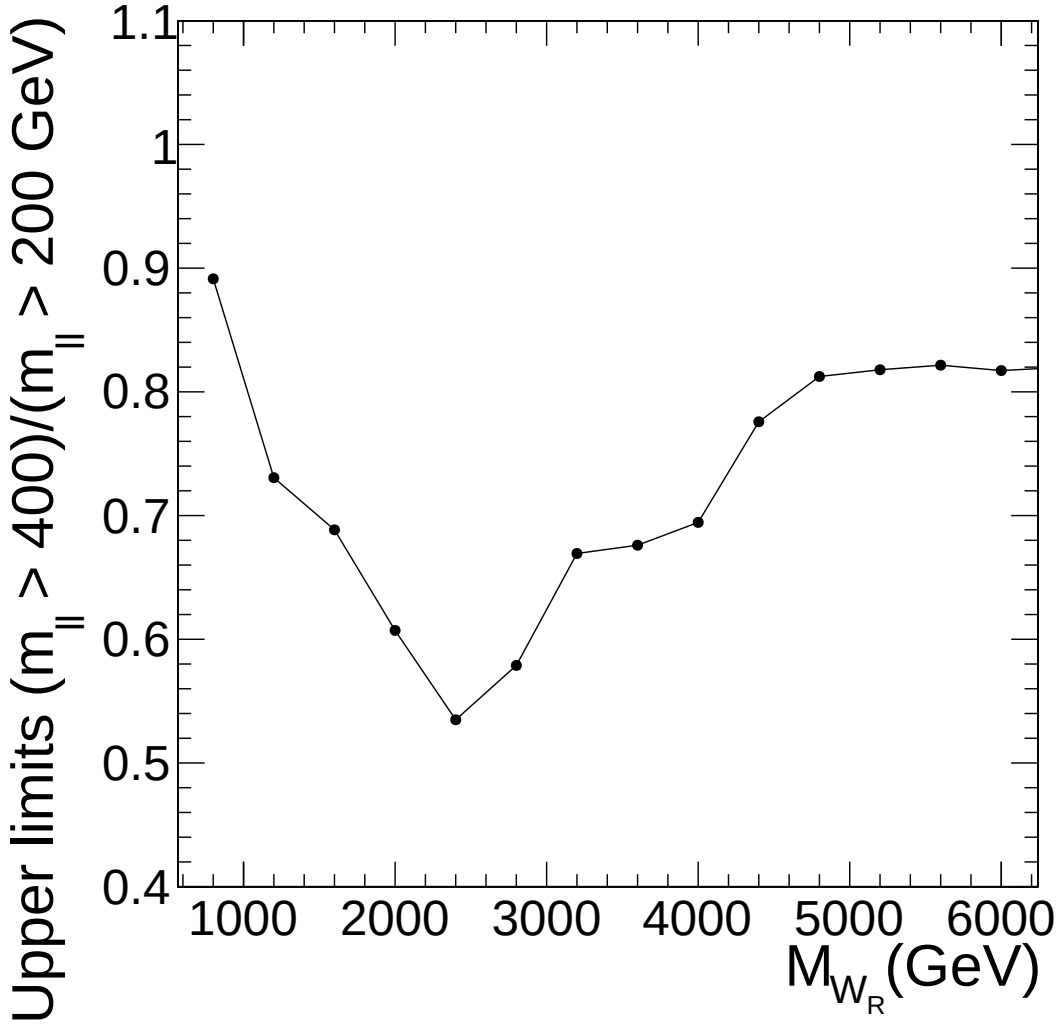

Figure 95: Ratio of the expected limits in the Muon channel of the resolved analysis with the $m_{ll} > 400$ GeV and $m_{ll} > 200$ GeV. The expected limits are calculated for signals with $m_{W_R} = m_N/2$. The expected limits are stronger for the $m_{ll} > 400$ GeV selection for all signals with $m_{W_R} > 1$ TeV.

A comparison is then done between the $m_{ll} > 400$ GeV selection and $m_{ll} > 450, 500, 550$ GeV selections. The ratio of the expected limits for these selections can be seen in Figure 96. The $m_{ll} > 400$ GeV gives the best expected limits, but only by $\sim 1\%$ for $m_{W_R} < 3.2$ TeV. The degradation of expected limits at low m_{W_R} becomes much more pronounced with the $m_{ll} > 550$ GeV selection.

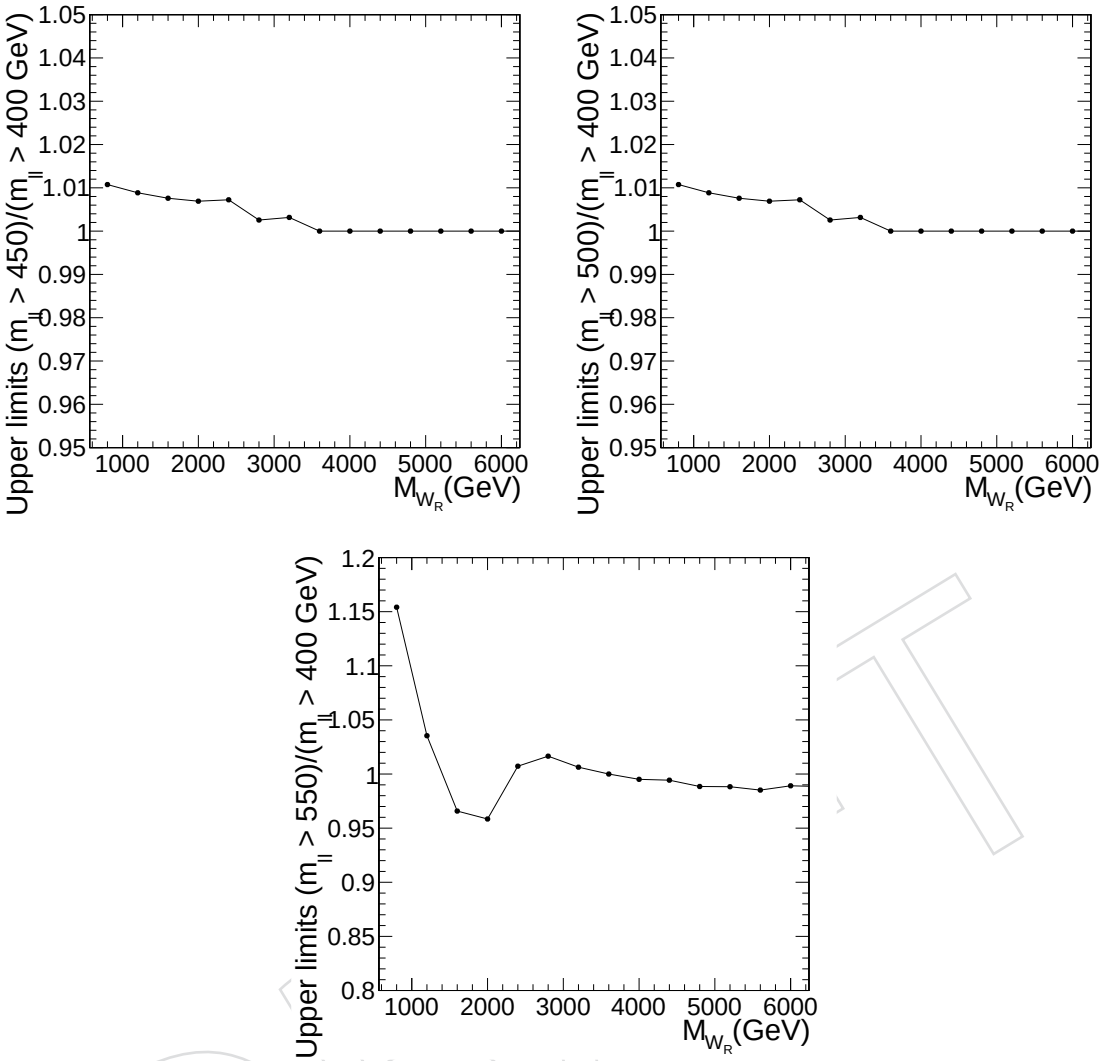

Figure 96: Ratio of the expected limits in the Muon channel of the resolved analysis with the $m_{ll} > 400$ GeV and $m_{ll} > 450, 500, 550$ GeV (top left, top right, bottom). The expected limits are calculated for signals with $m_{W_R} = m_N/2$. The expected limits are stronger for the $m_{ll} > 400$ GeV selection for all signals with $m_{WR} > 1$ TeV.

I Cutflow of samples

Table 46: Cutflow for resolved dielectron with 2016 samples.

Selection	$t\bar{t}$	DY	(3000,1400)	(4000,2000)	(5000,3000)
No cut	5.25E+06	7.59E+06	500.28	48.06	4.93
METFilter	5.25E+06	7.58E+06	499.48	48.00	4.93
Number of tight lepton is two	3.00E+04	1.94E+05	157.41	14.79	1.56
Trigger fired	2.97E+04	1.92E+05	157.41	14.79	1.56
Number of AK4 jets ≥ 2	2.02E+04	9.65E+04	151.55	14.43	1.53
$\Delta R > 0.4$	1.34E+04	5.27E+04	147.45	14.04	1.49
$m(\ell\ell) > 200$ GeV	5.21E+03	1.51E+03	135.91	12.97	1.38
$m(\ell\ell jj) > 800$ GeV	1.03E+03	5.19E+02	135.90	12.97	1.38
$m(\ell\ell) > 400$ GeV	3.22E+02	2.01E+02	130.80	12.71	1.36

Table 47: Cutflow for boosted dielectron with 2016 samples.

Selection	$t\bar{t}$	DY	(3000,200)	(4000,200)	(5000,200)
No cut	5.25E+06	7.59E+06	803.31	106.52	23.41
METFilter	5.25E+06	7.58E+06	802.49	106.39	23.38
Not resolved	2.86E+06	4.75E+06	642.09	84.10	17.62
Leading lepton is electron (muon)	1.29E+06	2.18E+06	307.49	40.43	8.35
Trigger fired	1.20E+06	2.04E+06	294.19	38.63	7.96
No $60 < m(\ell_{\text{Tight}}\ell_{\text{Loose}}) < 150$ GeV	1.19E+06	1.90E+06	293.87	38.60	7.93
Merged AK8 jet with $\Delta\phi > 2.0$	6.71E+03	1.63E+03	142.07	15.50	2.50
No extra tight lepton	6.69E+03	1.62E+03	141.74	15.48	2.50
Loose SF lepton inside the merged jet	1.79E+03	3.42E+02	127.28	13.99	2.25
No loose OF lepton inside the merged jet	1.76E+03	3.41E+02	125.85	13.79	2.21
$m(\ell_{\text{Tight}}\ell_{\text{Loose}}) > 200$ GeV	1.39E+03	3.17E+02	125.85	13.79	2.21
$m(\ell_{\text{Tight}}J) > 800$ GeV	1.43E+02	3.84E+01	125.17	13.63	2.15

Table 48: Cutflow for resolved dimuon with 2016 samples.

Selection	$t\bar{t}$	DY	(3000,1400)	(4000,2000)	(5000,3000)
No cut	5.25E+06	7.59E+06	500.28	48.06	4.93
METFilter	5.25E+06	7.58E+06	499.48	48.00	4.93
Number of tight lepton is two	4.32E+04	2.76E+05	205.37	20.25	2.07
Trigger fired	4.32E+04	2.76E+05	205.37	20.25	2.07
Number of AK4 jets ≥ 2	2.63E+04	9.98E+04	198.42	19.80	2.05
$\Delta R > 0.4$	2.30E+04	8.92E+04	185.06	18.47	1.92
$m(\ell\ell) > 200$ GeV	8.98E+03	2.43E+03	167.66	15.63	1.52
$m(\ell\ell jj) > 800$ GeV	1.75E+03	7.94E+02	167.66	15.63	1.52
$m(\ell\ell) > 400$ GeV	5.68E+02	2.97E+02	161.78	15.34	1.50

Table 49: Cutflow for boosted dimuon with 2016 samples.

Selection	$t\bar{t}$	DY	(3000,200)	(4000,200)	(5000,200)
No cut	5.25E+06	7.59E+06	803.31	106.52	23.41
METFilter	5.25E+06	7.58E+06	802.49	106.39	23.38
Not resolved	2.86E+06	4.75E+06	642.09	84.10	17.62
Leading lepton is electron (muon)	1.58E+06	2.57E+06	334.31	43.63	9.26
Trigger fired	1.51E+06	2.46E+06	276.74	34.33	7.50
No $60 < m(\ell_{\text{Tight}}\ell_{\text{Loose}}) < 150$ GeV	1.50E+06	2.29E+06	276.47	34.26	7.47
Merged AK8 jet with $\Delta\phi > 2.0$	8.37E+03	1.99E+03	171.28	19.88	3.61
No extra tight lepton	8.34E+03	1.99E+03	170.97	19.85	3.61
Loose SF lepton inside the merged jet	1.83E+03	3.49E+02	166.54	19.29	3.51
No loose OF lepton inside the merged jet	1.79E+03	3.49E+02	165.68	19.19	3.49
$m(\ell_{\text{Tight}}\ell_{\text{Loose}}) > 200$ GeV	1.39E+03	3.30E+02	165.67	19.19	3.49
$m(\ell_{\text{Tight}}\text{J}) > 800$ GeV	1.79E+02	5.42E+01	164.99	19.02	3.41

Table 50: Cutflow for resolved dielectron with 2017 samples.

Selection	$t\bar{t}$	DY	(3000,1400)	(4000,2000)	(5000,3000)
No cut	5.85E+06	2.32E+07	570.72	54.83	5.62
METFilter	5.84E+06	2.32E+07	569.90	54.73	5.62
Number of tight lepton is two	3.62E+04	2.71E+05	138.99	13.20	1.33
Trigger fired	3.60E+04	2.70E+05	138.99	13.20	1.33
Number of AK4 jets ≥ 2	2.18E+04	7.71E+04	133.17	12.86	1.31
$\Delta R > 0.4$	2.00E+04	6.63E+04	130.18	12.48	1.26
$m(\ell\ell) > 200$ GeV	7.29E+03	1.99E+03	118.81	11.44	1.15
$m(\ell\ell\text{jj}) > 800$ GeV	1.29E+03	5.92E+02	118.77	11.44	1.15
$m(\ell\ell) > 400$ GeV	4.08E+02	2.22E+02	114.64	11.22	1.14

Table 51: Cutflow for boosted dielectron with 2017 samples.

Selection	$t\bar{t}$	DY	(3000,200)	(4000,200)	(5000,200)
No cut	5.85E+06	2.32E+07	916.03	121.25	26.66
METFilter	5.84E+06	2.32E+07	914.65	121.06	26.61
Not resolved	3.38E+06	9.52E+06	719.00	94.45	19.81
Leading lepton is electron (muon)	1.54E+06	4.38E+06	323.94	42.22	8.95
Trigger fired	1.39E+06	3.95E+06	308.21	40.09	8.46
No $60 < m(\ell_{\text{Tight}}\ell_{\text{Loose}}) < 150$ GeV	1.38E+06	3.78E+06	307.97	40.00	8.43
Merged AK8 jet with $\Delta\phi > 2.0$	6.82E+03	1.60E+03	147.41	15.75	2.64
No extra tight lepton	6.81E+03	1.59E+03	147.13	15.73	2.63
Loose SF lepton inside the merged jet	1.79E+03	4.01E+02	133.14	14.17	2.34
No loose OF lepton inside the merged jet	1.75E+03	4.01E+02	131.29	14.00	2.30
$m(\ell_{\text{Tight}}\ell_{\text{Loose}}) > 200$ GeV	1.40E+03	3.85E+02	131.27	14.00	2.30
$m(\ell_{\text{Tight}}\text{J}) > 800$ GeV	1.37E+02	2.95E+01	130.54	13.81	2.24

Table 52: Cutflow for resolved dimuon with 2017 samples.

Selection	$t\bar{t}$	DY	(3000,1400)	(4000,2000)	(5000,3000)
No cut	5.85E+06	2.32E+07	570.72	54.83	5.62
METFilter	5.84E+06	2.32E+07	569.90	54.73	5.62
Number of tight lepton is two	5.05E+04	3.67E+05	244.13	23.75	2.44
Trigger fired	5.05E+04	3.67E+05	244.13	23.75	2.44
Number of AK4 jets ≥ 2	3.12E+04	1.06E+05	233.97	23.06	2.40
$\Delta R > 0.4$	2.68E+04	8.98E+04	219.17	21.68	2.26
$m(\ell\ell) > 200$ GeV	1.06E+04	2.93E+03	201.90	19.10	1.94
$m(\ell\ell\text{jj}) > 800$ GeV	2.01E+03	1.03E+03	201.87	19.09	1.94
$m(\ell\ell) > 400$ GeV	6.56E+02	4.27E+02	195.49	18.80	1.92

Table 53: Cutflow for boosted dimuon with 2017 samples.

Selection	$t\bar{t}$	DY	(3000,200)	(4000,200)	(5000,200)
No cut	5.85E+06	2.32E+07	916.03	121.25	26.66
METFilter	5.84E+06	2.32E+07	914.65	121.06	26.61
Not resolved	3.38E+06	9.52E+06	719.00	94.45	19.81
Leading lepton is electron (muon)	1.83E+06	5.14E+06	394.92	52.21	10.86
Trigger fired	1.74E+06	4.89E+06	332.25	43.49	9.21
No $60 < m(\ell_{\text{Tight}}\ell_{\text{Loose}}) < 150$ GeV	1.73E+06	4.67E+06	331.97	43.41	9.17
Merged AK8 jet with $\Delta\phi > 2.0$	8.64E+03	2.10E+03	205.02	24.64	4.48
No extra tight lepton	8.62E+03	2.09E+03	204.77	24.61	4.47
Loose SF lepton inside the merged jet	1.99E+03	4.48E+02	199.68	23.96	4.36
No loose OF lepton inside the merged jet	1.93E+03	4.47E+02	198.17	23.81	4.34
$m(\ell_{\text{Tight}}\ell_{\text{Loose}}) > 200$ GeV	1.50E+03	4.32E+02	198.12	23.81	4.34
$m(\ell_{\text{Tight}}\text{J}) > 800$ GeV	1.80E+02	4.90E+01	197.24	23.58	4.23

J Systematic uncertainty on the data-driven ttbar estimation

The $t\bar{t}$ background contribution is estimated directly from data in the flavor sideband CR, which has the same kinematics as the $t\bar{t}$ in the signal region. The contribution from other backgrounds in this CR are taken from simulation and subtracted from the data to produce a pure $t\bar{t}$ sample.

For this estimate, the assumption made on the conservation of the flavor in the decay is needed to ensure that there is no contamination from signal events. Thus, the decay of a real W_R boson at leading order cannot yield an $e\mu$ final state and the flavor sideband is dominated by $t\bar{t}$ events.

Table 54: The fraction (%) of signal yields compared to the total SM background at each flavor sideband.

m_{W_R}, m_N) GeV	Resolved sideband	Boosted sodeband (with μ-jet)	Boosted sodeband (with e-jet)
(3000,100)	0.011	0.055	0.027
(3000,200)	0.010	0.073	0.028
(3000,400)	0.072	0.253	0.121
(3000,600)	0.130	0.299	0.089
(3000,800)	0.109	0.234	0.064
(3000,1000)	0.170	0.199	0.069
(3000,1200)	0.116	0.168	0.067
(3000,1400)	0.105	0.150	0.062
(3000,1600)	0.096	0.152	0.050
(3000,1800)	0.079	0.145	0.052
(3000,2000)	0.053	0.159	0.029
(3000,2200)	0.043	0.103	0.024
(3000,2400)	0.026	0.051	0.015
(3000,2600)	0.012	0.045	0.012
(3000,2800)	0.006	0.012	0.003
(3000,2900)	0.002	0.006	0.002

To calculate the number of events from $t\bar{t}$ in the dimuon signal region, for both the boosted and resolved analyses, we used the $t\bar{t}$ MC to find the SFs $R_{e\mu/\mu\mu}$ between the flavor sideband and the signal regions. These SFs were evaluated from the ratio of the number of events in the final-state objects invariant mass distributions in the signal region over the invariant mass distribution in the flavor sideband. The number of events in the signal region is given by:

$$N_{t\bar{t}}(\text{signal region}) = N_{t\bar{t}}(\text{flavor sideband}) \times R_{ee,\mu\mu/e\mu} \quad (6)$$

Using the SFs we can account for the difference in efficiency and acceptance between electrons and muons in these final states.

The ratios between the signal region and the $e\mu$–sideband are obtained using $t\bar{t}$ MC samples, which are shown in Figs. 97–99. We fit the ratios with a constant polynomial function, and the fit results are summarized in Table 55.

The $m(W_R)$ distributions, for events in the $e\mu$–sideband, in data and simulation are shown in Figs. 100–102.

For the systematic uncertainty on the scale factors, a closure test is performed in the low invariant mass region for both flavor channels; all the requirements are the same as in the signal region, except that $m_{\ell\ell jj}$ ($m_{\ell J}$) are required to be less than 800 GeV for the resolved (boosted) re-

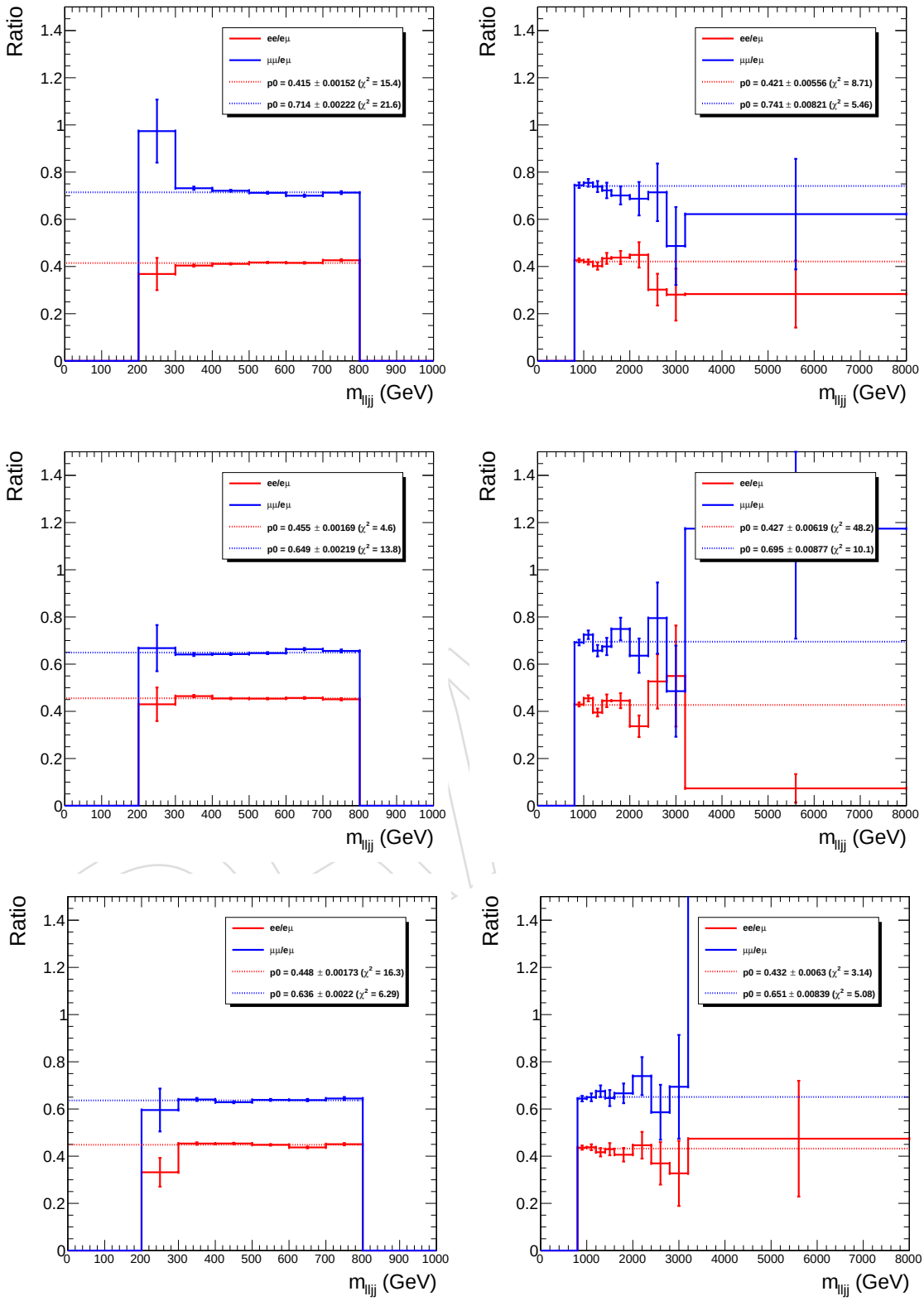

Figure 97: The signal region to eμ–sideband ratio as a function of the mass of W_R in the resolved category, for 2016 (upper), 2017 (middle) and 2018 (lower). The plots on the left (right) are obtained in low (high) invariant mass regions.

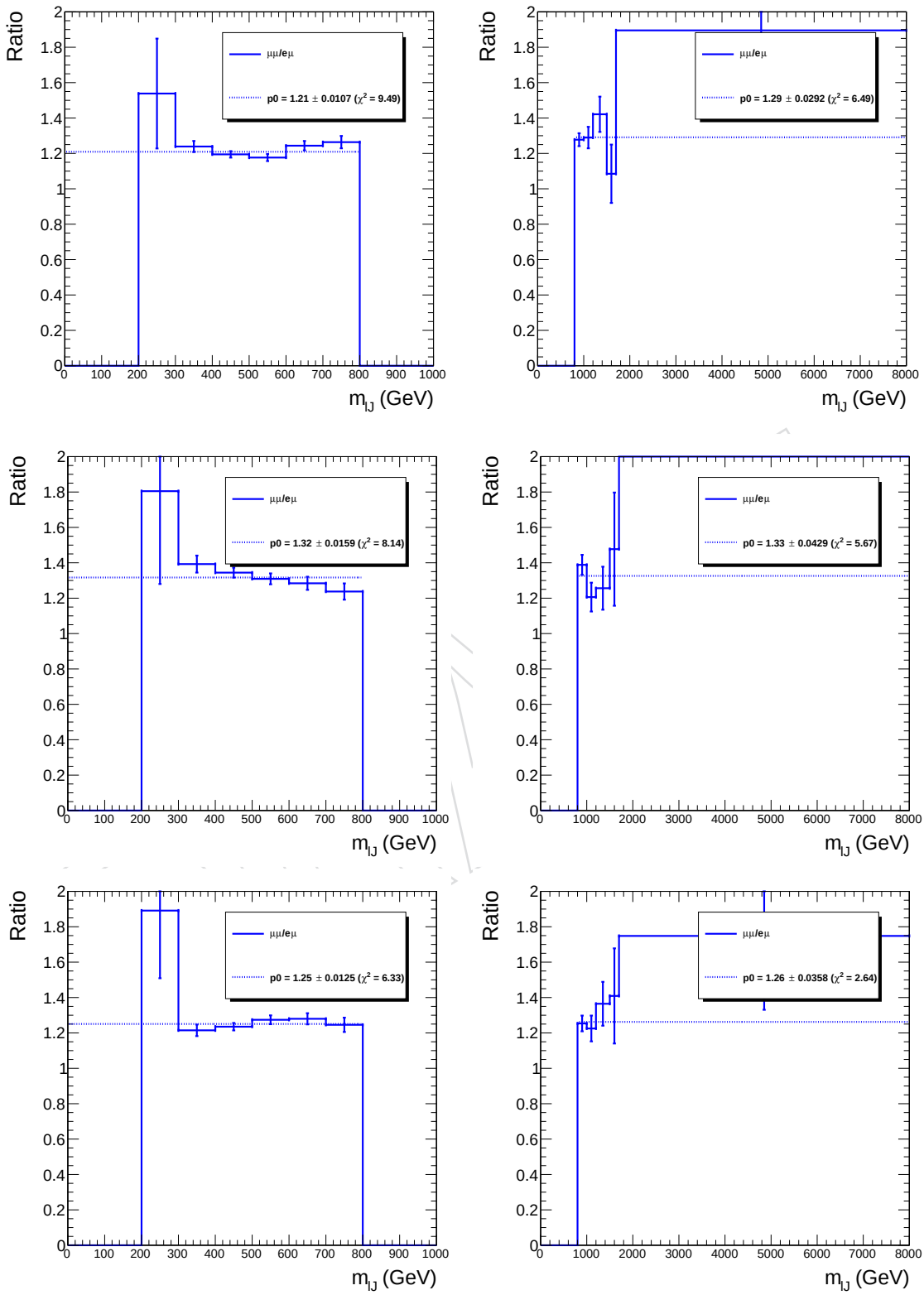

Figure 98: The signal region to eμ–sideband ratio as a function of the mass of W_R in the boosted category containing μ–jet, for 2016 (upper), 2017 (middle) and 2018 (lower).

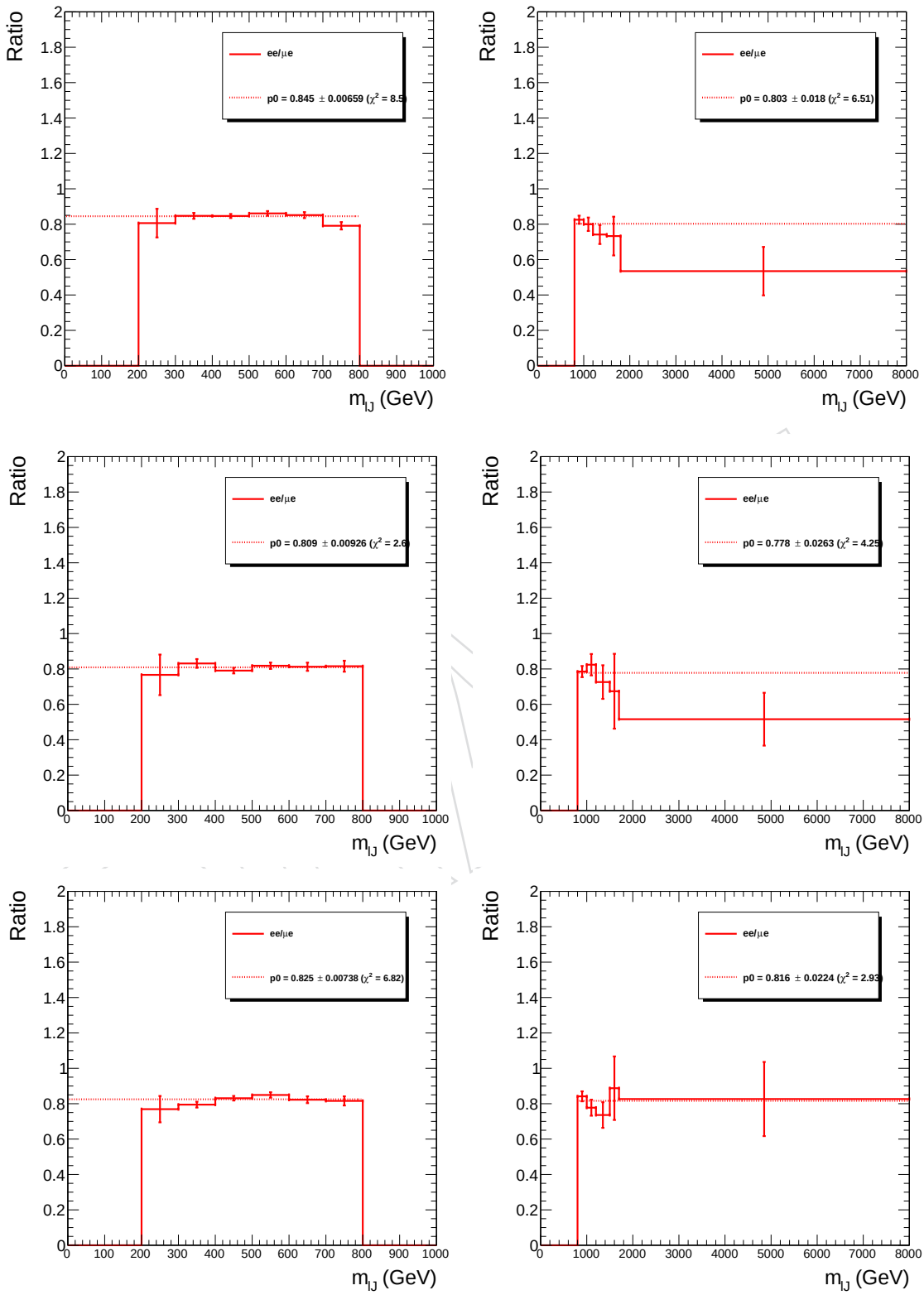

Figure 99: The signal region to eμ–sideband ratio as a function of the mass of W_R in the boosted category containing e–jet, for 2016 (upper), 2017 (middle) and 2018 (lower).

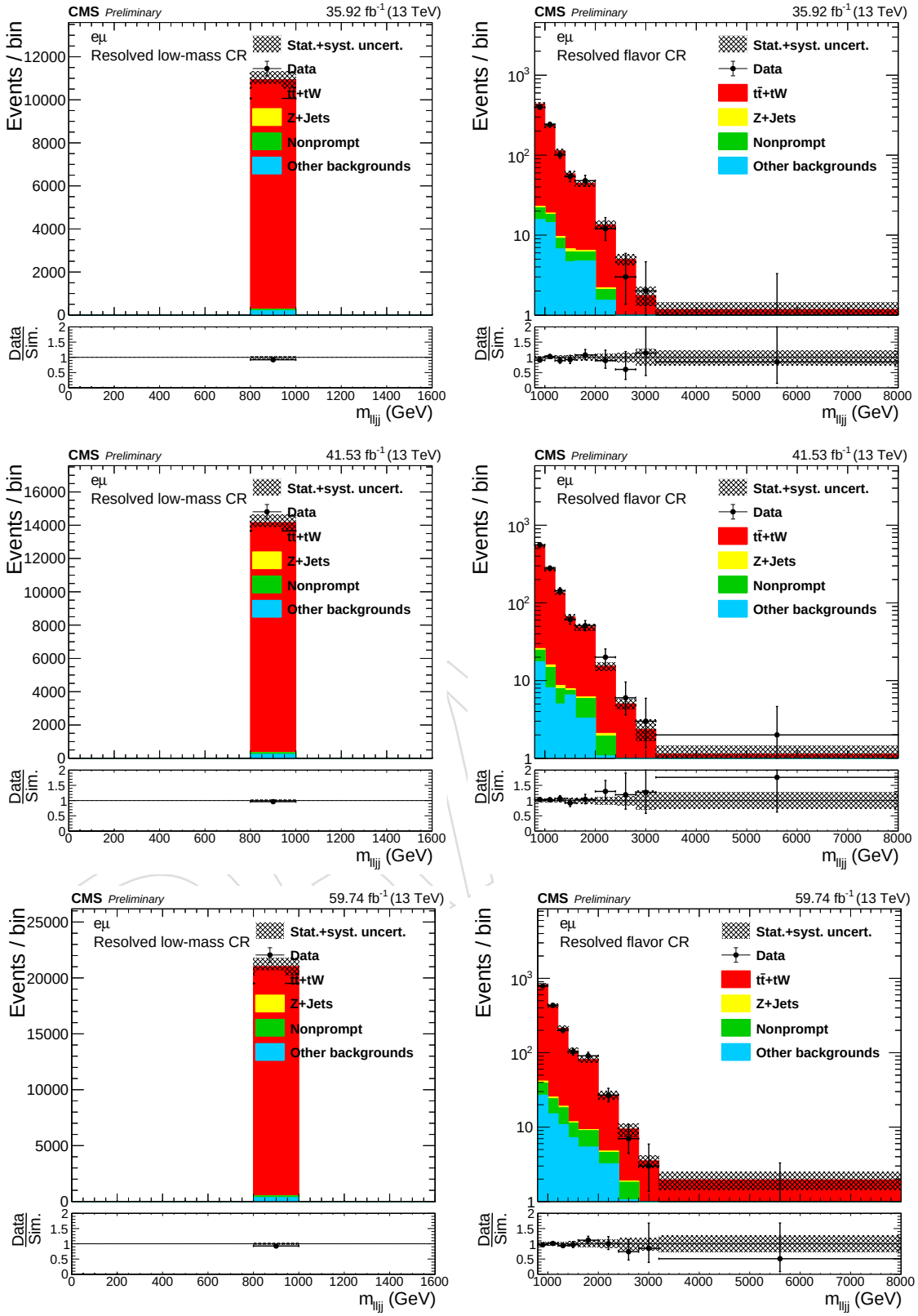

Figure 100: The reconstructed mass of W_R in the resolved flavor sideband region, for 2016 (upper), 2017 (middle) and 2018 (lower). The plots on the left (right) are obtained in low (high) invariant mass regions.

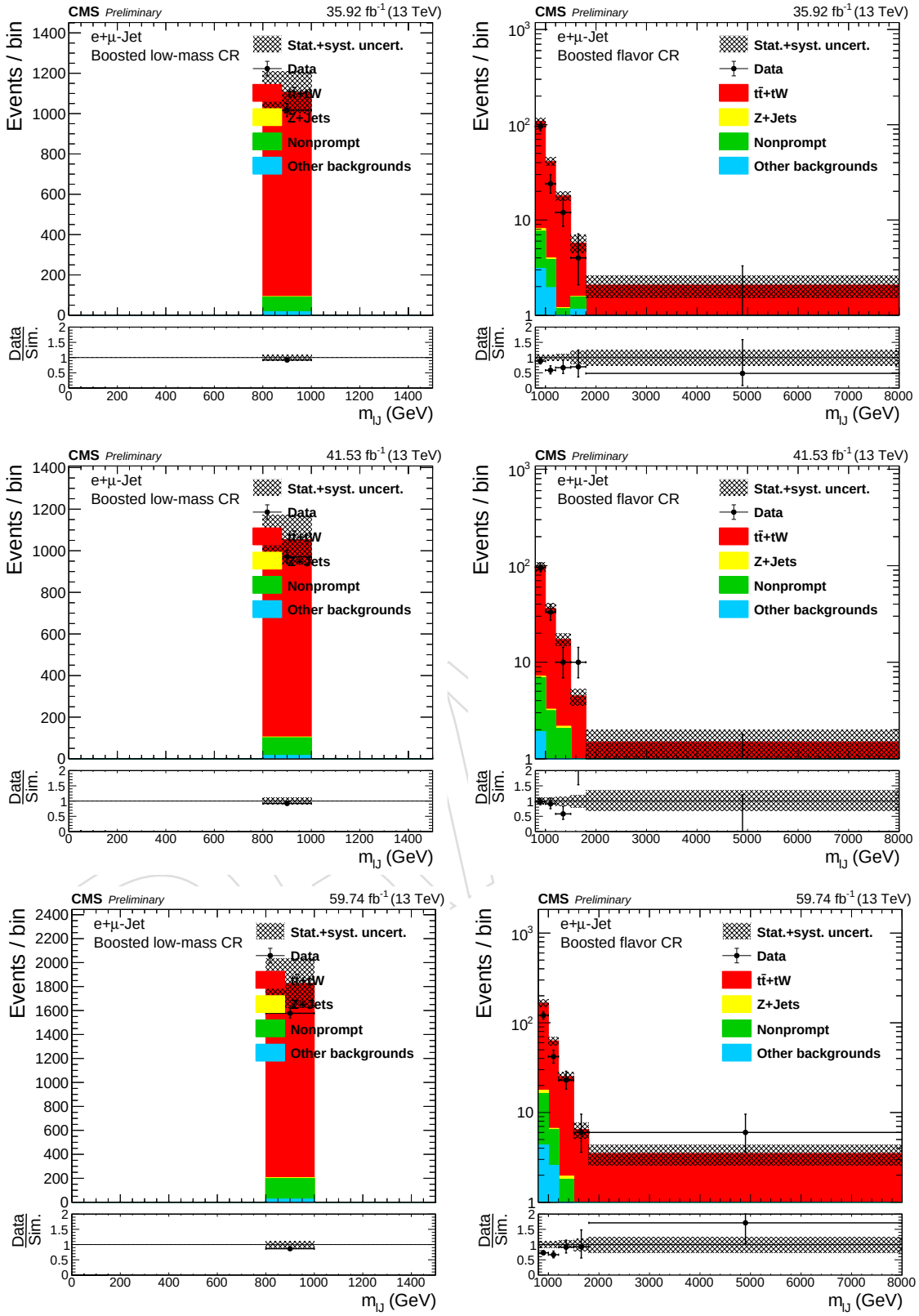

Figure 101: The reconstructed mass of W_R in the boosted flavor sideband region with μ–jet, for 2016 (upper), 2017 (middle) and 2018 (lower). The plots on the left (right) are obtained in low (high) invariant mass regions.

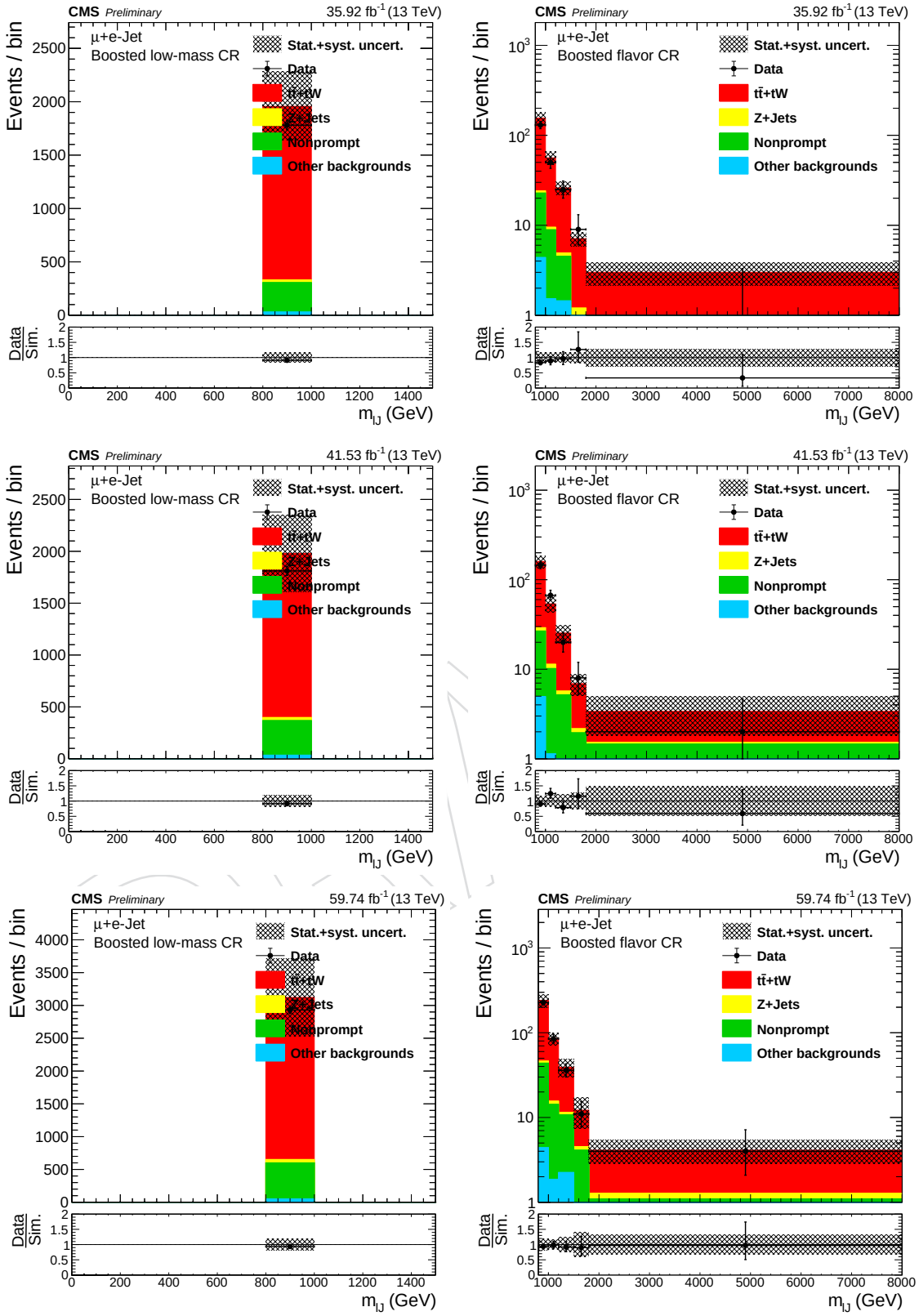

Figure 102: The reconstructed mass of W_R in the boosted flavor sideband region with e–jet, for 2016 (upper), 2017 (middle) and 2018 (lower). The plots on the left (right) are obtained in low (high) invariant mass regions.

Table 55: The fit results of the eμ–ratios, with the statistical uncertainties.

Year	Event Type	Resolved		Boosted	
		ee	$\mu\mu$	ee	$\mu\mu$
2016	$m(W_R) > 800$ GeV	0.421 ± 0.006	0.741 ± 0.008	0.804 ± 0.018	1.281 ± 0.029
	$m(W_R) \leq 800$ GeV	0.415 ± 0.002	0.714 ± 0.002	0.846 ± 0.007	1.212 ± 0.010
2017	$m(W_R) > 800$ GeV	0.431 ± 0.006	0.701 ± 0.009	0.786 ± 0.026	1.302 ± 0.041
	$m(W_R) \leq 800$ GeV	0.458 ± 0.002	0.652 ± 0.002	0.816 ± 0.009	1.306 ± 0.015
2018	$m(W_R) > 800$ GeV	0.432 ± 0.006	0.651 ± 0.008	0.815 ± 0.022	1.271 ± 0.036
	$m(W_R) \leq 800$ GeV	0.448 ± 0.002	0.636 ± 0.002	0.826 ± 0.007	1.249 ± 0.012

gion. The data and background, including data–driven estimation of $t\bar{t}$ contribution are shown in Fig. 103–104

To estimate the systematic uncertainty on our data-driven ttbar background estimation, we varied the uncertainty from 5 % to 60 % and checked the ratio of the observed data and preidictions in our low invariant mass control regions. Except the bins where we have very large statistical uncertaities (below 300 GeV), 20 % (30 %) uncertainty on the resolved (boosted) region was enough to cover the descrepancies between the data and the preiction. Figs. 105–116 show the agreement in the resolved low invariant mass control regions for our dimuon and dielectron regions across all three years of data taking. Figs. 117–128 show the agreement in the boosted low invariant mass control regions for our dimuon and dielectron regions across all three years of data taking.

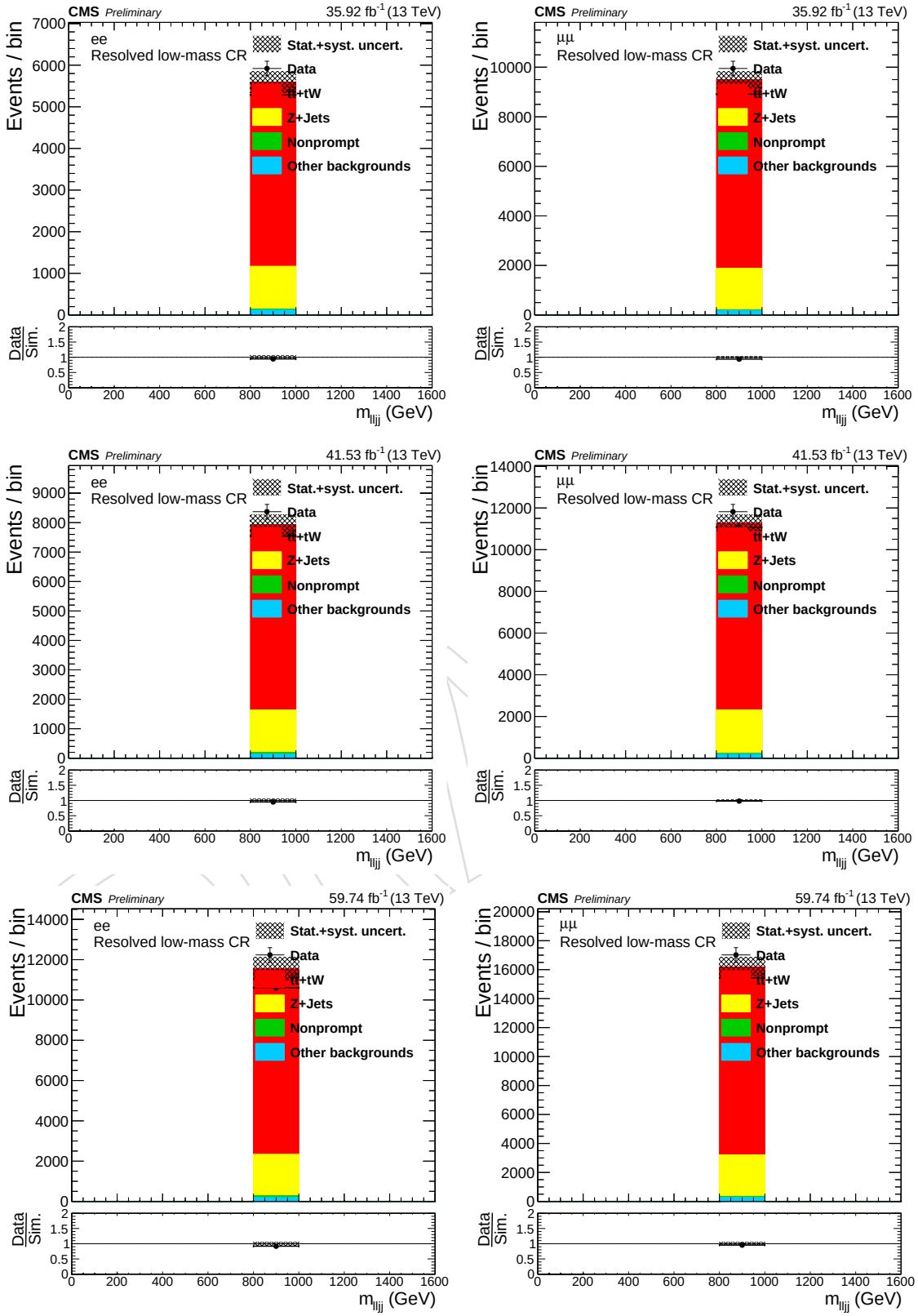

Figure 103: The reconstructed mass of W_R in the resolved region, for 2016 (upper), 2017 (middle) and 2018 (lower). The plots on the left (right) are obtained in dielectron (dimuon) events.

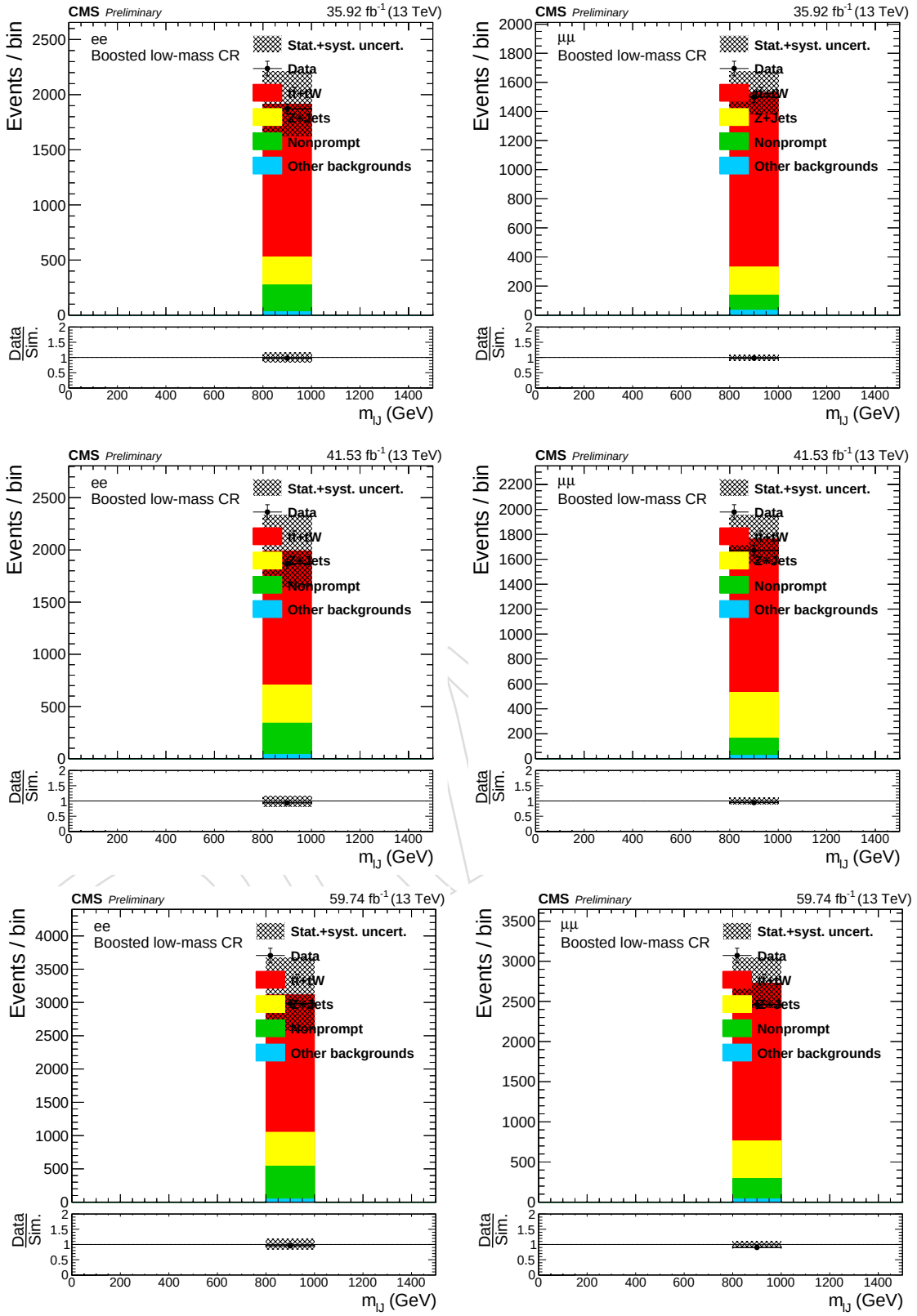

Figure 104: The reconstructed mass of W_R in the Boosted region, for 2016 (upper), 2017 (middle) and 2018 (lower). The plots on the left (right) are obtained in dielectron (dimuon) events.

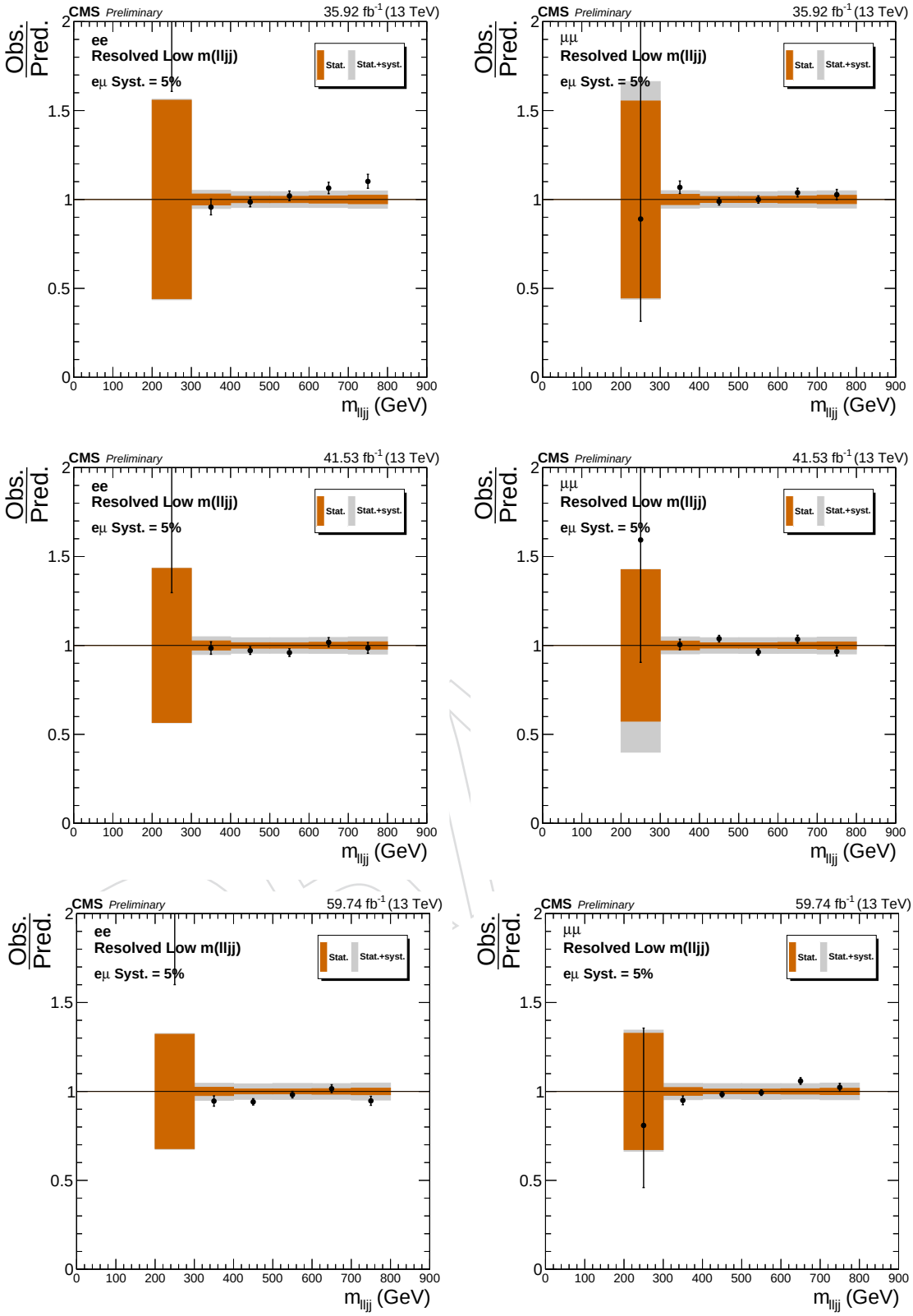

Figure 105: The ratio of observed and predicted yields in the resolved region as a function of the reconstructed mass of W_R for 2016 (upper), 2017 (middle) and 2018 (lower). The plots on the left (right) are obtained in dielectron (dimuon) events. A 5 % systematic uncertainty is assigned on the data-driven $t\bar{t}$ estimation.

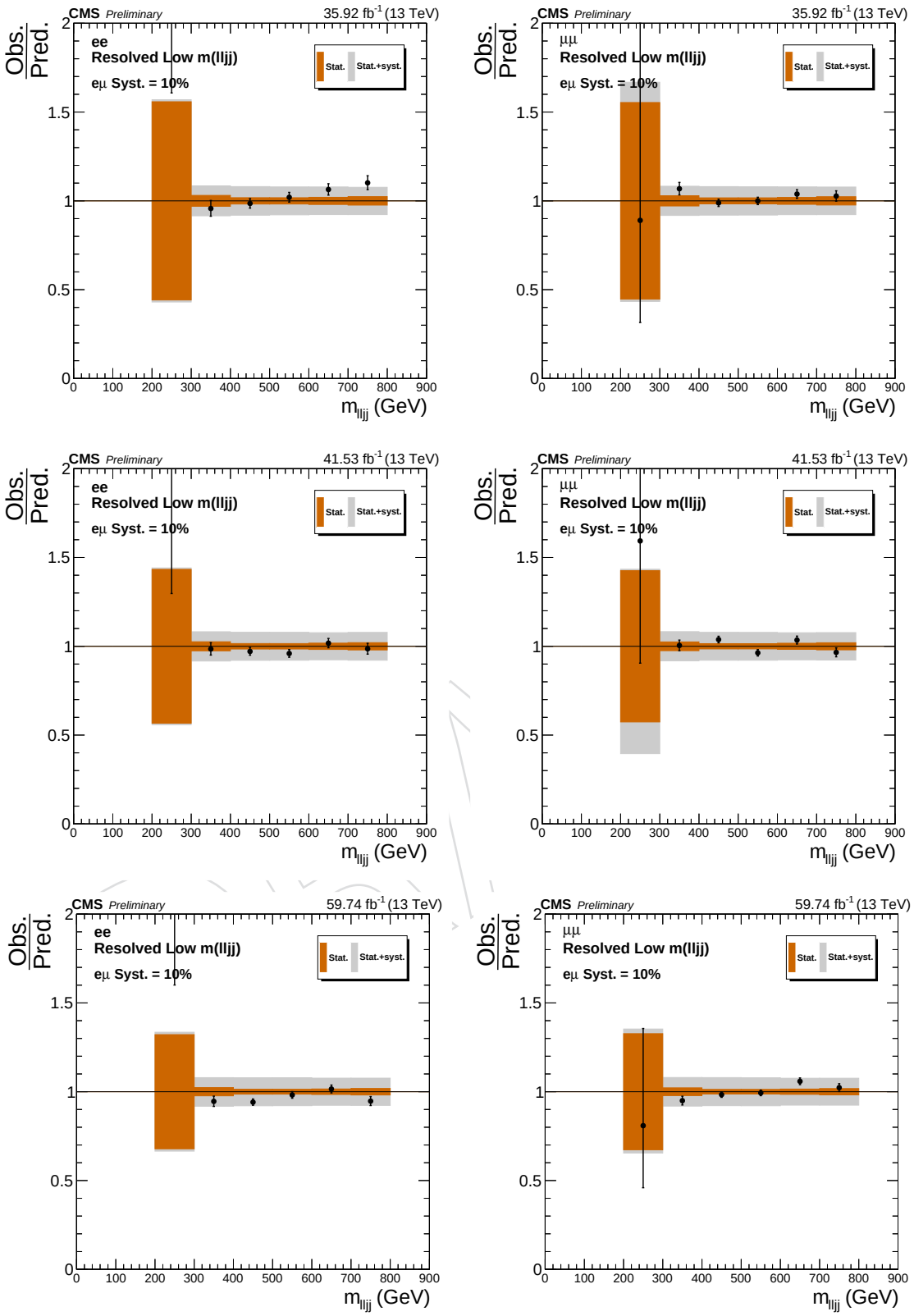

Figure 106: The ratio of observed and predicted yields in the resolved region as a function of the reconstructed mass of W_R for 2016 (upper), 2017 (middle) and 2018 (lower). The plots on the left (right) are obtained in dielectron (dimuon) events. A 10 % systematic uncertainty is assigned on the data-driven $t\bar{t}$ estimation.

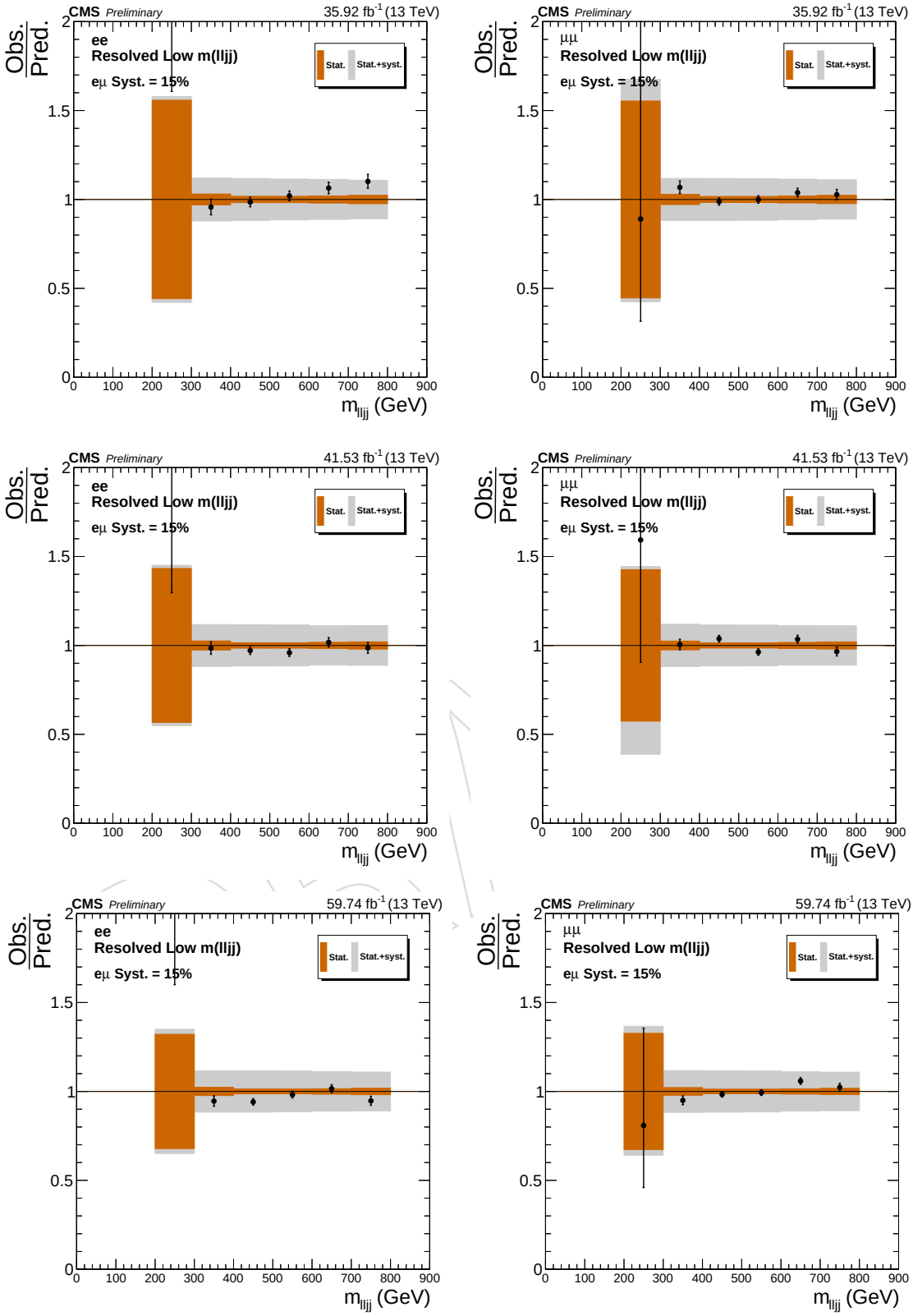

Figure 107: The ratio of observed and predicted yields in the resolved region as a function of the reconstructed mass of W_R for 2016 (upper), 2017 (middle) and 2018 (lower). The plots on the left (right) are obtained in dielectron (dimuon) events. A 15 % systematic uncertainty is assigned on the data-driven $t\bar{t}$ estimation.

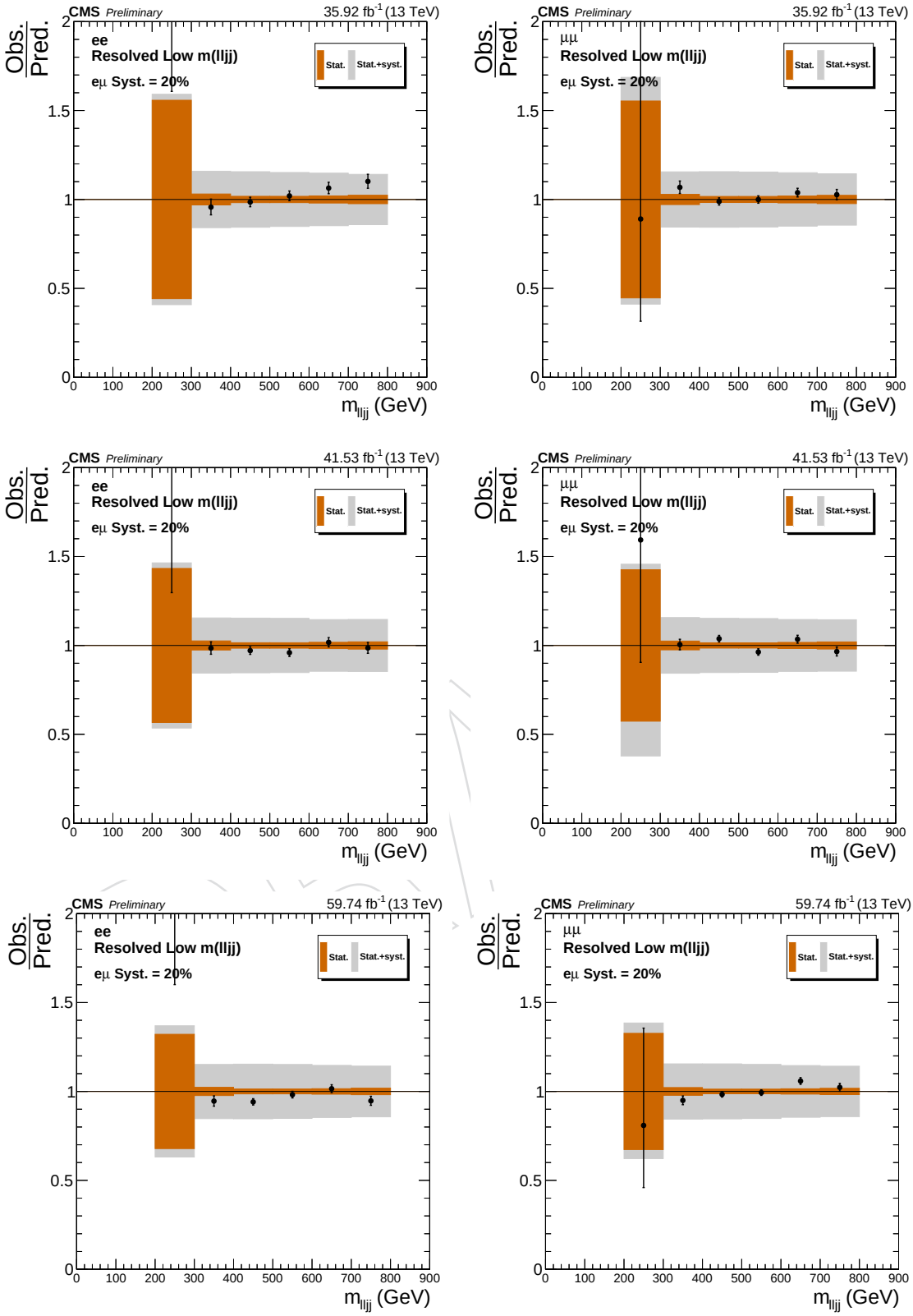

Figure 108: The ratio of observed and predicted yields in the resolved region as a function of the reconstructed mass of W_R for 2016 (upper), 2017 (middle) and 2018 (lower). The plots on the left (right) are obtained in dielectron (dimuon) events. A 20 % systematic uncertainty is assigned on the data-driven $t\bar{t}$ estimation.

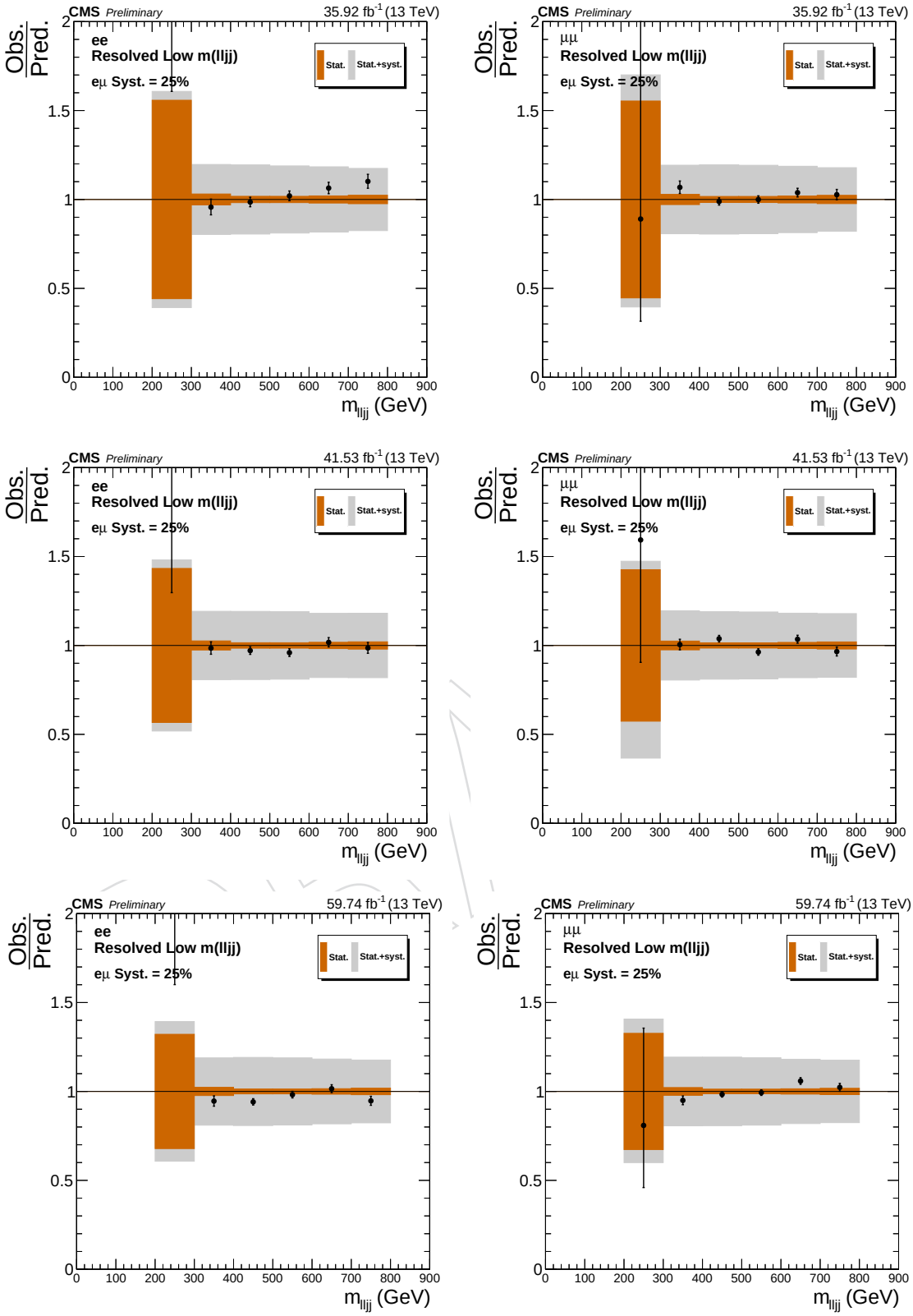

Figure 109: The ratio of observed and predicted yields in the resolved region as a function of the reconstructed mass of W_R for 2016 (upper), 2017 (middle) and 2018 (lower). The plots on the left (right) are obtained in dielectron (dimuon) events. A 25 % systematic uncertainty is assigned on the data-driven $t\bar{t}$ estimation.

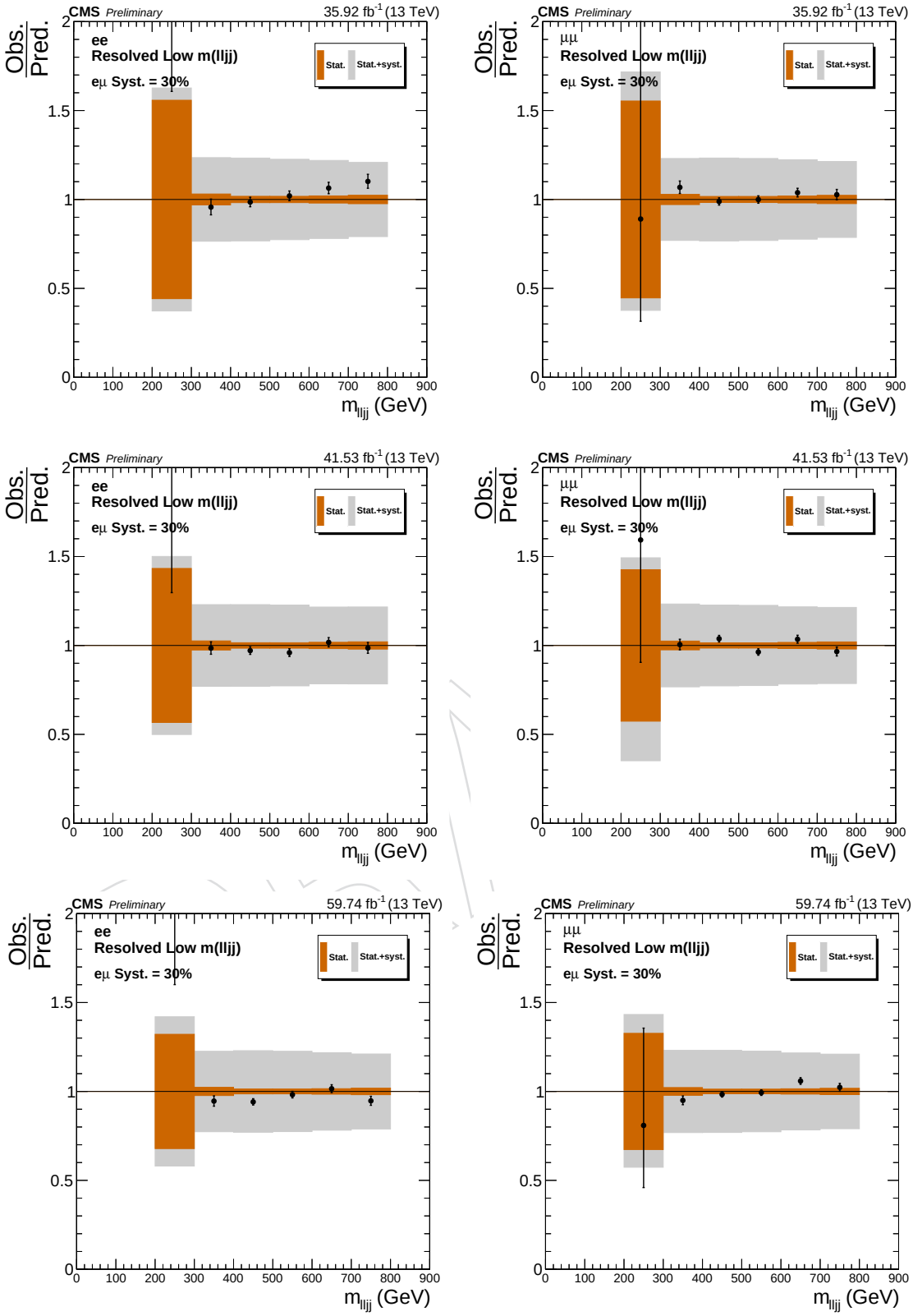

Figure 110: The ratio of observed and predicted yields in the resolved region as a function of the reconstructed mass of W_R for 2016 (upper), 2017 (middle) and 2018 (lower). The plots on the left (right) are obtained in dielectron (dimuon) events. A 30 % systematic uncertainty is assigned on the data-driven $t\bar{t}$ estimation.

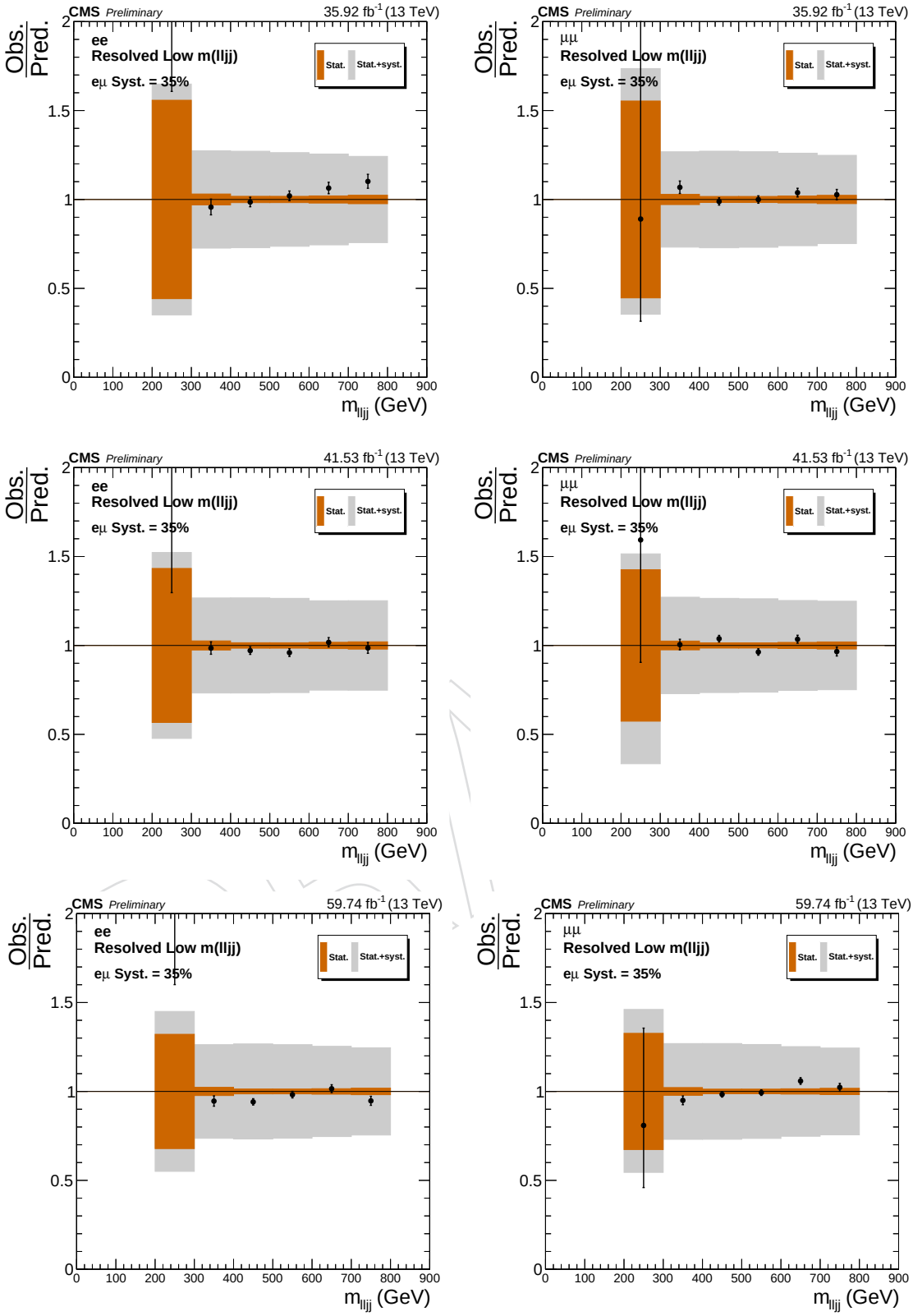

Figure 111: The ratio of observed and predicted yields in the resolved region as a function of the reconstructed mass of W_R for 2016 (upper), 2017 (middle) and 2018 (lower). The plots on the left (right) are obtained in dielectron (dimuon) events. A 35 % systematic uncertainty is assigned on the data-driven $t\bar{t}$ estimation.

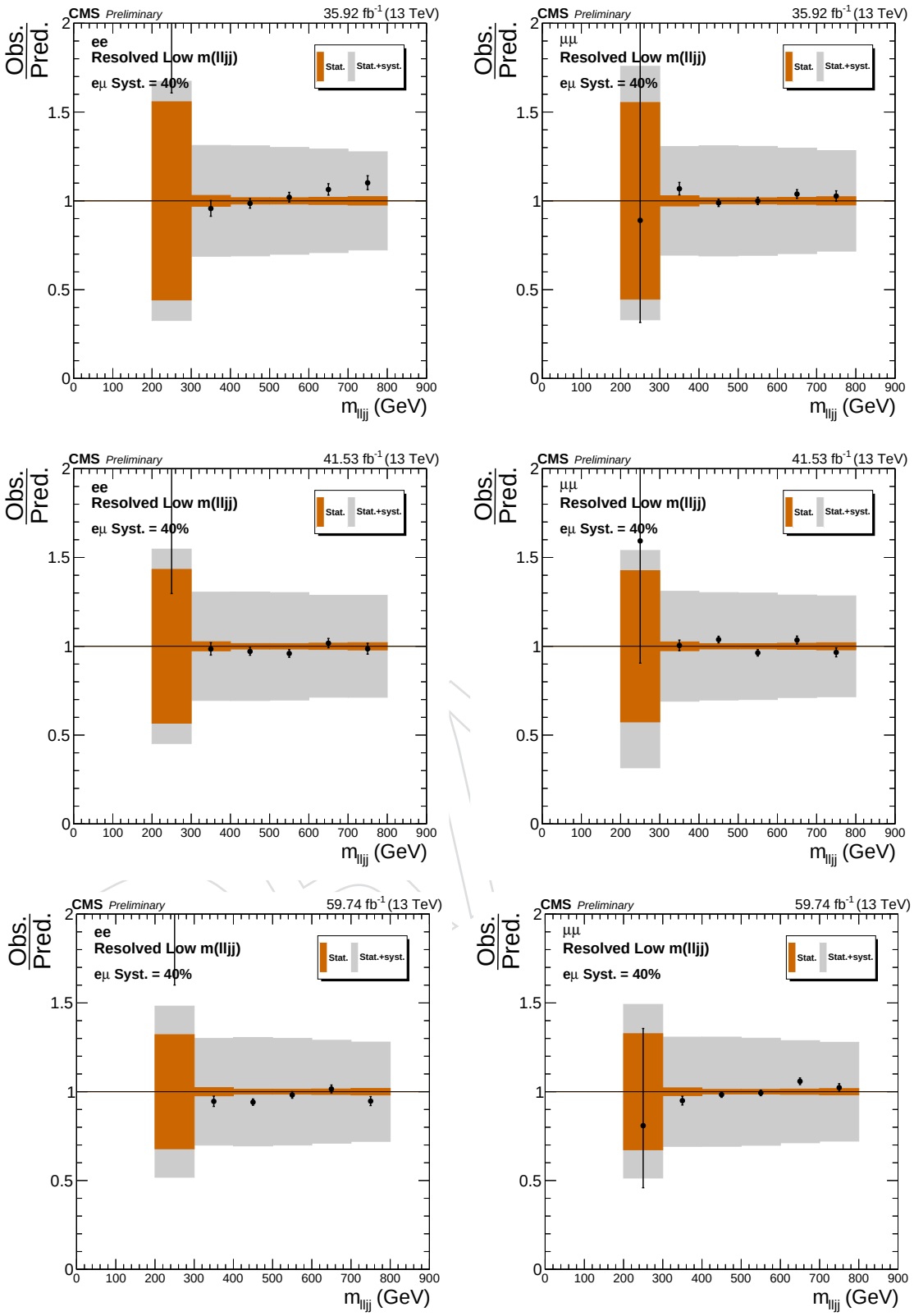

Figure 112: The ratio of observed and predicted yields in the resolved region as a function of the reconstructed mass of W_R for 2016 (upper), 2017 (middle) and 2018 (lower). The plots on the left (right) are obtained in dielectron (dimuon) events. A 40 % systematic uncertainty is assigned on the data-driven $t\bar{t}$ estimation.

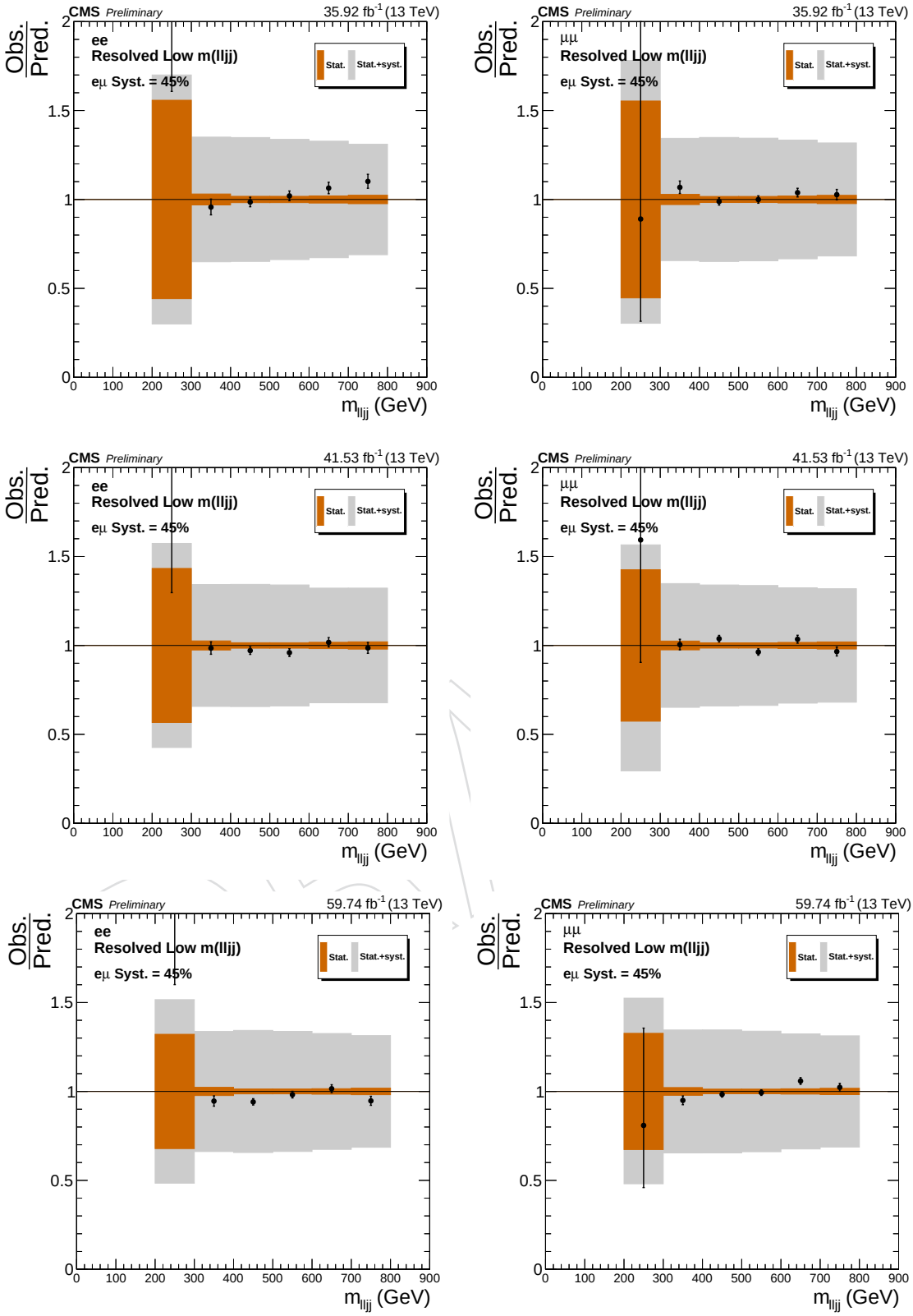

Figure 113: The ratio of observed and predicted yields in the resolved region as a function of the reconstructed mass of W_R for 2016 (upper), 2017 (middle) and 2018 (lower). The plots on the left (right) are obtained in dielectron (dimuon) events. A 45 % systematic uncertainty is assigned on the data-driven $t\bar{t}$ estimation.

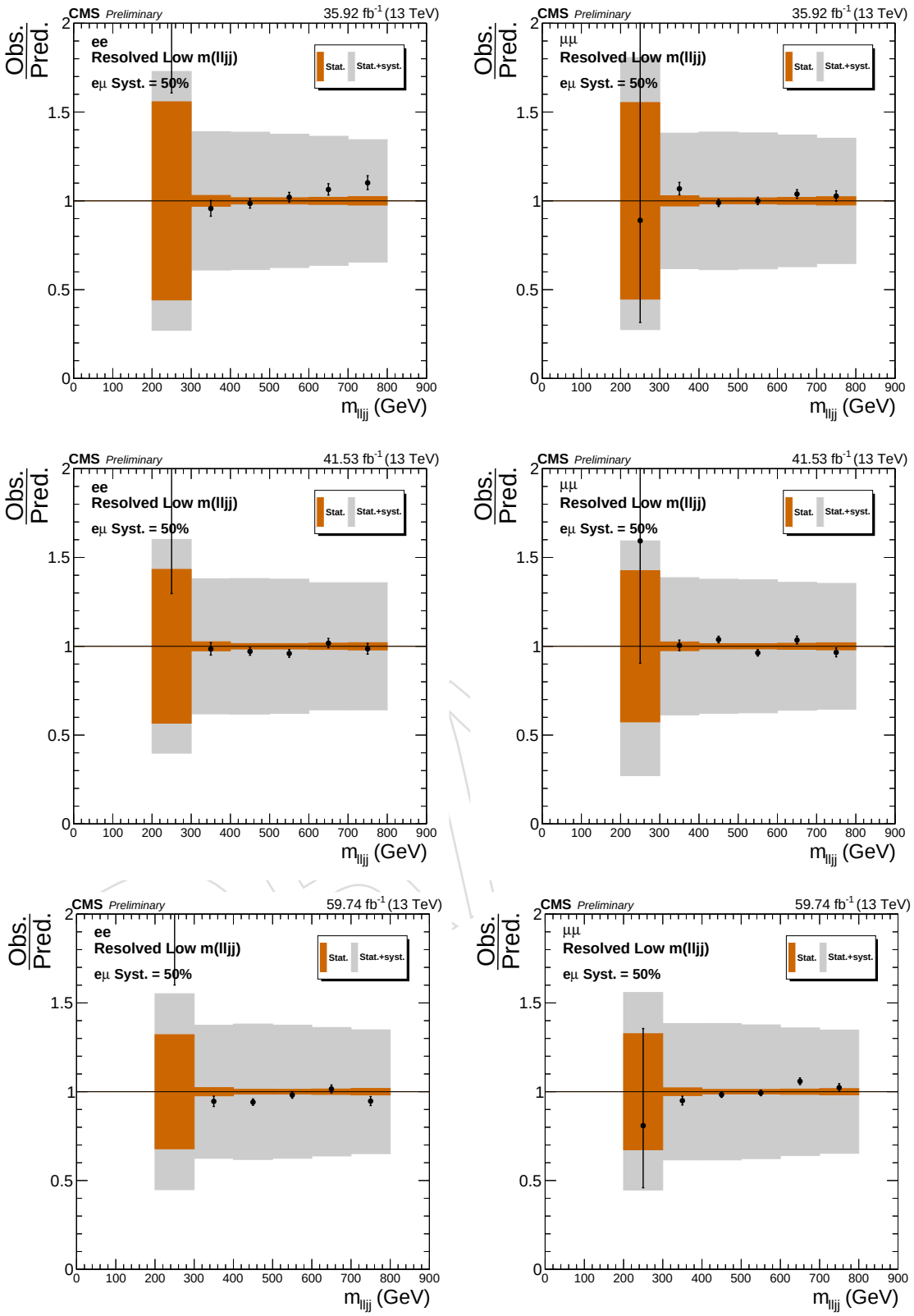

Figure 114: The ratio of observed and predicted yields in the resolved region as a function of the reconstructed mass of W_R for 2016 (upper), 2017 (middle) and 2018 (lower). The plots on the left (right) are obtained in dielectron (dimuon) events. A 50 % systematic uncertainty is assigned on the data-driven $t\bar{t}$ estimation.

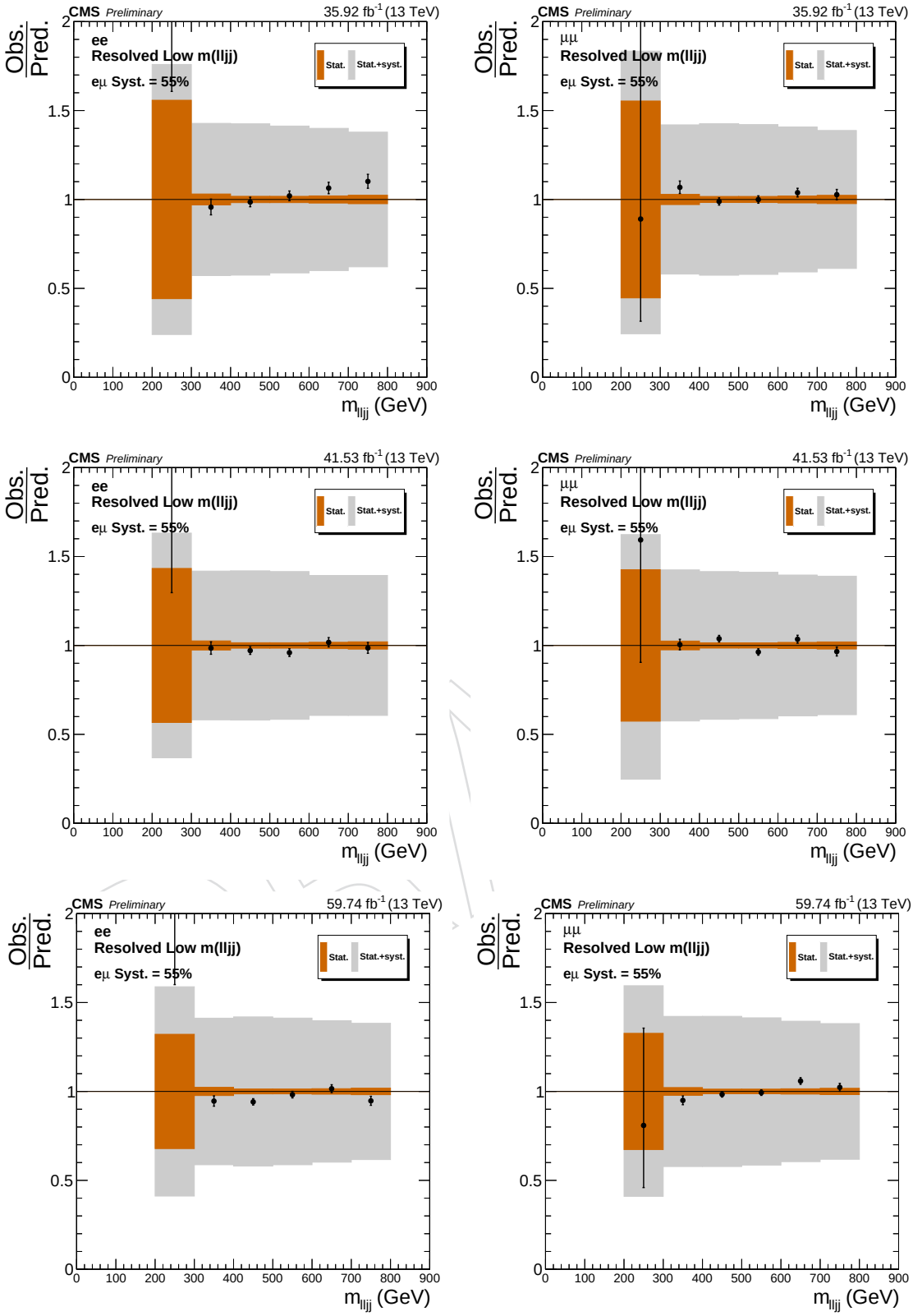

Figure 115: The ratio of observed and predicted yields in the resolved region as a function of the reconstructed mass of W_R for 2016 (upper), 2017 (middle) and 2018 (lower). The plots on the left (right) are obtained in dielectron (dimuon) events. A 55 % systematic uncertainty is assigned on the data-driven $t\bar{t}$ estimation.

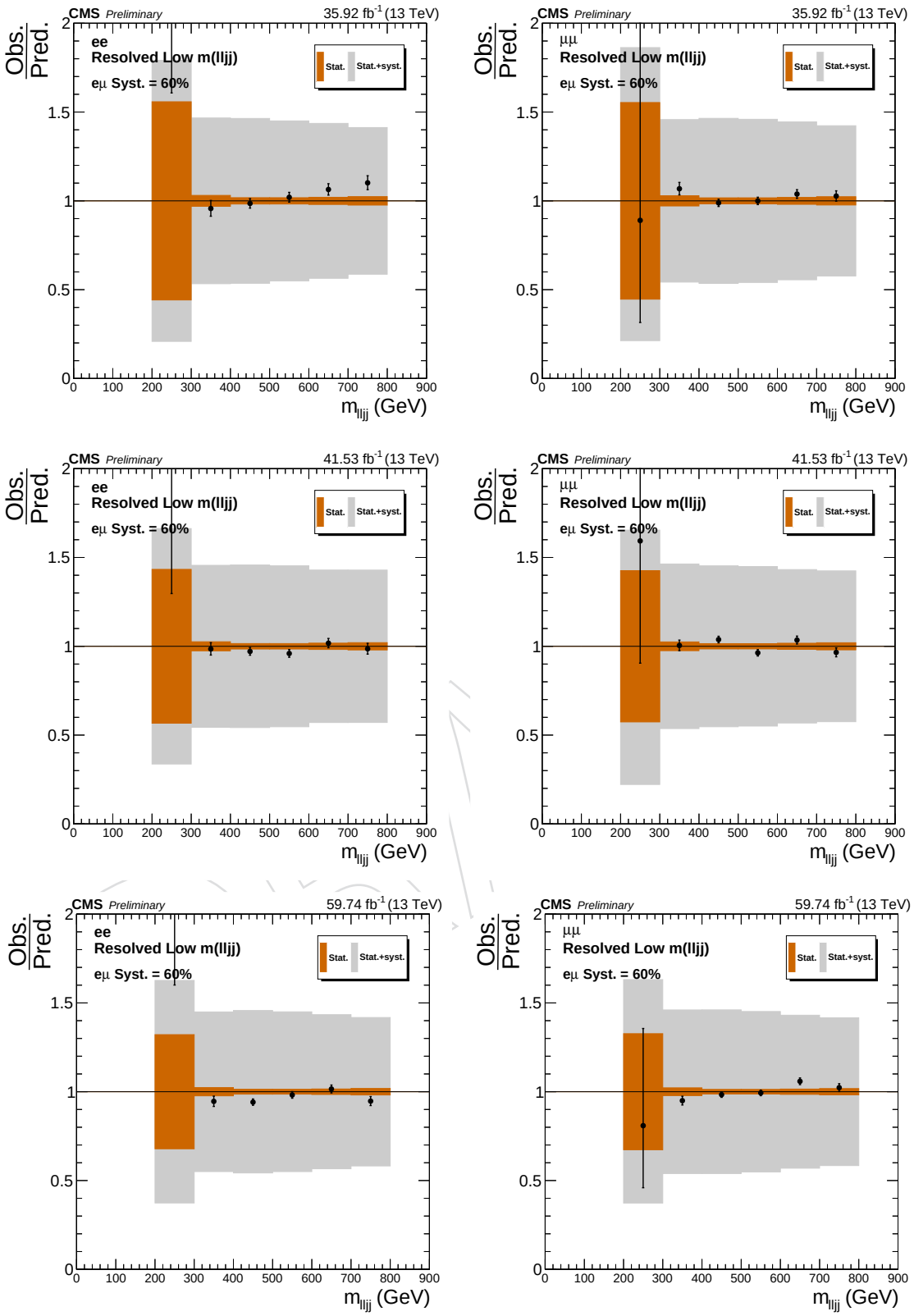

Figure 116: The ratio of observed and predicted yields in the resolved region as a function of the reconstructed mass of W_R for 2016 (upper), 2017 (middle) and 2018 (lower). The plots on the left (right) are obtained in dielectron (dimuon) events. A 60 % systematic uncertainty is assigned on the data-driven $t\bar{t}$ estimation.

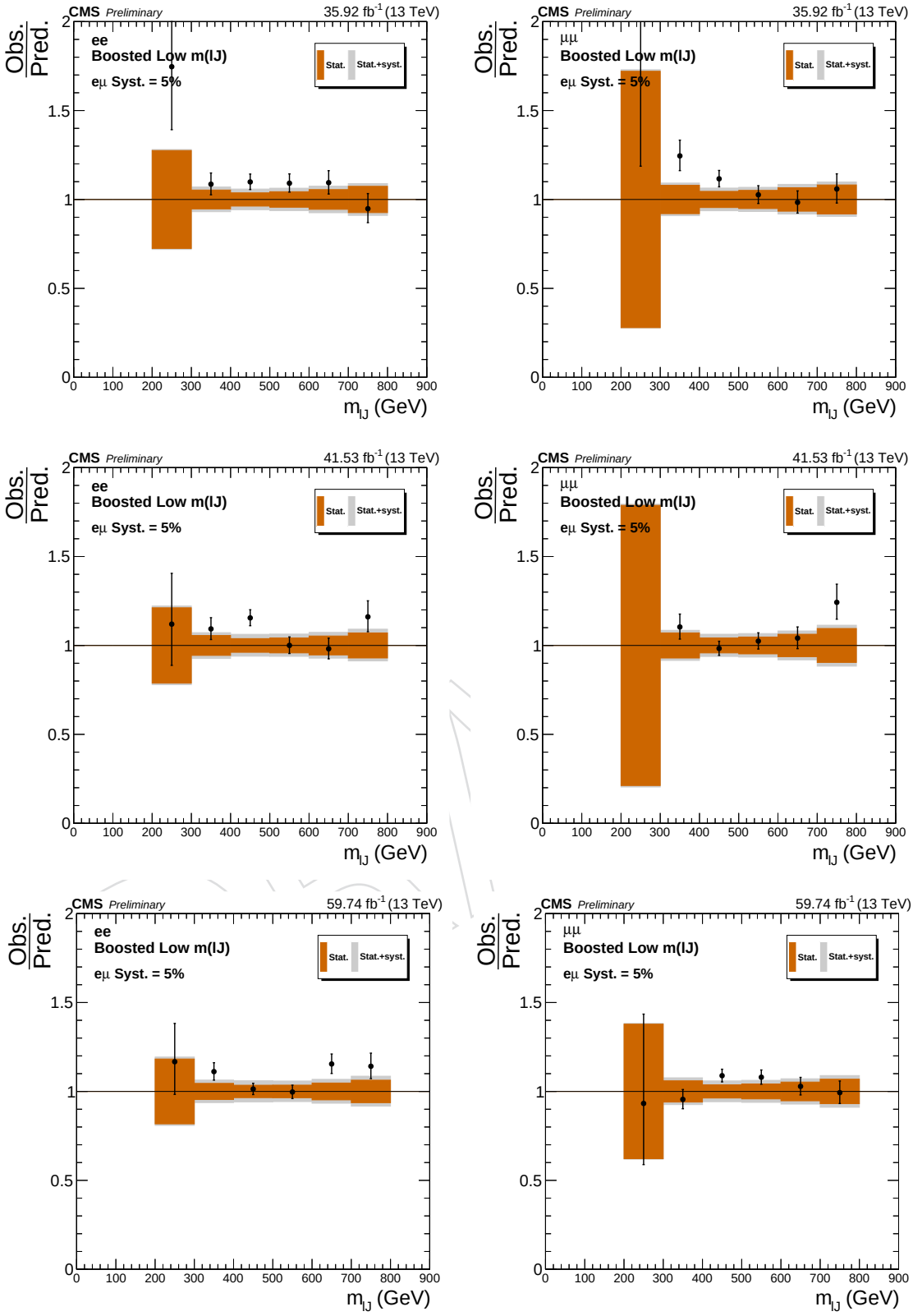

Figure 117: The ratio of observed and predicted yields in the boosted region as a function of the reconstructed mass of W_R for 2016 (upper), 2017 (middle) and 2018 (lower). The plots on the left (right) are obtained in dielectron (dimuon) events. A 5 % systematic uncertainty is assigned on the data-driven $t\bar{t}$ estimation.

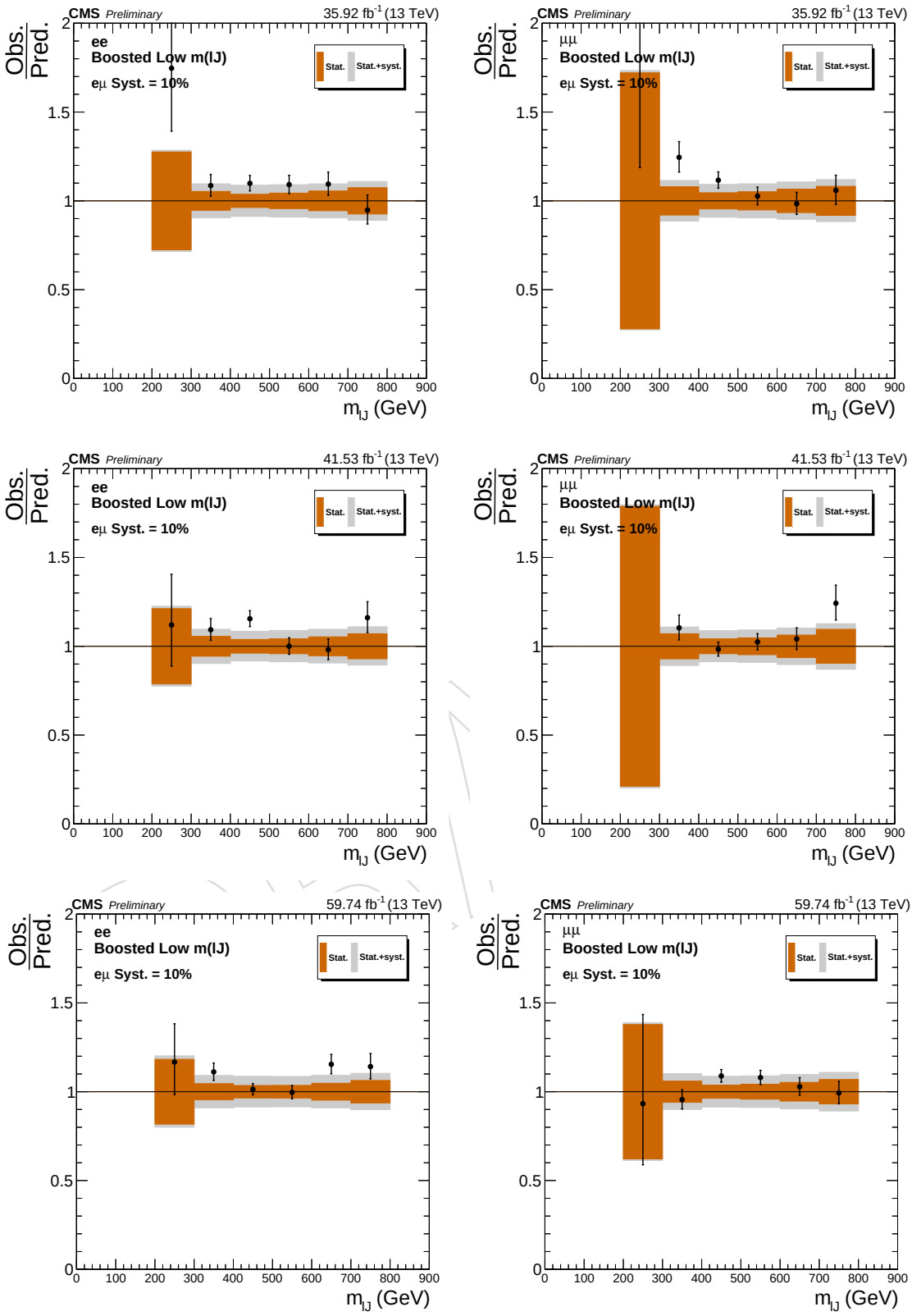

Figure 118: The ratio of observed and predicted yields in the boosted region as a function of the reconstructed mass of W_R for 2016 (upper), 2017 (middle) and 2018 (lower). The plots on the left (right) are obtained in dielectron (dimuon) events. A 10 % systematic uncertainty is assigned on the data-driven $t\bar{t}$ estimation.

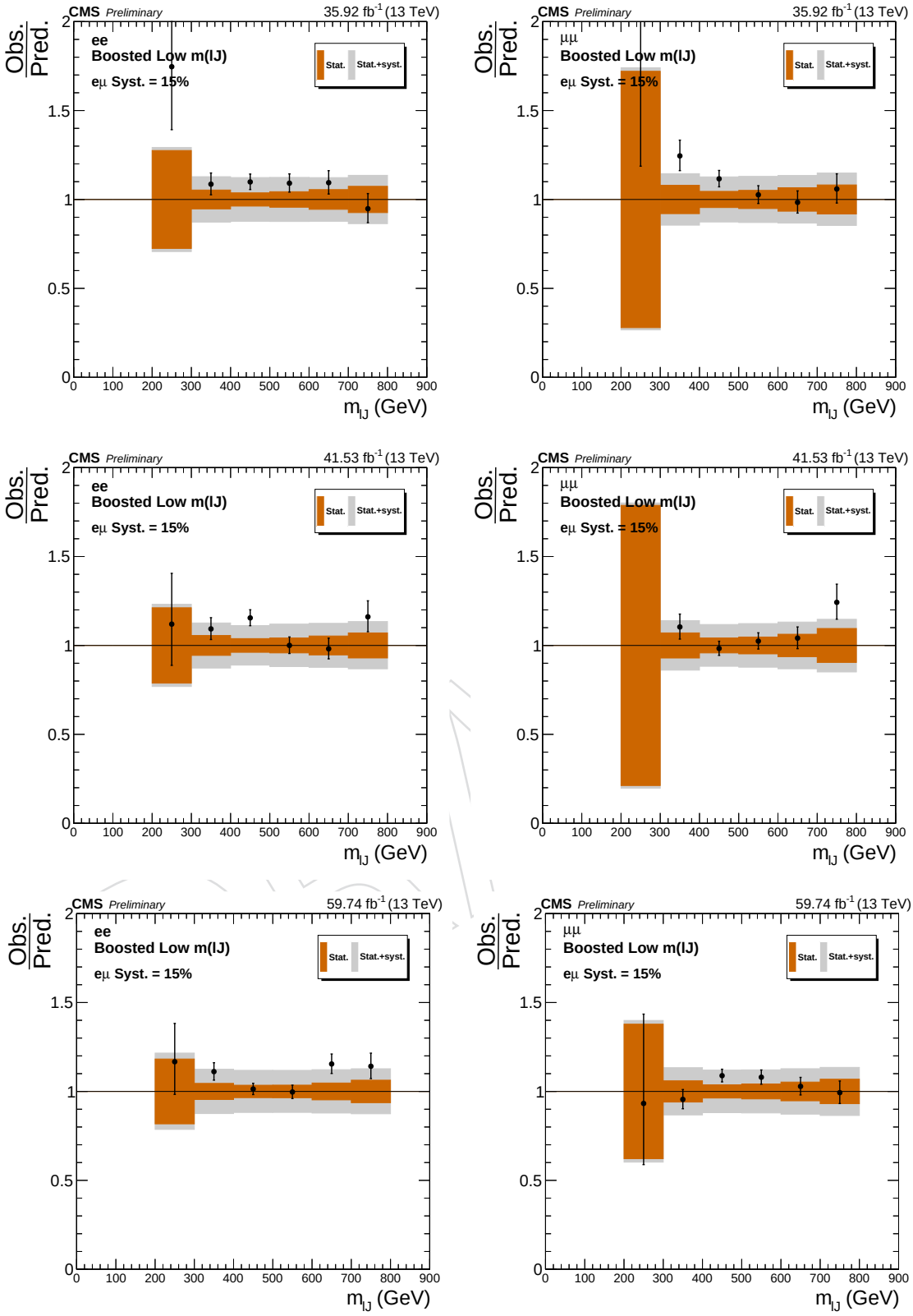

Figure 119: The ratio of observed and predicted yields in the boosted region as a function of the reconstructed mass of W_R for 2016 (upper), 2017 (middle) and 2018 (lower). The plots on the left (right) are obtained in dielectron (dimuon) events. A 15 % systematic uncertainty is assigned on the data-driven $t\bar{t}$ estimation.

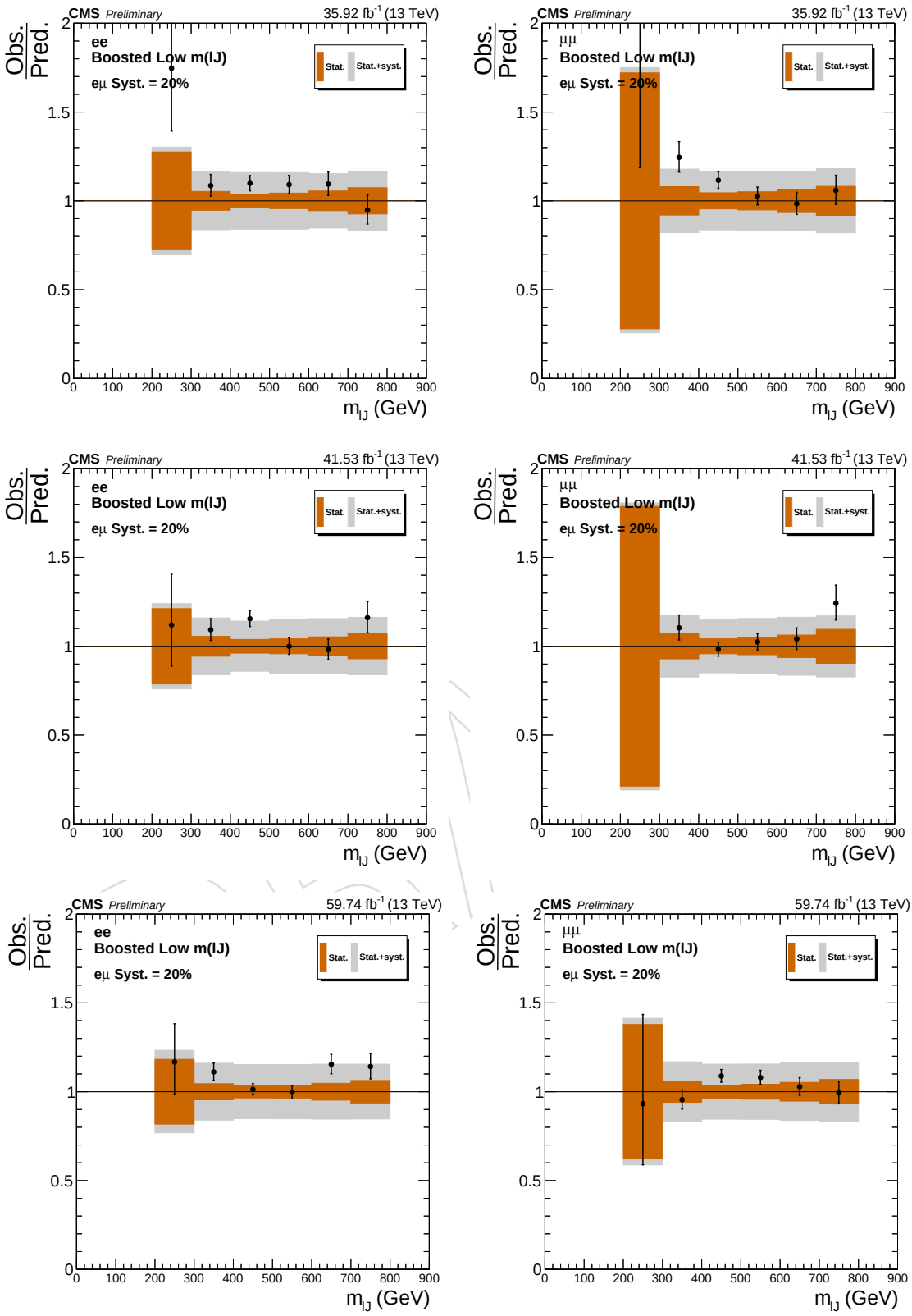

Figure 120: The ratio of observed and predicted yields in the boosted region as a function of the reconstructed mass of W_R for 2016 (upper), 2017 (middle) and 2018 (lower). The plots on the left (right) are obtained in dielectron (dimuon) events. A 20 % systematic uncertainty is assigned on the data-driven $t\bar{t}$ estimation.

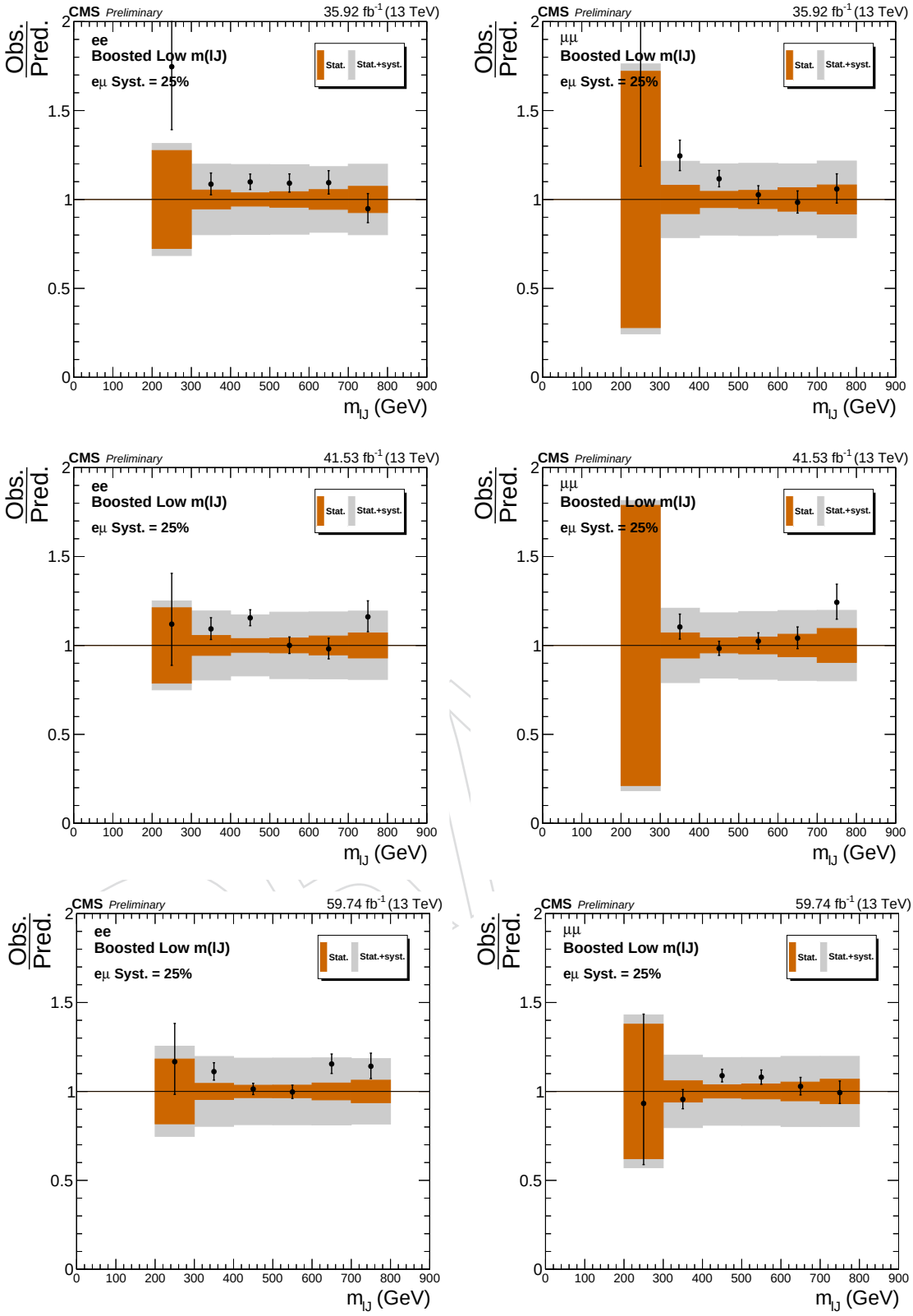

Figure 121: The ratio of observed and predicted yields in the boosted region as a function of the reconstructed mass of W_R for 2016 (upper), 2017 (middle) and 2018 (lower). The plots on the left (right) are obtained in dielectron (dimuon) events. A 25 % systematic uncertainty is assigned on the data-driven $t\bar{t}$ estimation.

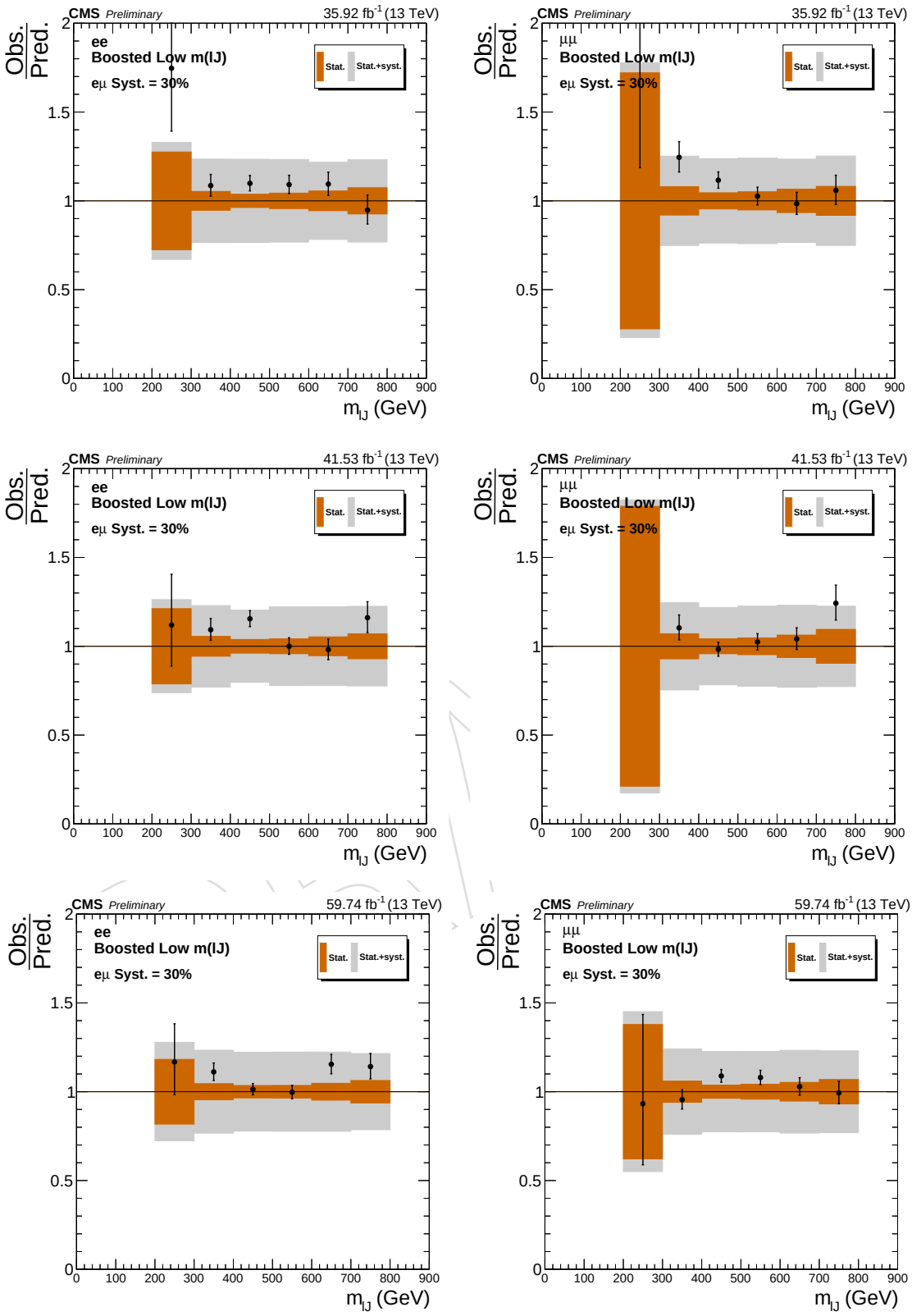

Figure 122: The ratio of observed and predicted yields in the boosted region as a function of the reconstructed mass of W_R for 2016 (upper), 2017 (middle) and 2018 (lower). The plots on the left (right) are obtained in dielectron (dimuon) events. A 30 % systematic uncertainty is assigned on the data-driven $t\bar{t}$ estimation.

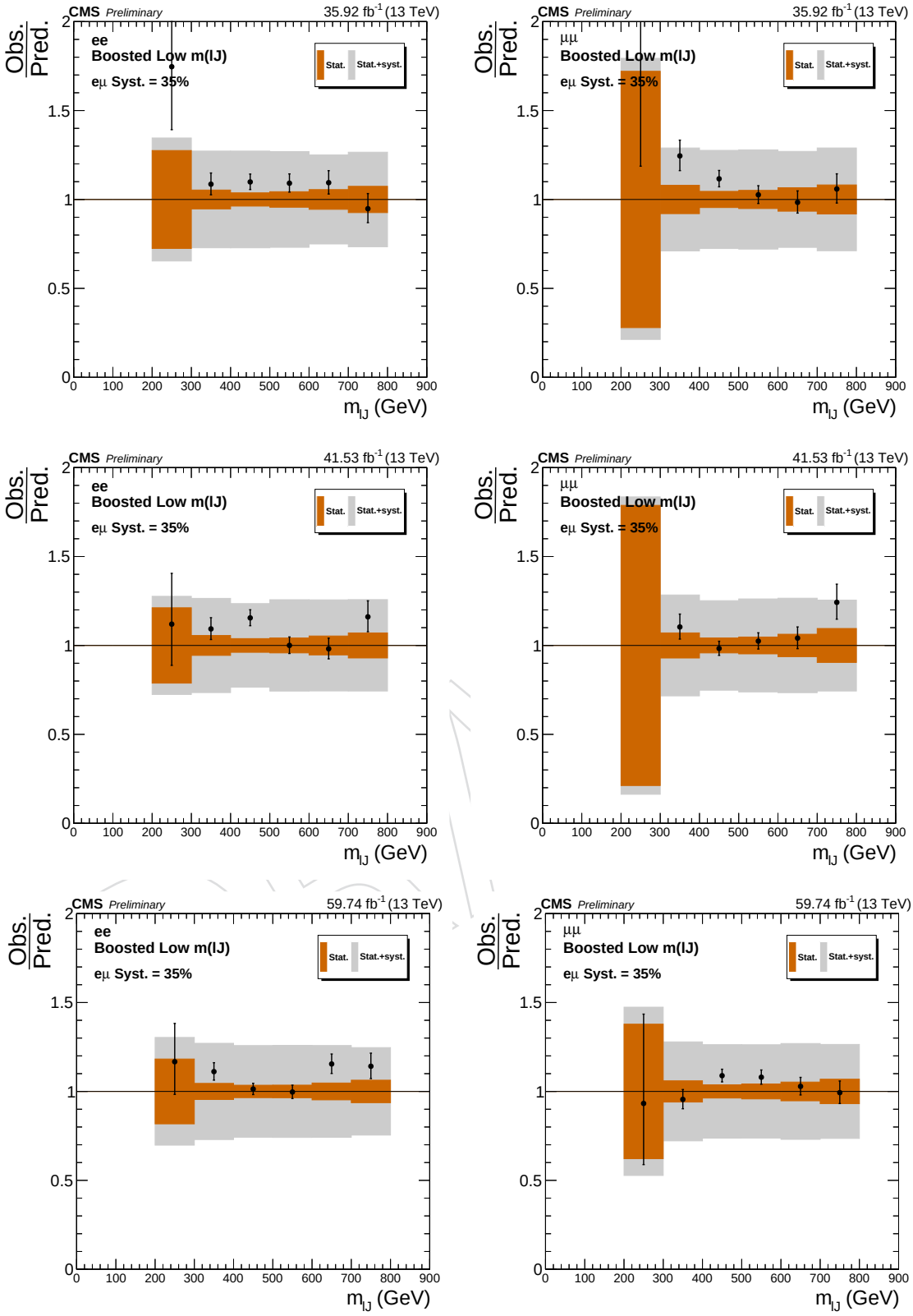

Figure 123: The ratio of observed and predicted yields in the boosted region as a function of the reconstructed mass of W_R for 2016 (upper), 2017 (middle) and 2018 (lower). The plots on the left (right) are obtained in dielectron (dimuon) events. A 35 % systematic uncertainty is assigned on the data-driven $t\bar{t}$ estimation.

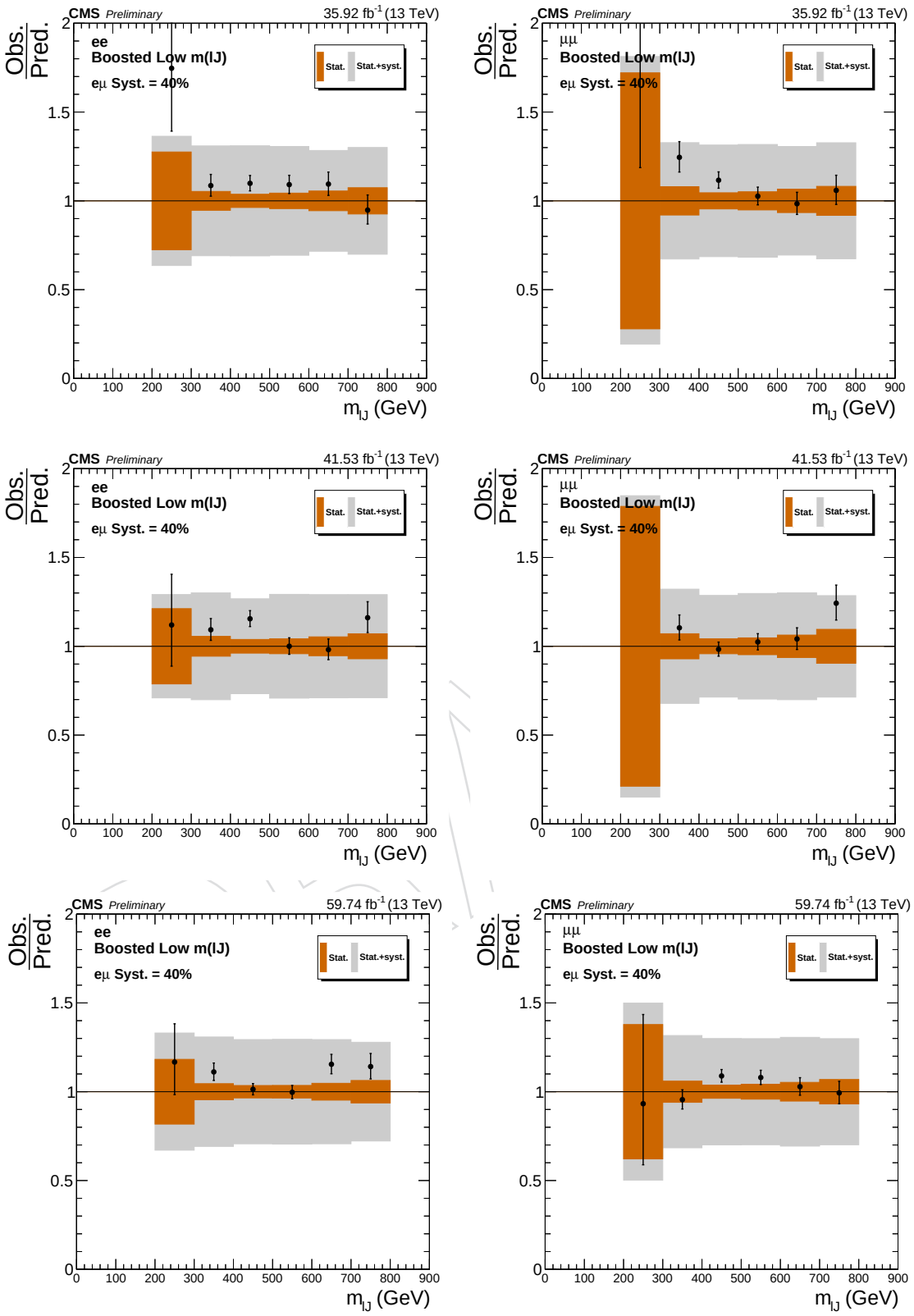

Figure 124: The ratio of observed and predicted yields in the boosted region as a function of the reconstructed mass of W_R for 2016 (upper), 2017 (middle) and 2018 (lower). The plots on the left (right) are obtained in dielectron (dimuon) events. A 40 % systematic uncertainty is assigned on the data-driven $t\bar{t}$ estimation.

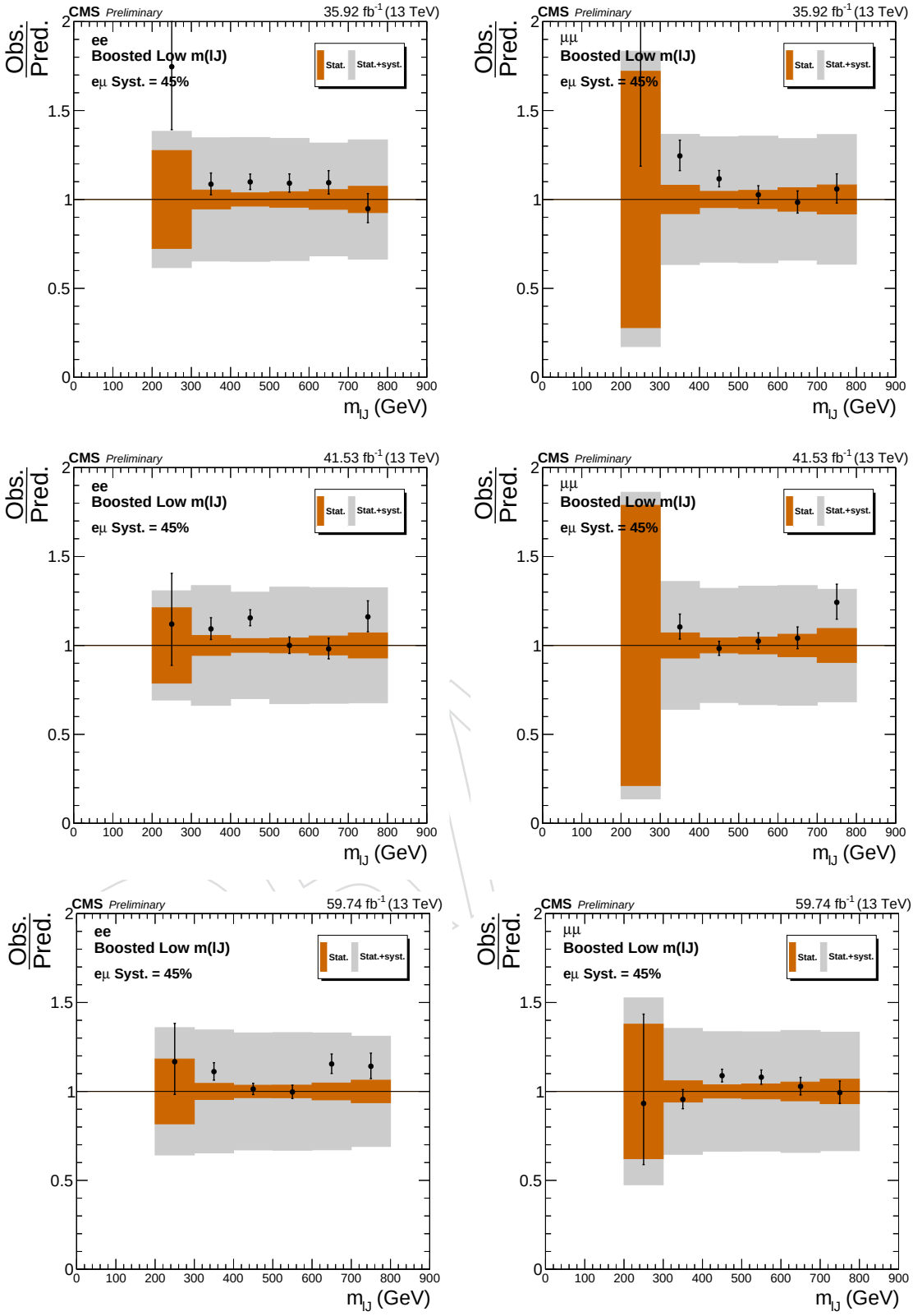

Figure 125: The ratio of observed and predicted yields in the boosted region as a function of the reconstructed mass of W_R for 2016 (upper), 2017 (middle) and 2018 (lower). The plots on the left (right) are obtained in dielectron (dimuon) events. A 45 % systematic uncertainty is assigned on the data-driven $t\bar{t}$ estimation.

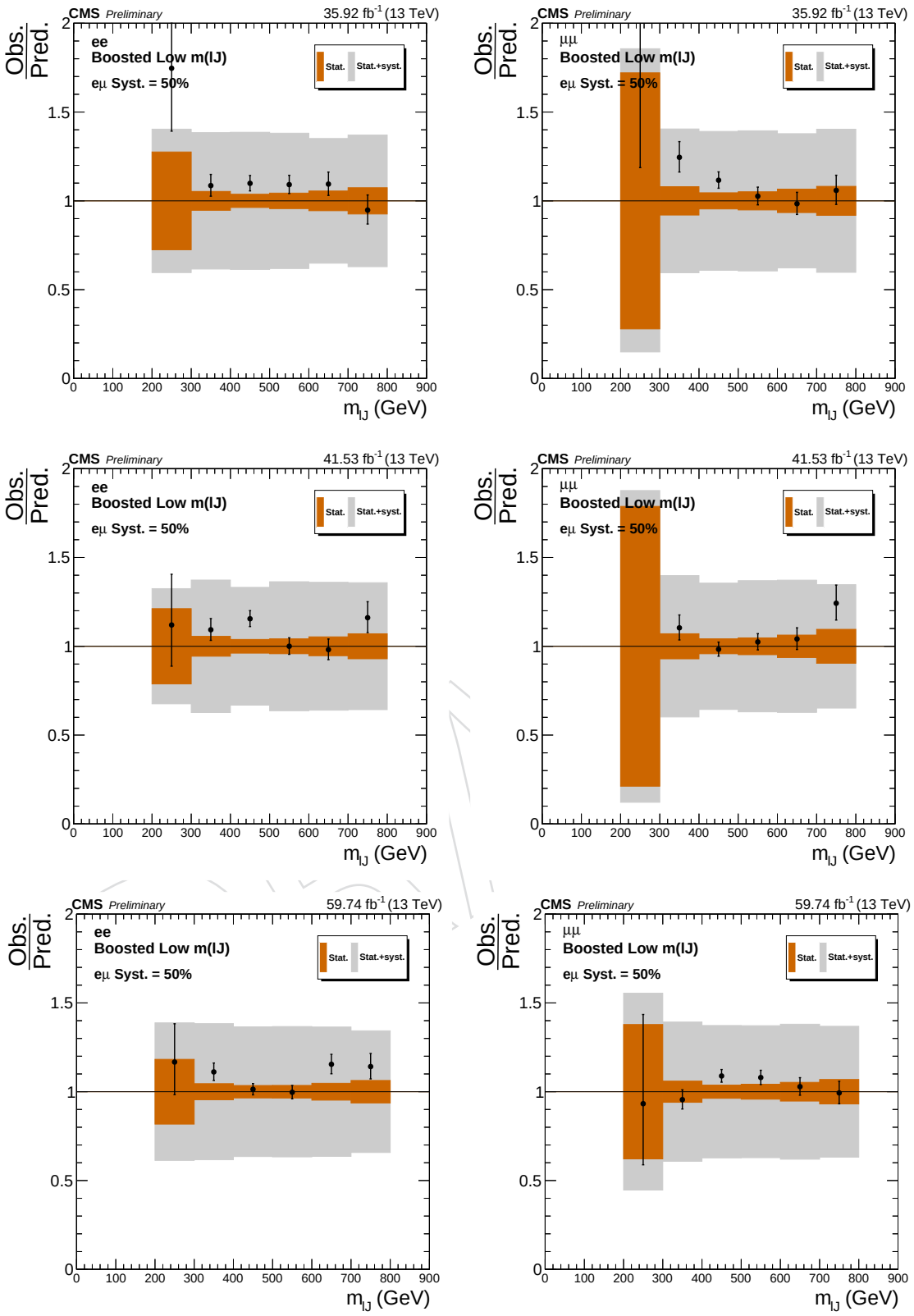

Figure 126: The ratio of observed and predicted yields in the boosted region as a function of the reconstructed mass of W_R for 2016 (upper), 2017 (middle) and 2018 (lower). The plots on the left (right) are obtained in dielectron (dimuon) events. A 50 % systematic uncertainty is assigned on the data-driven $t\bar{t}$ estimation.

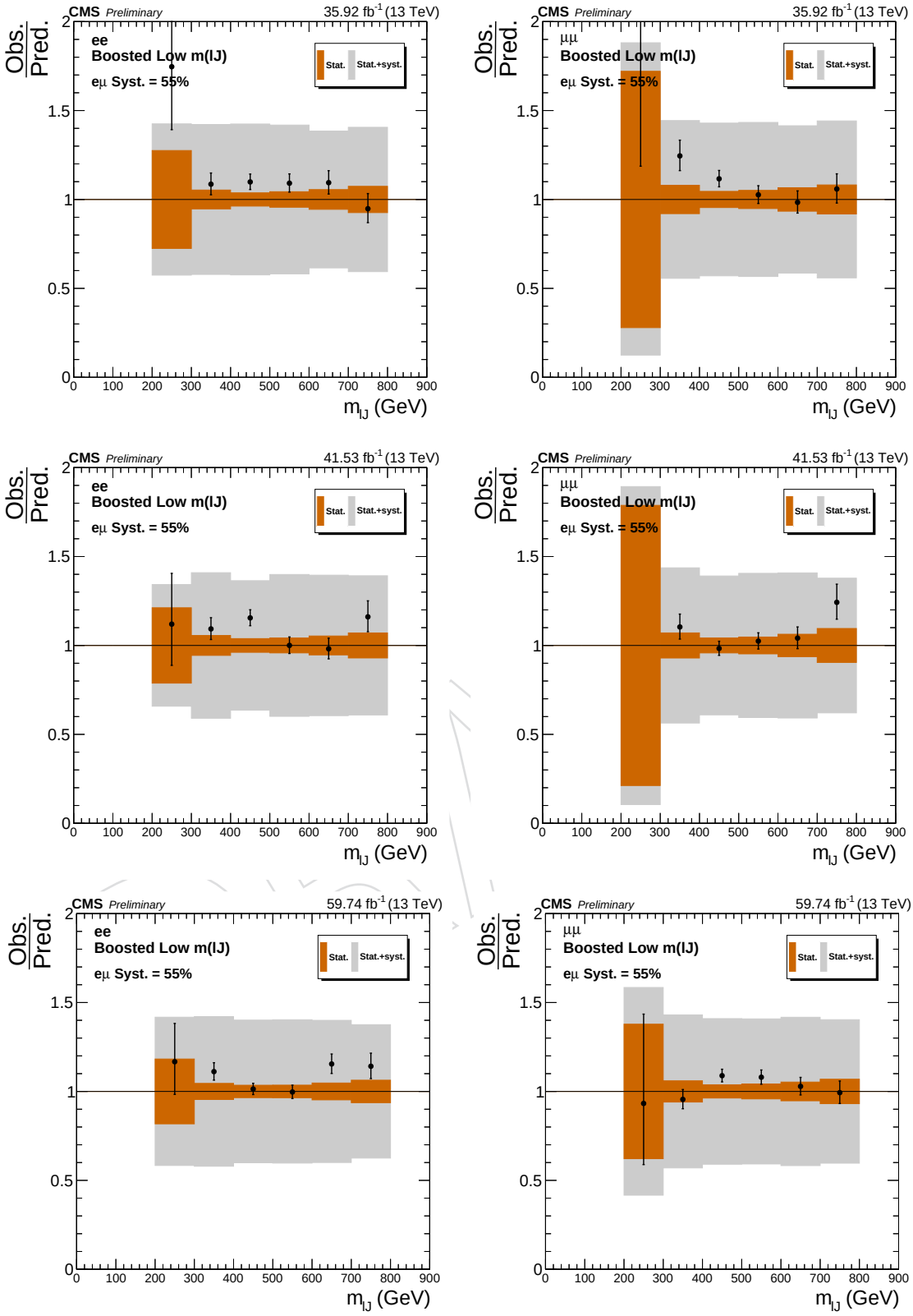

Figure 127: The ratio of observed and predicted yields in the boosted region as a function of the reconstructed mass of W_R for 2016 (upper), 2017 (middle) and 2018 (lower). The plots on the left (right) are obtained in dielectron (dimuon) events. A 55 % systematic uncertainty is assigned on the data-driven $t\bar{t}$ estimation.

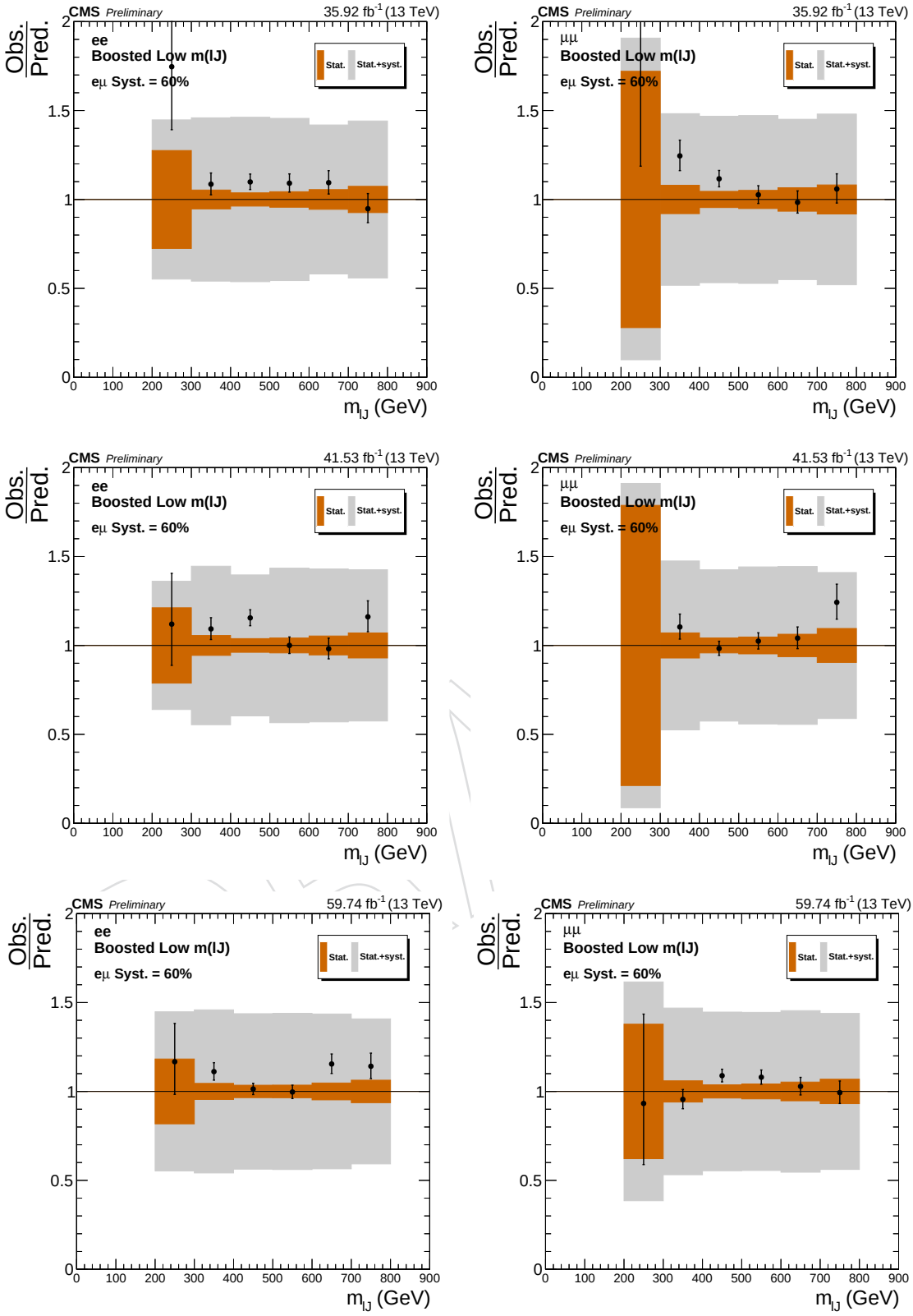

Figure 128: The ratio of observed and predicted yields in the boosted region as a function of the reconstructed mass of W_R for 2016 (upper), 2017 (middle) and 2018 (lower). The plots on the left (right) are obtained in dielectron (dimuon) events. A 60 % systematic uncertainty is assigned on the data-driven $t\bar{t}$ estimation.

K Comparing ATLAS's Boosted Results

During the work on this analysis, the ATLAS collaboration published a search for a W_R and boosted N with the 2016 and 2017 datasets [35]. Key differences between this analysis and our results are discussed in this appendix. While there are several minor differences, two differences in particular produce a large discrepancy in the final limit.

K.1 Theoretical signal uncertainties

Both analyses derive theoretical signal uncertainties based on the variation of the QCD scale, the parton distribution functions (PDFs) and α_s. As mentioned in Sec. 6, we use the NNPDF3.1 parton distribution set to estimate our PDF errors based on the PDF4LHC group recommendations. The ATLAS analysis utilizes the NNPDF2.3 parton distribution set. As shown in Figure 129, the different PDF sets give drastically different PDF uncertainties for our most boosted signal events, with the PDF uncertainty from the NNPDF3.1 set being $4-5\times$ larger than the PDF uncertainty obtained from the NNPDF2.3 set. Our PDF uncertainty is the dominant uncertainty for our analysis and by decreasing it by $4-5\times$ our limits improve considerably.

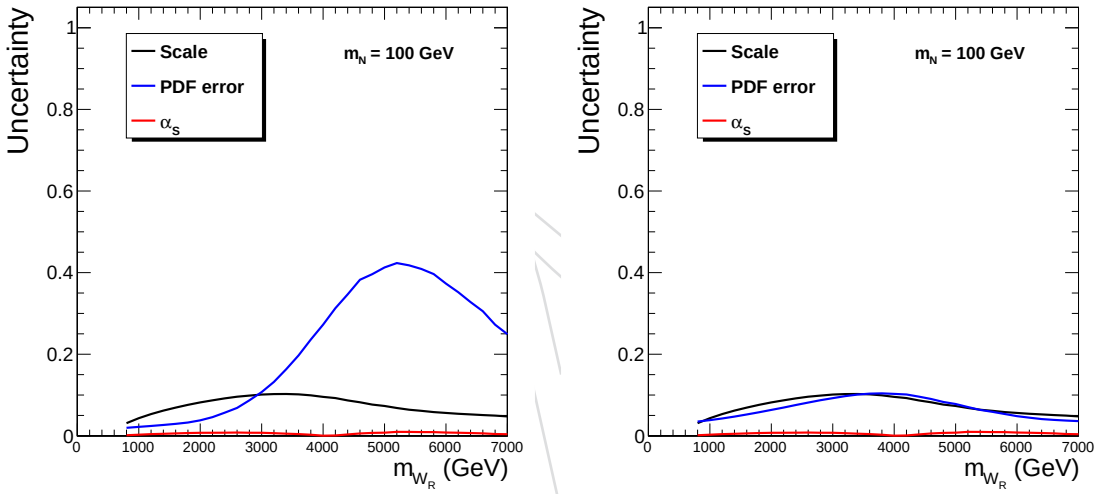

Figure 129: The QCD scale, parton distribution functions(PDFs) and α_s uncertainties plotted as a function of W_R mass for m_N = 100 GeV. On the left are the uncertainties calculated using NNPDF3.1 parton distribution set and on the right the NNPDF2.3 parton distribution set is used.

K.2 Generated signal topology

Both analyses produced signal samples based on the left-right symmetric model, where a W_R and N are produced and decay into a final state of two quarks and two same flavored leptons. The samples for both analyses were generated to LO using MADGRAPH 5. However, different UFOs were used by each group, and ATLAS generated the inclusive production and decay to all three lepton flavors, whereas we only generated samples that decay to the two lepton flavors considered in this analysis, electrons and muons. This is a minor difference and increases the signal acceptance of the ATLAS search by $\sim 3\%$, corresponding to when both tau's decay into electrons or muons.

Another discrepancy between the samples that causes a more significant difference is ATLAS produced only on-shell W_R's, whereas we produced samples with both on- and off-shell W_R's. In the boosted regime, off-shell W_R production is significant as lower N masses can still be

created with a light W_R. These are typically unfavored, as the W_R is off-shell, but W_R's in this analysis are heavy enough to be disfavored by production PDFs. Fig 130 shows the GEN W_R mass distribution for a highly boosted signal mass point. The lighter off-shell W_R's are more likely to be outside of our acceptance and often fail the selection, giving us a smaller event yield. This should not cause any difference in our expected upper limits on the cross section if the acceptance differences are taken into account, however this will effect the expected limit placed in the two-dimensional W_R vs N mass plain since it will change the signal cross sections. Taking into account the difference in decay modes, the LO cross sections used for the two analyses are approximately the same. This is unexpected since ATLAS signals only include on-shell production and should therefore have smaller cross sections. Due to these unexpected differences in the signal topology and cross sections between the analyses, a comparison of the expected limit contours in the two dimensional mass plane cannot be made. For reference, a comparison between these expected limit contours can be seen in Fig. 131.

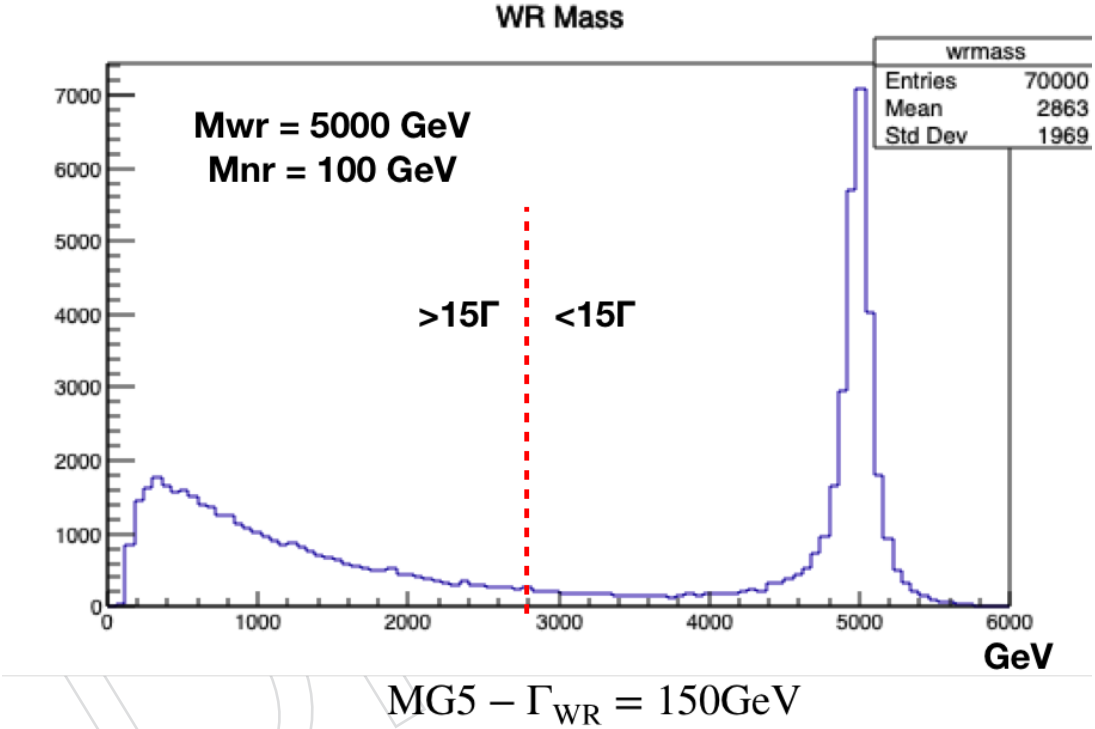

Figure 130: The generator level W_R mass distribution for the $m_{W_R} = 5000$, $m_N = 100\,\text{GeV}$ mass point. Madgraph defines on-shell as $15 \times \Gamma$, which is marked on the plot. Approximately 50% of events for this signal mass point are classified as off-shell.

K.3 Conclusion

The PDF uncertainties used by ATLAS and CMS produce significantly different expected limits, however, as cross-section limits for the ATLAS analysis were never published, a complete understanding of the differences between the CMS and ATLAS results cannot be made since the expected mass contours use different signal sample cross sections.

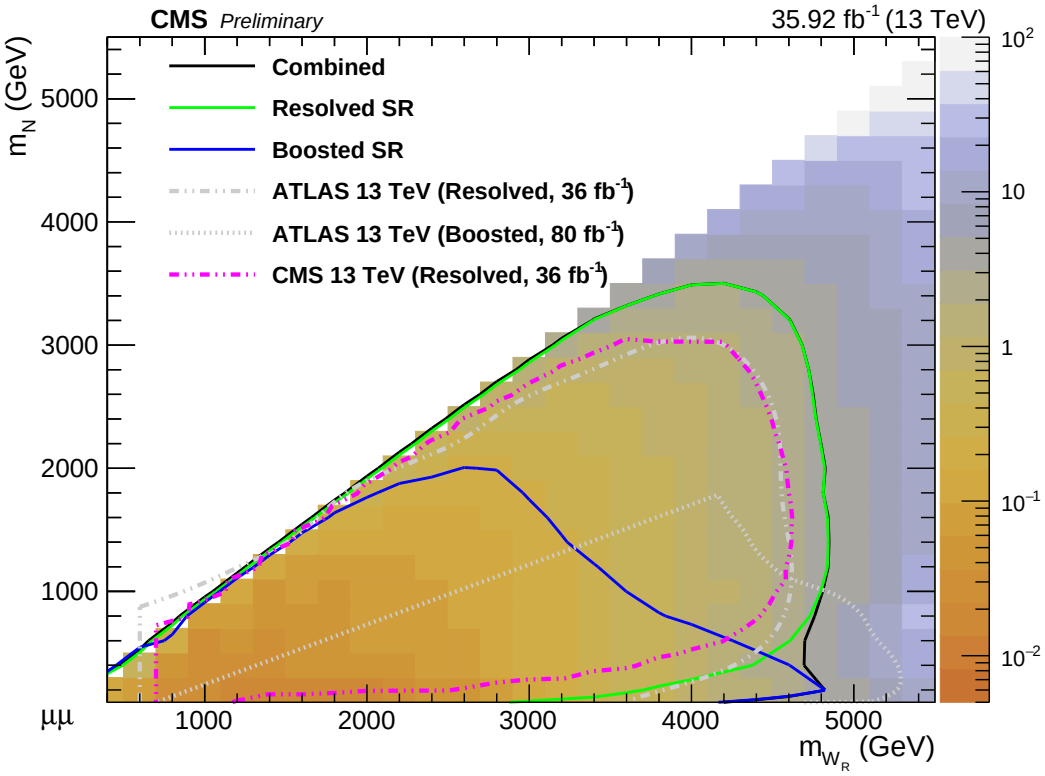

Figure 131: The expected limit contours in the two dimensional mass plane. The boosted results from ATLAS are included even though different signals have been used to produce these contours.

L Signal Injection

To determine the sensitivity of our background estimation to signal events, signal injection tests were performed. These were done by throwing background only toys based on our boosted $\mu\mu$ background predicitons for the 2016 dataset. Since we are mainly interested in signal events appearing in our high mass region where the background prediciton is small, we placed additional events in the highest mass bin($m_{lJ} > 1700GeV$) of the background only toy distribution and ran asymptotic limits. The observed and expected limits for the $m_N = 200$GeV mass points for 0, 1, 4, and 8 additional events can be seen in Fig 132. 8 additional events gives a 2 sigma excess across the m_{W_R} spectrum, which is reasonable given our background prediciton of about 4 events in this high mass bin.

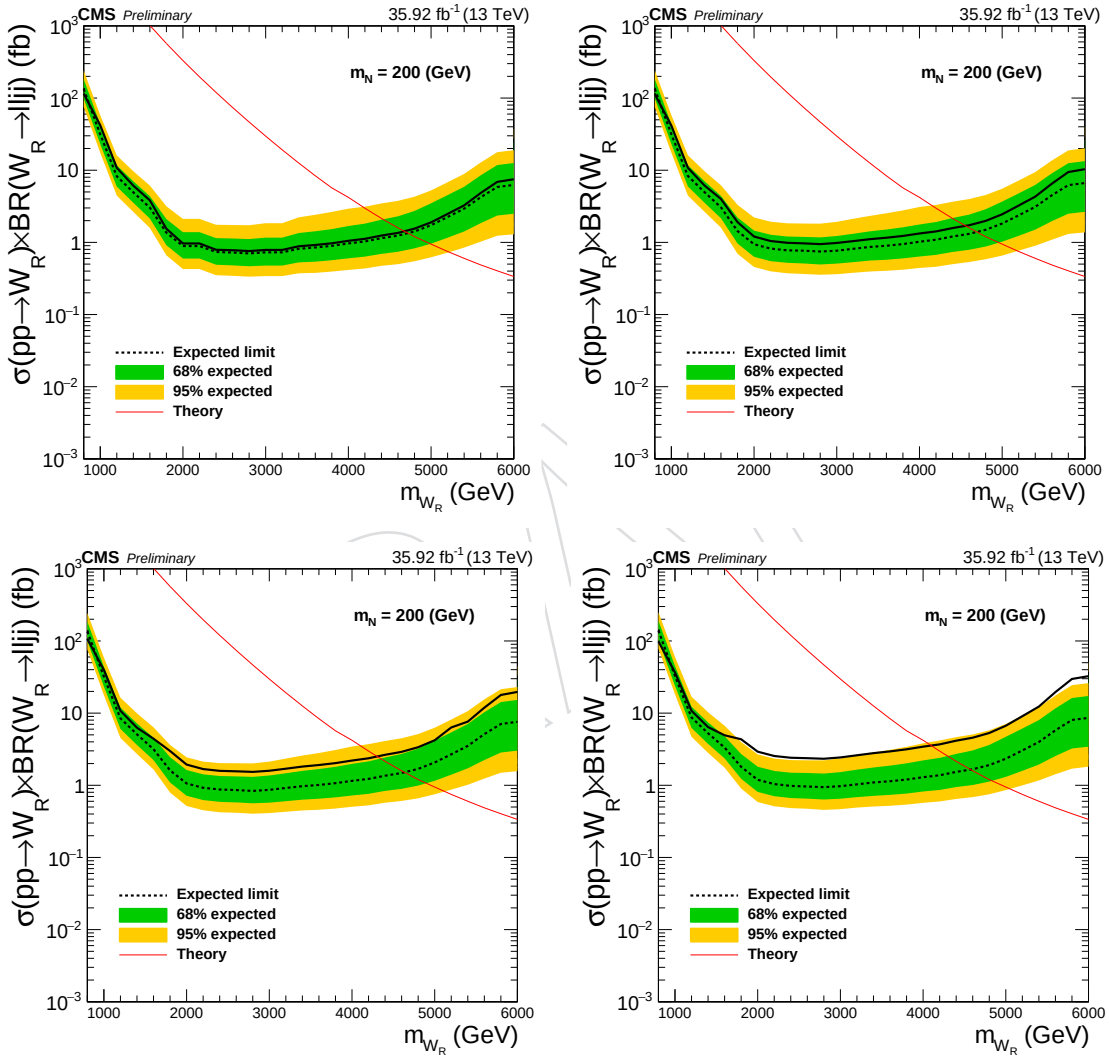

Figure 132: Boosted $\mu\mu$ asymptotic limits for the $m_N = 200$GeV mass points with 0(top left), 1(top right), 4(bottom left), and 8(bottom right) additional events added to the $m_{lJ} > 1700$GeV mass bin of a background only toy.

M LSF Validation

Due to the lack of a naturally occurring signal-like, 3-prong jet topology in SM processes, we used two different methods to measure the LSF_3 data-to-MC efficiency scale factor. The primary method that the scale factor was derived from is the "injected lepton method." As a cross-check, we also utilized the "semi-leptonic method." Both of these methods were discussed and approved by the JMAR group.

M.1 Injected Lepton Method

The injected lepton method artificially creates a 3-prong, signal-like jet by starting with a hadronically decaying, boosted W (2-prongs) and injecting either an electron or a muon into the event nearby it. To create a $t\bar{t}$ dominated sample, the selected boosted W events must fulfill the following criteria. The event is required to have one muon that passes the tight ID and isolation working point, $p_T > 53\,GeV$, and $|\eta| < 2.4$. The candidate events are also required to have $E_T^{miss} > 40\,GeV$ and the vectoral sum of the muon p_T and the E_T^{miss} is required to be greater than 200 GeV. The lead AK8 jet is the assumed boosted W and it is required to have a $p_T > 200\,GeV$, $|\eta| < 2.4$, and $N_2^{1,DDT} > 0$. $N_2^{1,DDT}$ is a 2-prong, jet tagger that is built from generalized energy correlation functions [36]:

$$N_2^1 = \frac{{}_2e_3^1}{({}_1e_2^1)^2}, \tag{7}$$

and then decorrelated from the jet $\rho = log(m_{SD}^2/p_T^2)$ follwing the procedure described in [37]. The decorrelation transformation fixes the background QCD efficiency at 26%.

The lepton is injected into the event by generating a single lepton event, where the p_T of the lepton is randomly selected between 50 and 350 GeV, which roughly corresponds to the p_T of leptons within jets within our signals, and the direction is randomly selected within a cone of $\Delta R < 0.8$ from the W jet. The single lepton is run through detector simulation and then merged with the original boosted W event, so that particle flow and jet clustering can be performed on the merged event. Leptons are injected into data and simulated events.

The LSF_3 distributions in data and MC are shown for the injected muon and injected lepton samples from all three years of data taking with the above event selection applied in Fig 133. Using the above event selection, 95% of events arise from $t\bar{t}$ and the remaining events come from W+jets and single top processes. Due to the small fraction of passing events from these backgrounds they are dropped from the scale factor measurement so that we did not have to inject leptons into these samples as well. Generator level matching is performed on the $t\bar{t}$ sample to ensure that at least one quark from the W and the injected lepton are within $\Delta R < 0.8$ of the jet.

M.1.1 Template fitting

To extract the scale factor, a template fitting method is performed in Combine where the template variable used is the LSF_3 value of the AK8 jet and a simultaneous fit is performed across the fail and pass samples. The pass and fail regions are tied together with the following equation applied to the matched ttbar events:

$$SF_{Fail} = \frac{N_{Pass} + N_{Fail} - N_{Pass} \times SF_{Pass}}{N_{Fail}}, \tag{8}$$

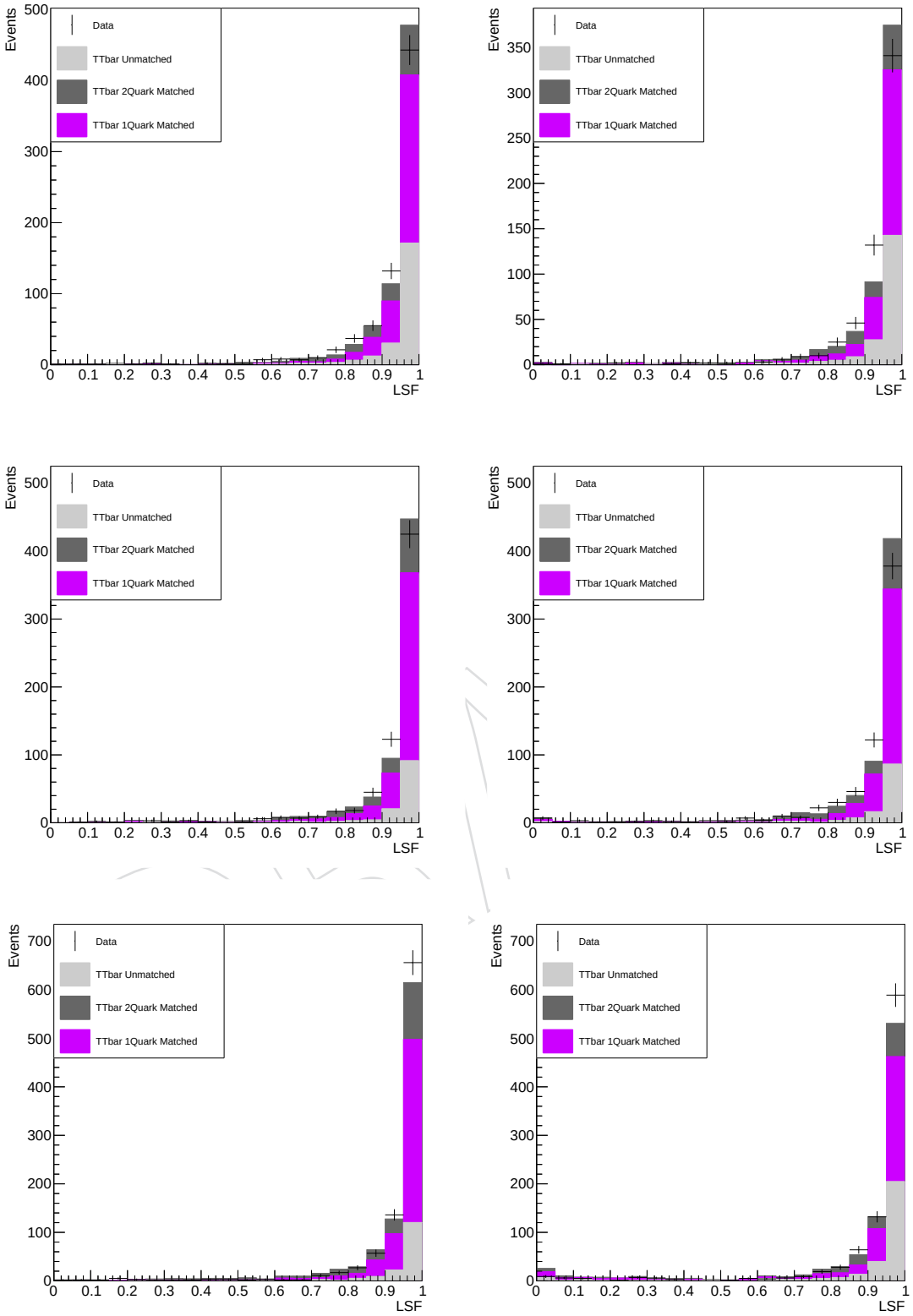

Figure 133: The LSF_3 distribution in data and simulation of the boosted, W jet with a muon (left) or an electron (right) injected into it for 2016 (upper), 2017 (middle), and 2018 (lower). The $t\bar{t}$ process has been split into 3 categories: where both generator quarks and the injected lepton are within $\Delta R < 0.8$ of the jet (2 quark matched), where one quark and the injected lepton are within $\Delta R < 0.8$ of the jet (1 quark matched), and where either neither quark or the injected lepton is not within $\Delta R < 0.8$ of the jet (unmatched). The W+jets and single top processes have been dropped and the $t\bar{t}$ simulation has been normalized to data to make up for the 5% contribution from these minor backgrounds.

where SF_{Pass} is the parameter of interest that is extracted from the simultaneous fit.

The following uncertainties are taken into account in the simultaneous fit:

- **Integrated luminosity**: The systematic uncertainty on the integrated luminosity are 2.5 %, 2.3 %, and 2.5 % for 2016, 2017 and 2018, respectively [30–32].
- **Pileup**: An uncertainty is estimated by varying the nominal minimum bias cross section of pp collisions at 13 TeV (69.2 mb) by 5 %.
- **Lepton trigger and selection**: Discrepancies in the lepton reconstruction, identification, and isolation efficiencies between data and simulation are corrected by applying a scale factor to all the simulated samples.
- **Jet energy scale and resolution**: The versions of JEC and JER are summarized in Table 15 and Table 16.
- **MC statistics**: A bin-wise statistical uncertainty is included to take into account the limited statistics available in our MC samples. This uncertainty is implemented through the Barlow-Beeston approach, where a single nuisance parameter is used in each bin to scale the sum of the process yields.
- **2-prong scale factor**: Discrepancies in the N_2^{DDT} selection efficiency between data and simulation are corrected by applying a scale factor to all the simulated samples.
- **Sample normalizations**: A 20% normalization uncertainty is applied to both the matched and unmatched $t\bar{t}$ templates.

M.1.2 Results

The pre- and post-fit LSF_3 templates for every year are shown in Fig 134-135 for the injected muon and injected electron samples, respectively. The extracted scale factors are listed in Table 56. Due to embedding a simulated lepton in both the data and MC samples, an additional uncertainty, corresponding to the lepton reconstruction uncertainty, has been added in quadrature to the scale factor uncertainty.

Table 56: The LSF scale factors for each year from the injected electron and muon samples.

Year	Injected e	Injected μ
2016	$1.04^{+0.09}_{-0.08}$	$1.01^{+0.06}_{-0.06}$
2017	$1.02^{+0.08}_{-0.08}$	$0.98^{+0.07}_{-0.07}$
2018	$1.05^{+0.07}_{-0.06}$	$1.04^{+0.06}_{-0.05}$

M.2 Semi-Leptonic Method

The semi-leptonic method measures the LSF_3 scale factor in a two-prong jet topology created from a leptonically decaying top, where the two-prongs originate from the b quark and lepton. We employ the tag-and-probe method to select for these events where our tag is the hadronically decaying top jet and our probe for LSF_3 is the leptonically decaying top jet on the opposite side of the event. Our tag selection requires the hadronic jet to have a p_T greater than 450 GeV as well as a soft drop mass window around the top mass ($105 < m_{SD} < 220$ GeV). Additionally, we use the tightest working point for the N-subjettiness ratio variable, requiring $\tau_{32} < 0.4$ to select for the three-prongness of the hadronically decaying top. To further define a hadronically decaying top we use the loose working point for a subjet b-tag discriminant, b-tag$_{DeepCSV} > 0.2217(0.1522, 0.1241)$ in 2016 (2017, 2018). We then require $d\phi(\text{Lep Jet}, \text{Hadronic Jet}) > 2$. Since there is a neutrino in the final of the semi-leptonic top jet we make a MET selection requiring more than 100 GeV of MET in the event.

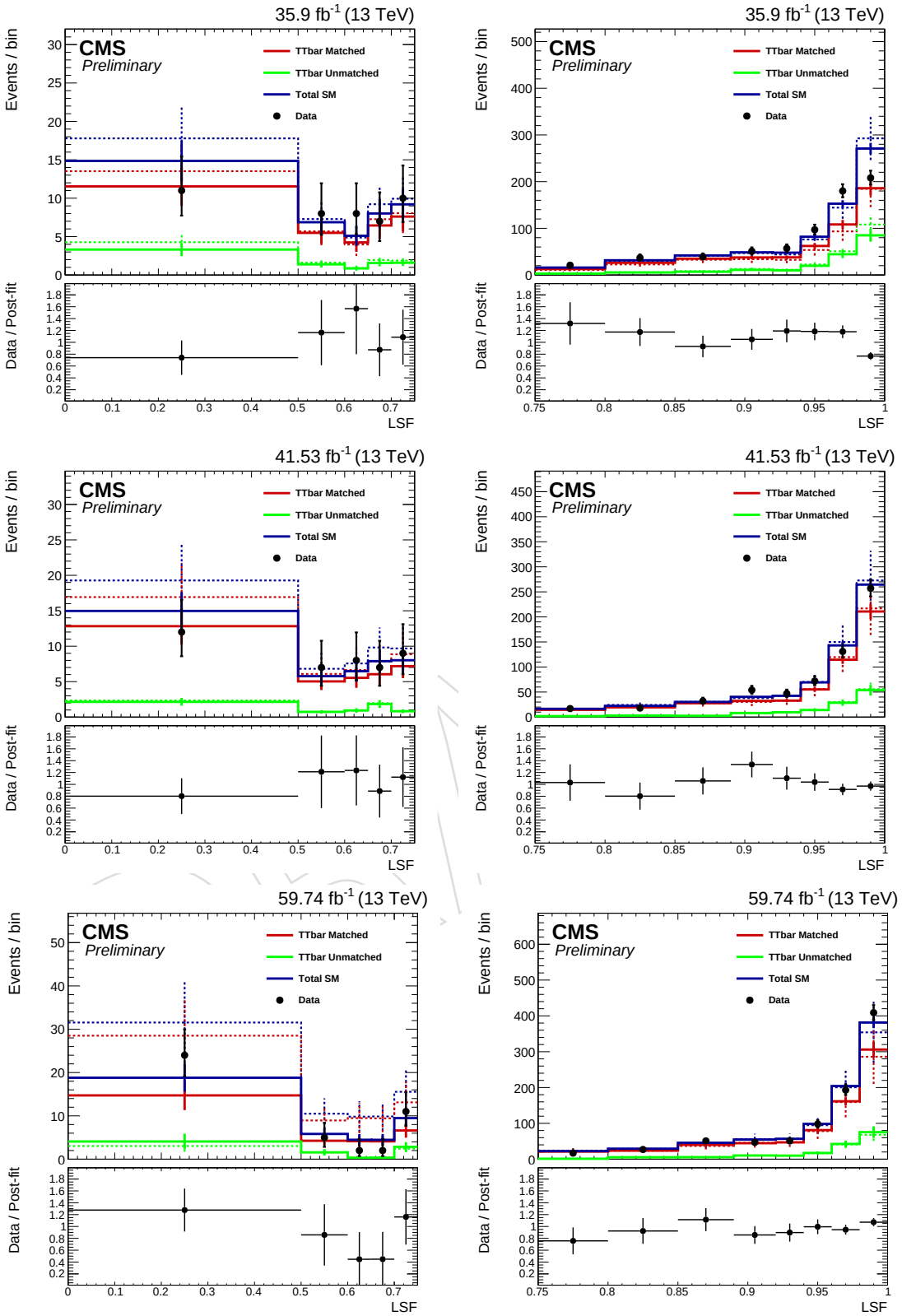

Figure 134: The pre- and post-fit failing (left) and passing (right) LSF_3 distributions in data and simulation of the boosted, W jet with a muon injected into it for 2016 (upper), 2017 (middle), and 2018 (lower). The $t\bar{t}$ process is considered matched when either one or two quarks from the W and the injected lepton are within $\Delta R < 0.8$ of the jet.

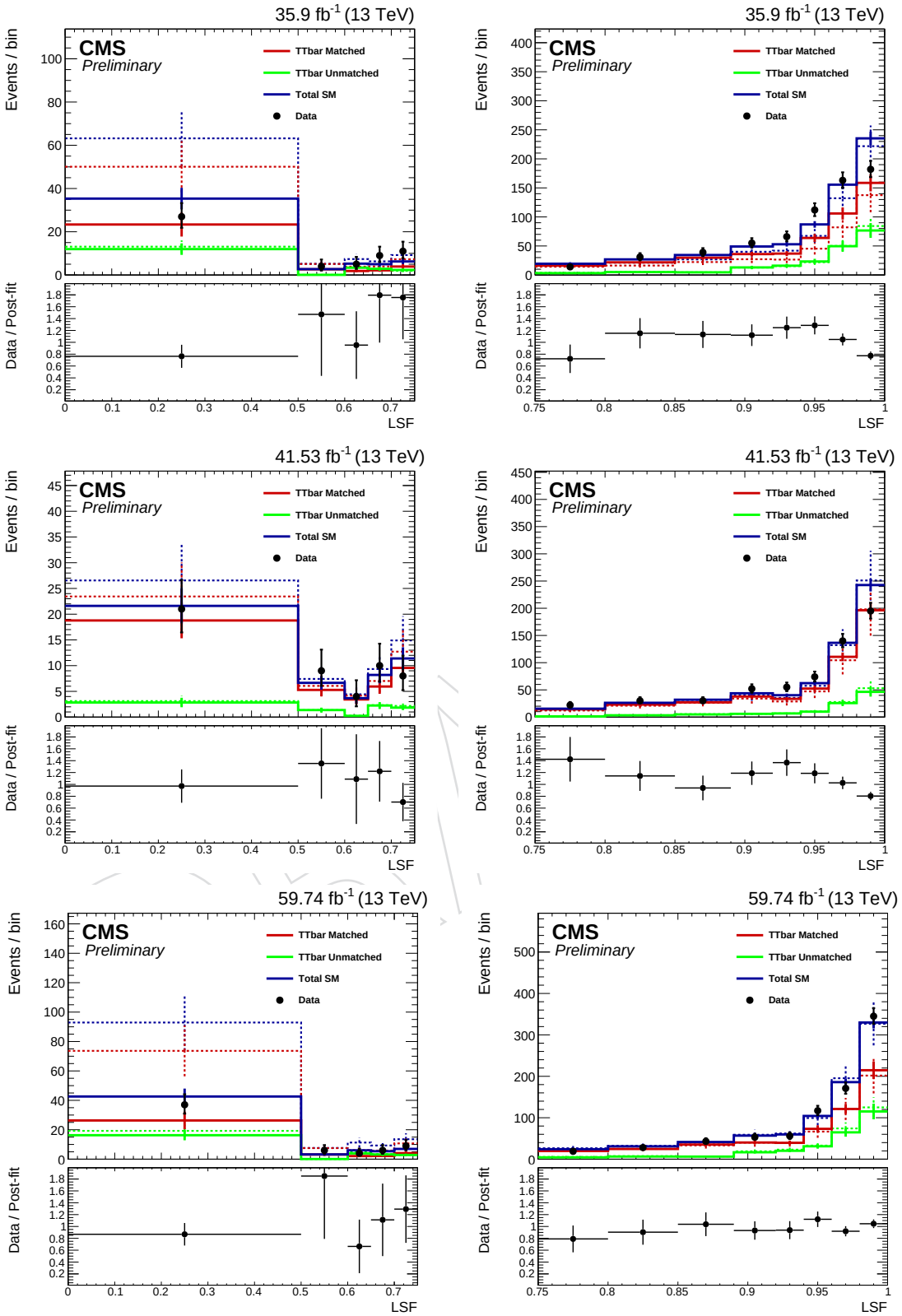

Figure 135: The pre- and post-fit failing (left) and passing (right) LSF_3 distributions in data and simulation of the boosted, W jet with an electron injected into it for 2016 (upper), 2017 (middle), and 2018 (lower). The $t\bar{t}$ process is considered matched when either one or two quarks from the W and the injected lepton are within $\Delta R < 0.8$ of the jet.

The LSF_3 distribution in this semi-leptonic $t\bar{t}$ sample can be seen Fig 136. Generator level matching is performed on the $t\bar{t}$ sample to ensure that the lepton from the W and the b quark are within $\Delta R < 0.8$ of the jet.

M.2.1 Template fitting

To extract the scale factor, the same template fitting method from the injected lepton method is used. However, we now use the m_{SD} distribution of the hadroncially decaying top jet as our templates because this distribution provides good separation between the background QCD and $t\bar{t}$ events.

The following uncertainties are taken into account in the simultaneous fit:

- **Integrated luminosity**: The systematic uncertainty on the integrated luminosity are 2.5 %, 2.3 %, and 2.5 % for 2016, 2017 and 2018, respectively [30–32].
- **Pileup**: An uncertainty is estimated by varying the nominal minimum bias cross section of pp collisions at 13 TeV (69.2 mb) by 5 %.
- **Jet energy scale and resolution**: The versions of JEC and JER are summarized in Table 15 and Table 16.
- **MC statistics**: A bin-wise statistical uncertainty is included to take into account the limited statistics available in our MC samples. This uncertainty is implemented through the Barlow-Beeston approach, where a single nuisance parameter is used in each bin to scale the sum of the process yields.
- **Top tagging**: Discrepancies in the top tagging selection efficiency between data and simulation are corrected by applying a scale factor to all the simulated samples.
- **Sample normalizations**: A 20% normalization uncertainty is applied all templates except for QCD where a 100% normalization uncertainty is applied.

M.2.2 Results

The pre- and post-fit m_{SD} templates for every year are shown in Fig 137. The extracted scale factors are listed in Table 57. The scale factors from the semi-leptonic method are consistently 1σ or slightly more below the scale factors from the injected lepton method.

Table 57: The LSF scale factors for each year from the semi-leptonic method.

Year	Scale Factor
2016	$0.87^{+0.08}_{-0.07}$
2017	$0.84^{+0.08}_{-0.07}$
2018	$0.91^{+0.06}_{-0.06}$

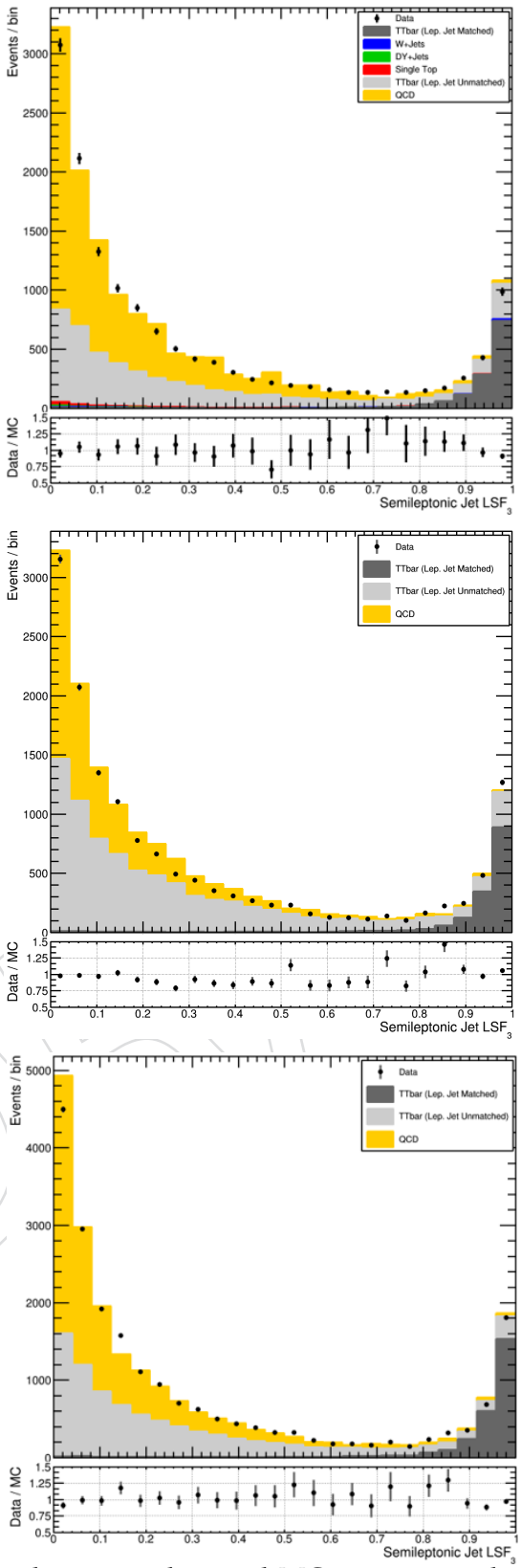

Figure 136: The LSF_3 distribution in data and MC in our semi-leptonic $t\bar{t}$ events from 2016 (top), 2017 (middle), and 2018 (bottom). The semileptonic jet corresponds to the highest p_T jet that was not hadronically top tagged. The matched $t\bar{t}$ corrsponds to the generator level lepton from the W and the b quark be within $\Delta R < 0.8$ of the jet.

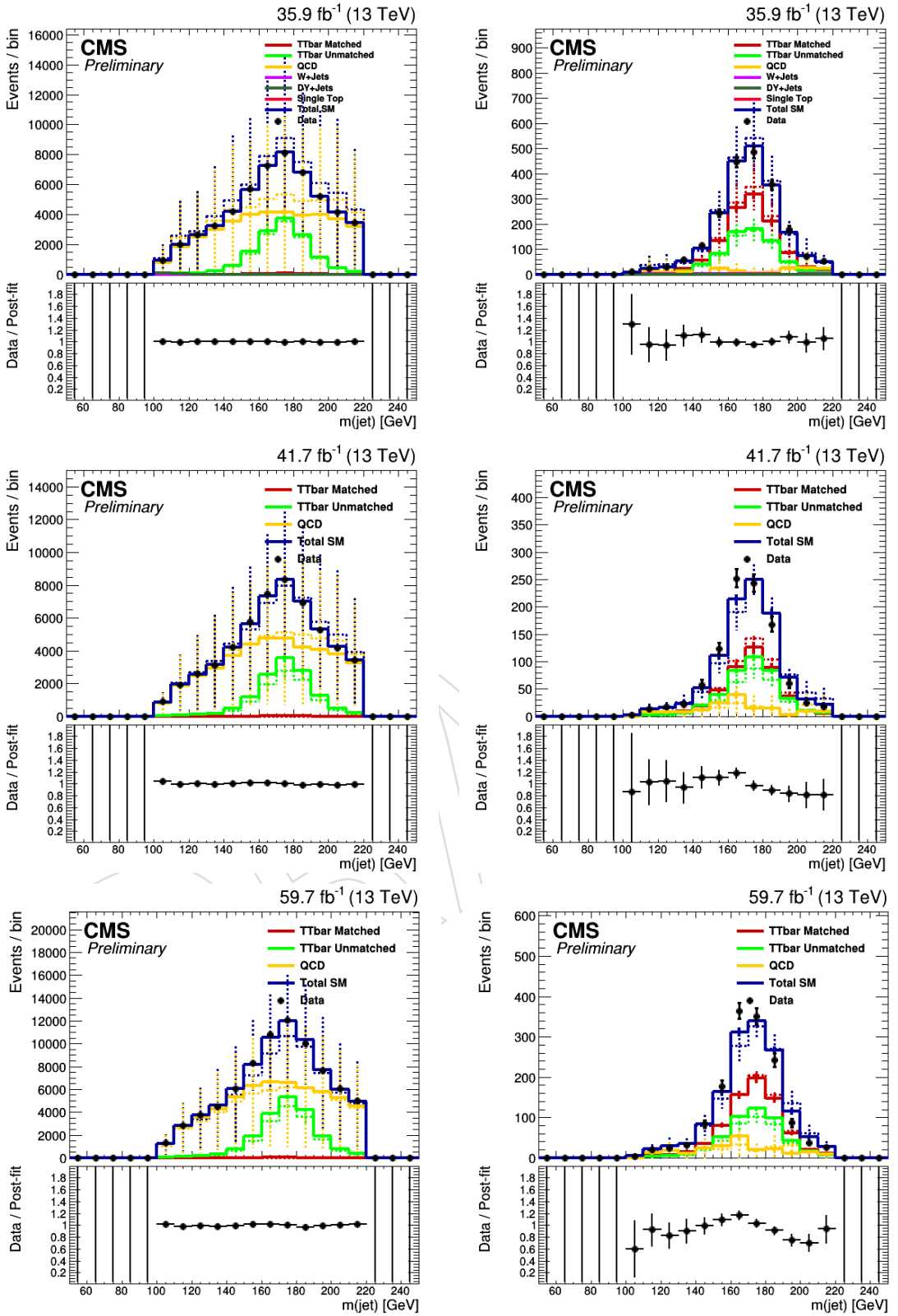

Figure 137: The pre- and post-fit m_{SD} distributions in data and simulation of the semi-leptonic $t\bar{t}$ events failing (left) and passing (right) the LSF_3 requirement for 2016 (upper), 2017 (middle), and 2018 (lower). The $t\bar{t}$ process is considered matched when the lepton from the W and the b quark are within $\Delta R < 0.8$ of the jet.

964 # N The impact and the pull of the nuisance parameters

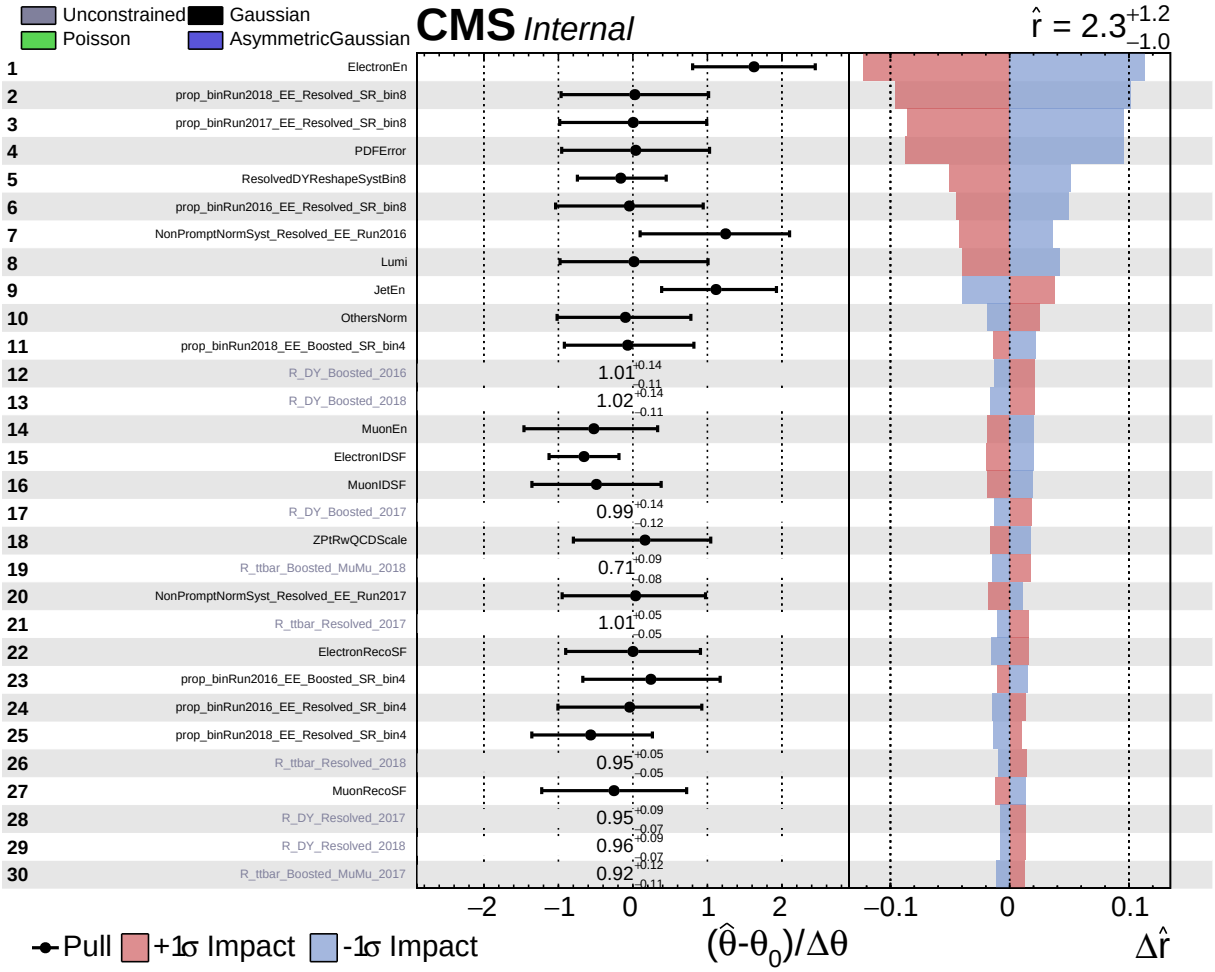

Figure 138: The impact and the pull of the nuisance paremeters in ee channel for $(m_{W_R}, m_N) = (5000, 3000)$ GeV signal (page 0 out of 6).

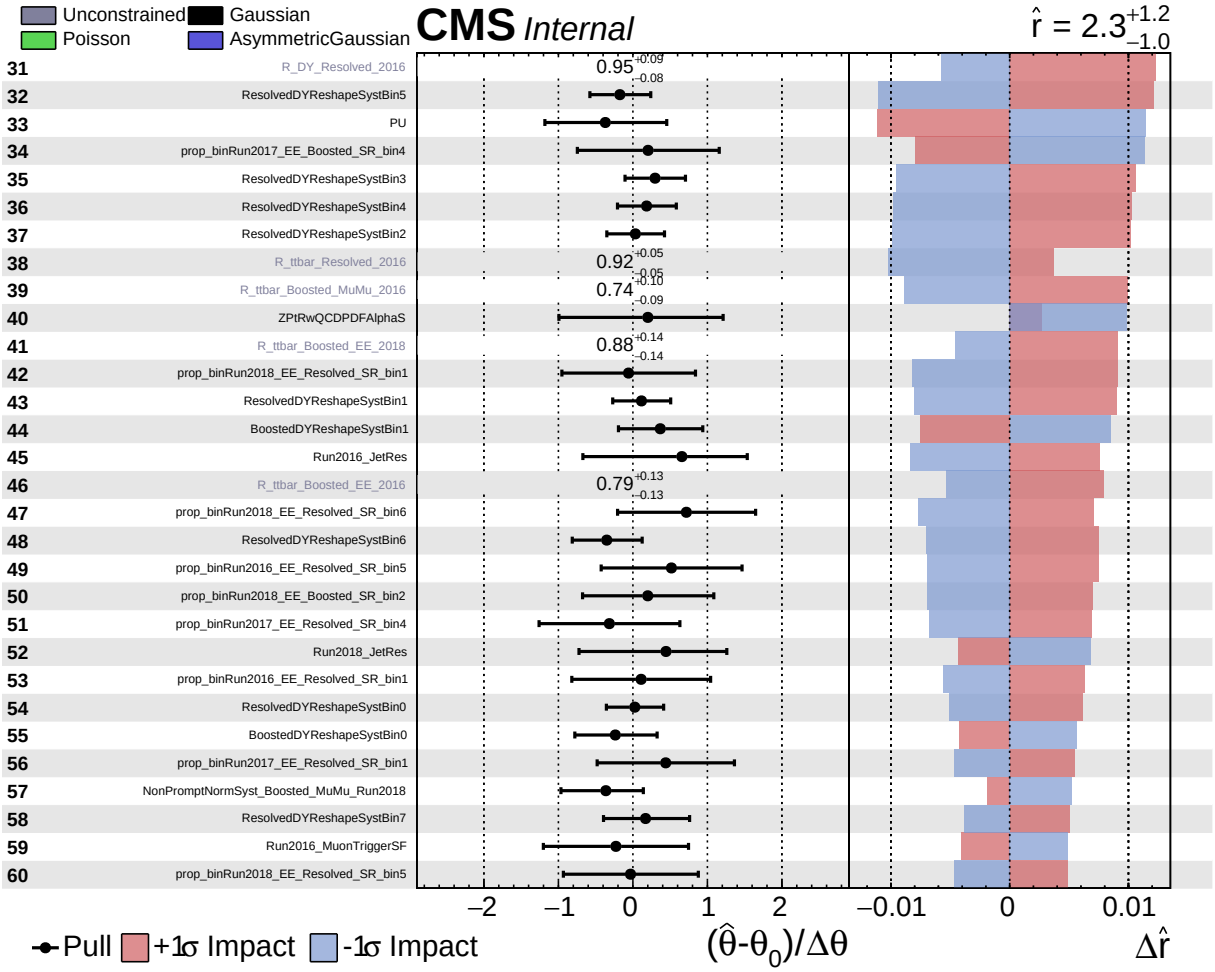

Figure 139: The impact and the pull of the nuisance paremeters in ee channel for $(m_{W_R}, m_N) = (5000, 3000)$ GeV signal (page 1 out of 6).

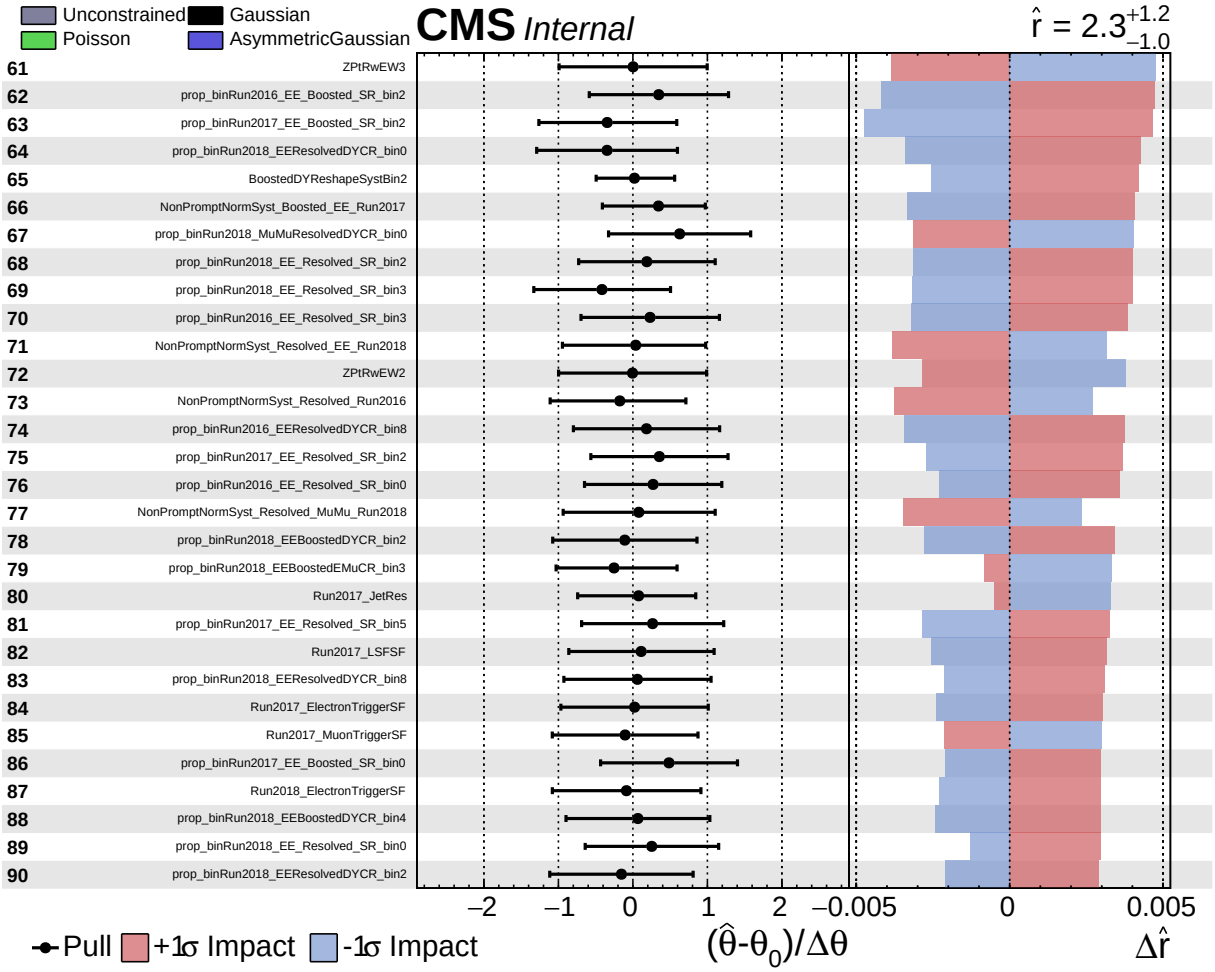

Figure 140: The impact and the pull of the nuisance paremeters in ee channel for $(m_{W_R}, m_N) = (5000, 3000)$ GeV signal (page 2 out of 6).

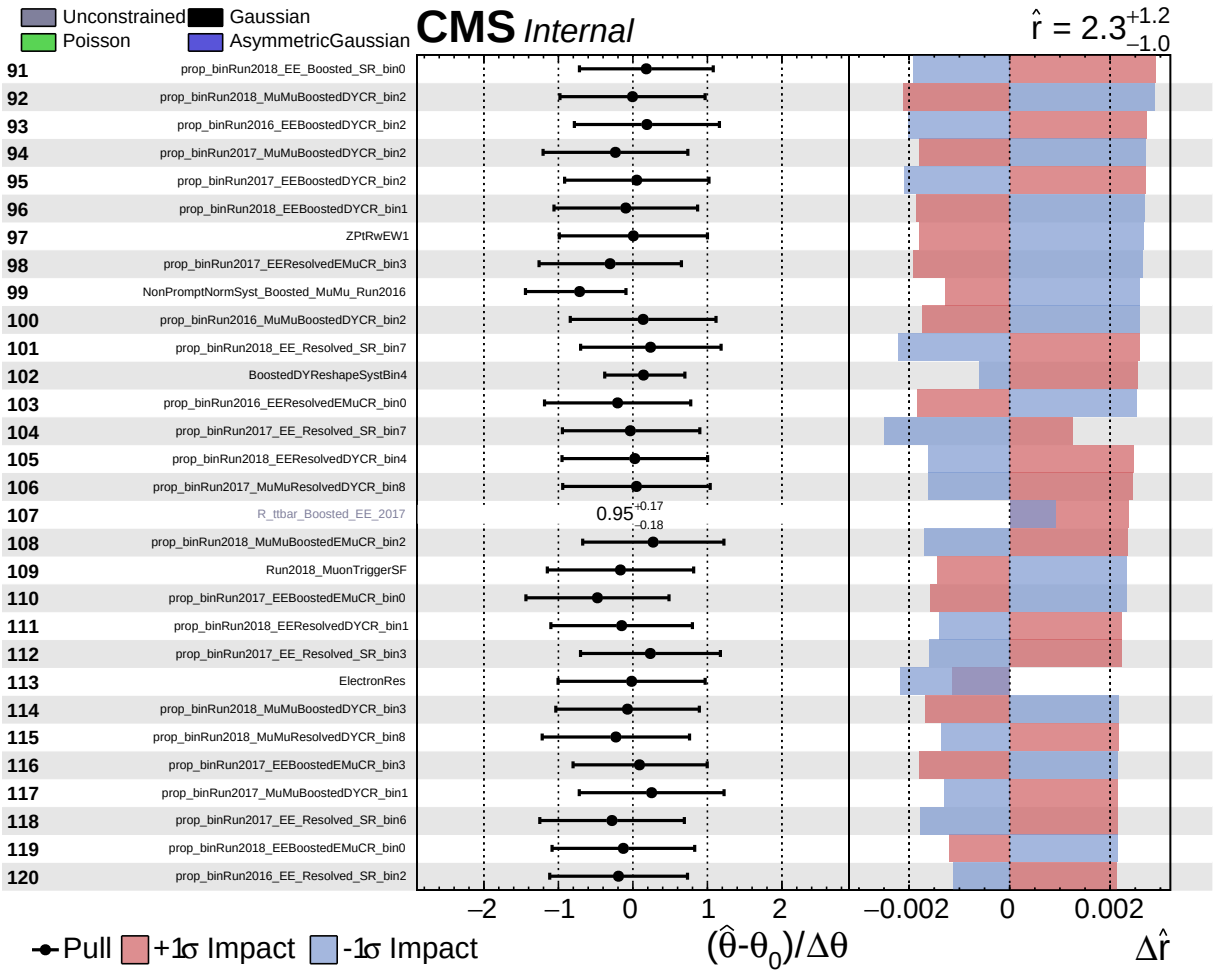

Figure 141: The impact and the pull of the nuisance paremeters in ee channel for $(m_{W_R}, m_N) = (5000, 3000)$ GeV signal (page 3 out of 6).

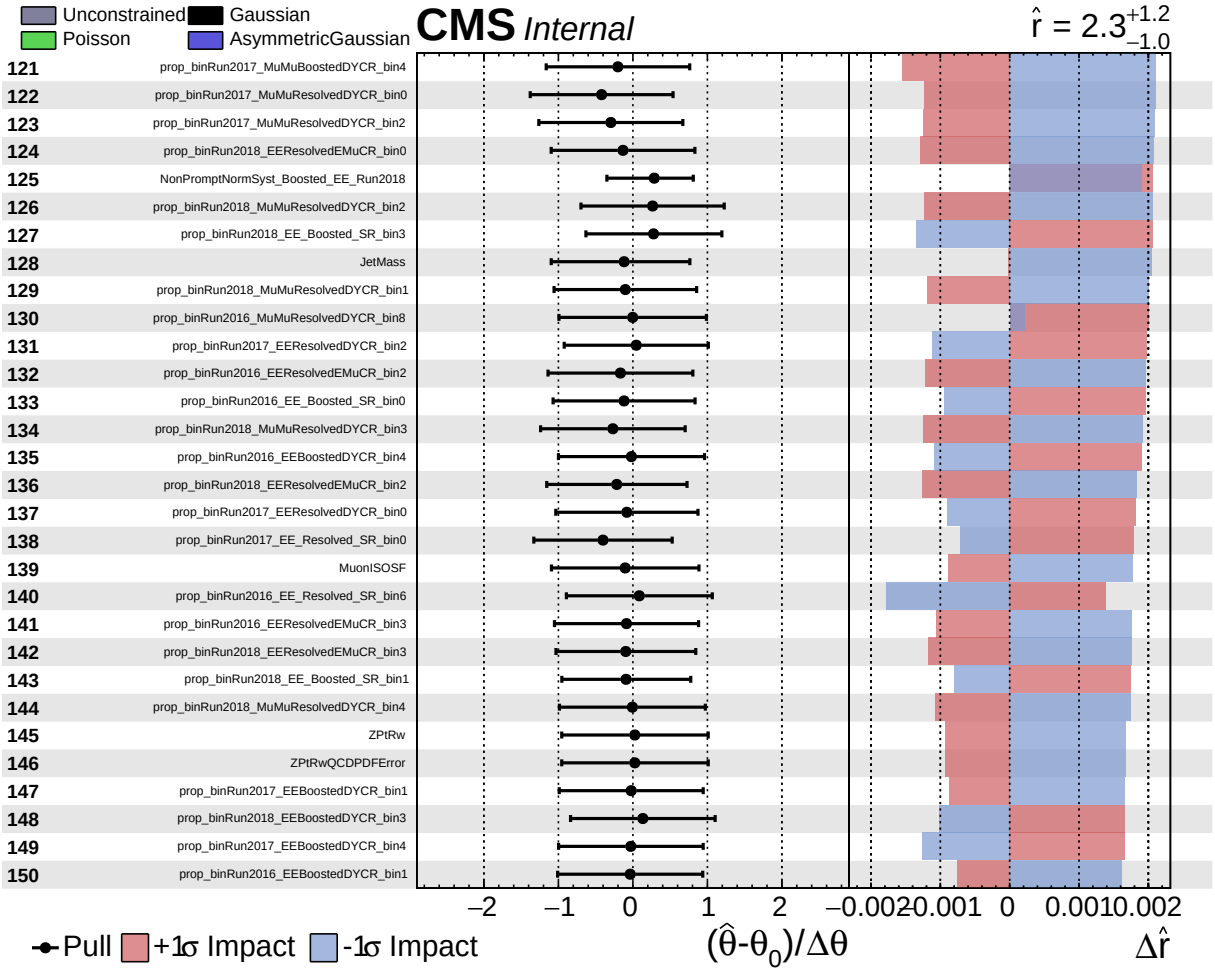

Figure 142: The impact and the pull of the nuisance paremeters in ee channel for $(m_{W_R}, m_N) = (5000, 3000)$ GeV signal (page 4 out of 6).

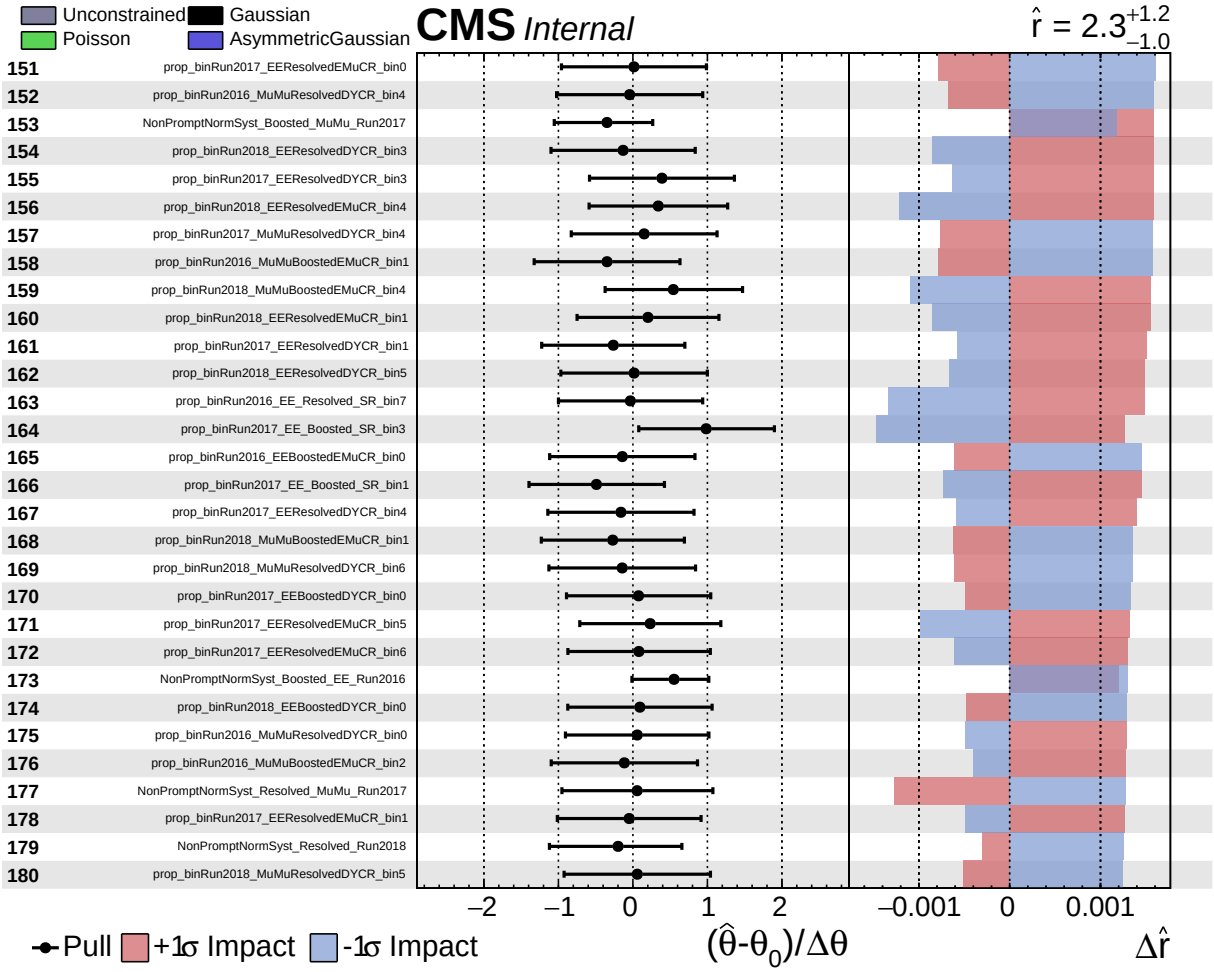

Figure 143: The impact and the pull of the nuisance paremeters in ee channel for $(m_{W_R}, m_N) = (5000, 3000)$ GeV signal (page 5 out of 6).

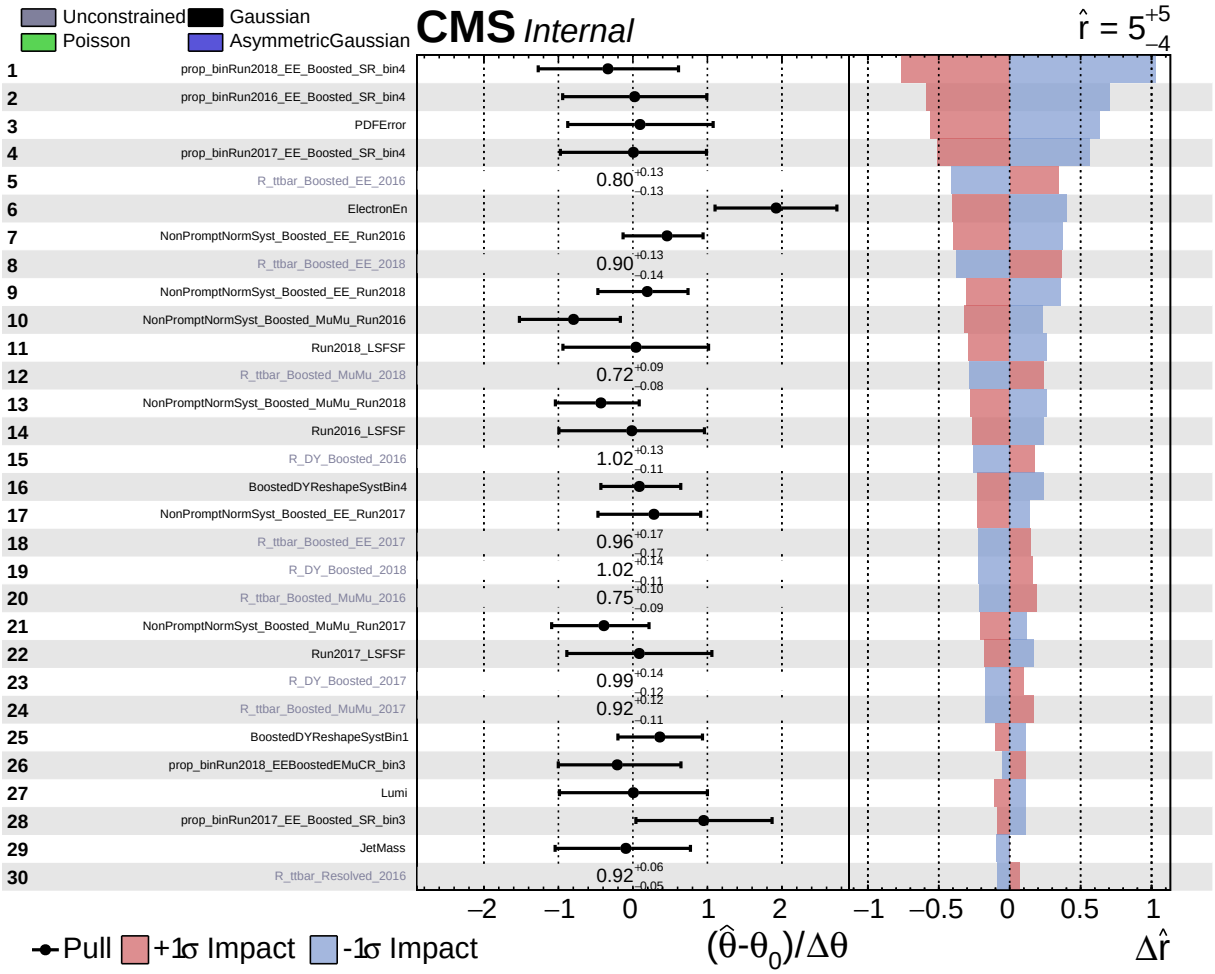

Figure 144: The impact and the pull of the nuisance paremeters in ee channel for $(m_{W_R}, m_N) = (5000, 200)$ GeV signal (page 0 out of 6).

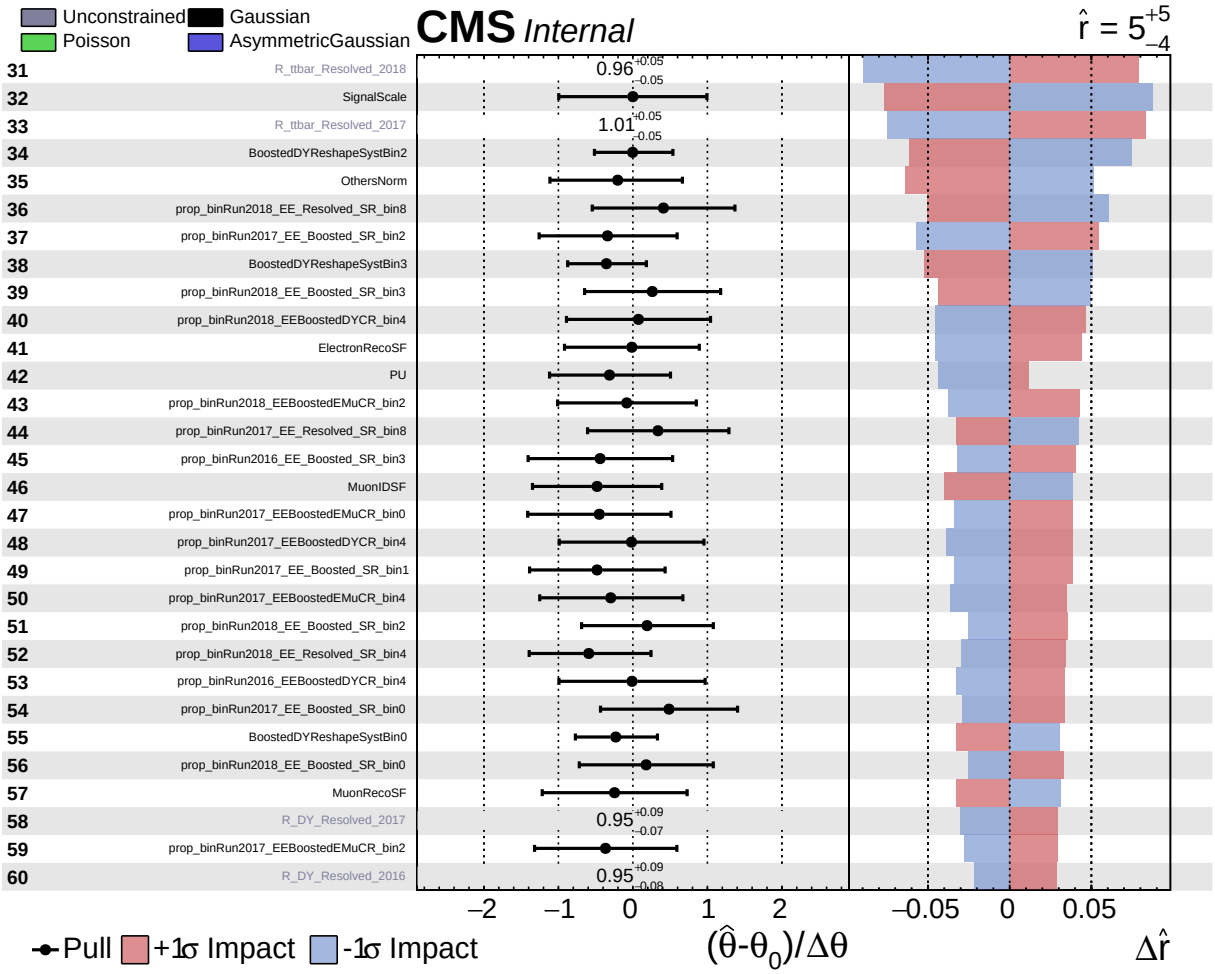

Figure 145: The impact and the pull of the nuisance paremeters in ee channel for $(m_{W_R}, m_N) = (5000, 200)$ GeV signal (page 1 out of 6).

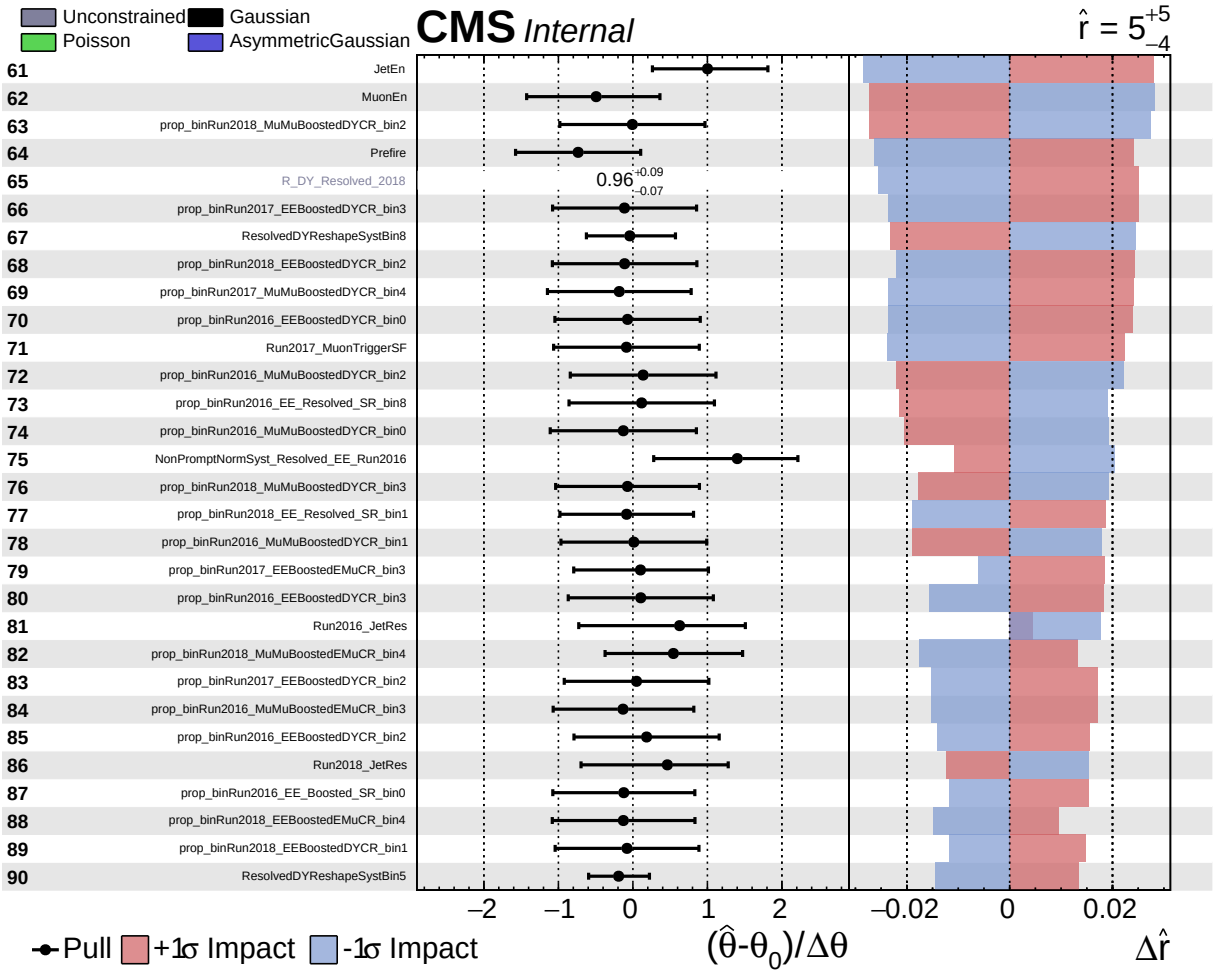

Figure 146: The impact and the pull of the nuisance paremeters in ee channel for $(m_{W_R}, m_N) = (5000, 200)$ GeV signal (page 2 out of 6).

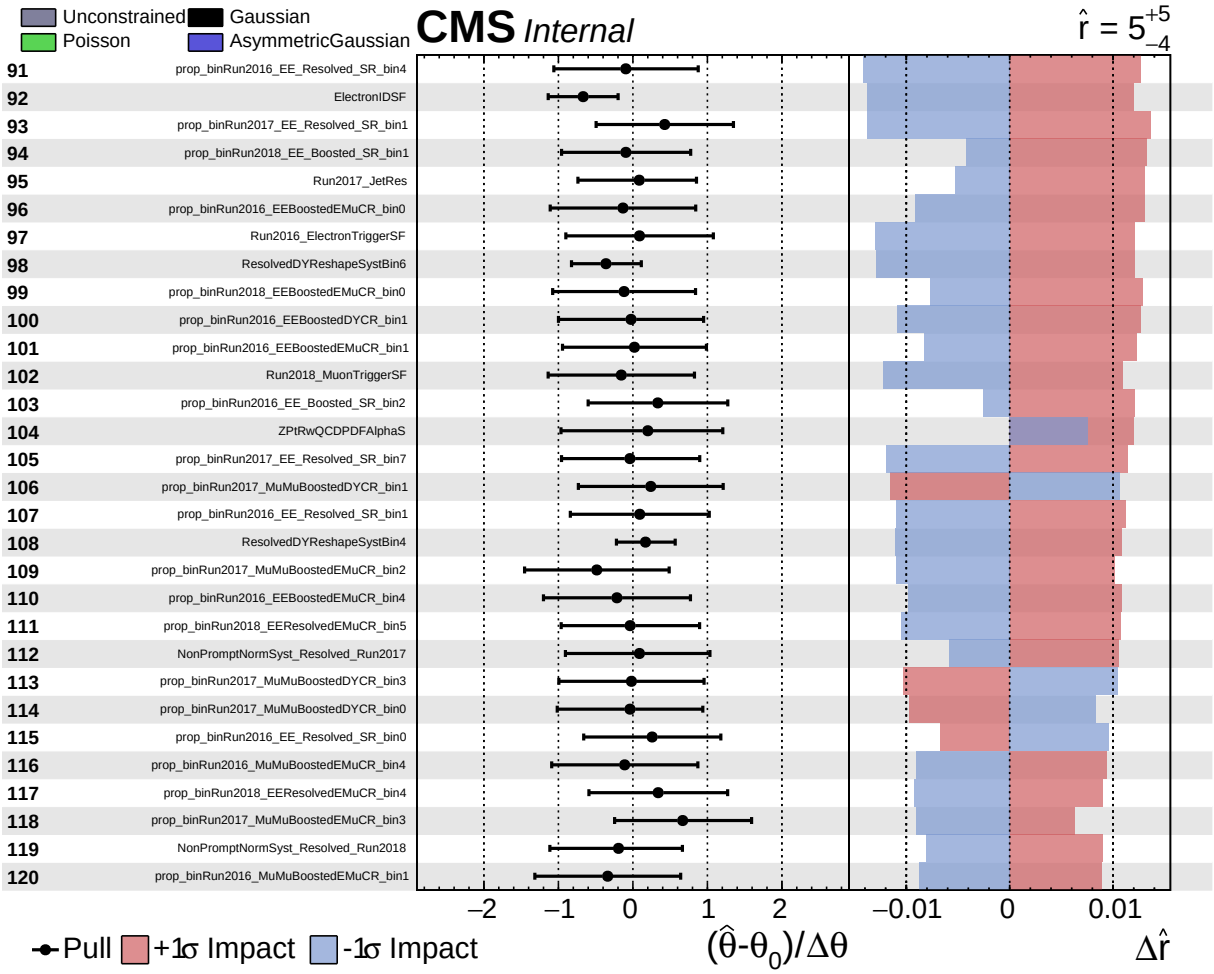

Figure 147: The impact and the pull of the nuisance paremeters in ee channel for $(m_{W_R}, m_N) = (5000, 200)$ GeV signal (page 3 out of 6).

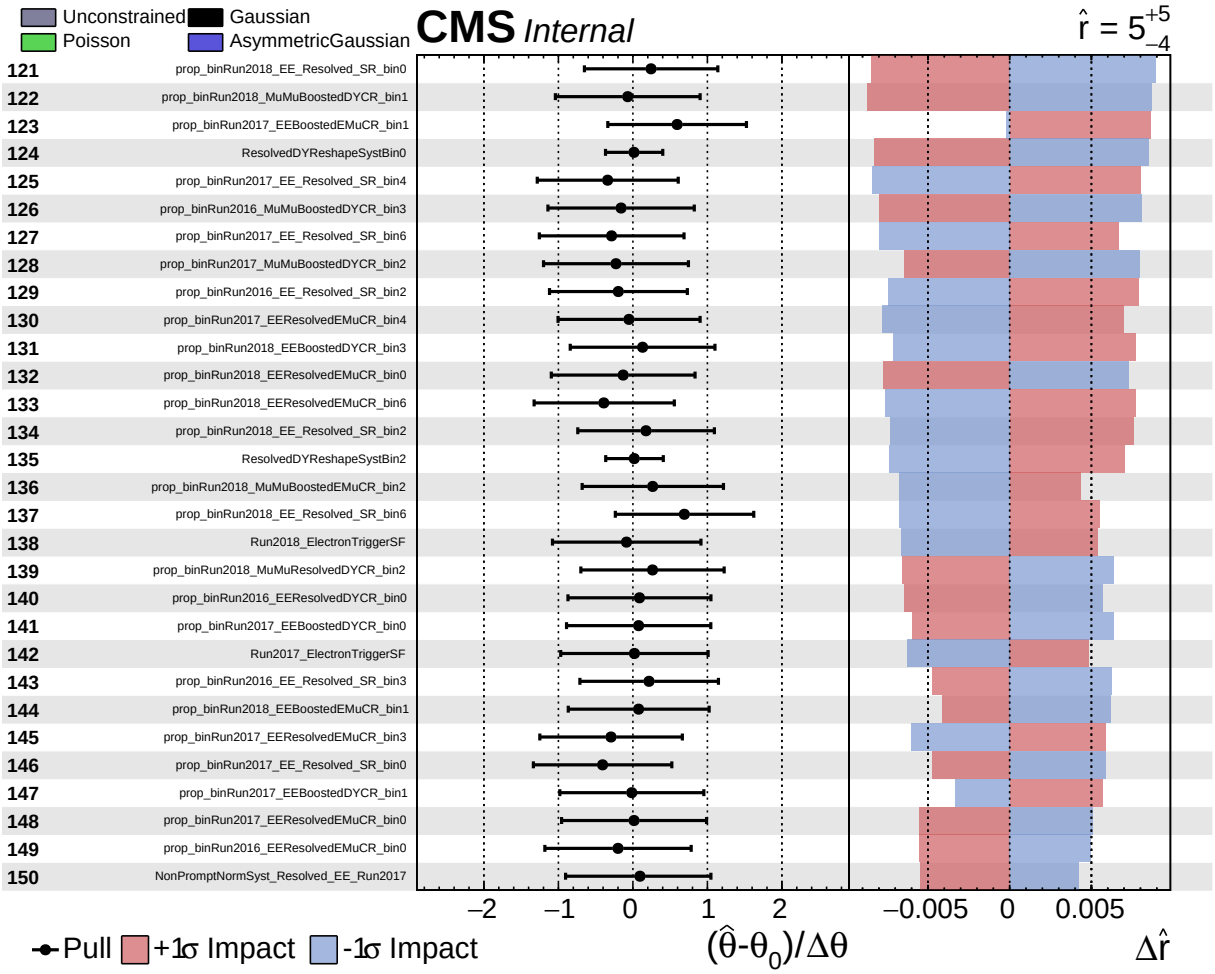

Figure 148: The impact and the pull of the nuisance paremeters in ee channel for $(m_{W_R}, m_N) = (5000, 200)$ GeV signal (page 4 out of 6).

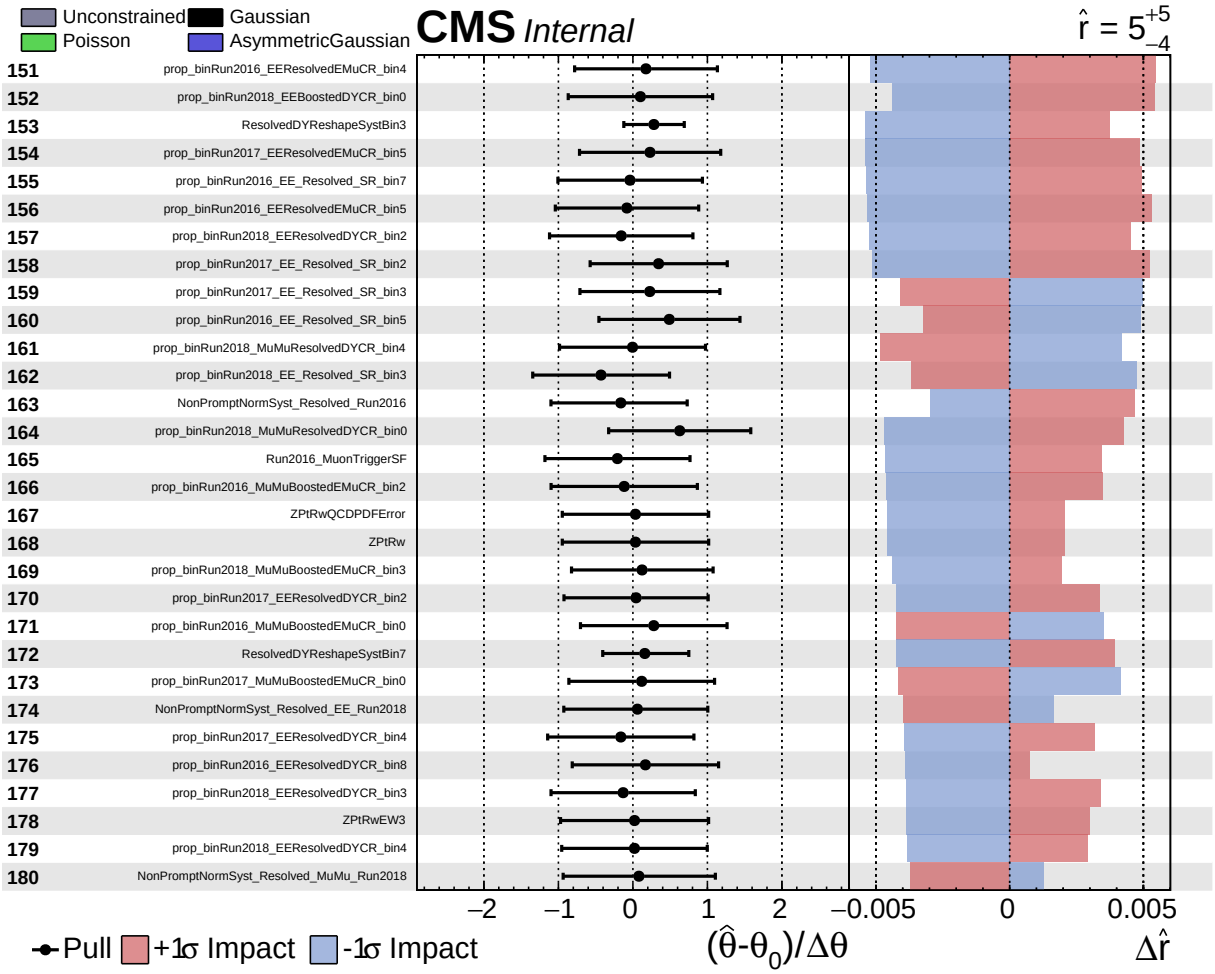

Figure 149: The impact and the pull of the nuisance paremeters in ee channel for $(m_{W_R}, m_N) = (5000, 200)$ GeV signal (page 5 out of 6).

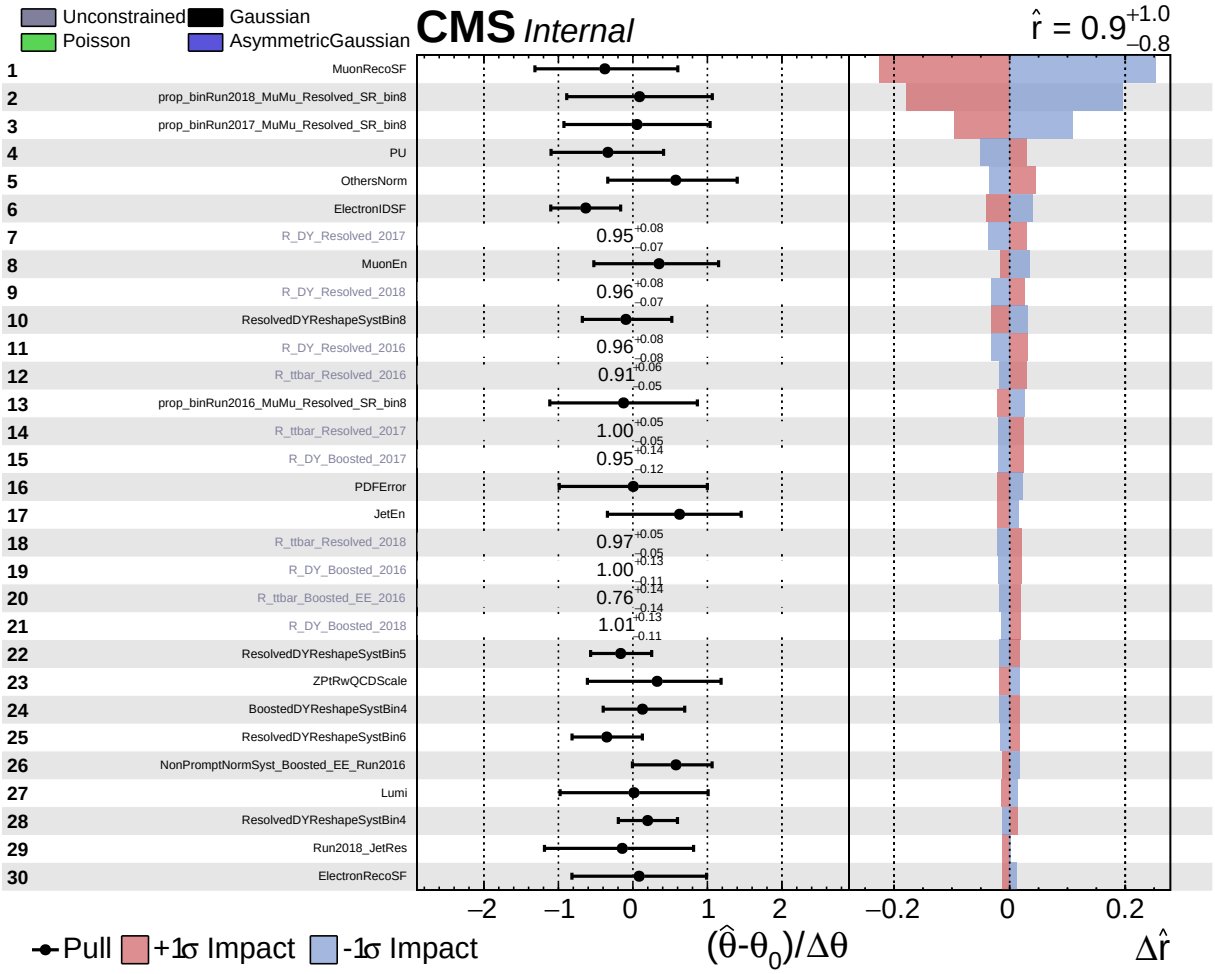

Figure 150: The impact and the pull of the nuisance paremeters in $\mu\mu$ channel for $(m_{W_R}, m_N) = (5000, 3000)$ GeV signal (page 0 out of 6).

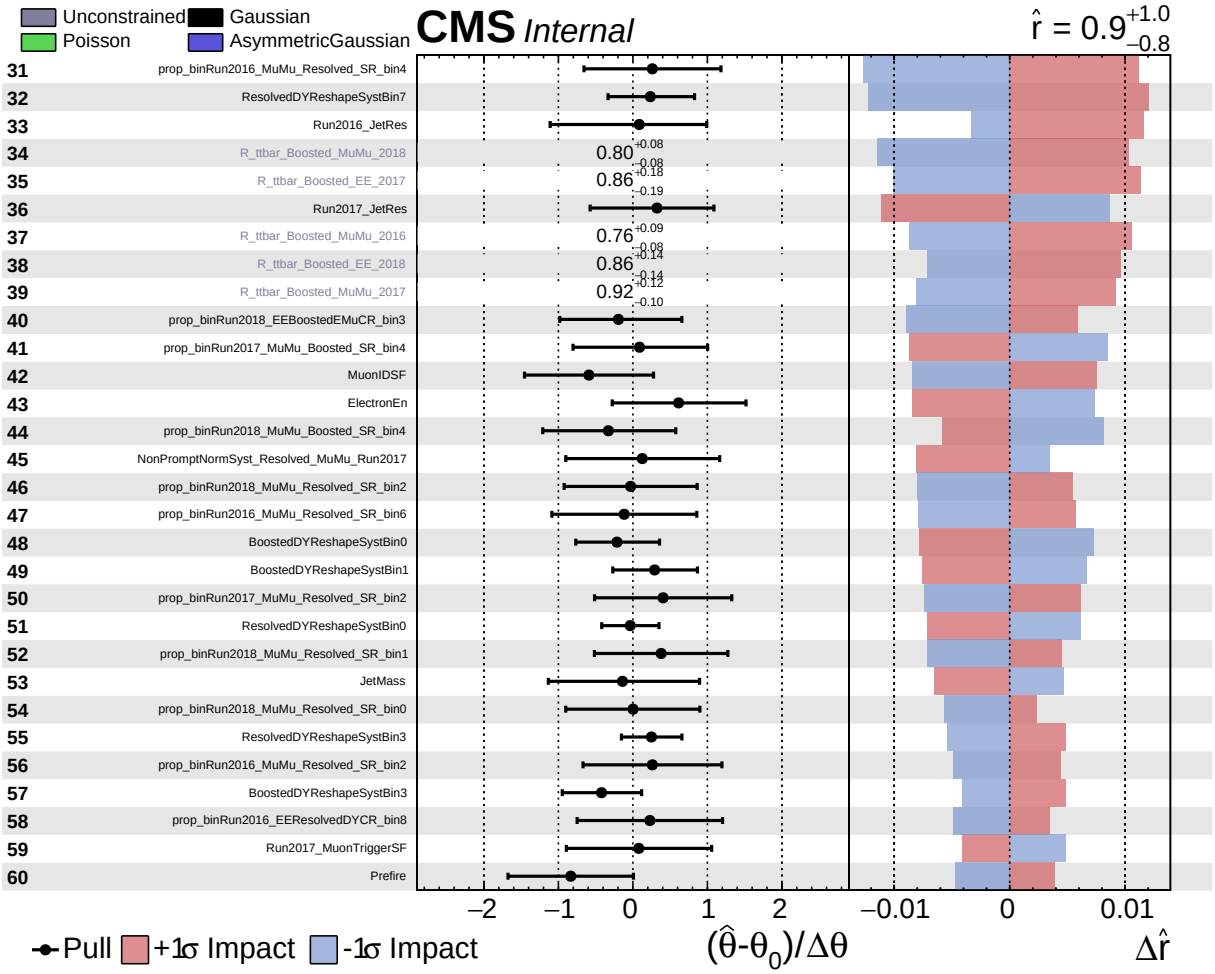

Figure 151: The impact and the pull of the nuisance paremeters in $\mu\mu$ channel for $(m_{W_R}, m_N) = (5000, 3000)$ GeV signal (page 1 out of 6).

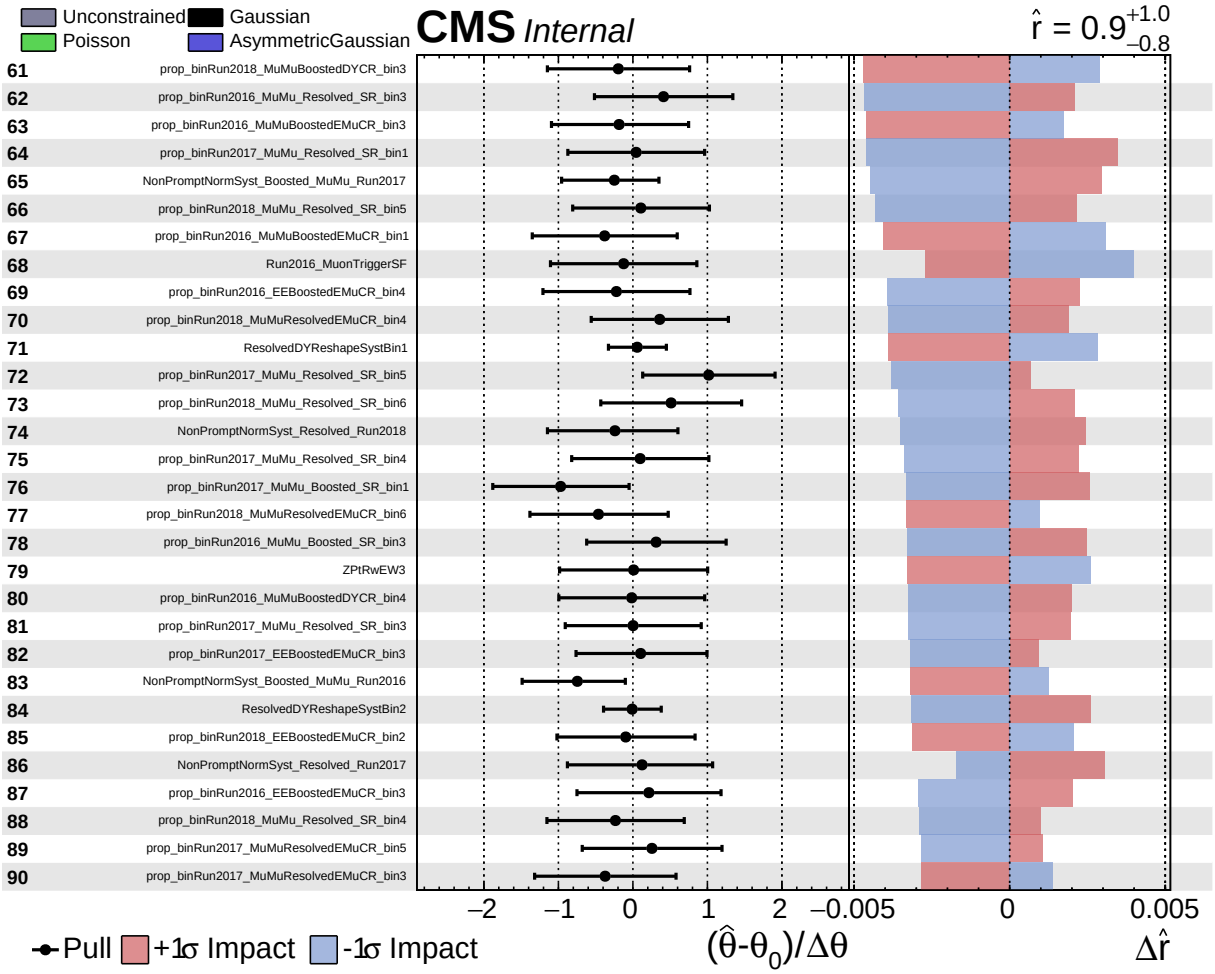

Figure 152: The impact and the pull of the nuisance paremeters in $\mu\mu$ channel for $(m_{W_R}, m_N) = (5000, 3000)$ GeV signal (page 2 out of 6).

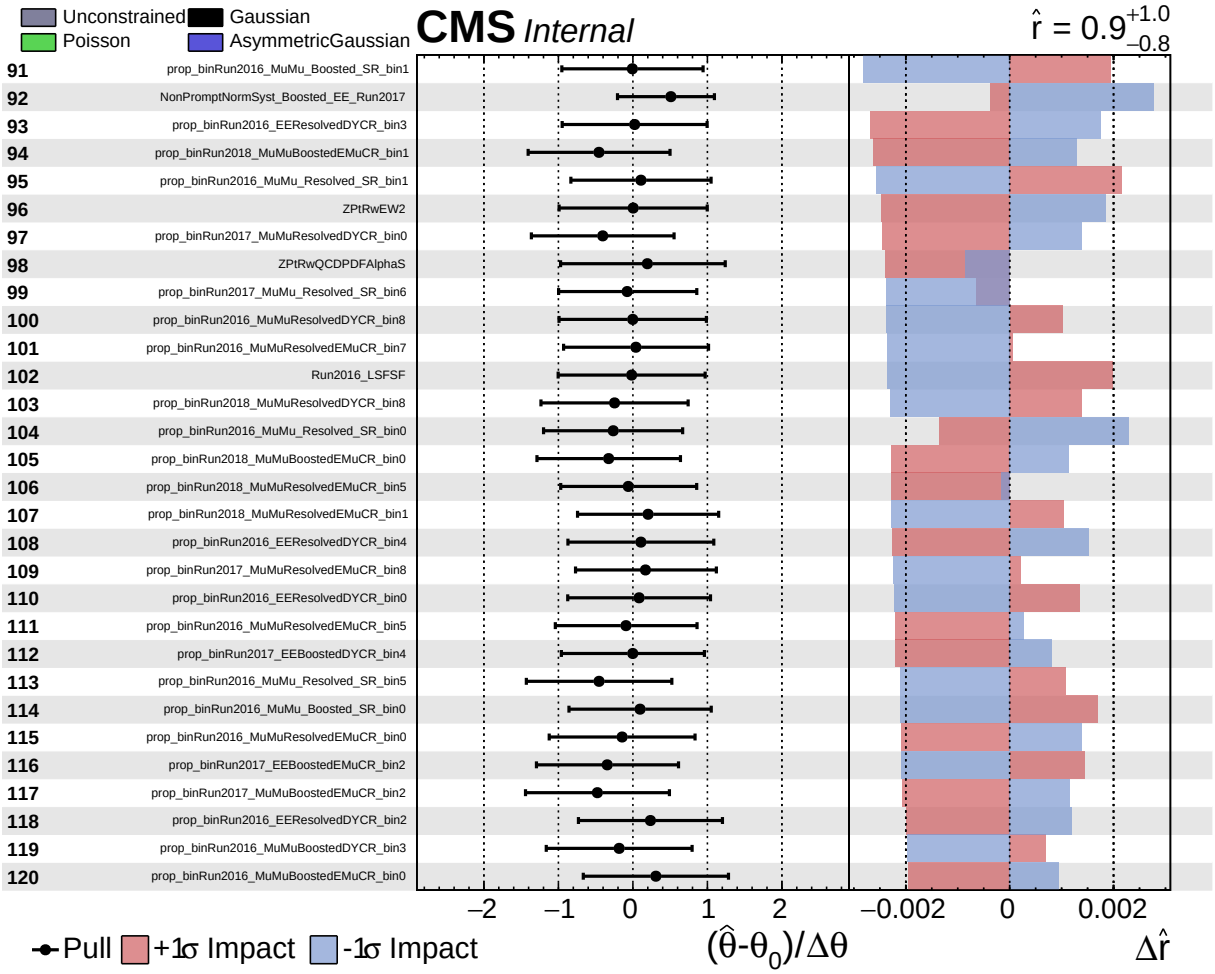

Figure 153: The impact and the pull of the nuisance paremeters in $\mu\mu$ channel for $(m_{W_R}, m_N) = (5000, 3000)$ GeV signal (page 3 out of 6).

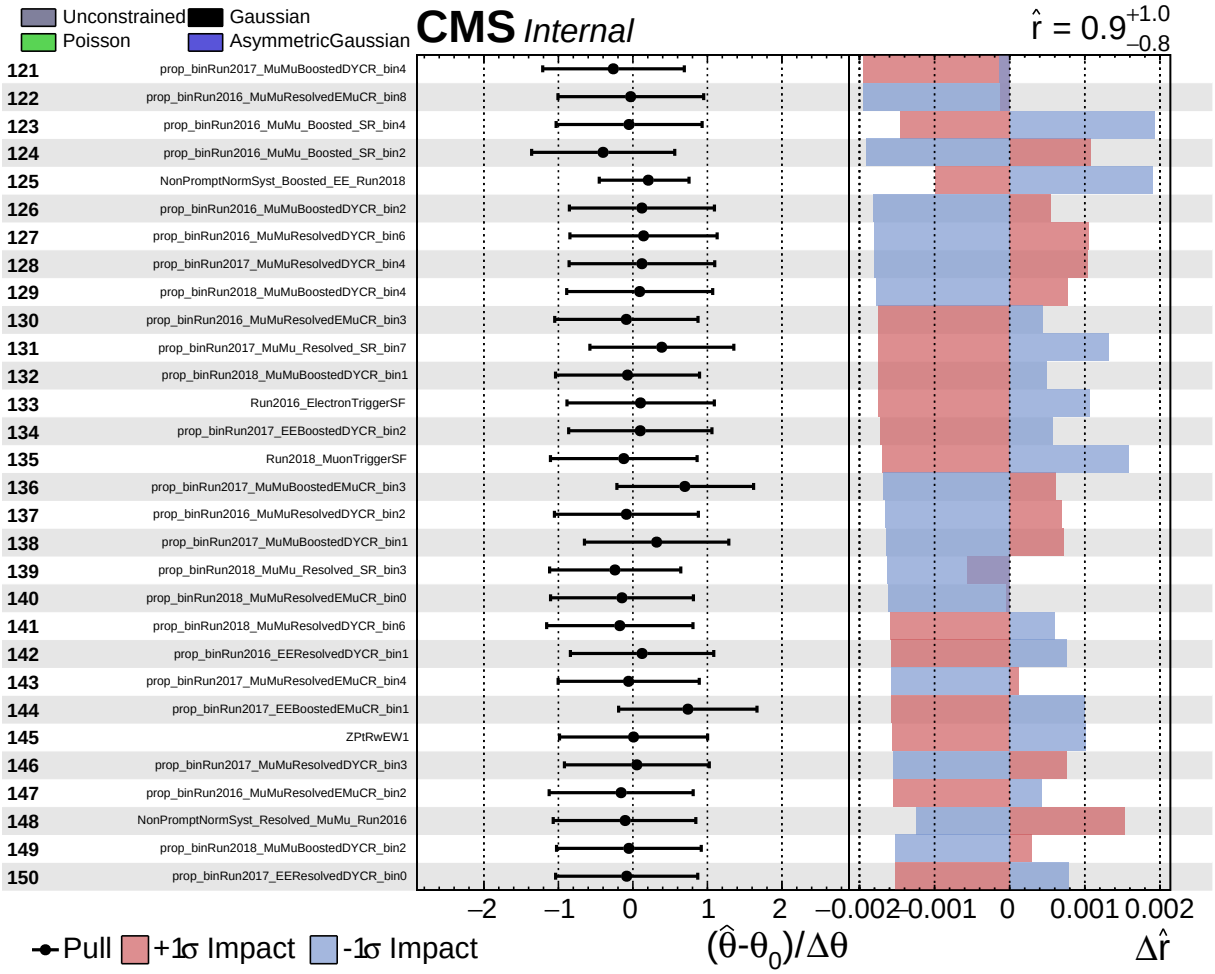

Figure 154: The impact and the pull of the nuisance paremeters in $\mu\mu$ channel for $(m_{W_R}, m_N) = (5000, 3000)$ GeV signal (page 4 out of 6).

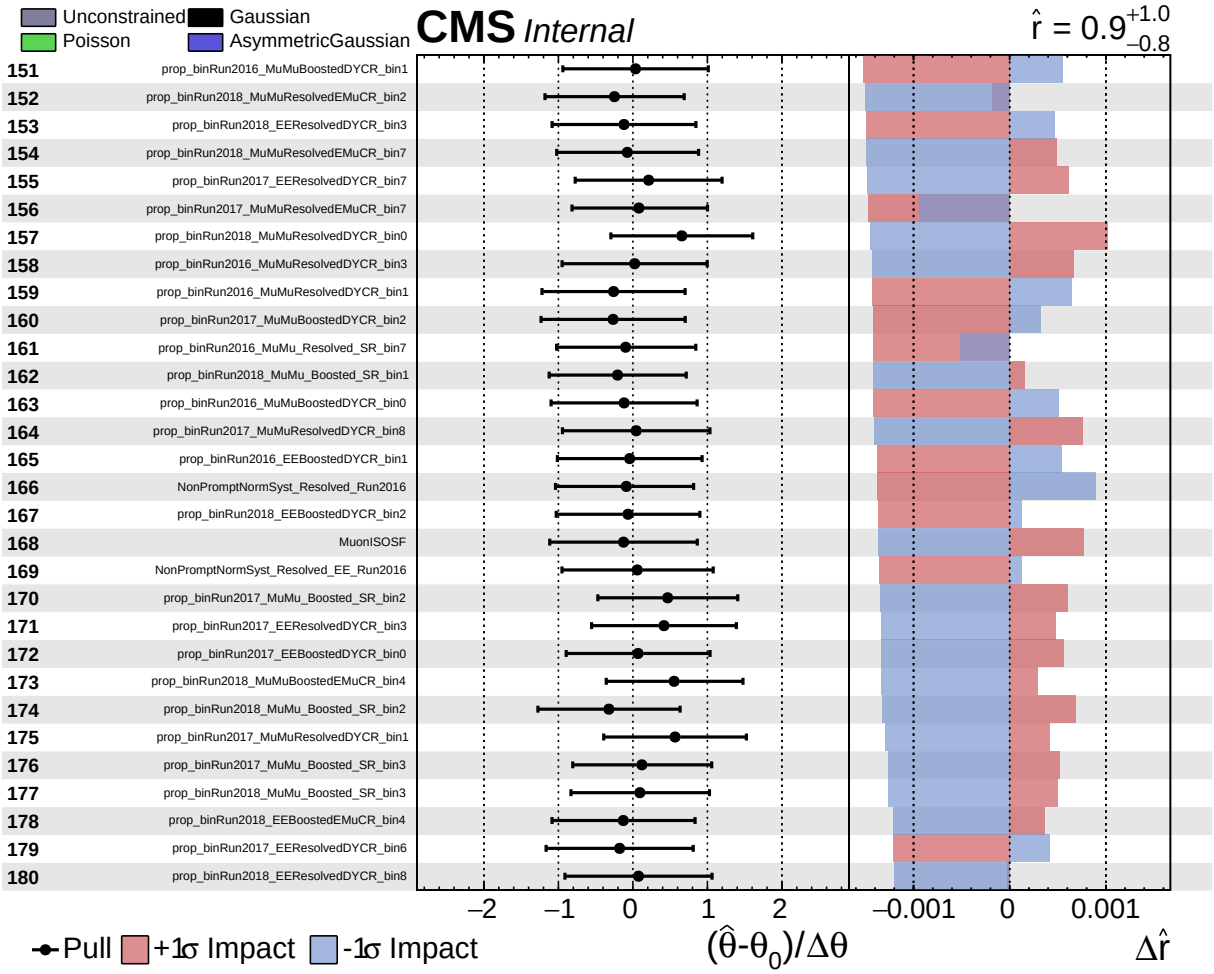

Figure 155: The impact and the pull of the nuisance paremeters in $\mu\mu$ channel for $(m_{W_R}, m_N) = (5000, 3000)$ GeV signal (page 5 out of 6).

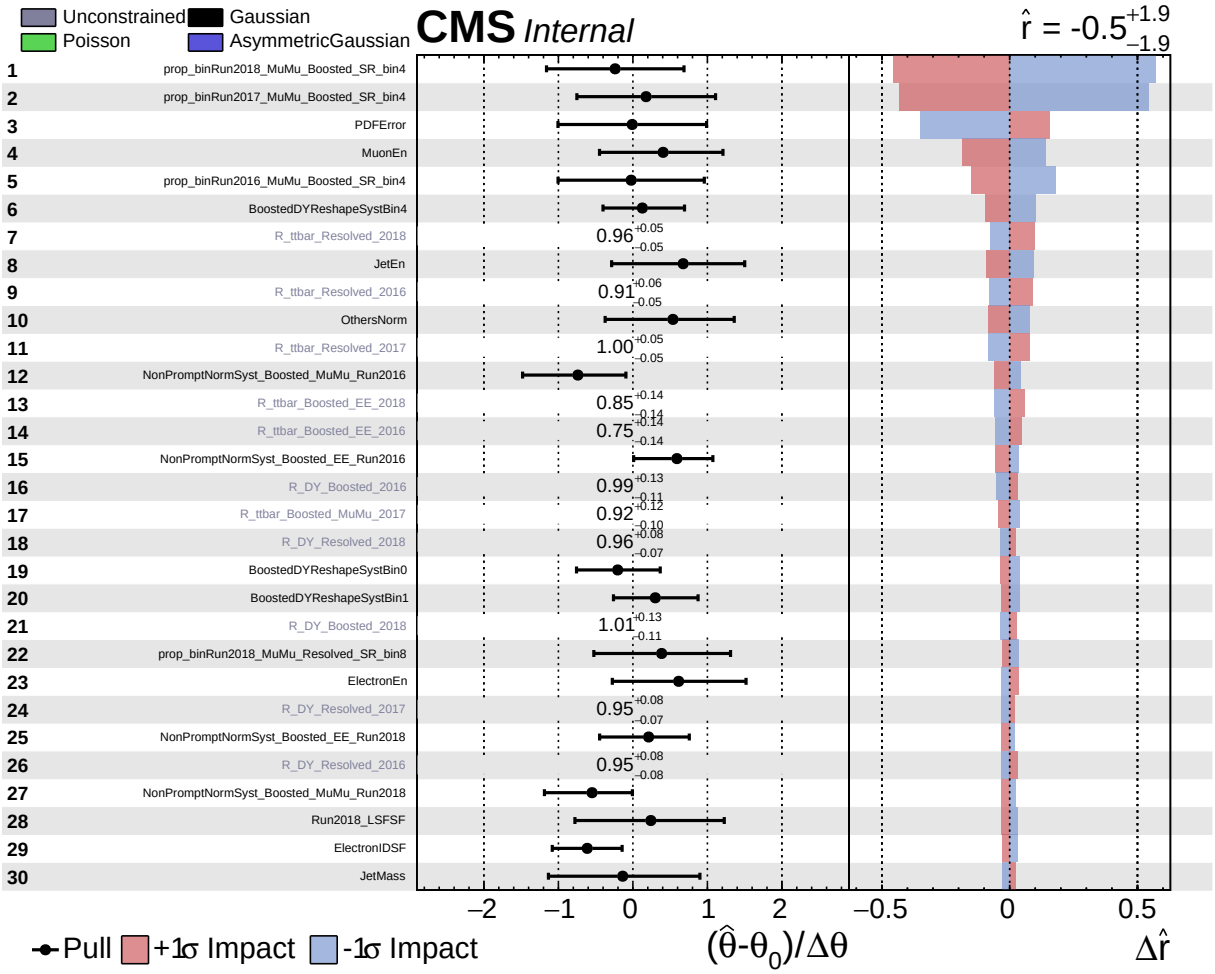

Figure 156: The impact and the pull of the nuisance paremeters in $\mu\mu$ channel for $(m_{W_R}, m_N) = (5000, 200)$ GeV signal (page 0 out of 6).

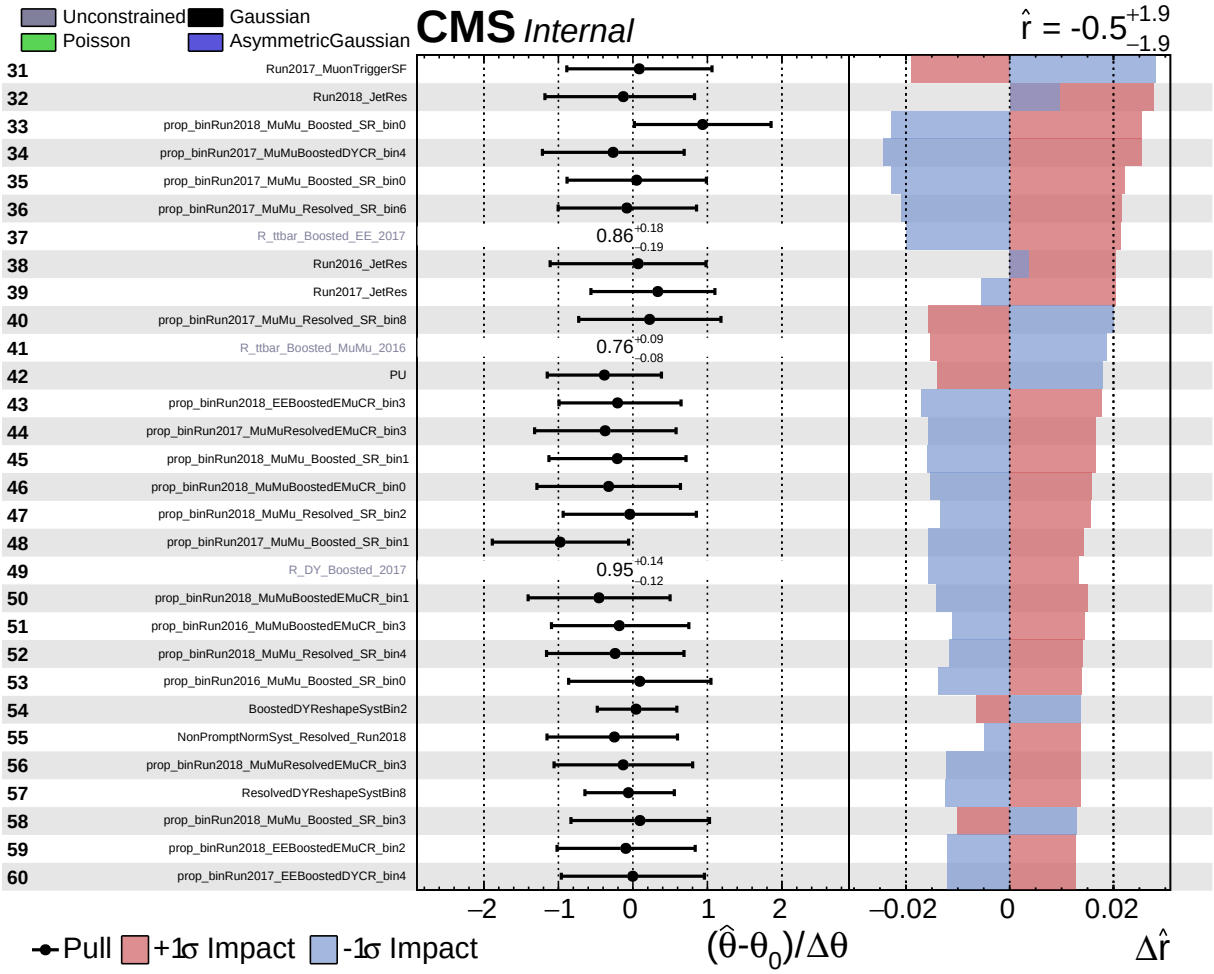

Figure 157: The impact and the pull of the nuisance paremeters in $\mu\mu$ channel for $(m_{W_R}, m_N) = (5000, 200)$ GeV signal (page 1 out of 6).

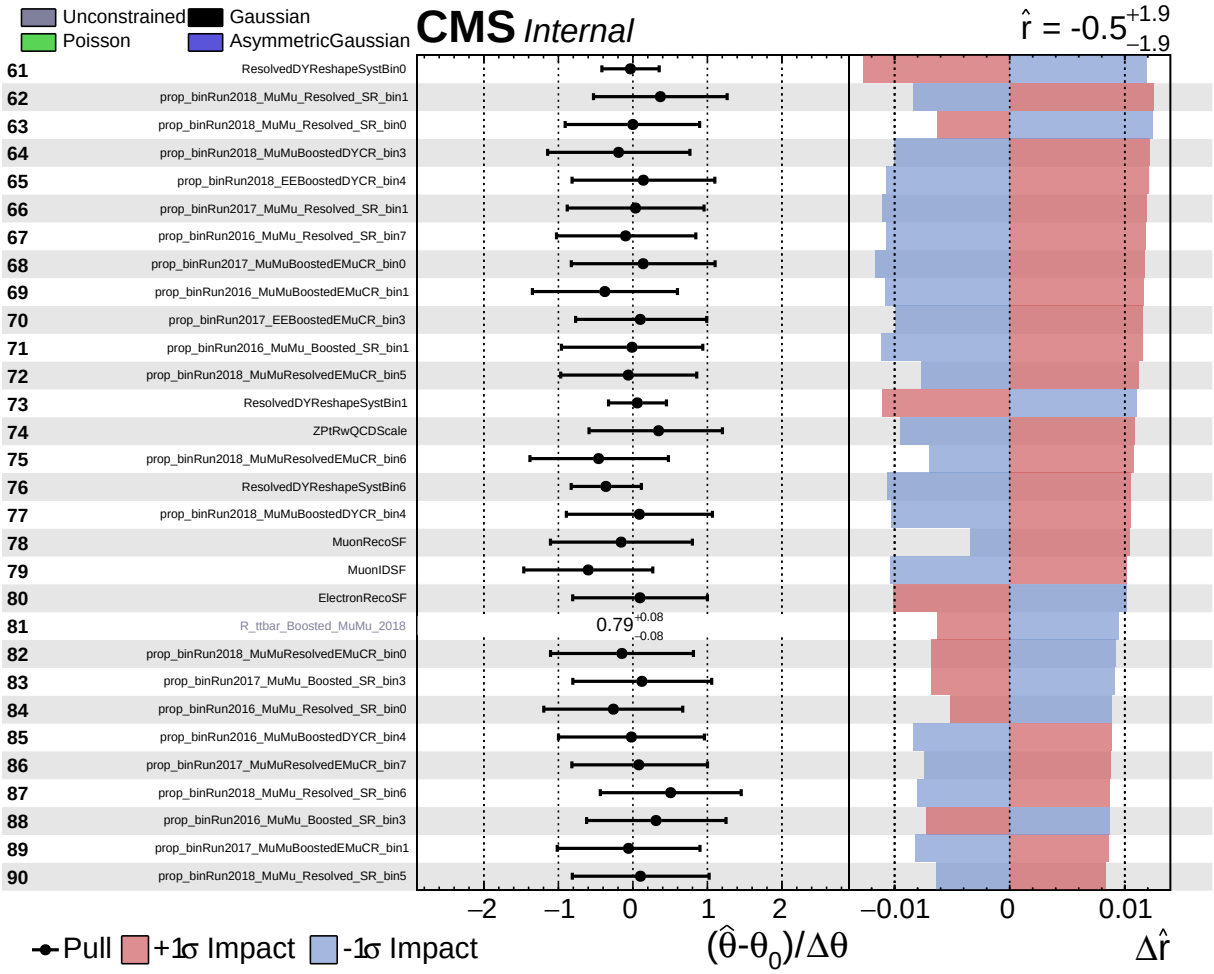

Figure 158: The impact and the pull of the nuisance paremeters in $\mu\mu$ channel for $(m_{W_R}, m_N) = (5000, 200)$ GeV signal (page 2 out of 6).

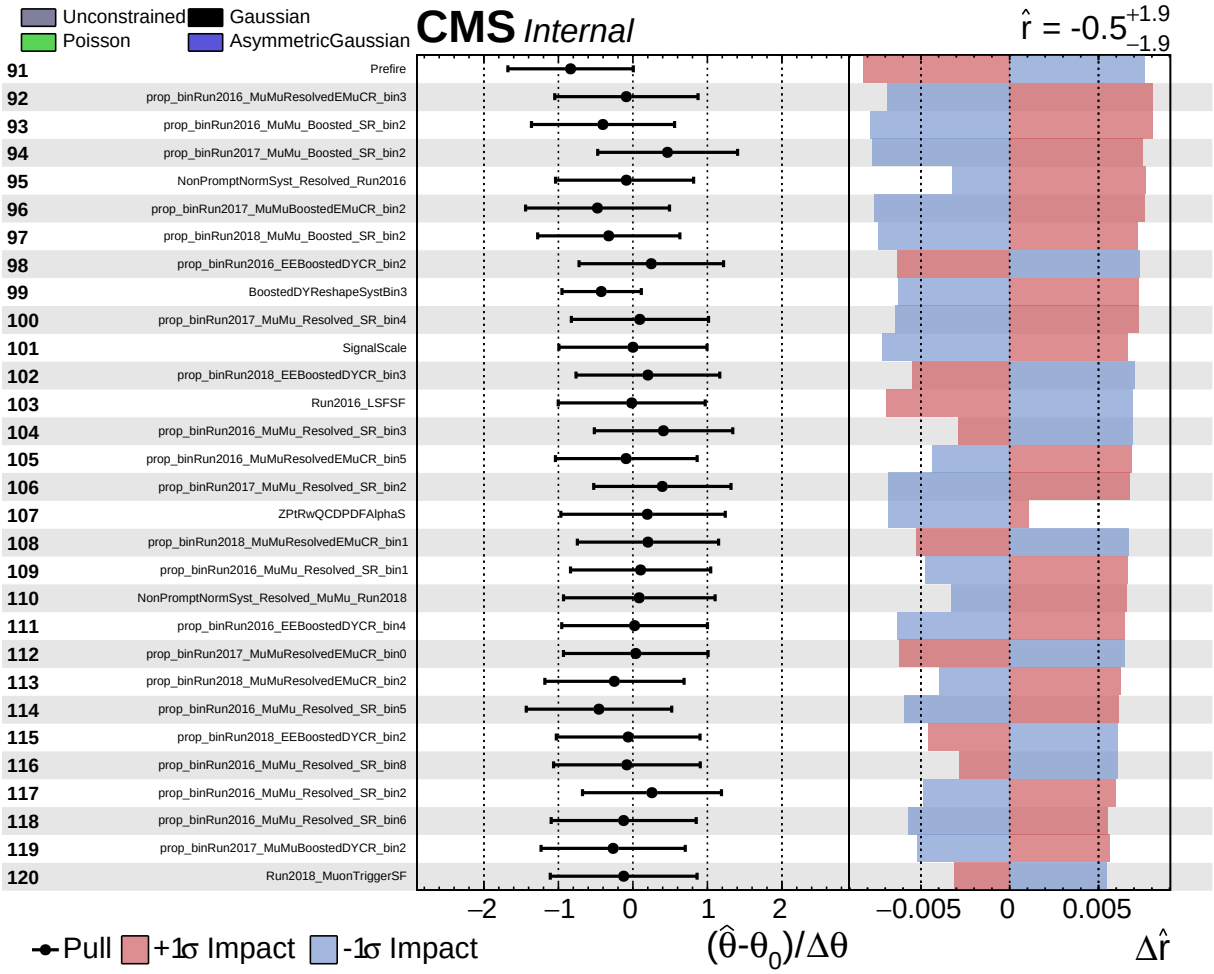

Figure 159: The impact and the pull of the nuisance paremeters in $\mu\mu$ channel for $(m_{W_R}, m_N) = (5000, 200)$ GeV signal (page 3 out of 6).

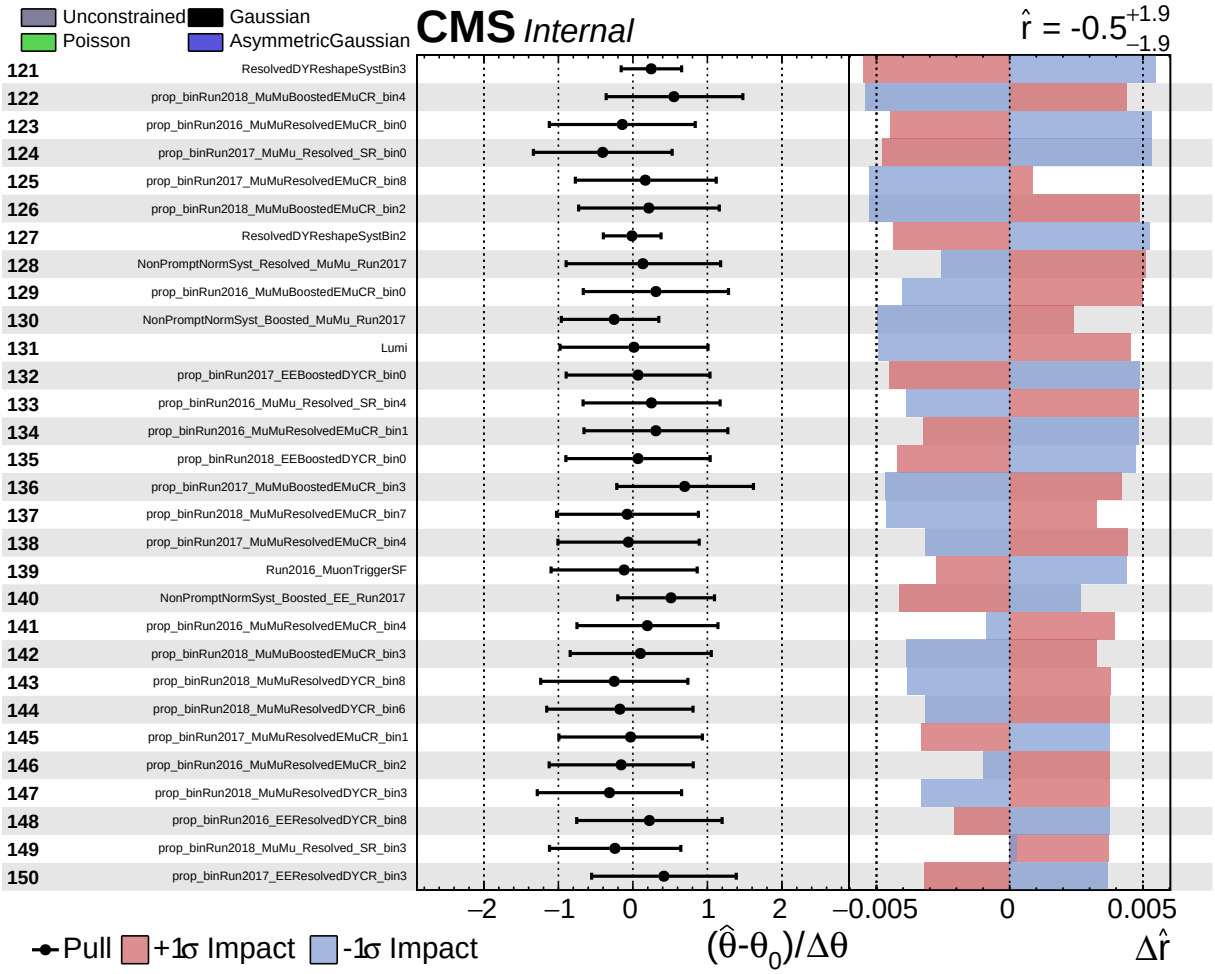

Figure 160: The impact and the pull of the nuisance paremeters in $\mu\mu$ channel for $(m_{W_R}, m_N) = (5000, 200)$ GeV signal (page 4 out of 6).

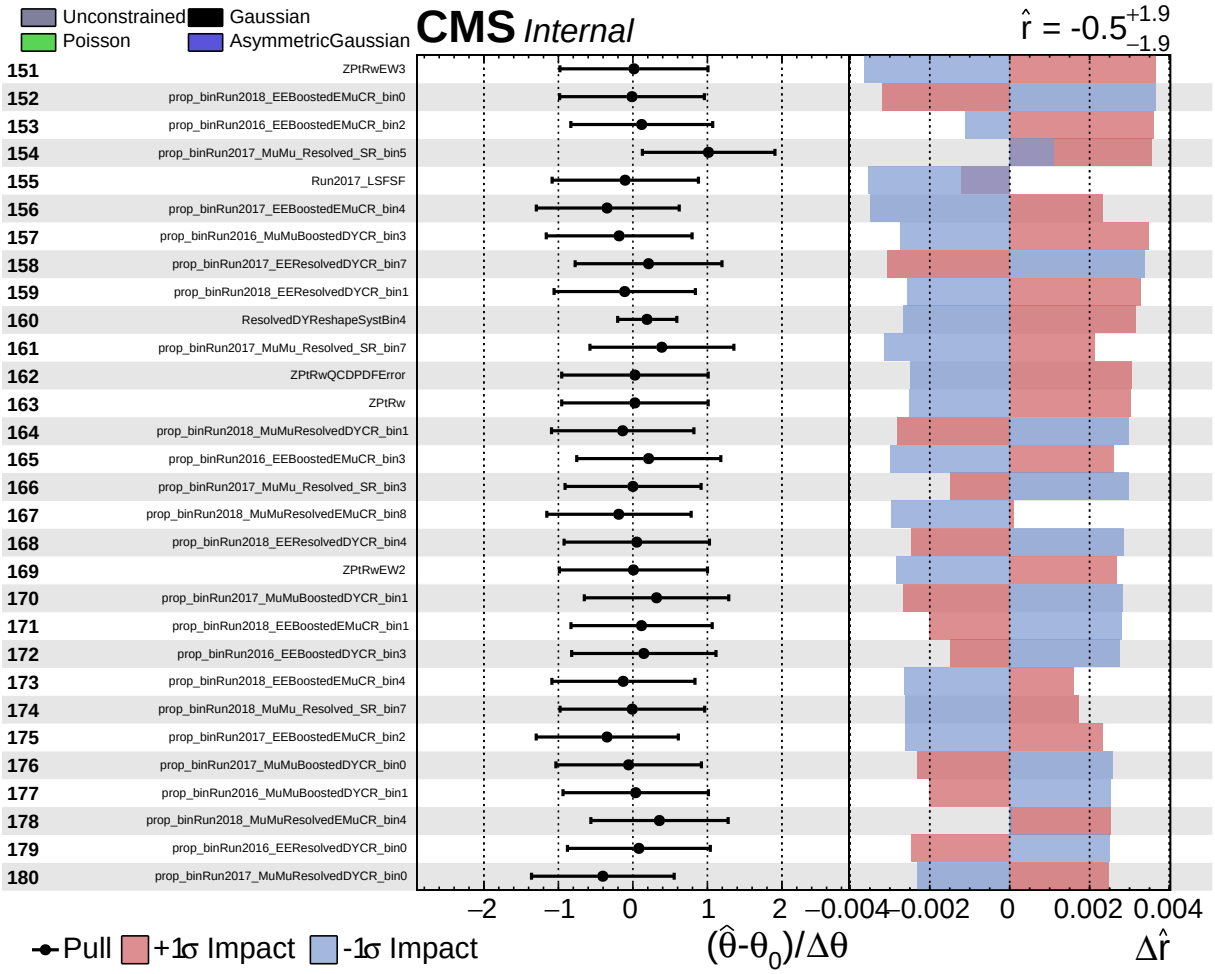

Figure 161: The impact and the pull of the nuisance paremeters in $\mu\mu$ channel for $(m_{W_R}, m_N) = (5000, 200)$ GeV signal (page 5 out of 6).

O The event information of high-mass events

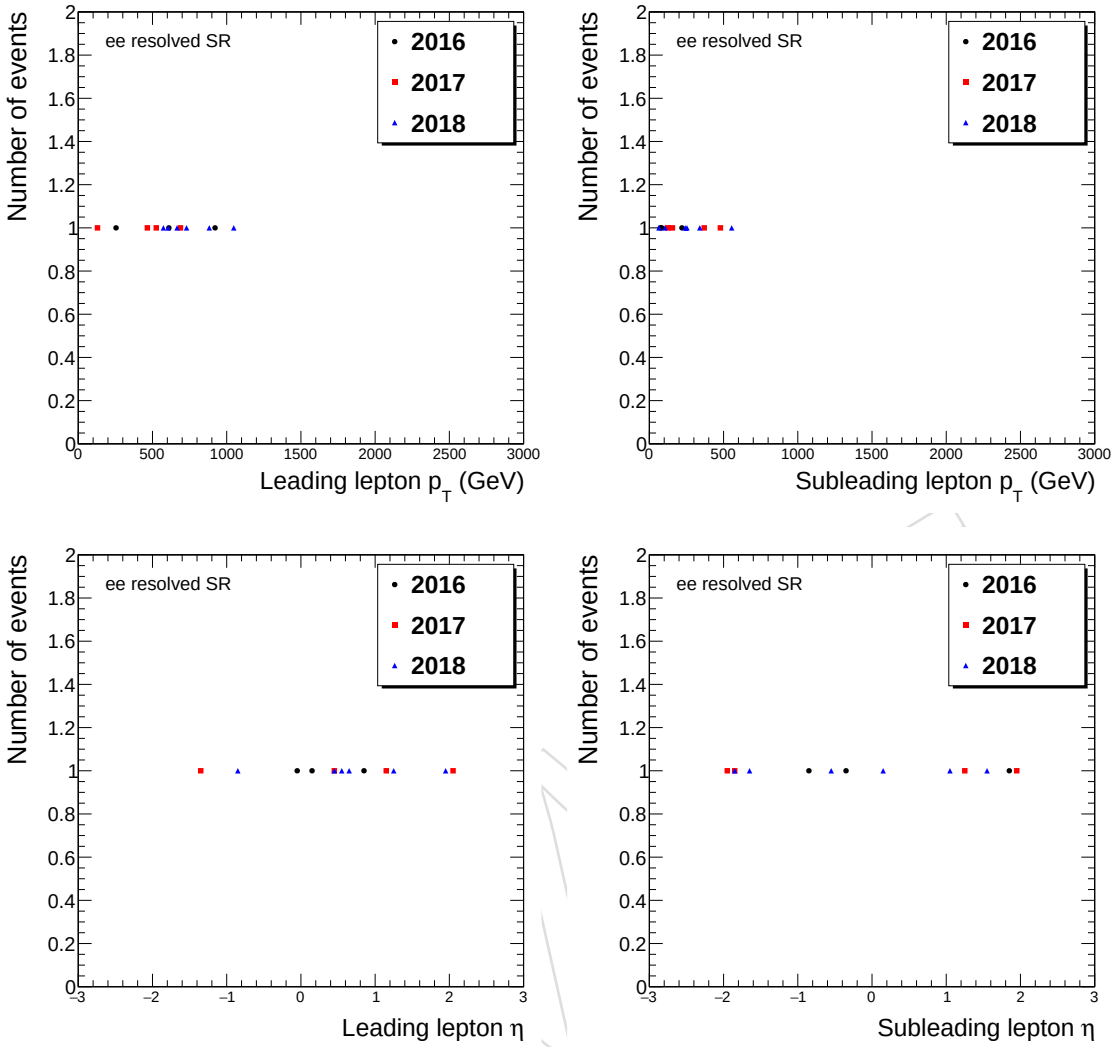

Figure 162: Lepton distributions of the high-mass dielectron data events in the resolved SR.

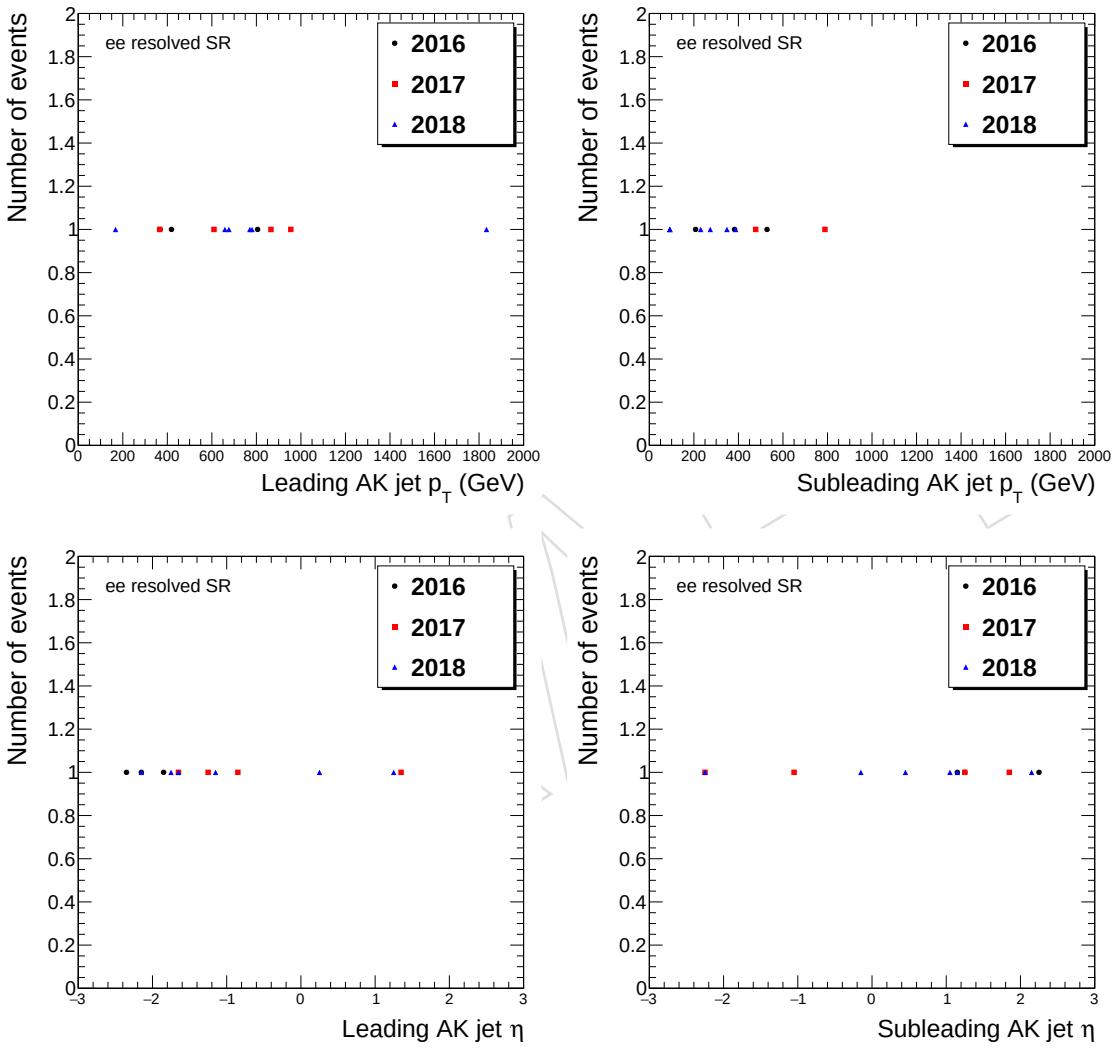

Figure 163: AK4 jet distributions of the high-mass dielectron data events in the resolved SR.

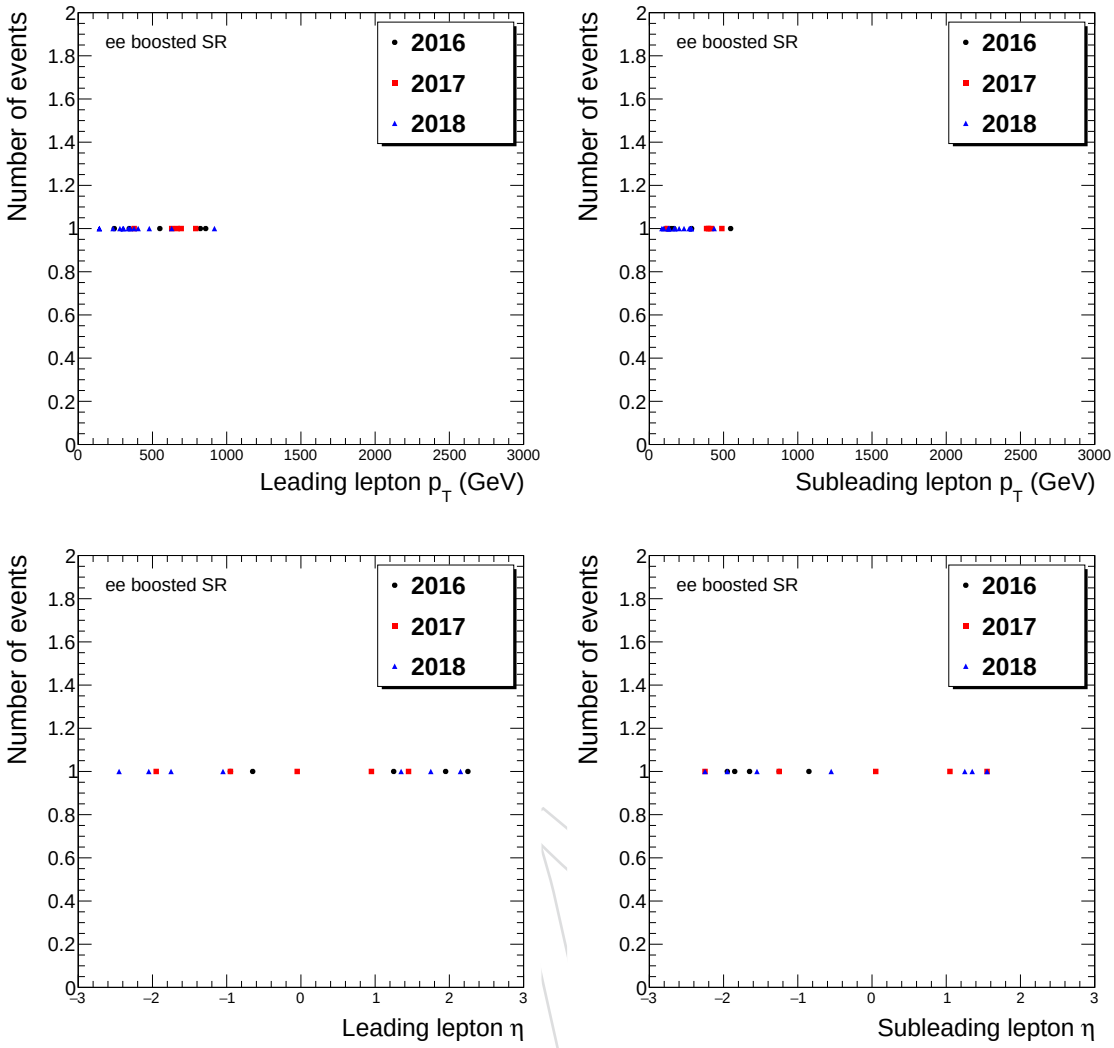

Figure 164: Lepton distributions of the high-mass dielectron data events in the Boosted SR.

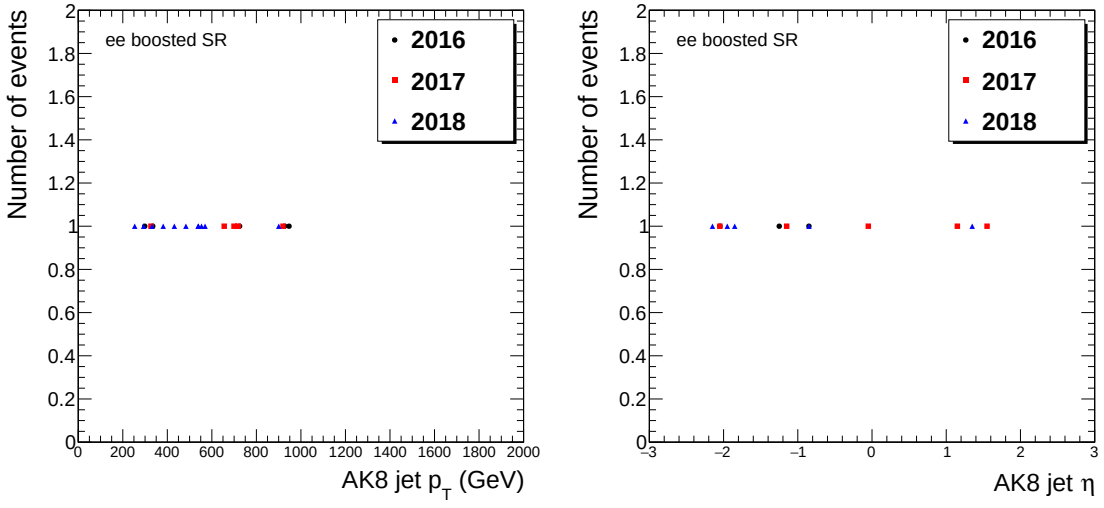

Figure 165: AK8 jet distributions of the high-mass dielectron data events in the Boosted SR.

Table 58: The object information of the resolved dielectron event in Run2016, (RunNumber, LumiSection, EventNumber) = (276935:118:94793071).

Object	p_{T} (GeV)	η	ϕ	mass (GeV)
Electron	610.39	-0.01	0.75	-0.00
Electron	83.50	-0.82	-1.87	-0.00
AK4	418.38	-2.39	-3.09	21.73
AK4	382.96	1.24	-1.67	39.57
$m(\ell\ell\mathrm{jj})$		3305.95 GeV		

Table 59: The object information of the resolved dielectron event in Run2016, (RunNumber, LumiSection, EventNumber) = (278406:329:470624728).

Object	p_{T} (GeV)	η	ϕ	mass (GeV)
Electron	921.68	0.18	1.06	-0.00
Electron	73.89	1.82	-1.96	0.00
AK4	805.76	-1.88	-1.57	47.71
AK4	528.99	1.18	3.08	33.32
$m(\ell\ell\mathrm{jj})$		4605.65 GeV		

Table 60: The object information of the resolved dielectron event in Run2016, (RunNumber, LumiSection, EventNumber) = (283359:19:28630266).

Object	p_{T} (GeV)	η	ϕ	mass (GeV)
Electron	254.88	0.87	-0.56	0.00
Electron	219.27	-0.33	1.16	0.00
AK4	367.47	-2.18	-2.43	40.03
AK4	207.21	2.29	1.56	15.82
$m(\ell\ell\mathrm{jj})$		3243.88 GeV		

Table 61: The object information of the boosted dielectron event in Run2016, (RunNumber, LumiSection, EventNumber) = (277096:1039:1850830067).

Object	p_{T} (GeV)	η	ϕ	mass (GeV)
Electron	343.80	2.23	-2.07	0.00
Electron	165.35	-1.65	1.73	0.00
AK8	298.36	-1.70	1.57	105.36
$m(\ell\ell\mathrm{jj})$		2332.55 GeV		

Table 62: The object information of the boosted dielectron event in Run2016, (RunNumber, LumiSection, EventNumber) = (278803:9:12981701).

Object	p_{T} (GeV)	η	ϕ	mass (GeV)
Electron	858.42	-0.94	-2.02	0.00
Electron	547.38	-0.83	1.31	-0.00
AK8	946.23	-0.81	1.17	265.58
$m(\ell\ell\mathrm{jj})$		1844.82 GeV		

Table 63: The object information of the boosted dielectron event in Run2016, (RunNumber, LumiSection, EventNumber) = (280385:1329:2495669340).

Object	p_{T} (GeV)	η	ϕ	mass (GeV)
Electron	822.09	-0.68	-1.09	-0.00
Electron	284.88	-1.26	2.25	-0.00
AK8	926.18	-1.23	2.09	207.16
$m(\ell\ell\mathrm{jj})$		1828.66 GeV		

Table 64: The object information of the boosted dielectron event in Run2016, (RunNumber, LumiSection, EventNumber) = (278820:375:671036081).

Object	p_{T} (GeV)	η	ϕ	mass (GeV)
Electron	242.71	1.96	-1.30	0.00
Electron	148.32	-1.93	1.98	0.00
AK8	334.31	-2.08	1.89	75.16
$m(\ell\ell\mathrm{jj})$		2192.35 GeV		

Table 65: The object information of the boosted dielectron event in Run2016, (RunNumber, LumiSection, EventNumber) = (281707:960:1568286511).

Object	p_{T} (GeV)	η	ϕ	mass (GeV)
Electron	549.08	1.25	-1.36	0.00
Electron	113.00	-1.87	1.85	-0.00
AK8	724.10	-1.63	1.85	116.08
$m(\ell\ell\mathrm{jj})$		2809.31 GeV		

Table 66: The object information of the resolved dielectron event in Run2017, (RunNumber, LumiSection, EventNumber) = (297485:217:372476529).

Object	p_{T} (GeV)	η	ϕ	mass (GeV)
Electron	129.70	2.05	1.41	0.00
Electron	123.82	-1.87	2.22	0.00
AK4	954.73	-1.25	-1.84	76.15
AK4	788.73	1.24	1.41	35.30
$m(\ell\ell\mathrm{jj})$		4204.11 GeV		

Table 67: The object information of the resolved dielectron event in Run2017, (RunNumber, LumiSection, EventNumber) = (297425:6:9086596).

Object	p_{T} (GeV)	η	ϕ	mass (GeV)
Electron	525.60	1.14	-2.01	0.00
Electron	478.68	1.95	1.71	0.00
AK4	365.72	-1.69	-0.52	49.35
AK4	191.60	-1.05	1.66	21.02
$m(\ell\ell\mathrm{jj})$		3769.68 GeV		

Table 68: The object information of the resolved dielectron event in Run2017, (RunNumber, LumiSection, EventNumber) = (305405:174:315138920).

Object	p_{T} (GeV)	η	ϕ	mass (GeV)
Electron	465.67	0.42	2.51	0.00
Electron	369.92	1.26	-0.98	0.00
AK4	609.02	-0.85	0.06	49.32
AK4	477.72	-2.23	3.07	34.77
$m(\ell\ell\mathrm{jj})$		3810.96 GeV		

Table 69: The object information of the resolved dielectron event in Run2017, (RunNumber, LumiSection, EventNumber) = (305204:890:1329763077).

Object	p_{T} (GeV)	η	ϕ	mass (GeV)
Electron	688.34	-1.36	-3.11	-0.00
Electron	155.08	-1.99	-1.06	-0.00
AK4	865.33	1.35	0.13	56.30
AK4	191.61	1.82	2.52	19.11
$m(\ell\ell\mathrm{jj})$		4383.5 GeV		

Table 70: The object information of the boosted dielectron event in Run2017, (RunNumber, LumiSection, EventNumber) = (300157:282:302943176).

Object	p_{T} (GeV)	η	ϕ	mass (GeV)
Electron	376.50	1.41	1.93	0.00
Electron	119.80	-2.26	-0.89	0.00
AK8	326.63	-2.07	-0.88	94.53
$m(\ell\ell\mathrm{jj})$		2058.61 GeV		

Table 71: The object information of the boosted dielectron event in Run2017, (RunNumber, LumiSection, EventNumber) = (304144:1866:2724236232).

Object	p_{T} (GeV)	η	ϕ	mass (GeV)
Electron	629.93	-0.99	-0.54	-0.00
Electron	385.41	1.09	2.35	-0.00
AK8	655.98	1.16	2.26	129.78
$m(\ell\ell\mathrm{jj})$		2096.99 GeV		

Table 72: The object information of the boosted dielectron event in Run2017, (RunNumber, LumiSection, EventNumber) = (304777:382:640645351).

Object	p_{T} (GeV)	η	ϕ	mass (GeV)
Electron	791.15	-0.03	-0.98	0.00
Electron	488.53	1.59	2.08	0.00
AK8	919.74	1.55	2.15	109.18
$m(\ell\ell\mathrm{jj})$		2270.07 GeV		

Table 73: The object information of the boosted dielectron event in Run2017, (RunNumber, LumiSection, EventNumber) = (304169:1202:1656789780).

Object	p_{T} (GeV)	η	ϕ	mass (GeV)
Electron	665.40	-1.91	-2.39	0.00
Electron	398.20	0.06	0.81	0.00
AK8	699.81	-0.01	0.87	174.42
$m(\ell\ell\mathrm{jj})$		2064.2 GeV		

Table 74: The object information of the boosted dielectron event in Run2017, (RunNumber, LumiSection, EventNumber) = (305898:128:142142616).

Object	p_{T} (GeV)	η	ϕ	mass (GeV)
Electron	693.07	0.92	-2.95	-0.00
Electron	417.30	-1.26	0.12	0.00
AK8	718.63	-1.20	0.13	99.30
$m(\ell\ell\mathrm{jj})$		2279.41 GeV		

Table 75: The object information of the resolved dielectron event in Run2018, (RunNumber, LumiSection, EventNumber) = (319993:883:1377163764).

Object	p_{T} (GeV)	η	ϕ	mass (GeV)
Electron	573.64	1.27	0.13	0.00
Electron	554.86	-1.82	-2.88	0.00
AK4	167.34	1.30	3.11	23.09
AK4	92.00	0.40	-1.77	12.32
$m(\ell\ell\mathrm{jj})$		3266.96 GeV		

Table 76: The object information of the resolved dielectron event in Run2018, (RunNumber, LumiSection, EventNumber) = (321305:1850:2884966010).

Object	p_{T} (GeV)	η	ϕ	mass (GeV)
Electron	882.61	0.52	-1.36	0.00
Electron	253.76	0.15	-0.45	0.00
AK4	770.45	-2.12	1.90	56.90
AK4	230.26	-0.19	2.35	28.44
$m(\ell\ell\mathrm{jj})$		3926.55 GeV		

Table 77: The object information of the resolved dielectron event in Run2018, (RunNumber, LumiSection, EventNumber) = (321475:890:1422339039).

Object	p_T (GeV)	η	ϕ	mass (GeV)
Electron	665.69	0.46	1.74	0.00
Electron	241.20	1.05	-2.65	0.00
AK4	676.91	-1.74	-0.41	27.94
AK4	387.19	2.14	-2.28	43.29
$m(\ell\ell$jj$)$	4773.57 GeV			

Table 78: The object information of the resolved dielectron event in Run2018, (RunNumber, LumiSection, EventNumber) = (323790:269:433645417).

Object	p_T (GeV)	η	ϕ	mass (GeV)
Electron	729.44	1.97	-1.06	-0.00
Electron	339.69	-1.65	2.46	0.00
AK4	658.76	-1.18	2.43	51.94
AK4	348.05	-2.28	0.12	22.99
$m(\ell\ell$jj$)$	6421.24 GeV			

Table 79: The object information of the resolved dielectron event in Run2018, (RunNumber, LumiSection, EventNumber) = (324420:57:119465165).

Object	p_T (GeV)	η	ϕ	mass (GeV)
Electron	1047.76	-0.87	-2.71	0.00
Electron	64.37	1.59	2.63	-0.00
AK4	1833.88	0.28	0.37	184.00
AK4	92.09	1.01	-2.75	16.16
$m(\ell\ell$jj$)$	3627.16 GeV			

Table 80: The object information of the resolved dielectron event in Run2018, (RunNumber, LumiSection, EventNumber) = (322106:674:1194162742).

Object	p_T (GeV)	η	ϕ	mass (GeV)
Electron	606.75	0.69	-2.33	0.00
Electron	105.18	-0.54	-0.38	0.00
AK4	780.91	-1.62	1.11	74.29
AK4	273.93	1.14	-2.56	38.94
$m(\ell\ell$jj$)$	3208.2 GeV			

Table 81: The object information of the boosted dielectron event in Run2018, (RunNumber, LumiSection, EventNumber) = (315489:682:368885503).

Object	p_T (GeV)	η	ϕ	mass (GeV)
Electron	479.00	-1.24	-0.41	0.00
Electron	167.12	1.14	2.34	0.00
AK8	553.43	1.29	2.47	105.30
$m(\ell\ell$jj$)$	1965.9 GeV			

Table 82: The object information of the boosted dielectron event in Run2018, (RunNumber, LumiSection, EventNumber) = (317435:62:81453320).

Object	p_{T} (GeV)	η	ϕ	mass (GeV)
Electron	629.82	-1.08	1.17	-0.00
Electron	233.92	1.16	-1.93	0.00
AK8	483.36	1.27	-1.88	80.95
$m(\ell\ell\mathrm{jj})$		1958.8 GeV		

Table 83: The object information of the boosted dielectron event in Run2018, (RunNumber, LumiSection, EventNumber) = (320065:158:256649322).

Object	p_{T} (GeV)	η	ϕ	mass (GeV)
Electron	350.16	2.15	-2.78	-0.00
Electron	134.38	-0.53	0.21	0.00
AK8	431.94	-0.85	0.20	124.29
$m(\ell\ell\mathrm{jj})$		1848.95 GeV		

Table 84: The object information of the boosted dielectron event in Run2018, (RunNumber, LumiSection, EventNumber) = (321414:959:1627087520).

Object	p_{T} (GeV)	η	ϕ	mass (GeV)
Electron	300.34	-1.78	-0.46	-0.00
Electron	84.04	1.76	2.81	0.00
AK8	381.87	2.15	3.08	113.38
$m(\ell\ell\mathrm{jj})$		2474.04 GeV		

Table 85: The object information of the boosted dielectron event in Run2018, (RunNumber, LumiSection, EventNumber) = (321975:333:589214395).

Object	p_{T} (GeV)	η	ϕ	mass (GeV)
Electron	337.26	1.79	1.64	-0.00
Electron	283.56	-1.58	-1.23	-0.00
AK8	433.01	-1.61	-1.18	85.72
$m(\ell\ell\mathrm{jj})$		2156.45 GeV		

Table 86: The object information of the boosted dielectron event in Run2018, (RunNumber, LumiSection, EventNumber) = (325022:177:255237941).

Object	p_{T} (GeV)	η	ϕ	mass (GeV)
Electron	280.02	1.64	2.91	0.00
Electron	127.45	-2.28	-1.12	0.00
AK8	293.27	-2.12	-0.99	116.53
$m(\ell\ell\mathrm{jj})$		1908.08 GeV		

Table 87: The object information of the boosted dielectron event in Run2018, (RunNumber, LumiSection, EventNumber) = (321818:597:1045679555).

Object	p_{T} (GeV)	η	ϕ	mass (GeV)
Electron	375.43	2.26	-0.92	0.00
Electron	200.17	-1.97	2.13	0.00
AK8	331.97	-1.92	2.02	94.40
$m(\ell\ell\mathrm{jj})$		2898.08 GeV		

Table 88: The object information of the boosted dielectron event in Run2018, (RunNumber, LumiSection, EventNumber) = (323474:232:434160282).

Object	p_T (GeV)	η	ϕ	mass (GeV)
Electron	403.41	-1.24	2.71	0.00
Electron	281.55	1.32	-0.26	0.00
AK8	569.19	1.41	-0.38	202.03
$m(\ell\ell$jj$)$		1948.36 GeV		

Table 89: The object information of the boosted dielectron event in Run2018, (RunNumber, LumiSection, EventNumber) = (324878:357:620269034).

Object	p_T (GeV)	η	ϕ	mass (GeV)
Electron	917.49	1.39	-2.45	0.00
Electron	436.74	1.25	0.84	-0.00
AK8	900.70	1.39	0.94	222.96
$m(\ell\ell$jj$)$		1831.3 GeV		

Table 90: The object information of the boosted dielectron event in Run2018, (RunNumber, LumiSection, EventNumber) = (323727:199:371091891).

Object	p_T (GeV)	η	ϕ	mass (GeV)
Electron	142.69	2.27	0.79	0.00
Electron	130.77	-1.78	-1.36	0.00
AK8	538.65	-1.67	-1.43	98.58
$m(\ell\ell$jj$)$		2016.43 GeV		

Table 91: The object information of the boosted dielectron event in Run2018, (RunNumber, LumiSection, EventNumber) = (320934:606:955636539).

Object	p_T (GeV)	η	ϕ	mass (GeV)
Electron	305.14	-2.08	-1.21	0.00
Electron	268.79	1.57	2.31	0.00
AK8	539.07	1.49	2.28	86.70
$m(\ell\ell$jj$)$		2488 GeV		

Table 92: The object information of the boosted dielectron event in Run2018, (RunNumber, LumiSection, EventNumber) = (321122:272:444385409).

Object	p_T (GeV)	η	ϕ	mass (GeV)
Electron	141.87	-2.40	-1.25	-0.00
Electron	96.97	1.74	1.80	0.00
AK8	253.56	2.11	1.73	105.59
$m(\ell\ell$jj$)$		1836.58 GeV		

Table 93: The object information of the boosted dielectron event in Run2018, (RunNumber, LumiSection, EventNumber) = (322118:160:290751203).

Object	p_T (GeV)	η	ϕ	mass (GeV)
Electron	234.32	1.68	1.68	-0.00
Electron	172.58	-1.78	-1.39	-0.00
AK8	433.14	-1.88	-1.63	143.42
$m(\ell\ell$jj$)$		1952.65 GeV		

P The kinematic distributions in the SRs

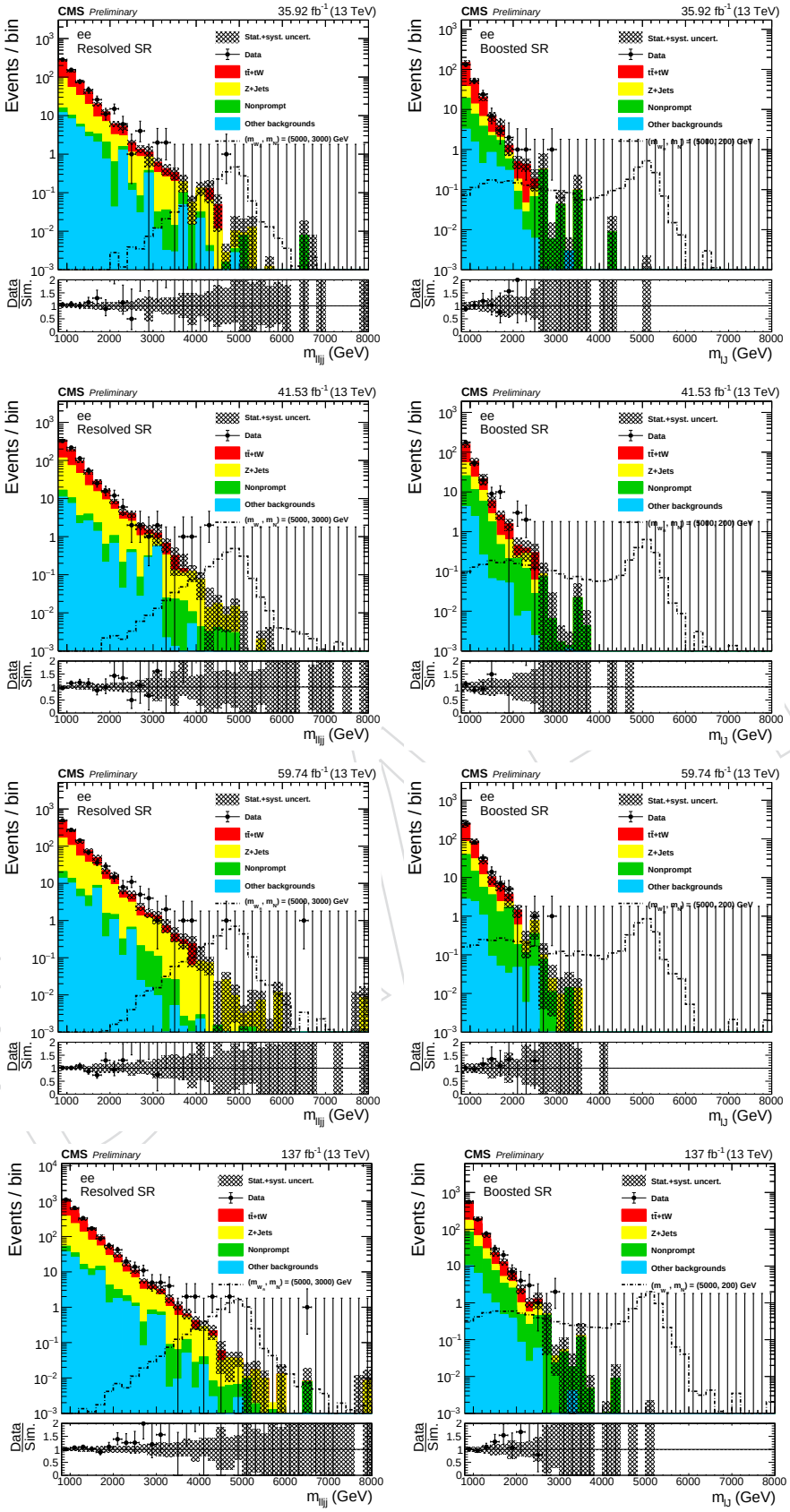

Figure 166: The mass distributions in the dielectron channel.

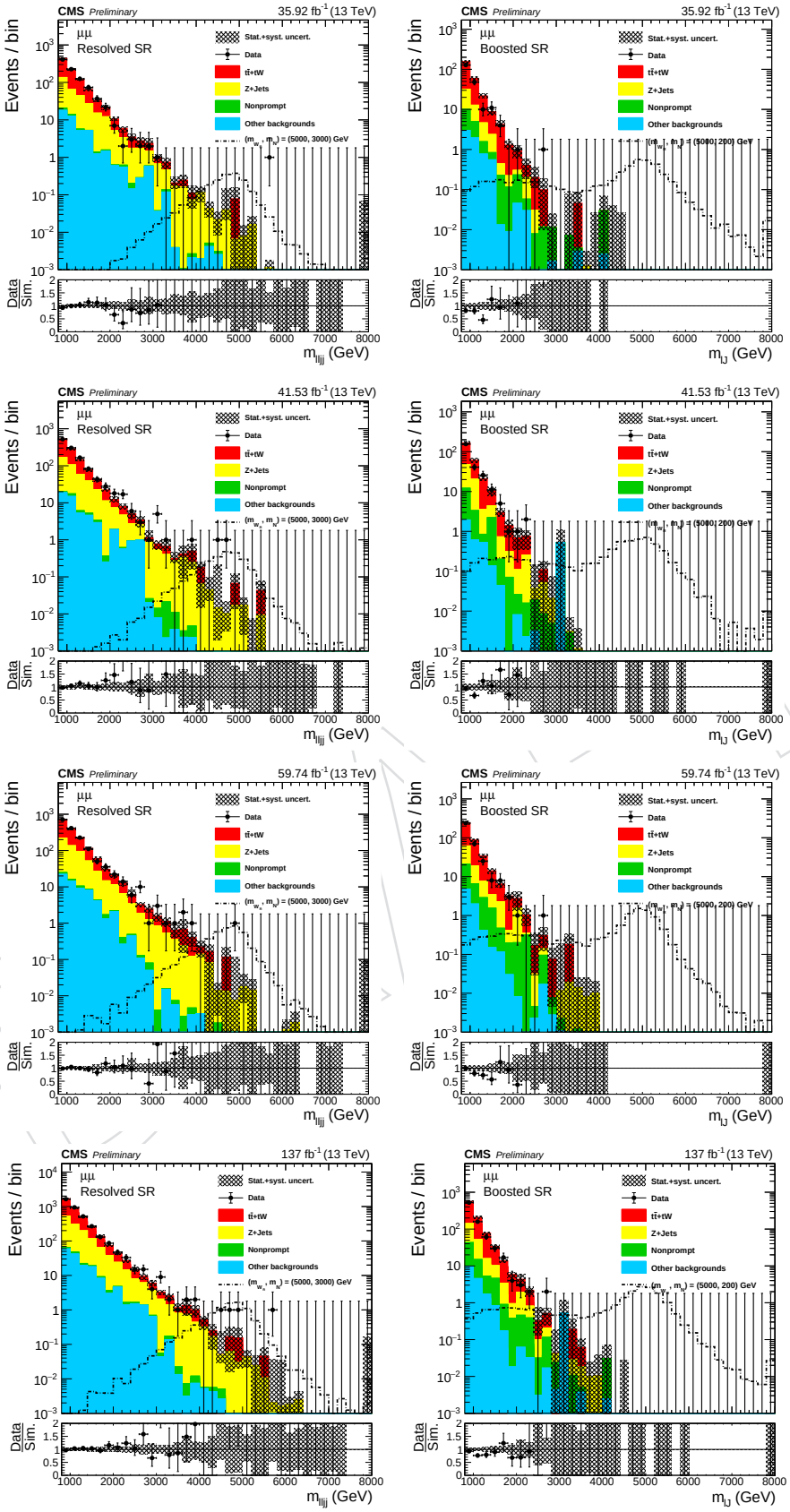

Figure 167: The mass distributions in the dimuon channel.

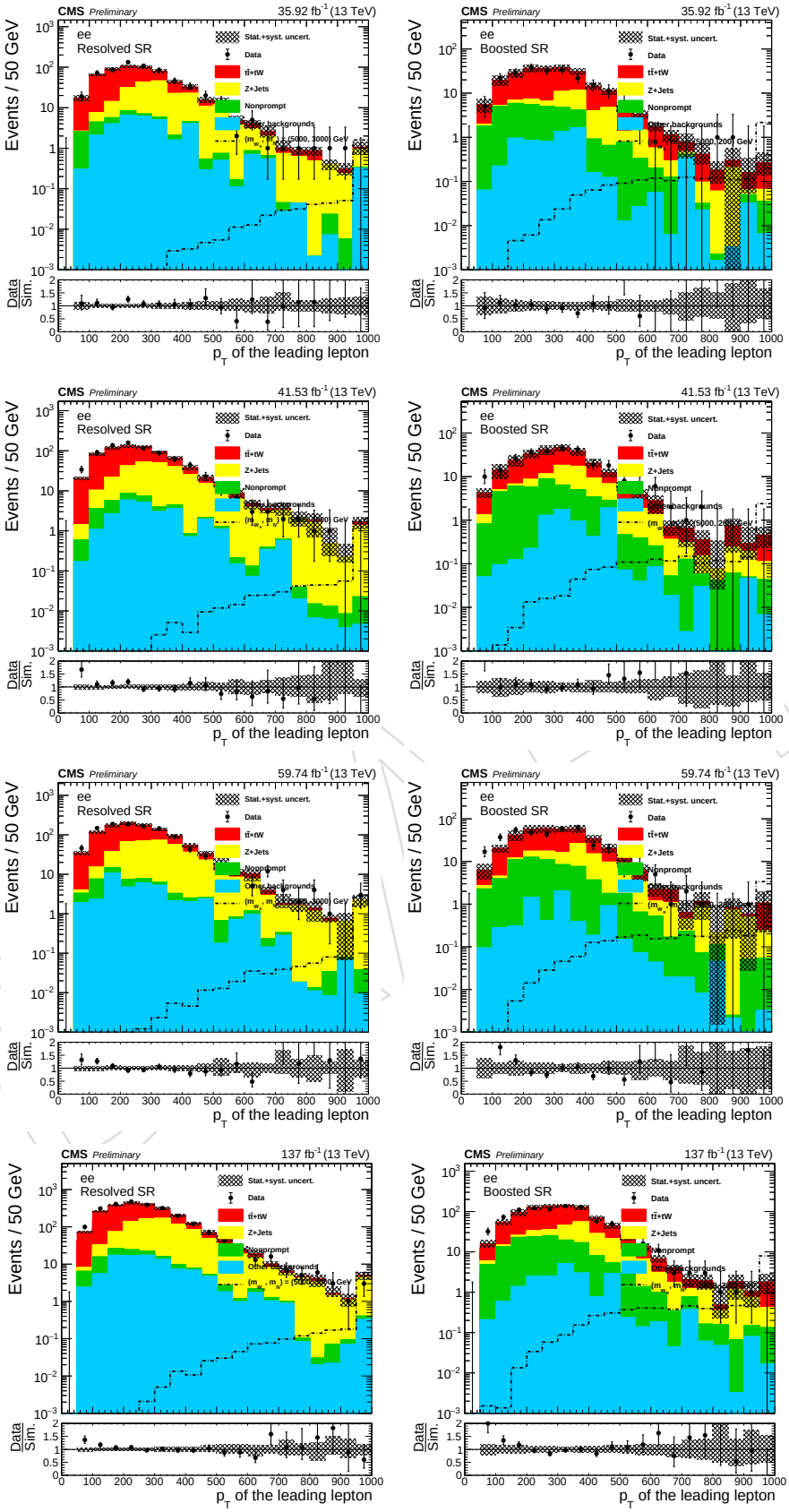

Figure 168: The leading lepton p_{T} distributions in the dielectron channel.

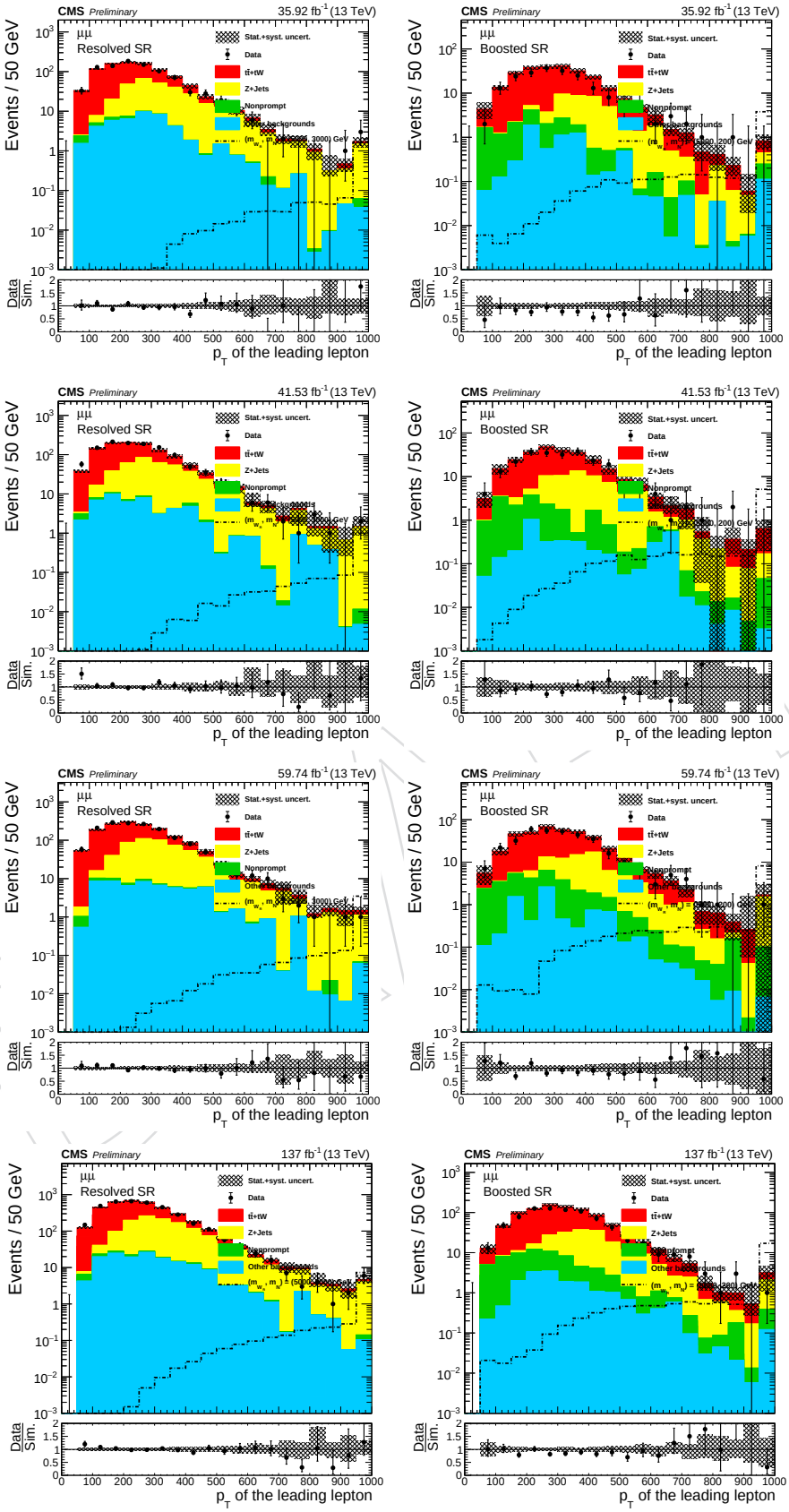

Figure 169: The leading lepton p_{T} distributions in the dimuon channel.

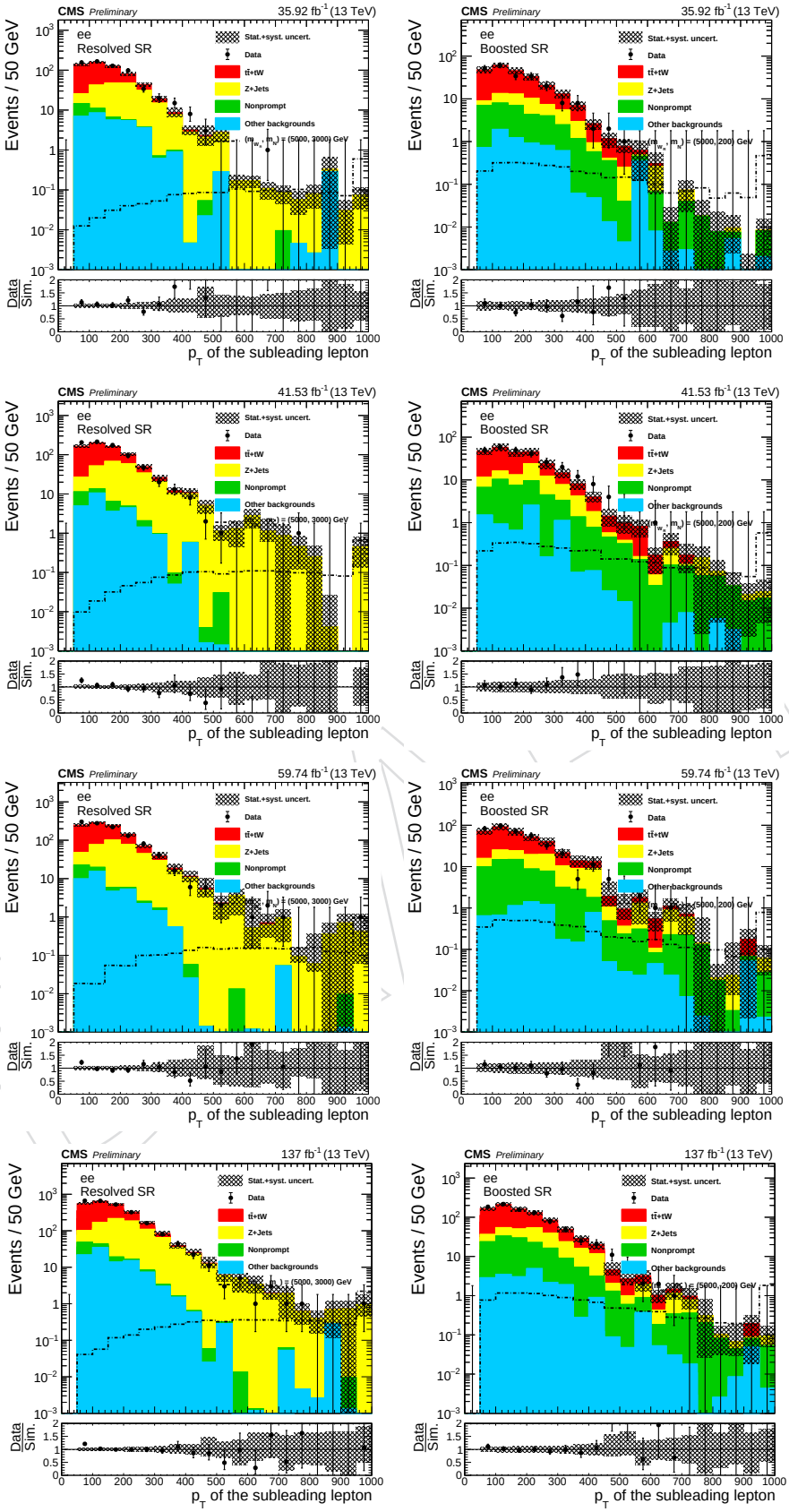

Figure 170: The subleading lepton p_{T} distributions in the dielectron channel.

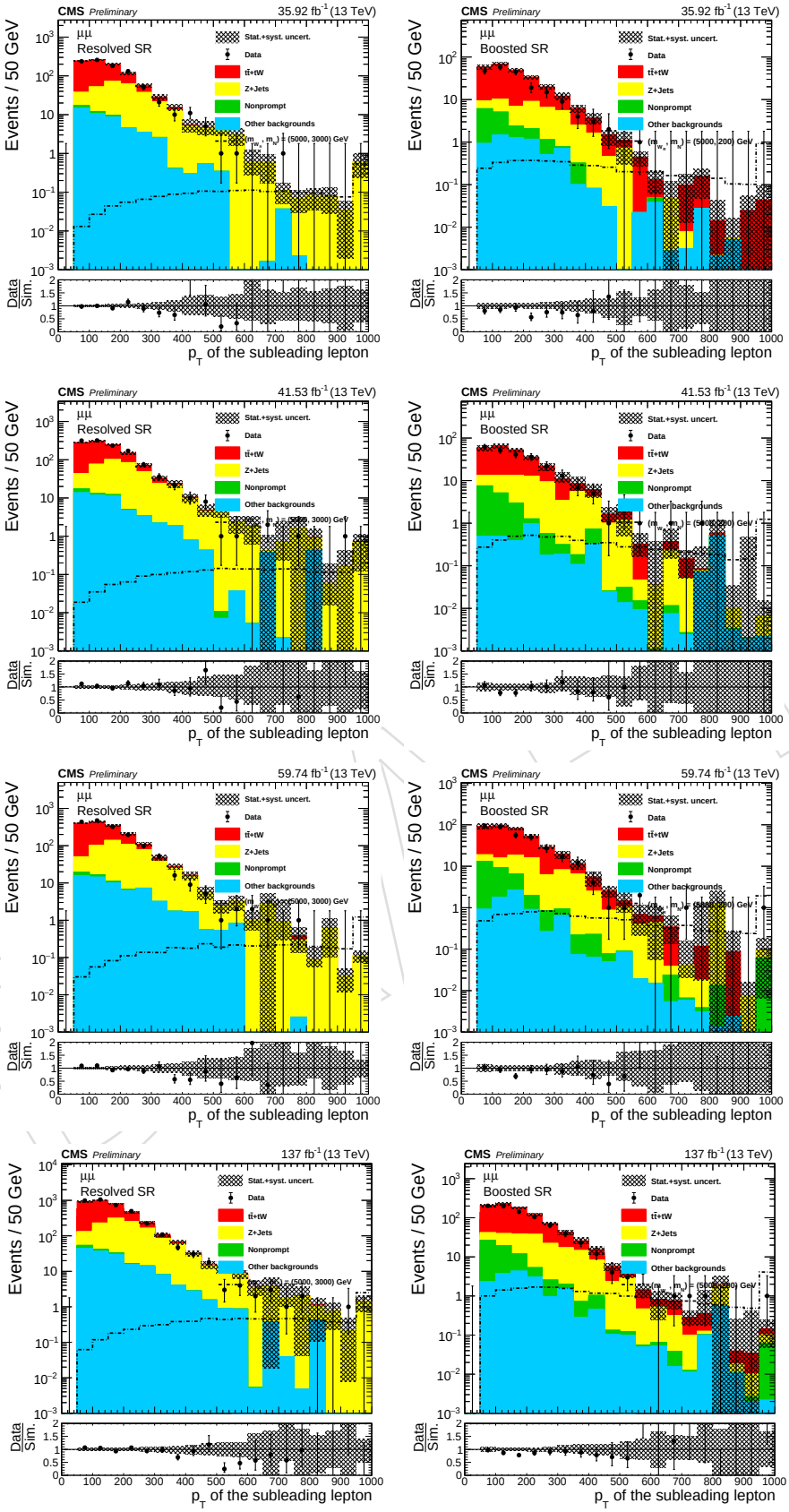

Figure 171: The subleading lepton p_{T} distributions in the dimuon channel.

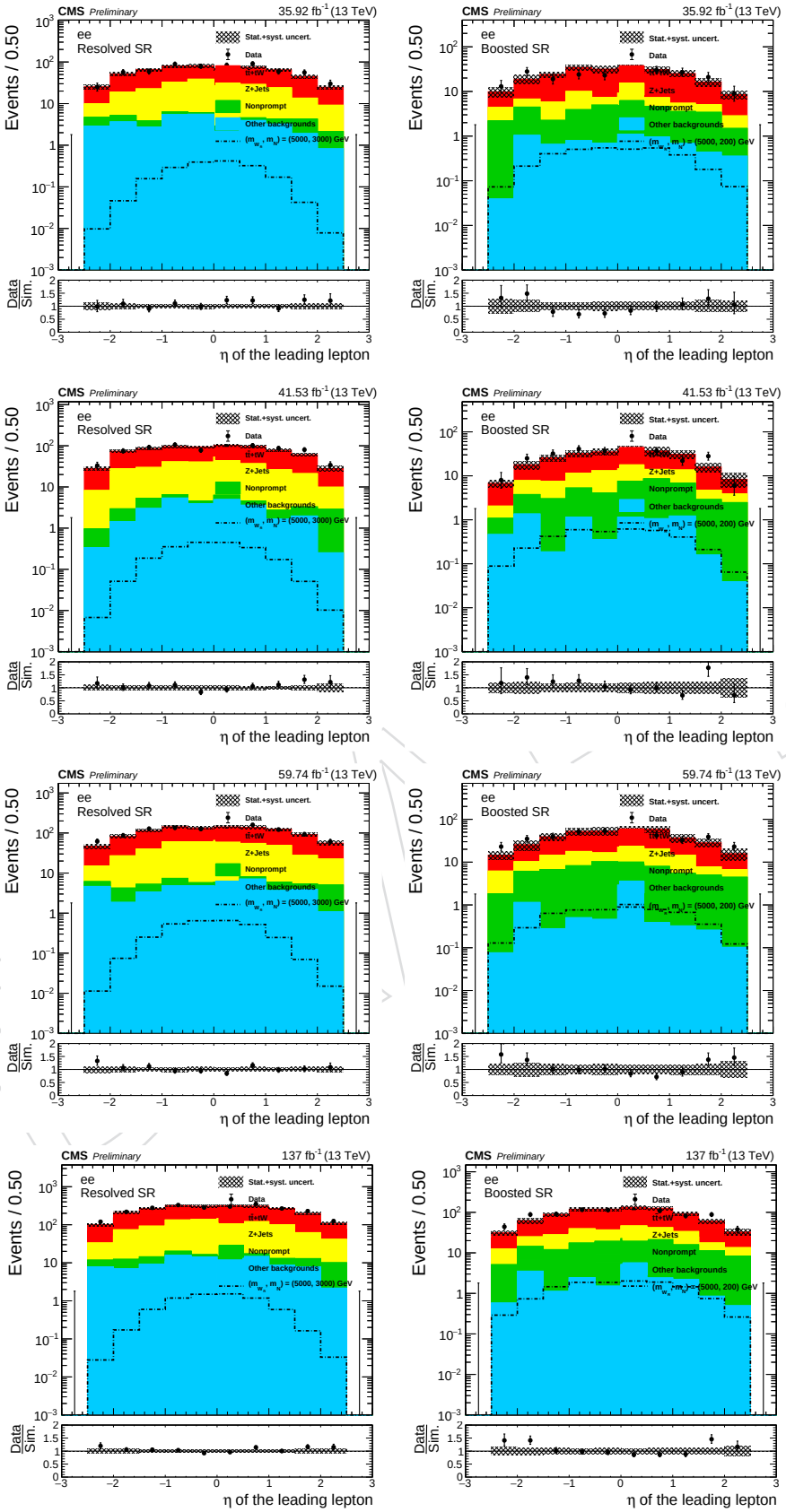

Figure 172: The leading lepton η distributions in the dielectron channel.

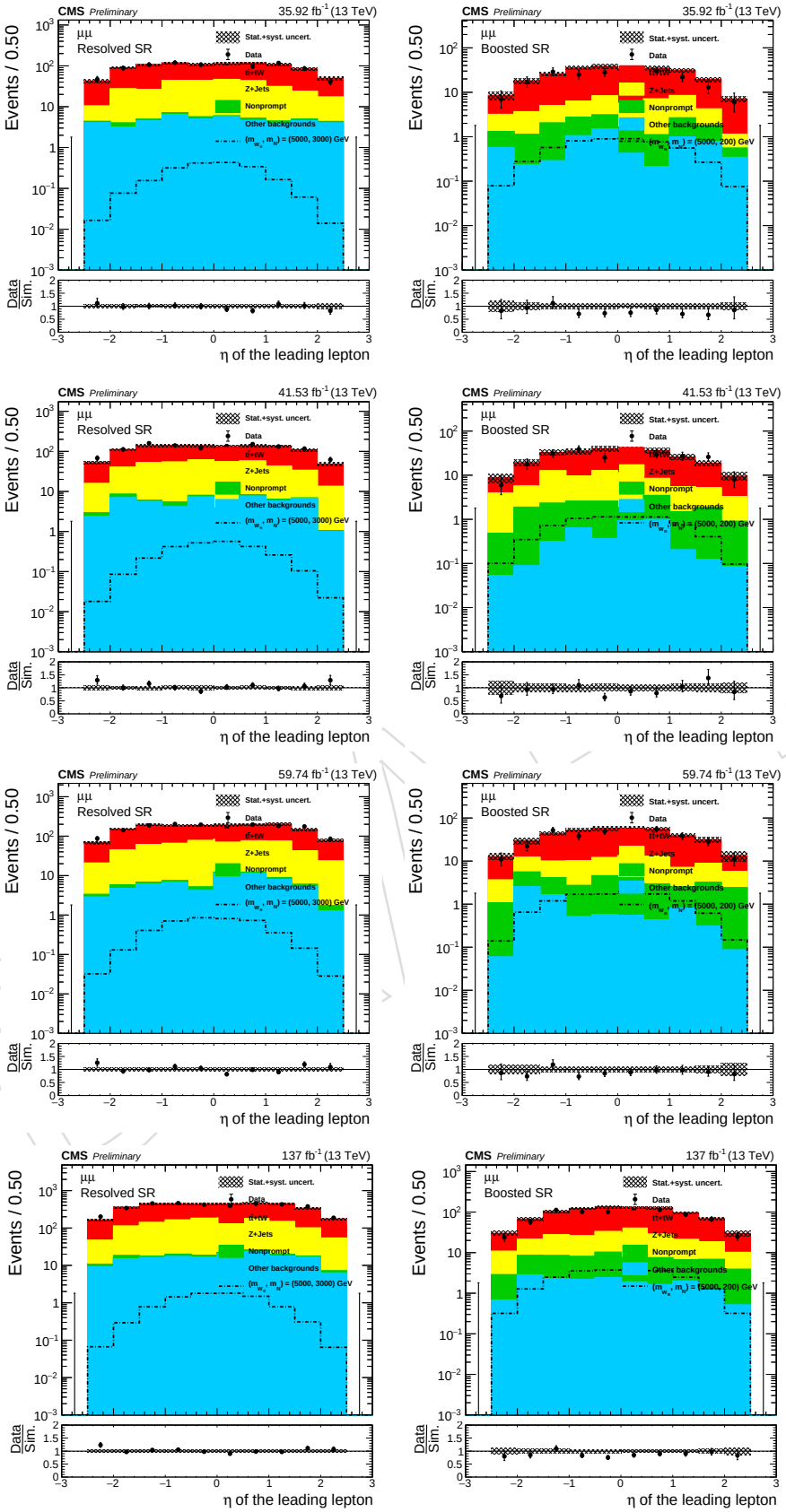

Figure 173: The leading lepton η distributions in the dimuon channel.

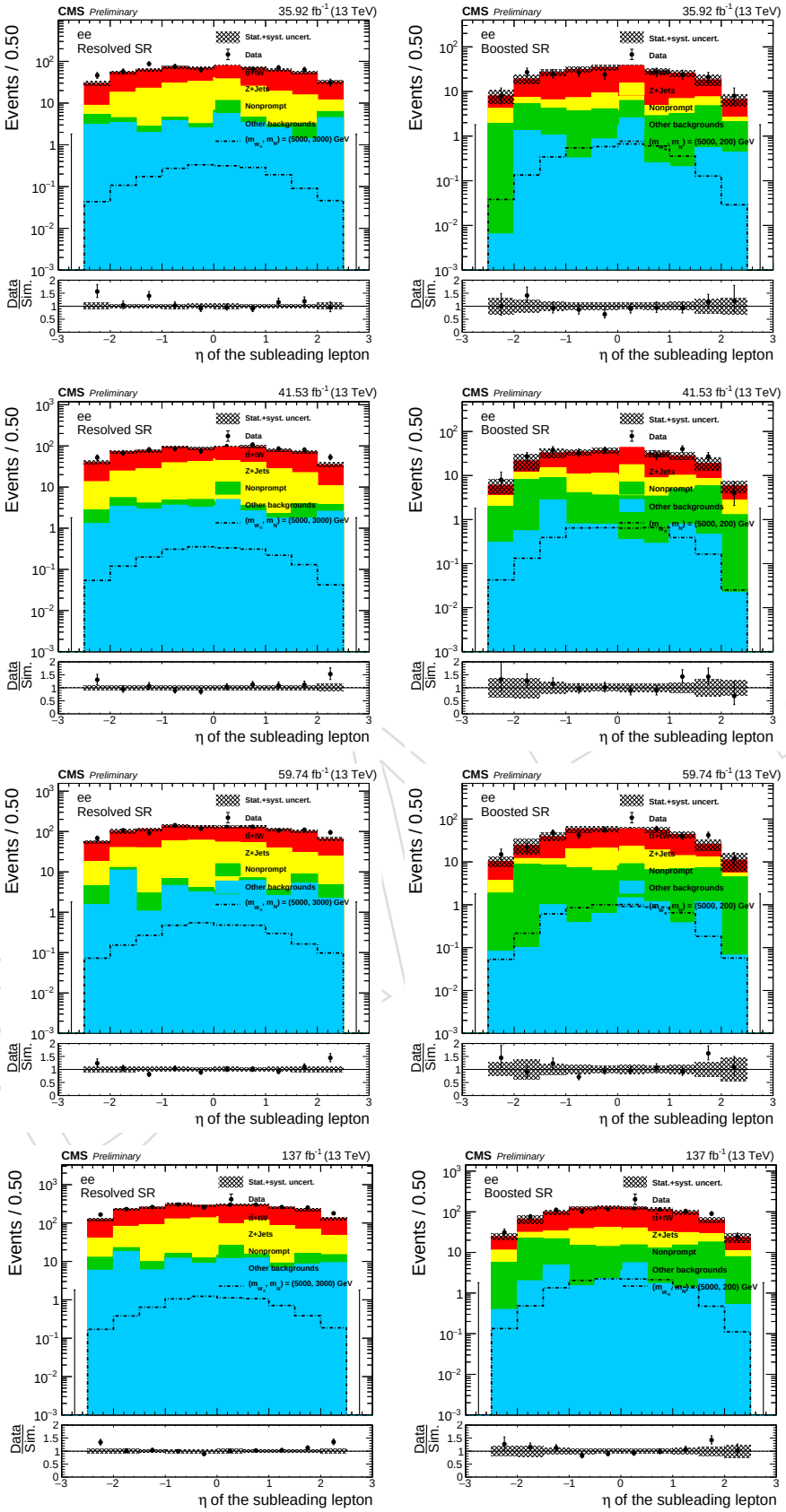

Figure 174: The subleading lepton η distributions in the dielectron channel.

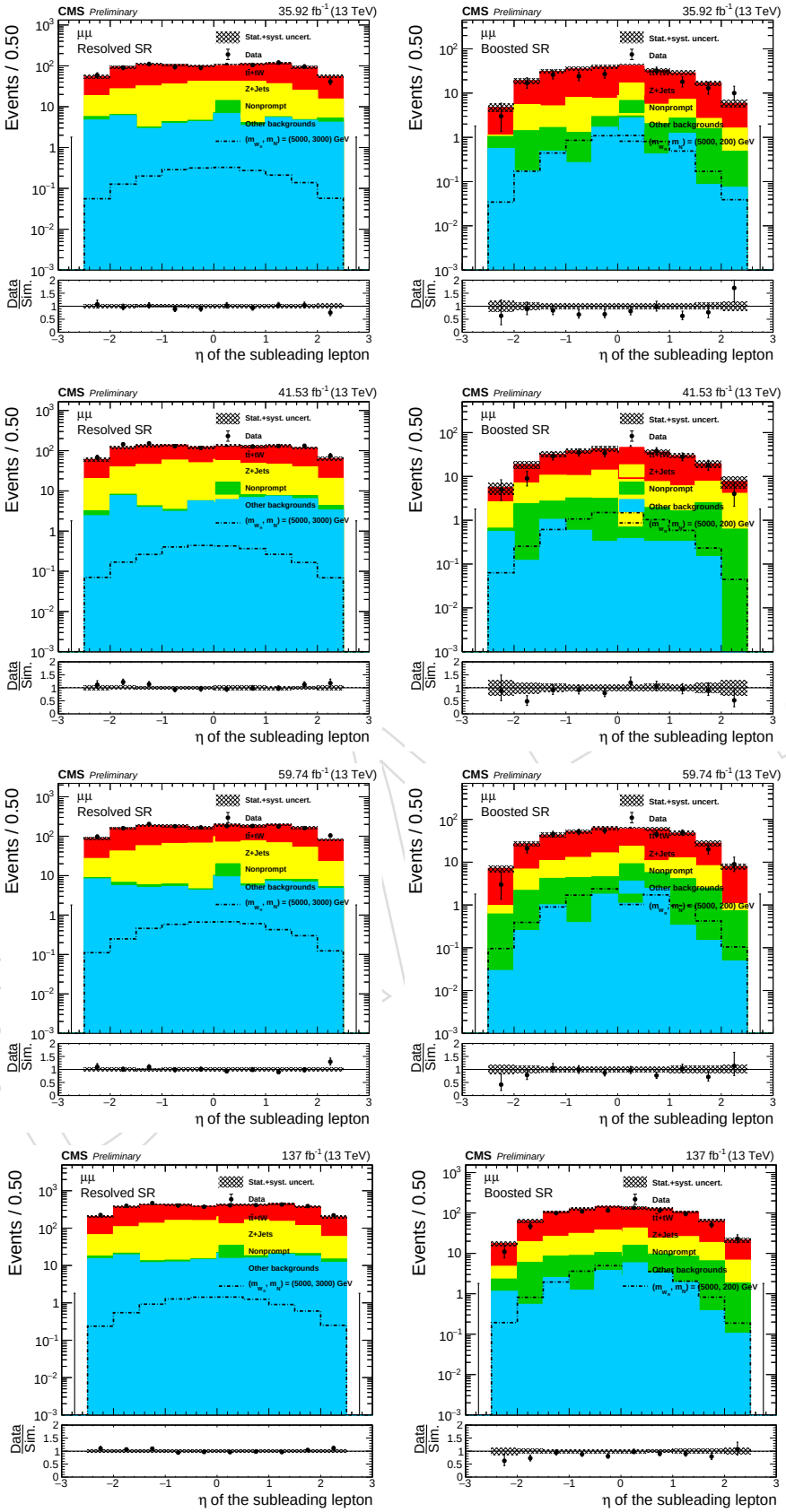

Figure 175: The subleading lepton η distributions in the dimuon channel.

Q The event display of high mass events

The event display of the highest mass event from each channel and region in 2016 data are shown in Fig. 176 - 177(dielectron resolved), Fig. 178 - 179(dielectron boosted), Fig. 180 - 181(dimuon resolved), and Fig. 182 - 183(dimuon boosted). The kinematics of the final state objects for these events are listed in Table 94(dielectron resolved), Table 95(dielectron boosted), Table 96(dimuon resolved), and Table 97(dimuon boosted).

Table 94: The object information of the resolved dielectron event, (RunNumber, LumiSection, EventNumber) = (278406:329:470624728). The event displays are shown in Fig. 176 and Fig. 177

Object	p_{T} (GeV)	η	ϕ	mass (GeV)
Electron	921.68	0.18	1.06	-0.00
Electron	73.89	1.82	-1.96	0.00
AK4	805.76	-1.88	-1.57	47.71
AK4	528.99	1.18	3.08	33.32
$m(\ell\ell\mathrm{jj})$	4605.65 GeV			

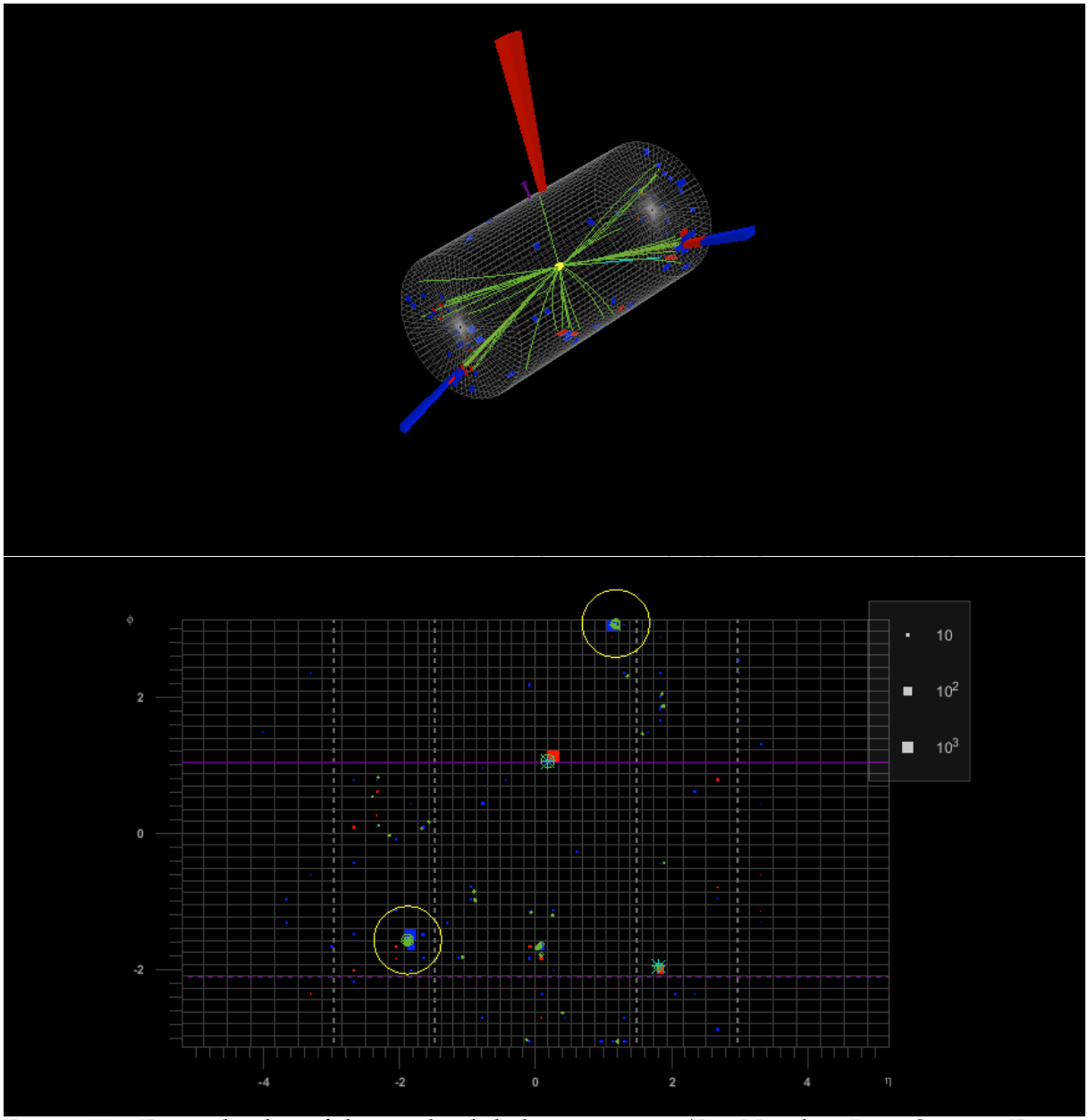

Figure 176: Event display of the resolved dielectron event, (RunNumber, LumiSection, EventNumber) = (278406:329:470624728) (page 1 out of 2).

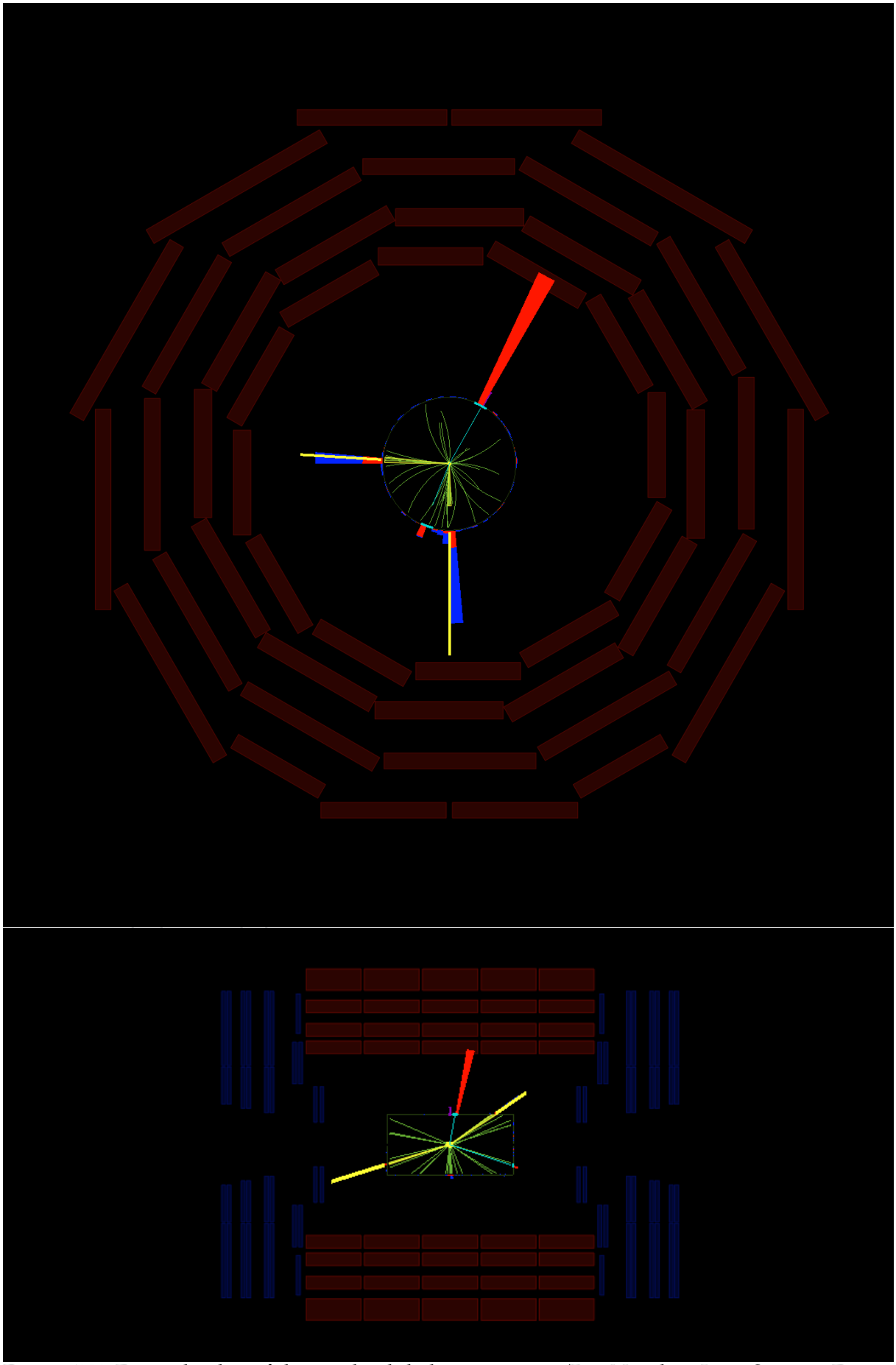

Figure 177: Event display of the resolved dielectron event, (RunNumber, LumiSection, EventNumber) = (278406:329:470624728) (page 2 out of 2).

Table 95: The object information of the boosted dielectron event, (RunNumber, LumiSection, EventNumber) = (281707:960:1568286511). The event displays are shown in Fig. 178 and Fig. 179

Object	p_{T} (GeV)	η	ϕ	mass (GeV)
Electron	549.08	1.25	-1.36	0.00
Electron	113.00	-1.87	1.85	-0.00
AK8	724.10	-1.63	1.85	116.08
$m(\ell\mathrm{J})$		2809.31 GeV		

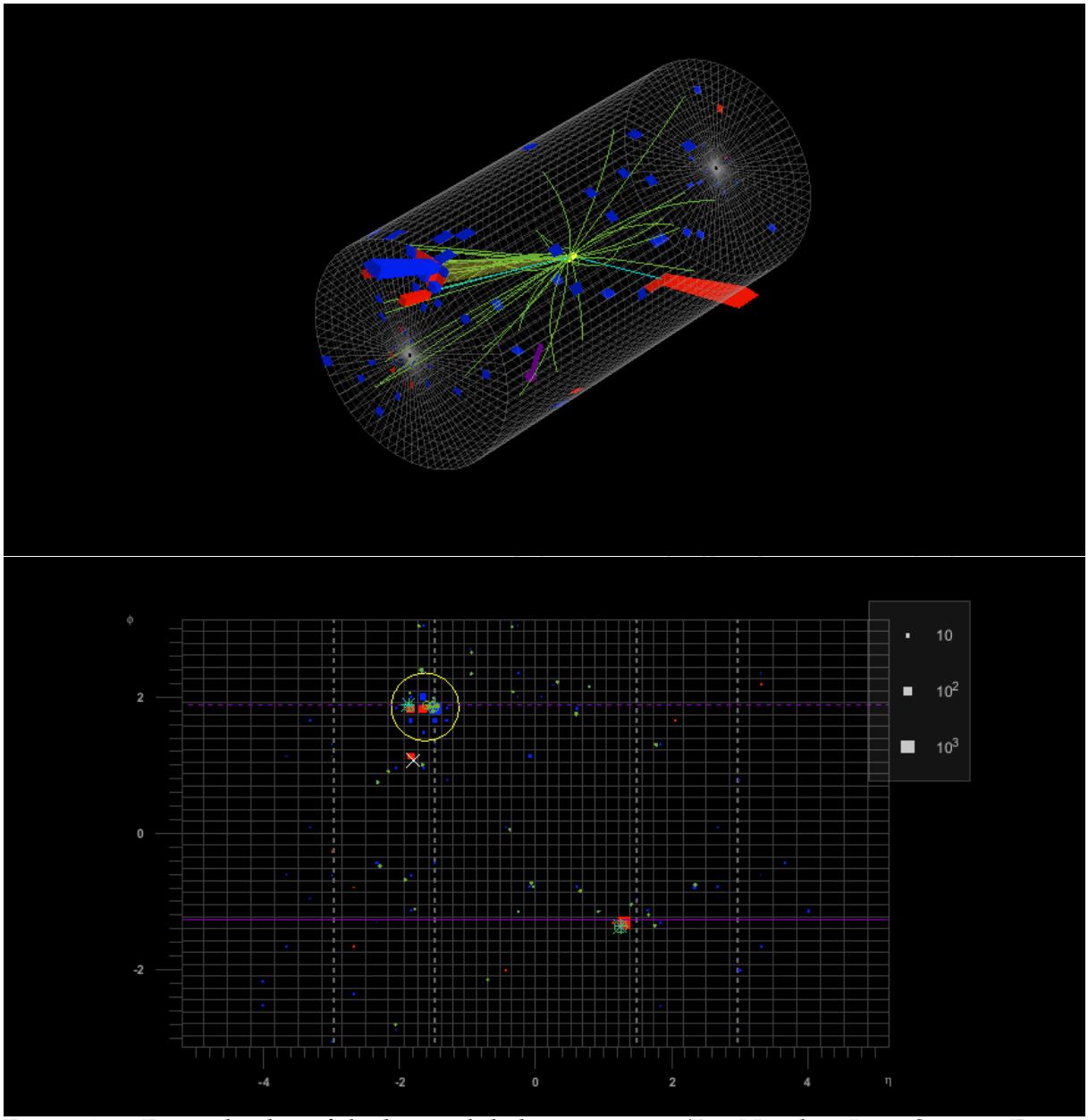

Figure 178: Event display of the boosted dielectron event, (RunNumber, LumiSection, EventNumber) = (281707:960:1568286511) (page 1 out of 2).

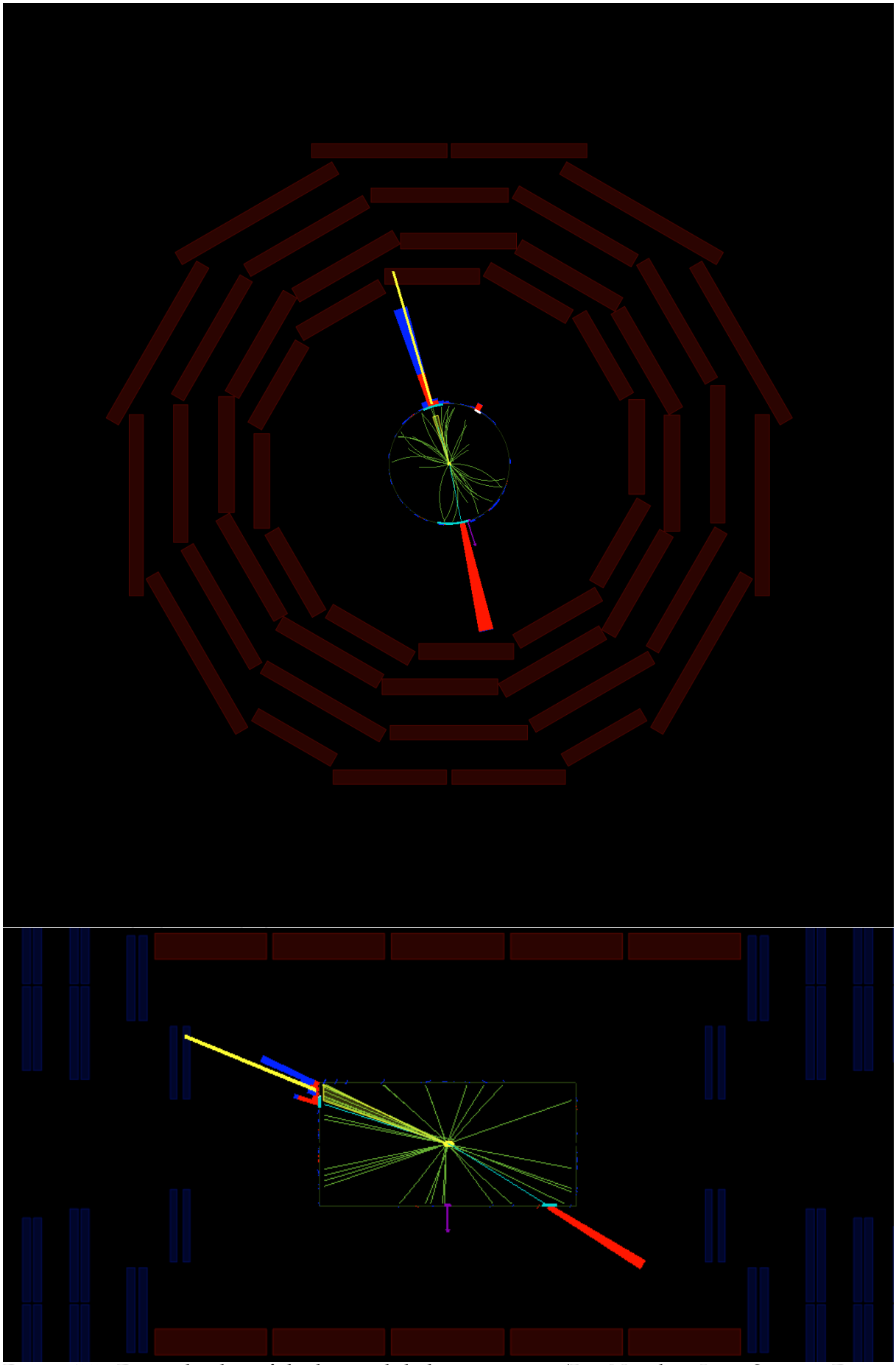

Figure 179: Event display of the boosted dielectron event, (RunNumber, LumiSection, EventNumber) = (281707:960:1568286511) (page 2 out of 2).

Table 96: The object information of the resolved dimuon event, (RunNumber, LumiSection, EventNumber) = (282800:174:315780535). The event displays are shown in Fig. 180 and Fig. 181

Object	p_{T} (GeV)	η	ϕ	mass (GeV)
Muon	1659.76	-0.12	0.25	0.11
Muon	227.03	0.63	-0.55	0.11
AK4	1604.18	-0.45	2.62	96.94
AK4	1349.24	-1.44	-1.80	55.66
$m(\ell\ell\mathrm{jj})$	5742.76 GeV			

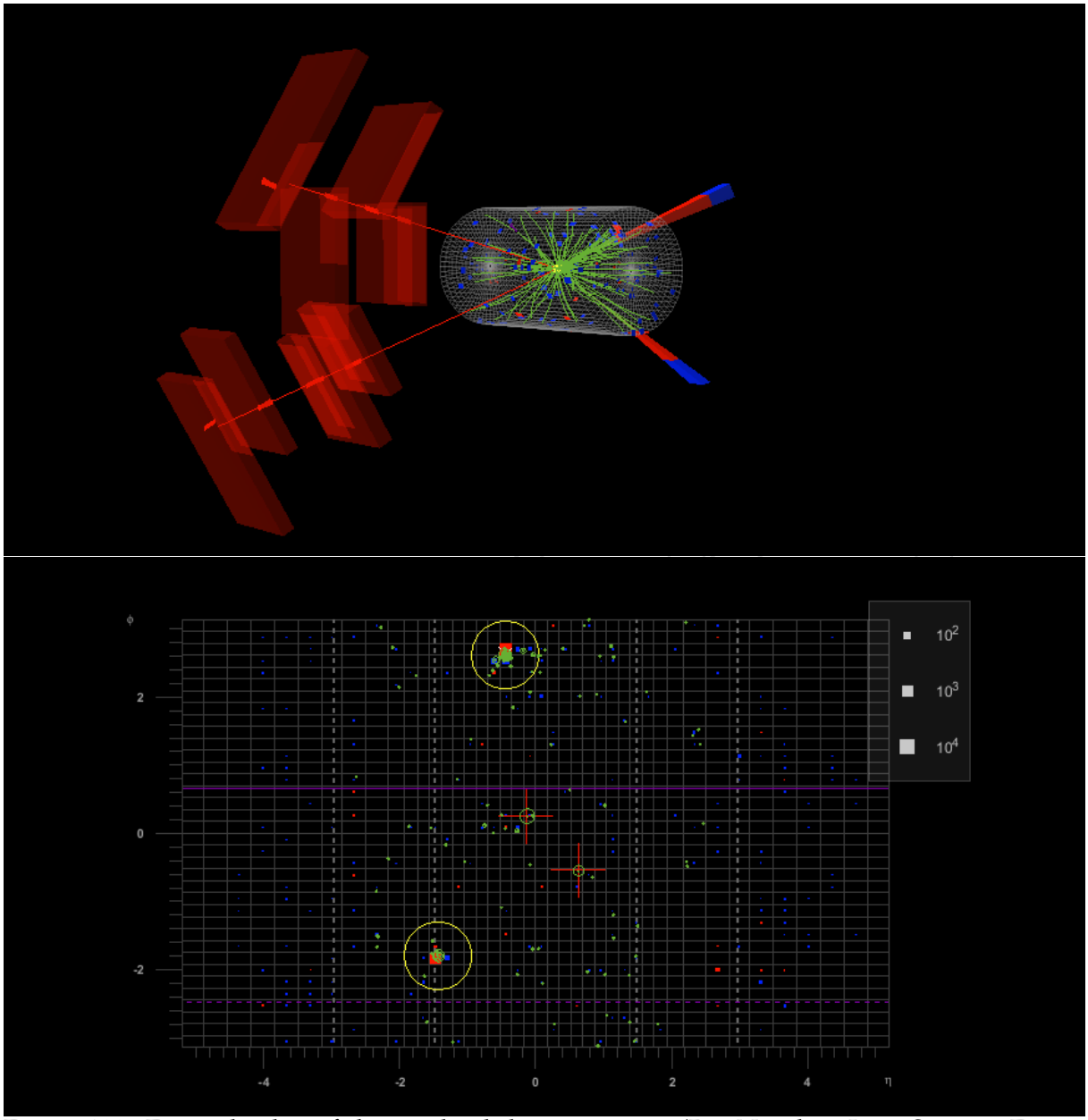

Figure 180: Event display of the resolved dimuon event, (RunNumber, LumiSection, EventNumber) = (282800:174:315780535) (page 1 out of 2).

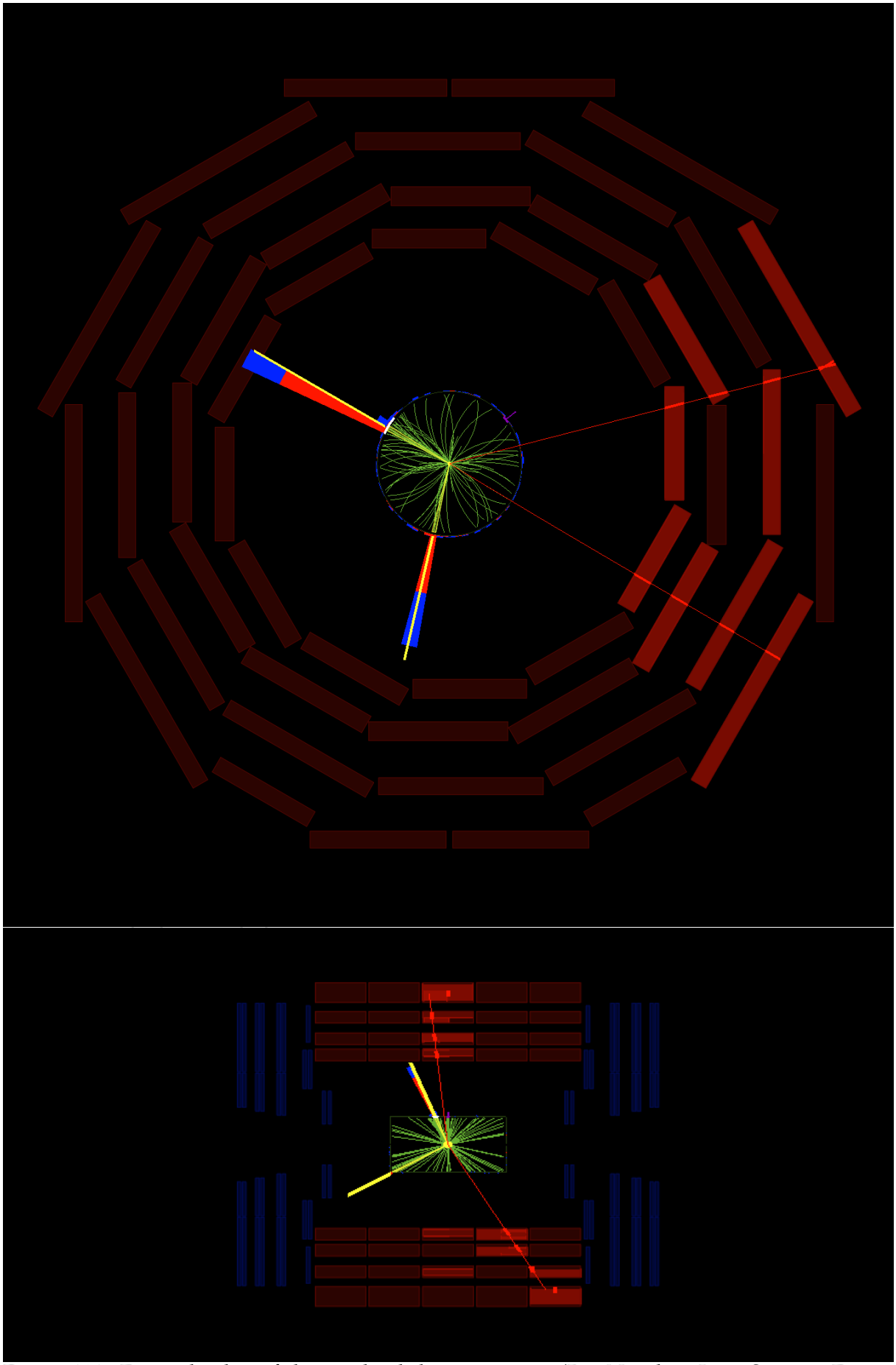

Figure 181: Event display of the resolved dimuon event, (RunNumber, LumiSection, EventNumber) = (282800:174:315780535) (page 2 out of 2).

Table 97: The object information of the boosted dimuon event, (RunNumber, LumiSection, EventNumber) = (274199:565:1035340729). The event displays are shown in Fig. 182 and Fig. 183

Object	p_{T} (GeV)	η	ϕ	mass (GeV)
Muon	457.33	-1.64	1.72	0.11
Muon	234.37	1.47	-1.26	0.11
AK8	590.88	1.57	-1.43	126.97
$m(\ell \mathrm{J})$	2699.16 GeV			

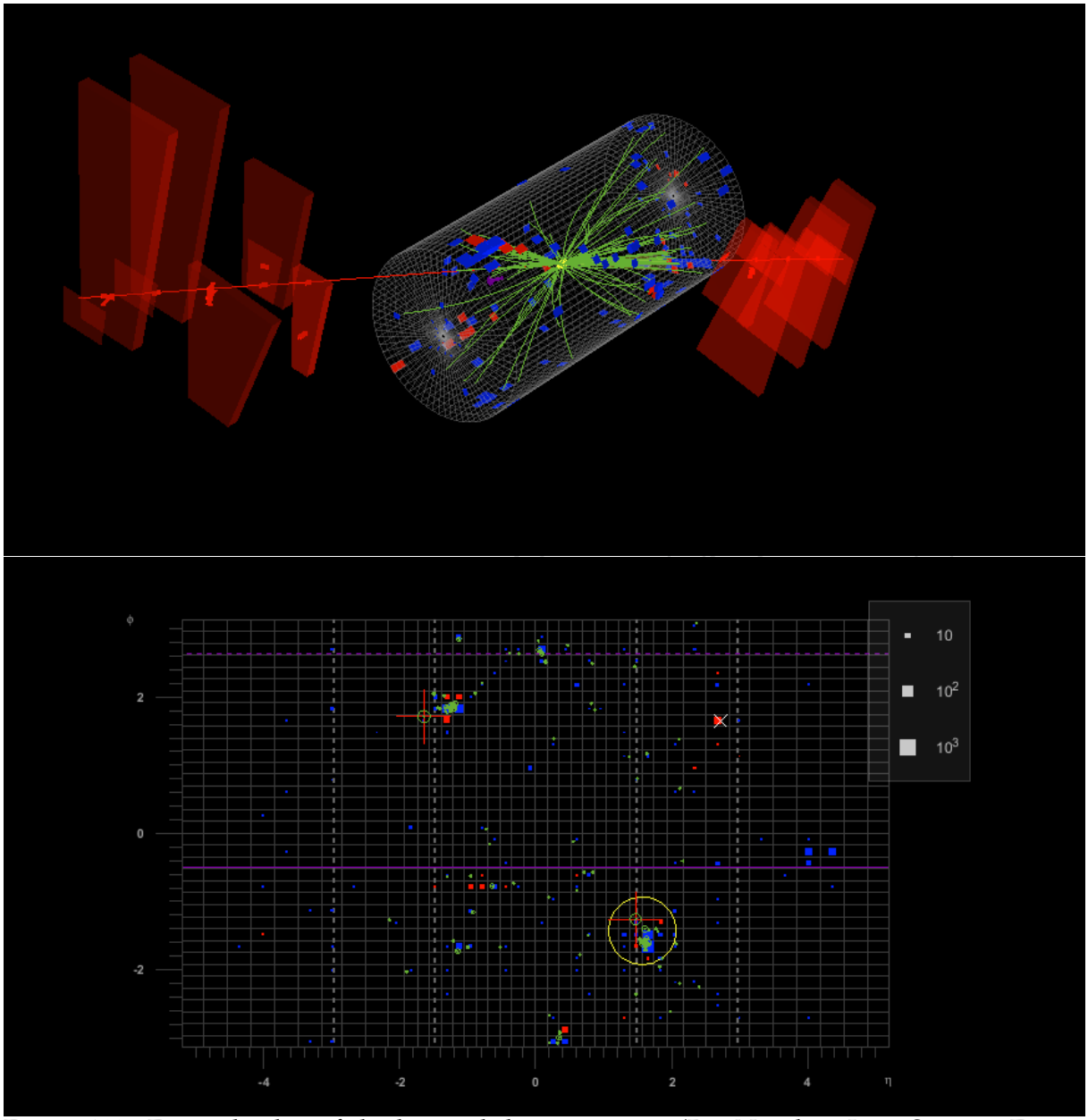

Figure 182: Event display of the boosted dimuon event, (RunNumber, LumiSection, EventNumber) = (274199:565:1035340729) (page 1 out of 2).

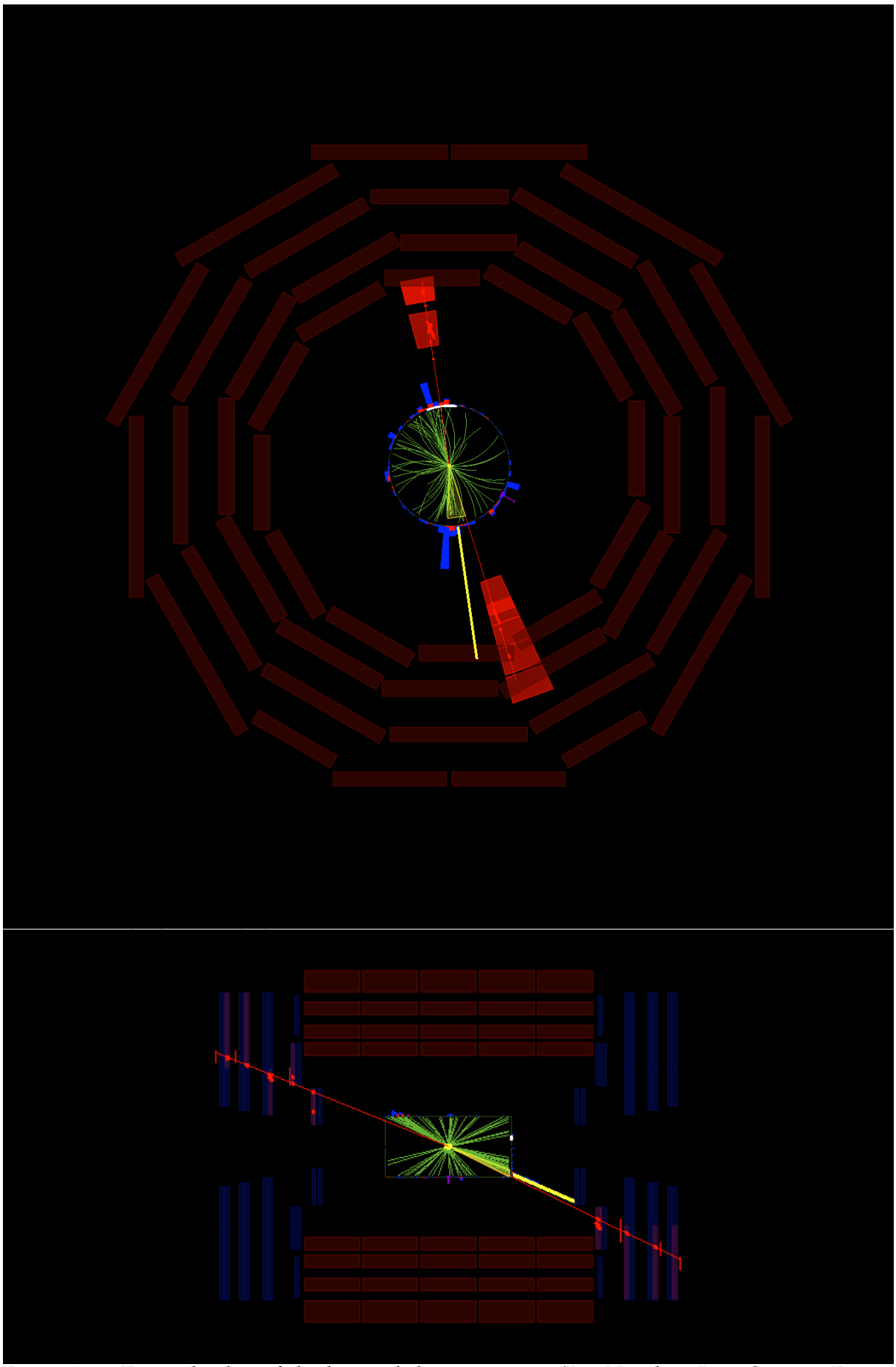

Figure 183: Event display of the boosted dimuon event, (RunNumber, LumiSection, EventNumber) = (274199:565:1035340729) (page 2 out of 2).

R ECAL spikes in 2018

An investigation of the ECAL spikes reported in the WPrime analysis are shown here. The ECAL clusters from the 6 events in 2018 in the highest m_{lljj} bin in the *ee* resolved signal region are shown in Fig 184–189. Every cluster looks ok and no spikes are seen, so this can not explain the excess seen in the *ee* resolved channel.

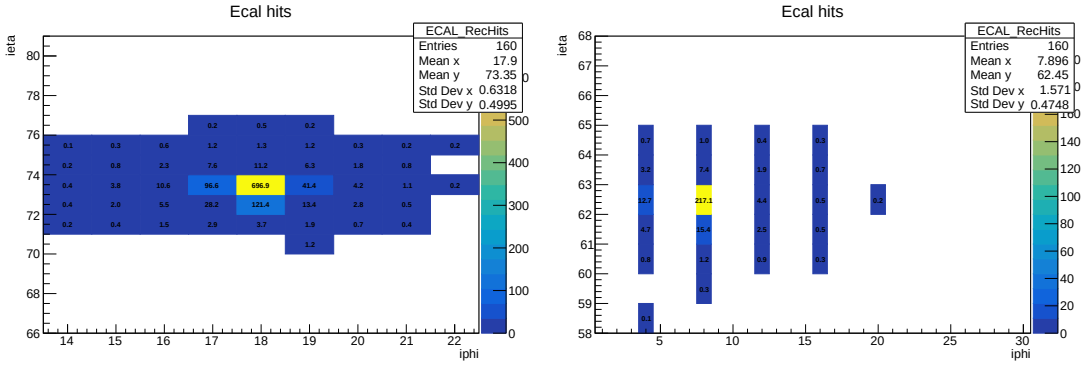

Figure 184: ECAL clusters in the first event in the highest m_{lljj} bin in the *ee* resolved signal region from 2018.

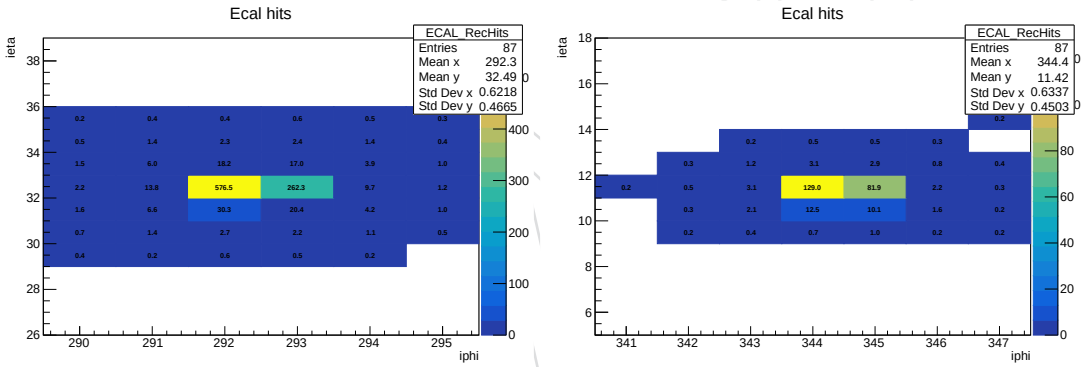

Figure 185: ECAL clusters in the second event in the highest m_{lljj} bin in the *ee* resolved signal region from 2018.

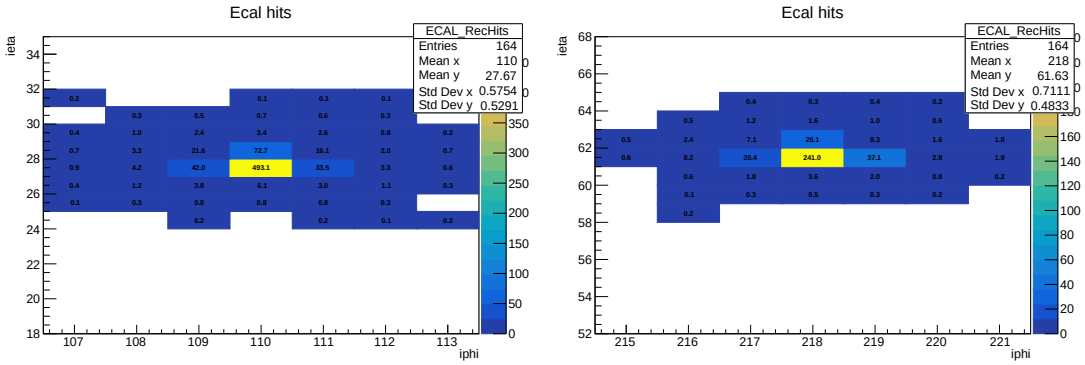

Figure 186: ECAL clusters in the third event in the highest m_{lljj} bin in the *ee* resolved signal region from 2018.

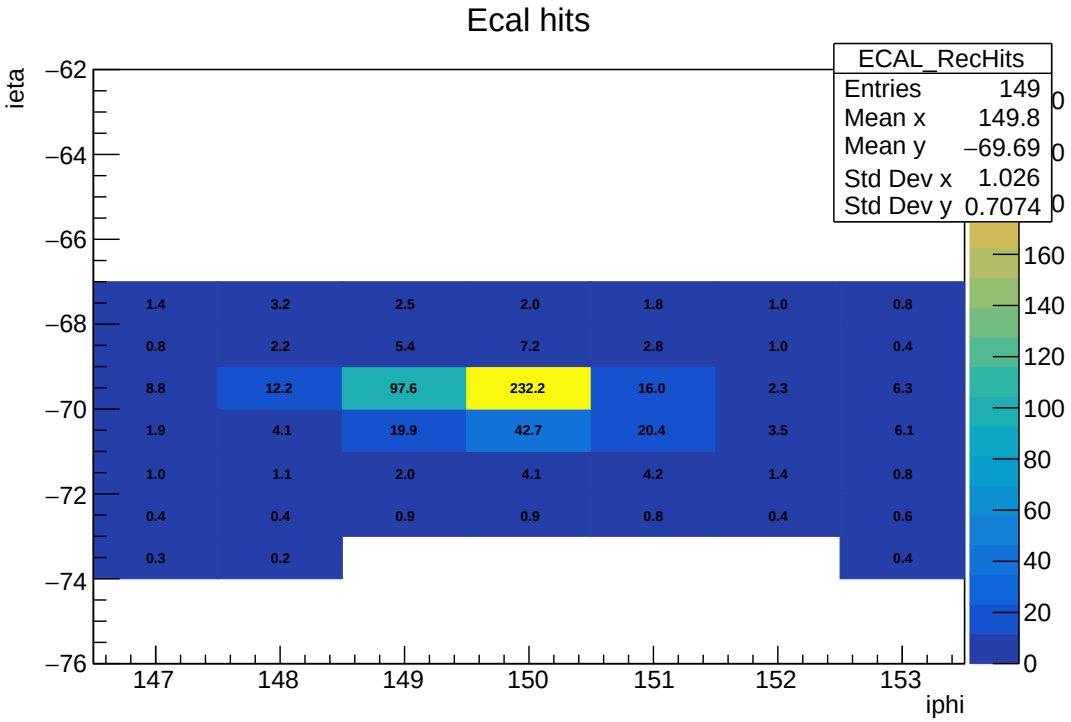

Figure 187: ECAL clusters in the fourth event in the highest m_{lljj} bin in the *ee* resolved signal region from 2018.

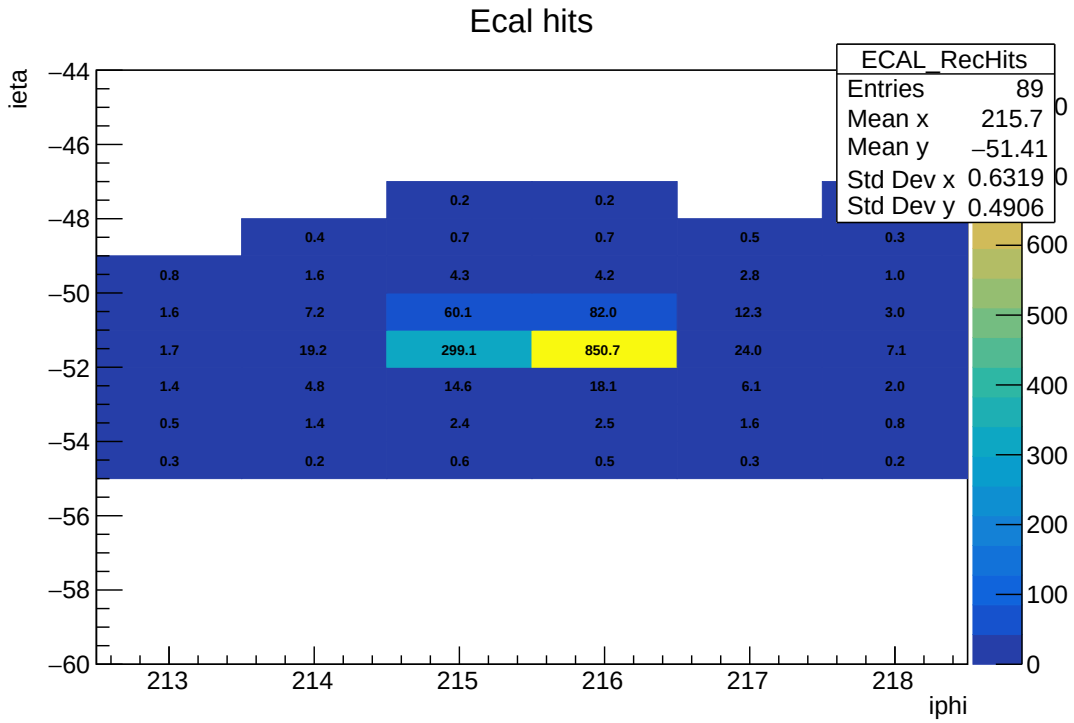

Figure 188: ECAL clusters in the fifth event in the highest m_{lljj} bin in the *ee* resolved signal region from 2018.

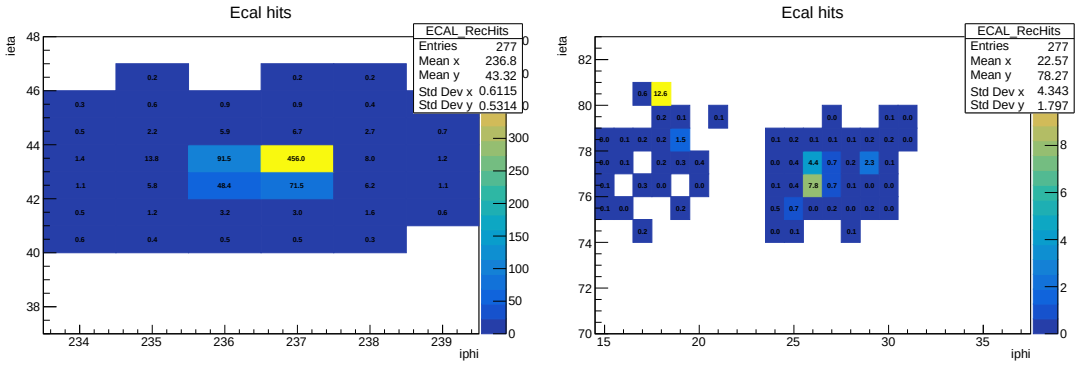

Figure 189: ECAL clusters in the sixth event in the highest m_{lljj} bin in the *ee* resolved signal region from 2018.